DARK MATTER: OBSERVATIONAL MANIFESTATION AND EXPERIMENTAL SEARCHES

DARK ENERGY AND DARK MATTER IN THE UNIVERSE

VOLUME 3

OBSERVATIONAL MANIFESTATION AND EXPERIMENTAL SEARCHES

NATIONAL ACADEMY OF SCIENCES OF UKRAINE
BOGOLYUBOV INSTITUTE FOR THEORETICAL PHYSICS
INSTITUTE FOR NUCLEAR RESEARCH
MAIN ASTRONOMICAL OBSERVATORY
NATIONAL SCIENCE CENTER
"KHARKIV INSTITUTE OF PHYSICS AND TECHNOLOGY"

MINISTRY FOR EDUCATION AND SCIENCE OF UKRAINE
TARAS SHEVCHENKO NATIONAL UNIVERSITY OF KYIV

НАЦІОНАЛЬНА АКАДЕМІЯ НАУК УКРАЇНИ
ІНСТИТУТ ТЕОРЕТИЧНОЇ ФІЗИКИ ім. М.М. БОГОЛЮБОВА
ІНСТИТУТ ЯДЕРНИХ ДОСЛІДЖЕНЬ
ГОЛОВНА АСТРОНОМІЧНА ОБСЕРВАТОРІЯ
НАЦІОНАЛЬНИЙ НАУКОВИЙ ЦЕНТР
"ХАРКІВСЬКИЙ ФІЗИКО-ТЕХНІЧНИЙ ІНСТИТУТ"

МІНІСТЕРСТВО ОСВІТИ І НАУКИ УКРАЇНИ
КИЇВСЬКИЙ НАЦІОНАЛЬНИЙ УНІВЕРСИТЕТ
імені ТАРАСА ШЕВЧЕНКА

За редакцією
В. Шульги

ТЕМНА ЕНЕРГІЯ І ТЕМНА МАТЕРІЯ У ВСЕСВІТІ

У ТРЬОХ ТОМАХ

ТЕМНА МАТЕРІЯ:

3 ТОМ

СПОСТЕРЕЖУВАНІ ПРОЯВИ ТА ЕКСПЕРИМЕНТАЛЬНІ ДОСЛІДЖЕННЯ

ПРОЕКТ
«УКРАЇНСЬКА НАУКОВА КНИГА
ІНОЗЕМНОЮ МОВОЮ»

КИЇВ
АКАДЕМПЕРІОДИКА
2015

DARK ENERGY AND DARK MATTER IN THE UNIVERSE

Editor
V. Shulga

IN THREE VOLUMES

DARK MATTER:

VOLUME 3
OBSERVATIONAL MANIFESTATION AND EXPERIMENTAL SEARCHES

PROJECT
«UKRAINIAN SCIENTIFIC BOOK
IN A FOREIGN LANGUAGE»

KYIV
AKADEMPERIODYKA
2015

UDK 524.7+529; 539.123.17, 539.12, 539.16, 539.143, 539.1.08
BBK 22.3, 22.6
D20

Reviewers:

V.A. ZAKHOZHAJ, Dr. Sci., Prof., Professor of the Department
of Astronomy and Space Informatics of the Physical Faculty
of the V.N. Karazin National University of Kharkiv
I.M. KADENKO, Dr. Sci., Prof., Head of the Department of Nuclear Physics
of the Taras Shevchenko National University of Kyiv

Approved for publication by the Scientific Councils of the following institutions:
Bogolyubov Institute for Theoretical Physics (03.07.2014, protocol No. 6)
Institute for Nuclear Research (26.06.2014, protocol No. 7)
Main Astronomical Observatory (10.07.2014, protocol No. 8)
the National Science Center
"Kharkiv Institute of Physics and Technology"
(27.08.2014, protocol No. 8)
of the National Academy of Sciences of Ukraine as well as
the Astronomical Observatory of the Taras Shevchenko National University of Kyiv
(05.06.2014, protocol No. 7)

Publication was made by a State contract promoting
the production of scientific printed material

D20 **Dark** energy and dark matter in the Universe: in three volumes / Editor V. Shulga. — Vol. 3. Dark matter: Observational manifestation and experimental searches / Vavilova I.B., Bolotin Yu.L., Boyarsky A.M., Danevich F.A., Kobychev V.V., Tretyak V.I., Babyk Iu.V., Iakubovskyi D.A., Hnatyk B.I., Sergeev S.G. — K. : Akademperiodyka, 2015. — 375 p.

ISBN 978-966-360-239-4
ISBN 978-966-360-287-5 (vol. 3)

This monograph is the third issue of a three volume edition under the general title "Dark Energy and Dark Matter in the Universe". The authors discuss the astrophysical direct and indirect manifestation and properties of dark matter in galaxies, galaxy clusters and groups; the different mechanisms of energy exchange between dark energy and dark matter that expand the capabilities of the Standard Cosmological Model; the experimental search for dark matter particle candidates (including the sterile neutrinos, solar axions, weakly-interacting massive particles, and superheavy dark matter particles) using space, ground-based, and underground observatories.

UDC 524.7+529; 539.123.17, 539.12, 539.16, 539.143, 539.1.08
BBK 22.3, 22.6

ISBN 978-966-360-239-4
ISBN 978-966-360-287-5 (vol. 3)

CONTENTS

FOREWORD OF THE EDITOR

This monograph is the third issue of a three volume edition under the general title "Dark Energy and Dark Matter in the Universe". The authors discuss the observational evidence of the dark matter in the large-scale structures of the Universe as well as the dark matter particle candidates.

The first Chapter of this volume has a special meaning for all the authors of the "Dark Energy and Dark Matter in the Universe" monograph because it includes the last papers and notes by Prof. P.I. Fomin, the leading scientist in the "CosmoMicroPhysics" scientific field in Ukraine. In these latter issues, which have been written altogether with A.P. Fomina, they have shown that the self-gravity and gravitational interaction of quantum vacuum fluctuations radically reduces the energy density of the physical vacuum relative to the predictions of local quantum field theory. In this case, the vacuum space becomes discrete and crystal-like on the Planck length scales. The development of vacuum condensates connected with breaking continuous symmetries produces additional reduction of the vacuum energy and makes it an acceptable candidate for dark energy manifesting itself as the acceleration of the cosmological expansion of space. The condition of spatial closeness allows one to give an upper bound on the vacuum energy density. Stationary radial flows of vacuum condensates are further used to explain the nature of dark matter.

As regards the term "CosmoMicroPhysics", it might be interesting to point out several facts related to the foundation of this research field in the former USSR. Dr. Yuri Shtanov, one of the authors of Volume 1 of this monograph related to the Dark Energy problem, recalls the story told him by late Prof. P.I. Fomin that it was him who first coined this term and proposed it to the Russian colleagues who were looking for a good Russian equivalent of the term "astroparticle physics".

The astrophysical direct and indirect evidence of the presence of dark matter in galaxy clusters and groups is discussed in Chapter 2, prepared by I. Vavilova and Iu. Babyk. The authors give a brief summary of the discovery of dark matter and dark matter models. The great attention is paid to the dark matter evaluation in the X-ray galaxy clusters, where the DM conception is widely applied to describe the density profiles at the wide scale of cluster's radii. The next Chapter, written by S. Sergeev and N. Pulatova, is related to consideration of the galaxies with active nuclei, including methods and results of evaluation of the masses of supermassive black holes in their centres as well as properties of host galaxies. While considering the galaxy groups, the problem of a common halo of groups and halo of individual galaxies in groups is discussed under the evaluation of the "mass-to-luminosity" ratio for sparse galaxy groups in the Local Supercluster and for samples detached from the SDSS spectroscopy survey (this Chapter is prepared by A. Elyiv, O. Melnyk, and I. Vavilova).

In the Chapter 5 "Interaction In The Dark Sector" prepared by Yu. Bolotin, A. Kostenko, D. Yerokhin, and O. Lemets, the authors consider in detail different topics associated with interaction in the dark sector. Although the Standard Cosmological Model postulates an absence of interaction between the dark components, there is no fundamental reason for this assumption in the absence of an underlying symmetry which would suppress the coupling. Furthermore, the latest observations (such as the PLANCK collaboration) at the very least do not eliminate this possibility. For these reasons, the study of dark sector interaction is an important field of study, and holds many possibilities. The greatest amount of attention is given to the mechanisms of energy exchange between dark energy and dark matter. We do not only introduce the reader to a large amount of interaction models used in literature (both linear and nonlinear), but also demonstrate how these models affect the dynamics of the Universe. It is shown that the inclusion of dark sector interaction on the one hand greatly expands the capabilities of the Standard Cosmological Model. On the other hand, it allows for a simple return to the fundamental results of the Standard Cosmological Model when the interaction is taken to be weak. The presence of interaction in the dark sector also simplifies the solution of a series of "classical" cosmological problems, such as the cosmic coincidence problem.

Right-handed (sterile) neutrinos are one of the most popular dark matter particle candidates. In the Chapter 6, which is written by A. Boyarsky and D. Iakubovsky, the authors quantify the properties of 'sterile neutrino Universe' depending on two basic parameters — the mass of sterile neutrino dark matter particle and its interaction strength with ordinary particles. In addition to model-independent analysis, throughout this Chapter, they rely on the baseline model — minimal extension of the Standard Model with three right-handed neutrinos. This popular model, dubbed νMSM, provides viable and unified description of three major "beyond the Standard Model" phenomena — dark matter, matter-antimatter asymmetry and neutrino oscillations. It is

among a very few models that provide testable resolution of these "beyond the Standard Model" puzzles in the situation when no new physics is found at the LHC (the so-called "nightmare scenario") and suggests how the nature of dark matter and other "beyond the Standard Model" phenomena may nevertheless be checked experimentally using existing experimental technologies and major infrastructure.

Particle properties play a key role in cosmology and astrophysics. Experimental investigations of neutrinoless double beta decay (an unique way to study neutrino and weak interactions) and solar axions (promising candidates for dark matter), measurements of neutrino fluxes from the Sun and the Earth, search for effects beyond the Standard Model (electric charge nonconservation, disappearance of nucleons, electromagnetic properties of neutrino), development of low counting experiments to search for dark matter are presented in this volume in the Chapter 7 prepared by F. Danevich, V. Kobychev, and V. Tretyak. The experiments call for extremely low counting rate and typically are carried out deep underground to minimize background caused by cosmic rays, and use low radioactive nuclear spectroscopy technique. Extremely low background conditions of the frontier astroparticle physics experiments provide also possibility to study very rare beta and alpha decays.

Among the numerous DM candidates ones of the most popular are weakly-interacting massive particles (WIMPs) due to the "WIMP miracle": thermally produced in hot early Universe particles with weak-scale mass and weak interaction velocity averaged cross-section automatically provide close to observed DM abundance. In the supersymmetry (SUSY) as the most promising theory for the extension of SM the lightest neutralino is a leading WIMP candidate. WIMPs can annihilate (or decay if they are metastable) into SM particles (protons-antiprotons, electrons-positrons, deuterons-antideuterons, neutrinos and photons) with energies of order of DM masses, i.e., into cosmic ray particles and photons in subGeV-TeV range. Annihilation or decay of more massive DM particles (superheavy dark matter (SHDM), WIMPZILLAS with masses up to GUT scale) could produce ultra high energy cosmic rays. These properties of DM particles open the possibility for indirect DM detection in cosmic ray window. The state-of-the-art in the search of the signatures of DM annihilation/decay in the observed spectrum of cosmic rays is discussed by B. Hnatyk in the Chapter 8.

This volume was prepared by the authors in 2012-2013 years and revised additionally in 2014.

V. SHULGA

ACKNOWLEDGMENTS

We are grateful to the National Academy of Sciences of Ukraine for the financial support of the Target Scientific Research Programs "Structure and Composition of the Universe: hidden mass and dark energy" (2007—2009) and "Astrophysical and cosmological problems of hidden mass and dark energy of the Universe" (2010—2012) ["CosmoMicroPhysics"] as well as the Target Program of the Space Scientific Research (2012—2016), within which this monograph was originated. We are thankful to academician Valery Shulga, the scientific manager of the "CosmoMicroPhysics" programs and editor of this monograph, for suggestion of its writing, participation in the formation of its content, and organization of its publication. We thank academician Yaroslav Yatskiv for his generous support of these Programs, interest in our research results, and organization of the publication of this monograph. We are also appreciating helpful and highly professional assistance from the staff of the "Akademperiodyka" publisher.

AUTHORS

Bologna—Dublin—Kharkiv—Kyiv—Leiden—Nauchnyj—Toronto,

October, 2013

1 CHAPTER

NOTES ON THE VACUUM NATURE OF DARK ENERGY AND DARK MATTER

P.I. Fomin, A.P. Fomina

1.1. On the gravitational mechanism of reducing the vacuum energy and the vacuum nature of dark energy

1.1.1. Introduction

The existence of the physical vacuum is the most important consequence of modern quantum field theories: the quantum electrodynamics, the Weinberg—Salam—Glashow theory of electroweak interactions, and the quantum chromodynamics — the theory of strong interactions. The physical vacuum can be regarded as a real relativistically invariant quantum medium (a kind of quantum fluid) filling out all the world space and realizing the lowest energy state of quantum fields. One can say that this is a remake of the classical "luminiferous ether". The real particles such as electrons, positrons, photons, hadrons etc. as well as all the macroscopic bodies are the quantum wave-like excitations of this medium endowed with certain quantum numbers ensuring their relative stability. The physical vacuum can be compared with an ocean with particles being oceanic waves. Waves may be created and destroyed, but the ocean is eternal.

All modern quantum field theories do not take into account gravitation, which is regarded as a superweak interaction, and describe local fields in the continuous Minkowski space without any parameters of non-locality such as fundamental length. A consequence of locality is the presence of ultraviolet divergences in quantum field theory. For instance, divergences are the integrals describing the field contribution to the electron mass and charge. There exists a phenomenological way of treating these divergences, the

so-called renormalization theory, consisting in isolating all such infinities in all orders of a perturbation theory and replacing them by finite experimental values of masses and charges. This operation, however, is not physically and mathematically consistent and closes the way to the theoretical explanation of the observed values of masses and charges. In the local quantum field theories, the value of the vacuum energy density also diverges. This infinity is replaced by zero in the renormalization theory under the assumption that the energy of all observed particles is measured from the vacuum energy [2].

The situation, however, fundamentally changes under the account of gravitation. In general relativity, every energy density, described by the stress-energy tensor on the right-hand side of the Einstein equations, gravitates (i.e., curves the spacetime metric). Therefore, one cannot simply neglect the vacuum energy density by subtracting its value.

The discovery of dark energy in cosmology and the estimate of its relatively low value (see the review paper [3] and references therein) raises the issue about the mechanism of radical reduction of the vacuum energy density with respect to the predictions of the local quantum field theories. We will show here that one of such powerful mechanisms is a self-gravity and gravitational interaction of the quantum fluctuations of vacuum. Gravity makes homogeneous vacuum gravitationally unstable, in a way, similarly to the Jeans instability of a uniform distribution of gravitating cosmic gas. Breaking out into ling-living quasilocal massless cells of Planckian size, the space of vacuum becomes discrete and crystal-like. Quantum field theory in such a space ceases to be local, similarly to the quantum theory of quasiparticle in a solid body. A fundamental Planck length

$$\ell_P = \sqrt{\frac{G\hbar}{c^3}} = 1.6 \times 10^{-33}\ \text{cm} \tag{1.1}$$

appears in the theory, and the "curse of divergences" is lifted from the quantum field theory. In such a scheme, now there is a prospect for the theoretical calculation of masses and charges of particles. For example, one can justify, in a certain approximation, the following formula for the electron mass [4]:

$$m_e = \frac{e^2}{\ell_P c^2} \exp\left(-A\frac{\hbar c}{e^2}\right), \tag{1.2}$$

which, for $A = 1/3$, gives $m_e \sim 10^{-27}$ g. If one formally switches off gravity ($G \to 0$) and runs ℓ_P to zero, one gets the original divergence.

Next, from the condition of topological closeness of the Universe, we obtain the upper bound for the vacuum energy density close to the currently observed value.

1.1.2. Gravitating fluctuations of the vacuum

In the relativistic domain, the energy and spatial dimensions of quantum fluctuations of the vacuum in quantum field theory without account of gravitation are regulated by the uncertainty relations:

$$\Delta E \Delta t \sim \hbar,\ \Delta E \sim c\Delta p,\ \Delta p \Delta q \sim \hbar. \tag{1.3}$$

Here, Δt is the lifetime of a fluctuation with energy ΔE, momentum dispersion Δp, and size Δq. Taking into account gravity, which reduces the total energy of fluctuation according to the law

$$\Delta E_{\rm tot} = \Delta E - \eta G \frac{\left(\Delta E/c^2\right)^2}{\Delta q} \geq 0 \tag{1.4}$$

(here, η is a numerical coefficient taking into account the form of a fluctuation; it will be specified below), one can replace the first of relations (1.3) by

$$\Delta E_{\rm tot} \Delta t \sim \hbar. \tag{1.5}$$

For long-living fluctuations ($\Delta t \to \infty$), from (1.4) and (1.5) we obtain the condition

$$\Delta E_{\rm tot} = \Delta E \left(1 - \frac{\eta G \Delta E}{c^4 \Delta q}\right) \sim \frac{\hbar}{c} \to 0. \tag{1.6}$$

It follows from (1.6) that, under the condition

$$\Delta E = \frac{c^4 \Delta q}{\eta G}, \tag{1.7}$$

there exist nontrivial fluctuations living infinitely long. Further, taking into account the second and third relation in (1.3), we get the equation for the size Δq of such a fluctuation:

$$\Delta E \sim c\Delta p \sim \frac{c\hbar}{\Delta q} = \frac{c^4 \Delta q}{\eta G}, \tag{1.8}$$

which gives

$$(\Delta q)^2 \sim \eta \frac{G\hbar}{c^3} = \eta \ell_P^2. \tag{1.9}$$

From the viewpoint of general relativity, equation (1.6) means spatial topological closeness of such gravitating configurations (see, e.g., [9]). The property of longevity of such fluctuations ($\Delta t \to \infty$) means that here we deal with a spontaneous phase transition of the vacuum with breaking of the translational symmetry of the homogeneous system. A gravitational vacuum condensate is formed.

Thus, the self-gravity of the quantum vacuum fluctuations turns the space of vacuum into a discrete crystal-like structure [5] consisting of massless and charge-neutral "Planck cells" of size (1.1). In this case, the energy density of the zero-point oscillations of the vacuum radically reduces from formally infinite (for local quantum field theories) to finite and even close to zero. Exactly this vacuum energy density, reduced by self-gravity, constitutes, according to our idea, the "dark energy" discussed in astrophysics. It does not appear possible at present to calculate its value from the first principles because it should essentially depend on the unknown structure of the discrete crystal-like space of the vacuum formed by interacting massless "Planck cells". Interaction between such cells due to their topological closeness can occur, for example, via quadrupole gravitational forces [6] and, as a whole, be similar to the van-der-Waals forces between electrically neutral atoms that form a crystal.

We have considered above the most extreme manifestation of the self-gravity of the vacuum in the form of gravitational self-closing of fluctuations of the Planck size. Somewhat lower, but also considerable, reduction of energy is produced, of course, by the mutual gravity of spatially close fluctuations of small sizes.

A substantial contribution into the lowering of the vacuum energy also comes from the origin of the so-called vacuum condensates connected with the dynamical breaking of various continuous symmetries in quantum field theory (see, e.g., [7]). These condensates are formed by binding of fermion particle-antiparticle vacuum pairs via strong gauge interactions. In this case, the vacuum of fermionic fields becomes as "bosonizing" and reduces its energy also by the suppression of the Pauli principle.

1.1.3. Estimate of the energy density from the condition of spatial closeness of the Universe

The modern idea that the Universe as a whole should have the topology of a closed three-dimensional sphere is connected, first and foremost, with the idea of quantum creation of our Universe from the vacuum of some "mother universe" [8]. Initially, the "daughter" universe is born small and then starts quickly growing in volume and internal mass (energy), for example, in the inflationary regime [10]. The size and energy density in this case are, to a certain extent, connected by the condition of closeness and, therefore, one can estimate the density from the known size. The condition of topological closeness of a gravitating system, according to general relativity [9], is accompanied by the zero total energy of such a system by virtue of the exact compensation of the positive proper energy (mass) of matter by the negative contribution from its self-gravity. In a simplified version, this condition can be

written, similarly to (1.4), as

$$E_{\text{tot}} = Mc^2 \left(1 - \eta \frac{GM}{c^2 a}\right) = 0, \tag{1.10}$$

where a is the size (radius) of such a spherical "zero-system", and η is a numerical factor dependent on its shape. This equation has two roots; one of them is trivial, $M = 0$, and the other is non-trivial:

$$M = \frac{c^2}{\eta G} a. \tag{1.11}$$

For a closed three-dimensional spherical universe, M is expressed through the mass density ρ as follows [9]:

$$M = 2\pi^2 a^3 \rho. \tag{1.12}$$

Substituting (1.12) into (1.11), we find the connection between ρ and a arising from the simplified condition (1.10) of the closeness of the universe:

$$\rho(a) = \frac{c^2}{2\pi\eta G a^3}. \tag{1.13}$$

Simplification in (1.10) and (1.13) consists in neglecting the term $\sim\dot{a}^2$, which is justified under the condition $\dot{a}^2 \ll c^2$. Taking into account this "energy of expansion" of the universe and introducing the Hubble parameter $H(t) \equiv \dot{a}/a$, we get the corresponding Friedmann equation

$$H^2(t) + \frac{c^2}{a^2(t)} = \frac{8\pi G}{3}\rho(t). \tag{1.14}$$

Dividing by H^2 and introducing the standard notation $\rho_c = 3H^2/8\pi G$, $c^2/H^2 = a_{\text{H}}^2$, where a_{H} is the Hubble radius, we write (1.14) in the form

$$1 + \frac{a^2}{a_{\text{H}}^2} = \frac{\rho}{\rho_c}. \tag{1.15}$$

Taking into account the known uncertainty in the determination of the modern value of the Hubble parameter,

$$H_0 = 50{-}80\,\frac{\text{km}}{\text{s}\,\text{Mpc}}, \tag{1.16}$$

we obtain the intervals for the corresponding uncertainties for ρ_c and a_{H}:

$$\rho_c = (0.5{-}1.3) \times 10^{-29}\,\frac{\text{g}}{\text{cm}^3}, \tag{1.17}$$

$$a_{\text{H}} = (1.8{-}1.1) \times 10^{28}\,\text{cm}. \tag{1.18}$$

We note that relation (1.15) describes the dependence of the total density of the proper mass (energy) of the universe on the critical density (1.17) and radius a. The fraction of dark energy in $\rho(a)$ depends on the whole physical history of the universe. Observations give that the fraction of dark energy ($\sim$72 %) together with dark matter ($\sim$24 %) dominate over the fraction of baryonic matter ($\sim$4 %). The smallness of the fraction of baryons is determined by the the physics of baryogenesis connected with the breaking of the baryon and lepton symmetry in the early universe and cannot be calculated without the quantitative deciphering of this physics.

As regards the fraction of dark matter, here we only announce the following. In the Chapter 1.2 devoted to this issue, we will show, proceeding from rather general assumptions, that one can justify theoretically the observed ratio $\rho_{\mathrm{DM}}/\rho_{\mathrm{DE}} \approx 1/3$.

In conclusion, we stress that formula (1.15) is obtained from the requirement of spatial closeness of the universe necessary for the possibility of its spontaneous quantum creation from the vacuum of some mother universe. This is a very important requirement since it is only a closed universe that does not require external energy for its creation.

We note that the current analysis based on the cosmological observations does not exclude the closed topology of the universe. It is clear from (1.15) that, for $a \gg a_{\mathrm{H}}$, the closed model approximately imitates the flat one, and these models may not be distinguishable observationally. A crucial theoretical argument in favor of a closed universe is the possibility of its spontaneous quantum creation.

1.1.4. Conclusion

From the macroscopic viewpoint, the physical vacuum as a continuous medium can be ascribed a stress-energy tensor of the form [9]

$$T_{\mu\nu} = (\varepsilon + p)u_\mu u_\nu - p g_{\mu\nu}, \tag{1.19}$$

where $g_{\mu\nu}$ is the metric tensor locally coinciding with the Minkowski tensor

$$\eta_{\mu\nu} = \mathrm{diag}\,(1, -1, -1, -1). \tag{1.20}$$

The vacuum is, by definition, a Lorentz-invariant state of quantum fields. The last term in (1.19) possesses this property, which is not true for its first term containing the four-velocity vector u_μ. Hence, it follows that the vacuum as a macroscopic medium should be characterized by negative pressure:

$$p = -\varepsilon,\ T_{\mu\nu} = \varepsilon g_{\mu\nu}. \tag{1.21}$$

It is this property that allows one to identify dark energy with the vacuum energy since the Friedmann equation for $\ddot{a}$ and equation (1.21) imply the "antigravity" property of the cosmological vacuum [3].

Taking into account the discussion of the previous sections, one can propose the following working model of the gravitating physical vacuum. On the Planckian spatial scales, the self-gravity of quantum fluctuations of the Planck sizes turns them into spatially closed massless "Planck cells" interacting with neighbors through quadrupole forces of the type of van-der-Waals forces. From the physical reasoning one can expect that this sufficiently rigid subsystem of vacuum forms a regular quantum-crystal lattice. This lattice is sort of filled with the mobile part of the gravitationally bound quantum fluctuations forming the "gravitational vacuum condensate" with positive energy as well as other vacuum condensates formed by bosonization of the fermionic degrees of freedom via strong gauge interactions. Vacuum condensates as coherent quantum-field subsystems similar to quantum fluids should be superfluous. In our future works, by laying this assumption as a basis for the "vacuum condensate" model of dark matter, we will try to show that this model leads to a sufficiently plausible estimate of the dark-matter density and spatial dimensions occupied by dark matter in the universe.

1.2. On the vacuum-condensate nature of dark matter

1.2.1. Introduction

In the previous section, *"On the gravitational mechanism of reducing the vacuum energy and the vacuum nature of dark energy"*, it is shown that the self-gravity and the mutual gravity of quantum vacuum fluctuations radically reduce the energy density of the physical vacuum, as compared with the predictions of the local quantum field theory. In this case, the space of vacuum becomes discrete and crystal-like at the Planck distances. The formation of vacuum condensates connected with the continuous symmetry breaking introduces an additional reduction of the vacuum density and makes it a suitable candidate for the role of "dark energy," which manifests itself in the acceleration of the cosmological expansion of space. The condition of the spatial closure of the universe allows us to give an upper bound for the vacuum energy density. The second part, devoted to *a vacuum model of dark matter*, is formulated below.

1.2.2. A vacuum model of dark matter

Our basic ideas are the following:

1. The intriguingly similar values of the mass density of "dark matter" (DM) and "dark energy" (DE) [1],

$$\frac{\rho_{\mathrm{DM}}}{\rho_{\mathrm{DE}}} \approx \frac{0,24 \cdot \rho_{\mathrm{c}}}{0,72 \cdot \rho_{\mathrm{c}}} \approx \frac{1}{3}, \tag{1.22}$$

suggest the idea of their common nature in seemingly different manifestations.

2. We assume that a common carrier of both $\rho_{\rm DE}$ and $\rho_{\rm DM}$ is the vacuum condensate (VC), which implements the lowest ("ground") energy state of the quantized fields.

3. This VC, being a quantum coherent state, is the analog of a superfluid quantum substance, and can flow onto gravitating bodies (Galaxies), into black holes and into hot areas (like the star centers) because of the "thermomechanical effect" inherent to superfluid substances.

4. We assume the steady inflow regime, i.e., $\partial/\partial t ... = 0$.

1.2.3. The mathematical realization

1. We assume that a massive galactic halo is formed by a stationary radial flow of VC, and preliminary we will take into account only its self-gravitation.

Under the outflow of VC from the boundary regions $r \sim R_{\rm halo}$, the density $\rho_{\rm VC}$ should be renewed there by quantum-field mechanisms that ensure the status of VC as *the ground* state of quantized fields [7]!

2. The stationarity of the flow implies:

$$4\pi r^2 \rho(r) V(r) = \dot{M}_0 = {\rm const}, \tag{1.23}$$

$$\frac{d}{dt}V(t,r) = \frac{d}{dt}V(r) = \dot{r}V'(r) = V(r)V'(r) = \frac{d}{dr}\frac{V^2(r)}{2} = -\frac{GM(r)}{r^2}, \tag{1.24}$$

$$M(r) = \int\limits_{r_0}^{r} 4\pi\rho(r) r^2 dr = \int\limits_{r_0}^{r} \frac{\dot{M}_0 dr}{V(r)}. \tag{1.25}$$

3. We will make the following ansatz:

$$V(r) \approx V_0 \sqrt{\ln \frac{Re}{r}}. \tag{1.26}$$

Then,

$$V^2(r) \approx V_0^2 \ln \frac{Re}{r},\ V(R) = V_0.$$

By virtue of the mean value theorem, we have,

$$M(r) = \dot{M}_0 \int\limits_{r_0}^{r} \frac{dr}{V(r)} \approx \frac{\dot{M}_0}{V_0} \int\limits_{r_0}^{r} \frac{dr}{\sqrt{\ln\left(Re/r\right)}} \approx \frac{\dot{M}_0}{V_0} \frac{r - r_0}{\sqrt{\ln\left(Re/\bar{r}\right)}},$$

so that

$$M(r) \approx \frac{\dot{M}_0}{V_0} \frac{r\left(1 - r_0/r\right)}{\sqrt{\ln\left(Re/\bar{r}\right)}} \approx \frac{\dot{M}_0}{V_0} \frac{r}{\sqrt{\ln\left(Re/\bar{r}\right)}},\ r \gg \bar{r} > r_0. \tag{1.27}$$

4. Now equation (1.24) takes the form

$$V_0^2 \frac{d}{dr} \ln \frac{Re}{r} \approx -\frac{2G\dot{M}_0}{rV_0\sqrt{\ln(Re/\bar{r})}},\ r \gg \bar{r} > r_0,$$

and becomes the identity when

$$V_0^3 \approx \frac{2G\dot{M}_0}{\sqrt{\ln(Re/\bar{r})}}. \tag{1.28}$$

5. $\rho(r) = \dfrac{\dot{M}_0}{4\pi V(r) r^2} = \dfrac{V_0^2}{8\pi G r^2} \dfrac{V_0\sqrt{\ln(Re/\bar{r})}}{V(r)} = \dfrac{V_0^2}{8\pi G r^2 \left[\frac{V(r)}{V(\bar{r})}\right]}.$

6. Since $V(R) = V_0$, we have

$$\rho(R) = \frac{V_0^2}{8\pi G R^2}\sqrt{\ln\frac{Re}{\bar{r}}},\ \rho(r) = \rho(R)\frac{R^2}{r^2\sqrt{\ln\frac{Re}{r}}}. \tag{1.29}$$

7. $M(r) = 4\pi\int\limits_{r_0}^{r} \rho(r) r^2 dr = 4\pi R^2 \rho(R) \int\limits_{r_0}^{r} \dfrac{dr}{\sqrt{\ln\frac{Re}{r}}} \approx 4\pi R^2 \rho(R) \dfrac{r}{\sqrt{\ln\frac{Re}{\bar{r}}}}.$ (1.30)

8. $M_{\text{halo}} = M(R) = \dfrac{4\pi R^3 \rho(R)}{\sqrt{\ln\frac{Re}{\bar{r}}}},\ R \approx R_{\text{halo}}.$ (1.31)

9. Now we consider the Metagalaxy (i.e., the closed Universe) with volume $V_{\text{Meta}} = 2\pi^2 R_{\text{Meta}}^3$. Let N_{Meta} be the number of "average" galaxies with the average halo radius R_{halo}.

Assuming that

$$\begin{cases} V_{\text{Meta}} = 2\pi^2 R_{\text{Meta}}^3, \\ R_{\text{Meta}} \le R_{\text{halo}} \cdot N_{\text{Meta}}^{1/3}, \\ \rho(R_{\text{halo}}) = \rho_{\text{VC}} = \rho_{\text{DE}}, \end{cases}$$

we have

$$V_{\text{Meta}} \le 2\pi^2 R_{\text{halo}}^3 N_{\text{Meta}}$$

and

$$M_{\text{DE}}^{\text{Meta}} = \rho_{\text{DE}} V_{\text{Meta}} \le 2\pi^2 \rho_{\text{DE}} R_{\text{halo}}^3 N_{\text{Meta}} \tag{1.32}$$

10. $M_{\text{halo}}^{\text{Meta}} = M_{\text{halo}} N_{\text{Meta}} = \dfrac{4\pi R_{\text{halo}}^3 \rho_{\text{DE}}(R) N_{\text{Meta}}}{\sqrt{\ln(R_{\text{halo}} e/\bar{r})}}.$ (1.33)

11. We calculate the ratio:

$$\frac{M_{\text{halo}}^{\text{Meta}}}{M_{\text{DE}}^{\text{Meta}}} \equiv \frac{M_{\text{DM}}}{M_{\text{DE}}} \ge \frac{4\pi R_G^3 N_{\text{Meta}} \rho_{\text{halo}}(R)}{2\pi^2 R_G^3 N_{\text{Meta}} \rho_{\text{DE}}} \frac{1}{\sqrt{\ln\frac{Re}{\bar{r}}}} =$$

$$= \frac{2}{\pi} \frac{1}{\sqrt{\ln\frac{Re}{\bar{r}}}} \frac{\rho_{\text{halo}}}{\rho_{\text{DE}}} = \frac{2}{\pi\sqrt{\ln\frac{Re}{\bar{r}}}}. \tag{1.34}$$

12. The results of observations give the estimate

$$\frac{M_{\rm halo}^{\rm Meta}}{M_{\rm DE}^{\rm Meta}} = \frac{0.24}{0.72} \sim \frac{1}{3} \geq \frac{2}{\pi\sqrt{\ln\frac{Re}{\bar r}}}, \tag{1.35}$$

whence

$$\sqrt{\ln\frac{Re}{\bar r}} \geq 2,\ \ln\frac{Re}{\bar r} \geq 4,$$

which is quite an acceptable requirement since

$$\ln\frac{R}{r_{\rm cp}} \geq 3,\ \frac{R}{r_{\rm cp}} \geq e^3,$$
$$\bar r \leq Re^{-3} = R\cdot 10^{-3/2.3} = R\cdot 10^{-1.3} \approx \frac{R_{\rm halo}}{20},$$
$$\bar r \leq 0.05\cdot R_{\rm halo}. \tag{1.36}$$

Taking

$$\bar R_{\rm halo} \sim 2.5\ {\rm Mpc} \sim 2.5\cdot 10^3\ {\rm kpc},$$

we obtain

$$\bar r \leq 2.5\cdot 50\ {\rm kpc} = 75\ {\rm kpc}. \tag{1.37}$$

For the Galaxy, we have $R_{\rm halo} \leq \frac{1}{2}L_{\rm Andromeda} \sim 300$ kpc, whence

$$\bar r_{\rm Galaxy} \leq 0.05\cdot 300\ {\rm kpc} < 15\ {\rm kpc}. \tag{1.38}$$

This is quite a reasonable value!

1.2.4. Conclusion

Thus, the performed calculations and final estimates based on the assumption that the vacuum condensate, with superfluidity property, is a common carrier of both $\rho_{\rm DE}$ and $\rho_{\rm DM}$ lead to the resulting value of the mass ratio (and, therefore, the corresponding densities) of dark matter and dark energy (1.35) which is close to the observed value of 1/3. We note that the approximations (1.26) and (1.30) made in our calculations are quite "mild," and affect our results very little.

Bibliography

1. A.D. Chernin, The space vacuum, UFN **171**, 1153 (2001).
2. A.I. Akhiezer and V.B. Berestetskii, Quantum Electrodynamics (Interscience Publishers, New York, 1965).
3. A.D. Chernin, Cosmic vacuum, Phys. Usp. **44**, 1099 (2001).
4. P.I. Fomin, Some questions of quantum electrodynamics at small distances, Fiz. Elem. Chast. Atom. Yad. **7**, 687 (1976).
5. P.I. Fomin, On the crystal-like nature of the physical vacuum at the Planck distances, in Problems of Physical Kinetics and Physics of Solid Body (Naukova Dumka, Kiev, 1990) [in Russian].
6. P.I. Fomin and V.V. Kuzmichev, Gravitational fields of massive and massless axial-symmetric quadrupoles in general relativity, Phys. Rev. D **49**, 1854 (1994).
7. P.I. Fomin, On the vacuum condensates and the problem of the nature of masses and innertia forces (National Scientific Center, Kharkov Institute of Physics and Technology, 2008).
8. P.I. Fomin, Gravitational instability of vacuum and the cosmological problem, Preprint ITP-73-137P [in Russian], Kiev (1973).
9. L.D. Landau and E.M. Lifshits, The Classical Theory of Fields (Pergamon Press, Oxford, 2003).
10. A.D. Linde, Particle Physics and Inflationary Cosmology (Harwood, Chur, Switzerland, 1990).

2 CHAPTER

DARK MATTER: OBSERVATIONAL MANIFESTATION IN GALAXY CLUSTERS

I.B. Vavilova, Iu.V. Babyk

2.1. Notes on the history of discovery of the dark matter

The structure of the Universe on the extragalactic scales is determined by the distribution of different types of matter. In terms of dark matter (DM) research, the heterogeneity of mass distribution, which is dominated by the DM contribution (since dark energy (DE) is distributed uniformly), is a key factor. To investigate this heterogeneity, the gravitational effects should be considered: kinematic characteristics of luminous matter, while its movement gives information on the gravitating mass; analysis of the "mass-to-luminosity" relation of galaxy or system of galaxies, which provides quantitative and qualitative information on the distribution of matter in the halo; gravity-relativistic effects in the propagation of light (gravitational lensing) and others. However, the first notes on the dark matter problem were related to our Galaxy and published 100 years ago.

2.1.1. Discovery of dark matter in galaxies, galaxy clusters and groups

Our Galaxy. The existence of matter which interacts gravitationally but is not seen via electromagnetic radiation has been considered since 1915 when Öpik [212] has tried to estimate the dynamical density of matter in the vicinity of Sun. The term "dark matter" was coined by Kapteyn in 1922 in his studies of the motions of stars in our Galaxy [148]. He found that no dark matter is needed in the galactic Solar neighborhood and confirmed the results by Öpik that

a dynamical density of stars is sufficient to explain their vertical motions near the plane of the Galaxy. But Jeans in 1922 [140] found that a dark matter probably exists in the vicinity of Sun. Later, in 1932, such a conclusion was supported by Öort [213] who suggested that there would be twice as much dark matter as visible matter in the Solar neighborhood. This was the first claim for evidence of dark matter. However, as we know, the following observations have shown that this claim about dark matter in the vicinity of Sun was to be wrong. Only through thirty years, as Einasto has pointed [101], in early 1950s Kuzmin et al. [161, 162] studied again this problem and obtained that the amount of dark matter in galactic plane is small. While, later, Hill [129], Öort [214], and Bahcall [2] have resulted that up to a half of matter in the vicinity of Sun may be unvisible.

It is obvious that establishing a presence, amount, and distribution of dark matter in the Milky Way is proved to be paved with more difficulties than in the case of external systems. Due to the problems of determining accurate distances to objects, whose velocities are known, and correcting for the motion of the Sun itself around the center of the Milky Way, large uncertainties are however introduced. For tracer objects not located in the Milky Way disc, e.g. globular clusters, the assumed shape of their orbits (circular, elliptical or radial) can also have a pronounced impact on the final result.

These difficulties aside, a consensus has been reached that our Galaxy does contain sizable amounts of dark matter, with a total mass of $\sim 10^{12}$ $M_{\odot}$. The DM distribution is however still a matter of debate, but it is widely accepted that its larger amount is concentrated in the halo as well as a partial "responsibility" for their amount is on the population of very cold stars, brown dwarfs, Jupiter-like objects etc. (see, for example, the Chapter "Ultracool dwarfs in our Galaxy" by Ya. Pavlenko in the volume 2 of this monograph).

In 2014 Jean Kovalevsky has written in the letter to Eric Hog in the comments on the future results by the GAIA space mission. "I think that astrometry could have some specific inputs into this challenging mystery [dark matter]. I especially think about building a detailed map of the gravitational field within the Galaxy. It is well known that the rotation of the Galaxy is reasonably well represented within about 7 kiloparsecs from its center, but further on, the velocities do not diminish as they should if there were only baryonic masses. I do not see how this can be done, but I guess that very accurate proper motions and parallaxes of stars in the outer galactic plane could be analyzed to give some hints about the repartition of dark matter, rather than presently modeled sphere. Another improvement by very detailed imaging would be the analysis of the gravitational lensing in many galactic clusters and henceforth the repartition and mass of dark matter. Other questions might also be tackled, like the presence or not of dark matter in globular clusters by studying the motions of outer members of the cluster" [133].

Galaxies. In 1970s several observations related to the rotational curves and kinematics of stars in the large disc galaxies indicated that dark matter is a common feature among galaxies [76, 105, 216, 236]. Ostriker & Peebles [215] showed that galactic discs by themselves would be unstable and suggested that they may be surrounded by spherical halos with huge masses. Hence, the important concept of dark halos, today believed to be common to all galaxies, was introduced (see, for example, [296]).

At around the same time, the first robust evidence in favor of dark matter in elliptical galaxies came from observations of their X-ray luminous gas. Many of the early attempts have been concentrated on the giant elliptical galaxy M87 at the centre of the Virgo cluster. Since the dark halo of M87 is embedded in the dark matter of the surrounding cluster, there are doubts about which system the detected dark matter should be attributed to. By the mid-1980s, a concordant picture had nonetheless emerged, in which the elliptical galaxies appeared to be surrounded by substantial amounts of invisible matter.

The first strong indications of dark matter in dwarf galaxies came in the early 1980s. Faber & Lin [111] studied dwarf spheroidals and found them to contain large amounts of dark matter. Subsequent studies (see, for example, review in [255]) have in fact shown that dwarf galaxies have higher mass-to-light ratios than normal galaxies. Smaller stellar populations, like globular clusters, do not appear to suffer from any significant missing matter problem. The DM manifestation in galaxy groups will be discussed in the Chapter 4 of this monograph.

Galaxy clusters.The first evidence about the existence of dark matter in clusters was made by Fritz Zwicky in 1933 [295]. Using measured redshifts of members (galaxies) in Coma, Zwicky found that the velocities of individual members of cluster are much larger than those expected from the estimated total mass of the cluster, calculated from masses of individual members. He has concluded that the cluster might contain a huge amount of some invisible matter (missing or dark matter), because it was only one way to keep the galaxy cluster from rapid expansion. He also assumed that the amount of invisible mass in Coma cluster exceeds the total mass of cluster galaxies at least in factor ten or more. In 1936 Smith was first who noticed in his study of the Virgo cluster [257] that the mass implied by cluster galaxy motions was largely exceeding that associated with the optical light component. Such result was confirmed by Zwicky in 1937, as a result, it was first evidence of the presence of invisible (dark) matter in other galaxy clusters. It would however take quite some time until 1970s, when the Zwicky's discovery became a well-recognized concept.

The rich galaxy clusters provide some of the best available sites for studying the nature and distribution of dark matter. Zwicky was the first who found that member galaxies in clusters are traveling too fast to be gravitationally bound unless the total mass in the cluster greatly exceeds that

expected from optical luminosities of member galaxies. Through sub sequent measurements the velocity dispersions of rich cluster were found typically to be 700 km s^{-1}, implying mass-to-light ratios of $M_{\rm total}/L_{\rm total} \sim 150$—$400 M_\odot/L_\odot$ [281]. Here $M_{\rm total}$ and $L_{\rm total}$ are the total dynamical mass and the total optical luminosity, respectively. In contrast, individual galaxies typically have mass-to-light ratios of $10 M_\odot/L_\odot$ in their optical luminous central region.

Clusters have the advantage of containing many more galaxies than typical groups. In some nearby clusters, several hundred galaxy velocities have been measured, thereby eliminating the statistical uncertainties that plague measurements of galaxy groups. The number of galaxies is so large that we can use the solutions of the collisionless Boltzmann equation to model the cluster. Such a procedure for the Coma cluster suggests mass-to-light ratio of $\sim 400 h M_\odot/L_\odot$ and Perseus cluster gives a value of $600 h M_\odot/L_\odot$. Clearly, these clusters contain a large amount of dark matter. Many clusters of galaxies contain hot gas that emits X-rays. Since the gas is in hydrostatic equilibrium, it can be used to trace the gravitational potential and mass distribution in clusters using Eq. (2.12). The principal obstacle in applying this method is the absence of spatially resolved spectral information, so that the temperature gradient term $d \ln T/d \ln r$ in Eq. (2.12) must be estimated by indirect methods.

Apart from these methods, a gravitational lensing — i.e. the effects associated with the gravitational deflection of light — has also played an important role in the study of dark matter. The notion that gravity can bend rays of light was proposed yet by Newton, although the magnitude of this effect cannot be correctly predicted by Newtonian gravity. Instead, the theory of general relativity is required. In 1919, Eddington measured the deflection of the light from a star as its ray of light crossed the edge of the Sun during a total solar eclipse, confirming Einstein's predictions. Zwicky (1937) was a first who suggested that gravitational lens effects could also be used to measure the total masses of extragalactic objects. It would however take quite some time until this technique became observationally feasible. The first extragalactic gravitational lens system, the quasar 0957 + 561 was discovered in 1979 [285]. In this case, a background quasar is spliting into two optical images by a foreground galaxy. Since then, more than a hundred candidate multiply-imaged quasars have been detected. In 1986, Lynds & Petrosian [172] announced the discovery of arc-like features in galaxy clusters. These arcs were later identified as images of galaxies located far behind the foreground cluster and having been distorted by its gravitational field. Such gravitational arcs provide an independent, non-dynamical estimate of the total mass of the lens cluster, and have subsequently confirmed the need for dark matter to explain the gravitational potential of these objects. A rich spectrum of other gravitational lens effects have also been discovered, many of which allows us to impose important constraints on the dark matter in the Universe (see, for example, the Chapters on the gravitatio-

nal lensing, which are presented by V. Shulga et al. and V. Zhdanov et al. in the volume 2 of this monograph). Among those, who first has paid an attention to the importance of studying the gravitational lens were the Ukrainian scientists Bliokh and Minakov.

Clusters have been formed via the collapse of cosmic matter over a region of several megaparsecs. Cosmic baryons, which represent approximately 15 % of the mass content of the Universe (see, Chapter 1 of this volume), follow the dynamically dominant dark matter during the collapse. As a result of adiabatic compression and shocks generated by supersonic motions during shell crossing and virialization, a thin hot gas permeating the cluster gravitational potential well is formed. For a typical cluster mass of 10^{14}—$10^{15} M_{\odot}$ this gas reaches temperatures of several 10^7 K, becomes fully ionized, and therefore emits via thermal bremsstrahlung in the X-ray band.

So, galaxy clusters have been regarded as the largest virialized systems in the Universe with dimensions of 1—5 Mpc across. Since the time scale for the cluster evolution is compatible with the age of the Universe, ∼10 Gyr, their properties should reflect the initial condition and the evolutional history over the cosmological time scale.

2.1.2. Dark matter models

Cold dark matter and Hot dark matter. Once it was recognized that most of the matter in the Universe was dark, this component was expected to dictate the conditions for the formation of large structures like galaxies and galaxy clusters. The fact that relativistic dark matter particles (i.e. moving close to the speed of light in the early Universe) — today referred to as hot dark matter (HDM) — like standard, low-mass neutrinos, would have severe trouble in explaining the observed structures soon became evident. The advantages of cold dark matter (CDM), i.e. dark matter consisting of particles with non-relativistic velocities early on, was made clear by Primack [226], Peebles [220] and Blumenthal et al. [39]. At present, CDM holds the position as the leading dark-matter model, although a number of recent problems (see below) may call for a revision of this scenario.

As the Universe has expanded, it passed from a state of radiation- to matter-domination at $\sim 4.7 \times 10^4$ yr after the Big Bang (in the $\Omega_m \approx 0.3$, $\Omega_\Lambda \approx 0.7$ scenario). If the Universe was purely baryonic, the overdense regions would not be able to collapse until after recombination. Such a scenario is inconsistent with the density fluctuations evident from the cosmic microwave background (CMB) and would lead to slower structure formation. Non-baryonic (dark) matter can on the other hand collapse before this epoch. In this case, the details of structure formation depend on the properties of the dark matter particles. In the case of particles moving with the relativistic velocities (i.e.

moving with velocities $v \sim c$; HDM) at the epoch of matter-radiation equality, free-streaming out of overdense regions would prevent early formation of low-mass structures. Structure formation would in this case progress according to a top-down scheme, in which overdensities of galaxy-cluster scale would collapse first, whereas smaller substructures, such as individual galaxies, would form through fragmentation at much later epochs.

Last results, which allow to observe galaxies already at high redshift, show that this scenario has now been dropped in favor of a bottom-up scheme, in which low-mass objects form first, and larger structures form through subsequent mergers and collapse. This can be achieved by non-baryonic matter which is non-relativistic (i.e. moving with $v < c$) at the epoch of radiation-matter equality. This component, known as cold dark matter (CDM), is still the leading contender for the non-baryonic dark matter of the Universe, and has been remarkably successful in explaining the observed large scale structures of the Universe. For a particle species in thermal equilibrium in the early Universe, the particle mass must be >1 keV in order for it to qualify as CDM. At masses of 1 keV, it would instead behave as HDM. Current cosmological observations constrain the non-baryonic matter component of the Universe to have an equation of state with $-1.5 \times 10^{-6} < w < 1.13 \times 10^{-6}$ [196], i.e. in excellent agreement with the CDM hypothesis ($w = 0$). The currently favored cosmology (with $\Omega_m \approx 0.3$, $\Omega_\Lambda \approx 0.7$), in which most of the matter is assumed to be CDM, is therefore often referred to as the ΛCDM model. In addition, the CDM model for structure formation assumes the primordial density fluctuations to be adiabatic and to follow a scale-invariant power spectrum (see, also, Chapter 1 by B. Novosyadlyj in the volume 1 of this monograph).

Despite a remarkable success in explaining the large scale structure of the Universe, the ΛCDM model is currently facing a number of potentially serious problems on the scales of individual dark halos. It must however be emphasized that many of these problems may in the end turn out to be related to how CDM halos and CDM-baryon interactions are simulated, rather than problems with the ΛCDM itself.

To resolve the various problems faced by CDM, a number of remedies have been suggested, varying from quite modest to very radical modifications of the assumptions going into the CDM model. A number of them are briefly reviewed below.

Warm dark matter. A dark matter species with intermediate velocities between those of HDM and CDM, so-called warm dark matter, would prevent gravitational clustering on small scales and inhibit the formation of such structures. This could potentially lower the densities in the centres of dark halos and reduce the number of subhalos, thereby removing two of the most serious problems faced by CDM. For particles which have been in thermal

equilibrium in the early Universe, the mass should be around ∼1 keV in order for them to act as warm dark matter (WDM).

Mixed dark matter. Mixed dark matter (MDM), i.e. a mixture of cold and hot dark matter, became fashionable for a few years in the mid-1990. The main virtue of this scenario was that it could reconcile the CMB observations of the time with (apparently spurious) reports of neutrino masses in the 20—30 eV range [226]. Interest in mixed dark matter declined, however, once the ΛCDM model entered the stage and provided a superior explanation for supernova type Ia data, the CMB anisotropy and the observed large scale structure of the Universe at both high and low redshift. While neutrinos are no longer believed to contribute substantially to the energy density of the Universe, they do appear to have non-zero masses in the right range to make them act as HDM. A small contribution from HDM (with $\Omega_{\rm HDM} \sim 0.01$) is still viable within the ΛCDM model, and could help to lower the central densities of dark halos somewhat [294].

Self-interacting dark matter. Introducing non-gravitational interactions among the dark matter particles gives rise to a complex phenomenology, the details of which have not yet been fully worked out. Elastic collisions among the dark matter particles could however both reduce the central halo densities and inhibit the formation of halo substructure, depending on the scattering cross-section [5,260]. Although a number of observational constraints have been imposed on the strength of the dark matter self-interaction, seemingly closing most of interesting parameter space, these constraints may not be as strong as originally claimed (see [5], for a review).

Self-annihilating or decaying dark matter. Dark matter particles, which self-annihilate upon collision, would decrease the densities in regions where collisions are most likely to occur, i.e. in the central regions of dark halos [147]. Alternatively, a component of dark matter, which decay into radiation or relativistic particles during early stages of structure formation, could also inhibit the formation of dense halo centers [65]. Although halo substructure will still form in such scenarios, star formation in subhalos may be quenched due to expansion of subhalos following the evaporation of dark matter. If some component of the dark matter is decaying into hydrogen-ionizing radiation at the current time, this could also help explain the scale-height of ionized gas in the Milky Way disc, which has long proved difficult to reconcile with known ionization sources in our Galaxy [253].

Fuzzy dark matter. Dark matter particles with low masses but extremely large effective sizes (e.g. of the same order as the constant density cores found in the center of many galaxies) cannot be concentrated on small scales, which would inhibit the formation of central density cusps and halo substructure [138].

2.2. Galaxy clusters: matter evolution and distribution

In this section we briefly describe the current scenario of the structure formation and its effects on the cluster evolution in order to provide a common picture as well as a background knowledge. We also mention previous results on the clusters by summarizing the observed properties of the hot gas. We notice that a cluster consists in average of 100—1000 member galaxies, ranging from the cD galaxy, which belongs to the most luminous galaxy class in the Universe, to dwarf galaxies.

2.2.1. General remarks on the evolution of galaxy clusters

Formation of galaxy clusters. It is significant to note that since the main properties of dark matter particles effect on the formation of the Universe, i.e. structure, so it can be concluded that dark matter is primary matter in the Universe. As a result, the studying of the dark matter problem is tightly related to the large scale structure of the Universe.

At present, the hierarchical clustering scenario is widely supported, as well as it is in agreement with the ΛCDM model. The fact that the galaxies have been observed at redshifts of ∼5, whereas the most distant observed clusters are at $z \sim 2$, is in favour that small systems have been formed first. According to the scenario of the evolution, large-scale structures of the Universe have formed from infinitesimally small density perturbations at the early epochs through the gravitational interaction. A number of N-body simulations for the structure formation support such a producing the large-scale structures as galaxy clusters and groups. This result is recognized as a strong support to the hierarchical clustering scenario. Since an early work by White [287] on the 700-body simulations, the recent calculations, which include N-body/gas-dynamical simulations, indicate that the clusters are formed through subcluster merger and/or capture of groups of galaxies [139, 140, 150, 203]).

Collapse condition. Let us briefly review the collapse scenario according to the spherical collapse model. First of all, consider a mass shell with a radius r_i at epoch $t = t_i$, which is moving with the general expansion until $t = t_i$ [225]. The kinetic energy per unit mass of the shell relative to the center is,

$$K_i = \frac{1}{2}(H_i r_i)^2, \tag{2.1}$$

where H_i is the Hubble constant at $t = t_i$. Suppose that the average density inside the shell, ρ_i, is higher than the homogeneous background, $\rho_{b,i}$, by a factor $1 + \delta$, i.e.

$$\rho_i = \rho_{b,i}(1 + \delta) = \frac{3}{8\pi G}\,\Omega_i H_i^2(1 + \delta), \tag{2.2}$$

where Ω_i is the density parameter at $t = t_i$. Then the potential energy per unit mass of the shell is,

$$W_i = -\frac{4\pi G\rho_i r_i^3}{3r_i} = -\Omega_i K_i(1+\delta). \tag{2.3}$$

Thus, the total energy is

$$E = K_i + W_i = \frac{W_i}{1+\delta}\left[\delta - \left(\frac{1}{\Omega_i - 1}\right)\right]. \tag{2.4}$$

Therefore, if $\Omega_i < 1$, when

$$\delta > \frac{1}{\Omega_i - 1}, \tag{2.5}$$

in other words, when

$$\rho_i = (1+\delta)\Omega_i\rho_{\mathrm{crit},i} > \rho_{\mathrm{crit},i}, \tag{2.6}$$

total energy is negative and the shell will eventually collapse. Here, we use the critical density $\rho_{\mathrm{crit},z}$ at the redshift z as,

$$\rho_{\mathrm{crit},z} = \frac{3H_z^2}{8\pi G}, \tag{2.7}$$

where

$$H_z = H_0 E(z),\ E^2(z) = \Omega_0(1+z)^3 + \Omega_\Lambda,\ \Omega_0 = \frac{8\pi G\rho_0}{3H_0^2};\ \Omega_\Lambda = \frac{\Lambda}{3H_0^2}. \tag{2.8}$$

Here ρ_0 is the non-relativistic matter density, R is the radius of curvature, H_0 is the current Hubble constant, and Λ is the cosmological constant.

If the density parameter, Ω_i, is close to unity, density perturbations with a small amplitude can collapse. Thus, galaxy clusters were effectively formed in such epochs. For a large initial over-dense spheres behave during the expansion is stopped at an early stage and the system collapses into a virialized system.

From cold collapse to hierarchical clustering. N-body simulations of the gravitational collapse of a collisionless system of particles pre-date the CDM model. Early simulations, in the 1960's, focused on the formation of elliptical galaxies from the collapse of a cold top-hat perturbation of stars. The resulting virialisation process gave rise to equilibrium structures with de Vaucouleurs or Einasto (Eq. (2.54)) type density profiles, similar to observations of elliptical galaxies. It is remarkable that the end state of almost any gravitational collapse, independently on the small scale structure and hierarchical merging pattern, leads to a similar global structure of the final equilibrium system.

Computer simulations in the 1970's attempted to follow the expansion and a collapse of a spherical overdensity to relate to the observed properties of virialised structures such as galaxy clusters. A random distribution of particles with a Poisson power spectrum led to the initial formation of many bound

clumps, however it was observed that these bound structures were destroyed as the final system formed — resulting in a smooth distribution of matter. This overmerging problem persisted for over two decades and motivated the development of semi-analytical models for galaxy formation.

During the 1980's, it was proposed that cosmic structure formation follows a dominant, non-baryonic CDM component. Cold dark matter could consist of new and yet undiscovered weakly-interacting massive particles (WIMPs), which occur for example in super-symmetric extensions of the Standard Model of particle physics. "Cold" means that these particles have rather small thermal velocities, which allows the formation of very small structures, typically down to far below one solar mass (see, Section 2.1.2). CDM together with the dark energy (usually denoted "Λ") are the dominant components of the ΛCDM model, in which all the ordinary matter accounts for only 4.6 percent of the total. ΛCDM has by now become the "Standard Cosmological Model" and its parameters (and therefore the initial conditions for structure formation) are now known to a reasonable precision. Computer simulations allow to follow the non-linear evolution of perturbations, starting from realistic and well constrained cosmological initial conditions. The final quasi-equilibrium structures are the dark matter halos that are observed to surround galaxies and galaxy clusters. Large cubes of the universe were simulated in an attempt to match the large scale clustering of galaxies. Some of the most basic properties of collapsed structures were discovered — the distribution of halo shapes, spin parameters etc. It was not until the simulations by Dubinski & Carlberg [96] that individual objects were simulated at sufficiently high resolution to resolve their inner structure on scales that could be compared with observations. Using a million particle simulation of a cluster mass halo run on a single work-station for an entire year, these authors found central cusps and density profiles with a continuously varying slope as a function of radius. They fit the Hernquist profiles to their initial simulations but an Navarro—Frenk—White (NFW) profile provides an equally good fit (see, Section 2.2.3).

Navarro, Frenk, and White published results of simulations of halo density profiles from scales of galaxies to galaxy clusters. They demonstrated that all halos could be reasonably well fit by a simple function (see Eq. (2.22)) with a concentration parameter that was related to the halo mass. However, with less than 10^4 particles only the mass profile beyond about 5—10 % of the virial radius was resolved reliably. Shortly afterwards, simulations with 10^6 particles showed cusps steeper than r^{-1} down to their innermost resolved point near one percent of the virial radius. These simulations also resolved the overmerging problem — the resolution was sufficient to resolve cusps in the progenitor halos enabling the structures to survive the merging hierarchy. The final surviving substructure population is a relic of the entire merger history of a given CDM halo.

2.2.2. Hydrostatic equilibrium and gravitational mass distribution

Since the collision time scale for ions and electrons in the intracluster media (ICM) are much shorter than the time scales of the heating or cooling, we can treat the gas as a fluid [250]. In general, the time required for a sound wave in the intracluster gas to cross a cluster (sound crossing time) is shorter than the probable age of a cluster. Therefore we can assume that the ICM is under the hydrostatic equilibrium, so that the pressure gradient is balanced with the gravitational force as,

$$\bigtriangledown P_{\rm gas} = -\mu m_{\rm p} n_{\rm gas} \bigtriangledown \phi. \tag{2.9}$$

Here $P_{\rm gas}$ and $n_{\rm gas}$ are the ICM pressure and number density, ϕ is the gravitational potential, and $\mu \sim 0.6$ is the mean molecular weight relative to the proton mass $m_{\rm p}$. Since the ICM density is quite low, the ICM pressure can be expressed as

$$P_{\rm gas} = n_{\rm gas} kT = \frac{\rho_{\rm gas}}{\mu m_{\rm p}} kT, \tag{2.10}$$

where k is the Boltzmann constant, and $\rho_{\rm gas}$ is the ICM density. When we assume a spherical symmetry, the equation (2.9) becomes

$$\frac{dP_{\rm gas}}{dr} = -\mu m_{\rm p} n_{\rm gas} \frac{GM_{\rm tot}(<r)}{r^2}, \tag{2.11}$$

where G is the gravitational constant, and $M_{\rm tot}(<r)$ is the gravitational (total) mass (i.e. the dark matter + galaxies + hot gas) within the radius r. Thus, we obtain the total mass of a galaxy cluster as

$$M_{\rm tot}(<r) = -\frac{r^2 k}{\mu m_{\rm p} G n_{\rm gas}} \frac{d}{dr}(n_{\rm gas} T) = -\frac{kTr}{\mu m_{\rm p} G} \left(\frac{d \ln n_{\rm gas}}{d \ln r} + \frac{d \ln T}{d \ln r} \right), \tag{2.12}$$

that is to say, once we measure the ICM density distribution $n_{\rm gas}(r)$ and the temperature distribution $T(r)$, we can estimate the total mass distribution.

If the heat conduction were sufficiently rapid compared to the other important time scales, the gas would become isothermal. Substituting the equation 2.10 into the equation 2.9 and assuming the ICM temperature T is constant, we obtain

$$\frac{dln\rho_{\rm gas}}{dr} = -\frac{\mu m_{\rm p}}{kT} \frac{d\phi(r)}{dr}. \tag{2.13}$$

Similarly, assuming that the galaxies are in hydrostatic equilibrium, the hydrostatic equation of the galaxies is written as,

$$\frac{dln\rho_{\rm gas}}{dr} = -\frac{1}{\sigma^2} \frac{d\phi(r)}{dr}. \tag{2.14}$$

From equations (2.13) and (2.14), we obtain

$$\rho_{\rm gas} \propto \rho_{\rm gal}^{\beta}, \tag{2.15}$$

where

$$\beta \equiv \frac{\mu m_{\rm p} \sigma^2}{kT}. \tag{2.16}$$

King has derived [152] an analytic approximation to the isothermal sphere of self-gravitational isothermal collision-less particles. The density profiles of galaxies have been found to be well approximated with the King profile,

$$\rho_{\rm gal}(r) \sim \rho_{\rm King}(r) = \rho_{\rm King}(0) \left[1 + \left(\frac{r}{r_c}\right)^2\right]^{-\frac{3\beta}{2}}. \tag{2.17}$$

Then the isothermal gas distribution may be represented as

$$\rho_{\rm gas}(r) = \rho_{\rm gas}(0) \left[1 + \left(\frac{r}{r_c}\right)^2\right]^{-\frac{3}{2}\beta}. \tag{2.18}$$

The surface brightness profile of an isothermal spherical plasma with a radial density profile given by equation (2.18) is calculated by integrating the local emission per unit volume given by $L_X = EM \times S \times \Lambda(T, Z)$ and the EM given by $EM = \int n_{\rm e}^2 dl$ along the line of sight (l). The X-ray surface brightness $S(r)$ at projected radius r can will be obtain as

$$S(r) = S(0) \left[1 + \left(\frac{r}{r_c}\right)^2\right]^{-3\beta+\frac{1}{2}}. \tag{2.19}$$

Once we have obtained the β profile parameters to characterize the surface brightness distribution, we can estimate the three-dimensional density profile of the gas. Here, the total X-ray luminosity $L_X(<R)$ within the radius R is written as,

$$L_X(<R) = \int_0^R S(r)dr = \frac{\pi^{3/2} n_0^2 r_c^3 \Lambda}{3\beta - 1} \left[1 - \left(\frac{r_c^2}{r_c^2 + R^2}\right)^{3\beta-2}\right] \frac{\Gamma(3\beta - 3/2)}{\Gamma(3\beta - 1)}, \tag{2.20}$$

where the n_0 is the ICM number density at $r = 0$. In order to estimate the 3-dimensional density profile based on the equation (2.19), we can calculate the n_0 using equation (2.20). When we obtained the 3-dimensional β-model density profile, we derive the total mass of the cluster inside a radius s from the assumption of hydrostatic equilibrium Eq. (2.12),

$$M(r) = \frac{3kT\beta r}{\mu m_{\rm p} G} \frac{(r/r_c)^2}{1 + (r/r_c)^2} \propto \beta T r. \tag{2.21}$$

It has been known that the observed X-ray surface brightness of galaxy clusters are well fitted by equation (2.19) with $\beta \sim 0.7$ on average [60, 61, 64]. However recent observational studies of the clusters with Chandra and XMM-Newton observation, which have unprecedented imaging capability and large effective area, reveal that a lot of clusters could not represent by the simple β-profile (see, Section 2.3).

2.2.3. Dark matter density distribution

Navarro—Frank—White model. As discussed in the previous subsection, the gas density profiles of X-ray clusters of galaxies are known to be approximated by equation (2.18). Theoretically, this is consistent with the observed indication that luminous member galaxies obey the King profile and the assumption of the hydrostatic equilibrium of cluster gas. The galaxies in clusters, however, constitute a very small fraction of the gravitational mass of the entire cluster because of the presence of dark matter. Recent high-resolution N-body hydrodynamical simulations have strongly suggested that dark halos of cluster scales are described by a family of fairly universal density profiles. Navarro, Frenk & White [201—203] found from their numerical simulations of structure formation that the virialized dark matter halos with masses over several orders of magnitude follow a universal density profile,

$$\rho_{\rm DM}(r) = \frac{\rho_s}{(r/r_s)(1 + r/r_s)^2}, \tag{2.22}$$

where ρ_s and r_s are characteristic density and length, respectively. ρ_s is related to the critical density of the Universe $\rho_{\rm crit}$ and characteristic density δ_c through $\rho_s = \delta_c \rho_{\rm crit}$. Instead of the flat core of the King profile, the NFW profile has a core with $\propto r^{-1}$ dependence.

Suto, Sasaki & Makino [265] generalize the NFW profile in equation (2.22) and consider a set of density profiles describing the dark matter halo

$$\rho_{\rm DM}(x) = \frac{\rho_s}{x^\mu (1 + x^\nu)^\lambda}, \tag{2.23}$$

where $x \equiv r/r_s$ is the dimensionless radius in units of the characteristic scale r_s. Then the total mass of the dark matter halo within the radius r is given by

$$M(r) = 4\pi \rho_s r_s^3 m(r/r_s), \tag{2.24}$$

with

$$m(x) = \int_0^x \frac{u^{2-\mu}}{(1 + u^\nu)^\lambda} du. \tag{2.25}$$

Using equation (2.22) we proceed by computing the mass by integrating over the volume:

$$M \equiv 4\pi \int_0^R \frac{\rho_0 r^2}{\frac{r}{r_0}(1+r/r_0)^2} dr = 4\pi r_0^3 \rho_0 \left[\ln\left(1+\frac{R}{r_0}\right) - \frac{R}{R+r_0} \right]. \tag{2.26}$$

The mean radius $\langle R \rangle$ can then be defined with

$$M\langle R \rangle \equiv 4\pi \int_0^R \frac{\rho_0 r^3}{\frac{r}{r_0}(1+r/r_0)^2} dr = 4\pi r_0^4 \rho_0 \left[\frac{R}{r_0} - 2\ln\left(1+\frac{R}{r_0}\right) + \frac{R}{R+r_0} \right], \tag{2.27}$$

which after considering Eq. (2.101) can be written as follows:

$$\langle R \rangle = r_0 \frac{\left[\frac{R}{r_0} - 2\ln\left(1+\frac{R}{r_0}\right) + \frac{R}{R+r_0} \right]}{\left[\ln\left(1+\frac{R}{r_0}\right) - \frac{R}{R+r_0} \right]}. \tag{2.28}$$

We can then get the shape parameter r_0 by numerically inverting $\langle R \rangle$ and use it to define the NFW density parameter ρ_0 from the observed mass M contained within the radius R by inverting Eq. (2.101):

$$\rho_0 = \frac{M}{4\pi r_0^3 \left[\ln\left(1+\frac{R}{r_0}\right) - \frac{\frac{R}{r_0}}{1+\frac{R}{r_0}} \right]}. \tag{2.29}$$

The kinetic energy density is defined in terms of the average velocity dispersion, σ_υ, to be

$$\rho_K = 1/23/V \int \rho \sigma_\upsilon^2 dV = 9/2 \frac{r_0^3}{R^3} \rho_0 \int_0^R \frac{r}{[r+r_0]^2} \sigma_\upsilon^2 dr. \tag{2.30}$$

Assuming a constant average velocity dispersion, it reads

$$\rho_K = 1/2M/V 3\sigma_\upsilon^3 = 9/2 \frac{r_0^3}{R^3} \rho_0 \left[\ln\left(1+\frac{R}{r_0}\right) - \frac{R}{R+r_0} \right]. \tag{2.31}$$

The potential energy is given by

$$\rho_W = -\frac{4\pi}{4\pi R^3/3} \int_0^R \frac{\rho(r) G M(r)}{r} r^2 dr =$$

$$= -\frac{3GM^2}{4\pi R^3 r_0} \frac{\left[\left(1+\frac{R}{r_0}\right) \frac{1}{2} \left(1+\frac{R}{r_0}\right) - \ln\left(1+\frac{R}{r_0}\right) - \frac{1}{2} \right]}{\left[\left(1+\frac{R}{r_0}\right) \ln\left(1+\frac{R}{r_0}\right) - \frac{R}{r_0} \right]^2}. \tag{2.32}$$

The existence of interaction between dark energy and dark matter is estimated by comparing the ratio ρ_K/ρ_W with the expected –1/2 value arising from the virial theorem. Taking the ratio of last two equations we can find:

$$\frac{\rho_K}{\rho_W} = -\frac{3/2\frac{r_0}{GM}\sigma_v^2\left[\left(1+\frac{R}{r_0}\right)\ln\left(1+\frac{R}{r_0}\right)-\frac{R}{r_0}\right]^2}{\left[\left(1+\frac{R}{r_0}\right)1/2\left(1+\frac{R}{r_0}\right)-\ln\left(1+\frac{R}{r_0}\right)-1/2\right]}. \tag{2.33}$$

Throughout our analysis, the errors of the ratios are computed according to the following equation:

$$\Delta\left(\frac{\rho_K}{\rho_W}(o_i)\right) = \sqrt{\sum_{p_i \epsilon o_i}\left(\frac{\partial \rho_K/\rho_W}{\partial p_i}\Delta(p_i)\right)^2}, \tag{2.34}$$

where o_i are the parameters carrying measurement errors and are defined for each cluster as $o_i = \sigma_v, M$ and as $o_i = \sigma_v, r_0, \rho_0$.

If one neglects the gas and galaxy contributions to the gravitational mass, the gas density profile $\rho_{\rm gas}$ in hydrostatic equilibrium with the above dark matter potential satisfies the equation (2.11) and described as

$$\frac{d\ln\rho_{\rm gas}}{dr} = -\frac{\mu m_{\rm p}}{kT}\frac{GM(r)}{r^2}. \tag{2.35}$$

Equation (2.35) can be formally integrated to yield

$$\ln\frac{\rho_{\rm gas}(r)}{\rho_{\rm gas,0}} = -B\int_0^{r/r_s}\frac{m(x)}{x^2}dx, \tag{2.36}$$

where $B = \dfrac{4\pi G\mu m_{\rm p}\rho_s r_s^2}{kT}$.

Isothermal profile. Introduced first as the natural outcome of spherically symmetric dark matter self-gravitating infall, the isothermal density profile is simpler then the NFW one:

$$\rho = \frac{\rho_0}{\left(\frac{r}{r_0}\right)^2}. \tag{2.37}$$

Here the fiducial radius r_0 and the density ρ_0, or mass $M_0 = 4\pi/3\rho_0 r_0^3$, are arbitrary as the profile is self-similar: there is no characteristic scale, so we can chose the mass and total radius of the halo as the fiducial values, $M_0 = M$, $r_0 = R$. The mass is found by integrating Eq. (2.37) over the volume:

$$M \equiv 4\pi\int_0^R\frac{\rho_0 r^2}{\left(\frac{r}{r_0}\right)^2}dr = 4\pi r_0^2 R\rho_0 = M_0\frac{R}{r_0}. \tag{2.38}$$

The mean radius we can find with

$$M\langle R\rangle \equiv 4\pi \int\limits_0^R \frac{\rho_0 r^3}{\left(\frac{r}{r_0}\right)^2} dr = 2\pi r_0^2 \rho_0 R^2, \tag{2.39}$$

which after considering Eq. (2.38) can be written as follows:

$$\langle R\rangle = \frac{R}{2}. \tag{2.40}$$

The new kinetic energy density is now defined to be

$$\rho_K = 1/23/V \int \rho\sigma_v^2 dV = 9/2\frac{r_0^2}{R^3}\rho_0 \int\limits_0^R \sigma_v^2 dr = \frac{9}{8\pi}\frac{M_0}{R^3 r_0}\int\limits_0^R \sigma_v^2 dr. \tag{2.41}$$

Assuming a constant average velocity dispersion, it reads

$$\rho_K = \frac{1}{2}\frac{M}{V}3\sigma_v^2 = \frac{9}{8\pi}\frac{M_0}{R^3 r_0}R\sigma_v^2. \tag{2.42}$$

The potential energy is given by

$$\rho_W = -\frac{4\pi}{4\pi R^3/3}\int\limits_0^R \frac{\rho(r)GM(r)}{r} r^2 dr = -\frac{3GM_0^2}{4\pi R^2 r_0^2} = -\frac{3GM^2}{4\pi R^4}. \tag{2.43}$$

Taking the ratio of two last equations we find:

$$\frac{\rho_K}{\rho_W} = -\frac{3}{2}\frac{r_0}{GM_0}\sigma_v^2 = -\frac{3}{2}\frac{R}{GM}\sigma_v^2. \tag{2.44}$$

Moore's profile. We consider the Moore density profile that also arises as a suitable dark halo profile from N-body simulations [193–195]. It is believed to be quite accurate to describe galaxy size halo formation:

$$\rho = \frac{\rho_0}{\left(\frac{r}{r_0}\right)^{3/2}}\left[1 + \left(\frac{r}{r_0}\right)^{3/2}\right], \tag{2.45}$$

where ρ_0 and r_0 are the new mass density and shape parameters, respectively. The mass is found by integrating Eq. (2.45) over the volume:

$$M = 4\pi\rho_0 \int\limits_0^R \frac{r^2}{\left(\frac{r}{r_0}\right)^{3/2}\left[1 + \left(\frac{r}{r_0}\right)^{3/2}\right]} dr = \frac{8\pi}{3} r_0^3 \rho_0 \ln\left(1 + \left(\frac{R}{r_0}\right)^{3/2}\right). \tag{2.46}$$

The mean radius can then be defined with

$$M\langle R\rangle = 4\pi r_0^3 \rho_0 \int_0^R \frac{\left(\frac{r}{r_0}\right)^{3/2}}{1+\left(\frac{r}{r_0}\right)^{3/2}} dr, \tag{2.47}$$

and considering Eq. (2.46), it can be written as:

$$\langle R\rangle = \frac{3}{2} r_0 \left[\frac{R}{r_0} + \frac{\pi}{3\sqrt{3}} + \frac{1}{3}\ln\left(\frac{1-\sqrt{\frac{R}{r_0}}+\frac{R}{r_0}}{\left(1+\sqrt{\frac{R}{r_0}}\right)^2}\right) - \frac{2}{\sqrt{3}}\arctan\left[\frac{2\sqrt{\frac{R}{r_0}}-1}{\sqrt{3}}\right]\right] \Bigg/ \Bigg/ \ln\left(1+\left(\frac{R}{r_0}\right)^{3/2}\right). \tag{2.48}$$

We can get the shape parameter r_0 numerically by inverting $\langle R\rangle$, which can be then used to define the Moore density parameter, ρ_0, with the observed mass, M, contained within the radius, R, by inverting Eq. (2.46):

$$\rho_0 = \frac{3M}{8\pi r_0^3 \ln\left(1+\left(\frac{R}{r_0}\right)^{3/2}\right)}. \tag{2.49}$$

Thus, the kinetic energy density is defined to be

$$\rho_K = \frac{1}{2}\frac{3}{V}\int \rho\sigma_\upsilon^2 dV = \frac{9}{2}\frac{\rho_0 r_0^3}{R^3}\int_0^R \frac{r^{1/2}}{r^{3/2}+r_0^{3/2}}\sigma_\upsilon^2 dr. \tag{2.50}$$

Assuming a constant average velocity dispersion, it reads

$$\rho_K = 1/2M/V3\sigma_\upsilon^2 = 3\rho_0\left(\frac{r_0}{R}\right)^3 \ln\left(1+\left(\frac{R}{r_0}\right)^{3/2}\right)\sigma_\upsilon^2 = \frac{9}{8\pi}\frac{M}{R^3}\sigma_\upsilon^2. \tag{2.51}$$

The potential energy is given by

$$\rho_W = -\frac{4\pi}{4\pi R^3/3}\int_0^R \frac{\rho(r)GM(r)}{r} r^2 dr =$$

$$= -\frac{8\pi G r_0^5 \rho_0^2}{R^3}\int_0^{\frac{R}{r_0}} \frac{\ln(1+X^{3/2})}{X^{1/2}(1+X^{3/2})} dX = -\frac{8\pi G r_0^5 \rho_0^2}{R^3} F\left(\frac{R}{r_0}\right). \tag{2.52}$$

Taking the ratio of four last equations we find:

$$\frac{\rho_k}{\rho_W} = -\frac{r_0}{GM}\frac{\ln^2\left(1+\left(\frac{R}{r_0}\right)^{3/2}\right)}{F\left(\frac{R}{r_0}\right)}\sigma_v^2. \tag{2.53}$$

Einasto's profile. The Einasto density profile was originally used to describe the internal density profiles of galaxies and has been proposed as a better fit model for ΛCDM haloes [102]:

$$\rho = \rho_{\rm e}\exp\left[-d_n\left(\left(\frac{r}{r_{\rm e}}\right)^{1/n}-1\right)\right] = \rho_0\exp\left[-2n\left(\frac{r}{r_{-2}}\right)^{1/n}\right], \tag{2.54}$$

where $\rho_0 = \rho_{\rm e}e^{d_n}$ is the central density and r_{-2} the radius at which the slope $d\ln\rho/d\ln r = -2$, the isothermal value. The radius $r_{\rm e}$ is defined such that it contains half the total mass and d_n is an integration boundary to ensure that. n gives the strength of the density fall. From Eq. (2.54) the corresponding mass then reads:

$$M = 4\pi\int_0^R \rho_0\exp\left[-2n\left(\frac{r}{r_{-2}}\right)^{1/n}\right]r^2dr. \tag{2.55}$$

The mean radius then becomes defined with

$$M\langle R\rangle = 4\pi\int_0^R \rho_0\exp\left[-2n\left(\frac{r}{r_{-2}}\right)^{1/n}\right]r^3dr. \tag{2.56}$$

We can get the shape parameter r_{-2} from observing the mean intergalactic distance and numerically solving together the last two equations.

We can then use it to compute the central density parameter ρ_0 by making use of Eq. (2.55). The kinetic and potential energy densities are computed from their definition

$$\rho_K = \frac{1}{2}\frac{3}{V}\int\rho\sigma_v^2dV\rho_W, \tag{2.57}$$

$$\rho_W = -\frac{4\pi}{4\pi R^3/3}\int_0^R\frac{\rho(r)GM(r)}{r}r^2dr, \tag{2.58}$$

through numerical integration. Note that it is possible to perform the integrations analytically as done for the previous cases and find expressions relating the profile parameters and the virial ratio to the data M, $\langle R\rangle$ and σ. However, since these expressions for the Einasto profile are not particularly illuminating we will omit them in our studies (see, Chapter 2.6).

Burkert's profile. The Burkert density profile for dark matter halo given as [55]

$$\rho = \frac{\rho_s}{(1 + (r/r_s))[1 + (r/r_s)^2]}, \tag{2.59}$$

where the central density ρ_s is taken to be $0.05 M_\odot/pc^3$, and the scale radius r_s is computed from the mass of the DM halo $M_{200} = 10^{11} M_\odot$. In the inner part of the Burkert halo the profile has a core structure, while the slope approximates to –3 in the infinity. The cumulative mass profile with such a distribution diverges as $r \to \infty$. In fact, the Burkert profile is a phenomenological formula, which provides a good fit to the observed data to less than the virial radius $r_{\rm vir}$ and not valid to arbitrarily large distance from the galactic center. Instead of truncating the profile sharply at $r_{\rm vir}$, we have chosen an exponential cut-off for $r > r_{\rm vir}$, which sets in at $r_{\rm vir}$ and turn-off in a scale $r_{\rm decay}$

$$\rho = \frac{\rho_s}{(1+c)(1+c^2)} \left(\frac{r}{r_{\rm vir}}\right)^\alpha \exp\left[-\frac{r - r_{\rm vir}}{r_{\rm decay}}\right] \text{ for } (r > r_{\rm vir}), \tag{2.60}$$

where $c \equiv r_{\rm vir}/r_s$ is the concentration parameter. In order to ensure a smooth transition between last two equations ar $r_{\rm vir}$, we require the logarithmic slope there to be continuous. This leads to

$$\alpha = \frac{3 r_{\rm vir}}{r_{\rm decay}} - \frac{2c^2}{1+c^2} - \frac{c}{1+c}. \tag{2.61}$$

We consider the simulations between a minimum radius $r_{\rm min}$ and a maximum radius $r_{\rm max}$. The minimum radius is chosen such that it has sufficient particles for us to analyze. The maximum radius is equal to the virial radius plus several $r_{\rm decay}$. Here we adopt three $r_{\rm decay}$ ($r_{\rm decay} = 0.1\, r_{\rm vir}$). In addition, we add a boundary at the maximum radius. If the halo is stable, it is in homeostasis, that is, at any time the number of particles which move out off the boundary is equal to that of particles which move in. In the case of Burkert halo, the hallo will not be stable in the outer region, if not adding such a boundary.

King's profile. King introduced [152] two dynamical models of self-gravitating stellar systems. These were successfully applied to globular clusters and later extended to elliptical galaxies. A King profile can be described in terms of the following parameters: tidal radius r_t, central brightness $\sum_0$ and core radius r_c, at which the brightness is $\sum_0 /2$. Generally the curves are labeled in terms of a quantity $c = \log(r_t/r_c)$. For sufficiently small r, all King curves have a zero gradient. The model with $r = \infty$ has a slope of –1 at large r and corresponds to the isothermal sphere (see, Eq. (2.17) and Section 2.2.2).

King's profiles are based on specific dynamical models, and provide good fits to globular cluster surface brightness. However, recent studies have shown that these are not really suitable for clusters and galaxies.

Sersic's profile. This profile describes how the intensity I of a galaxy cluster varies with distance R from its center. The Sersic profile has the form

$$\ln I(R) = \ln I_0 - kR^{1/n}, \tag{2.62}$$

where I_0 is the intensity at $R = 0$. The parameter n, called Sersic index, controls the degree of curvature of the profile. The smaller the value of n, the less centrally concentrated the profile is and shallower the logarithmic slope at small radii is:

$$\frac{d\ln I}{d\ln R} = -(k/n)R^{1/n}. \tag{2.63}$$

2.2.4. Dark matter halo in galaxies and galaxy cluster: controversies

The problem of dark matter haloes formation has a long history going back to the seminal paper by [124, 125], who studied the density profile formation using the collapse of a spherical perturbation in an expanding background (see [78, 81] for a review, and [79, 80, 84] for the changes to halo formation due to dark energy, and [21] for limits of the dark matter scenario). Due to this approach and several following analytical models, for example [43, 97, 132], it was found that the density profiles are described by power-laws in all the radius range. More recent semi-analytical models (e.g., [19, 20, 82, 99, 100, 262, 268, 288, 289]) showed that the profile is not a power-law, similarly to N-body simulations results (e.g., for example, [139,140,203] NFW), and [53,141,153,195,204,205,224]) found that the spherically averaged density profiles of the N-body dark matter halos are similar, regardless of the mass of the haloes or the cosmological model [58, 84, 88—90].

The NFW profile is given (2.22), where ρ_c is the critical density of the Universe at the cluster's redshift z, and Δ_c is the virial over density. The scale radius r_s is connected to the virial radius $r_{\rm vir}$ through the concentration parameter $c = r_{\rm vir}/r_s$ [1].

In NFW works, it was shown that the concentration parameter is larger for smaller mass haloes, since these haloes formed before the high mass ones, when the Universe was denser. The concentration—mass relation has been studied by many authors. In works [53, 107], it was suggested explanation of the concentration-mass relation through simple models. The model in [53] used two parameters K, determining the initial concentration parameter of collapsing haloes, and F, ratio among the initial collapse mass and the final virial mass

[1] The value of $r_{\rm vir}$ in a spherical model collapse is analytically defined as $r_{\rm vir} = 178$ (for the CDM model) being approximated to r_{180}, while the density contrast corresponding to $r_{\rm vir} = r_{101}$ [48] in the ΛCDM cosmology. The values of the virial radius are inevitably in observations, somewhat arbitrary, the typical values are r_{500} or r_{200} [153].

of the halo at present. Two parameters power-laws were used in [94, 256], and more recently in [38, 107].

The logarithmic density slope at the small scales that is also known as the inner slope is given by

$$\alpha = -\frac{d\log\rho}{d\log r}\bigg|_{r\to 0} = 1. \tag{2.64}$$

The quoted profile diverges as $\rho \propto r^{-1}$ in the inner part, and at large radii behaves as $\rho \propto r^{-3}$. The inner slope is even steeper in [167] profile ($\rho \propto r^{-1.5}$). More recent simulations (e.g., [127,261]) showed that density profiles are better fitted by the Einasto profile, which becomes shallower towards the centre of the halo (see Section 2.2.3 in detail). The Einasto profile is a rolling power-law first introduced to describe the distribution of stars in Milky Way. It takes the form:

$$\ln(\rho/\rho_{-2}) = -\frac{2}{\alpha}[(r/r_{-2})^{\alpha} - 1], \tag{2.65}$$

where ρ_{-2} is the density at r_{-2}, and r_{-2} is the radius at which the logarithmic slope of the density is isothermal (i.e. –2), analogous to r_s in the NFW profile.

Unfortunately, N-body simulation predictions are not supported by the observations. Observations of the inner part of density profiles of dwarfs galaxies and dwarfs galaxies with low surface brightness are characterized by a core-like structure (e.g. [10, 64, 71, 72, 90, 117, 121, 151, 194, 245, 283]), and a similar problem is evidenced when studying the clusters of galaxies inner profile. Density profiles of clusters has been studied through X-ray observations, strong and weak lensing. For what concerns the mass determination of galaxy clusters using X-ray observations, one usually assumes that the ICM (intra-cluster medium) is in the hydrostatic equilibrium and the cluster is approximately spherical. In this case, we have Eq. (2.70). Gas density, $\rho_{\rm gas}$, is usually described by the β model [60, 64] based on the assumption that the galaxy density mass distribution is in a good agreement with a King profile, and the gas is in the hydrostatic equilibrium as Eq. (2.87). The model's parameters are determined analyzing the X-ray surface brightness profile obtained from X-ray image analysis. The total mass $M(r)$ can be obtained when $\rho_{\rm gas}$ and $T(r)$ are got through X-ray observations. A precise mass determination (in the NFW model) gives a consistent description of the mass distribution in the relaxed clusters [54, 223, 277].

X-ray temperature measurements give some information on the galaxy cluster structure in the range 50—500 kpc [48]. At smaller radii, the temperature determination is limited by the instrumental resolution and cluster's substructuring [252]. X-ray measurements are also limited by the "cooling flows" presence and the breaking of the assumption for hydrostatic equilibrium [15]. The inner slope calculation of the density profiles with the X-ray observational data brought to the discrepant values (e.g., 0.6 [110], 1.2 [166], 1.9 [14]).

Another technique used to study the DM distribution in clusters is gravitational lensing. Weak lensing of background galaxies is used to reconstruct the mass distribution in the outer parts of clusters [62]. The resolution that can be achieved is able to constrain profiles inside 100 kpc. Strong lensing is used to study the DM distribution in the inner parts of clusters, it has a typical sensitivity to the projected mass distribution inside $\simeq$100—200 kpc, with limits at $\simeq$10—20 kpc [6, 120, 168, 269].

Discrepant results have been sometime obtained when using the lensing method. Smith et al. [257] found $\alpha > 1$ at 1 % of $r_{\rm vir}$ by studying the tangential and radial arcs of A383. A much smaller value α was obtained in [208, 248], for the same cluster, using lensing and through the aid of stellar kinematics of the central region. Tyson et al. [270] found $\alpha = 0.57 \pm 0.024$ for CL 0024 + 1654, while Kneib et al. [154] found that a NFW profile fits the profile in the radius range 0.1-several $r_{\rm vir}$. Sand et al. [246] found a cored profile with $\alpha = 0.35$ for MS 2137.3 – 2353, while Gavazzi et al. [119] concluded that the precise value of the slope depends on the mass-to-luminosity ratio of the Brightest Cluster Galaxy (BCG).

In summary, N-body simulations are not always in agreement with the inner slopes of dwarf galaxies, LSBs and clusters of galaxies, and in the case of clusters of galaxies, observations may even disagree for the very same cluster [252, 258, 271]. Several could be the reasons of the discrepancy (e.g., (a) different definition of the slope, which sometimes refers to the DM and sometimes to the total mass; (b) use of observational techniques with different/limited dynamic range in radius; (c) not taking into account the stellar mass of the BCG). In order to obtain more sure constraints on the central part of the density profiles, one should use combined methods [207] (weak + strong lensing); [47] (weak + strong lensing); [174] (X-ray + weak lensing), or better constraints on the central part of the density profiles can be obtained through stellar kinematics of the central galaxy ($\simeq$1—200 kpc region).

The authors [247] studied the clusters MS 2137 – 23; A383; A963; RXJ1133; MACS 1206; A1201, separating the contribution to the halo coming from the dark matter from that coming from the baryonic and stellar mass of the BCG. They found a profile flatten than $\alpha < 1$ except for RXJ1133. Newman et al. [208] found $\alpha < 1$ (95 % CL (confidence level)) for A383. A detailed analysis of DM and baryonic distributions in A611 is presented in [207], where finding a slope $\alpha < 0.3$ (68 % CL).

Summarizing, at least some clusters of galaxies have inner density-profile slopes shallower that those obtained in N-body simulations, in agreement with what happens, as previously reported, with the density profiles of dwarfs galaxies and LSBs. We want to recall here that, similarly to Sand's result concerning the quoted clusters, the galaxies NGC 2976, NGC 4605, NGC 5949, NGC 5963 and NGC 6689, have inner slopes going from very flat to cuspy, and [70],

using a sample from The HI Nearby Galaxy Survey (THINGS) found that the best fit to rotation curves, and then the inner slope α of their density profile, depends on their mass. Several papers have shown the fundamental role of baryons in shaping the density profiles of structures. Different processes have been pointed out capable of flattening the inner density profile, transferring energy from stellar baryons to the dark matter, heating it and lowering the central dark matter density [80, 118,149, 150, 158, 171, 173, 179, 183, 190, 237, 238, 286].

2.3. Dark matter in the X-ray galaxy clusters

With cosmic X-ray observation, which started in the 1960s, clusters were found to be the most luminous class of X-ray sources in the Universe after some types of active galactic nuclei (AGNs). The X-ray emission originates from the inracluster medium (ICM), a hot (10^7—10^8 K) and low density (10^{-4}—10^{-2} cm^{-3}) plasma in the intracluster space. Extensive observations with previous X-ray satellites such as HEAO-1, Einstein, Ging, ROSAT, and ASCA provided measurements of densities and temperatures of the ICM. These results implied that the mass if the ICM is comparable to, or even greater than that of the stellar component in member galaxies. Characteristic emission lines from ionized heavy elements (mainly from iron) were detected in the X-ray spectra of clusters. The implied sub-solar metallicity of the ICM indicates that the ICM is a mixture of the primordial gas and that reprocessed in the stellar interior. Moreover, X-ray observations of the ICM have provided independent and more accurate measurements of the total mass, and hence of the dark matter, in clusters of galaxies. A rough agreement between the optical and X-ray measurements of the total cluster mass supports the basic assumption that the ICM is in hydrostatic equilibrium (see Section 2.2). According to a contemporary consensus, about 5—10 % of a cluster mass is in the stellar component, another 10—20 % is in the ICM, and the rest is in the dark matter (see Fig. 2.1).

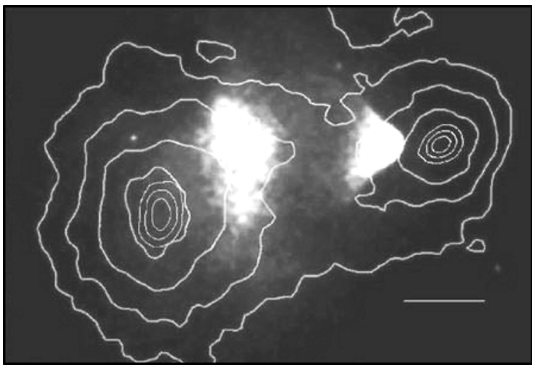

Fig. 2.1. The Bullet Cluster (image of merger galaxy cluster is taken from Chandra X-ray Center (2008))

The Bullet cluster provides the best current evidence for the nature of dark matter. It consists of two subclusters, a larger one on the left, and a smaller one on the right. They have recently collided and traveled through each other. One component of the image is an optical image which shows the vi-

sible galaxies. Superposed on it, in red, is an X-ray image, which shows the heated intergalactic gas, that has been slowed down by the collision and left behind the galaxy components of the clusters. The blue color is another superposed image, which represent an estimate of the total mass distribution of the cluster, based on gravitational lensing.

The first observations showed that such structures are associated with deep gravitational potential wells, containing galaxies with a typical velocity dispersion along the line of sight of $\sigma_v \sim 10^3$ km s^{-1}. The crossing time for a cluster of size R can be defined as

$$t_{\rm cr} = \frac{R}{\sigma_v} \approx 1 \left(\frac{R}{\rm Mpc}\right)\left(\frac{\sigma_v}{10^3 \text{ km s}^{-1}}\right)^{-1} \text{ Gyr}. \tag{2.66}$$

Therefore, in a Hubble time, $t_{\rm H}$ 10 h^{-1} Gyr, such a system has enough time in its internal region, 1 h^{-1} Mpc, to dynamically relaxed condition that cannot be attained in the surrounding, ∼10 Mpc, environment. Assuming virial equilibrium, the typical cluster mass is

$$M \approx \frac{R\sigma_v^2}{G} \approx \left(\frac{R}{1 \text{ h}^{-1} \text{ Mpc}}\right)\left(\frac{\sigma_v}{10^3 \text{ km s}^{-1}}\right)^2 10^{15} \text{ h}^{-1}\, M_\odot. \tag{2.67}$$

Observations of galaxy clusters in the X-ray band have revealed a substantial fraction (∼15 %) of the cluster mass to be in the form of hot diffuse gas, permeating its potential well. If this gas shares the same dynamics as member galaxies, then it is expected to have a typical temperature

$$k_{\rm B}T = \mu m_{\rm p} \sigma_v^2 \approx 6 \left(\frac{\sigma_v}{10^3 \text{ km s}^{-1}}\right)^2 \text{ keV}, \tag{2.68}$$

where $m_{\rm p}$ is the proton mass and μ is the mean molecular weight ($\mu = 0.6$ for a primordial composition with a 76 % fraction contributed by hydrogen). Observational data for distant clusters (see Fig. 2.2) actually follow this relation, although with some scatter and with a few outliers. This correlation indicates that the idealized picture of clusters as relaxed structures in which both gas and galaxies feel the same dynamics is a reasonable representation.

At the high energies implied by Eq. (2.68), the ICM behaves as a fully ionized plasma, whose emissivity is dominated by thermal bremsstrahlung. By integrating the above equation over the energy range of the X-ray emission and over the gas distribution, one obtains X-ray luminosities $L_X \sim 10^{43}$–10^{45} erg s^{-1}. That is why X-ray clusters are the powerful luminous sources which are identified as the extended ones at the large cosmological distances.

Assuming spherical symmetry, the condition of hydrostatic equilibrium connects the local gas pressure P to its density ρ_g according to

$$\frac{dP}{dR} = -\frac{GM(<R)\rho_g(R)}{R^2}. \tag{2.69}$$

By inserting the equation of state for a perfect gas, $P = \rho_g k_{\rm B} T/\mu m_{\rm p}$, into Eq. (2.69), one can express $M(<R)$, the total gravitating mass within R, as

$$M(<R) = -\frac{k_{\rm B} T R}{G\mu m_{\rm p}} \left(\frac{d\log(\rho_g)}{d\log(R)} + \frac{d\log(T)}{d\log(R)} \right). \tag{2.70}$$

If R is the virial radius, then at redshift z we have $M \propto R^3 \rho_0 (1+z)^3 \times$ $\times\, \Delta_{\rm vir}(z)$, where ρ_0 is the mean cosmic density at present time and $\Delta_{\rm vir}(z)$ is the mean overdensity within a virialized region. For an Einstein—de-Sitter cosmology, $\Delta_{\rm vir}$ is constant and therefore, for an isothermal gas distribution, Eq. (2.70) implies $T \propto M^{2/3}(1 + + z)$. Such relations show how quantities such as ρ_g and T, which can be obtained from X-ray observations, are directly related to the cluster mass. Thus, in addition to providing an efficient method to detect clusters, X-ray studies of the ICM allow one to measure the total gravitating cluster mass, which is the quantity predicted by theoretical models for cosmic structure formation. A widely used description of the gas density profile is the β-model (see, Section 2.2.2),

$$\rho_g(r) = \rho_{g,0} \left[1 + \left(\frac{r}{r_c} \right)^2 \right], \tag{2.71}$$

which was introduced by Cavaliere & Fusco-Femiano [60, 64] to describe an isothermal gas in hydrostatic equilibrium within the potential well associated with a King dark-matter density profile. The parameter β is the ratio between kinetic dark-matter energy and thermal gas energy. This model is a useful guideline for interpreting cluster emissivity, although over limited dynamical ranges. Now, with the Chandra and XMM-Newton satellites, the X-ray emissivity can be mapped with high angular resolution and over larger scales. These new data have shown that Eq. (2.71) with an unique β value cannot always describe the surface brightness profile of clusters.

Kaiser [145] described the thermodynamics of the ICM by assuming it: "to be entirely determined by gravitational processes, such as adiabatic compression during the collapse and shocks due to supersonic accretion of the surrounding gas. As long as there are no preferred scales both in the cosmological framework (i.e., $\Omega_m = 1$ and power-law shape for the power spectrum at the cluster scales) and in the physics (i.e., only gravity acting on the gas and pure bremsstrahlung emission), then clusters of different masses are just a scaled version of each other, because bremsstrahlung emissivity predicts $L_X \propto M \rho_g T^{1/2}$, $L_X \propto T_X^2 (1+z)^{3/2}$ or, equivalently $L_X \propto M^{4/3}(1+z)^{7/2}$. Furthermore, if we define the gas entropy as $S = T/n^{2/3}$, where n is the gas density assumed fully ionized, we obtain $S \propto T(1+z)^{-2}$".

It was soon recognized that X-ray clusters do not follow these scaling relations. As we discussed in the previous sections, the observed luminosity-

temperature relation for clusters is $L_X \propto T^3$ for $T \gtrsim 2$ keV and possibly even steeper for $T \lesssim 1$ keV groups. This result is consistent with the finding that $L_X \propto M^\alpha$ with $\alpha \simeq 1.8 \pm 0.1$ for the observed mass-luminosity ratio (see bottom panel of Fig. 2.2). Furthermore, the low-temperature systems are observed to have shallower central gas-density profiles than the hotter systems, which turns into an excess of entropy in low-T systems with respect to the $S \propto T$ predicted scaling.

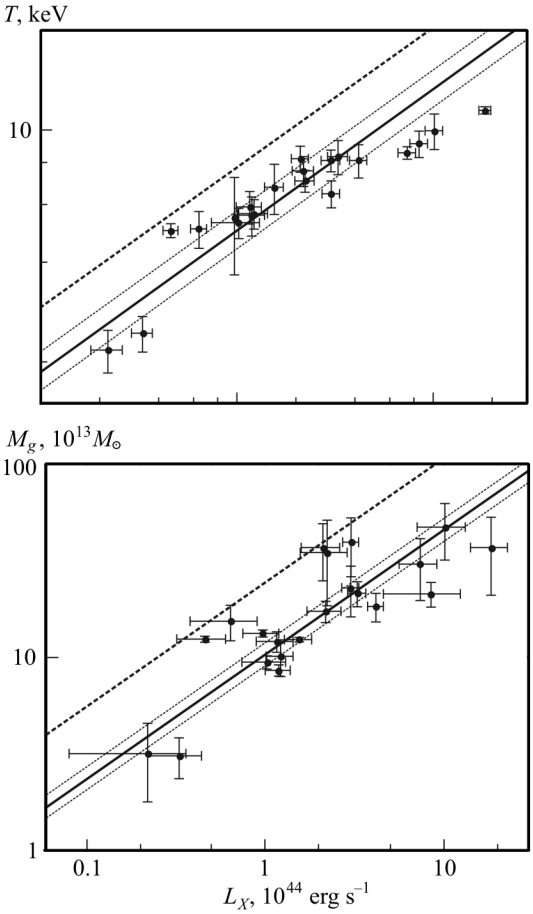

Fig. 2.2. (Top) The relation between luminosity and intracluster temperature, T, for distant ($z > 0.15$) galaxy clusters. (Bottom) The relation between X-ray luminosity and the mass contained within the radius encompassing an average density $200\rho_c$. The two solid and dotted lines are the best power-law fit with 1σ confidence level, the two dashed lines represent L_X-T relation for nearer clusters. The figures are taken from Babyk & Vavilova [30]

A possible interpretation for the breaking of the scaling relations assumes that the gas has been heated at some earlier epoch by feedback from a non-gravitational astrophysical source. This heating would increase the entropy of the ICM, place it on a higher adiabat, prevent it from reaching a high central density during the cluster gravitational collapse and, therefore, decrease the X-ray luminosity. For a fixed amount of extra energy per gas particle, this effect is more prominent for poorer clusters, i.e., for those objects whose virial temperature is comparable with the extra-heating temperature. As a result, the self-similar behavior of the ICM is expected to be preserved in hot systems, whereas it is bro ken for colder systems.

X-ray studies of galaxy clusters provide:

1) an efficient way of mapping the overall structure and evolution of the Universe;

2) an invaluable means of understanding their internal structure and the overall history of cosmic baryons.

2.3.1. Evolution of the X-ray galaxy clusters

The evolution of the Universe is divided broadly into the structure formation and the chemical evolution. Clusters of galaxies are regarded as useful probes to study the both evolutions by several reasons:

1) since the dynamical time-scale of clusters is close to Hubble time, clusters retain the cosmological initial conditions well;

2) clusters can be approximated that they consist of dark matter, hot gas, and galaxies, and also the shape is almost spherical, thus they are easy to deal with;

3) though a part of metals produced in galaxies run away into ICM, they do not escape from clusters.

We can thus obtain the total metal abundance without emission. In order to obtain the properties of clusters, X-ray observations are particularly suited, because the X-ray-emitting gas gives us the physical parameters such as temperature, mass, and metal abundance.

Galaxy clusters form through the hierarchical accretion of cosmic matter. The end products of this process are the virialized structures that feature, in the X-ray band, similar radial profiles of the surface brightness $S_{\rm b}$ [277, 283] and of the plasma temperature $T_{\rm gas}$ [245, 256]. Such measurements have definitely improved in recent years thanks to the arcsec resolution and large collecting area of the present X-ray satellites, like Chandra and XMM-Newton, but still remain difficult, in particular in the outskirts, because of the low surface brightness associated to these regions. Present observations provide routinely reasonable estimates of the gas density, $n_{\rm gas}$, and temperature, $T_{\rm gas}$, up to about R_{2500} ($\sim 0.3\, R_{200}$; R_{Δ} is defined as the radius of the sphere that encloses a mean mass density of Δ times the critical density at the cluster's redshift; R_{200} defines approximately the virialized region in galaxy clusters). Only few cases provide meaningful measurements at R_{500} ($\sim 0.7\, R_{200}$) and beyond [272, 281]. The X-ray surface brightness is a quantity much easier to characterize than the temperature and it is still rich in physical information being proportional to the emission measure, i.e. to the gas density, of the emitting source.

Clusters of galaxies are the largest collapsed structures in the Universe with total masses up to $10^{15} M_{\odot}$. Over 80 % of their mass resides in the form of dark matter. The remaining mass is composed of baryons, most of which (about 85 %) is a diffuse, hot $T > 10^7$ K plasma (the intracluster medium, ICM) that radiates primarily in the X-ray band. Thus in galaxy clusters, through the radiation from the hot gas and the galaxies, we can observe and study the interplay between the hot and cold components of the baryonic matter and the dark matter. X-ray observations of the evolving cluster population provide a unique opportunity to address such open and fundamental questions:

1. How do hot diffuse baryons dynamically evolve in dark matter potentials?

2. How and when was the excess energy which we observe in the intergalactic medium generated?

3. What is the cosmic history of heavy-element production and circulation?

Clusters grow via accretion of dark and luminous matter along filaments and merger of smaller clusters and groups. X-ray observations show that many present epoch clusters are indeed not relaxed systems, but are scarred by shock fronts and contact discontinuities, and that the fraction of unrelaxed clusters likely increases with redshift. Although the gas evolves in concert with the dark matter potential, this gravitational assembly process is complex, as illustrated by the temporary separations of dark and X-ray luminous matter in massive merging clusters such as the "Bullet Cluster" (see Fig. 2.1). In addition to the X-ray emitting hot gas, the relativistic plasma seen through synchrotron emission in merging clusters is an important ICM component with at present few observational constraints.

High-resolution X-ray spectral imaging can determine the subcluster velocities and directions of motions by combining redshifts measured from X-ray spectra (which give relative line-of-sight velocities) and total subcluster velocities deduced from temperature and density jumps across merger shocks or cold fronts [281]. These measurements combined with high quality lensing observations from instruments such as the LSST will probe how the hot gas reacts in the evolving dark matter potential.

Sensitive hard X-ray (10—40 keV) imaging can reveal inverse Compton emission from ICM. Although this emission has so far not even clearly been detected, it promises unique information on the energy density of the relativistic particles, and when combined with next generation radio observations like SKA, would probe the history of magnetic fields in clusters. Capabilities like those of IXO are needed to understand these observationally elusive, but important components of the ICM.

Further crucial insight into cluster assembly can be gleaned from measurements of the dark matter distribution in the most relaxed systems. Cosmological numerical simulations of large-scale structure collapse robustly predict that the dark matter distribution should be cuspy, vary with system mass, and evolve with time. Current X-ray observations of bright, local systems confirm the cuspy nature of the distribution, and show some indication for a variation with mass [223]. With, IXO, we can dramatically increase the mass range available for these test, and, for the first time, tackle the question of evolution by determining the mass profiles up to high redshift ($z \sim 2$), even for low mass systems.

One of the most important revelations from X-ray observations, supported by recent optical and IR studies, is that non-gravitational processes, particularly galaxy feedback from outflows created by supernovae and supermassive black holes (SMBH), must play a fundamental role, both in the history of all massive galaxies and in the evolution of groups and clusters as a whole.

Galaxy feedback is lakely to provide the extra energy required to keep the gas in cluster cores from cooling all the way down to molecular clouds, to cure the over-cooling problem, to regulate star formation, and to produce the red sequence.

It is now well established from XMM-Newton and Chandra observations of local clusters and groups that their hot atmospheres have much more entropy than expected from gravitational heating alone [54, 262]. Determining when and how this non-gravitational excess energy was acquired will be an essential goal of the next generation X-ray observatory. Galaxy feedback is a suspected source, but understanding whether the energy was introduced early in the formation of the first halos (with further consequence on galaxy formation history), or gradually over time by AGN feedback, SN driven galactic winds, or an as-yet unknown physical process, is crucial to our understanding of how the Universe evolved.

The various feedback processes, as well as cooling, affect the intergalactic gas in different ways, both in terms of the level of energy modification and the time-scale over which this occurs. Measuring the evolution of the gas entropy and metallicity from the epoch of cluster formation is the key information required to disentangle and understand the respective role for each process. Since non-gravitational effects are most noticeable in groups and poor clusters, which are the building blocks of today's massive clusters, these systems are of particular interest.

The first open question concerns the production of heavy elements over cosmic time. Chandra and XMM-Newton observations of clusters hint at a Fe abundance evolution from $z = 1$ to the present [36, 180]. To give a definitive answer on when the metals are produced, we need to extend abundance studies to higher redshifts and for all astrophysical abundant elements. In local systems, the abundance pattern of elements from O to Fe group, that are produced by supernovae, indicate that both type I and type II SN contribute to the enrichment [146]. However, these measurements only provide a fossilized integral record of the past SN enrichment and thus the evolution of supernovae remains largely unconstrained. Furthermore, the main source of C and N, which can originate from a wide variety of sources (including stellar mass loss from intermediate mass stars, whose cosmic history is poorly known) is still under debate.

The second fundamental — and even more complex — open question is how the metals produced in the galaxies are ejected and redistributed in the ICM. Although AGN outflows as well as galaxy — galaxy interactions can add metals to the ICM, studies of local cluster abundance profiles suggest that the metal enrichment of the ICM is due primarily to galactic winds and ram pressure stripping of enriched gas from galaxies by the ICM [146], an example being the ram-pressure stripped tail of the Virgo cluster galaxy M86. These processes

would result in different distributions for the metallicity within the cluster and over time. For example, at high redshifts, galactic winds are expected to be effective at enriching the ICM, while at lower redshifts, when massive clusters have formed, the dense ICM, especially in the cluster cores, can ram-pressure strip the enriched gas from galaxies and can even suppress galactic winds and quench star formation. The enriched material is not expected to be immediately mixed with the ICM, and in fact in the brightest, best studied nearby clusters, current X-ray observations show that the metallicity distribution in the ICM is inhomogeneous [251]. Thus by mapping the metallicity in samples of clusters over cosmic time, one can untangle the various transport processes that contribute to the enrichment. In addition, if the mass in metals is calculated assuming that the metallicity is uniform, this will miss estimate the true metal mass in the clusters.

Measurements of the metallicity distribution in clusters, for a wide range of masses, dynamical states, and redshifts, are required in order to understand the ejection and redistribution process within clusters. These studies would also have far reaching consequences for our understanding of the excess energy that is present in the ICM, as some of the transport processes (SNe winds and AGN outflows) also inject energy into the ICM, as well as for our understanding of environmental effects on the galaxy star formation history, when combined with optical and IR observations.

Past and current X-ray mission allow us to observe only a fraction of the volume occupied by the ICM. Indeed, typical measures of the surface brightness, temperature and metal abundance extend out to a fraction of the virial radius. The coming into operation of the second generation of medium energy X-ray telescopes at the turn of the millennium, has resulted in relatively modest improvements in our ability to characterize cluster outskirts.

2.3.2. Observational studies of X-ray cluster evolution

X-ray emission process. The X-ray spectrum emitted from an ionized plasma of the low density ($\sim 10^{-3}$ cm^{-3}) ICM is described with a combination of thermal bremsstrahlung (free-free) emission and line emission from heavy elements. In the temperature range of typical cluster (1 kV $< kT <$ 10 keV) the total emission is dominated by the free-free emission if the abundance of heavy elements does not exceed the solar abundance by very much. The emissivity of the free-free emission at a frequency ν from hot plasma with an electron temperature of T_g is given by

$$\epsilon_\nu = \frac{2^5 \pi e^6}{2 m_\mathrm{e} c^3} \left(\frac{2\pi}{2 m_\mathrm{e} k}\right)^{1/2} n_\mathrm{e} \sum_i Z_i^2 n_i g_{ff}(Z, T_g, \nu) \times \\ \times T_g^{-1/2} \exp(-h\nu/kT_g) = \Lambda(T, Z, \nu) n_\mathrm{e}^2, \tag{2.72}$$

where Z_i and n_i are the charge and number density of the ion i, respectively, and n_e is the electrons number density. The Gaunt factor is a correction factor for quantum mechanical effects and is approximately $g_{ff} \sim 0.9(h\nu/kT)^{-0.3}$. The emissivity in a given bandpass, $\nu_1 < \nu < \nu_2$, is then

$$\epsilon^{ff} = \int_{\nu_1}^{\nu_2} \epsilon_\nu^{ff} d\nu = \Lambda(T, Z) n_e^2. \tag{2.73}$$

The $\Lambda(T, Z)$ is the cooling function, with T and Z representing the plasma temperature and the heavy element abundance, respectively. The contribution of the bremsstrahlung continuum to Λ increases as $\propto T^{1/2}$. It is useful to define the emission integral as

$$EI = \int n_e^2 dV, \tag{2.74}$$

where V is the volume of the cluster. If we assume that the ICM has a spatially-uniform temperature and abundance in the volume V, and that the ICM density is constant over the projected sky area S, then the luminosity L_X is given as

$$L_X = \int \epsilon^{ff} dV = EM \times S \times \Lambda(T, Z). \tag{2.75}$$

The EM is the emission measure defined as

$$EM = \int n_e^2 dl, \tag{2.76}$$

where l is the depth of the plasma along the line of sight. The emission integral determines the normalization of the spectrum, and the shape of the spectrum depends only on the temperature T and the heavy element abundance Z, and EI (or EM if S is known) from the observed X-ray spectra.

Emission of atomic lines becomes significant when the ICM temperature falls below a few keV. Since the temperature of the ICM is the same order as the K-shell ionization potentials of heavy elements such as O, Ne, Mg, Si, S and Fe, these elements become mainly He/H-like ions and are completely ionized. these ions are excited during collisions, and then emit their resonance K-lines. In lower temperature clusters, in which Fe ions are not only He-like but also of a low ionization status, the spectrum exhibits resonance L-lines at ∼1 keV. The emission lines and continuum spectra from the ionization equilibrium plasma have been calculated by various authors, [54, 223, 283], and so on (MEKAL model is usually applied to describe emission from hot plasma).

The MEKAL model is the model which describe the emission from hot intracluster diffuse gas (ICM) and named by Mewe—Kaastra—Liedahl. Mewe et al. [187, 188] calculated the atomic data for a hot optical thin plasma in

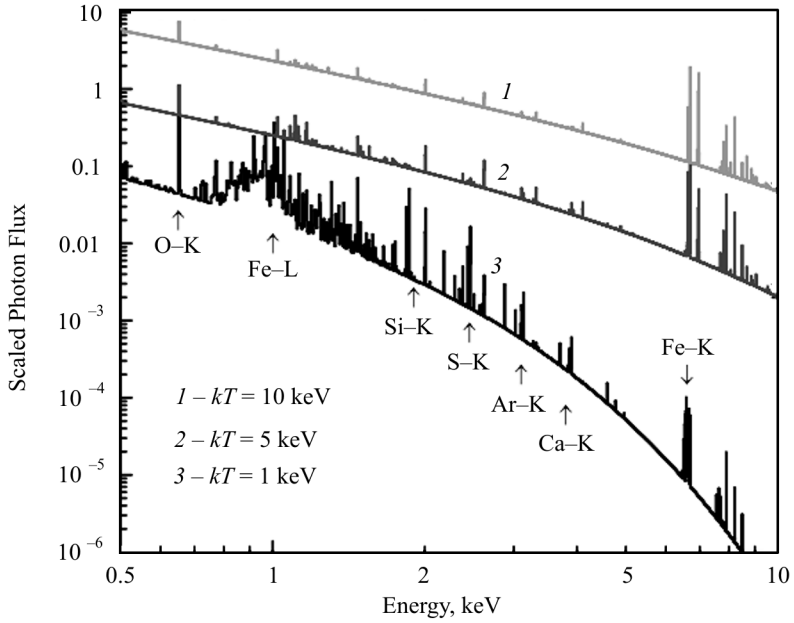

Fig. 2.3. Calculated X-ray spectra from optically thin hot plasma with various temperatures. The MEKAL plasma emission code is used, assuming a metal abundance of 0.3 solar. Vertical scale is arbitrary

1985, also Kaastra [143] then wrote the first code for fitting from these data in 1992 and then Liedahl et al. [167] improved the data for the Fe lines in 1995. This model is one of the most used models when fitting spectral data today and is the standard model in Xspec.

The MEKAL model (see Fig. 2.3) is the Xspec implementation and it takes a number of input parameters: temperature, metalicity, hydrogen density and normalization parameter. We will call the set of input parameters, $par = n_{\rm H}, Z, z, Norm, (E_0, E_1)$, which also contains the energy interval of the observation.

The amount of radiation that a volume of gas outputs is given by the emissivity $\epsilon = \Lambda(T)n^2$, where n^2 is the number density of the gas inside the volume we are looking at. The functional form $\Lambda_{par}(T)$ we select that to extract must be a function of temperature alone. That means that we need to fix the input parameters *par*, so that Xspec will output $\Lambda(T)$ and so that the values makes sense for the specific combination of instrument and source. But first we take a look at the definition of Λ:

$$\Lambda = \frac{L}{n_{\rm e}^2}, \tag{2.77}$$

which has the unit of energy per second times volume or $\mathrm{erg\,cm^3\,s^{-1}}$ or even

photons $\mathrm{cm}^3\,\mathrm{s}^{-1}$. Xspec calculates the flux form a model spectrum $M(E)$ like,

$$F = \frac{1}{E_1 - E_0} \int\limits_{E_0}^{E_1} M(E) dE. \tag{2.78}$$

This has the unit of either $\mathrm{erg\,cm}^{-2}\,\mathrm{s}^{-1}$ or photons $\mathrm{cm}^{-2}\,\mathrm{s}^{-1}$. And now we want to turn flux into luminosity per electrons squared:

$$\Lambda_{par} = \frac{L}{n_\mathrm{e}^2} = \frac{4\pi d_l^2 F}{n_\mathrm{e}^2}. \tag{2.79}$$

For specific combination of parameter par Xspec calculated the flux like:

$$F_{par} = \frac{Norm}{E_1 - E_0} \int\limits_{E_0}^{E_1} f(E) dE, \tag{2.80}$$

where $Norm$ and E_0 and E_1 are the normalization and energy band parameters in $par = n_H, Z, z, Norm, (E_0, E_1)$ and $f(E)$ is the functional form of the spectrum that Xspec calculates. In the documentation of Xspec [16] it is stated how $Norm$ should be interpreted:

$$Norm = \frac{10^{-14} \int n_\mathrm{e} n_H dV}{4\pi d_l^2 (1+z)^2}. \tag{2.81}$$

Metal distribution. The iron abundance in the intracluster gas is observed to be $\sim$0.3 solar, with only small variations ($\pm\sim$0.1) from cluster to cluster [275—278, 283]. A strong correlation between the total iron mass in clusters and the total luminosity of the E + SO cluster galaxies is observed [176]. The metal enrichment of the intracluster gas is likely caused by gas stripped out of the elliptical galaxy members. The iron abundance profile as a function of radius from the cluster center is generally flat, i.e., a constant abundance at all radii (except for some poor, low-mass clusters dominated by a single massive galaxy).

The existence and distribution of the chemical elements and their isotopes are a consequence of nuclear processes that taken place in the past in the Big Bang and subsequently in stars and in the interstellar medium where they are still ongoing. These processes have been studied theoretically and observationally (see, for example, the Chapter prepared by Pilyugin in the volume 2 of this monograph).

The main source of metal production is supernovae (SN), which are classified roughly into Type Ia and Type II. Type Ia SN are important contributors to iron-group elements in the galaxy. Type II SN are explosions of massive

stars, which have short lives of about 10 Myr with initial mass above about $10\,M_{\odot}$. Type II SN produce mainly α elements such as O, Ne, Mg, Si and S. The metal abundances for the elements are given by X-ray spectroscopy of the ICM. Since part of metals are transferred into ICM by galactic wind or ram pressure stripping, observation of the ICM, not galaxy only, gives total abundance. The observed ratio of Fe to α elements constrains the ratio of Type Ia to Type II and the explosion rate. This enables ua to study other essential subjects such as the initial mass function, and star formation rate based on z-evolution.

Sinse heavy elements can be produced only by thermonuclear reactions in stars and by supernovae, the presence of the emission lines found in the spectra from the ICM implies that heavy elements processed in galaxies largely contaminate the ICM.

Moreover, recent observational studies of the clusters with Chandra and XMM-Newton unveil a lot of new interesting abundance distribution in the cluster.

2.3.3. The distribution of baryon matter in the nearby X-ray galaxy clusters

To analyze the evolution of the baryon mass function of galaxy clusters we should provide relevant measurements for galaxy clusters at all redshifts, including the small ones. With this aim and to reveal the distribution of visible/dark matter we compiled a sample of 34 X-ray nearby galaxy clusters ($z < 0.2$). These clusters were selected from a larger sample of *Chandra* X-ray galaxy clusters ($0.01 < z < 1.5$), which is described fully in our work [34] (hereafter BVP sample). The main criteria were that clusters should be sufficiently symmetrical and each X-ray cluster image should trace the surface brightness profile at larger as possible radii. To satisfy the second statement we selected clusters with a wide exposure interval (not less 5000 s) and, moreover, under the condition that a virial radius fits on the line of sight. The value of a virial radius was taken as R_{200} (a providing accuracy is sufficient for the purposes of our study). Following these criteria, we excluded A754, A1750, A2151, etc. clusters from our BVP sample, nevertheless that are at $z < 0.2$, because of their irregular morphology or double structure. Our sample of 34 nearby X-ray galaxy clusters is given in Table 2.1.

We have measured the brightness profiles in concentric rings of equal logarithmic width, which were centered on the cluster's maximum brightness; the radii's ratio of inner and outer rings is equal to 1.1. We have used two types of profiles: the average azimuthal brightness profiles and profiles in six angle sectors 0—60, ..., 300—360. It allowed us to verify the choice of other "reasonable" centroid profiles: the measured surface brightness distribution at large radii were practically identical.

As for a cosmic X-ray background, we have measured it individually for each cluster because of a significant contribution to the overall brightness of X-ray galaxy cluster may occur even at large distances from the center. Usually, the X-ray cluster's surface brightness is about 5—20 % of the background near

Table 2.1. **The sample and results of approximation of the surface brightness profiles of galaxy clusters on $z < 0.2$ using β-model**

Name	T, keV	z	R_{200}, Mpc	β	β_{out}	r_c, kpc
A13	$5.76^{+0.15}_{-0.15}$	0.094	$1.51^{+0.47}_{-0.33}$	0.65 ± 0.08	0.68 ± 0.03	84 ± 8
A85	$6.20^{+0.40}_{-0.15}$	0.055	$2.71^{+0.65}_{-0.73}$	0.75 ± 0.03	0.76 ± 0.03	374 ± 54
A119	$5.71^{+0.16}_{-0.15}$	0.044	$2.66^{+0.13}_{-0.15}$	0.64 ± 0.06	0.61 ± 0.04	342 ± 49
A400	$2.33^{+0.21}_{-0.17}$	0.024	$1.55^{+0.24}_{-0.13}$	0.55 ± 0.07	0.58 ± 0.03	185 ± 20
A401	$8.16^{+0.87}_{-0.78}$	0.074	$3.07^{+1.21}_{-0.99}$	0.63 ± 0.07	0.69 ± 0.02	267 ± 51
A478	$6.90^{+0.35}_{-0.35}$	0.088	$2.60^{+0.41}_{-0.55}$	0.75 ± 0.04	0.80 ± 0.06	311 ± 30
A496	$4.89^{+0.12}_{-0.14}$	0.033	$1.93^{+0.48}_{-0.35}$	0.70 ± 0.06	0.75 ± 0.03	237 ± 22
A539	$3.33^{+0.29}_{-0.31}$	0.028	$1.88^{+0.33}_{-0.18}$	0.69 ± 0.03	0.73 ± 0.04	244 ± 33
A644	$6.59^{+0.17}_{-0.17}$	0.070	$2.92^{+0.77}_{-0.81}$	0.71 ± 0.03	0.71 ± 0.04	244 ± 41
A780	$4.33^{+0.15}_{-0.18}$	0.054	$1.69^{+0.48}_{-0.37}$	0.65 ± 0.08	0.61 ± 0.04	119 ± 25
A1413	$6.77^{+0.36}_{-0.26}$	0.14	$1.83^{+0.66}_{-0.57}$	0.68 ± 0.01	0.70 ± 0.02	219 ± 17
A1651	$6.11^{+0.20}_{-0.21}$	0.085	$2.45^{+0.46}_{-0.37}$	0.70 ± 0.02	0.77 ± 0.04	256 ± 43
A1689	$9.02^{+0.40}_{-0.30}$	0.183	$2.23^{+0.03}_{-0.07}$	0.75 ± 0.05	0.81 ± 0.06	265 ± 64
A1795	$6.88^{+0.14}_{-0.14}$	0.063	$2.46^{+0.36}_{-0.54}$	0.77 ± 0.06	0.88 ± 0.07	377 ± 48
A2029	$8.45^{+0.47}_{-0.45}$	0.077	$2.94^{+0.96}_{-0.82}$	0.68 ± 0.03	0.66 ± 0.04	277 ± 74
A2052	$3.22^{+0.22}_{-0.22}$	0.035	$1.93^{+0.55}_{-0.61}$	0.64 ± 0.03	0.66 ± 0.03	133 ± 35
A2063	$4.21^{+0.55}_{-0.36}$	0.035	$2.01^{+0.45}_{-0.37}$	0.68 ± 0.02	0.69 ± 0.04	210 ± 45
A2124	$10.88^{+1.78}_{-2.01}$	0.065	$2.16^{+0.63}_{-0.61}$	0.67 ± 0.03	0.59 ± 0.04	254 ± 73
A2142	$9.57^{+0.92}_{-1.11}$	0.091	$2.82^{+0.59}_{-0.61}$	0.75 ± 0.05	0.73 ± 0.04	387 ± 47
A2163	$14.01^{+1.89}_{-1.45}$	0.203	$4.22^{+0.68}_{-0.66}$	0.73 ± 0.04	0.87 ± 0.04	417 ± 36
A2199	$4.15^{+0.23}_{-0.21}$	0.030	$2.14^{+0.28}_{-0.19}$	0.64 ± 0.03	0.67 ± 0.05	155 ± 25
A2218	$7.39^{+1.03}_{-0.89}$	0.175	$1.65^{+0.16}_{-0.12}$	0.66 ± 0.03	0.71 ± 0.03	234 ± 46
A2255	$7.30^{+1.20}_{-1.20}$	0.081	$3.21^{+0.46}_{-0.27}$	0.74 ± 0.04	0.73 ± 0.06	552 ± 37
A2256	$7.53^{+0.91}_{-0.75}$	0.058	$3.33^{+0.62}_{-0.58}$	0.72 ± 0.03	0.75 ± 0.04	436 ± 57
A2462	$2.55^{+0.71}_{-0.66}$	0.073	$2.51^{+0.27}_{-0.22}$	0.65 ± 0.03	0.66 ± 0.04	221 ± 36
A2597	$4.39^{+0.45}_{-0.51}$	0.085	$2.01^{+0.57}_{-0.73}$	0.66 ± 0.03	0.66 ± 0.04	166 ± 45
A2657	$3.77^{+0.81}_{-0.77}$	0.040	$1.98^{+0.15}_{-0.11}$	0.75 ± 0.05	0.73 ± 0.02	372 ± 40
A2717	$2.31^{+0.34}_{-0.15}$	0.049	$2.16^{+0.79}_{-0.81}$	0.68 ± 0.03	0.66 ± 0.02	71 ± 3
A3112	$4.86^{+0.56}_{-0.67}$	0.075	$2.43^{+0.31}_{-0.26}$	0.61 ± 0.04	0.65 ± 0.03	119 ± 12
A3391	$7.01^{+0.63}_{-0.73}$	0.051	$2.45^{+0.84}_{-0.35}$	0.55 ± 0.01	0.56 ± 0.03	210 ± 17
A3571	$8.21^{+0.86}_{-0.73}$	0.039	$2.88^{+0.46}_{-0.37}$	0.69 ± 0.03	0.61 ± 0.05	271 ± 32
A4038	$3.32^{+0.53}_{-0.42}$	0.030	$1.87^{+0.25}_{-0.17}$	0.60 ± 0.04	0.61 ± 0.03	162 ± 43
A4059	$4.11^{+0.35}_{-0.32}$	0.047	$2.03^{+0.28}_{-0.34}$	0.65 ± 0.04	0.66 ± 0.03	222 ± 48
AWM4	$2.44^{+0.19}_{-0.25}$	0.032	$1.73^{+0.27}_{-0.22}$	0.62 ± 0.04	0.67 ± 0.07	125 ± 42

the radius R_{200}. Since, in many cases, this radius is a quite close to the size of the telescope's field of view, it is practically impossible to isolate the studied image for a direct determination of the background level.

Thus, we have considered that the surface brightness cluster radius at large radii should follow the exponential law, and therefore the observation surface brightness could be approximated as $\mathrm{Ar}^{-\gamma}+$ const . Thus, this approximation in the range of radii $r > R_{200}/3$ allows us to find the intensity level of the background. According to the observations of distant clusters, in which the level of background can be measured directly, we verified that this method gives the correct result.

Finally, using observations of blank fields, we checked the images alignment quality: the difference between the background level in the center and on the end of the image does not exceed ∼5 % after eliminating all the sources. We notice that this 5 % variation in the background levels gives an additional uncertainty of β-parameter of the β-model at $\delta\beta \sim 0.3$—0.4 and 2.1 % uncertainty in the value of R_δ. We used the cosmological parameters $H_0 = 73$ km/s/Mpc, $\Omega_M = 0.27$, and $\Omega_\Lambda = 0.73$ in our study.

Modeling the surface brightness profiles. We used the *Sherpa* software package and β-model [60,64] to determine the galaxy cluster brightness profiles:

$$S(r) = S_0 \left(1 + r^2/r_c^2\right)^{-3\beta+0.5}, \tag{2.82}$$

S_0, r_c and β are the free parameters. Such a model was used firstly by Jones & Forman 1999 [142] when analyzing the images of galaxy clusters based on the data from "Einstein" X-ray space observatory. The value of β for those clusters was in the range from 0.5 to 0.8 (the better value is 0.67). The authors noticed also a non-significant correlation between β-parameter and temperature of clusters: X-ray clusters with a higher temperature have a higher value of β-parameter.

The numerical simulations of that times provided more steeper profiles of density matter distribution, and $\beta \approx 0.8$—1, which was contrary to the observations. Bartelmann & Meneghetti [37] argued argued that the surface brightness profiles may curl at the larger radii but we can not observe such a process because the brightness of cluster is decreasing due to the influence of background. They proposed to check an accuracy of modeling of brightness profiles using β-model, because it allows to determine the mass of cluster under the condition of the hydrostatic equilibrium of intracluster gas [136]. We decided to apply a simple β-model for analyzing the observational surface brightness profiles in the studied nearby X-ray clusters as well as to clear up how such a procedure likely the azimuthal corrections of surface brightness profiles in galaxy clusters is fair one.

The most number of X-ray clusters with a normal morphology consists of a strong central peak of surface brightness, which is usually explained as

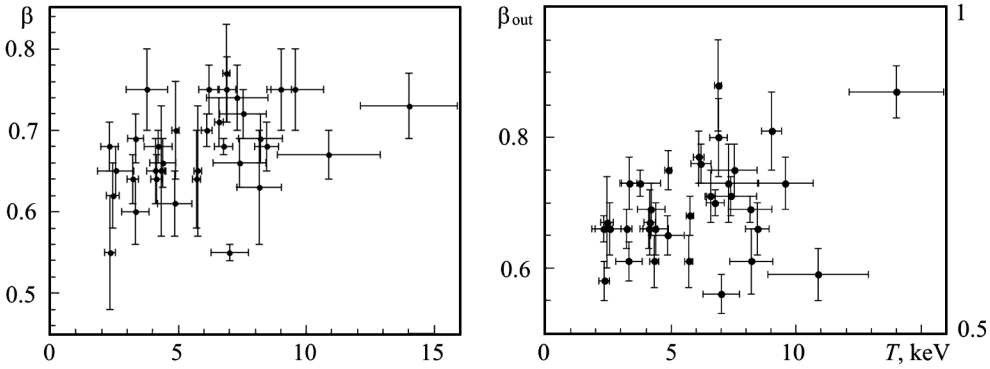

Fig. 2.4. The correlation between β and temperature of galaxy clusters. Top: β is taken from approximation at all range of radii. Down: β is taken from approximation at $0.3R_{200} < R < 1.5R_{200}$. The figures are taken from [32]

a consequence of radiative cooling of the gas. Using the central parts of such clusters the approximation by β-model leads to the small values of the core radius r_c and β-parameter as well as to the weak data approximation in general. Obviously, a central part of the X-ray galaxy cluster images must be excluded during their processing, if the aim of a study concerns with a correct analysis of the gas distribution at large cluster's radii.

There are several approaches to this problem. For example, [142] increased gradually a value of the minimal radius until the approximation of the surface brightness profile not leads to the acceptable values of χ^2. A new method to resolve such a problem is concerns with the search of the required radius parameter while a gas radiative cooling does not affect the distribution of a gas in the galaxy cluster till a typical value of a gas cooling time not exceeds the age of the Universe. Such a method, where a gas radiative cooling parameter described in a value of the radius $R_{\rm col}$, and a gas radiative cooling time is 1.3×10^{10} years, was introduced and analyzed [287]. Taking into account these results and the aforementioned analytical approximation we calculated $R_{\rm col}$ parameter and excluded range of radii $r < R_{\rm col}$ for each cluster from our sample.

Our results on the approximation of surface brightness profiles are given in Table 2.1. The values obtained for the nuclei radii r_c are often comparable with the $R_{\rm col}$ parameter in the case of clusters with the central peaks of a surface brightness, indicating thus that r_c can not be reliably measured. Meanwhile, the value of β-parameter is measured accurately and reliably as well as such an approximation responds well to the observations.

The obtained values of β-parameter are shown in Fig. 2.4. If we compare these values with those from the work [142], where β-parameter had a fairly narrow range 0.7 ± 0.1, we may conclude as follows from Fig. 2.4: only a few nearby Chandra X-ray clusters from our sample have $\beta < 0.6$.

As concerns with the question on the correlation between β-parameter and cluster's temperature T (left panel in Fig. 2.4). Our analysis allows to conclude that the previous statement about the absense of $\beta - T_X$ correlation was based on the small values of $\beta \sim 0.5$ for the cold X-ray clusters ($T \sim 3$ keV), which are characterized by the steeper surface brightness profiles. The most likely explanation for this discrepancy is related to the incomplete removal of the cooling central parts during processing the data on X-ray clusters in earlier works. We considered the same radial range (by the coordinate's position): $0.3\,R_{200}(T) < R < 1.5\,R_{200}(T)$. The nuclei r_c parameter can not be determined in this range from the Chandra data, so we fixed it at $0.1\,R_{200}$ or at the value that was obtained in the entire range of radii during approximation. Since r_c is usually much less than $0.3\,R_{200}(T)$, so the data approximation is equivalent to the application of a power law model, $S \sim r^{-6\beta+1}$.

The obtained values of $\beta_{\rm out}$ are given in Table 2.1 and are presented dependently on the cluster's temperature T in Fig. 2.4 (right panel). The measured slope of a surface brightness profile in the outer part of this Figure was slightly steeper than it follows from approximating β-model across the range of radii. An extreme case is related to the A2163 cluster, where β is changed to 0.17. The swirled surface brightness profile of the A2163 at $r > 0.3\,R_{200}(T)$ is obvious (Fig. 2.4). We notice that the changes of β in the outer parts of the clusters are much smaller, $\Delta\beta \approx 0.05$, as well as are not statistically significant for the most of galaxy clusters of our sample.

Thus, we concluded on the correlation between $\beta_{\rm out}$ parameter and cluster's temperature T. It is caused mainly by a group of five hot ($T = 6$—10 keV) clusters (A85, A401, A478, A644, A1413, etc.) with $\beta > 0.7$, as well as by a strong twist profile of the hottest A2163 cluster. However, one can see from Fig. 2.4 that there are systematic changes in the slope of surface brightness profile at the large radii of clusters, which are within the scatter at the high temperatures. We notice that the observed trend is a weak for $\beta \approx 0.67$ for clusters with $T = 3$ keV to $\beta \approx 0.7$—0.75 with $T = 10$—13 keV.

"Mass-temperature-radius of cluster" relation. Under the condition of spherical symmetry of the cluster and the observed surface brightness profile we can find the volume of emitting ability, which is then easily transferred to the gas density profile, using the fact that the plasma radiating capacity in the soft X-ray range is proportional to the square of the density and dependent very weakly on the temperature.

The theory of the formation of clusters provides correlation between mass and temperature of clusters, $M \sim T^{3/2}$. Since the mass and radius corresponding to this density contrast associated as $M_{200} \sim R_{200}^3$, we can expect the following correlation R_{200} and temperature: $R_{200} \sim T^{1/2}$. Since most of the baryons are concentrated in the X-ray intergalactic gas, this ratio $(R_{200} - T_X)$ for baryons can be easily verified.

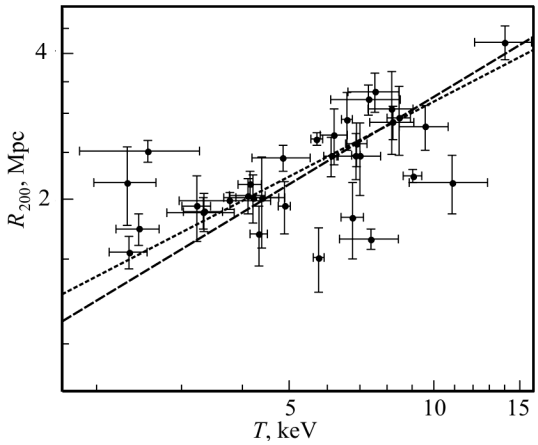

Fig. 2.5. The correlation of R_{200} and temperature clusters. Doted line shows approximations with power law model, and dashed line shows theoretical model from correlation $R \sim T^{0.5}$. This figure is taken from [32]

The contrast of baryon density is defined as the ratio of the mass of gas within a certain radius and the value of $(4\pi/3)\rho_0 R^3 \times \times (1+z)^3$, where ρ_0 is the current density of baryons in the Universe. This compares reliably the relative content of light elements from the theory of primary nucleosynthes, $\rho_0 = (5.55 \pm \pm 0.28) \times 10^9 M_\odot\,\mathrm{Mpc}^{-3}$. Radius R_{200} is sufficiently close to the virial radius $r_{\mathrm{vir}}(T)$. Correlation between the cluster's radius R_{200} and temperature T is shown in Fig. 2.5. We notice that since the measurement of the mass of gas is almost independent of temperature clusters, measuring R and T are also statistically independent. The observed correlation has a small scatter and close to the theoretically expected correlation of $R \sim T^{0.5}$. Note, that even A3391 with abnormally flat surface brightness profile is well accumulated within the average dependence. The measured correlation $R_{200} - T_X$ was modeled [17] using a power law model that allowed us also to consider both statistical and internal variations in the data on both axes.

The variation has value only 5.5 % for R_{200} at this temperature. Although the obtained slopes differ formally from the theoretical value of 0.5 for 2—3σ, the discrepancy between the best approximation and the power law $R \sim T^{0.5}$ lies completely within the scatter of data. The resulting ratio is as follows:

$$R_{200} = 850\ \mathrm{kpc} \times T^{0.61 \pm 0.04}\ \mathrm{keV}. \tag{2.83}$$

Main difference with other relations, such as luminosity-temperature or size-temperature, are related to the fact that the data, which are depending on the parameters of concentrated gas distribution, were obtained from the inner parts of cluster, but the correlation between R_{200} and T was obtained based on the data from the outer parts. So, the properties of the central parts of clusters can strongly affect various non-gravitational processes, which are not important at large radii, where the main part of the cluster's mass is concentrated.

Small scatter observed in the correlation $R_{200} - T$ can help us to find upper limit on variation in the proportion of baryons in total mass between

different clusters and its systematic dependence on temperature. We used the theoretically expected fact that the total mass of the cluster within a radius of density contrast correlated with temperature as $M_{\rm tot} \sim T^{3/2}$. Observed ratio for baryons, $R \approx \text{const} \times T^{1/2}$ is equivalent $M_{\rm gas} \sim T^{3/2}$. It means that $f_{\rm gas} = M_{\rm gas}/M_{\rm tot} \approx \text{const}$. Since the hot gas is the dominant baryon component in clusters, we can conclude that the proportion of baryons in total mass is constant too. The best approximation is $R_{200} \sim T^{0.57}$ and corresponds to a small change in gas content in total mass: $f_{\rm gas} \sim T^{0.2}$. However, if we consider the fraction of stars in the mass of baryons, which is higher in cold clusters, then this trend is significantly reduced and we can count that for wide range of temperatures the fraction of baryon mass in total mass of clusters is constant.

We now consider possible the variations of $f_{\rm gas}$ between different clusters with a given temperature. In the outer parts of the clusters radial correlation of the contrast density of gas is $\delta \sim r^{-3\beta}$. Accordingly, the observed 6.5 %-variations within the fixed $\delta_{\rm gas}$ corresponds to approximately $3\beta \times 6.5\,\%$ variation of contrast at a given radius. Hence, we can predict that the total mass of clusters clearly related to temperature.

In fact, the ratio $M_{\rm tot} - T$ has scatter of $f_{\rm gas}$ for clusters with a given mass of somewhat reduced. Thus, the findings suggest that the contribution of baryons in the total mass is constant, the same for different clusters of galaxies, and is independent from their temperature.

Vikhlinin et al. [278] calculated the correlation ratio between the baryon's mass and the total X-ray luminosity of clusters. This ratio provides an opportunity to make a rough estimate of the mass in those situations when the quality of the X-ray data are not available. More importantly that an availability of $M - L$ ratio helps to determine the volume, which is covered by the survey, with any restriction on the flow, depending on the mass of the cluster, and thus, finally, the mass function. These authors obtained also an integral function of the baryon mass which takes into account a statistical measurement error of the mass function of close clusters as well as distortions caused by the measurement errors for the masses of individual clusters.

We measured the mass profiles of intracluster gas in all the studied galaxy clusters using Chandra data and aforementioned analysis. Afetr a very accuracy applying the correlation ratio between the mass of hot gas and total optical luminosity taken from [278], we found not only the mass of gas, but also the total mass of baryons (intracluster gas + stars) for the X-ray nearby clusters:

$$M_b = M_g \times \left[1.33 + 0.05 \left(\frac{M_g}{10^{15} M_\odot}\right)^{-0.52}\right]. \qquad (2.84)$$

Here, M_b is the mass of baryons at the contrast $\delta = 200$, M_g is the mass of gas at the same contrast without a fraction of stars. The fraction of stars in the

total mass of baryons is significant and equal ∼10—15 % for massive clusters. Considering that the mass ratio of the gas and stars do not evolve at large z (i.e., galaxies do not associate themselves hot intergalactic gas), this ratio can be used for a measurement of the total baryonic mass of distant clusters, for which the sufficient quality optical observations are not available yet.

Thus, the baryon mass function for X-ray galaxy clusters at the small redshifts can be estimated with the use of Eq. (2.84). Observations of Chandra distant clusters can give us an opportunity to measure the baryon mass function also at the large redshifts (see, for example, the related articles by Schmidt & Allen [252] and on the distinguished use of this approach by Babyk, Del Popolo, Vavilova [34]).

2.3.4. $L_X - T - M_{\rm gas}$ relations in the distant X-ray galaxy clusters

The correlations between different physical parameters of galaxy clusters allow to get information about the global properties of clusters. The observations of the diffuse X-ray emitting medium (ICM) of galaxy clusters provide such parameters like its temperature (T), X-ray luminosity (L_X) and, after estimations, the mass (M_g). There are difficulties for theoretical predictions of these relations (e.g. [209, 211]). A correlation between the mass of hot intergalactic gas, temperature and X-ray luminosity of clusters has a small scatter that indicates a similar formation history for all clusters [91, 175, 197]. However, the detailed studies showed that the observational correlation coefficient is at odds with theoretical predictions. One of the most famous example is the slope of $L_X \sim T^{2.7}$ for hot clusters [175], while the theory provides $L_X \sim T^2$ [91]. Such differences can be explained by the fact that a heated intergalactic medium plays an important role in the non-gravitational processes as early heating of massive supernova [61] or radiation cooling as well as the associated active star formation [284].

Among the works on the $L_X - T$ relation for galaxy clusters at the large redshifts we note the followings. In a series of papers, Mushotzky and co-authors [197,198] have analyzed this ratio for a large sample of distant clusters observed by ASKA and did not find the evolution in $L_X - T$ relation. However, the later observations [17, 210] gave a support to an evolution parameterised in the form $L_X(z) \sim (1+z)^A$, where $A = 1.3$—1.5. A similar result for 12 distant galaxy clusters was obtained by [135]. Nevertheless that a value $L_X - T$ for clusters has a considerable scatter, the dispersion in $L_X - T$ for the nearer clusters can be reduced if the central region is excluded when the temperature and luminosity of clusters are evaluated [115,175] (hereafter FRB) [13, 116, 136].

A $L_X - T$ relation was derived for galaxy clusters in series of papers [61—63] and [78, 84, 88]. Del Popolo et al. [78] used two models. The first model is

a modification of the self-similar model, while the second one is a modification of the punctuated equilibrium model [62]. They have shown that the above models lead, in X-rays, to a $L_X - T$ relation as $L \sim T^5$ at the scale of groups, flattening to $L \sim T^3$ for the rich clusters and converging to $L \sim T^2$ at the higher temperatures. A principal result of these works is that the non-similarity in the $L_X - T$ relation can be explained by a simple model that takes into account the amount of the angular momentum acquisition by the protostructures during their expansion and collapse. It is important to note that this result is in disagreement with a widely accepted idea that the non-similarity is due to the non-gravitating processes, such a heating andor cooling.

In addition, Cavaliere et al. [62] have predicted the $L_X - T$ relation, which is consistent with the data as for a shape and scatter. For getting this result, they combine the mass distribution provided by the canonical hierarchical clustering under the condition that the initial perturbation spectra are dominated by cold dark matter but include enough baryons to account for the high abundance sampled by the X-ray clusters. Thus they have obtained the z-resolved luminosity functions, with the associated source counts and redshift distributions. They have predicted also the complementary contribution by the unresolved groups and clusters to the soft X-ray background.

The mass-temperature relations and its time evolution for galaxy clusters in different cosmological models were analyzed by Del Popolo [83]. The first one is based upon a modification of the top-hat model in order to take into account an angular momentum acquisition by protostructures and an external pressure term in the virial theorem. The second one is based on the merging-halo formalism, accounting for the fact that massive clusters accrete a matter quasi-continuously. The final result is that, in both models, the $M - T$ relation shows a break at $T \sim 3$—4 keV. The behavior of the $M - T$ relation is as usual, $M \sim T^{3/2}$, at the high-mass end, and $M \sim T^{\gamma}$, with a value depending on the chosen cosmology. Another recent observational studies accentuate on the possible existence of a break in the $M - T$ relation. For example, Finoguenov et al. [115] have investigated $M - T$ relation in the low-mass clusters and found that $M \propto T^{\sim 2}$ as compared to $M \propto T^{\sim 3/2}$ in the higher mass clusters using the resolved temperature profile of X-ray clusters observed by ASCA. Suggestions have been made to explain this behavior by attributing it to the effect of formation redshift, cooling and heating processes.

We consider the luminosity-temperature-mass of gas ($L_X - T - M_g$) relations for galaxy clusters at the higher redshifts ($0.4 < z < 1.4$). Our sample consists of 22 clusters with a large exposure time, which allows to determine the temperature of clusters with an accuracy better than 10—15 %. Using the Chandra data we were able to determine the evolution of these relations more accurately. For most of galaxy clusters (first of all, from MACS and RCS surveys) these results were obtained for the first time. We derived constraints

on the mass-temperature relation of gas in galaxy clusters from their observed luminosity-temperature relation. We parameterized the $M_g - T$ relation as a single power-law and derived the best-fit values of their amplitude and slope from the observed $L_X - T$ relation. We also derived the $L_X - M_g$ relation for our sample using a power-law model to describe this relation.

The most important observations of intracluster medium are conducted in the soft X-ray range (0.5—10.0 keV) with the third generation of X-ray Space Observatories. They allow us to measure the temperature and luminosity, and from these readings we can find the total mass of a galaxy cluster within a scaled radius assuming the hydrostatic equilibrium of gas with the gravitational cluster potential. Since, the ICM emits extremely X-ray luminous, these observatories may detect clusters out of $z > 1$. The distant clusters provide the most important information for cosmological estimations, including the scaling relationship between the main observed parameters and total mass (see, for example, [115,175,199]). Various kind of such relations were predicted via self-similar models of galaxy clusters [144], but the observed scaling relations are still different from the theoretical models.

The correlations between temperature, luminosity and mass of clusters give a great opportunity to get important information about the global properties of galaxy clusters. There are many difficulties with the theoretical predictions of these correlations. A small scatter in relations between temperature, luminosity and mass of clusters indicates the similar nature of formation for all galaxy clusters. On the other hand, the detailed analysis showed significant uncertainties in the correlation coefficient between observations and theory. For example, the $L_X - T$ relation has an observational slope of 2.7 [23—26, 30, 33, 78], while theory gives a slope only of 2 (e.g., [10,11,275]). Such uncertainty can be explained by the presence of non-gravitational processes or radiation cooling inside these clusters.

A $L_X - T$ relation was studied in series of papers [10, 11, 78]. Del Popolo et al. [78] used self-similar model, and modification of the punctuated equilibrium model from previous researches. They found that both models lead to $L_X - T$ relation so flattening to $L_X \propto T^3$ for the rich clusters but converging to $L_X \propto T^2$ at the higher temperatures. The main result of these researches is that the non-similarity in $L_X - T$ relation can be explained using a simple model taking into account the amount of the angular momentum acquisition by the substructures during their collapse and expansion.

The scaling relations between the luminosity, temperature, and mass of gas ($L_X - T - M_g$) are well-described for the relaxed clusters at the low redshifts ($z < 0.15$) [276, 277], while the relations at the higher redshifts are less well determined. The $L_X - T - M_g$ correlations at very high redshifts have not yet been well studied, however, more and more clusters are being detected at these redshifts, which will provide a great opportunity for cosmological researches

in the coming years. Being in the deepest gravitational potential wells, the galaxy clusters reside an excellent cosmological probe as a tracer of the peaks of structure formation.

Sample and methods. We accentuate on measuring the physical parameters (temperature, surface brightness, total mass profiles, etc.) and the scaling relation for yet one distant galaxy cluster XLSSJ 022403 — 041328. This galaxy cluster was discovered by the XMM-Newton Observatory as an extended X-ray source within the XMM Large-Scale Structure Survey [10, 221, 272]. Later on, after conducting the analysis of NIR (K_s-band) and $R - z$ observations, its belonging to the higher redshift cluster population was confirmed ($z = 1.05$) by [11]. One can receive the more information also by [217] on the XMM-LSS Class 1 cluster sample (pertaining to the first 5 deg of the survey) and its cosmological modeling, [170] on the X-ray analysis methodology, and [290] for an extensive spectral analysis and other parameters of X-ray distant clusters in the XMM LSS survey, as well as their optical assessments [3]) including the additional data on the studied galaxy cluster.

The gas in cluster is trapped by the cluster's gravitational potential well. If the hot gas is supported by its own pressure against gravitational infall, it must obey the equation of hydrostatic equilibrium. The intercluster gas in the most of clusters appears to be in an approximate hydrostatic equilibrium Eq. (2.69). It was used the assumptions of spherical symmetry of clusters. Since the density and pressure of hot gas have very low values, we can use the ideal gas law,

$$P = \frac{\rho_g k T_g(r)}{\mu m_{\rm p}}, \tag{2.85}$$

where μ is the mean molecular weight of the gas, and $m_{\rm p}$ is the proton mass. Combining the equation (2.69) and equation (2.85), the total mass of cluster as a function of the projected radius is as follows in Eq. (2.70).

Assuming an isothermal and spherical distribution of gas in clusters with temperature T, the equation (2.70) becomes

$$M_T = -\frac{kTr}{G\mu m_{\rm p}} \left(\frac{d\ln\rho_g}{d\ln r}\right), \tag{2.86}$$

where r is the outer radius of the cluster and μ is constant with radius, since the chemical composition of the gas is expected to be uniform throughout the cluster.

Assuming an isothermal spherical gas in the hydrostatic equilibrium, the density profile of the X-ray emitting gas can be approximated by an isothermal β-model [60]

$$\rho_g(r) = \rho_0 \left(1 + \left(\frac{r}{r_c}\right)^2\right)^{-3/2\beta}, \tag{2.87}$$

where $\rho_g(r)$ is the density of the gas as a function of the cluster's projected radius r, r_c is the core radius, and ρ_0 is the density in the cluster's center. The values of β and r_c are obtained by analysis of the X-ray surface brightness profile for each cluster.

X-ray image analysis allows the determination of the X-ray surface brightness profile. The assumption that the hot gas is isothermal one leads to a β-model for the cluster's brightness profile

$$S(r) = S_0 \left(1 + \left(\frac{r}{r_c}\right)^2\right)^{-3\beta+1/2} + C, \tag{2.88}$$

where $S(r)$ is the X-ray brightness as a function of the projected cluster's radius r. S_0, r_c, β and C are free parameters by fitting the model to the X-ray brightness profile. In general, the X-ray surface brightness profile is approximated well by the β-model.

There are cases, when the standard β-model leads to underestimating the brightness in the central region of the clusters. The central X-ray excess is one of the first pieces of evidence of cooling flows in galaxy clusters [142]. For simplicity in our study, we use a single β-model [239].

The mass of the hot gas in the ICM is determined by the integration of the gas density profile (Eq. (2.87)) over the volume of the cluster within a defined radius R_{200},

$$M_g = \int\limits_{200} \rho dV. \tag{2.89}$$

Equation (2.89) can be written as

$$M_g = 4\pi\rho_0 \int\limits_0^{R_{200}} r^2 \left(1 + \left(\frac{r}{r_c}\right)^2\right)^{-3/2\beta} dr. \tag{2.90}$$

The value of ρ_0 is derived from combining the results obtained from fitting a model to the X-ray spectrum, and from the best fit parameters obtained by fitting a β-model to the X-ray surface brightness profile. The result obtained by integrating the density profile over a defined volume of the cluster depends on the cosmology assumed because of the projected radius of the cluster is calculated using the cluster's angular distance d_A [113].

$L_X - T - M_{\mathrm{gas}}$ correlations. The obtained values of $L_X - T$ for the distant galaxy clusters are shown in Fig. 2.6. Variation in the ratio is very small. It is almost entirely due to the measurement errors. The slope is consistent with the ratio for clusters from our sample at the lower redshifts [25] (see Section 2.3.3). We used normalization parameter on z as $L \sim (1+z)^{A_{L_XT}} T^{\beta_{L_XT}}$ and found that $\beta_{L_XT} = 2.55 \pm 0.07$, and $A_{L_XT} = 1.50 \pm 0.23$ at the confidence level 68 %.

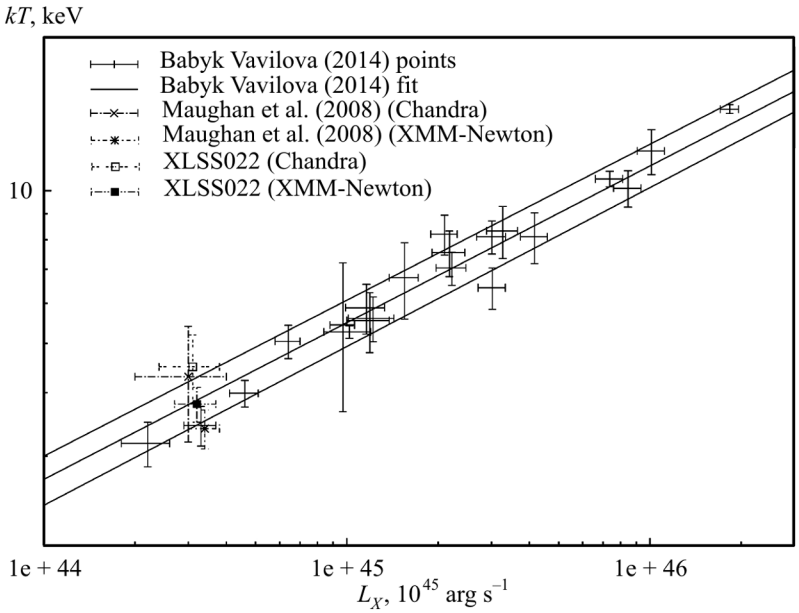

Fig. 2.6. The scaled $L-T$ relation of sample clusters observed by Chandra and XMM-Newton. The lines correspond to the normalization parameter $L_g(1+z)^{A_{LT}}T^{\beta_{LT}}$ with $A_{LT} = 1.50 \pm 0.23$, while $\beta_{LT} = 2.55 \pm 0.07$; a standard deviation is at 1σ confidence level. The figure is taken from [29]

The $L_X - T$ relation has been studied well at the lower redshifts, however, the situation at the higher redshifts is less clear. Henry et al. [128] found that there is moderate to no evolution out to a redshift of 0.33. Muzhotsky et al. [197] found evidence for no evolution out to a redshift of 0.4. Fairley et al. [112] found that $L_X \sim (1+z)^{0.60\pm0.38}T^{3.15}$ for an $\Omega_m = 0.3$, which is consistent with no evolution in the $L_X - T$ relation out to a redshift of 0.8. Borgani et al. [46] constrained β_{L_XT} to be between 3 and 4. Using their constraints on β_{L_XT}, they found $1 < A < 3$ for an $\Omega_m = 1.0$ and $A = 0$ implied a low density universe. Muzhotsky et al. [197] found $A = 0$ also. Donahue et al. [95] found a slightly negative value of A (for $\Omega_m = 0.3$, $\Omega_\Lambda = 0.7$, $A = -0.8^{+0.9}_{-1.1}$), and rule out $A = 1.5$; their results were also consistent with $A = 0$. Reichart et al. [230] determined the $L_X - T$ relation for cooling flow's corrected luminosities and temperatures. They found $\beta_{L_XT} = 2.80 \pm 0.15$ and $A = 1.53^{+0.54}_{-1.22}$ for our chosen cosmological parameters. These results are in a good agreement with our estimations [28,29]. Horner et al. [136] found $\beta_{L_XT} = 2.98 \pm 0.14$ and $A = 0.02 \pm \pm 0.16$ for no cooling flow corrections that is in confirmation with our results.

Using spherically symmetric clusters, the value of gas mass can be estimated from a surface brightness profile. We decided to measure the mass of gas within radius R_{200} (our sample includes only two clusters in the temperature

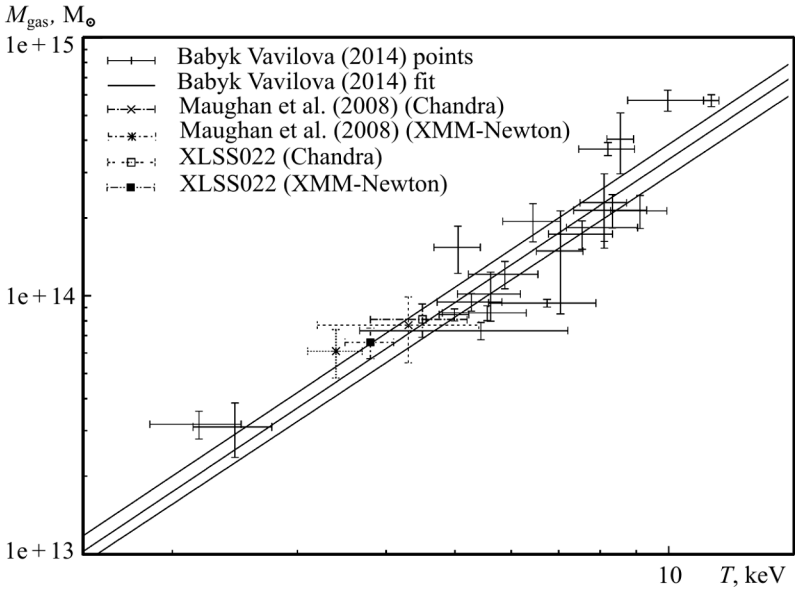

Fig. 2.7. The scaled $M-T$ relation of sample clusters observed by Chandra and XMM-Newton. The lines correspond the normalization parameter $M_g(1+z)^{A_{MT}}T^{\beta_{MT}}$ with $A_{MT}=-0.58\pm0.13$, and $\beta_{MT}=1.77\pm0.16$; a standard deviation (1σ confidence level). The figure is taken from [29]

range from 2 to 3 keV, so we can say anything about the break in $M_g - T$ scaling relation).

The relation $M_{g,200}-T$ is shown in Fig. 2.7. We used a functional relation of the following form $M_g \sim (1+z)^{A_{M_gT}}T^{\beta_{M_gT}}$ with parameters $\beta_{M_gT}=1.77\pm$ $\pm\,0.16$, and $A_{M_gT}=-0.58\pm0.13$.

The cluster formation simulations [186], which include supernova heating, produce a slightly steeper slope ($M_g \propto T^{1.61}$) compared to the self-similar slope 1.5 in their results of simulations with no winds. They show that if all the wind energy is thermalized and retained within a virial radius, the temperature for the masses $\sim 10^{13} M_\odot$ may increase by 100 %, which would totally break the scaling at the low temperatures. [206] found $\beta_{M_gT}=1.79\pm0.14$. In addition, [157] found $\beta_{M_gT}=1.65\pm0.15$ using the Chandra sample of galaxy clusters at $z=0.4$—0.7 spanning a temperature interval of $3\,\mathrm{keV} < T < 14\,\mathrm{keV}$.

Relationship between the mass and luminosity ($M_g - L_X$) of gas is shown in Fig. 2.8. This value is useful in assessing the functions of the distant clusters by their X-ray luminosity. We used the functional relation as $M_g \sim (1+z)^{A_{M_gL_X}}L^{\beta_{M_gL_X}}$. We found $\beta_{M_gL_X}=0.73\pm0.15$ and obtained $A_{M_gL_X}\approx -1.86\pm0.34$ for our model of the Universe. One can see that the most independent M_g-T relation observations are consistent with our results and with the preheating scenario.

Thus, the relationship between X-ray temperature, luminosity and mass of gas at $z > 0.4$ has a strong evolution in relationship with respect to the correlations observed at the lower z. The evolution in the ratio $M_g - L_X$ and $M_g - T$ for baryon matter and non-baryon cause ought to be the same.

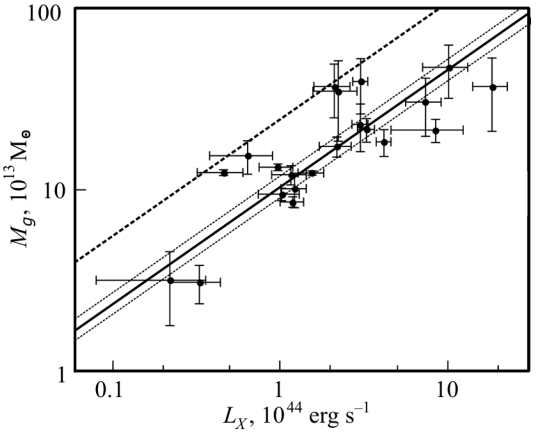

Fig. 2.8. The relation between the luminosity of clusters in 0.5—7 keV energy range and the mass of hot gas at R_{200}. The dotted line represents the $M - L_X$ relation for galaxy clusters at the lower redshifts. The solid line is moved on $(1 + z)^{1.94}$. The two dotted lines show 68 % standard deviation. The figure is taken from [28]

Both the observed strong evolution based on $M_g - L_X$ is weak, and negative evolution of the luminosity function mean that the mass function evolves strongly: the spatial density of clusters of the fixed mass at high-z is much smaller than in the current epoch of cosmological parameters [108, 109, 297]. The ratio between $M_g - T - L_X$, which we derived for the considered X-ray clusters at the higher redshifts ($0.4 < z < 1.4$), indicates that clusters of galaxies in the past had an higher density, they were hotter and had a higher luminosity at the fixed mass than predicted actually with the scaling relations obtained on the gravitational structure formation [52].

Using the new Chandra data on the cluster's temperatures, luminosities and mass of X-ray hot intercluster gas, we obtain the $L_X - T - M_X$ relations in the 2—11 keV temperature interval with a greatly reduced scatter. The large redshift sample has provided an evidence that clusters do not evolve self-similarly in the last ∼11 Gyr. Our normalization of the $M_g - T$ relation is also in a good agreement with those derived from the high-resolution numerical simulations (e.g., [45]) that undertaken to model the non-gravitational processes in the ICM (radiative cooling, star formation, and feedback from supernova). We have presented the constraints on the mass-temperature relation of hot gas of galaxy clusters.

For $M_g - T$ relation we found that

$$M_{200} = (4.93 \pm 0.64) \times 10^{13} \left(\frac{kT}{1\ \mathrm{keV}}\right)^{1.5} \mathrm{h}^{-1} M_\odot, \tag{2.91}$$

which can be compared with

$$M_{200} = 5.88 \times 10^{13} \left(\frac{kT}{1\ \mathrm{keV}}\right)^{1.5} \mathrm{h}^{-1} M_\odot, \tag{2.92}$$

taken by [4].

We revealed the constraints on the luminosity-temperature, the temperature-mass and the mass-luminosity relations of distant galaxy clusters based on the Chandra observations. Our analysis adopted a simple parameterized model for these relations. We note that the evolution in such relations with redshift is a very sensitive to values of cosmological parameters [7, 91, 176]. In overall, the clusters at the higher-z have stronger dependencies between $L_X - T - M_g$ correlations that those for clusters at the lower-z. For the most of galaxy clusters (first of all, from MACS and RCS surveys) these results are obtained for the first time. We are in progress to compare such evolutions ($L_X - T - M_g$) using the non-X-ray data for the studied galaxy clusters taking into account the properties, which are not being sources directly from X-ray range [12].

Our results showed that the $M_g - T$ relation at the high redshifts has a strong evolution with respect to those at the small redshifts. It is significant to note that the $M - T$ relation has smaller variations than that predicted by the theory ($M \sim T^{3/2}$). This difference can be explained by the fact that heated intergalactic medium plays a significant role in non-gravitational processes, as early heating by massive supernovae, radiation cooling. In general, the main physical characteristics are consistent with the self-similar evolution of the cluster population. We note that the temperature values for this cluster are reliable [222] and confirm the potential to investigate the evolution of X-ray clusters in a statistical manner over a wide, uniformly-selected redshift, and $0.7 < T < 14$ keV temperature, intervals using the XMM LSS survey.

The simulations of cluster formation, which include non-gravitational processes, show a steeper slope for $M_g - T_X$ relation ($\sim$1.61) compared to the self-similar slope ($\sim$1.5) [186]. As a result, if all the wind energy is thermalized and retained within the virial radius, the temperature for the masses (in $10^{13} M_\odot$) may rise by 100 %, which would totally break the scaling relation at the low temperatures [27, 30, 78]. We did not find any evidence of the presence of a spectral break in $M - T$ relation at lower ($\sim$1—2 keV) temperatures (after adding new points). The assumption of virial equilibrium leads to the expected relation $M \propto T^{3/2}$ between total mass and temperature. A topic of vigorous debate over the previous years that used recent investigations of the X-ray mass-temperature relation have shown one percent-level agreement in normalization showing that the slope is not greatly different from the self-similar expectation [78], although it may be slightly steeper [30]. We note that for the distinguished analysis the more ambitious surveys covering 7000 deg^2 should provide the 1 % accuracy in the estimation of the $M - T$ relation normalizations (see, for accentuation, [42]).

$L - T$ relation. Our results may also be used to test the evolution between luminosity and temperature of ICM. We used the normalization parameter $L_X (1+z)^{A_{LT}} T^{\beta_{LT}}$ with $A_{LT} = 1.50 \pm 0.23$, while $\beta_{LT} = 2.55 \pm 0.07$. Fig. 2.6

shows the results of $L-T$ relation, where our measurements together with the data [180] are shown on a graph together.

There are a couple of models to describe the $L-T$ relation, for example, adiabatic, shock etc. The adiabatic model predicts a single, scale-free relation $L \propto T^{3.5}$, or $L \propto T^3$ if the gas equilibrium distributed to virial radius. However, at the cluster scales the universal baryonic fraction, one expects saturation toward the scaling of $L \propto T^2$ of the shock model. On the other hand, at the group scales a much steeper dependence is indicated by observations. Such opposite departures of the $L-T$ correlation from a single power-law are beyond the reach of the adiabatic model, but within the predictions of the shock model. It is therefore instructive to consider trends in the $L-T$ relation in anticipation of a larger sample of distant clusters from the continuing XMM LSS survey as that was concluded yet by [222].

Kaiser [144] described the thermodynamical processes of the ICM by assuming it to be entirely determined by the gravitational processes, such as adiabatic compression during the collapse and shocks due to supersonic accretion of the surrounding gas. There are no preferred scales in the cosmological framework (i.e. $\Omega_m = 1$), and in physics (i.e. only gravity acting on the gas and pure thermal, bremsstrahlung emission), then clusters of different masses are just a scaled version of each other. Because bremsstrahlung emissivity predicts $L_X \propto M\rho_{\rm gas}T^{1/2}$, as result, $L_X \propto T_X^2(1+z)^{3/2}$ or, equivalently for the L_X-M relation as $L_X \propto M^{4/3}(1+z)^{7/2}$.

The assumption of pure thermal, bremsstrahlung is quite accurate above approximately 2 keV, but at lower temperatures the line emission becomes significant, unless the value of metals is very low. We quantified that the value of metal abundance does not effect on the value of temperature, i.e. total mass, significantly. [41] have determined the dependence of the metal abundance on the redshift and virial radius as $Z(r,z) = Z_0(1+(r/0.15_{r_{500}})^2)^{-a}(z/0.6)^{-\gamma}$ with the best-fit model parameters of $Z_0 = 0.36 \pm 0.03$, $a = 0.32 \pm 0.07$, and $-\gamma = 0.25 \pm 0.57$. This relation depicts an important negative trend of Z with the radius and, although no important evolution with the redshift is detected. It represents the first time that the abundance measured in ICM has been parameterized as a function of both r and z in a way that could be directly compared with the models of diffusion of metals. Pure thermal, bremsstrahlung emission itself does not exactly scale as was predicted ($T^{1/2}$), due to the additional Gaunt factor [276]. However, this factor varies by less than 4 % in the 1—10 keV temperature band. In contrast, the line emission reaches about 18 % of the total emission at 2 keV for a typical abundance of $0.3\,Z_\odot$. This extra line emission tends to flatten the slope of the $L_X - T$ relation, as low-T clusters are boosted in luminosity more than their high-T counterparts. This effect is amplified, because low-T clusters tend to have higher abundances.

$M - T$ relation. The four data points (two from our research and two ones taken from [180]) are plotted in Fig. 2.7. We used the normalization parameter $M_g(1+z)^{A_{MT}}T^{\beta_{MT}}$ to describe the $M-T$ correlation with $A_{MT} = -0.58 \pm 0.13$, and $\beta_{MT} = 1.77 \pm 0.16$. Our measurements and calculations made by Maughan et al. [180] are in a very good agreement with our previous relations for 21 distant clusters observed by the Chandra. They are consistent also with the $M-T$ relation obtained by Kotov & Vikhlinin [157] for clusters at $0.4 < z < 0.7$ observed by XMM-Newton.

2.4. Dark matter halo in the massive X-ray galaxy clusters

In the present section, we use Chandra X-ray data to study the properties of 128 dynamically relaxed galaxy clusters. We selected the sample with redshift range from 0.01 to 1.4. with the aim to recover their total and gas mass profiles and analysis of the measured distribution of c_{200}, M_{200} and baryonic mass content. We determine the baryons content of each cluster subtracting the DM from the total mass. Point out that fitting the density profile with a generalized NFW model:

$$\rho(r) = \frac{\rho_0}{(r/r_s)^{\alpha}(1 + r/r_s)^{3-\alpha}} \tag{2.93}$$

the slope α is correlated with the baryonic mass content of the cluster, in agreement with several studies [66, 232—234, 254].

2.4.1. Main properties of the Chandra massive X-ray galaxy clusters at $z < 1.4$

The main criterion to generate the studied sample of galaxy clusters was the value of the X-ray flux. This value should be low enough to represent the largest number of galaxy clusters, while at the same time, the value of the X-ray flux should be high enough to measure the total mass of clusters more carefully. Usually, for the energy range 0.5—7.0, the flux is considering as $f_X = 7.0 \times 10^{-12}$ erg s^{-1} cm^{-2} [177, 282]. In our study we selected the clusters having a larger value of the X-ray flux before mentioned. In addition to flux criteria, a second criterion was to use a wide range of redshifts. The cluster with highest redshift used is ISCS J1438 + 3414 having $z \sim 1.41$, while the most of clusters has a redshift in the range 0.01—0.3, and in general $0.01 \leq z \leq 1.4$. We added to our sample 14 MACS and 8 RCS clusters as some of the most distant objects which are observed by Chandra. All the target clusters have the mass weighted X-ray temperatures measured within the radius r_{2500}, $kT_{2500} \leq 5$ keV.

To minimize systematic scatter and to allow the most precise test of the CDM model predictions, we used only highly relaxed clusters. All other clusters

in the sample have a regular X-ray morphology, indicative of a relaxed state and allowing reliable determination of the total mass profile through the hydrostatic equilibrium equation. We did not take into account observations of clusters when the exposition time was smaller then 5 ks. This helped to decrease the uncertainties in the spectrum modeling, and mass of clusters determination. The list of observations results are presented in Table 2.2. It is significant to note that coordinates of clusters were taken from the NED archive, where these coordinates, in turn, were taken from the paper by [2]. Since the quoted authors [2] used the Palomar telescope for its determination, some differences between optically defined coordinates from NED and X-ray peak from intracluster gas have been noted. These differences are not so critical or significant, however, we have used the central coordinates from maximum of X-ray emission.

Advanced β-model. As we already told, because of the beta-model has some limitations, we introduced a more precise model to get the distribution of hot gas of galaxy cluster.

In order to get the hot gas distribution in galaxy clusters, we will solve numerically the system of the following differential equations:

$$\frac{1}{\rho_g}\frac{\partial \rho_g}{\partial x_i} = -\frac{\mu m_{\rm p}}{kT_g(r)}\frac{\partial \phi(r)}{\partial x_i}, \tag{2.94}$$

for the gas distribution, where $x_i = (x, y, z)$ are the Cartesian coordinates, μ is the molecular weight, $m_{\rm p}$ is the proton mass, k is the Boltzman constant, and ϕ is the gravitational potential. We performed the numerical integration of the system of Eq. (2.94) through the Euler method. The integration step was chosen in such a manner that the maximum error in the resulting X-ray brightness was not bigger than 0.1 %.

After getting the gas density (ρ_g), we were able to obtain the emission measure profile in the X-ray energy band. The emission flux, that comes from the observed regions, is proportional to the square of the integral density of hot gas, ρ_g^2, along the line of sight. We used the metal abundance of 0.3 and assumed $n_{\rm e}/n_{\rm p} = 1.17$ and $\rho_g = 1.35\, m_{\rm p} n_{\rm p}$, where $n_{\rm e}$ and $n_{\rm p}$ are the electron and proton concentrations, respectively [282]. We have to note that from the model, we can obtain the gas density with precision of some constant factor a, which depends on the integration boundary conditions of Eq. (2.94). Therefore, the real density $\rho_g^{\rm real}$ of gas is equal to $\rho_g^{\rm real} = a \cdot \rho_g^{\rm sim}$, where $\rho_g^{\rm sim}$ (sim stands for "simulations") is the density of gas obtained by solving the previous differential equations. So, we can write $\rho_g^{\rm sim} \equiv \rho_g$ in Eq. (2.94). Thus the value of $\mathrm{EM_{sim}}$, namely EM from simulations (see Section 2.3.2), can be found as:

$$\mathrm{EM_{sim}} = \int n_{\rm e} n_{\rm p} dV = 0.64/m_{\rm p}^2 \int (\rho_g^{\rm sim})^2 dV. \tag{2.95}$$

Table 2.2. **The massive Chandra X-ray galaxy clusters: total and baryonic masses, dark matter profiles. Columns list the target name, redshift, number of ID observation, the total mass in clusters at radius R_{200}, the mass of baryonic matter in clusters, and the fraction of baryonic matter in total mass, and, in the case of the gNFW, we give the inner value of slope, α**

Cluster	z	ObsID	M_{200}, 10^{14} $M_\odot$	$M_{\rm b}$, 10^{13} $M_\odot$	$f_{M_{\rm b}/M_{\rm tot}}$	α
A85	0.055	904	$25.68^{+4.89}_{-3.18}$	$42.86^{+4.83}_{-6.46}$	0.166	$0.85^{+0.16}_{-0.28}$
A119	0.044	7918	$24.06^{+4.16}_{-2.18}$	$47.97^{+8.35}_{-9.12}$	0.199	$0.82^{+0.27}_{-0.25}$
A133	0.056	2203	$16.34^{+3.55}_{-2.17}$	$35.02^{+3.87}_{-6.45}$	0.214	$0.69^{+0.08}_{-0.08}$
A168	0.045	3203	$6.74^{+2.03}_{-1.78}$	$19.76^{+2.17}_{-3.17}$	0.293	$1.01^{+0.17}_{-0.11}$
A209	0.206	522	$12.05^{+2.34}_{-2.11}$	$10.47^{+1.85}_{-1.82}$	0.087	$1.72^{+0.16}_{-0.13}$
A262	0.016	2215	$2.93^{+0.73}_{-0.67}$	$7.25^{+1.53}_{-1.67}$	0.246	$0.69^{+0.03}_{-0.04}$
A383	0.187	524	$5.63^{+2.04}_{-1.19}$	$11.03^{+3.11}_{-2.18}$	0.195	$1.58^{+0.22}_{-0.22}$
A399	0.072	3230	$37.90^{+3.94}_{-4.11}$	$94.53^{+10.11}_{-9.16}$	0.249	$0.51^{+0.17}_{-0.15}$
A401	0.074	518	$37.97^{+4.16}_{-2.81}$	$75.91^{+6.31}_{-5.83}$	0.199	$0.86^{+0.29}_{-0.37}$
A478	0.088	1669	$23.35^{+2.62}_{-2.17}$	$30.86^{+2.88}_{-3.17}$	0.132	$0.96^{+0.22}_{-0.16}$
A496	0.033	931	$9.10^{+1.19}_{-1.27}$	$10.86^{+1.51}_{-1.22}$	0.119	$0.82^{+0.05}_{-0.07}$
A521	0.250	430	$7.21^{+1.16}_{-1.13}$	$14.47^{+1.95}_{-2.17}$	0.200	$0.93^{+0.12}_{-0.13}$
A539	0.028	5808	$8.38^{+1.46}_{-1.77}$	$15.06^{+1.25}_{-1.19}$	0.179	$1.08^{+0.21}_{-0.22}$
A576	0.039	3289	$21.11^{+2.16}_{-1.19}$	$23.87^{+2.14}_{-2.11}$	0.113	$0.74^{+0.18}_{-0.18}$
A644	0.070	2211	$32.55^{+3.51}_{-2.99}$	$44.62^{+3.17}_{-2.91}$	0.137	$1.03^{+0.11}_{-0.06}$
A697	0.280	4217	$13.56^{+1.27}_{-1.14}$	$13.49^{+1.17}_{-1.19}$	0.099	$0.94^{+0.14}_{-0.13}$
A754	0.054	577	$40.30^{+3.71}_{-3.16}$	$61.80^{+6.17}_{-5.19}$	0.153	$1.08^{+0.12}_{-0.09}$
A773	0.217	533	$14.09^{+1.72}_{-1.28}$	$24.47^{+2.15}_{-1.98}$	0.173	$0.82^{+0.13}_{-0.11}$
A907	0.150	3205	$6.54^{+0.73}_{-0.72}$	$13.12^{+1.13}_{-1.19}$	0.200	$1.12^{+0.13}_{-0.12}$
A963	0.206	903	$8.22^{+1.24}_{-0.91}$	$22.63^{+2.14}_{-2.19}$	0.275	$1.52^{+0.13}_{-0.12}$
A1060	0.012	2220	$9.81^{+1.32}_{-1.16}$	$24.28^{+2.16}_{-1.93}$	0.247	$0.89^{+0.08}_{-0.11}$
A1068	0.138	1652	$7.71^{+0.71}_{-0.78}$	$14.64^{+1.16}_{-1.19}$	0.189	$0.98^{+0.19}_{-0.19}$
A1201	0.169	4216	$5.43^{+0.59}_{-0.66}$	$9.79^{+1.15}_{-0.93}$	0.180	$1.72^{+0.10}_{-0.10}$
A1240	0.159	4961	$7.34^{+0.94}_{-0.81}$	$16.42^{+1.73}_{-1.67}$	0.223	$0.91^{+0.08}_{-0.08}$
A1361	0.117	2200	$11.07^{+1.34}_{-1.18}$	$21.56^{+2.15}_{-2.17}$	0.194	$0.80^{+0.29}_{-0.28}$
A1413	0.140	537	$8.53^{+1.18}_{-0.92}$	$14.48^{+1.42}_{-1.18}$	0.169	$0.93^{+0.08}_{-0.08}$
A1446	0.104	4975	$12.66^{+1.26}_{-1.15}$	$28.20^{+2.16}_{-2.17}$	0.222	$1.34^{+0.73}_{-0.72}$
A1569	0.074	6100	$14.35^{+1.34}_{-1.11}$	$37.01^{+3.26}_{-3.17}$	0.257	$0.67^{+0.18}_{-0.19}$
A1644	0.047	2206	$14.60^{+1.47}_{-1.17}$	$33.95^{+4.12}_{-3.16}$	0.232	$0.75^{+0.07}_{-0.07}$
A1650	0.084	5823	$39.44^{+3.74}_{-2.78}$	$81.43^{+5.85}_{-4.81}$	0.206	$0.43^{+0.12}_{-0.22}$
A1651	0.085	4185	$19.48^{+2.45}_{-2.17}$	$37.81^{+3.75}_{-3.61}$	0.194	$0.91^{+0.22}_{-0.08}$
A1664	0.128	1648	$22.84^{+2.81}_{-2.19}$	$40.35^{+3.71}_{-3.78}$	0.176	$0.72^{+0.26}_{-0.25}$
A1689	0.183	540	$16.09^{+2.81}_{-1.73}$	$39.52^{+4.17}_{-3.92}$	0.245	$1.10^{+0.18}_{-0.16}$
A1736	0.046	4186	$8.11^{+1.15}_{-1.18}$	$11.26^{+1.93}_{-2.18}$	0.138	$1.08^{+0.13}_{-0.27}$
A1795	0.063	493	$19.34^{+2.18}_{-2.16}$	$20.46^{+3.16}_{-2.19}$	0.105	$1.04^{+0.45}_{-0.28}$
A1835	0.253	495	$22.86^{+2.86}_{-3.11}$	$41.93^{+5.16}_{-4.28}$	0.183	$0.68^{+0.13}_{-0.15}$
A1914	0.171	542	$76.85^{+5.81}_{-5.28}$	$93.76^{+9.61}_{-10.27}$	0.121	$0.43^{+0.18}_{-0.18}$

Continuation of the tabl. 2.2

Cluster	z	ObsID	M_{200}, 10^{14} $M_\odot$	M_b, 10^{13} $M_\odot$	$f_{M_\mathrm{b}/M_\mathrm{tot}}$	α
A1995	0.318	906	$45.32^{+5.16}_{-3.18}$	$56.22^{+6.17}_{-4.91}$	0.124	$0.55^{+0.18}_{-0.18}$
A2029	0.077	891	$33.43^{+3.71}_{-4.12}$	$42.42^{+5.18}_{-4.19}$	0.126	$0.91^{+0.37}_{-0.17}$
A2034	0.113	2204	$19.98^{+2.54}_{-1.37}$	$21.22^{+1.93}_{-2.18}$	0.106	$1.06^{+0.37}_{-0.27}$
A2052	0.035	890	$9.12^{+1.26}_{-1.72}$	$13.45^{+2.46}_{-1.28}$	0.147	$1.62^{+0.27}_{-0.22}$
A2063	0.035	6263	$10.30^{+1.94}_{-1.29}$	$20.06^{+2.47}_{-2.46}$	0.194	$0.80^{+0.27}_{-0.28}$
A2065	0.073	3182	$39.43^{+5.82}_{-4.18}$	$94.05^{+10.27}_{-11.28}$	0.238	$0.41^{+0.29}_{-0.27}$
A2124	0.065	3238	$13.12^{+1.37}_{-1.27}$	$20.67^{+2.15}_{-2.19}$	0.157	$0.91^{+0.12}_{-0.16}$
A2142	0.091	1228	$29.87^{+2.47}_{-3.17}$	$21.69^{+3.16}_{-1.28}$	0.072	$0.93^{+0.12}_{-0.17}$
A2147	0.035	3211	$10.93^{+1.27}_{-1.28}$	$18.09^{+2.52}_{-1.27}$	0.165	$1.12^{+0.19}_{-0.19}$
A2163	0.203	545	$111.18^{+5.92}_{-7.38}$	$143.51^{+14.92}_{-15.37}$	0.129	$0.51^{+0.14}_{-0.15}$
A2199	0.030	497	$12.38^{+2.18}_{-1.29}$	$24.25^{+2.38}_{-2.19}$	0.195	$0.90^{+0.39}_{-0.10}$
A2204	0.152	499	$23.35^{+3.16}_{-2.17}$	$43.67^{+5.82}_{-5.19}$	0.186	$0.85^{+0.36}_{-0.37}$
A2218	0.175	553	$6.46^{+0.82}_{-0.83}$	$8.95^{+2.15}_{-0.93}$	0.138	$1.78^{+0.14}_{-0.15}$
A2219	0.225	896	$36.49^{+4.92}_{-3.39}$	$47.06^{+5.38}_{-4.19}$	0.128	$0.83^{+0.37}_{-0.33}$
A2244	0.097	4179	$36.52^{+3.16}_{-3.18}$	$35.20^{+4.16}_{-3.82}$	0.096	$0.81^{+0.16}_{-0.17}$
A2256	0.058	519	$47.78^{+5.37}_{-5.29}$	$57.77^{+5.97}_{-6.92}$	0.120	$1.12^{+0.11}_{-0.27}$
A2319	0.056	3231	$46.00^{+4.57}_{-5.82}$	$71.45^{+8.14}_{-6.93}$	0.155	$0.86^{+0.12}_{-0.10}$
A2390	0.228	500	$28.21^{+3.15}_{-2.39}$	$50.89^{+5.67}_{-4.86}$	0.180	$0.94^{+0.12}_{-0.11}$
A2462	0.073	4159	$20.73^{+2.47}_{-2.49}$	$28.33^{+3.14}_{-3.11}$	0.136	$1.21^{+0.15}_{-0.10}$
A2537	0.295	4962	$16.12^{+2.16}_{-2.19}$	$31.45^{+4.28}_{-3.19}$	0.195	$1.18^{+0.13}_{-0.11}$
A2589	0.041	3210	$10.05^{+1.27}_{-1.29}$	$18.43^{+3.15}_{-2.91}$	0.183	$1.34^{+0.17}_{-0.17}$
A2597	0.085	922	$10.76^{+1.27}_{-1.22}$	$12.34^{+1.27}_{-1.28}$	0.114	$0.92^{+0.11}_{-0.18}$
A2634	0.031	4816	$11.88^{+2.15}_{-1.27}$	$22.11^{+2.63}_{-2.18}$	0.186	$1.21^{+0.19}_{-0.24}$
A2657	0.040	4941	$9.89^{+2.17}_{-1.28}$	$19.53^{+2.15}_{-2.72}$	0.197	$1.18^{+0.13}_{-0.15}$
A2667	0.230	2214	$19.71^{+2.61}_{-1.27}$	$37.59^{+4.72}_{-3.18}$	0.190	$0.74^{+0.14}_{-0.11}$
A2670	0.076	4959	$16.62^{+1.25}_{-1.62}$	$30.09^{+3.61}_{-3.18}$	0.180	$0.74^{+0.12}_{-0.12}$
A2717	0.049	6973	$12.94^{+2.11}_{-1.26}$	$25.13^{+2.34}_{-2.15}$	0.194	$1.03^{+0.14}_{-0.15}$
A2744	0.308	2212	$22.17^{+2.14}_{-2.26}$	$48.97^{+5.16}_{-4.72}$	0.220	$0.70^{+0.12}_{-0.13}$
A3112	0.075	6972	$18.84^{+3.14}_{-2.16}$	$13.61^{+2.17}_{-1.27}$	0.072	$0.83^{+0.15}_{-0.18}$
A3158	0.060	3712	$25.80^{+3.17}_{-2.72}$	$16.76^{+2.15}_{-1.27}$	0.065	$0.95^{+0.14}_{-0.12}$
A3266	0.059	899	$33.25^{+4.16}_{-3.27}$	$42.05^{+5.42}_{-4.17}$	0.126	$1.23^{+0.15}_{-0.17}$
A3376	0.045	3202	$26.61^{+3.72}_{-2.91}$	$30.67^{+4.27}_{-3.27}$	0.115	$1.63^{+0.35}_{-0.17}$
A3391	0.051	4943	$18.91^{+1.25}_{-1.28}$	$30.61^{+4.28}_{-3.27}$	0.161	$0.72^{+0.19}_{-0.18}$
A3395	0.050	4944	$33.67^{+4.27}_{-4.12}$	$45.40^{+6.87}_{-5.28}$	0.134	$0.82^{+0.14}_{-0.13}$
A3526	0.011	504	$8.26^{+0.72}_{-0.28}$	$18.24^{+2.36}_{-1.92}$	0.220	$0.69^{+0.14}_{-0.13}$
A3558	0.048	1646	$21.27^{+3.27}_{-2.16}$	$28.64^{+4.25}_{-2.37}$	0.134	$0.76^{+0.18}_{-0.28}$
A3562	0.049	4167	$14.05^{+1.56}_{-1.46}$	$33.07^{+4.27}_{-3.27}$	0.235	$0.67^{+0.18}_{-0.19}$
A3571	0.039	4203	$30.41^{+3.75}_{-3.84}$	$39.35^{+4.46}_{-3.28}$	0.129	$0.91^{+0.17}_{-0.19}$
A3667	0.055	889	$26.84^{+2.48}_{-2.46}$	$44.18^{+4.56}_{-4.74}$	0.164	$0.87^{+0.17}_{-0.16}$
A3827	0.098	7920	$78.90^{+5.26}_{-4.27}$	$70.79^{+8.36}_{-6.48}$	0.089	$0.53^{+0.24}_{-0.34}$
A3921	0.093	4973	$29.61^{+2.15}_{-1.77}$	$18.56^{+2.36}_{-2.74}$	0.062	$1.16^{+0.48}_{-0.29}$

Continuation of the tabl. 2.2

Cluster	z	ObsID	M_{200}, 10^{14} $M_\odot$	$M_{\rm b}$, 10^{13} $M_\odot$	$f_{M_{\rm b}/M_{\rm tot}}$	α
A4038	0.030	4992	$8.26^{+1.18}_{-0.92}$	$14.98^{+2.10}_{-1.48}$	0.180	$0.77^{+0.12}_{-0.13}$
A4059	0.047	897	$10.72^{+0.92}_{-1.28}$	$13.64^{+1.25}_{-1.28}$	0.127	$0.83^{+0.12}_{-0.15}$
AWM4	0.032	9423	$6.55^{+0.85}_{-0.37}$	$15.61^{+1.47}_{-1.47}$	0.238	$1.52^{+0.25}_{-0.22}$
CLJ1226.9 + 3332	0.890	3180	$143.19^{+15.26}_{-17.26}$	$94.12^{+10.16}_{-9.27}$	0.065	$0.52^{+0.16}_{-0.11}$
Coma (A1656)	0.023	10672	$41.94^{+4.72}_{-3.92}$	$76.82^{+7.62}_{-4.58}$	0.183	$0.63^{+0.16}_{-0.16}$
IIIZw54	0.0311	4182	$8.81^{+1.04}_{-0.93}$	$17.99^{+1.74}_{-2.15}$	0.204	$1.43^{+0.28}_{-0.27}$
ISCSJ1438 + 3414	1.41	10461	$293.15^{+18.27}_{-36.84}$	$316.22^{+112.92}_{-74.83}$	0.107	$0.35^{+0.14}_{-0.14}$
MACSJ0011.7 − 1523	0.379	3261	$48.34^{+3.82}_{-4.15}$	$59.97^{+4.88}_{-4.28}$	0.124	$0.63^{+0.16}_{-0.18}$
MACSJ0159.8 − 0849	0.405	3265	$44.00^{+4.84}_{+4.44}$	$52.57^{+5.18}_{-4.92}$	0.119	$0.72^{+0.24}_{-0.36}$
MACSJ0242.6 − 2132	0.314	3266	$27.44^{+1.99}_{-2.19}$	$48.48^{+4.28}_{-4.83}$	0.176	$0.64^{+0.17}_{-0.17}$
MACSJ0429.6 − 0253	0.399	3271	$18.50^{+1.82}_{-1.63}$	$31.31^{+3.24}_{-3.18}$	0.169	$0.93^{+0.17}_{-0.17}$
MACSJ0647.7 + 7015	0.59	3196	$89.51^{+10.14}_{-9.28}$	$98.25^{+8.12}_{-7.28}$	0.109	$0.77^{+0.37}_{-0.27}$
MACSJ0744.8 + 3927	0.697	536	$106.48^{+8.82}_{-6.18}$	$97.81^{+9.16}_{-7.99}$	0.091	$0.65^{+0.19}_{-0.19}$
MACSJ1115.8 + 0129	0.355	3275	$23.59^{+4.17}_{-3.18}$	$49.38^{+4.76}_{-5.17}$	0.209	$0.64^{+0.26}_{-0.25}$
MACSJ1311.0 − 0311	0.49	3258	$55.11^{+4.84}_{-5.58}$	$68.15^{+7.15}_{-6.72}$	0.123	$0.54^{+0.23}_{-0.13}$
MACSJ1423.8 + 2404	0.545	4195	$48.21^{+4.72}_{-4.72}$	$34.90^{+3.26}_{-3.55}$	0.072	$0.63^{+0.18}_{-0.18}$
MACSJ1427.6 − 2521	0.318	3279	$25.04^{+2.36}_{-2.26}$	$34.75^{+3.17}_{-3.33}$	0.138	$0.84^{+0.33}_{-0.23}$
MACSJ1720.3 + 3536	0.391	3280	$40.70^{+5.17}_{-4.92}$	$37.61^{+4.29}_{-4.83}$	0.092	$0.79^{+0.17}_{-0.17}$
MACSJ1931.8 − 2635	0.352	3282	$32.78^{+3.91}_{-4.19}$	$42.24^{+7.11}_{-6.18}$	0.129	$0.77^{+0.38}_{-0.33}$
MACSJ2129.4 − 0741	0.589	3199	$96.66^{+10.26}_{-10.15}$	$95.79^{+7.91}_{-6.19}$	0.099	$0.64^{+0.18}_{-0.18}$
MACSJ2229.8 − 2756	0.324	3286	$46.06^{+4.92}_{-5.17}$	$35.64^{+4.82}_{-5.19}$	0.077	$0.84^{+0.19}_{-0.19}$
MKW3s	0.045	900	$12.02^{+2.47}_{-3.19}$	$20.87^{+3.99}_{-4.18}$	0.173	$0.85^{+0.17}_{-0.19}$
MKW4	0.020	3234	$2.22^{+1.84}_{-2.10}$	$7.69^{+1.94}_{-2.19}$	0.346	$1.75^{+0.28}_{-0.27}$
MKW8	0.027	4942	$7.47^{+1.48}_{-2.57}$	$8.34^{+2.37}_{-1.87}$	0.111	$1.83^{+0.18}_{-0.17}$
PKS0745 − 19	0.103	508	$33.52^{+3.17}_{-3.17}$	$30.04^{+2.84}_{-2.93}$	0.089	$1.88^{+0.18}_{-0.19}$
RXCJ0043.4 − 2037	0.292	9409	$6.38^{+0.82}_{-0.84}$	$10.29^{+2.55}_{-3.19}$	0.161	$1.43^{+0.18}_{-0.18}$
RXCJ0232.2 − 4420	0.283	4993	$18.25^{+2.16}_{-1.82}$	$16.51^{+1.48}_{-1.55}$	0.090	$1.31^{+0.34}_{-0.38}$
RXCJ0307.0 − 2840	0.253	9414	$12.62^{+1.72}_{-1.82}$	$21.28^{+2.10}_{-2.11}$	0.128	$1.21^{+0.19}_{-0.19}$
RXCJ0516.7 − 5430	0.294	9331	$13.96^{+1.54}_{-1.22}$	$17.59^{+2.10}_{-1.99}$	0.126	$1.34^{+0.17}_{-0.16}$
RXCJ0547.6 − 3152	0.148	9419	$11.06^{+1.17}_{-1.10}$	$18.82^{+2.12}_{-2.18}$	0.150	$1.64^{+0.15}_{-0.15}$
RXCJ0605.8 − 3518	0.141	12899	$6.37^{+0.75}_{-0.72}$	$13.84^{+1.38}_{-1.28}$	0.117	$1.54^{+0.19}_{-0.19}$
RXCJ1131.9 − 1955	0.307	3276	$15.43^{+1.45}_{-1.66}$	$20.92^{+2.10}_{-1.28}$	0.115	$1.42^{+0.18}_{-0.18}$
RXCJ2014.8 − 2430	0.161	11757	$10.53^{+1.48}_{-1.47}$	$18.27^{+1.58}_{-1.93}$	0.123	$1.64^{+0.19}_{-0.18}$
RXCJ2129.6 + 0005	0.235	552	$8.46^{+0.94}_{-1.10}$	$12.27^{+1.33}_{-1.26}$	0.115	$1.73^{+0.24}_{-0.22}$
RXCJ2337.6 + 0016	0.273	3248	$8.50^{+1.01}_{-0.89}$	$13.75^{+1.44}_{-1.55}$	0.131	$1.67^{+0.19}_{-0.19}$
ZwCL1215	0.075	4184	$33.71^{+4.17}_{-4.29}$	$36.33^{+3.17}_{-2.38}$	0.118	$0.74^{+0.14}_{-0.13}$
RCSJ0224 − 0002	0.778	4987	$10.51^{+1.11}_{-1.28}$	$22.45^{+0.19}_{-0.11}$	0.113	$1.02^{+0.15}_{-0.14}$
RCSJ0439 − 2904	0.951	3577	$3.79^{+0.56}_{-0.27}$	$9.01^{+1.66}_{-2.18}$	0.207	$1.84^{+0.36}_{-0.33}$
RCSJ1107 − 0523	0.735	5825	$5.27^{+0.74}_{-0.45}$	$12.65^{+1.47}_{-1.48}$	0.219	$1.53^{+0.54}_{-0.53}$
RCSJ1419.2 + 5326	0.64	3240	$12.91^{+1.64}_{-1.72}$	$33.91^{+2.88}_{-3.17}$	0.222	$0.67^{+0.12}_{-0.13}$
RCSJ1620 + 2929	0.87	3241	$7.57^{+1.02}_{-1.04}$	$14.15^{+1.47}_{-1.82}$	0.147	$1.04^{+0.14}_{-0.15}$

End of the tabl. 2.2

Cluster	z	ObsID	M_{200}, 10^{14} $M_\odot$	$M_{\rm b}$, 10^{13} $M_\odot$	$f_{M_{\rm b}/M_{\rm tot}}$	α
RCSJ2156 + 0123	0.335	674	$22.80^{+3.28}_{-2.88}$	$42.97^{+5.82}_{-5.28}$	0.181	$0.58^{+0.11}_{-0.12}$
RCSJ2318 + 0034	0.78	4938	$28.37^{+4.11}_{-3.18}$	$51.45^{+5.27}_{-5.82}$	0.141	$0.64^{+0.15}_{-0.14}$
RCSJ2319 + 0038	0.904	5750	$40.96^{+4.25}_{-5.22}$	$91.91^{+8.88}_{-9.45}$	0.204	$0.54^{+0.15}_{-0.16}$
RXJ0439.0 + 0520	0.208	527	$9.11^{+1.75}_{-2.27}$	$11.43^{+2.16}_{-1.37}$	0.225	$1.04^{+0.29}_{-0.38}$
RXJ0848.7 + 4456	0.570	927	$3.32^{+0.73}_{-0.77}$	$9.36^{+3.56}_{-2.19}$	0.241	$1.01^{+0.14}_{-0.15}$
RXJ0849 + 4452	1.26	945	$4.67^{+0.66}_{-0.47}$	$67.87^{+6.48}_{-6.84}$	0.165	$0.55^{+0.17}_{-0.16}$
RXJ0910 + 5422	1.106	2227	$64.92^{+5.67}_{-7.34}$	$66.84^{+6.77}_{-7.55}$	0.143	$0.63^{+0.13}_{-0.13}$
RXJ1113.1 − 2615	0.730	915	$5.30^{+0.73}_{-0.48}$	$12.72^{+1.49}_{-1.48}$	0.219	$1.04^{+0.33}_{-0.37}$
RXJ1221.4 + 4918	0.700	1662	$46.64^{+5.22}_{-3.49}$	$75.08^{+6.32}_{-4.29}$	0.151	$0.54^{+0.18}_{-0.18}$

Using equation (2.95), we found the next expression:

$$\mathrm{norm_{sim}} = \mathrm{EM_{sim}} \times 10^{-14}/[4\pi(D_A(1+z))^2], \tag{2.96}$$

where $\mathrm{norm_{sim}}$ is the value of $\mathrm{norm_{MEKAL}}$ in numerical simulations, D_A is the angular distance to cluster. From the observational data we got the normalization parameter of the best-fit MEKAL model, $\mathrm{norm_{MEKAL}}$, which was fitted by the $\mathrm{norm_{sim}}$ values obtained from the simulations. Since the $\mathrm{norm_{MEKAL}}$ parameter can be expressed by:

$$\mathrm{norm_{MEKAL}} = \frac{0.64}{m_{\rm p}^2} \int \frac{(\rho_g^{\rm real})^2 dV \times 10^{-14}}{[4\pi(D_A(1+z))^2]}, \tag{2.97}$$

by using Eq. (2.95, 2.96) and Eq. (2.97), we obtain that the normalization factor a is given by:

$$a = \sqrt{\frac{\mathrm{norm_{MEKAL}}}{\mathrm{norm_{sim}}}}. \tag{2.98}$$

Therefore we are able to obtain the field of hot gas density $\rho_g^{\rm real} = a \cdot \rho_g^{\rm sim}$ and the emission measure $\mathrm{EM_{real}}$, using $\rho_g^{\rm real}$ into Eq. (2.95) instead of $\rho_g^{\rm sim}$.

For each cluster, we performed a series of numerical simulations of the emission measure profile. In our model we used two free parameters ρ_0 and r_s from NFW model. Sorting them out in the acceptable ranges for $\rho_0 = 10^{-25}$—10^{-18} and $r_s = 0.1$ to 2 Mpc, we selected such pair of values, which is the best convenient for describing the observational cluster profile. Using the χ^2 test we found the values ρ_0 and r_s with 90 % confidence level. Using these parameters we have reconstructed the density profiles for DM and gas.

Galaxy cluster's mass profile. In order to calculate the total mass profiles of galaxy clusters, the spherical symmetry and hydrostatic equilibrium

of clusters was assumed. We have determined the total mass of clusters using two independent methods. In the first one, we have parameterized the cluster total mass profiles (luminous + dark matter) using NFW model (slope $\alpha = 1$, method 1). The gas profiles were also calculated at this stage (see [252]).

In method 2, we modeled the total mass profile as composed of three components: the dark matter halo (fitted with a generalized NFW profile), the gaseous component (an improvement on the beta model described in the previous paragraph), and the luminous component of the central galaxy (approximated with a Jaffe profile [139]). For the density profile of DM, we used the NFW model having a DM density profile given by Eq. (2.22) and a mass profile, within a fixed radius given by

$$M(<r) = 4\pi\rho_0 r_s^3 \left[\ln\left(1 + \frac{r}{r_s}\right) - \frac{r}{r_s + r}\right], \tag{2.99}$$

where ρ_0, and r_s were defined in section on the density profiles.

Mass contribution of X-ray diffused gas. As pointed out in [252], they obtained the gas profiles through the method 1 and did not involve a functional form for the gas profile.

In the method 2, in order to approximate the gas contribution to the total mass allowing us to get the DM profile, it is necessary to apply a model for the gas density profile. The so called beta model [60, 64], which is widely used, is given by Eq. (2.71). This model is not quite precise for the gas distribution determination. It overestimates the baryons density at high radii leading to the flatter profiles in cluster centre, and to the biases in the gas distribution and gas fraction in clusters. According to [252], the beta model has a slight influence on the DM profile since a gas fraction is only 10 % of the total mass. So, we improved the gas modeling (see subsection on the advanced β model) and introduced a model that gives the better results than the beta model.

Stellar component. The studied clusters have a single, optically dominant BCG near their centers. It allows determining the mass of the stars in the central galaxy through the Jaffe model [139] with the same parameters as in [252]:

$$\rho_J(r) = \frac{\rho_{0,J}}{(r/r_c)^2(1 + r/r_c)^2}, \tag{2.100}$$

where $\rho_{0,J}$ is the central density and r_c is the core radius. The total mass profile was obtained adding the stellar mass to the generalized NFW potential of DM, and the beta model for describing the emitting gas. Due to a small effect of the including the model for the central galaxy on the results, we limited the modeling of the stellar mass only to the central galaxy, since the effect of the others is even less than the central one. Thus, two parameters of the model, ρ_J, and r_c were fixed as the following: $R_e = 0.76\, r_c = 25$ kpc, and

$\rho_{0,J} = M_J/(4\pi r_c^3)$, where $M_J = 1.14 \times 10^{12} M_\odot$ is the estimated value of the stellar mass of the BCG of MS 2137 – 2353. We recall that the effective radius R_e is the radius containing half of the light. The stellar mass of all clusters is assumed to be the same. It was shown by SA07, even using a different model for the stars of the central galaxy (for example, [274]) does not change the results.

Mass profiles scaling. Simple analytical and numerical simulations of structure formation predict that galaxy clusters are self-similar, both for what concerns as the DM component and the hot ICM (intra-cluster medium). Scaling laws relate each physical property to the total mass M of the cluster, and to redshift [52, 59, 83, 145, 267].

The DM density profiles are approximately universal on a large mass scale [139]. In our work we scaled the mass profiles with R_{200} and M_{200} (here R_{200} is the radius within which the mean halo density is 200 times the critical density, and M_{200} is the total mass of galaxy cluster inside a sphere with radius R_{200}). We defined the total mass within a given overdensity Δ as:

$$M_\Delta = \frac{4}{3}\pi\Delta\rho_c R_\Delta^3, \tag{2.101}$$

where (see section 1) $R_\Delta^3 = c_\Delta r_s$ is the radius within which the mean cluster overdensity is Δ times ρ_c and the relation with the concentration c_Δ and the scale radius r_s holds by definition of the NFW mass profile (we assumed $\Delta = 200$).

The important aim of our study is to analyze if the baryonic content in the galaxy clusters has influences on the slope of the density profile. Thus, we calculated the fraction M_b/M_{200} for each object from our sample, this ratio will be obtained subtracting the DM mass from the total mass in each cluster. Taking into account R_{200_2} values for the clusters, the total mass profile of which is M_{200}, modeled with our introduced method 2, namely, considering a three-component model (luminous (stellar) matter, M_*, gaseous fraction, $M_{\rm gas}$, and dark matter, $M_{\rm DM}$), we can obtain the total mass for each cluster:

$$M_{\rm tot_2} = M_* + M_{\rm gas} + M_{\rm DM} = M_b + M_{\rm DM}. \tag{2.102}$$

Taking into account R_{200_1} values for the clusters modeled with method 1, namely, considering a two-component model (luminous (stellar) matter and dark matter), we can obtain the total mass for each cluster by this method:

$$M_{\rm tot_1} = M_* + M_{\rm DM}. \tag{2.103}$$

Then the baryonic mass is given by:

$$M_{\rm b} = M_{\rm tot_2} - M_{\rm tot_1} + M_* = M_{\rm gas} + M_*. \tag{2.104}$$

As the result we get a relation between the obtained values of α, namely, the fits to the dark matter component through a gNFW model, and the baryonic content $M_{\rm b}$.

2.4.2. Total mass and dark matter profiles

Total mass profile. We summarized our results obtained from the modeling the total mass profiles of the Chandra galaxy clusters with a NFW model ($\alpha = 1$) in Table 2.2. We note that the quoted authors used both the NFW model and the singular isothermal sphere model (SI) ($\rho(r) \propto r^{-2}$). They concluded that the latter model is a much worse fit for almost all clusters in the sample. So, we used only the NFW model in our study.

The first column in Table 2.2 includes the target name, redshift, number of ID observation, the total mass in clusters at radius R_{200}, the mass of baryonic matter in clusters, and the fraction of baryonic matter in total mass, and, in the case of the gNFW, we give the inner value of slope, α. Confidence levels are 68 %. The NFW model is a good fit for the most clusters, similarly to SA07. We have found that for 110 of 128 clusters, the probability of the χ^2/d.o.f. value based on a χ^2 distribution is 0.04 or better, and only for 18 clusters the probability drop is below 0.002. Combining the results for all studied galaxy clusters, the NFW model gave a total χ^2 of 2603.48 for 1267 d.o.f.

Dark matter profile. As already reported, we considered two approaches. In the first case, we examined the models, in which the inner slope of the DM profile was fixed at $\alpha = 1$ accordingly to the NFW model. In the second case, we decomposed the total mass of galaxy cluster in its DM, diffused gas, and BCG components. Our results, when the cluster mass distributions were separated in the dark matter halo (fitted with a gNFW model), the X-ray emitting halo, and the luminous mass of the central galaxy.

We calculated also the concentration parameter for each cluster to obtain the mass-concentration parameter: $c_{\rm vir} \equiv c_{200}$ and $M_{\rm vir} \equiv M_{200}$ [2]. We define the concentration parameters, similarly to [252], as $c_{\rm vir} = (r_{\rm vir}^{\rm total}/r_s^{\rm dark})$ [3].

The simplest analytic form that describes the mass-concentration relation is a power-law model:

$$c(z) = \frac{c_0}{(1+z)^b}\left(\frac{M}{8\times 10^{14}{\rm h}^{-1}M_\odot}\right)^a. \qquad (2.105)$$

The relation between concentration and total masses for CDM haloes is not so well represented by Eq. (2.105) with $b = 1$ [94, 252]. In order to improve the description of Chandra data, we assumed differently from [53] to consider a redshift evolution, namely $b \neq 1$ in Eq. (2.105). The motivation to the new redshift dependence comes from the fact that clusters are more complicated objects than those assumed in [53]. They contain X-ray emitting gas and stars, as well as DM. At the highest mass, [53] argued that [292] model

[2] We note that $c_{\rm vir}$, and $M_{\rm vir}$ in [252] are connected through the equation $M_{\rm vir} = \frac{4}{3}\pi r_{\rm vir}^3 \Delta_c(z)\rho_c$, with $\Delta_c = 178\Omega_m(z)^{0.45}$ [163].

[3] Both the virial radii and virial masses are calculated for the total mass model, including all the mass components.

could overpredict the evolution of $c_{\rm vir}$ with z, and moreover, to date the mass-concentration relation studies includes few clusters in the largest mass range in Chandra data.

The result from a standard χ^2 fit, and using the three free parameters c_0, a and b, is shown by the thick solid line (average value) and thin solid lines ($\pm 2\sigma$ CL) in Fig. 2.9. We have concluded that this model (b not equal 1) gives an improved description of our sample with $\chi^2 = 288.7$ for 125 d.o.f. then the same model with $b = 1$. For 34 galaxy clusters and with similar model, [252] have obtained the best-fitting parameters $c_0 = 7.55 \pm 0.90$, $a = -0.45 \pm 0.12$ and $b = 0.71 \pm 0.52$ with $\chi^2 = 41.5$ for 29 degrees of freedom. We have also compared our results to that of [97] and [38], plotted in Fig. 2.9. As shown, these two models are in a good agreement with our data, and our mass-concentration relation. Using the best-fit parameters from our fit, we determine the intrinsic scatter in our sample as $\sim$0.2, which is also in a good agreement with simulations and previous works [53, 252].

The inner slope of DM profiles. Finally, we fitted the DM profiles by means of a gNFW model to have hints on the inner slopes of the density profiles. The results are summarized in Table 2.2. The goodness of fit for 110 from 128 galaxy clusters give χ^2/d.o.f. value with probability of 0.03 or better.

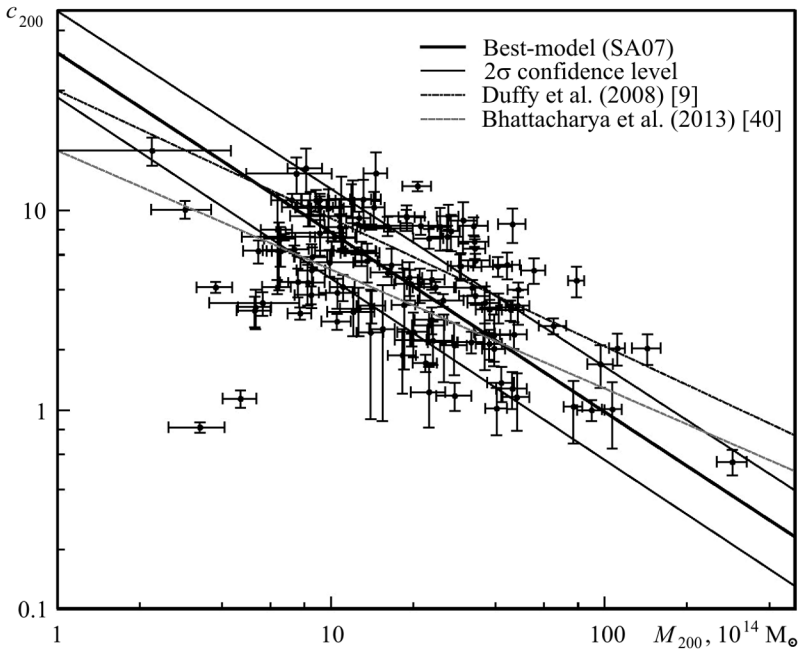

Fig. 2.9. The mass-concentration relation for the total mass ($c_{200} - M_{200}$). Thick (thin) solid line: best-fitting model and 2σ CL. The dashed line represents the [97] model, and the dotted line the [38] model (see the text for details). The image is taken from [30]

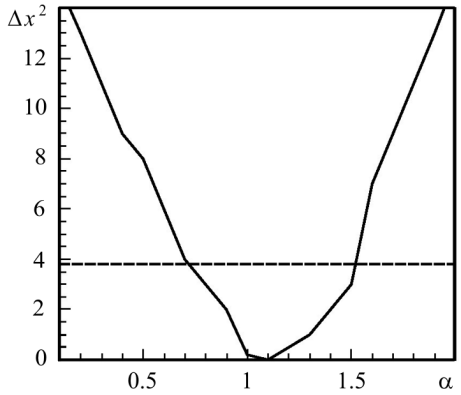

Fig. 2.10. The summed χ^2 values as a function of α for the clusters, for which the NFW model provides a reasonable fit to the data. The dashed line indicates the 2 σ confidence levels. Overall best fit: $\alpha = 1.10^{+0.40}_{-0.48}$ (95 % confidence level). The image is taken from [30]

The value of α obtained is $\alpha = 1.1 \pm \pm 0.4$ (95 % confidence limits) from the summed χ^2 data. The result was obtained summing the χ^2 (as a function of α) for the 128 clusters (Fig. 2.10). This result is consistent with predictions from CDM simulations.

Similarly to [252], in order to get α on the combined DM profile, we summed χ^2 values as function of α for the clusters for which the NFW model provides a reasonable fit to the data. We showed the results in Fig. 2.11. The best fit is $\alpha = 1.10^{+0.40}_{-0.48}$ (95 % confidence limits).

Note, that three separate components (DM, gas and BCG) to model were included in the fits. The values of the slope are in the range $0.4 < \alpha < 1.8$ and the density profile for the largest number of clusters is compatible with the expectation from ΛCDM model $0.7 < \alpha < 1.5$. Some clusters (∼32 %) have a flatter profile than the cuspy dark matter profile predicted by CDM simulations. A few clusters have the slopes smaller than 0.7 and they are usually characterized by an higher $M_{\rm b}$, when comparing the clusters with larger α.

The correlation between the gas fraction and the inner slope indicates that the baryonic component affect the dark matter distribution in the central region of cluster, which is in agreement with some other results [84].

2.4.3. Inner slope and baryons content of DM density profile

We discussed that there are clusters which have no the best fitted profiles by the NFW model. Among the processes able to produce the flat profile, the role of baryons has been several times claimed. Recently, [79] studied the effect of baryons, and the central BCG in shaping the inner density profile. It was also shown how higher content of baryons can give rise to profiles similar to A611 and A383, which have the slopes flatter than NFW profile, and small baryonic content can produce steeper inner profiles in agreement with the NFW model (MACS J 1423.8 + 2404, RXJ1133).

Being motivated by the previous arguments, we studied the eventual correlation among the inner density profile slope, α, and the baryonic content of the studied X-ray galaxy clusters. We performed an analysis, in which the

total mass was separated in the DM halo, the X-ray emitting halo, and the luminous mass of the BCG. We fitted the DM profile with a gNFW model and calculated α, and reported the values in Table 2.2. $M_{\rm b}$ was calculated from the analysis of the baryonic content, summing the diffuse gas content and the baryons contained in the central BCG in each cluster. We plotted the inner slope, α, versus the baryonic content at the radius of R_{200} in Fig. 2.11. The plot shows a tight correlation between the inner slope α and the baryonic content: the larger is the baryonic content the flatter is the inner profile. This result is in agreement with studies of the role of baryons on the inner slope of clusters.

We have fitted the $\alpha_{\rm gNFW} - M_{\rm b}$ relation using a simple power-law model ($y(x) = k^* x^{-b}$), and found the slope $b = 1.72 \pm 0.37$ at 68 % confidence level. We calculated the intrinsic systematic scatter that can be present in the $\alpha - M_{\rm b}$ relation. Using the simple power law model with k and b as free parameters we found that the scatter is $\Delta \lg(b) \sim 0.2$. The flattening of the slope can be interpreted as due to the fact that the presence of a larger quantity of baryons guarantees a larger transfer of energy and angular momentum from baryons to DM, with the result that DM moves to larger orbits, reducing the inner density and forming haloes rounder than those seen in DM simulations

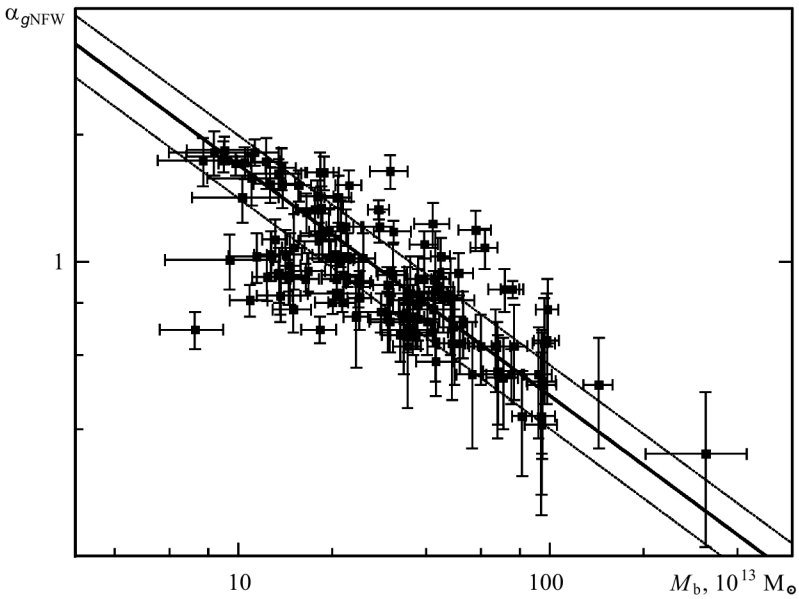

Fig. 2.11. $\alpha_{\rm gNFW} - M_{\rm b}$ relation for all sample of galaxy clusters. The data were obtained fitting the DM profiles of clusters with the gNFW model. The baryonic mass was obtained, as described in the text, by subtracting the DM component from the total mass. The solid line represents the power-low fit with slope $b = 1.72 \pm 0.37$ (68 % confidence level). The dashed lines correspond to the region enclosed by the mean $\pm 1\sigma$ standard deviation. The image is taken from [30]

[1, 68, 131]. However, as reported in the introduction, the slopes flatter than those obtained in the simulations, $\alpha < 0.7$ are observed in some clusters and the largest number of dwarf galaxies and LSBs. A few of our studied clusters have slopes $\alpha < 0.7$.

As already reported, NFW N-body simulations predicted a profile with inner slope $\propto r^{-1}$ and an outer one $\propto r^{-3}$. More recently, it has been shown that the density profiles are better fitted by an Einasto profile which becomes shallower towards the centre of the halo (e.g. [205]). In any case, the lower values for the inner slope obtained in N-body simulations are $\alpha = 0.8$ at 120 pc [261] in agreement with the analytical and numerical works to solve the Jeans equation [22, 69]. Inner density slopes in the range $0.7 < \alpha < 1.5$ could be considered in agreement with ΛCDM predictions [252].

Given the several and noteworthy pieces of evidence supporting ΛCDM on large scales, the discrepancy could be connected to the fact that baryonic physics is a fundamental issue in cluster formation. It could originate just because we are comparing dissipationless systems generated by N-body simulations with real, dissipational structures, whose physics is different from the dissipationless physics typical of DM. We should not forget that the inner 10 kpc of clusters are dominated by baryons whose presence strongly influence the DM distribution. While baryons can steepen the inner slope of the density profile of clusters through the adiabatic contraction of DM [40, 123, 126], heating of DM due to dynamical friction with cluster galaxies can counteract the adiabatic contraction effect and flatten the inner profile.

Other mechanisms can give rise to flattening of the inner slope of the density profile. The spatial distributions of components constituting the cluster can be changed by feedback processes [178], gas cooling, star formation, and dynamical interactions between different mass components (e.g., BCG galaxy and the ICM in relaxed clusters). The already reported adiabatic contraction steepens the density profile and may produce a rounder halo. AGN feedback can flatten the inner density profile [178], as supernovae feedback can flatten the inner profile of galaxies [266]. SMBH outburst also produces changes in the inner gas distribution [164], and gravitational interaction (galaxy-galaxy, ram pressure stripping, etc.) play a role in this very dense environment [37, 67, 185, 273].

Comparison with other studies of the inner DM slopes. We here discuss how our results compare to previous studies of the inner density slope of density profiles. The inner slopes of clusters are compatible in our and [252] study. Other clusters, like A383, A611, A963, A1835, A2029, A2204, A2589 were studied by others authors. For example, A611 was studied in [207] who combined weak lensing from multicolor Subaru imaging, strong lensing using data of Hubble Space Telescope and stellar velocity dispersion measures (Keck Telescope), sampling the dark matter profile from 3 kpc to 3.25 Mpc. It was

found values of $r_s = 320^{+240}_{-110}$ kpc and $c = 5.1^{+1.7}_{-1.6}$ are in agreement with [252], but $\alpha < 0.3$(<0.56, <0.65) at 68 % (95 %, 99 %) CL. [252] found a value of the slope $\alpha = 0.64^{+0.94}$.

A383 was studied in [247] finding a flat inner DM slope ($\alpha = 0.45^{+0.2}_{-0.25}$), and in [208] who found $\alpha < 1$ at (95 % CL) and a best fit (inferred from weak and strong lensing, kinematics and X-ray data) of $\alpha = 0.59^{+0.30}_{-0.35}$. [252] found $\alpha < 0.8$, we found $\alpha = 1.1 \pm 0.4$. A flat slope was obtained also for A963 [22], but [37, 67, 252] found values consistent with the NFW model. We found $\alpha = 1.52^{0.13}_{-0.12}$. In the case of A2029, [122] found $\alpha = 1.19 \pm 0.04$ similarly to [252], and we got $0.91^{+0.37}_{-0.17}$. In the case of A1835, A2029, A2204, [15] by means of Chandra data obtained $\alpha \simeq 0.9$, $\alpha \simeq 1.85$, and $\alpha \simeq 1.8$, respectively, much larger than [252] values and ours.

A detailed analysis of DM and baryonic distributions in A611 and A383 is presented in [207, 208] combining weak lensing, strong lensing and stellar velocity dispersion for the BCG, and finding slopes flatter than the NFW predictions. According to these authors, degeneracies in constraining the DM profile can be broken only simultaneously using the three techniques. In reality, the X-ray observations alone give information on clusters on cluster structure in the range 50—500 kpc. At smaller radii, temperature determination is limited by instrumental resolution, substructure, and they are also limited by "cooling flows" presence and the breaking of assumption of hydrostatic equilibrium. So, if the point of view by Newman et al. [207, 208] is correct, for clusters containing larger quantity of baryons the inner profile may be flatter than X-ray observations provide.

Effect of the BCG model on the results. In principle, one expects that the mass and model used to describe the BCG can influence the inner density slope. In order to understand, if this is the case, Schmidt & Allen [252] tried to understand how important was the role of central BCG in MS 2137.3 – 2353 (for which [204,205] found a flat profile). This BCG is one of the most massive in the sample. Varying the ratio M/L_V and recalculating the α value, they obtained a flattening of the profile for larger M/L_V, but in any case the inner slope was still compatible with a NFW fit. As already reported, the modeling of the mass associated to stars in the other galaxies in cluster has a negligible effect on the result, since stars have a small contribution ($\simeq$2 %) to the total system mass [169].

Systematic uncertanities. The clusters used in our analysis, are the most massive dynamically relaxed clusters known, and this should be a good issue to let us think that hydrostatic equilibrium assumption is robust. Uncertainties remain in disentangling DM and baryonic matter, geometric effects, could introduce some systematic uncertainties.

Other systematic uncertainties that could change the results is the presence of non-thermal pressure support (due to gas motions, cosmic rays or

magnetic fields). However for relaxed clusters, bulk and/or turbulent motions, if present, could cause changes in the mass measurements of 10—20 % accuracy [93, 200, 228]. Similar effects are expected by magnetic pressure [149]. Effects of magnetic pressure on X-ray measurements were studied by [7]. Magnetic pressure in relaxed clusters could produce effects of the order of 10—20 %, for individual cluster, on measurements [114, 159, 160, 182, 191, 293].

Another important issue to recall is the fact that in our study the X-ray data only extend to about r_{2500} (approximately a quarter to a third of the virial radius in most clusters). Extrapolating the allowed range of NFW mass models (discussed in the previous sections) to these larger radii gives also rise to some systematic uncertainty [57].

General remarks. We presented the reconstruction the reconstruction of the total mass (the fraction of dark matter, intercluster gas, and brightest galaxy of cluster) of 128 X-ray galaxy clusters in the redshift range 0.01—1.4, which is based on the Chandra observations. We measured the total mass M_{200} and the baryonic mass M_b, and also the concentration parameter c_{200}, that characterized the size of halo of dark matter for all the objects of our sample. We confirm that a tight correlation between c_{200} and M_{200}, $c \propto M_{\rm vir}^a/(1+z)^b$ with $a = -0.56 \pm 0.15$ and $b = 0.80 \pm 0.25$ (95 % CL) is present, which is in a good agreement with the predictions from numerical simulations and previous observations. Fitting the inner dark matter density slope α with a generalized NFW model, we got $\alpha = 1.10 \pm 0.48$ at 2σ confidence level combining the results for our entire sample for which the model gives a good description of the data. We obtained that the tight correlation between the inner slope of the density profile of dark matter α and the baryonic mass content M_b for massive galaxy clusters is present, namely, α is decreasing with increasing the baryonic mass content. We used the simple power-law model to fit the $\alpha - M_b$ distributions and found an inner slope $b = 1.72 \pm 0.37$ (68 % CL) of the density profile of dark matter.

2.5. Conclusion

The large scale structure of the Universe is defined by increasing dark matter density and by the dynamical interaction of dark energy and dark matter. A sufficient success was reached in recent years in constraining the cosmological parameters, and in reconstructing the evolution in the large-scale structure of the dark matter distribution, but we still lack an understanding the evolution of the baryonic component of the Universe. We do not understand well how the baryonic matter was collected in dark matter gravitational wells and participated in the formation of galaxies and their groups/clusters.

Recent observations with theoretical researches show that a baryonic structure formation on different scales is interrelated; galaxy formation is dependent

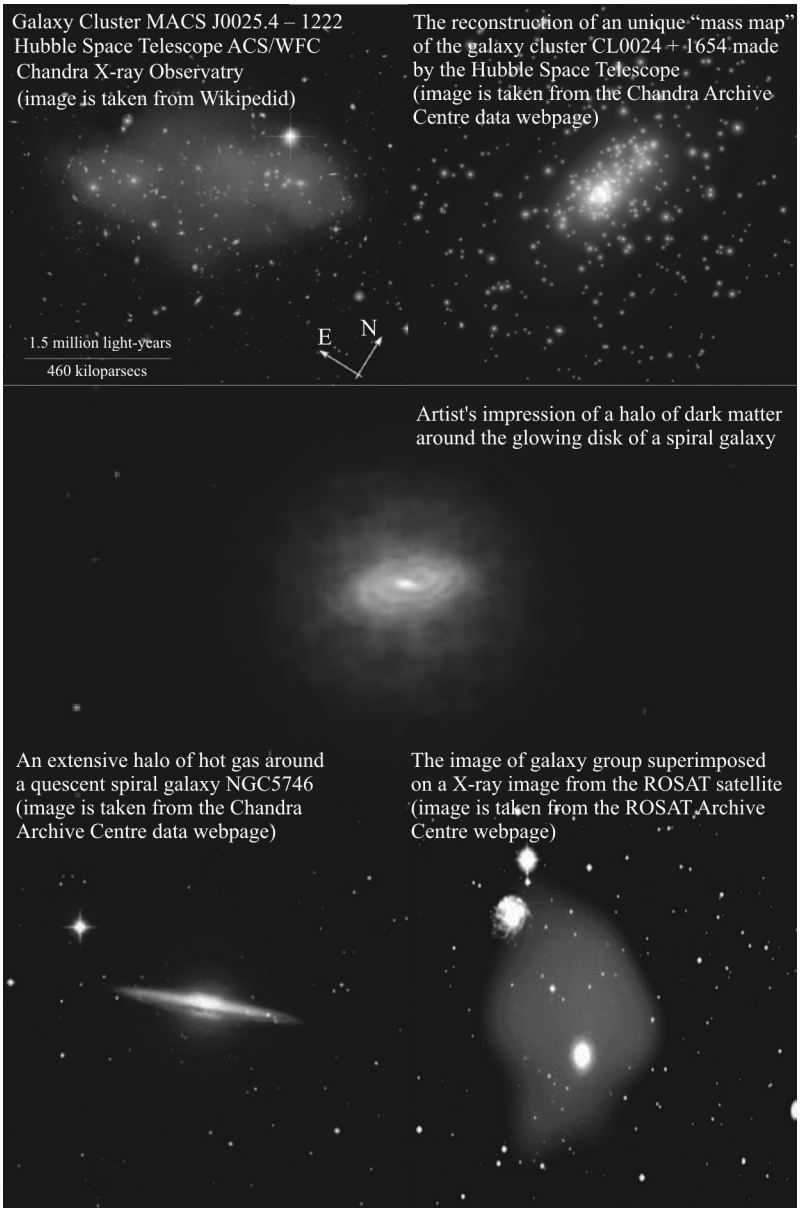

Fig. 2.12. Dark matter observational manifestation in galaxy clusters

on the large scale environment where galaxies were born and on the chemical and physical properties of the environment from which they were formed. The main progress in the studying of the behavior of baryonic matter has been gotten by observations and by studies the evolution of the cold and hot components of the Universe. The progress in this research field is going from the high energy spectral range data.

All the knowledge about baryons comes from studies of galaxy clusters in the nearby Universe ($z < 0.5$). High spatial and spectral resolutions of X-ray observations of clusters give us a great opportunity to define the thermodynamic properties and metal abundance of the clusters at $z \sim 2$. In addition, a high spectral resolution of X-ray observations also helps us to probe the hot gas in different cosmological tests.

One of the main question in astrophysics is about the origin and evolution of heavy elements. This is related to the star formation history, the physical properties of environment where heavy elements have been produced, the circulation of energy and matter during different evolutionary phases of the Universe, etc. Galaxy clusters are great laboratories to study a nucleosynthesis. Using optical/IR/sub-mm observatories we can derive information on the history of star formation, but only with X-ray observations we can determine the metal distribution in the intracluster gas at high redshifts.

A major challenging goal of a future next generation X-ray observatory is thus to study the properties of the first small clusters emerging at $z \sim 2$ and directly trace their thermodynamic and energetic evolution to the present epoch. Some observational confirmations of DM presense in galaxy clusters are given in Fig. 2.12.

Acknowledgements

We thank our coauthor, Dr. A. Del Popolo [27, 31, 34], since the materials of these cited papers were used in this chapter, as well as Dr. F. Pace for a helpful discussion. We thank the HEASARC Data Archive for the high quality data. The data obtained from the Chandra, XMM-Newton, and Suzaku Data Archives were used in our research. We thank all the staff members involved in the Chandra, XMM-Newton, and Suzaku projects.

Bibliography

1. M.G. Abadi et al., Galaxy-induced transformation of dark matter haloes, Mon. Not. R. Astron. Soc. **407**, 435 (2010).
2. G.O. Abell, H. Corwin, R. Olowin, A catalog of rich clusters of galaxies, Astrophys. J. S. **70**, 1 (1989).
3. C. Adami et al., The XMM-LSS survey: optical assessment and properties of different X-ray selected cluster classes, Astron. Astrophys.. **526**, 18 (2011).
4. N. Afshordi & R. Cen, Mass-Temperature Relation of Galaxy Clusters: A Theoretical Study, Astrophys. J. **564**, 669 (2002).
5. K. Ahn & P.R. Shapiro, Formation and evolution of self-interacting dark matter haloes, Mon. Not. R. Astron. Soc. **363**, 1092 (2004).
6. A.N. Alexandrov, V. Sliusar, V. Zhdanov, Caustic Crossing Events and Source Models in Gravitational Lens Systems, arXiv:1105.0114. (2011).
7. S.W. Allen, R.W. Schmidt, A.C. Fabian, Chandra observations of RX J1347.5−1145: the distribution of mass in the most X-ray-luminous galaxy cluster known, Mon. Not. R. Astron. Soc. **335**, 256 (2002).
8. S.W. Allen et al., GINGA and EXOSAT observations of the Perseus cluster of galaxies, Mon. Not. R. Astron. Soc. **254**, 51 (1992).
9. A. Alshino et al., Evolution of the X-ray profiles of poor clusters from the XMM-LSS survey, Mon. Not. R. Astron. Soc. **407**, 2543 (2010).
10. S. Andreon et al., The XMM-LSS project: a short presentation of the survey and of the first results, Memorie della Societa Astronomica Italiana Supplement. **3**, 188 (2003).
11. S. Andreon et al., Batch discovery of nine $z \sim 1$ clusters using X-ray and K or R, z' images, Mon. Not. R. Astron. Soc. **359**, 1250 (2005).
12. S. Andreon et al., Cluster X-ray luminosity-temperature relation at $z \geq 1.5$, Mon. Not. R. Astron. Soc. **412**, 2391 (2011).
13. S. Apunevych et al., Dark matter and dark energy in the Universe: Astrophysical reasons and theoretical models, Kinematics and Physics of Celestial Bodies. **25**, 55 (2009).
14. J.S. Arabadjis, M.W. Bautz, G.P. Garmire, Chandra Observations of the Lensing Cluster EMSS 1358 + 6245: Implications for Self-interacting Dark Matter, Astrophys. J. **572**, 66 (2002).
15. J.S. Arabadjis, M.W. Bautz, G. Arabadjis, Extracting the Dark Matter Profile of a Relaxed Galaxy Cluster, Astrophys. J. **617**, 303 (2004).

16. K.A. Arnaud, XSPEC: The First Ten Years. Astronomical Data Analysis Software and Systems V, A.S.P. Conference Series. **101**, 17 (1996).
17. K.A. Arnaud, N. Aghanim, D. Neumann, The X-ray surface brightness profiles of hot galaxy clusters up to vec $z \sim 0.8$: Evidence for self-similarity and constraints on Ω_0, Astron. Astrophys.. **389**, 1 (2002).
18. Y. Ascasibar & M. Markevitch, The Origin of Cold Fronts in the Cores of Relaxed Galaxy Clusters, Astrophys. J. **650**, 102 (2006).
19. Y. Ascasibar, Y. Hoffman, S. Gottlober, Secondary infall and dark matter haloes, Mon. Not. R. Astron. Soc. **376**, 393 (2007).
20. Y. Ascasibar et al., On the physical origin of dark matter density profiles, Mon. Not. R. Astron. Soc. **352**, 1109 (2004).
21. A. Astashenok & A. Del Popolo, Cosmological measure with volume averaging and the vacuum energy problem, Class. Quantum Grav. **29**, 5014 (2012).
22. C.G. Austin et al., Semianalytical Dark Matter Halos and the Jeans Equation, Astrophys. J. **634**, 756 (2005).
23. Iu. Babyk et al., The mass distribution in the galaxy cluster Abell 2744, Kinematics and Physics of Celestial Bodies **28**, 69 (2012).
24. Iu. Babyk, O. Melnyk, A. Elyiv, The distribution of dark matter and intracluster gas in galaxy clusters, AASP **2**, 56 (2012).
25. Iu. Babyk, Physical properties of X-ray gas in galaxy cluster CL 0024 + 17, Bulletin Crimean Astrophysical Observatory **108**, 87 (2012).
26. Iu. Babyk, Physical Properties of Galaxy Cluster Abell 13, Journal of physical studies **16**, 7 (2012).
27. Iu. Babyk & A. Del Popolo, Correlations in Relaxed Clusters of Galaxies, Baltic Astronomy **23**, 9 (2014).
28. Iu. Babyk & I. Vavilova, The Chandra X-ray galaxy clusters at $z < 1.4$: constraints on the evolution of $L_X - T - M_g$ relations, Astrophys. & Space Science **349**, 415 (2014).
29. Iu. Babyk & I. Vavilova, The distant galaxy cluster XLSSJ 022403.9 − 041328 on the $L_X - T_X - M$ scaling relations using Chandra and XMM-Newton observations, Astrophys. & Space Science **353**, 613 (2014).
30. Iu. Babyk, A Distant Chandra Galaxy Cluster CL J1415.1 + 3612: Constraint on Evidence of the Cool-core Phenomenon, Baltic Astronomy **23**, 93 (2014).
31. Iu. Babyk, A. Del Popolo, I. Vavilova, Chandra X-ray galaxy clusters at $z < 1.4$: constraints on the inner slope of density profiles, Astronomy Reports. **58**, 1 (2014).
32. Iu. Babyk & I. Vavilova, The Distribution of Baryon Matter in the Nearby X-ray Galaxy Clusters, Odessa Astron. Public. **25**, 119 (2012).
33. Iu. Babyk & I. Vavilova, Comparison of Optical and X-ray Mass Estimates of the Chandra Galaxy Clusters at $z < 0.1$, Odessa Astron. Public. **26**, 175 (2013).
34. Iu. Babyk, I. Vavilova, A. Del Popolo, The Dark Matter Haloes of Chandra X-ray Galaxy Clusters and Baryons Effect, arXiv:1208.2424. (2012).
35. N. Bahcall et al., The Cosmic Triangle: Revealing the State of the Universe, Science **284**, 1482 (1999).
36. I. Balestra et al., Tracing the evolution in the iron content of the intra-cluster medium, Astron. Astrophys. **462**, 429 (2007).
37. B. Bartelmann & M. Meneghetti, Do arcs require flat halo cusps? Astron. Astrophys. **418**, 413 (2004).

38. S. Bhattacharya et al., Dark Matter Halo Profiles of Massive Clusters: Theory versus Observations, Astrophys. J. 766, 32 (2011).
39. G.R. Blumenthal et al., Formation of galaxies and large-scale structure with cold dark matter, Nature **311**, 517 (1984).
40. G.R. Blumenthal et al., Contraction of dark matter galactic halos due to baryonic infall, Astrophys. J. **301**, 27 (1986).
41. A. Baldi et al., An XMM-Newton spatially-resolved study of metal abundance evolution in distant galaxy clusters, Astron. Astrophys. **537**, 142 (2012).
42. J. Berge et al., Combined analysis of weak lensing and X-ray blind surveys, Astron. Astrophys. **385**, 695, (2008).
43. E. Bertschinger, Self-similar secondary infall and accretion in an Einstein-de Sitter universe, Astrophys. J. S. **58**, 39 (1985).
44. S. Borgani et al., Measuring Ω_M with the ROSAT Deep Cluster Survey, Astrophys. J. **561**, 13 (2001).
45. S. Borgani et al., X-ray properties of galaxy clusters and groups from a cosmological hydrodynamical simulation, Mon. Not. R. Astron. Soc. **348**, 1078 (2004).
46. S. Borgani et al., Cosmological Constraints from the ROSAT Deep Cluster Survey, Astrophys. J. **517**, 40 (1999).
47. M. Brada et al., Strong and weak lensing united, Astron. Astrophys. **437**, 49 (2005).
48. M. Brada et al., Dark Matter and Baryons in the X-Ray Luminous Merging Galaxy Cluster RX J1347.5−1145, Astrophys. J. **681**, 187 (2008).
49. N. Brickhouse et al., Coronal Structure and Abundances of Capella from Simultaneous EUVE and ASCA Spectroscopy, Astrophys. J. **530**, 387 (2000).
50. T. Broadhurst et al., Large-scale distribution of galaxies at the Galactic poles, Nature **343**, 726 (1990).
51. T. Broadhurst & A. Jaffe, Using the Comoving Maximum of the Galaxy Power Spectrum to Measure Cosmological Curvature, Clustering at High Redshift, ASP Conference Series **200**, 241 (2000).
52. G. Bryan & M. Norman, Statistical Properties of X-Ray Clusters: Analytic and Numerical Comparisons, Astrophys. J. **495**, 80 (1998).
53. J.S. Bullock et al., A Universal Angular Momentum Profile for Galactic Halos, Astrophys. J. **555**, 240 (2001).
54. D.A. Buote et al., The X-Ray Concentration-Virial Mass Relation, Astrophys. J. **664**, 123 (2007).
55. A. Burkert, The Structure of Dark Matter Halos in Dwarf Galaxies, Astrophys. J. **447**, L25 (1995).
56. S. Burles et al., Sharpening the Predictions of Big-Bang Nucleosynthesis, Phys. Rev. Let. **82**, 4176 (1999).
57. V.F. Cardone et al., Secondary infall model and dark matter scaling relations in intermediate-redshift early-type galaxies, Mon. Not. R. Astron. Soc. **416**, 1822 (2011).
58. V.F. Cardone & A. Del Popolo, Newtonian acceleration scales in spiral galaxies, Mon. Not. R. Astron. Soc. **427**, 3176 (2012).
59. V.F. Cardone, M.P. Leubner, A. Del Popolo, Spherical galaxy models as equilibrium configurations in non-extensive statistics, Mon. Not. R. Astron. Soc. **414**, 2265 (2011).

60. A. Cavaliere & R. Fusco-Femiano, X-rays from hot plasma in clusters of galaxies, Astron. Astrophys. **49**, 137 (1976).
61. A. Cavaliere, N. Menci, P. Tozzi, The Luminosity-Temperature Relation for Groups and Clusters of Galaxies, Astrophys. J. **484**, 21 (1997).
62. A. Cavaliere, N. Menci, P. Tozzi, Diffuse Baryons in Groups and Clusters of Galaxies, Astrophys. J. **501**, 493 (1998).
63. A. Cavaliere, N. Menci, P. Tozzi, Hot gas in clusters of galaxies: the punctuated equilibria model, Mon. Not. R. Astron. Soc. **308**, 599 (1999).
64. A. Cavaliere & R. Fusco-Femiano, The Distribution of Hot Gas in Clusters of Galaxies, Astron. Astrophys. **70**, 677 (1978).
65. R. Cen, Decaying Cold Dark Matter Model and Small-Scale Power, Astrophys. J. **546**, L77 (2001).
66. R. Cen et al., Properties of Cold Dark Matter Halos at $z > 6$, astro-ph/0403352. (2004).
67. N. Dalal & C.R. Keeton, (Lack of) lensing constraints on cluster dark matter profiles, astro-ph/0312072. (2003).
68. V.P. Debattista et al., The Causes of Halo Shape Changes Induced by Cooling Baryons: Disks versus Substructures, Astrophys. J. **681**, 1076 (2008).
69. W. Dehnen & D.E. McLaughlin, Dynamical insight into dark matter haloes, Mon. Not. R. Astron. Soc. **363**, 1057 (2005).
70. W.J.G. de Blok et al., High-Resolution Rotation Curves and Galaxy Mass Models from THINGS, Astron. J. **136**, 2648 (2008).
71. W.J.G. de Blok & A. Bosma, High-resolution rotation curves of low surface brightness galaxies, Astron. Astrophys. **385**, 816 (2002).
72. W.J.G. de Blok, A. Bosma, S. McGaugh, Simulating observations of dark matter dominated galaxies: towards the optimal halo profile, Mon. Not. R. Astron. Soc. **340**, 657 (2003).
73. A. Del Popolo, Dark matter, density perturbations, and structure formation, Astron. Rep. **51**, 169 (2007).
74. A. Del Popolo, Non-baryonic dark matter in cosmology, AIP Conference Series **1548**, 2 (2013).
75. A. Del Popolo, F. Pace, J.A. Lima, Spherical collapse model with shear and angular momentum in dark energy cosmologies, Mon. Not. R. Astron. Soc. **430**, 628 (2013).
76. A. Del Popolo et al., Shear and rotation in Chaplygin cosmology, Phys. Rev. D **87**, 043527 (2013).
77. A. Del Popolo, F. Pace, J.A. Lima, Extended Spherical Collapse and the Accelerating Universe, International J. Modern Phys. D **22**, 1350038 (2013).
78. A. Del Popolo, N. Hiotelis, J. Penarrubia, A Theoretical Study of the Luminosity-Temperature Relation for Clusters of Galaxies, Astrophys. J. **628**, 76 (2005).
79. A. Del Popolo, On the density-profile slope of clusters of galaxies, Mon. Not. R. Astron. Soc. **424**, 38 (2012).
80. A. Del Popolo & P. Kroupa, Density profiles of dark matter haloes on galactic and cluster scales, Astron. Astrophys. **502**, 733 (2009).
81. A. Del Popolo, F. Pace, J. Lima, Spherical collapse model with shear and angular momentum in dark energy cosmologies, Mon. Not. R. Astron. Soc. **430**, 628 (2013).

82. A. Del Popolo & M. Gambera, Peak mass in large-scale structure and dynamical friction, Astron. Astrophys. **308**, 373 (1996).
83. A. Del Popolo, A theoretical study of the mass-temperature relation for clusters of galaxies, Mon. Not. R. Astron. Soc. **336**, 81 (2002).
84. A. Del Popolo, Density profile slopes of dwarf galaxies and their environment, Mon. Not. R. Astron. Soc. **419**, 971 (2012).
85. A. Del Popolo, The Cusp/Core Problem and the Secondary Infall Model, Astrophys. J. **698**, 2093 (2009).
86. A. Del Popolo, V.F. Cardone, G. Belvedere, Surface density of dark matter haloes on galactic and cluster scales, Mon. Not. R. Astron. Soc. **429**, 1080 (2013).
87. A. Del Popolo et al., Density profiles of dark matter halos in an improved secondary infall model, Astron. Astrophys. **353**, 427 (2000).
88. A. Del Popolo, On the universality of density profiles, Mon. Not. R. Astron. Soc. **408**, 1808 (2010).
89. A. Del Popolo, Non-power law behavior of the radial profile of phase-space density of halos, JCAP **07**, 14 (2011).
90. A. Del Popolo & V.F. Cardone, Statistical properties of the dark matter haloes of dwarf galaxies and correlations with the environment, Mon. Not. R. Astron. Soc. **423**, 1060 (2012).
91. L. David et al., A catalog of intracluster gas temperatures, Astrophys. J. **412**, 479 (1993).
92. J. Dickey & F. Lockman, H I in the Galaxy, ARA&A. **28**, 215 (1990).
93. K. Dolag & S. Schindler, The effect of magnetic fields on the mass determination of clusters of galaxies, Astron. Astrophys. **364**, 491 (2000).
94. K. Dolag et al., Numerical study of halo concentrations in dark-energy cosmologies. Astron. Astrophys. **416**, 853 (2004).
95. M. Donahue et al., The Second Most Distant Cluster of Galaxies in the Extended Medium Sensitivity Survey, Astrophys. J. **527**, 525 (1999).
96. J. Dubinski & R. Carlberg, The structure of cold dark matter halos, Astrophys. J. **378**, 496 (1991).
97. A.R. Duffy et al., Dark matter halo concentrations in the Wilkinson Microwave Anisotropy Probe year 5 cosmology, Mon. Not. R. Astron. Soc. **390**, L64 (2008).
98. H. Ebeling et al., The ROSAT Brightest Cluster Sample (BCS): The Cluster X-Ray Luminosity Function within $z = 0.3$, Astrophys. J. **479**, 101 (1997).
99. A. El-Zant et al., Dark Halos: The Flattening of the Density Cusp by Dynamical Friction, Astrophys. J. **560**, 636 (2001).
100. A. El-Zant et al., Flat-cored Dark Matter in Cuspy Clusters of Galaxies, Astrophys. J. **607**, L75 (2004).
101. J. Einasto, Dark Matter, arXiv:0901.0632. (2009).
102. J. Einasto, Large scale structure, New astronomy reviews **45**, 355 (2001).
103. J. Einasto et al., A 120-Mpc periodicity in the three-dimensional distribution of galaxy superclusters, Nature **385**, 139 (1997).
104. J. Einasto et al., The supercluster-void network — III. The correlation function as a geometrical statistic, Mon. Not. R. Astron. Soc. **289**, 813 (1997).
105. J. Einasto, A. Kaasik, E. Saar, Dynamic evidence on massive coronas of galaxies, Nature **250**, 309 (1974).
106. V. Eke et al., Measuring Ω_0 using cluster evolution, Mon. Not. R. Astron. Soc. **298**, 1145 (1998).

107. V.R. Eke et al., The Power Spectrum Dependence of Dark Matter Halo Concentrations, Astrophys. J. **554**, 114 (2001).
108. S. Ettori & A. Fabian, ROSAT PSPC observations of 36 high-luminosity clusters of galaxies: constraints on the gas fraction, Mon. Not. R. Astron. Soc. **305**, 834 (1999).
109. S. Ettori & A. Fabian, Chandra constraints on the thermal conduction in the intracluster plasma of A2142, Mon. Not. R. Astron. Soc. **317**, 57 (2000).
110. S. Ettori et al., Deep inside the core of Abell 1795: the Chandra view, Mon. Not. R. Astron. Soc. **331**, 635 (2002).
111. S.M. Faber & D.N. Lin, Is there nonluminous matter in dwarf spheroidal galaxies, Astrophys. J. **266**, L17 (1983).
112. B. Fairley et al., The WARPS survey — IV. The X-ray luminosity-temperature relation of high-redshift galaxy clusters, Mon. Not. R. Astron. Soc. **315**, 669 (2000).
113. L. Ferramacho, A. Blanchard, Gas mass fraction from XMM-Newton and Chandra high redshift clusters and its use as a cosmological test, Astron. Astrophys. **463**, 423 (2007).
114. J.A. Fillmore & P. Goldreich, Self-similar gravitational collapse in an expanding universe, Astrophys. J. **281**, 1 (1984).
115. A. Finoguenov, T.H. Reiprich, H. Bohringer, Details of the mass-temperature relation for clusters of galaxies, Astron. Astrophys. **368**, 749 (2001).
116. A. Finoguenov et al., XMM-Newton study of $0.012 < z < 0.024$ groups — I. Overview of the IGM thermodynamics, Mon. Not. R. Astron. Soc. **374**, 737 (2007).
117. R.A. Flores & J.R. Primack, Observational and theoretical constraints on singular dark matter halos, Astrophys. J. **427**, L1 (1994).
118. L. Gao & S.D. White, Assembly bias in the clustering of dark matter haloes, Mon. Not. R. Astron. Soc. **377**, L5 (2007).
119. R. Gavazzi et al., A radial mass profile analysis of the lensing cluster MS 2137.3 – 2353, Astron. Astrophys. **403**, 11 (2003).
120. R. Gavazzi, Projection effects in cluster mass estimates: the case of MS 2137 – 23, Astron. Astrophys. **443**, 793 (2005).
121. G. Gentile et al., The cored distribution of dark matter in spiral galaxies, Mon. Not. R. Astron. Soc. **351**, 903 (2004).
122. F. Governato et al., Bulgeless dwarf galaxies and dark matter cores from supernova-driven outflows, Nature **463**, 203 (2010).
123. O.Y. Gnedin et al., Response of Dark Matter Halos to Condensation of Baryons: Cosmological Simulations and Improved Adiabatic Contraction Model, Astrophys. J. **616**, 16 (2004).
124. J.E. Gunn & J.R. Gott, On the Infall of Matter Into Clusters of Galaxies and Some Effects on Their Evolution, Astrophys. J. **176**, 1 (1972).
125. J.E. Gunn, Massive galactic halos. I — Formation and evolution, Astrophys. J. **218**, 592 (1977).
126. M. Gustafsson, M. Fairbairn, J. Sommer-Larsen, Baryonic pinching of galactic dark matter halos, Phys. Rev. D **74**, 123522 (2006).
127. E. Hayashi et al., The inner structure of ΛCDM haloes — II. Halo mass profiles and low surface brightness galaxy rotation curves, Mon. Not. R. Astron. Soc. **355**, 794 (2004).

128. J. Henry, L. Jiao, I. Gioia, Temperatures of distant clusters of galaxies, Astrophys. J. **432**, 49 (1994).
129. E.R. Hill, Dark matter, Bull. Astron. Inst. Netherlands **15**, 1 (1960).
130. N. Hiotelis & A. Del Popolo, Anomalous diffusion models for the formation of dark matter haloes, Mon. Not. R. Astron. Soc. **436**, 163 (2013).
131. N. Hiotelis, Density profiles in a spherical infall model with non-radial motions, Astron. Astrophys. **382**, 84 (2002).
132. Y. Hoffman & J. Shaham, Local density maxima — Progenitors of structure, Astrophys. J. **297**, 16 (1985).
133. E. Hog, The Astrometric Foundation of Astrophysics, arxiv.org/1408.2122. (2014).
134. E. Hog, Absolute astrometry in the next 50 years, arxiv.org/1408.2190. (2014).
135. B. Holden et al., Moderate-Temperature Clusters of Galaxies from the RDCS and the High-Redshift Luminosity-Temperature Relation, Astron. J. **124**, 33 (2002).
136. D. Horner, R. Mushotzky, C. Scharf, Observational Tests of the Mass-Temperature Relation for Galaxy Clusters, Astrophys. J. **520**, 78 (1999).
137. J. Henry & K. Arnoud, A measurement of the mass fluctuation spectrum from the cluster X-ray temperature function, Astrophys. J. **372**, 410 (1991).
138. W. Hu, R. Barkana, A. Gruzinov, Fuzzy Cold Dark Matter: The Wave Properties of Ultralight Particles, Phys. Rev. Let. **85**, 1158 (2000).
139. W. Jaffe, A simple model for the distribution of light in spherical galaxies, Mon. Not. R. Astron. Soc. **202**, 995 (1983).
140. J.H. Jeans, The motions of stars in a Kapteyn universe, Mon. Not. R. Astron. Soc. **82**, 122 (1922).
141. Y.P. Jing & Y. Suto, The Density Profiles of the Dark Matter Halo Are Not Universal, Astrophys. J. **529**, L69 (2000).
142. C. Jones & W. Forman, The structure of clusters of galaxies observed with Einstein, Astrophys. J. **276**, 38 (1984).
143. J. Kaastra & R. Mewe, X-ray emission from thin plasmas. I — Multiple Auger ionisation and fluorescence processes for Be to Zn, Astron. Astrophys. Suppl. Ser. **97**, 443 (1993).
144. N. Kaiser, Evolution of clusters of galaxies, Astrophys. J. **383**, 104 (1991).
145. N. Kaiser, Evolution and clustering of rich clusters, Mon. Not. R. Astron. Soc. **222**, 323 (1986).
146. W. Kapferer et al., Metal enrichment of the intra-cluster medium over a Hubble time for merging and relaxed galaxy clusters, Astron. Astrophys. **466**, 813 (2007).
147. M. Kaplinghat, L. Knox, M.S. Turner, Annihilating Cold Dark Matter, Phys. Rev. Let. **85**, 3335 (2000).
148. J.C. Kapteyn, First Attempt at a Theory of the Arrangement and Motion of the Sidereal System, Astrophys. J. **55**, 302 (1922).
149. V.E. Karachentseva & I.B. Vavilova, Clustering of dwarf galaxies with low surface brightness. II. The Virgo cluster, Kinematics and Physics of Celestial Bodies **11**, 38 (1995).
150. V.E. Karachentseva & I.B. Vavilova, Clustering of low surface brightness dwarf galaxies. I. General properties, Bulletin of the Special Astrophysical Observatory **37**, 98 (1994).

151. V.E. Karachentseva & I.B. Vavilova, Clustering of Low Surface Brightness Dwarf Galaxies in the Local Supercluster, European Southern Observatory Conference and Workshop Proceedings **49**, 91 (1994).
152. I. King, The structure of star clusters. III. Some simple dynamical models, Astron. J. **71**, 64 (1966).
153. A. Klypin et al., Resolving the Structure of Cold Dark Matter Halos, Astrophys. J. **554**, 903 (2001).
154. J.-P. Kneib et al., A Wide-Field Hubble Space Telescope Study of the Cluster Cl 0024 + 1654 at $z = 0.4$. II. The Cluster Mass Distribution, Astrophys. J. **598**, 804 (2003).
155. R. Knop et al., New Constraints on Ω_M, Ω_Λ, and w from an Independent Set of 11 High-Redshift Supernovae Observed with the Hubble Space Telescope, Astrophys. J. **598**, 102 (2003).
156. O. Kotov & A. Vikhlinin, XMM-Newton Observations of Evolution of Cluster X-Ray Scaling Relations at $z = 0.4$—0.7, Astrophys. J. **633**, 781 (2005).
157. O. Kotov & A. Vikhlinin, Chandra Sample of Galaxy Clusters at $z = 0.4$—0.55: Evolution in the Mass-Temperature Relation, Astrophys. J. **641**, 752 (2006).
158. Y. Kulinich, B. Novosyadlyj, S. Apunevych, Non-linear power spectra of dark and luminous matter in halo model of structure formation, arXiv:1203.5297. (2012).
159. R. Kuzio de Naray, S.S. McGaugh, W.J.G. de Blok, Mass Models for Low Surface Brightness Galaxies with High-Resolution Optical Velocity Fields, Astrophys. J. **676**, 920 (2008).
160. R. Kuzio de Naray, S.S. McGaugh, J.C. Mihos, Constraining the NFW Potential with Observations and Modeling of Low Surface Brightness Galaxy Velocity Fields, Astrophys. J. **692**, 1321 (2009).
161. G. Kuzmin, Proper movements of the galactic-equatorial A and K stars of the perpendicularly galactic plane and dymanic density of the Galaxy, Tartu Astr. Obs. Publ. **32**, 5 (1952).
162. G. Kuzmin, Tartu Astr., On the question of the size of the dynamic parameters of C and density of matter in the vicinity of the Sun, Obs. Publ. **33**, 3 (1955).
163. O. Lahav et al., Dynamical effects of the cosmological constant, Mon. Not. R. Astron. Soc. **251**, 128 (1991).
164. L. Lanz et al., Constraining the Outburst Properties of the SMBH in Fornax A Through X-ray, Infrared, and Radio Observations, Astrophys. J. **721**, 1702 (2010).
165. M. Le Delliou & R.N. Henriksen, Non-radial motion and the NFW profile, Astron. Astrophys. **408**, 27 (2003).
166. A.D. Lewis, D.A. Buote, J.T. Stocke, Chandra Observations of A2029: The Dark Matter Profile Down to below $0.01 r_{\rm vir}$ in an Unusually Relaxed Cluster, Astrophys. J. **586**, 135 (2003).
167. D. Liedahl et al., New calculations of Fe L-shell X-ray spectra in high-temperature plasmas, Astrophys. J. **438**, 115 (1995).
168. M. Limousin et al., Strong lensing in Abell 1703: constraints on the slope of the inner dark matter distribution, Astron. Astrophys. **489**, 23 (2008).
169. Y.-T. Lin & J.J. Mohr, K-band Properties of Galaxy Clusters and Groups: Brightest Cluster Galaxies and Intracluster Light, Astrophys. J. **617**, 879 (2004).

170. E.J. Lloyd-Davies et al., The XMM Cluster Survey: X-ray analysis methodology, Mon. Not. R. Astron. Soc. **418**, 14 (2011).
171. A. Loeb & P.J.E. Peebles, Cosmological Origin of the Stellar Velocity Dispersions in Massive Early-Type Galaxies, Astrophys. J. **589**, 29 (2003).
172. R. Lynds & V. Petrosian, Giant Luminous Arcs in Galaxy Clusters, Bull. Am. Astron. Soc. **18**, 1014 (1986).
173. C.-P. Ma, P. Chang, J. Zhang, Is the Radial Profile of the Phase-Space Density of Dark Matter Halos a Power-Law? arXiv:0907.3144. (2009).
174. A. Mahdavi et al., Joint Analysis of Cluster Observations. I. Mass Profile of Abell 478 from Combined X-Ray, Sunyaev—Zel'dovich, and Weak-Lensing Data, Astrophys. J. **664**, 162 (2007).
175. M. Markevitch, The $L_X - T$ Relation and Temperature Function for Nearby Clusters Revisited, Astrophys. J. **504**, 27 (1998).
176. M. Markevitch et al., Chandra Observation of Abell 2142: Survival of Dense Subcluster Cores in a Merger, Astron. Astrophys. J. **541**, 542 (2000).
177. M. Markevitch, A. Vikhlinin, P. Mazzotta, Nonhydrostatic Gas in the Core of the Relaxed Galaxy Cluster A1795, Astrophys. J. **562**, L153 (2001).
178. D. Martizzi et al., The effects of baryon physics, black holes and active galactic nucleus feedback on the mass distribution in clusters of galaxies, Mon. Not. R. Astron. Soc. **422**, 3081 (2012).
179. S. Mashchenko, H.M.P. Couchman, J. Wadsley, The removal of cusps from galaxy centres by stellar feedback in the early Universe, Nature. **442**, 539 (2006).
180. B. Maughan J. et al., Testing the galaxy cluster mass-observable relations at $z = 1$ with XMM-Newton and Chandra observations of XLSSJ 022403.9 – 041328, Mon. Not. R. Astron. Soc. **387**, 998 (2008).
181. B. Maughan et al., Images, Structural Properties, and Metal Abundances of Galaxy Clusters Observed with Chandra ACIS-I at $0.1 < z < 1.3$, Astrophys. J. S. **174**, 117 (2008).
182. S.S. McGaugh et al., The Baryon Content of Cosmic Structures, Astrophys. J. **708**, L14 (2010).
183. P.J. McMillan & W. Dehnen, Halo evolution in the presence of a disc bar, Mon. Not. R. Astron. Soc. **363**, 1205 (2005).
184. Y. Mellier, Probing the Universe with Weak Lensing, Ann. Rev. Astron. Astrophys. **37**, 127 (1999).
185. O.V. Melnik, A.A. Elyiv, I.B. Vavilova, Mass-to-light ratios for galaxy pairs and triplets in various environments, Kinematics and Physics of Celestial Bodies **25**, 43 (2009).
186. C. Metzler & A. Evrard, Simulations of Galaxy Clusters with and without Winds: I. The Structure of Clusters, astro-ph/9710324. (1997).
187. R. Mewe, E.H. Gronenschild, G.H. van den Oord, Calculated X-radiation from optically thin plasmas. V, Astron. Astrophys. Suppl. Ser. **62**, 197 (1985).
188. R. Mewe, J.R. Lemen, G.H.J. van den Oord, Calculated X-radiation from optically thin plasmas. VI — Improved calculations for continuum emission and approximation formulae for nonrelativistic average Gaunt factors, Astron. Astrophys. Suppl. Ser. **65**, 511 (1986).
189. C. Miller & D. Batuski, The Power Spectrum of Rich Clusters on Near Gigaparsec Scales, astro-ph/0002295. (2000).

190. M. Milosavljevic, D. Merritt, Formation of Galactic Nuclei, Astrophys. J. **563**, 34 (2001).
191. J. Miralda-Escude, Gravitational lensing by a cluster of galaxies and the central cD galaxy: Measuring the mass profile, Astrophys. J. **438**, 514 (1995).
192. J. Mohr et al., The X-Ray Size-Temperature Relation for Intermediate-Redshift Galaxy Clusters, Astrophys. J. **544**, 109 (2000).
193. B. Moore et al., Cold collapse and the core catastrophe, Mon. Not. R. Astron. Soc. **310**, 1147 (1999).
194. B. Moore, Evidence against dissipation-less dark matter from observations of galaxy haloes, Nature **370**, 629 (1994).
195. B. Moore et al., Resolving the Structure of Cold Dark Matter Halos, Astrophys. J. **499**, L5 (1998).
196. C.M. Muller, Cosmological bounds on the equation of state of dark matter, Phys. Rev. D **71**, 047302 (2005).
197. R. Mushotzky et al., The Luminosity-Temperature Relation at $z = 0.4$ for Clusters of Galaxies, Astrophys. J. **482**, 13 (1997).
198. R. Mushotzky et al., Resolving the extragalactic hard X-ray background, Nature **404**, 459 (2000).
199. A. Muzzin et al., Discovery of a Rich Cluster at $z = 1.63$ Using the Rest-frame 1.6 μm "Stellar Bump Sequence" Method, Astrophys. J. **767**, 39 (2013).
200. D. Nagai, A. Vikhlinin, A.V. Kravtsov, Testing X-Ray Measurements of Galaxy Clusters with Cosmological Simulations, Astrophys. J. **655**, 98 (2007).
201. J.F. Navarro, C.S. Frenk, S.D. White, Simulations of X-ray clusters, Mon. Not. R. Astron. Soc. **275**, 720 (1995).
202. J.F. Navarro, C.S. Frenk, S.D. White, The Structure of Cold Dark Matter Halos, Astrophys. J. **462**, 563 (1996).
203. J.F. Navarro, C.S. Frenk, S.D. White, A Universal Density Profile from Hierarchical Clustering, Astrophys. J. **490**, 493 (1997).
204. J.F. Navarro et al., The inner structure of ΛCDM haloes — III. Universality and asymptotic slopes, Mon. Not. R. Astron. Soc. **349**, 1039 (2004).
205. J.F. Navarro et al., The diversity and similarity of simulated cold dark matter haloes, Mon. Not. R. Astron. Soc. **402**, 21 (2010).
206. J. Nevalainen et al., The Cluster $M - T$ Relation from Temperature Profiles Observed with ASCA and ROSAT, Astrophys. J. **532**, 694 (2000).
207. A.B. Newman et al., The Distribution of Dark Matter Over Three Decades in Radius in the Lensing Cluster Abell 611, Astrophys. J. **706**, 1078 (2009).
208. A.B. Newman et al., The Dark Matter Distribution in A383: Evidence for a Shallow Density Cusp from Improved Lensing, Stellar Kinematic, and X-ray Data, Astrophys. J. **728**, L39 (2011).
209. M. Norman, Simulating Galaxy Clusters, astro-ph/1005.1100. (2010).
210. M. Novicki, M. Sornig, J.P. Henry, The Evolution of the Galaxy Cluster Luminosity-Temperature Relation, Astron. J. **124**, 2413 (2002).
211. B. Novosyadlyj, Large-Scale Structure of the Universe Formation: Theory and Observations, J. Phys. Stud. **11**, 226 (2007).
212. E. Opik., Absorption of light in space as viewed from the Standpoint of Galactic dynamics, Bull. de la Soc. Astr. de Russie **21**, 150 (1915).
213. J.H. Öort, The force exerted by the stellar system in the direction perpendicular to the galactic plane and some related problems, Bull. Astron. Inst. Netherlands **6**, 249 (1932).

214. J.H. Öort, Determination of Kz and on the mass density near the Sun, Bull. Astron. Inst. Netherlands **15**, 45 (1960).
215. J.P. Ostriker & P.J. Peebles, A Numerical Study of the Stability of Flattened Galaxies: or, can Cold Galaxies Survive?, Astrophys. J. **186**, 467 (1973).
216. J.P. Ostriker, P.J. Peebles, A. Yahil, The size and mass of galaxies, and the mass of the universe, Astrophys. J. **193**, L1 (1974).
217. F. Pacaud et al., The XMM-LSS survey: the Class 1 cluster sample over the initial 5 $\deg^2$ and its cosmological modelling, Mon. Not. R. Astron. Soc. **382**, 1289 (2007).
218. B. Parodi et al., Supernova Type Ia Luminosities, Their Dependence on Second Parameters, and the Value of H_0, Astrophys. J. **540**, 634 (2000).
219. S. Perlmutter et al., Measurements of Ω and Λ from 42 High-Redshift Supernovae, Astrophys. J. **517**, 565 (1999).
220. P.J. Peebles, Large-scale background temperature and mass fluctuations due to scale-invariant primeval perturbations, Astrophys. J. **263**, L1 (1982).
221. M. Pierre et al., The XMM-LSS survey. Survey design and first results, J. Cosmol. Astropart. Phys. **09**, 011 (2004).
222. M. Pierre et al., The XMM Large-Scale Structure survey: a well-controlled X-ray cluster sample over the D1 CFHTLS area, Mon. Not. R. Astron. Soc. **372**, 591 (2006).
223. E. Pointecouteau, M. Arnaud, G.W. Pratt, The structural and scaling properties of nearby galaxy clusters. I. The universal mass profile, Astron. Astrophys. **435**, 1 (2005).
224. C. Power et al., The inner structure of ΛCDM haloes — I. A numerical convergence study, Mon. Not. R. Astron. Soc. **338**, 14 (2003).
225. G. Pratt, M. Arnaud, E. Pointecouteau, Structure and scaling of the entropy in nearby galaxy clusters, Astron. Astrophys. **446**, 429 (2006).
226. J.R. Primack, Whatever Happened to Hot Dark Matter? astro-ph/0112336. (2001).
227. D. Rapetti, S. Allen, A. Mantz, The prospects for constraining dark energy with future X-ray cluster gas mass fraction measurements, Mon. Not. R. Astron. Soc. **388**, 1265 (2008).
228. E. Rasia et al., Systematics in the X-ray cluster mass estimators, Mon. Not. R. Astron. Soc. **369**, 2013 (2006).
229. J. Raymond & B. Smith, Soft X-ray spectrum of a hot plasma, Astrophys. J. S. **35**, 419 (1977).
230. D. Reichart, F. Castander, R. Nichol, A Bayesian Inference Analysis of the X-Ray Cluster Luminosity-Temperature Relation, Astrophys. J. **516**, 1 (1999).
231. T. Reiprich & H. Bohringer, The Mass Function of an X-Ray Flux-limited Sample of Galaxy Clusters, Astrophys. J. **567**, 716 (2002).
232. M. Ricotti, M.I. Wilkinson, On the origin of dark matter cores in dwarf galaxies, Mon. Not. R. Astron. Soc. **353**, 867 (2004).
233. M. Ricotti, A. Pontzen, M. Viel, Is the Concentration of Dark Matter Halos at Virialization Universal?, Astrophys. J. **663**, L53 (2007).
234. M. Ricotti, Dependence of the inner dark matter profile on the halo mass, Mon. Not. R. Astron. Soc. **344**, 1237 (2003).
235. A. Riess et al., Observational Evidence from Supernovae for an Accelerating Universe and a Cosmological Constant, Astron. J. **116**, 1009 (1998).

236. M.S. Roberts & R.N. Whitehurst, The rotation curve and geometry of M31 at large galactocentric distances, Astrophys. J. **201**, 327 (1975).
237. E. Romano-D et al., Erasing Dark Matter Cusps in Cosmological Galactic Halos with Baryons, Astrophys. J. **685**, L105 (2008).
238. E. Romano-D et al., Dissecting Galaxy Formation. I. Comparison Between Pure Dark Matter and Baryonic Models, Astrophys. J. **702**, 1250 (2009).
239. M. Roncarelli et al., Simulated X-ray galaxy clusters at the virial radius: Slopes of the gas density, temperature and surface brightness profiles, Mon. Not. R. Astron. Soc. **373**, 1339 (2006).
240. P. Rosati et al., The ROSAT Deep Cluster Survey: The X-Ray Luminosity Function out to $z = 0.8$, Astrophys. J. **492**, 21 (1998).
241. B. Roukema & G. Mamon, Tangential large scale structure as a standard ruler: curvature parameters from quasars, Astron. Astrophys. **358**, 395 (2000).
242. V.C. Rubin & W.K.J. Ford, Rotation of the Andromeda Nebula from a Spectroscopic Survey of Emission Regions, Astrophys. J. **159**, 379 (1970).
243. H. Russell et al., Direct X-ray spectral deprojection of galaxy clusters, Mon. Not. R. Astron. Soc. **390**, 1207 (2008).
244. S. Sakai et al., The Hubble Space Telescope Key Project on the Extragalactic Distance Scale. XXIV. The Calibration of Tully-Fisher Relations and the Value of the Hubble Constant, Astrophys. J. **529**, 698 (2000).
245. P. Salucci et al., The universal rotation curve of spiral galaxies — II. The dark matter distribution out to the virial radius, Mon. Not. R. Astron. Soc. **378**, 41 (2007).
246. D.J. Sand, T. Treu, R.S. Ellis, The Dark Matter Density Profile of the Lensing Cluster MS 2137−23: A Test of the Cold Dark Matter Paradigm, Astrophys. J. **574**, L129 (2002).
247. D.J. Sand et al., Separating Baryons and Dark Matter in Cluster Cores: A Full Two-dimensional Lensing and Dynamic Analysis of Abell 383 and MS 2137−23, Astrophys. J. **674**, 711 (2008).
248. D.J. Sand et al., The Dark Matter Distribution in the Central Regions of Galaxy Clusters: Implications for Cold Dark Matter, Astrophys. J. **604**, 88 (2004).
249. J. Sanders et al., A deeper X-ray study of the core of the Perseus galaxy cluster: the power of sound waves and the distribution of metals and cosmic rays, Mon. Not. R. Astron. Soc. **381**, 1381 (2007).
250. C. Sarazin, Book-Review — X-Ray Emission from Clusters of Galaxies, British Astron. Assoc. Journal. **98**, 212 (1988).
251. J. Sauvageot, E. Belsole, G.W. Pratt, The late merging phase of a galaxy cluster: XMM EPIC observations of A 3266, Astron. Astrophys. **444**, 673 (2005).
252. R.W. Schmidt & S.W. Allen, The dark matter haloes of massive, relaxed galaxy clusters observed with Chandra, Mon. Not. R. Astron. Soc. **379**, 209 (2007).
253. D.W. Sciama, Dark matter decay and the ionization of H I regions in the Galaxy, Astrophys. J. **364**, 549 (1990).
254. J.D. Simon et al., High-Resolution Measurements of the Halos of Four Dark Matter-Dominated Galaxies: Deviations from a Universal Density Profile, Astrophys. J. **621**, 757 (2005).
255. J.D. Simon, Dark Matter in Dwarf Galaxies: Observational Tests of the Cold Dark Matter Paradigm on Small Scales. Dissertation for a Ph.D. (University of California, Berkeley, 2005).

256. L.D. Shaw et al., Statistics of Physical Properties of Dark Matter Clusters, Astrophys. J. **646**, 815 (2006).
257. G.P. Smith et al., A Hubble Space Telescope Lensing Survey of X-Ray Luminous Galaxy Clusters. I. A383, Astrophys. J. **552**, 493 (2001).
258. G.P. Smith et al., A Hubble Space Telescope lensing survey of X-ray luminous galaxy clusters — IV. Mass, structure and thermodynamics of cluster cores at $z = 0.2$, Mon. Not. R. Astron. Soc. **359**, 417 (2005).
259. D. Spergel et al., Three-Year Wilkinson Microwave Anisotropy Probe (WMAP) Observations: Implications for Cosmology, Astrophys. J. S. **170**, 377 (2007).
260. D.N. Spergel & P.J. Steinhardt, Observational Evidence for Self-Interacting Cold Dark Matter, Phys. Rev. Let. **84**, 3760 (2000).
261. J. Stadel et al., Quantifying the heart of darkness with GHALO — a multibillion particle simulation of a galactic halo, Mon. Not. R. Astron. Soc. **398**, L21 (2009).
262. K. Subramanian, R. Cen, J.P. Ostriker, The Structure of Dark Matter Halos in Hierarchical Clustering Theories, Astrophys. J. **538**, 528 (2000).
263. P. Schuecker et al., The REFLEX galaxy cluster survey. VII. Ω_m and σ_8 from cluster abundance and large-scale clustering, Astron. Astrophys. **398**, 867 (2003).
264. M. Sun et al., Chandra Studies of the X-Ray Gas Properties of Galaxy Groups, Astrophys. J. **693**, 1142 (2009).
265. Y. Suto, S. Sasaki, N. Makino, Gas Density and X-Ray Surface Brightness Profiles of Clusters of Galaxies from Dark Matter Halo Potentials: Beyond the Isothermal β-Model, Astrophys. J. **509**, 544 (1998).
266. M. Teyssier, K. Johnston, M. Kuhlen, Identifying Local Group field galaxies that have interacted with the Milky Way, Mon. Not. R. Astron. Soc. **426**, 1808 (2012).
267. R. Teyssier et al., Self-similar Spherical Collapse Revisited: A Comparison between Gas and Dark Matter Dynamics, Astrophys. J. **480**, 36 (1997).
268. C. Tonini, A. Lapi, P. Salucci, Angular Momentum Transfer in Dark Matter Halos: Erasing the Cusp, Astrophys. J. **649**, 591 (2006).
269. V.S. Tsvetkova et al., Search for dark matter using the phenomenon of strong gravitational lensing, Kinematics and Physics of Celestial Bodies **25**, 28 (2009).
270. J.A. Tyson, J.A. Kochanski, I.P. dell'Antonio, Detailed Mass Map of CL 0024 + + 1654 from Strong Lensing, Astrophys. J. **498**, L107 (1998).
271. K. Umetsu, T. Broadhurst, Combining Lens Distortion and Depletion to Map the Mass Distribution of A1689, Astrophys. J. **684**, 177 (2008).
272. I. Valtchanov et al., The XMM-LSS survey. First high redshift galaxy clusters: Relaxed and collapsing systems, Astron. Astrophys. **423**, 75 (2004).
273. I.B. Vavilova et al., Triplets of Galaxies in the Local Supercluster. I. Kinematic and Virial Parameters, Kinematika i Fizika Nebesnykh Tel **21**, 1 (2005).
274. G. de Vaucouleurs, Recherches sur les Nebuleuses Extragalactiques, Annales d'Astrophysique **11**, 247 (1948).
275. A. Vikhlinin, Predicting a Single-Temperature Fit to Multicomponent Thermal Plasma Spectra, Astrophys. J. **640**, 710 (2006).
276. A. Vikhlinin et al., Chandra Sample of Nearby Relaxed Galaxy Clusters: Mass, Gas Fraction, and Mass-Temperature Relation, Astrophys. J. **640**, 691 (2006).
277. A. Vikhlinin et al., Chandra Temperature Profiles for a Sample of Nearby Relaxed Galaxy Clusters, Astrophys. J. **628**, 655 (2005).

278. A. Vikhlinin et al., Heating versus Cooling in Galaxies and Clusters of Galaxies, in H. Bohringer, G.W. Pratt, A. Finoguenov, P. Schuecker, eds, Springer, Berlin, 48 (2007).
279. A. Vikhlinin, M. Markevitch, S. Murray, A Moving Cold Front in the Intergalactic Medium of A3667, Astrophys. J. **551**, 160 (2001).
280. A. Vikhlinin et al., Chandra Cluster Cosmology Project III: Cosmological Parameter Constraints, arXiv:0812.2720. (2008).
281. A. Vikhlinin et al., Evolution of the Cluster X-Ray Scaling Relations since $z > > 0.4$, Astrophys. J. **578**, 107 (2002).
282. A. Vikhlinin, W. Forman, C. Jones, Outer Regions of the Cluster Gaseous Atmospheres, Astrophys. J. **525**, 47 (1999).
283. A. Vikhlinin et al., Chandra Temperature Profiles for a Sample of Nearby Relaxed Galaxy Clusters, Astrophys. J. **628**, 655 (2005).
284. G. Voit et al., Regulation of the X-ray luminosity of clusters of galaxies by cooling and supernova feedback, Nature **414** 425, (2001).
285. D. Walsh, R.F. Carswell, R.J. Weymann, $0957 + 561$ A, B — Twin quasistellar objects or gravitational lens, Nature **279**, 381 (1979).
286. M.D. Weinberg, N. Katz, Bar-driven Dark Halo Evolution: A Resolution of the Cusp-Core Controversy, Astrophys. J. **580**, 627 (2002).
287. S. White et al., The baryon content of galaxy clusters: a challenge to cosmological orthodoxy, Nature **366**, 429 (1993).
288. S.D.M. White, D. Zaritsky, Models for Galaxy halos in an open universe, Astrophys. J. **394**, 1 (1992).
289. L.L. Williams, A. Babul, J.J. Dalcanton, Investigating the Origins of Dark Matter Halo Density Profiles, Astrophys. J. **604**, 18 (2004).
290. J.P. Willis et al., Distant galaxy clusters in the XMM Large Scale Structure survey, Mon. Not. R. Astron. Soc. **430**, 134 (2013).
291. J.P. Willis et al., The XMM Large-Scale Structure survey: an initial sample of galaxy groups and clusters to a redshift $z < 0.6$*, Mon. Not. R. Astron. Soc. **363**, 675 (2005).
292. D.H. Zhao et al., Mass and Redshift Dependence of Dark Halo Structure, Astrophys. J. **597**, L9 (2003).
293. L. Zappacosta et al., The Absence of Adiabatic Contraction of the Radial Dark Matter Profile in the Galaxy Cluster A2589, Astrophys. J. **650**, 777 (2006).
294. A.R. Zentner & J.S. Bullock, Inflation, cold dark matter, and the central density problem, Phys. Rev. D **66**, 043003 (2002).
295. F. Zwicky, On the Masses of Nebulae and of Clusters of Nebulae, Astrophys. J. **86**, 217 (1937).
296. X. Yang et al., Evolution of the galaxy — dark matter connection and the assembly of galaxies in dark matter halos, arXiv:1110.1420v. (2011).
297. Ya.S. Yatskiv et al., General Relativity Theory: Tests through Time, ISBN 966-02-3728-6 (2005).
298. Ya.S. Yatskiv et al., General Relativity Theory: Horizons for Tests, ISBN 978-966-02-6940-8 (2013).

3 CHAPTER

SUPERMASSIVE BLACK HOLES IN GALACTIC NUCLEI AND THEIR RELATION TO THE HOST GALAXY PROPERTIES

S.G. Sergeev, N.G. Pulatova

3.1. Supermassive black holes in AGNs: brief review

Active galactic nuclei (AGN) are relativistic objects with a number of extreme properties: the presence of supermassive black hole (SMBH), the largest luminosity in our Universe, and the variable brightness in all wavelengths from gamma rays to radio waves. The huge amount of energy is released via accretion of gas onto SMBH. This giant luminosity in the continuum makes a strong light pressure. To compensate this pressure, there should be a strong gravitational field created by a body with a mass of millions of solar masses. On the other hand, the rapid variability of AGNs is the evidence that the millions of solar masses must be concentrated in a very small volume. Thus it was assumed that the AGN phenomenon is caused by SMBH surrounded by accretion disk. This assumption was subsequently proved by observations. The most direct evidence for existing of SMBHs in AGNs is the discovery of X-ray iron line, which arises in the accretion disk at a distance of only few gravitational radii from the central mass (e.g., [86]). So, the central mass in AGNs is a supermassive black hole.

A black hole can be detected by the dynamics of the surrounding material. The most direct and efficient method for determining the masses of the SMBHs in galactic nuclei is based on the study of the dynamics of stars and gas. Such studies are mainly carried out with the Hubble Space Telescope (HST) for nearby galaxies, where the region of gravitational domination of the central black hole is spatially resolved (e.g., [37, 47, 83, 89]). Observations with HST

allow to study the dynamics of matter in the galaxy up to distances of several million gravitational radii from the black hole. As was found by observations with HST, at least 30 % of all galaxies have such SMBHs, while AGNs constitute only 1—2 % of all galaxies. So the most galactic nuclei with SMBH is not active because a lack of accreting gas in these nuclei. Such SMBHs manifest themselves by the gravitational field only and they are *a real dark matter*.

The SMBHs are more common in more massive galaxies. Almost all massive galaxies are thought to contain an SMBH. The observational evidences and theoretical suggestions show that there are an upper limit on the SMBH masses of $10^{10} M_\odot$ (e.g., [59]).

As was found from observations, SMBH masses are in the range from millions to billions of solar masses. Such masses are much less than the masses of the host galaxies $M_{\rm host}$. As compared to the bulge masses, the $M_{\rm BH}/M_{\rm bulge}$ ratio is only 0.0014 ± 0.0004 according to [46] or $\sim$0.006 according to [55]. The mean $M_{\rm BH}/M_{\rm host}$ ratio for the Local Universe was found to be as small as $\sim$0.002 [24, 57] or even more less if we consider total gravitational mass $M_{\rm tot}$ that includes dark matter mass $M_{\rm DM}$. Under such mass ratio, the radius of the gravitational influence of a typical SMBH is negligible with respect to the size of its host galaxy.

For AGNs, it is very difficult to determine masses of SMBH from the stellar dynamics because the strong radiation of the central source suppresses the weak radiation of stars in the vicinity of the black hole. In early studies, it was proposed several methods for determination the masses (e.g., [2, 31, 54, 95]), of which one should note the photoionization method proposed in 1980 by Dibai [31]. However, the most direct method for the determination black hole masses in AGNs is reverberation mapping technique (e.g., [9, 50, 68, 69]) which is based on the dynamics of gas that emits the broad lines. The broad-line emission is a result of the high-energy continuum that ionizes and heats nuclear gas. It is so called broad-line region (BLR). Here we approach to a black hole up to distances of several hundreds of gravitational radii. In the gravity-dominated motion, the mass related to the distance $c\,\tau$ and velocity $\sigma_{\rm line}$ by the following equation:

$$M_{\rm BH} = \frac{f\, c\, \tau\, \sigma_{\rm line}^2}{G}, \tag{3.1}$$

where G is the gravitational constant, c is the speed of light, τ is a delay between the line and continuum flux variations, $\sigma_{\rm line}$ is the line width, and f is a factor of order unity that depends on the structure and kinematics of the broad line region. The delay τ is determined by the centroid of the cross-correlation function between line and continuum flux variations at the level of 0.8 of the maximum. The width $\sigma_{\rm line}$ is measured by the profile dispersion. It was shown that (e.g., [81]): $f = 1.5$ for the spherically symmetrical free-fall motion of

gas in the BLR, $f = 3.0$ for Keplerian orbits with random inclinations, and $f = 2.0/\sin^2 i$ for the Keplerian disk with the inclination angle of the disk axis to the line-of-sight equals i. Onken et al. [61] have calibrated the factor f by comparing the "reverberation" masses and the masses obtained by the velocity dispersion of stars in the spherical component of galaxies (i.e., from the $M_{\rm BH} - \sigma_*$ relation) and it was found to be: $f = 5.5 \pm 1.7$. The value of this coefficient has been updated in by [41, 92]. Using the reverberation method, there were measured masses of the central black holes in more than forty AGNs [8, 28, 71]. It was found that the black hole mass depends on the luminosity of the nucleus as $M \propto L^{0.79 \pm 0.09}$ [71]. The large scatter of the data points on the mass-luminosity diagram is caused by uncertainties in the mass measurements as well as real differences related to the differences in the accretion rate and the uncertainties in the inclination angle of the accretion disk.

The purposes of this review are:

1. To overview observed correlations among dark matter halos, the properties of galaxies that resides inside these halos, and, especially, the connection of both halos and galaxies to the SMBH masses.

2. To overview modern views and theories about origin of the dark matter halos, their role in the formation of galaxies and SMBHs, and co-evolution of dark matter, galaxies, and SMBHs.

3. To summarize results on mass determination of the SMBHs by reverberation method.

4. To summarize results obtained in the Crimean Astrophysical Observatory, especially the determination of mass of the SMBHs.

3.2. Spatially resolved kinematics of galaxies and observed correlations

A concept of dark matter in galaxies has arisen from the studies of spatially resolved kinematics of gas (emission lines) or/and stars (stellar absorption lines), e.g., [14–17, 63]. This concept has been supported by theoretical expectations that galaxies are surrounded by extended halos of dark matter [12, 91]. Typically, the rotation curves were found to consist of a linear part near a central region, which is indication of a solid body rotation, and of a flat part with about a constant rotation velocity in an outer region of galaxies. The mass distribution necessary to produce such rotation curves was found to be strongly different from the brightness distribution with the dynamic masses to be much larger than the light masses, especially in the outer parts of galaxies. For some galaxies, the rotation curves were more complicated, e.g., with some radial asymmetry. Examples of the rotation curves of galaxies are shown in Fig. 3.1.

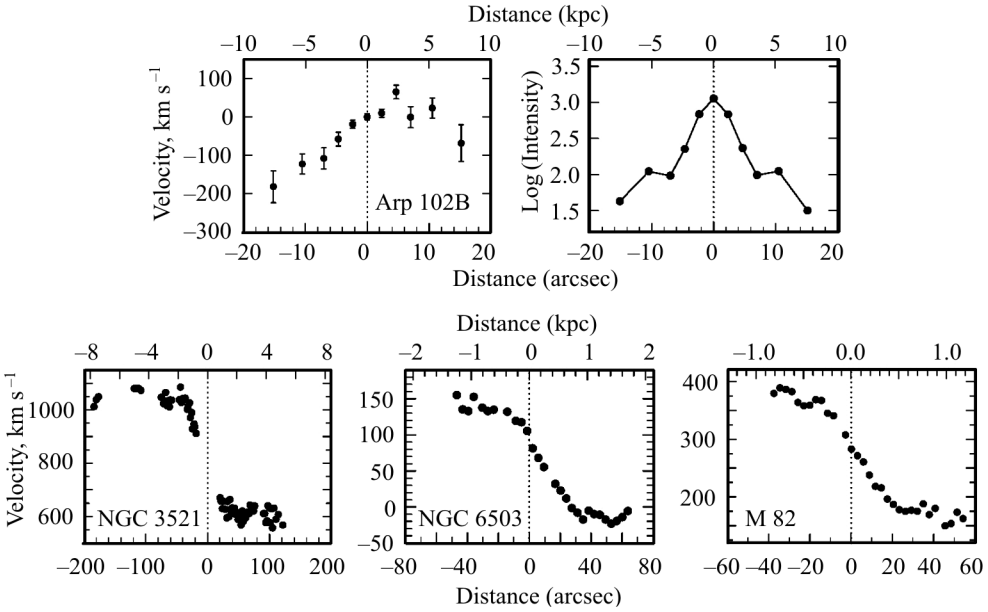

Fig. 3.1. Examples of the observed rotation curves of galaxies. Top-Left: Rotation curve of the Arp 102B elliptical galaxy along the position angle of 90 degree obtained from stellar absorption lines. The velocities are in the nucleus frame. Top-Right: Brightness distribution of the Arp 102B galaxy along the position angle of 90 degree obtained from absorption line intensities. Both velocity and brightness curves are preliminary unpublished results from CCD spectra obtained at the 2.6-m Telescope in 2005—2010. Bottom: Rotations curves of the NGC 3521, NGC 6503, and M 82 spiral galaxies along major axes according to [15—17] (emission line of gas). The velocities are given in the heliocentric frame

Similarly, the application of virial theorem to the clusters of galaxies leds to the missing mass problem — the evidence for the existence of large amount of dark matter in individual galaxies or/and in systems of galaxies (e.g., [64, 67]).

There was compiled a catalog of the galaxy rotation curves [3] containing information about 271 galaxies from 332 papers. Later compilation of spatially resolved kinematics of galaxies [66] contains 4165 observations of 2070 galaxies referring to 743 published papers of which a largest source is [58]. See also a review paper "Rotation curves of spiral galaxies" [74]. The catalog is updated on a regular basis. The updated version of the catalog can be accessed at the HYPERLEAD database at http://leda.univ-lyon1.fr/05/. This database gives central velocity dispersion and rotation velocity. The observed *central velocity dispersion* represents the internal motions of stars along a column crossing the center of a galaxy. It can be derived from the measurement of the line widths from spectra obtained at the central part of galaxies. Usually, it is the width of the hydrogen radio line at 21 cm or the width of the optical

stellar lines. It is reduced to a common standard aperture of $0.595\,\mathrm{h}^{-1}\,\mathrm{kpc}$. Observed *maximum rotation velocity* (usually designated as V_{rot} or V_{circ}) is calculated from the rotation curves (generally in H_α) or/and by analyzing 21-cm line width at different intensity levels. Note, that the rotation velocity in the outer parts of galaxies must be sensitive to the mass of the dark matter halo, since the dark halo gravity controls the matter motion in this region. Since the rotation velocity often remains almost a constant after reaching a peak value (a "turn off") in the rotation curve, the maximum rotation velocity can be roughly treated as a proxy for the mass of the dark matter halo. For example, for a dark matter density profile $\rho(r) \propto r^{-2}$, the velocity is: $V(r) = \sqrt{GM(<r)/r}$ and after integration of $M(r)$ from 0 to r, we obtain that the rotation velocity is independent on r: $V(r) = \mathrm{const}$. However, above assumption lacks both theoretical and observational support. In a reality, the maximum rotation velocity must depends on both the dark and light matter distributions. Navarro, Frenk, and White have proposed, from the N-body simulation, the following dark matter profile [60] (see Section 2.2.3):

$$\rho(r) = \frac{\rho_s}{(r/r_s)(1 + r/r_s)^2},$$

where r_s is a characteristic "inner" radius, and ρ_s is a corresponding inner density.

Much progress has been made recent years in understanding correlations between the masses of dark matter halos, the properties of the galaxies that reside in them, and the masses of the central black holes. The observed relationships among above things are important in order to understand formation of galaxies and their evolution over cosmic time. These relationships are considered below.

3.2.1. The relation between black hole masses and properties of host galaxies

It was found that the SMBH masses are correlated with the large-scale properties of their host galaxies and especially with the properties of the spheroidal component of galaxies. The SMBH masses are closely tied to the bulge luminosity, L_{bulge} [40,45,52], the mass of the bulge [46,55], the central light concentration [39], the stellar velocity dispersion σ_* [38,45,52], and some other. A key relationship is between black hole mass and bulge stellar velocity dispersion, or so called $M_{\mathrm{BH}} - \sigma_*$ relation, observed in both quiescent [38,45,52] and active galaxies [41,44,61]. According to [38] "the intrinsic scatter in black hole mass mass at fixed σ_* is probably less than 0.15 dex". The $M_{\mathrm{BH}} - \sigma_*$ relation was predicted theoretically [35,84] and then was explained by various analytical methods and from numerical simulations. According to [45] this

relation is as follows:

$$M_{\rm BH} = (8.12 \pm 0.08) + (4.24 \pm 0.41) log(\sigma_*/200), \qquad (3.2)$$

where $M_{\rm BH}$ is in Solar mass units and σ_* is in $\mathrm{km\,s^{-1}}$. The high degree of the $M_{\rm BH} - \sigma_*$ correlation permits to determine black hole masses via bulge velocity dispersions, that is much easier than the stellar dynamics studies with HST, and so, it can be used to infer $M_{\rm BH}$ in large sample of galaxies. The stars outside the region of the gravitational domination of a black hole "know" about the existence of the black hole! Fig. 3.2 illustrates $M_{\rm BH} - \sigma_*$ relation for active galaxies (see also [44]). The σ_* velocities are central velocity dispersion from HYPERLEDA database (see http://leda.univ-lyon1.fr/) and the black hole masses are reverberation masses from various studies. Both $M_{\rm BH}$ and σ_* are also given in Table 3.1.

The $M_{\rm BH} - L_{\rm bulge}$ relation, although suffered from a large scatter (a factor of several in $M_{\rm BH}$), indicates that the formation of SMBHs is connected to the formation of bulges. Häring and Rix have found the $M_{\rm BH} - L_{\rm bulge}$ relation is very tight (an observed scatter of 0.30 dex, including measurement errors) and almost linear: $M_{\rm BH} \sim M_{\rm bulge}^{1.12 \pm 0.06}$ [46]. Perhaps SMBH masses are correlated with the bulge properties rather than with the dark matter halos (see below).

3.2.2. The relation among properties of host galaxies and mass of dark matter halos

The majority of work in the literature is concentrated to the relation between halo mass and galaxy luminosity or stellar mass and the relation between halo mass and galaxy kinematics, such as central velocity dispersion or rotation velocity (e.g., [5, 23, 34, 88]).

Tully—Fisher relation. The Tully—Fisher relation is an observed correlation between the optical absolute luminosity and disk circular velocity ($V_{\rm circ}$) in the outer parts of galaxies where the matter motion is controlled by dark matter gravity. It was discovered by Tully and Fisher [88] for disk type galaxies. They measured luminosity versus 21-cm neutral hydrogen emission line width for a sample of 10 spiral galaxies. Later, this relation has been investigated using other measures of disk rotation, such as optical H_α emission line. Note that the Tully—Fisher relation suggest a tight correlation between the mass of the dark matter halos and the mass of a disk component of galaxies because $V_{\rm circ}$ is a rough representation for the mass of the dark matter in a galaxy, while the absolute luminosity represents the mass of the light matter. Fig. 3.3 illustrates the observed Tully—Fisher relation according to the catalog data by Mathewson, Ford, and Buchhorn [58]. To make this figure from the catalog data, we took the total I_c (Cousins) magnitudes corrected for the internal and external extinction, the maximum rotation velocity, and the

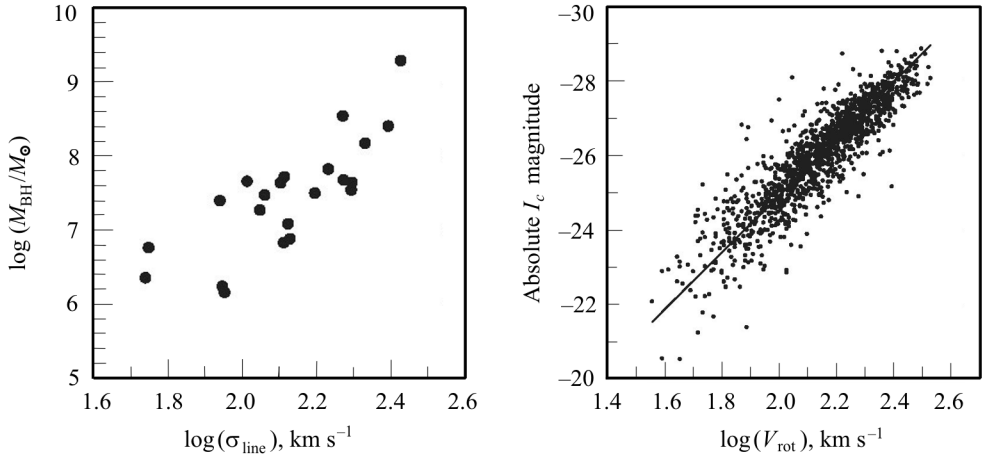

Fig. 3.2. Central velocity dispersion — black hole mass relationship ($M_{\rm BH} - \sigma_*$) for AGNs

Fig. 3.3. Observed Tully—Fisher relationship between the absolute luminosity and the maximum rotation velocity according to the catalog data from [58]. The solid line is the linear regression. This relation suggests a close link between the mass of the dark halos and the mass of their spiral hosts

line-of-sight velocity converted to the Local Group frame. The Hubble constant to calculate absolute I_c magnitudes was assumed to be $70\,\mathrm{km\,s^{-1}}$ Mpc. We have applied the reduced major-axis linear regression to the data on Fig. 3.3 and the following dependence between the absolute I_c magnitude and the maximum rotation velocity has been found:

$$I_c = (-9.620 \pm 0.239) + (-7.654 \pm 0.108)\log(V_{\rm circ}),$$

where $V_{\rm circ}$ is in $\mathrm{km\,s^{-1}}$. The power index of above relation for usual scale (not magnitudes) is equal to 7.654/2.5, i.e., $I_{\rm abs} \propto V_{\rm circ}^{3.06 \pm 0.04}$ [1]. Note that rms uncertainty in magnitude does not exceed 0.6 mag.

Faber—Jackson relation. The Faber—Jackson relation is the first scaling relation discovered by Faber and Jackson [34] for elliptical galaxies. This is a power law relation linking absolute luminosity to central velocity dispersion of early-type galaxies. It suggests, from the $M_{\rm BH} - \sigma_*$ relation, that for elliptical galaxies, the absolute luminosity and the masses of SMBHs are linked each together as well (see also black hole mass — bulge luminosity relation above).

Later there were attempts undertaken to find more general relations linking effective radius, mean effective surface brightness, central velocity dispersion, and total absolute magnitude. These relations are very useful tools for understanding the processes of formation and evolution of galaxies.

[1] Cf.: Ordinary linear regression gives: $L \propto V^{-2.74 \pm 0.04}$. In the original paper by Tully and Fisher [88], it was claimed that $L \propto V^{2.5 \pm 0.3}$.

Table 3.1. **Central velocity dispersion and black hole mass estimates for AGNs**

Target	σ_*, km s^{-1}	Type	BH mass, $10^7\,M_\odot$	$\log \lambda L_\lambda$, ergs s^{-1}	Reference
NGC 5548	197.60 ± 10.90	S0-a	6.54 ± 0.25	43.51	[7]
NGC 4151	103.20 ± 9.90	SABa	$4.57^{+0.57}_{-0.47}$	42.64	[6, 75]
NGC 4051	88.40 ± 3.10	SABb	$0.158^{+0.050}_{-0.065}$	41.93	[27]
NGC 4593	197.60 ± 29.50	Sb	0.98 ± 0.21	43.09	[25]
Mrk 279	197.00 ± 12.00	S0	3.49 ± 0.92	43.88	[71, 73]
3C 390.3	268.00 ± 15.00	—	196 ± 30	43.92	[76, 79]
Ark 120	214.80 ± 13.90	E	15.0 ± 1.9	44.23	[32, 71, 81]
Mrk 6a	—	S0-a	18 ± 2	43.32	[33, 80, 81]
1E 0754.6 + 3928	—	—	10	44.65	[77]
Mrk 290	—	E	2.43 ± 0.37	43.49	[28]
Mrk 817	127.00 ± 12.00	S0-a	$4.33^{+1.05}_{-1.07}$	43.82	[28]
NGC 3227	134.60 ± 5.70	SABa	$0.763^{+0.162}_{-0.172}$	42.38	[28]
NGC 3516	157.10 ± 13.40	S0	$3.17^{+0.28}_{-0.42}$	42.88	[28]
Mrk 335	—	E?	2.5 ± 0.3	43.70	[42, 43]
Mrk 1501	—	—	18.4 ± 2.7	44.32	[42]
3C 120	170.90 ± 17.10	S0	6.7 ± 0.6	43.96	[42]
PG 2130 + 099	—	—	4.6 ± 0.4	44.15	[42]
PG 0026 + 129	—	—	39.3 ± 9.6	45.02	[71]
PG 0052 + 251	—	—	36.9 ± 7.6	44.96	[71]
Fairall 9	248.2 ± 21.8	S0	25.5 ± 5.6	44.25	[71]
Mrk 590	187.9 ± 6.7	Sa	4.75 ± 0.74	43.81	[71]
Mrk 79	130.0 ± 10.0	Sb	5.24 ± 1.44	43.72	[71]
PG 0804 + 761	—	—	69.3 ± 8.3	44.94	[71]
PG 0844 + 349	—	—	9.24 ± 3.81	44.35	[71]
Mrk 110	87.1 ± 12.0	—	2.51 ± 0.61	43.72	[71]
PG 0953 + 414	—	—	27.6 ± 5.9	45.22	[71]
NGC 3783	115.1 ± 20.6	SBa	2.98 ± 0.54	43.26	[71]
PG 1211 + 143	—	—	14.6 ± 4.4	44.75	[71]
PG 1226 + 023	—	—	88.6 ± 18.7	45.96	[71]
PG 1229 + 204	—	—	7.32 ± 3.52	44.08	[71]
PG 1307 + 085	—	—	44.0 ± 12.3	44.88	[71]
PG 1411 + 442	—	—	44.3 ± 14.6	44.63	[71]
PG 1426 + 015	—	—	129.8 ± 38.5	44.72	[71]
PG 1613 + 658	—	E	27.9 ± 12.9	44.98	[71]
PG 1617 + 175	—	E	59.4 ± 13.8	44.48	[71]
PG 1700 + 518	—	—	$78.1^{+18.2}_{-16.5}$	45.63	[71]
Mrk 509	—	—	14.3 ± 1.2	44.28	[71]
NGC 7469	133.0 ± 6.4	Sa	1.22 ± 0.14	43.72	[71]
Mrk 142	—	—	$0.219^{+0.078}_{-0.085}$	43.62	[8]
SBSG 1116 + 583A	55.9 ± 20.0	—	$0.58^{+0.21}_{-0.19}$	42.93	[8]
Arp 151	129.7 ± 7.5	S0	$0.678^{+0.097}_{-0.126}$	42.73	[8]
Mrk 1310	54.9 ± 17.5	E	$0.226^{+0.091}_{-0.091}$	42.84	[8]
Mrk 202	89.7 ± 7.9	—	$0.144^{+0.087}_{-0.060}$	42.87	[8]
NGC 4748	—	S?	$0.26^{+0.11}_{-0.13}$	42.97	[8]
NGC 6814	111.80 ± 17.50	SABb	$1.86^{+0.35}_{-0.36}$	42.24	[8]

a – According to [42] the BLR size in Mrk 6 is equal to 10.1 ± 1.1 light days, while the black hole mass is equal to $(13.6 \pm 1.2) \times 10^7\,M_\odot$.

3.2.3. The relation among masses of the dark halos, masses of the supermassive black holes, and the total masses of galaxies

Theoretical models of SMBH formation predict that the black hole mass $M_{\rm BH}$ has to be connected to the total mass of the host galaxy, including dark matter, rather than to the bulge mass (e.g., [1, 85]). The key ingredient in these studies is that the formation of the SMBHs is controlled by the dark matter halos and there must be a tight correlation between SMBH masses ($M_{\rm BH}$) and the masses of the dark matter halos ($M_{\rm DM}$).

Since the correlation between σ_* and the circular velocity $V_{\rm circ}$ was found in several studies, it was suggested from the $M_{\rm BH} - \sigma_*$ relation [36, 65] that there is a link between $M_{\rm BH}$ and $V_{\rm circ}$, or equivalently, with the mass of the dark matter halo because $V_{\rm circ}$ is a velocity in the outer parts of galaxies where the motion is controlled by dark matter halo.

However, it is difficult to find observation support for above relation since measurement of the total mass is non-trivial. Most direct observational methods to obtain the total mass of galaxies are the galaxy-galaxy lensing [12, 13, 49] and satellite kinematics in combination with the spatially resolved kinematics of galaxies [11, 93, 94]. Unfortunately, a mass estimate for individual galaxies is usually too insignificant statistically. The indirect observational evidence that SMBHs and dark matter halos are tightly connected has been provided by Ferrarese [36], who studied the correlation between bulge velocity dispersion σ_* and the observed circular velocity $V_{\rm circ}$ for a sample of 20 elliptical and 16 spiral galaxies. As already mentioned above, $V_{\rm circ}$ is dependent on the total gravitational mass, $M_{\rm tot}$, and the $\sigma_* - V_{\rm circ}$ relation is translated into an equivalent$M_{\rm BH} - M_{\rm tot}$ correlation. Ferrarese argued that the scatter in the $M_{\rm BH} - M_{\rm DM}$ relation could be even smaller than that in $M_{\rm BH} - \sigma_*$ relation. More direct evidence for the correlation between $M_{\rm BH}$ and the total gravitational mass of the host galaxy, $M_{\rm tot}$, was found by Bandara et al. [4] who used 43 galaxy-scale strong gravitational lenses from the Sloan Lens Survey to measure $M_{\rm tot}$, while $M_{\rm BH}$ was determined from the $M_{\rm BH} - \sigma_*$ relation. The best fit correlation was found to be:

$$\log(M_{\rm BH}) = (8.18 \pm 0.11) + (1.55 \pm 0.31)(\log(M_{\rm tot}) - 13.0)$$

over 2 orders of magnitude in $M_{\rm BH}$. This result is in a striking agreement with the result of simulation of the co-evolution of the SMBH and galaxy populations [10]. Since the power index of the $M_{\rm BH} - M_{\rm tot}$ relation is greater than 1, it indicates that massive halos are more efficient in forming black holes. Volonteri et al. [90] proposed that dark matter halos play role in both the formation and growth of SMBHs.

However, Kormendy and Bender [53] argued that "supermassive black holes do not correlate with dark matter halos of galaxies". They studied a sample of

bulgeless galaxies and concluded that there is almost no correlation between the SMBH and dark the matter halo, unless the galaxy also contains a bulge. Indeed, it is known that SMBH masses do correlate with galaxy bulges (e.g., $M_{\rm BH} - \sigma_*$ relation), while Tully—Fisher relation [88] indicates that the dark matter correlates closely with galaxy disks. So, it can be concluded that black holes do not correlate directly with dark matter. Indeed, if $V_{\rm circ}$ is a proxy for the dark matter halo mass then less strong (more scatter) $M_{\rm BH} - V_{\rm circ}$ relation and more strong (less scatter) $M_{\rm BH} - \sigma_*$ relation suggests that SMBH masses are more coupled to the baryonic, rather than to the dark matter [5]. Volontery et al. [90] claimed, however, that "although the black hole masses are not uniquely determined by dark matter halo mass, when considered for the current sample as a whole, the $M_{\rm BH} - V_{\rm circ}$ correlation may be as strong (or as weak) as $M_{\rm BH} - \sigma_*$". There were pointed out by [22, 48] that the $V_{\rm circ} - \sigma_*$ relation actually depends on galaxy morphology (or equivalently, on its light concentration) thus precluding a simple connection between $M_{\rm BH}$ and $V_{\rm circ}$. Treuthardt et al. [87] have noted that the SMBH–bulge connection is no so tight because discovery of SMBHs in the centers of late-type galaxies with little or no bulge and the mass of SMBHs may be tied to the dark matter halo virial mass, or its concentration.

Thus recent papers have argued both for [4, 36, 90] and against [53] a tight correlation between SMBHs and dark matter halos. Perhaps, the mass of SMBHs is indeed related to the bulge properties rather than to the mass of dark mater halo.

3.3. Researches at the Crimean Astrophysical Observatory

3.3.1. Pre-CCD era

The Crimean Astrophysical Observatory keeps one of the first position in the world in the study of AGNs. It carried out researches in this area since the 1960s. Thus, the CrAO is to be at the very beginning of studies of the AGN phenomenon. The term "broad-line region" (BLR), that is now widely used, has appeared after the pioneer works of V.I. Pronik and E.A. Dibai [29,30]. Systematic observations of the emission lines in AGNs were initiated in the CrAO since 1972 by K.K. Chuvaev, who is really pioneered spectroscopic monitoring of AGNs [19–21, 72]. However, the fact that the activity phenomenon is directly related to the presence of supermassive black holes in galactic nuclei has been realized much later, only in the 1980s, and the researches in this area basically begin in the CCD era. It must also be mentioned the outstanding contribution to the study of AGNs of our colleagues from the Southern Station of the Sternberg Astronomical Institute of the Moscow State University, which is located in the close vicinity of the CrAO. For the

first time (and much earlier than other similar studies), the reverberation-mapping method has been applied to determine the size of BLR in the nucleus of NGC 4151 by Cherepashchuk & Lyutyi in 1973 [18]. Dibai [31] was the first who have developed the photoionization method to measure masses of the central black holes in AGNs. He has measured black hole masses of many AGNs and obtained accretion rates onto black holes. Again, this study was performed much earlier than other similar studies and it was really a pioneer work.

3.3.2. CCD era

The CrAO was a pioneer of CCD observations among the astronomical institutes of the Soviet Union. The spectral observations with the Astromed-2000 CCD have been started at the 2.6-m Shajn Telescope in 1985. The observations of AGNs with this telescope have been initialized by V.I. Pronik, who has developed a special spectrograph for this purpose. The first CCD spectra of AGNs have been acquired in February 1988 by V.I. Pronik and S.G. Sergeev. During the next several years, the CCD observations of AGNs have been continued on a regular basis (usually once per month). The main target was the NGC 4151 nucleus.

At present, the instrumental setup for spectral observations of AGNs includes a modern SPEC-10 CCD and the computer controlled "SPEM" spectrograph mounted in the Nasmith focus of the 2.6-m Shajn Telescope. The spectropgraph with the CCD camera is shown in Fig. 3.4. At present, more than 1500 spectra of about thirty AGNs are obtained with this CCD.

In the beginning of our monitoring program, we had no more than one observational set (2—3 nights) per month. Since 1993, the observational rate has been increased up to 2 sets per month. The spectra were registered at the two separate spectral regions near *ha* and *hb* lines. The "extraction window" is equal to 11 arcs. Most of observations were performed with position angle of the entrance slit of 90 degree (i.e., the slit is aligned on right ascension). The typical exposure time is from twenty minutes to one hour. Generally, all the spectra were obtained with a single exposure within a night.

As a rule, four short-time ($\sim$5—30^s) exposures of bright standard stars (B—A spectral type) per each galaxy exposure have been obtained at approximately the same zenith distance. Only a single star has been selected for a given galaxy. The spectral energy distribution for this star has been taken from [51]. The standard star spectra were used to remove telluric absorption features from the galactic spectra as well as to provide the relative flux calibration. Using the standard star, we have also measured the "seeing" defined as full width at half-maximum (FWHM) of the cross-dispersion profile on CCD image.

We have considered the following uncertainties in our measurements of the broad line fluxes and continuum fluxes:

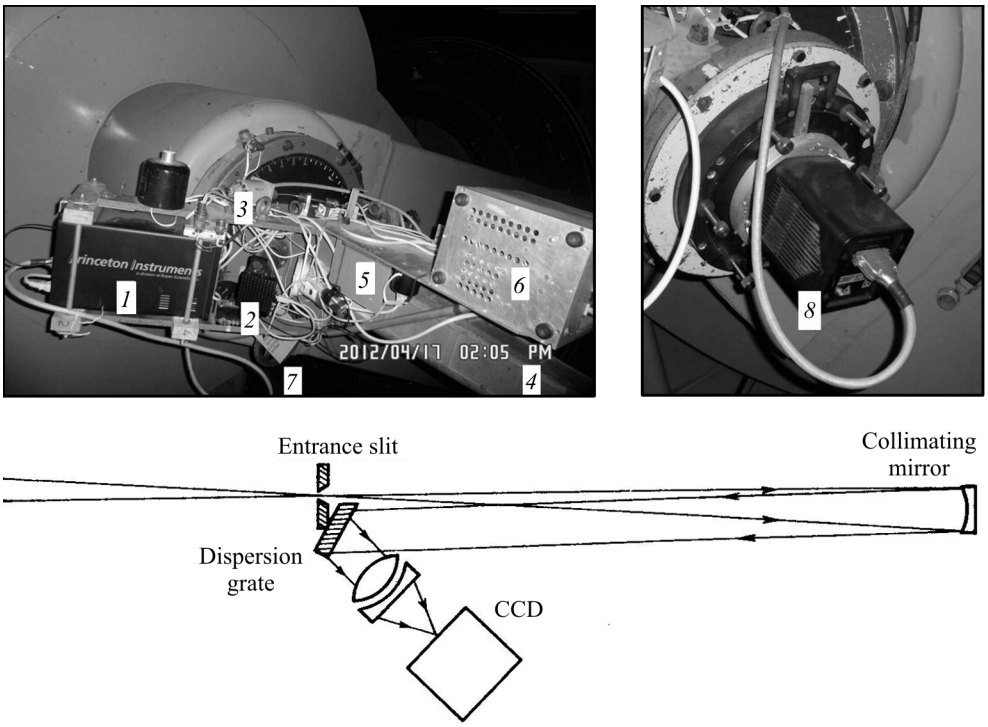

Fig. 3.4. Top: "SPEM" spectrograph mounted in the Nasmyth focus of the 2.6-m Shajn Telescope. Digits denote: *1* – Controller of the SPEC-10 CCD camera; *2* — Meade CCD camera to view and to track targets; *3* — Unit to set a title of the grating dispersion unit by steeper engine; *4* — Collimator; *5* — 12 V Power supply; *6* — Unit to control the spectrograph; *7* – Wheel to change a position angle; and *8* — SPEC-10 CCD camera. Bottom: Optical scheme of the spectrograph

1. The error related to the S/N of source spectra.
2. The atmospheric dispersion.
3. The effect of "seeing".

Two-dimensional images of AGNs were unbiased and then corrected for the flat field. The sky background spectra were subtracted from the extracted nucleus spectra and then wavelength calibrated. After flux calibration using comparison star spectra, the final absolute calibration in flux was performed using the narrow-line fluxes which were assumed to be constant over the duration of the monitoring program.

A powerful and effective software tool for observations, and for data processing and analysis, more than 100 programs have been developed, including:

1. Computer-controlled interface for the 70-cm AZT-8 Telescope [82] and for the SPEM spectrograph.

2. The programs for photometric observations and for spectroscopic observations.

3. The program for the primary processing of the CCD images.

4. The program to view two-dimensional images and to extract one-dimensional spectra.

5. "SPE" program and related programs, including command interpreter, for processing and analysis of one-dimensional spectra.

Observational and instrumental setup, data processing and analysis are described in [56, 79, 80].

One of the major goal of our scientific program is the reverberation mapping studies, i.e., determination the size, geometry, and kinematics of the broad-line region (BLR) as well as masses of the central black holes from the time delay between line and continuum flux variations. The first estimates of the BLR size and the black hole mass were obtained at CrAO for the NGC 4151 nucleus [75, 76]. In subsequent years, the number of such estimates for various AGNs has increased significantly. E.g., Sergeev et al. in 1999 have determined or revised black hole masses for total of 12 AGNs using Crimean observational data as well as literature data [81].

The Crimean reverberation program is generally intended for the AGNs with a moderate or high absolute luminosity, for which a temporal resolution of order ten days is sufficient to determine the time lag. However, to obtain reliable lag estimates, especially for the low-luminosity AGNs, the international cooperation is strongly required. The Crimean observatory participates in the international programs of spectroscopic and photometric monitoring of AGNs (such as AGN Watch, see [28, 70] for example). The Crimean team takes part in the determination the sizes and masses in total of eleven AGNs (e.g., [28]). For Mrk 6 [33, 80, 81] and 1E $0754.6+3928$ [77] the sizes and masses have been determined for the first time, and by the efforts of the Crimean team only. The position of 1E $0754.6+3928$ in the black hole mass–luminosity diagram agrees with the positions of similar AGNs (so called narrow-line Seyfert I galaxies) and can be explained by an enhanced mass accretion rate in the central source. In contrast to 1E $0754.6+3928$, our reverberation results on 3C 390.3 suggests even larger black hole mass to its nucleus than previously though, and, therefore, lower accretion rate, thus providing more evidence for anti-correlation between broad line widths and Eddington luminosity ratios [76, 96—98]. Summary of the reverberation measurements of the black hole masses from various studies is present in Table 3.1. CrAO made a contribution to the determination of the black hole masses in the first 17 targets of the table. Also given in this table are the central velocity dispersion, σ_*, from the HYPERLEDA catalog, the host galaxy type, the absolute luminosity of the nucleus, $\log \lambda L_\lambda$, obtained from optical spectra in various studies, and the last table column gives references.

The reverberation BLR sizes and black hole masses allow to establish the most important relationships for AGNs: the size-luminosity and the mass-

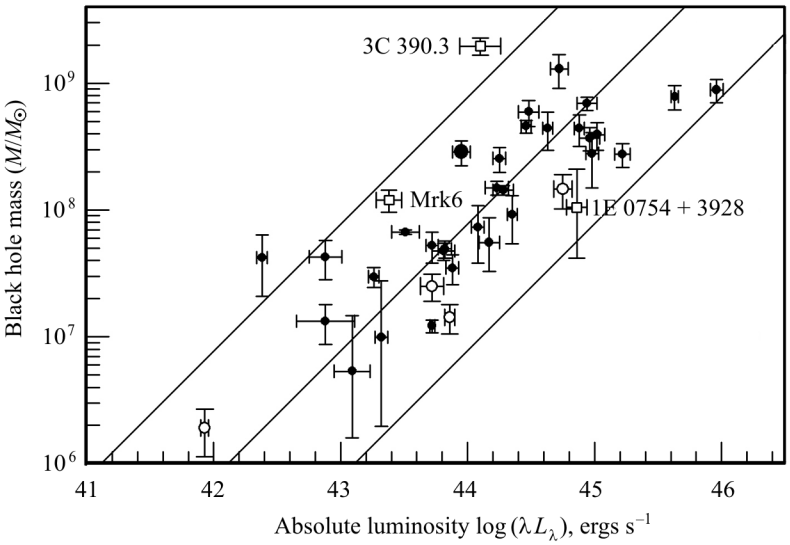

Fig. 3.5. Luminosity — black hole mass relationship. The data for reverberation-mapped AGNs are from [71] (see their table 8 and fig. 16). Open circles show the AGNs of the NLS1 type. Open squares show the AGNs, for which the reverberation masses were measured at the CrAO: 3C 390.3 [76, 79], 1E 0754.6 + 3928 [77], and Mrk 6 [33, 80, 81]. The large filled circle represents data for 3C 390.3 from [71]. The diagonal lines show the Eddington limit $L_{\rm Edd}$, $0.1L_{\rm Edd}$, $0.01L_{\rm Edd}$

luminosity diagrams [8, 71]. These relationships are often considered in the frame of the AGN models. The mass-luminosity relationship is shown in Fig. 3.5. Also shown in Fig. 3.5 are estimates of the black hole masses made by the Crimean team only.

However, there remained some doubts about the correctness of the reverberation method because it is only valid under virial assumption, i.e., under gravitationally dominated gas motions in the BLR. The reverberation mapping and stellar dynamic mass measurements for NGC 4151 nucleus have been compared by Onken et al. in 2007 [62] and both mass estimates were found to be in a reasonable agreement. The role of the CrAO in this project was to carry out regular photometric measurements of the brightness of the NGC 4151 nucleus to watch whether its brightness is low enough to initialize observations with the Hubble Space Telescope. NGC 4151 is now among the small sample of galaxies in which the SMBH mass has been constrained from two independent techniques.

In order to check the virial assumption, the lag estimates were obtained as a function of the line-of-sight velocity of the Hβ line profile in six AGNs by Denney et al. [26, 28]. They found indications of apparent infall, outflow, and virialized motions, which would indicate that the BLR is a complicated region that differs from object to object. This fact put limitations on the preci-

sion of the mass estimates by the reverberation technique and thus introduce more scattering in the $M_{\rm BH} - L$ relationship derived from the reverberation method.

The large archive of many AGN spectra observed at CrAO allows us to achieve a signal-to-noise ratio high enough to study kinematics of the host galaxies along the slit position angle of 90 degree from the galaxy centers to far peripheral regions. Recently, we have undertaken such a study for the Arp 102B galaxy (unpublished). The rotation curve and brightness profile of this galaxy is shown in Fig. 3.1. The rotation curve has been obtained by measuring centroids of the stellar absorption features at various distances from the galaxy center, while the profile brightness has been obtained by measuring intensities of these features. It is seen, that the brightness profile is nearly symmetric, while the rotation curve is strongly asymmetric relatively to the galaxy center. The "turn off" in the rotation curve is poorly seen, probably because uncertainties for outer galaxy regions are large enough.

3.4. Summary

The observed correlations among dark matter halos, the properties of galaxies that resides inside these halos, and, especially, the connection of both halos and galaxies to the SMBH masses are briefly reviewed. Special attention has been paid to the supermassive black holes (SMBHs) in galactic nuclei and to the AGN phenomenon. We have also reviewed modern views and theories about origin of the dark matter halos, their role in the formation of galaxies and SMBHs, and co-evolution of dark matter, galaxies, and SMBHs. It was described the reverberation method to determine SMBH masses in AGNs. It is shown that the Crimean Astrophysical Observatory (CrAO) has traditionally been one of the leaders in studying AGNs. In particular, the CrAO contributed to:

1. Determination SMBH masses for a number of AGNs.

2. Refining the "mass–luminosity" and the "radius–luminosity" relationships for AGNs (black hole mass, nucleus absolute luminosity, and the size of the broad line region).

3. Comparison reverberation masses and the masses obtained by other methods.

4. Verification of the virial assumptions for the gas motion in the broad line region.

We also present first preliminary result on the spatially resolved kinematics of AGN hosts observed spectroscopically at CrAO.

The most of SMBHs do not cause the activity phenomenon, so they are a real dark matter. But their contributions to the total galaxy masses are negligible: 0.2 % (on average) or more less if we consider total gravitational mass,

including dark matter mass, and so the radius of the gravitational influence of SMBH is negligible as well.

It is not clear how tight is the SMBH phenomenon connected to the dark matter halo. Some authors believe that there is a tight correlation between black hole mass, $M_{\rm BH}$, and dark matter mass, $M_{\rm DM}$. If so, the obtained SMBH masses can be used as a proxy for the dark matter masses. However, other authors argued that there is no correlation between $M_{\rm BH}$ and $M_{\rm DM}$. The Tully—Fisher $L - V_{\rm circ}$ relation suggests that the masses of spiral galaxies are tightly correlated with the masses of the dark matter, while $M_{\rm BH} - \sigma_*$ relation suggests that SMBH masses are tightly connected to the properties of galaxy bulges. Whether $M_{\rm BH}$ is correlated with $M_{\rm DM}$ or not, is probably dependent on how strong is $V_{\rm circ} - \sigma_*$ correlation. It seems that the last correlation is poor rather than strong.

Bibliography

1. F.C. Adams, D.S. Graff, and D.O. Richstone, A Theoretical Model for the $M_{\rm BH}-\sigma$ Relation for Supermassive Black Holes in Galaxies, Astrophys. J. **551**, L31 (2001).
2. S.M.V. Aldrovandi, Supermassive black holes and emission lines of active galaxies and QSOs — Accretion rate, black hole mass, and photoionization models, Astron. Astrophys. **97**, 122 (1981).
3. G.C. Baiesi-Pillastrini, G.G.C. Palumbo, and G. Vettolani, Galaxies rotation curves — A catalogue, Astron. Astrophys. Suppl. Ser. **53**, 373 (1983).
4. K. Bandara, D. Crampton, and L. Simard, A Relationship Between Supermassive Black Hole Mass and the Total Gravitational Mass of the Host Galaxy, Astrophys. J. **704**, 1135 (2009).
5. A. Beifiori, S. Courteau, E.M. Corsini, and Y. Zhu, On the correlations between galaxy properties and supermassive black hole mass, Mon. Not. R. Astron. Soc. **419**, 2497 (2012).
6. M.C. Bentz et al., A Reverberation-based Mass for the Central Black Hole in NGC 4151, Astrophys. J. **651**, 775 (2006).
7. M.C. Bentz et al., NGC 5548 in a Low-Luminosity State: Implications for the Broad-Line Region, Astrophys. J. **662**, 205 (2007).
8. M.C. Bentz et al., The Lick AGN Monitoring Project: Broad-line Region Radii and Black Hole Masses from Reverberation Mapping of Hβ, Astrophys. J. **705**, 199 (2009).
9. R.D. Blandford, C.F. McKee, Reverberation mapping of the emission line regions of Seyfert galaxies and quasars, Astrophys. J. **255**, 419 (1982).
10. C.M. Booth and J. Schaye, Joop Dark matter haloes determine the masses of supermassive black holes, Mon. Not. R. Astron. Soc. **405**, L1 (2010).
11. F.C. van den Bosch, P. Norberg, H.J. Mo, and X. Yang, Measurement of Mass and Beta-Lifetime of Stored Exotic Nuclei, Mon. Not. R. Astron. Soc. **352**, 1302 (2004).
12. T.G. Brainerd, R.D. Blandford, and I. Smail, Weak Gravitational Lensing by Galaxies, Astrophys. J. **466**, 623 (1996).
13. F. Brimioulle, S. Seitz, M. Lerchster, R. Bender, and J. Snigula, Dark matter halo properties from galaxy-galaxy lensing, Mon. Not. R. Astron. Soc. **432**, 1046 (2013).
14. E.M. Burbidge, G.R. Burbidge, K.H. Prendergast, The Rotation and Mass of NGC 2146, Astrophys. J. **130**, 739 (1959).

15. E.M. Burbidge, G.R. Burbidge, D.J. Crampin, V.C. Rubin, The Rotation and Mass of NGC 3521, Astrophys. J. **139**, 1058 (1964).
16. E.M. Burbidge, G.R. Burbidge, D.J. Crampin, V.C. Rubin, The Rotation and Mass of NGC 6503, Astrophys. J. **139**, 539 (1964).
17. E.M. Burbidge, G.R. Burbidge, V.C. Rubin, A Study of the Velocity Field in M82 and its Bearing on Explosive Phenomena in that Galaxy, Astrophys. J. **140**, 942 (1964).
18. A.A. Cherepashchuk, V.M. Lyutyi, Rapid Variations of Hα Intensity in the Nuclei of Seyfert Galaxies NGC 4151, 3516, 1068, Astrophys. Lett. **13**, 165 (1973).
19. K.K. Chuvaev, Hβ Profile Variations in the Spectrum of Seyfert Galaxy NGC 5548 Nucleus, IAU Symp. 121: Observational Evidence of Activity in Galaxies **121**, 203 (1987).
20. K.K. Chuvaev, Multiyear spectral observations of active galactic nuclei in the optical range. I — The galaxy NGC 1275, Krymskaia Astrofizicheskaia Observatoriia, Izvestiia **81**, 138 (1990).
21. K.K. Chuvaev, Multiyear spectral observations of the nuclei of active galaxies in the optical spectral region. II — Variations of the H-beta-line profile in the spectrum of the nucleus of the galaxy MKN 6", Krymskaia Astrofizicheskaia Observatoriia, Izvestiia **83**, 194 (1991).
22. S. Courteau, M. McDonald, L.M. Widrow, J. Holtzman, The Bulge-Halo Connection in Galaxies: A Physical Interpretation of the Vc-σ0 Relation, Astrophys. J. Lett. **655**, L21 (2007).
23. A.A. Dutton, C. Conroy, F.C. van den Bosch, F. Prada, and S. More, The kinematic connection between galaxies and dark matter halo, Mon. Not. R. Astron. Soc. **407**, 2 (2010).
24. R. Decarli, R. Falomo, A. Treves, M. Labita, J.K. Kotilainen, and R. Scarpa, The quasar MBH-Mhost relation through cosmic time — II. Evidence for evolution from $z = 3$ to the present age, Mon. Not. R. Astron. Soc. **402**, 2453 (2010).
25. K.D. Denney et al., The Mass of the Black Hole in the Seyfert 1 Galaxy NGC 4593 from Reverberation Mapping, Astrophys. J. **653**, 152 (2006).
26. K.D. Denney et al., Diverse Kinematic Signatures from Reverberation Mapping of the Broad-Line Region in AGNs, Astrophys. J. **704**, L80 (2009).
27. K.D. Denney et al., A Revised Broad-line Region Radius and Black Hole Mass for the Narrow-line Seyfert 1 NGC 4051, Astrophys. J. **702**, 1353 (2009).
28. K.D. Denney et al., Reverberation Mapping Measurements of Black Hole Masses in Six Local Seyfert Galaxies, Astrophys. J. **721**, 715 (2010).
29. E.A. Dibai and V.I. Pronik, Spectrophotometric Investigation of the Nucleus of NGC 1068, Astrophys. **1**, 78 (1965).
30. E.A. Dibai and V.I. Pronik, Физические условия в ядре галактики NGC 1275, Krymskaia Astrofizicheskaia Observatoriia, Izvestiia **35**, 87 (1966).
31. E.A. Dibai, The Mass/Luminosity Relation for Active Galaxy Nuclei, Soviet Astronomy **24**, 389 (1980). (transleted from AZh **57**, 677).
32. V.T. Doroshenko, S.G. Sergeev, and V.I. Pronik, The Seyfert 1 galaxy Ark 120. Spectral variability in 1992 2005, Astron. Rep. **52**, 442 (2008).
33. V.T. Doroshenko, S.G. Sergeev, S.A. Klimanov, V.I. Pronik, Yu.S. Efimov, and S.V. Nazarov, Broad-line region kinematics and black hole mass in Markarian 6, Mon. Not. R. Astron. Soc. **426**, 416 (2012).

34. S.M. Faber, R.E. Jackson, Velocity dispersions and mass-to-light ratios for elliptical galaxies, Astrophys. J. **204**, 668 (1976).
35. A.C. Fabian, The obscured growth of massive black hol, Mon. Not. R. Astron. Soc. **308**, L39 (1999).
36. L. Ferrarese, Beyond the Bulge: A Fundamental Relation between Supermassive Black Holes and Dark Matter Ha, Astrophys. J. **578**, 90 (2002).
37. L. Ferrarese and H. Ford, Supermassive Black Holes in Galactic Nuclei: Past, Present and Future Research, Space Science Reviews **116**, 523 (2005).
38. K. Gebhardt et al., A Relationship between Nuclear Black Hole Mass and Galaxy Velocity Dispersion, Astrophys. J. Lett. **539**, L13 (2000).
39. A.W. Graham, P. Erwin, N. Caon, and I. Trujillo, A Correlation between Galaxy Light Concentration and Supermassive Black Hole Mass, Astrophys. J. Lett. **563**, L11 (2001).
40. A.W. Graham, The black hole mass — spheroid luminosity relation, Mon. Not. R. Astron. Soc. **379**, 711 (2007).
41. A.W. Graham, C.A. Onken, E. Athanassoula, and F. Combes, An expanded Mbh-σ diagram, and a new calibration of active galactic nuclei masses, Mon. Not. R. Astron. Soc. **412**, 2211 (2011).
42. C.J. Grier et al., Reverberation Mapping Results for Five Seyfert 1 Galaxies, Astrophys. J. **755**, 60 (2012)
43. C.J. Grier et al., A Reverberation Lag for the High-ionization Component of the Broad-line Region in the Narrow-line Seyfert 1 Mrk 335, Astrophys. J. Lett. **744**, L4 (2012).
44. C.J. Grier, P. Martini, L.C. Watson, B.M. Peterson, M.C. Bentz, K.M. Dasyra, M. Dietrich, L. Ferrarese, R.W. Pogge, Y. Zu, Stellar Velocity Dispersion Measurements in High-luminosity Quasar Hosts and Implications for the AGN Black Hole Mass Scale, Astrophys. J. **773**, 90 (2013).
45. K. Gultekin et al., The $M - \sigma$ and $M - L$ Relations in Galactic Bulges, and Determinations of Their Intrinsic Scatter, Astrophys. J. **698**, 198 (2009).
46. N. Häring and H.-W. Rix, On the Black Hole Mass-Bulge Mass Relation, Astrophys. J. Lett. **604**, L89 (2004).
47. R.J. Harms et al., HST FOS spectroscopy of M87: Evidence for a disk of ionized gas around a massive black hole, Astrophys. J. **435**, L35 (1994).
48. L.C. Ho, Bulge and Halo Kinematics Across the Hubble Sequence, Astrophys. J. **668**, 94 (2007).
49. Henk Hoekstra, H.K.C. Yee, and M.D. Gladders, Properties of Galaxy Dark Matter Halos from Weak Lensing, Astrophys. J. **606**, 67 (2004).
50. S. Kaspi, W.N. Brandt, Maoz Dan, H. Netzer, D.P. Schneider, and O. Shemmer, Reverberation Mapping of High-Luminosity Quasars: First Results, Astrophys. J. **659**, 997 (2007).
51. A.V. Kharitonov, V.M. Tereshchenko, and L.N. Kni'azeva, Spektrofotometricheskiĭ katalog zvezd, Alma-Ata: Izd-vo "Nauka" Kazakhskoĭ SSR (1988).
52. J. Kormendy and D. Richstone, Inward Bound — The Search For Supermassive Black Holes In Galactic Nuclei, Ann. Rev. Astron. Astrophys. **33**, 581 (1995).
53. J. Kormendy and R. Bender, Supermassive black holes do not correlate with dark matter haloes of galaxies, Nature **469**, 377 (2011).

54. S.A. Lushchenko, M. Maksumov, Masses of hypothetical black holes in quasars and galactic nuclei, Akademiia Nauk Tadzhikskoi SSR, Doklady **21**, 25 (1978).
55. J. Magorrian et al., The Demography of Massive Dark Objects in Galaxy Centers, Astrophys. J. **115**, 2285 (1998).
56. Yu.F. Malkov, V.I. Pronik, and S.G. Sergeev, Complex variability pattern in NGC 4151. I. Sequences on the line-continuum diagram. Astron. Astrophys. **324**, 904 (1997).
57. A. Marconi and L.K. Hunt, The Relation between Black Hole Mass, Bulge Mass, and Near-Infrared Luminosity, Astrophys. J. **589**, L21 (2003).
58. D.S. Mathewson, V.L. Ford, and M. Buchhorn, A southern sky survey of the peculiar velocities of 1355 spiral galaxies, Astrophys. J. Suppl. Ser. **81**, 413 (1992).
59. P. Natarajan and E. Treister, Is there an upper limit to black hole masses?, Mon. Not. R. Astron. Soc. **393**, 838 (2009).
60. J.F. Navarro, C.S. Frenk, and S.D.M. White, A Universal Density Profile from Hierarchical Clustering, Astrophys. J. **490**, 493 (1997).
61. C.A. Onken, L. Ferrarese, D. Merritt, B.M. Peterson, R.W. Pogge, M. Vestergaard, and Amri Wandel, Supermassive Black Holes in Active Galactic Nuclei. II. Calibration of the Black Hole Mass-Velocity Dispersion Relationship for Active Galactic Nuclei, Astrophys. J. **615**, 645 (2004).
62. C.A. Onken et al., The Black Hole Mass of NGC 4151: Comparison of Reverberation Mapping and Stellar Dynamical Measurements, Astrophys. J. **670**, 105 (2007).
63. J.H. Oort, Some Problems Concerning the Structure and Dynamics of the Galactic System and the Elliptical Nebulae NGC 3115 and 4494, Astrophys. J. **91**, 273 (1940).
64. G. Paal, Evolutionary approach to the missing mass problem of clusters of galaxies, Astron. Nachr. **297**, 311 (1976).
65. A. Pizzella, E.M. Corsini, B.E. Dalla, M. Sarzi, L. Coccato, F. Bertola, On the Relation between Circular Velocity and Central Velocity Dispersion in High and Low Surface Brightness Galaxies, Astrophys. J. **631**, 785 (2005).
66. Ph. Prugniel, A. Zasov, G. Busarello, and F. Simien, A catalogue of spatially resolved kinematics of galaxies: Bibliography, Astron. Astrophys. Suppl. Ser. **127**, 117 (1998).
67. K. Rines, A. Diaferio, P. Natarajan, The Virial Mass Function of Nearby SDSS Galaxy Clusters, Astrophys. J. **657**, 183 (2007).
68. E. Perez, A. Robinson, L. de la Fuente, The response of the broad emission line region to ionizing continuum variations. III — an atlas of transfer functions, Mon. Not. R. Astron. Soc. **256**, 103 (1992).
69. B.M. Peterson, Reverberation mapping of active galactic nuclei, Publ. Astron. Soc. Pacif. **105**, 247 (1993).
70. B.M. Peterson et al., Steps toward Determination of the Size and Structure of the Broad-Line Region in Active Galactic Nuclei. XVI. A 13 Year Study of Spectral Variability in NGC 5548, Astrophys. J. **581**, 197 (2002).
71. B.M. Peterson et al., Central Masses and Broad-Line Region Sizes of Active Galactic Nuclei. II. A Homogeneous Analysis of a Large Reverberation-Mapping Database, Astrophys. J. **613**, 682 (2004).

72. V.I. Pronik, K.K. Chuvaev, Hydrogen lines in the spectrum of the galaxy Markaryan 6 during its activity, Astrophys. **8**, 112 (1972).
73. M. Santos-Lleo et al., Monitoring of the optical and 2.5—11.7 μm spectrum and mid-IR imaging of the Seyfert 1 galaxy Mrk 279 with ISO, Astron. Astrophys. **369**, 57 (2001).
74. Y. Sofue and V. Rubin, Rotation Curves of Spiral Galaxies, Ann. Rev. Astron. Astrophys. **39**, 137 (2001).
75. S.G. Sergeev, Gas kinematics: Estimation of the broad-line region size and the central source mass from the profile variability of the H alpha line in NGC 4151, Astron. Rep. **38**, 162 (1994).
76. S.G. Sergeev, Variations of the broad H-alpha line profile in NGC 4151 as evidence for the complex kinematics of gas in the nucleus, Astrophys. Space Sci. **197**, 77 (1992).
77. S.G. Sergeev, S.A. Klimanov, N.G. Chesnok, and V.I. Pronik, Optical variability of the active galactic nucleus 1E 0754.6 + 3928 and reverberation-based mass estimate for the central black hole, Astron. Lett. **33**, 429 (2007).
78. S.G. Sergeev, S.A. Klimanov, V.T. Doroshenko, Yu.S. Efimov, S.V. Nazarov, and V.I. Pronik, Variability of the 3C 390.3 nucleus in 2000—2007 and a new estimate of the central black hole mass, Mon. Not. R. Astron. Soc. **410**, 1877 (2011).
79. S.G. Sergeev, V.I. Pronik, B.M. Peterson, E.A. Sergeeva, and W. Zheng, Variability of the Broad Balmer Emission Lines in 3C 390.3 from 1992 to 2000, Astrophys. J. **576**, 660 (2002).
80. S.G. Sergeev, V.I. Pronik, E.A. Sergeeva, and Yu.F. Malkov, Markarian 6 Nucleus since 1992, Astrophys. J. Suppl. Ser. **121**, 159 (1999).
81. S.G. Sergeev, V.I. Pronik, E.A. Sergeeva, and Yu.F. Malkov, A Link between the Hβ Equivalent Width, Profile Width, BLR Size, and Optical Luminosity from a Small Sample of Well-studied Active Galactic Nuclei, Astron. J. **118**, 2658 (1999).
82. S.G. Sergeev, S.A. Klimanov, N.N. Okhmat, and G.A. Sivtsov, Upgrading and automating the AZT-8 70-cm telescope, Bulletin of the Crimean Astrophysical Observatory **106**, 92 (2010).
83. K.L. Shapiro et al., The black hole in NGC 3379: a comparison of gas and stellar dynamical mass measurements with HST and integral-field data, Mon. Not. R. Astron. Soc. **370**, 559 (2006)
84. J. Silk and M.J. Rees, Quasars and galaxy formation, Astron. Astrophys. **331**, L1 (1998).
85. J. Silk and M.J. Rees, Quasars and galaxy formation, Astron. Astrophys. **331**, L1 (1998).
86. Y. Tanaka et al., Gravitationally redshifted emission implying an accretion disk and massive black hole in the active galaxy MCG-6-30-15, Nature **375**, 659 (1995).
87. P.S. Treuthardt, S. Marc, A.D. Sierra, I. Al-Baidhany, H. Salo, D. Kennefick, J. Kennefick, and C.H.S. Lacy, On the link between central black holes, bar dynamics and dark matter haloes in spiral galaxies, Mon. Not. R. Astron. Soc. **423**, 3118 (2012).
88. R.B. Tully and J.R. Fisher, A new method of determining distances to galaxies, Astron. Astrophys. **54**, 661 (1977).

89. M. Valluri, D. Merritt, and E. Emsellem, Difficulties with Recovering the Masses of Supermassive Black Holes from Stellar Kinematical Data, Astrophys. J. **602**, 66 (2004).
90. M. Volonteri, P. Natarajan, and K. Gültekin, How Important is the Dark Matter Halo for Black Hole Growth?, Astrophys. J. **737**, 50 (2011).
91. S.D.M. White and M.J. Rees, Core condensation in heavy halos — A two-stage theory for galaxy formation and clustering, Mon. Not. R. Astron. Soc. **183**, 341 (1978).
92. J.-H. Woo et al., The Lick AGN Monitoring Project: The MBH-σ^* Relation for Reverberation-mapped Active Galaxies, Astrophys. J. **716**, 269 (2010).
93. I.A. Yegorova, A. Pizzella, and P. Salucci, Probing dark matter haloes of spiral galaxies at poorly explored distances using satellite kinematics, Astron. Astrophys. **532**, A105 (2011).
94. D. Zaritsky and S.D.M. White, The massive halos of spiral galaxies, Astrophys. J. **435**, 599 (1994).
95. A.S. Zentsova, A method for estimating the mass of the central bodies in active galaxy nuclei and quasars, Pisma v Astronomicheskii Zhurnal **8**, 535 (1982).
96. N. Chesnok, S. Sergeev, and I. Vavilova, Photometric and kinematic properties of non-isolated and isolated AGNs, In: "Astrophysics and Cosmology after Gamow", Proceedings of the 4th Gamow International Conference on Astrophysics and Cosmology After Gamow and the 9th Gamow Summer School "Astronomy and Beyond: Astrophysics, Cosmology, Radio Astronomy, High Energy Physics and Astrobiology". AIP Conference Proceedings **1206**, 328—334 (2010).
97. N. Chesnok, S. Sergeev, I. Vavilova, Optical and X-ray variability of Seyfert galaxies NGC 5548, NGC 7469, NGC 3227, NGC 4051, NGC 4151, Mrk 509, Mrk 79, and Akn 564 and quasar 1E 0754, Kinematics and Physics of Celestial Bodies **25**, Iss. 2, 107—113 (2009).
98. E. Breedt, I.M. McHardy, P. Arévalo, P. Uttley, S.G. Sergeev, T. Minezaki, Y. Yoshii, Y. Sakata, P. Lira, N.G. Chesnok, Twelve years of X-ray and optical variability in the Seyfert galaxy NGC 4051, Mon. Not. R. Astron. Soc. **403**, Iss. 2, 605—619 (2010).

4 CHAPTER

DARK AND BARYONIC MATTER DISTRIBUTION IN THE SPARSELY POPULATED GALAXY GROUPS

A.A. Elyiv, O.V. Melnyk, I.B. Vavilova

4.1. Dark matter halo in galaxy groups

Where is the dark matter located in galaxies and clusters? is one of the important questions related to the large-scale structure of the Universe. Observational manifestation in favour of dark matter in the halos of individual galaxies includes rotation curves for spiral galaxies, star motions for elliptical galaxies, and X-ray observations. For groups and clusters the evidence for dark matter in a common halo includes the virial theorem, gravitational lensing, and the temperature of the hot int-racluster gas (ICM). Bahcall et al. [2] suggested that a virial paradox could be resolved if dark matter is concentrated in galaxy halos extending up to 200 kpc.

In 1966, Karachentsev [34] was the first who argued that there is a steady growth of mass-to-luminosity ratio (M/L) with galaxy system population from pairs to superclusters. In 2002, when the needed observational data were accumulated, Girardi et al. [28] compared virial mass-to-luminosity ratios for poor groups up to rich clusters and found that the mass of systems grows with system population faster than luminosity $(M/L)^{1.34\pm0.03}$ (the range covers 30—1000 $M_\odot/L_\odot$)). Evaluation of the virial masses of poor groups meets several difficulties because of the non-stationary properties of these systems and projection effects. Thus, virial mass estimates may vary by a few orders of magnitude. It is not a trivial task also to derive galaxy group properties or determine the algorithms for selection of galaxies into groups. For instance, Karachentsev [41] obtained the following values of the M/L ratio for the

7 nearest galaxy groups with populations from 8 to 29 galaxies: median $M_{\rm vir}/L = 29\,M_\odot/L_\odot$ with a range of values for individual groups from 8 up to $88\,M_\odot/L_\odot$; the virial mass of the Local Group is equal to (1.29 ± 0.14) $10^{12}\,M_\odot$; the virial mass-to-luminosity ratio for the Local Group is equal to $12.8 \pm 1.4\,M_\odot/L_\odot$ (size is about 1 Mpc). These estimates were based on the direct measurement of distances, and they are much less than, for example, median estimate by Tully [86] for galaxy groups of the Local Supercluster, $M_{\rm vir}/L = 94\,M_\odot/L_\odot$.

Physical properties of galaxies depend on the formation conditions and evolution. In addition to intrinsic evolution, galaxies are exposed to significant environmental influence (among others [7,8,18,20,50,62,67,101]). The density of galaxies (number of galaxies per volume unit) or luminosity density as well as the number of galaxies in group/cluster or distance to the nearest galaxy is often implied as regarding the environment.

The influence of an environment can be found till 1 Mpc and even farther [7, 46], where small galaxy groups are observed. We obtained that the Dressler effect may be observed even in such poor groups as galaxy triplets and even pairs [22, 58, 63, 97]. The study of "enviromental effects" in such poor galaxy groups is helpful for understanding the galaxy evolution on intermediate scales between isolated galaxies and rich groups/clusters. The isolated galaxies that have not sufficiently undergone the influence of environment allow us to consider them as the "autonomous laboratories" for studying evolutionary processes in the galaxies. Individual properties of isolated galaxies (mass, luminosity, morphology, colour-index etc.) can be served as the standard when studying galaxies in the different environment (see, for example, [42] (KIG), [62,73,75,81,98]).

The dark matter in small groups seems to be distributed in the whole volume of system in the case of compact groups and to be concentrated in the halo of individual galaxies in the case of sparsely galaxy groups [16,59–61,64]. At the same time the amount of dark matter in galaxy groups is not enough to be explained in frame of the Standard Cosmological Model.

In this section we will analyze the mass-to-luminosity ratio for homogeneous samples of the sparsely populated galaxy groups of the Local Supercluster and groups selected from the Sloan Digital Spectroscopic Survey (SDSS).

4.1.1. Methods for identifying galaxy groups

For studying galaxy properties in different environment it is important to define the galaxy's isolation degree. The principle of overdensity in comparison with background is widely used for the group identification by different selection methods. The richer the group population, the overdensity is more strong and therefore more likely that such a galaxy group is physically

bound. Poor groups identification depends strongly on the limiting parameters of the method. These systems can be easily confused with the random physically not bound systems. For this reason, many authors prefer to study rich groups/clusters only. That is why the elaboration of the reliable methods for identifying small groups will allow us to pay more attention to these structures.

For example, 2D method for galaxy pairs and triplets selection was used in studies [35,36,43,44] with taking into account the isolation degree in comparison with the foreground and the background, while the environment of each pair and triplet was inspected using POSSI, POSSII and ESO/SERC plates. This method selects effectively the isolated systems, which are compact in a projection with characteristic distance between galaxies $R \sim 50$—100 kpc. Another approach was developed by these authors in [39], where the tidal index for each galaxy was introduced to study global properties of nearest galaxies in different environments.

With appearance of the large databases and surveys (LEDA, NED, SDSS, CfA2, SSRS2, DEEP2, 2dF etc.) and the data on the the galaxy' radial velocities, an application of three-dimensional methods for detachment of galaxy groups became generally accepted.

3D methods of group's identification use as a rule the two limited parameters: projected distance between galaxies R and radial velocity difference ΔV. For example, the isolation criterion was ignored in [3, 4, 26, 103], where the selected close galaxy pairs from CfA2 catalogue with $R < 50$ kpc and $\Delta V < 1000$ km s^{-1} have been considered. Patton et al. [68] have investigated galaxy pairs from SSRS2. They considered all pairs with $R < 100$ kpc and didn't find pairs with the signs of interaction with $\Delta V > 600$ km s^{-1}, but most of galaxy pairs with interaction signs had $R < 20$ kpc and $\Delta V < 500$ km s^{-1} (see, also, [17,69,70,105]). Nikolic et al. [65] obtained similar results for galaxies pairs from SDSS. These authors found that a star-formation rate is significantly enhanced for the projected separations less then 30 kpc. Lambas et al. [49] and Alonso et al. [1] have considered galaxy pairs with $R < 1$ Mpc and $\Delta V < 1000$ km s^{-1} from 2dF survey. They analyzed the star formation activity in the pairs as a function of both relative projected distance and relative radial velocity and found that the star formation activity in galaxy pairs is significantly enhanced over that in isolated galaxies at similar redshifts for $R < 25$ kpc and $\Delta V < 100$ km s^{-1}. Soares [80] has showed that more than half of the simulated pairs with projected distance $R \leq 50$ kpc have 3D separations greater than 50 kpc. Therefore, for the selection of real physical pair it is important to take into account the signs of interaction, but that is not always possible.

Triplets of galaxies are less studied than pairs. Mainly, they have been selected from the catalogues of galaxy groups of different population. For example, we compared the kinematic, dynamical, configurational, and morphological properties of triplets from the various galaxy samples formed by different me-

thods ([45, 57, 59, 60, 94], including the galaxy triplets selected in [85]) and obtained that physical properties of galaxy groups strongly depend on selection criteria.

One major question is what method is most effective for selecting group members within a volume-limited catalogue? Various methods are widely used including the Boxcounts [76,108], n-point Correlation functions [220], Percolation [77], Hierarchical analysis [55], nearest neighbor (friend-of-friend clustering) analysis [9], taxonomic studies [71], Wavelets [23, 24, 78, 92], Fractals [14, 96], Fourier-transforms [79], Voronoi tessellation [31, 56], Void probability functions [21, 104] as well as its modifications. The best approach is to apply several methods for identifying groups from the same catalogue, because it allows us to avoid selection effects, which are inherent in each of these methods when you try to select physically bound galaxies.

Most authors mentioned above used simple selection algorithms for pair identification: they consider all pairs with the fixed limitation parameters R and ΔV, which describe properties of galaxy pair only as a separate system, without information about their neighbours. Contrary to this in our several works an another approach was developed. Namely, this is the second-order Voronoi tessellation for galaxy pairs identification, where the fundamental elements are pairs, as well as the third-order Voronoi tessellation for galaxy triplets identification, where the fundamental elements are triplets. The geometric properties of the high-order tessellations give information about relative location of neighbouring galaxies. This allowed to analyse the correlations of group properties with environment. The high-order (second or third -order) Voronoi tessellation method has not been applied earlier for groups detection, unlike the first-order Voronoi tessellation. These methods were applied by us to the galaxies from SDSS DR5 spectroscopic survey with known redshifts and the galaxy sample of the Local Supercluster [58] allowing us realizing the 3D approach [22].

4.1.2. High-order Voronoi tessellation

Voronoi diagram was introduced by G. Voronoi in 1908 [99]. The most popular is the first-order Voronoi diagram (so called Voronoi tessellation), Fig. 4.1. It is a geometric method of space partition on regions. Each region consists of one nucleus and all the points of space that are closer to a given nucleus than to other nuclei [51, 56]. Kiang found analytic function of Voronoi cell volume distribution for random points in 2D and 3D space [47].

A Voronoi tessellation is used widely in astrophysics, especially for modelling the galaxy and void large-scale structure distribution [30, 88, 90, 91, 106, 107], for studying periodicity in deep pencil-beam sky surveys [29, 32, 83, 89, 102], extragalactic radiosources distribution [6], for modeling of the cosmic microwave background anisotropy [13, 83] etc. Ebeling & Wiedenmann [19] were the first who applied Voronoi tessellation for finding groups and clusters

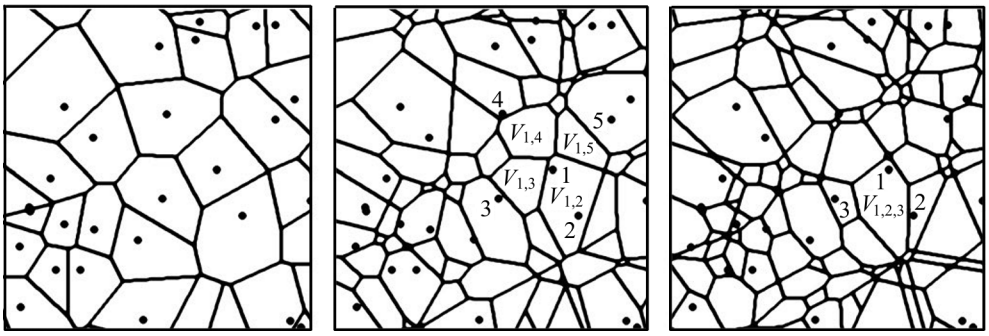

a *b* *c*

Fig. 4.1. 2D Voronoi tessellation of the first- (*a*), second- (*b*) and third- (*c*) order for the same distribution of the random nuclei

of galaxies in 2D case (see, also, on the early review, the textbook for students prepared by Vavilova [93] in 1998). Later such approach was used by [3, 48, 66, 72, 74].

3D Voronoi tessellation for galaxy groups identification was realized by Marinoni et al. [54] and Cooper et al. [15]. The application of 3D Voronoi tessellation to DEEP2 survey was introduced by Gerke et al. [27]. We applied at first the first-order 3D Voronoi tessellation for the identification of galaxy groups in the Local Supercluster [58] and demonstrated that the first-order tessellation is more useful for searching the rich clusters of galaxies than the small groups. In the first-order Voronoi tessellation the key parameter is the volume of galaxy's Voronoi cell V. This parameter characterizes a galaxy environmental density. The condition of cluster/group membership of certain galaxy is the relatively small value of V. This condition is true when the galaxy is surrounded by close neighbouring galaxies (Fig. 4.1). That is why the first order Voronoi tessellation is not corrected for the identifying small isolated galaxy systems (see aforementioned paper for details).

Contrary to the first-order tessellation the second-order tessellation for set S distribution of nuclei is the partition of the space which associates a region $V_{1,2}$ with each pairs of nuclei 1 and 2 from S in such a way that all points in $V_{1,2}$ are closer to 1 and 2 than other nuclei from S. Region $V_{1,2}$ is a *common cell* for nuclei 1 and 2[1]. In such a way the second-order Voronoi tessellation is available for the identification of single galaxies and pairs. The third-order Voronoi tessellation is appropriate for the triplets identification. It is the partition of the space which associates a region $V_{1,2,3}$ with each triplet of nuclei 1, 2, 3 in such a way that all points in $V_{1,2,3}$ are closer to nuclei 1, 2, 3 than other nuclei from S [51].

[1] However it is not necessary that these nuclei lie in the common cell. For example nuclei 1 and 5 create the common cell $V_{1,5}$ and they do not lie in this cell (Fig. 4.1).

We considered galaxies as the nuclei of the Voronoi tessellation taking into account equatorial coordinates α, δ and radial velocities of galaxies V_h only. For the constructing of the 3D Voronoi tessellations it is necessary to determine the distances in 3D space. Spatial distance between two galaxies one can split on projected (tangential) distance r and radial v (difference of the radial velocities). We can determine the projected distance with a relatively high accuracy, while radial component has errors owing to inaccuracy of radial velocity measurement of each galaxies and existing strong peculiar velocities (due to virial motions of galaxies in groups and clusters). As a result the galaxy distribution in space of radial velocities is extended along radial component, so-called fingers-of-god effect. This is attributed to the random velocity dispersions in galaxy volume-limited sample that deviate a galaxy's velocity from pure Hubble flow, stretching out a group of galaxies in redshift space [33]. Various authors take into account this effect in their own way in dependence on the specificity of their problem. For example, Marinoni et al. [54] chose some cylindrical window of clusterization, which is extended along the radial component. We propose other approach that is based on the introduction of weight for a radial component. Such approach allows us to avoid a problem of tangential and radial distance inequivalence and to apply high-order 3D Voronoi tessellation method [22, 58].

The second-order Voronoi tessellation was applied by us for the identification of pairs and single galaxies in the following way. Each galaxy i from set S forms the common cells with the certain number of neighbouring galaxies. So under *neighbouring galaxies* of galaxy i we understand only galaxies which create common cells with this galaxy. For example, galaxy 1 creates only 4 common cells ($V_{1,2}$, $V_{1,3}$, $V_{1,4}$, $V_{1,5}$) with neighbouring galaxies 2, 3, 4 and 5, respectively (Fig. 4.1). Each pair of galaxies i, j is characterized by the dimensionless parameters $p_{i,j}$:

$$p_{i,j} = \frac{\sqrt[D]{V_{i,j}}}{m_{i,j}}, \tag{4.1}$$

where D — space dimension, $V_{i,j}$ — the area (for 2D) or volume (for 3D) of cell, $m_{i,j}$ — distance between galaxies i and j.

Each galaxy has the set of $p_{i,j}$ parameters. For example, galaxy 1 has the set $p_{1,2}$, $p_{1,3}$, $p_{1,4}$, $p_{1,5}$. We choose the maximum value from the set of parameters for galaxy 1: $p_{\max}(1) = \max(p_{1,2}, p_{1,3}, p_{1,4}, p_{1,5})$. In general case for galaxy i: $p_{\max}(i) = \max(p_{i,j})$ where j assume numbers of k neighbours.

We named the *geometric pair* in the second-order Voronoi tessellation such a pair which contains two galaxies with the common cell that have the same $p_{\max}$ parameters, $p_{\max}(1) = p_{\max}(2) = p$. The parameter p characterizes a *degree of geometric pair isolation*. Under degree of pair isolation we understand the overdensity under background. We used the principle which was applied in [36] for the selection of isolated galaxy pairs: if all galaxies have the same

angular diameter, a neighbour of a pair of galaxies should be located on the sky more than five times farther from a pair than the separation of the pair members from each other. In our 3D approach the degree of pair isolation is described by the relation between volume $V_{1,2}$ of common cell (it characterizes distance to neighbours) and the distance $m_{1,2}$ between pair members according to (4.1). For example, strongly isolated pair has a large value of p due to a large $V_{1,2}$ and small $m_{1,2}$ (Eq. (4.1)).

We also introduced the parameter p_e which describes only *pair environment* and does not depend on distance between pair members directly. We defined it as the mean value of $p_j(1)$ and $p_l(2)$ parameters of the first and second galaxy, excepting p from both sets:

$$p_e = \frac{\sum\limits_{j=2}^{k} p_j(1) + \sum\limits_{l=2}^{n} p_l(2)}{k+n-2}, \tag{4.2}$$

where k and n — number of neighbouring galaxies for 1 and 2 galaxies of geometric pair, respectively. We start sums from $j=2$ and $l=2$ for excepting $2 \cdot p$, because the first galaxy is neighbour for the second galaxy and vice versa. Therefore $k+n-2$ is sum of neighbouring galaxies of pair members excepting of pair galaxies as neighbouring for each other. Parameter p_e depends on the distribution of neighbouring galaxies. Small value of p_e points out that such pair is located in loose environment. In such case the average volume of common cells of pair components with neighbouring galaxies is relatively small, and distance between them is large, see Eq. (4.1).

Single galaxy is a galaxy which is not member of any geometric pair. The single galaxies are field galaxies in the environment of geometric pairs. Every single galaxy has the own neighbours, single galaxies and geometric pair members can be among them. According to the second-order Voronoi tessellation the larger is the degree of galaxy isolation, the greater is the number of neighbours, but these neighbours locate farther. The best parameter which describes the isolation degree of the single galaxy is the mean value of all parameters p_j of this galaxy:

$$s = \frac{\sum_{j=1}^{k} p_j}{k}, \tag{4.3}$$

where k is the number of neighbours. Therefore the smaller is s value, the more isolated is the single galaxy.

Method of the third-order Voronoi tessellation can be introduced the same as the second-order approach. All points of the common triplet's cell are the most closer to galaxies of this triplet than to other galaxies. Similarly to the parameter $p_{i,j}$ for pairs we set up the parameter $t_{i,j,u}$ for triplets:

$$t_{i,j,u} = \frac{\sqrt[D]{V_{i,j,u}}}{\max(m_{i,j}, m_{i,u}, m_{j,u})}, \tag{4.4}$$

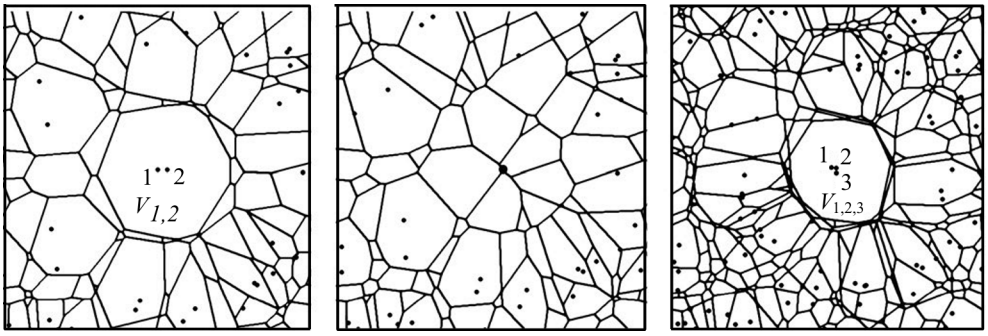

a *b* *c*

Fig. 4.2. Different configurations of the galaxies: isolated close pair (*a*) and isolated single galaxy (*b*) in the second-order tessellation; isolated close triplet in the third-order tessellation (*c*)

where D — space dimension, $V_{i,j,u}$ — the area (for 2D) or volume (for 3D) of cell, $m_{i,j}$, $m_{i,u}$, $m_{j,u}$ — distances between galaxies in the triplet.

Geometric triplet in the third-order Voronoi tessellation contains three galaxies that have the common cell and the same maximal parameters $t_{\max}(1) = t_{\max}(2) = t_{\max}(3) = t$. The parameter t characterizes a *degree of geometric triplet isolation*. We defined parameter of *triplet environment* t_e as the mean value of parameters $t_i(1)$, $t_j(2)$ and $t_u(3)$, except t from three sets:

$$t_e = \frac{\sum\limits_{i=2}^{k} t_i(1) + \sum\limits_{j=2}^{n} t_j(2) + \sum\limits_{u=2}^{q} t_u(3)}{k+n+q-3}, \tag{4.5}$$

here in case of third-order Voronoi tessellation k, n and q denote the number of *neighbouring triplets* which contain galaxies 1, 2 and 3, respectively (Fig. 4.1). Therefore $k+n+q-3$ is number of neighbouring triplets for certain triplet, which contain at least one galaxy from this triplet. For the triplet with highest degree of standing out against a background, the isolation parameter t has the highest value. At the same time, if the triplet neighbours locate far from it, parameter t_e has the small value (see, Fig. 4.2).

Parameters p, s, t are the basic ones and define the isolation degree of galaxy pair, single galaxy or triplet in comparison with background, respectively. Parameters p_e and t_e are additional ones and contain information about the distribution of the neighbouring galaxies (environment). Similarly to the second- and third-order Voronoi tessellation it is possible to apply more high-order Voronoi tessellation for the identification of galaxy quartets, quintets and so on.

4.2. Galaxy groups at the small redshifts

4.2.1. Galaxy sample from the SDSS spectroscopic survey

For our investigation we used Northern part of the SDSS DR5 spectroscopic survey. Our sample is volume-limited and consists of objects that are classified as galaxies. The primary sample had contained approximately 11000 galaxies with radial velocities from 2500 $\mathrm{km\,s^{-1}}$ to 10000 $\mathrm{km\,s^{-1}}$, $H_0 = 75\ \mathrm{km\,s^{-1}\,Mpc^{-1}}$. It is known that completeness of SDSS is poor for the bright galaxies because of spectroscopic selection criteria and the difficulty of obtaining correct photometry for object with large angular size. We tried to decrease this effect's influence in a way to limiting of our sample $V_h > 2500$ km $\mathrm{s^{-1}}$, i.e. in the way not to take into account nearest objects with the large angular diameter. Such a volume limiting also helps us to avoid influence of Virgo cluster where strong peculiar motion exists. We checked additionally all pairs of galaxies with a small angular resolution and excluded identical objects (parts of galaxies), which are presented twice and more in SDSS survey. All galaxy velocities V_h were corrected for the Local Group centroid V_{LG} accordingly to [40]. When we had applied the high-order Voronoi tessellation method to SDSS catalogue we limited our sample $3000\ \mathrm{km\,s^{-1}} \leq V_{\mathrm{LG}} \leq 9500\ \mathrm{km\,s^{-1}}$. We did not consider also galaxies that located within 2° near borders, because the correct estimation of Voronoi cell volume is not possible in this case. Our volume-limited sample is completed up to 17.7^m but contains also about 100 more fainter galaxies. Final number of galaxies in the sample was 6786.

We applied the second-order 3D Voronoi tessellation to our sample of 6786 galaxies and obtained 2196 geometric pairs and 2394 single galaxies (65 % galaxies of whole sample are in pairs and 35 % are singles). We divided our samples of geometric pairs and singles on four equal parts by the parameter of isolation p and s, respectively. A quatre of each sample with the highest isolation degree we called as *isolated* (549 pairs and 598 singles). It means that the isolated pairs and singles have $p > Q_3$ and $s < Q_1$, respectively, Q_3 is third quartile and Q_1 is the first quartile. Independently we applied the third-order 3D Voronoi tessellation to our galaxy sample and obtained 1182 geometric triplets (52 % of whole sample). The quatre (297) of triplet sample with the highest isolation degree $t > Q_3$ we called as *isolated*.

We cross-correlated our results with other samples. In the first order we compared pairs and triplets of our sample with Tago et al. (2008) groups selected by modified friends-of-friends method using the same release of SDSS. From 965 galaxies of Tago's pairs that are located in our region of investigation, 686 galaxies (343 pairs or 71 %) coincide with our pairs with different isolation degree. Median value of isolation parameter p is 9.89 that does not differ

strongly from our isolation limit ($Q_3 = 10.17$). Other 121 galaxies coincide with one of our pair members, median value of p for these pairs is 3.94. We can conclude that they locate in the field. The remaining 158 galaxies coincide with our single galaxies having isolation degree $s = 0.87$ i.e. the also associated with the field galaxies (our isolation limit is less than $Q_1 = 0.57$). 63 triplets (51 %) by Tago et al. triplets [84] that fall in our region coincide with our triplets. Median value of isolation degree for these triplets $t = 4.83$ is higher than our isolation limit $Q_3 = 3.90$.

We also compared our pairs with 28 isolated pairs from [36] that located in our region of investigation: 16 pairs coincide with our pairs (median value of isolation degree $p = 21.16$ is very high). Among 7 our "pairs" one of the component is interacting galaxy which corresponds to the pair from [36], second component is more fainter galaxy, these "pairs" are not isolated (median value of p is 3.95). Such cases appear because of difficulties in spectroscopic measurement of interacting (very close) galaxies in SDSS. The remaining 5 pairs coincide by components with different pairs and single galaxies with small isolation degree because of these pairs are surrounded by fainter satellites. We found that 10 from 36 KIG galaxies coincided with our single galaxies, but 24 KIG galaxies fall in our pairs with different isolation degree (median value is not very high $p = 5.8$). Such difference can be explained by the presence of fainter galaxy in immediate vicinity of KIG galaxy. Actually, all 34 isolated galaxies with fainter satellites from [73], which locate in our region, coincide with our pairs and triplets.

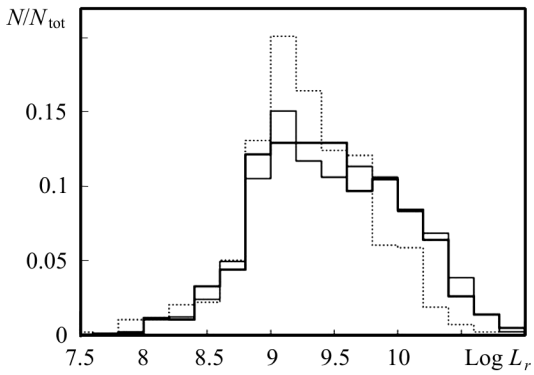

Fig. 4.3. Luminosity distributions of isolated galaxies (dotted line), galaxies in isolated pairs (solid line), galaxies in isolated triplets (thick line)

Table 4.1. **Comparison between the luminosities of the galaxies from different samples**

Sample of galaxies	$L_r \times 10^9 (L_\odot)$	
	Median	Mean (SD)
All single	$2.23^{+3.66}_{-1.15}$	5.17 (8.00)
All geometric pairs	$2.38^{+4.27}_{-1.29}$	5.79 (8.66)
All geometric triplets	$2.48^{+1.36}_{-9.14}$	6.00 (8.77)
Isolated	$1.80^{+3.10}_{-0.77}$	3.52 (4.47)
Isolated pairs	$2.89^{+7.20}_{-1.73}$	6.74 (9.46)
Isolated triplets	$2.68^{+6.80}_{-1.52}$	6.53 (9.97)

We may conclude: singles, pairs and triplets of galaxies obtained by the high-order Voronoi tessellation are in a good agreement with other samples, especially it concerns the systems with the high isolation degrees. Some lack of coincidence can be

explained by differences in primary catalogues, for example, by the magnitude depth or spectroscopy of interacting galaxies in SDSS.

In addition to the isolation and environmental parameters p, p_e, s, t and t_e, we calculated also other characteristics [37, 94]: root-mean-square (rms) velocity of galaxies with respect to the group centre (in $\mathrm{km\,s^{-1}}$), $S_v = \left[\frac{1}{N}\sum_{k=1}^{N}(V_{\mathrm{LG}}^k - \langle V_{\mathrm{LG}}\rangle)^2\right]^{1/2}$, $S_v = \Delta V/2$ for pairs, N is the number of galaxies in the group; harmonic mean radii of the system (in kpc) — $R_h = \left[\frac{1}{3}\sum_{i,k} R_{ik}^{-1}\right]^{-1}$, where $R_{ik} = X_{i,k}\langle V_{\mathrm{LG}}\rangle H_0^{-1}$ and X_{ik} is the relative angular distance; R — maximal distance between galaxies in triplets, for galaxy pair $R_h = R$; dimensionless crossing time

$$\tau = 2H_0 R_h / S_v \tag{4.6}$$

expressed in units of the cosmological time H_0^{-1}; virial mass

$$M_{\mathrm{vir}} = 3\pi N(N-1)^{-1} G^{-1} S_v^2 R_h \tag{4.7}$$

in $M_\odot$; galaxy luminosity L_r, which corresponds to Petrosian magnitude in r-band, $L_\odot$; mass-to-luminosity ratio $M_{\mathrm{vir}}/L = M_{\mathrm{vir}}/\sum L_r$ in $M_\odot/L_\odot$.

4.2.2. Luminosity-density relation

As considering the luminosity-density relation (for example, [67], and references therein) we can note the following: galaxies are more luminous in the high density regions than in the field. Karachentseva et al. [41] showed that galaxies even in such poor groups as the triplets are more luminous than the isolated galaxies. We compared the luminosities of single/isolated galaxies with the luminosities of galaxies in pairs and triplets. One can see from Table 4.1 and Fig. 4.3 that the median and mean values of luminosities are greater for galaxies in pairs and triplets than for single/isolated galaxies. The mean values of luminosities of isolated galaxies and galaxies in isolated pairs differ significantly (with the probability of >0.99 by t-criterium), but differences for "All" samples are not statistically significant. The same conclusions we made from comparison of the sample of single/isolated galaxies with galaxies in triplets.

So, galaxies in isolated pairs and triplets are two times more luminous than isolated galaxies. It is necessary to note that our method of group identification doesn't take into account individual physical characteristics of galaxies, therefore the effects of selection are absent here. The fact that for "All" samples the mean values have small difference may serve as the evidence of influence of non-physical (accidental) groups in these samples, the wide systems are dominated among them.

4.2.3. Mass-to-luminosity ratio

For studying dark matter presence and distribution in small galaxy groups we used the mass-to-luminosity ratio ($M_{\rm vir}/L$) as the quantitative indicator of dark matter contribution. We checked the mass-to-luminosity ratio in dependence on isolation degree of pairs and triplets. We plotted the dependencies of system isolation p, t on $M_{\rm vir}/L$ in the narrow bins of R, because the isolation parameters p, t and virial mass $M_{\rm vir}$ depend on the projected distance between the galaxies R (see Eqs. (4.1), (4.4), and (4.7)). Fig. 4.4 presents the dependence of slope α in p, $t - M_{\rm vir}/L$ relation on R, and Fig. 4.5 presents dependence of correlation coefficient on R (details in signatures to the figures).

We see from Fig. 4.4 that if the system is located in denser environment, it has greater value of $M_{\rm vir}/L$ ($\alpha < -0.1$, correlation coefficient <–0.3). Moreover, such dependencies are true only on the scales approximately up to 150—200 kpc for pairs and up to 250—300 kpc for triplets. For greater values of R the p, $t - M_{\rm vir}/L$ dependencies were not observed. This conclusion only confirms our results where we showed that the widest systems most probably are accidental formations, because they don't stand out against a background. The strong dependence of morphology on the nearest neighbour was found at the distances of about 200 $\rm h^{-1}$ kpc. On the other hand, several authors (see, for example, [1, 17, 49, 70, 103]) on the base of analysis of physical properties such as star formation rate and colour indices concluded that differences between galaxies in pairs and fields galaxies are significant in pairs with $R < 20$—50 kpc. Dependence on velocity dispersion is weaker, but Lambas et al. [49] and Alonso et al. [1] found significant differences in $\Delta V < 100$ km s^{-1}.

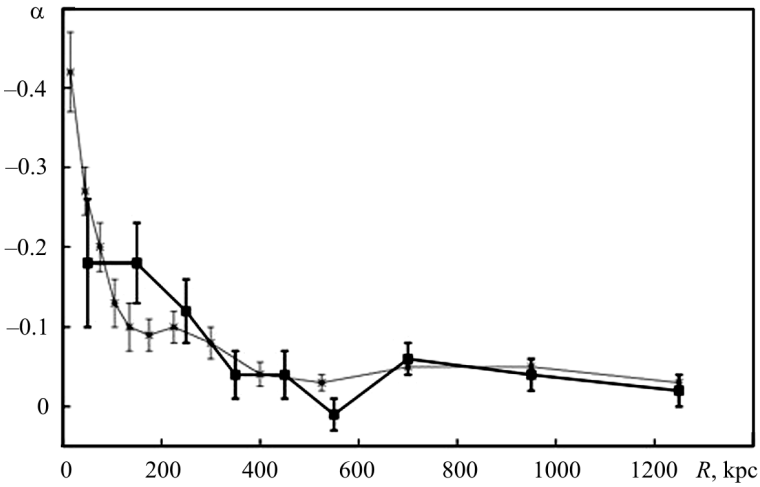

Fig. 4.4. Dependence between slope α and R: for the pairs $\log(p) = \alpha \log(M_{\rm vir}/L) + b$ (thin line) and for the triplets $\log(t) = \alpha \log(M_{\rm vir}/L) + b$ (thick line)

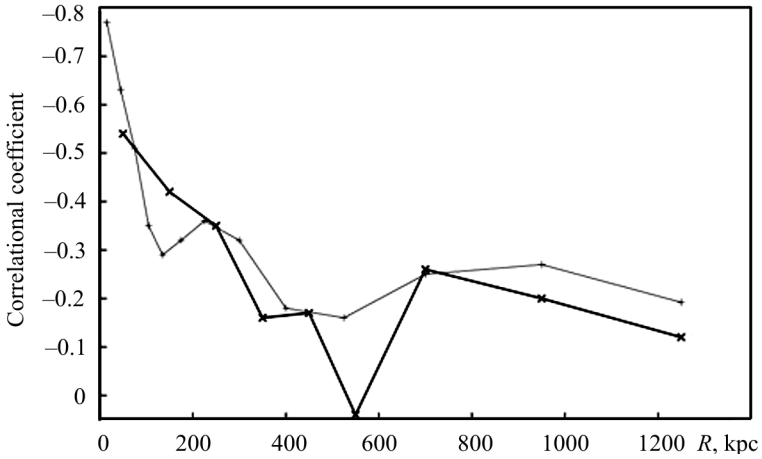

Fig. 4.5. Dependence between correlation coefficient in relations from Fig. 4.4 on R: for the pairs (thin line) and for the triplets (thick line)

Because of maximal distance R is a constant, enhancement of $M_{\rm vir}/L$ value is a result of increase of rms velocities in groups. In other words, if the relatively compact pairs and triplets located in denser environment, then they have greater value of mass-to-luminosity ratio due to larger virial motions. The same result was obtained by Einasto et al. [20]. The authors found that sparsely populated groups in the neighbourhood of a rich cluster are typically 2.5 times more massive and 1.6 times more luminous than groups on average, and these loose groups have velocity dispersions 1.3 times greater than groups on average.

Table 4.2 presents the medians and quartiles of system crossing time τ and mass-to-luminosity ratio $M_{\rm vir}/L$ for samples of pairs and triplets that characterized by different isolation degree and compactness.

From Table 4.2 and Fig. 4.5 follows that values of $M_{\rm vir}/L$ at $R < 50$ kpc for pairs and $R < 100$ kpc for triplets is 7—8 $M_\odot/L_\odot$ and increase with enhancing of R_h faster for triplets than for pairs.

Table 4.2. **Medians and quartiles of the system crossing time and mass-to-luminosity ratio for pairs and triplets**

Pairs	N	τ	$M_{\rm vir}/L$	Triplets *	N	τ	$M_{\rm vir}/L$
$p > Q_3$	519	$1.12^{+1.24}_{-0.59}$	12^{+37}_{-10}	$t > Q_3$	297	$1.06^{+0.88}_{-0.42}$	44^{+60}_{-28}
$R < 50$	133	$0.18^{+0.20}_{-0.07}$	7^{+28}_{-6}	$R < 100$	16	$0.24^{+0.07}_{-0.08}$	8^{+16}_{-3}
$R < 100$	335	$0.40^{+0.47}_{-0.21}$	9^{+31}_{-8}	$R < 200$	70	$0.43^{+0.49}_{-0.24}$	20^{+46}_{-13}
$R < 150$	549	$0.61^{+0.63}_{-0.32}$	14^{+44}_{-11}	$R < 300$	136	$0.70^{+0.33}_{-0.28}$	24^{+41}_{-16}
$R < 200$	684	$0.70^{+0.75}_{-0.34}$	17^{+50}_{-14}	$R < 400$	240	$0.71^{+0.39}_{-0.30}$	31^{+49}_{-18}

* Maximal distance R correlates with R_h: $R = 1.41 \cdot R_h + 266$, the correlation coefficient is 0.87 for triplets, and $R = R_h$ for pairs.

The values of $M_{\rm vir}/L$ are in a good agreement with the corresponding values within IQR for groups which were selected by dynamical method. The values of $M_{\rm vir}/L$ are $18^{+39}_{-14}\ M_\odot/L_\odot$ and $32^{+34}_{-22}\ M_\odot/L_\odot$ for pairs and triplets, respectively ([53] and for triplets [94]) $35^{+30}_{-23}\,M_\odot/L_\odot$. The median of most compact triplets is in agreement with median $M_{\rm vir}/L = 13^{+16}_{-11}\,M_\odot/L_\odot$ obtained for interacting triplets, where star formation rate is high [57]. The median of isolated triplets is in a good agreement with median $M_{\rm vir}/L = 47^{+48}_{-33}\ M_\odot/L_\odot$ which corresponds to the sample of isolated Northern [37] and Southern [44] triplets (N&S triplets). An observable agreement with previous results is additional evidence of the correctness of applying the high-order Voronoi tessellation method for identification of pairs and triplets.

4.3. Poor galaxy groups in the Local Supercluster

We reviewed results published since 1990 yrs and found that estimates of $M_{\rm vir}/L$ for galaxy groups derived by the different authors are in a range of 30—200 $M_\odot/L_\odot$. Such a result depends on the galaxy population in groups, applied method of clustering, measurement accuracy of distances (radial velocities), and completeness of samples at the faint end of the luminosity function. Moreover, Tully et al. [48], (2006) found a special class of galaxy groups, which consist wholly of dwarfs of low surface brightness, for which the M/L is 100—1000 $M_\odot/L_\odot$. During the last years we undergone exhaustive investigation of the physical properties of poor groups in the Local Supercluster (LS) [22, 45, 53, 59—61, 94, 97]. The goal of these investigations was to estimate mass-to-luminosity ratios and to analyze the location of the dark matter in sparsely populated groups.

4.3.1. Homogeneous galaxy sample

The catalogue of LS galaxies [53] was compiled from the LEDA database. After excluding questionable and fake objects objects, the final catalogue consists of 7087 galaxies with known radial velocities up to 3100 km/s, magnitudes, morphological types, and sizes. The examination of objects proceeded independently with NED, POSS-I plates, and ESO/SERC plates. Due to selection effects, especially as concerns the faint end of the luminosity function, the catalogue is not homogeneous.

The catalog is fairly inhomogeneous, in particular, there is no clear boundary absolute magnitude (as would be in the case of observations with a single instrument). The sample is selective in depth relative to the LS dwarf (low-luminosity) galaxies. The presence of a large number of dwarf galaxies in the Local Group, i.e., in the immediate neighborhood of the Galaxy, also affects the sample inhomogeneity. In addition, since the radial velocities are

used as distance estimates, the supercluster is more elongated along the radial component. Calculating the Voronoi cell volumes for the galaxies of this sample, we would obtain much smaller volumes for nearby galaxies than those for distant ones. Therefore, it is inappropriate to directly apply the geometrical Voronoi tessellation method to such an inhomogeneous catalog.

Without consideration of the luminosity function and galaxy dynamics, a homogeneous catalog can be compiled by two techniques.

The first one is implemented by limiting the sample in absolute magnitude; $M^0_{\rm abs} = -17.5^m$ for the LS. The boundary apparent magnitude is 15.5^m and the absolute magnitude $M_{\rm abs}$ of a galaxy with $m = 15.5^m$ at a distance of 3100 $\mathrm{km\,s^{-1}}$ is $M^0_{\rm abs}$. In this case, galaxies more luminous than $M_{\rm abs}$ remain in the catalog.

The second technique provides for the inclusion of all catalog galaxies. It involves an artificial re-scaling of the distances in such a way that the concentration of galaxies varies with sample depth as a power law with the same index as that for the full homogeneous catalog. The slope was estimated for a homogeneous (in luminosity) catalog ($M_{\rm abs} < -17.5^m$) to be $\beta = 0.7$ (see below). If this value is extrapolated to the LS sample under consideration, then the variation in galaxy concentration with distance will be related to the real galaxy distribution in space and not to the deficit of low-luminosity galaxies at large distances. Consider this approach in more detail.

Let us introduce a new distance as a function of the radial velocity, $u = f(v)$. The concentration of galaxies in the "new" space varies as $\rho(u) = A \cdot u^{-\beta}$.

The concentration of galaxies at distance v is

$$\rho(v) = \frac{dn}{4\pi v^2 dv} \tag{4.8}$$

in the "old" space and

$$\rho(u) = \frac{dn}{4\pi u^2 du} = A \cdot u^{-\beta} \tag{4.9}$$

in the new space.

We find from Eqs. (4.8) and (4.9) that $\dfrac{\rho(v)}{A \cdot u^{-\beta}} = \dfrac{u^2}{v^2}\dfrac{du}{dv}$ or

$$A \int u^{2-\beta} du = \int \rho(v) v^2 dv. \tag{4.10}$$

The number of galaxies within the sphere of radius v is

$$N(<v) = \int_0^v 4\pi v^2 \rho(v) dv. \tag{4.11}$$

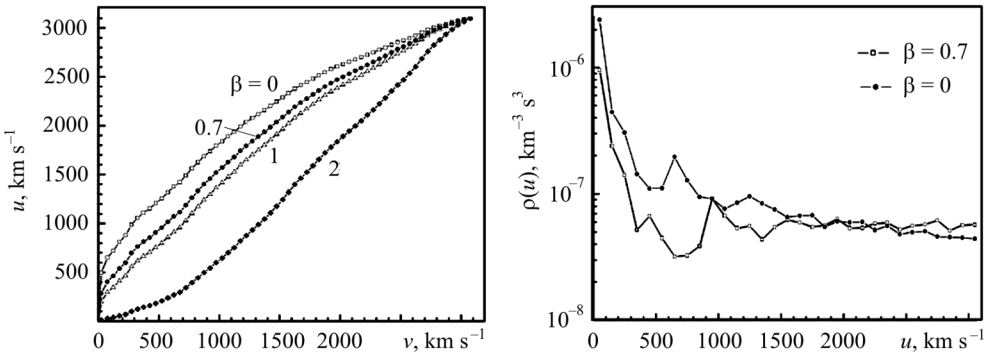

Fig. 4.6. New distance u versus radial velocity v

Fig. 4.7. Galaxy concentration in the new space versus new distance u

Substituting (4.11) into (4.10) and integrating yields

$$u(v) = \left(\frac{3-\beta}{4\pi A} N(<v)\right)^{\frac{1}{3-\beta}}. \tag{4.12}$$

We set the boundary condition $u(v_{\max}) = v_{\max}$, where $v_{\max} = 3100$ km s^{-1} is the maximum radial velocity. Using the boundary condition, we obtain the constant from Eqs. (4.12): $A = \dfrac{(3-\beta)N}{4\pi v_{\max}^{3-\beta}}$, where $N = 7064$ is the number of galaxies in the sample. Then,

$$u(v) = v_{\max} \left(\frac{N(<v)}{N}\right)^{\frac{1}{3-\beta}}. \tag{4.13}$$

This approach (distance re-scaling) can be interpreted as the choice of a unit of length for the corresponding supercluster depth. It allows nearby small and distant large groups to be reduced to the same scale. Latter equation relates the "old" distance v to the "new" distance u. This relation is shown in Fig. 4.7 for the following values of the parameter β: $\beta = 0$, 1, and 2 that correspond to uniform, pancake, and threadlike galaxy distributions in depth (Fig. 4.6), respectively. We decided to dwell on $\beta = 0.7$ [3] and to consider $\beta = 0$ in order to determine how sensitive the method is to this parameter.

In Fig. 4.7, the concentration of galaxies is plotted against distance u in the new space. The concentration now varies within one order of magnitude, in accordance with the specified slope β and has no sharp negative trend toward the supercluster boundary. Fig. 4.8 (a and b) show the galaxy distributions in the v and u spaces; for comparison, Fig. 4.8, c shows a random distribution of the same number of galaxies. Also there are shown the distributions of galaxies from the absolute-magnitude-limited LS subsamples: galaxies with $M_{\rm abs} < -17.5^m$ (Fig. 4.8, d), luminous galaxies with $M_{\rm abs} < -19^m$ (Fig. 4.8, e)

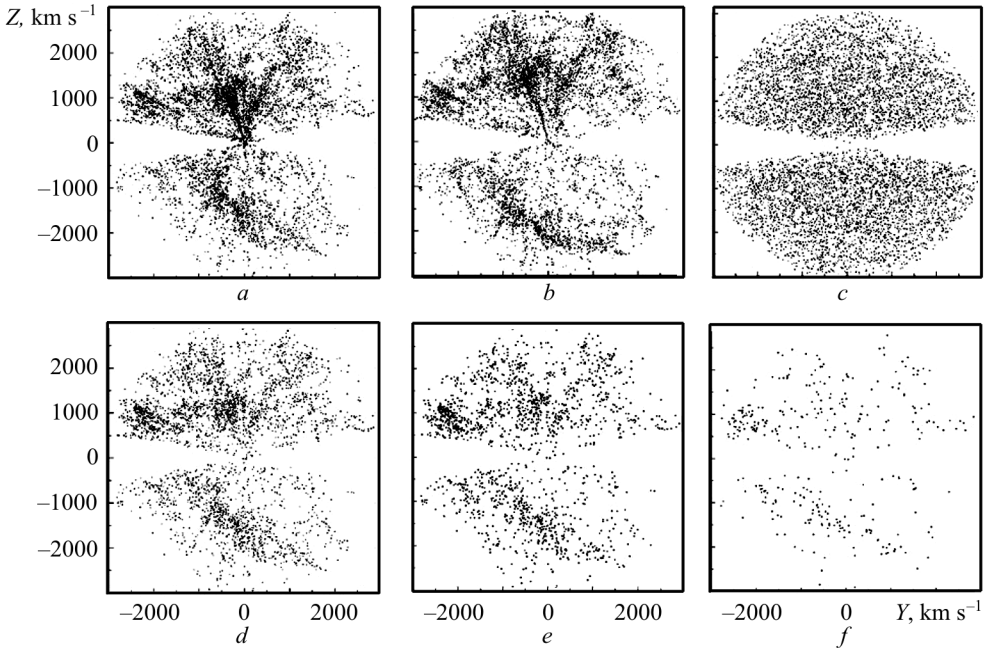

Fig. 4.8. Projection of the LS sample galaxies onto the plane perpendicular to the galactic plane: a — in the v space; b — in the u space; c — a random distribution of the same number of galaxies; d — the distribution of LS galaxies with $M_{\rm abs} < -17.5^m$ in the v space; e — the distribution of LS galaxies with $M_{\rm abs} < -19^m$ in the v space; f — the distribution of LS galaxies with $M_{\rm abs} < -20.5^m$ in the v space

and the most luminous galaxies with $M_{\rm abs} < -20.5^m$. Even a visual comparison demonstrates that the galaxy distributions in these subsamples are different. The distribution of the most luminous galaxies with $M_{\rm abs} < -20.5^m$ is closer to the random one (but does not correspond to it). This effect in the distribution of galaxies may depend not on their luminosity, but on their number (the fewer the galaxies, the weaker their clustering.

4.3.2. Methods

We applied two different methods to the LS catalogue for detecting groups:

Dynamical method was introduced by Karachentsev [38], whose criterion for membership is based on the assumption of closed Keplerian motions of companions around the dominating component of a system within their radius of gravitational influence. The criterion accounts for individual galaxy properties and excludes optically projected groups. The resulting catalogue includes 238 poor groups (4—10 members) containing a total of 1315 galaxies.

Geometrical method. Geometrical method of 3D-Voronoi tessellation introduced by Melnyk et al. [58] is based only on galaxy positions and allows

identifying over dense regions of galaxies compared to the background. To avoid aforementioned selection effects, we over scaled the space of radial velocities in such a manner that the concentration of galaxies increased with radial velocity as a power law function with the same exponent as for the full homogeneous catalogue. This method is sensitive to both elongated and spherical structures while, for instance, the wavelet transform is more sensitive to identifying spherical structures and substructures [95]. In this sample there are 226 poor groups containing 1222 galaxies. To reveal how the different group membership methods affect the derived properties of galaxy groups selected from the same catalogue (Local Supercluster), we compared groups obtained by Voronoi tessellation with those groups obtained by Karachentsev's dynamical method. The number of groups, for which all members coincide, is 22 % on average (most of them are pairs and triplets). This value is in a good agreement with results by Garsia [25], when hierarchical and percolation methods have been applied to the same catalogue.

When the percolation and hierarchical methods are applied, this effect is taken into account by introducing a luminosity function in the calculation of clustering parameters; in this case, the sample is limited in apparent magnitude m. In the dynamical method the sample is not m-limited and this effect is indirectly taken into account in the dynamical clustering conditions (more luminous and more massive galaxies are considered to be group members, being at a larger distance from one another than less massive ones).

We have calculated a set of median values of the following physical parameters for poor LS groups (4—10 members) selected by Voronoi tessellation and dynamical methods (value in parentheses), respectively: velocity dispersion of galaxies $S_v = 34$ km/s (58 km/s), harmonic radius of the group $R_h = 240$ kpc (183 kpc), dimensionless crossing time (in units of the Hubble time $1/H_0$ $s = 1.02$ (0.48), the logarithm of the virial mass $\log M_{\rm vir} = 11.89$ (12.31), the logarithm of the luminosity of galaxy groups $\log L = 10.32$ (10.52). The luminosity was calculated using LEDA total B magnitude corrected for extinction. Throughout we assume a Hubble constant of $H_0 = 75$ km/(s Mpc). Median value of mass-to-luminosity ratio is $M_{\rm vir}/L = 34\, M_\odot/L_\odot$ ($50\, M_\odot/L_\odot$), mean value is $76\, M_\odot/L_\odot$ ($78\, M_\odot/L_\odot$), SD is 130 (82). These results agree at the 80 % confidence level. The differences arise since the Voronoi technique is more sensitive to selecting large and elongated structures. For instance, some groups detected by Voronoi tessellation can include at least two groups detected individually by the dynamical method. For isolated systems, we find perfect coincidence between these two methods.

4.3.3. Dark matter and properties of galaxy triplets in the Local Supercluster

From the larger catalogue, we identified a sample of 173 groups of galaxy triplets that includes about 14 % of the total number of LS galaxies [94]. We have considered also two samples for comparison: the joint sample of the Northern and Southern triplets [43, 44] and the sample of triplets from the catalogue of Interacting galaxies by Vorontsov—Velyaminov et al. [100]. The velocity dispersions for galaxy triplets of both samples are less than 300 km/s because the majority of physically non-bound triplets have $S_v > 300$ km/s [37]. We will refer to these samples as N&S and Interacting triplets, respectively. The general properties of these galaxy triplets were considered in [57, 59, 94].

We used also two samples of isolated galaxies: non-clustering galaxies from the LS catalogue [45,53] and isolated galaxies from the KIG catalogue. We will refer to these samples as ILS and KIG, respectively. For LS triplets we find a harmonic radius $R_h = 160$ kpc (median value), relative fraction of E/S0 is 18 %, and median value of crossing time of the system is $s = 0.87$. For Northern & Southern (N&S) triplets, $R_h = 55$ kpc, E/S0 galaxy fraction is 25 %, and $s = 0.09$. For Interacting triplets, $R_h = 28$ kpc, E/S0 faction is 30 %, and $s = 0.04$. For comparison, ILS and KIG samples contain 11 % and 19 % of early type galaxies, respectively.

We suggest that the Dressler effect (higher fraction of E/S0 galaxies associated with denser systems) is seen even in such poor groups as galaxy triplets. Therefore, the analysis of morphological content and crossing times suggests that LS triplets are dynamically younger systems whereas N&S and Interacting triplets are dynamically older systems. We note that LS triplets were selected in radial velocity space whereas N&S and Interacting triplets were selected by visual inspection of POSS-1, 2 plates. For this reason, the latter samples are more compact and, so, dynamically older systems. We present our new results for the mean colour indices of galaxies from these samples as well as the colour indices for galaxies of early and late types in Table 4.3. The mean indices show that galaxies in triplets are redder than isolated galaxies, and early type galaxies in triplets are redder than isolated early type galaxies. These differences are not significant when you consider subsamples of early and late galaxy types separately. When you consider complete samples, these differences are significant at the confidence level 95 %. This result can be explained by morphological content (aforementioned Dressler effect). From modelling the dynamical evolution of triplets, more than half of the time two components are close to each other while the third component is at a relatively large distance from the pair. Such a configuration is called hierarchical. We have analyzed also the projected configurations of triplets from these samples and

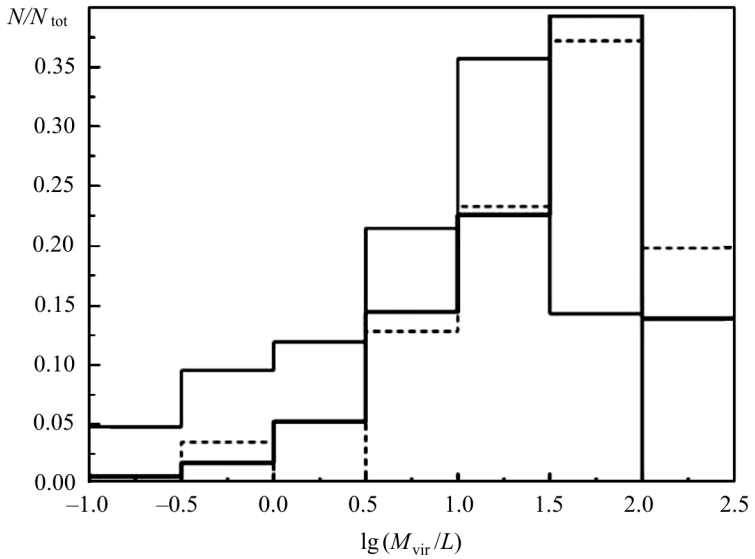

Fig. 4.9. Distribution of the mass-to-luminosity ratio for LS triplets (thick line), Northern and Southern triplets (dashed line), Interacting triplets (thin line), respectively

found an excess of hierarchical configurations in LS triplets (3r) compared to the N&S and Interacting triplet samples [59]. Chernin et al. [12] argued that the observed configuration of triplet can be a good indicator of the distribution of dark matter.

Thus, our results suggest that for the LS triplets dark matter is located in the individual galaxy halos which are the dynamically younger systems while for the Interacting and late type N&S triplets the dark matter preferentially lies in a common halo.

The distributions of virial mass-to-luminosity ratio for these samples are given in Fig. 4.9 and Fig. 4.10. One can see that Interacting triplets have systematically smaller $M_{\rm vir}/L$ values than LS triplets and N&S. Thus, the median luminosity for the Interacting triplet sample ($L = 5.66 \times 10^{10}\,L_{\odot}$), exceeds that for the LS triplets ($1.57 \times 10^{10}\,L_{\odot}$) and N&S triplets ($4.14 \times \times 10^{10}\,L_{\odot}$). The mean values of the mass-to-luminosity ratio and standard deviations (value in parentheses) for LS triplets, N&S triplets, and Interacting triplets are $53\,M_{\odot}/L_{\odot}$ (65), $77\,M_{\odot}/L_{\odot}$ (98), $27\,M_{\odot}/L_{\odot}$ (61), respectively. The median values of the mass-to-luminosity ratio for these samples are $35\,M_{\odot}/L_{\odot}$, $47\,M_{\odot}/L_{\odot}$, $13\,M_{\odot}/L_{\odot}$, respectively. For the hierarchical triplets in these same subsamples, the $M_{\rm vir}/L$ ratios are $24\,M_{\odot}/L_{\odot}$, $21\,M_{\odot}/L_{\odot}$, $14\,M_{\odot}/L_{\odot}$, respectively. We note that the values for LS and N&S hierarchical triplets are lower than the values for the total samples. The values for the Interacting triplets are equal. This could be additional evidence for the higher compactness of interac-

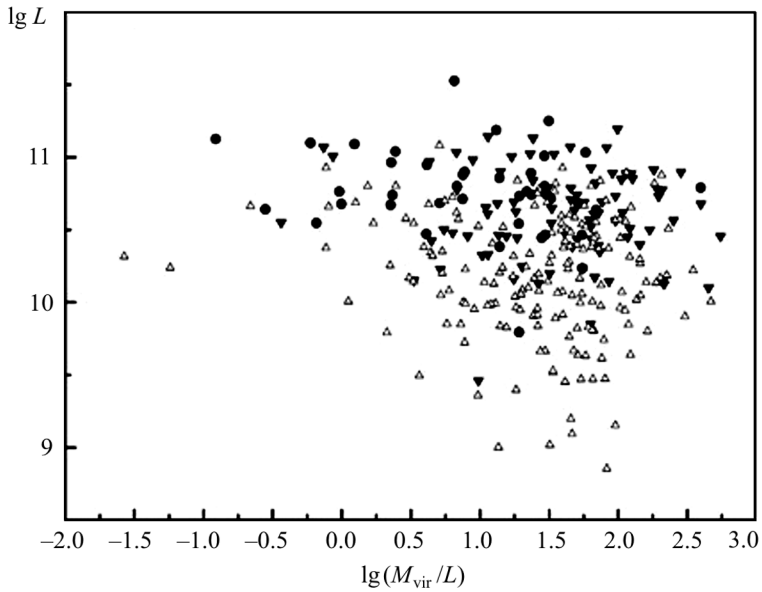

Fig. 4.10. Luminosity vs. mass-to-luminosity ratio. Triangles designate LS triplets, inverted triangles — Northern and Southern triplets, circles — Interacting triplets

ting systems while it is not possible to distinguish between a common dark matter halo and individual dark matter haloes associated with each galaxy. The examples of galaxy triplets are presented in Fig. 4.11.

4.4. Conclusion

For the first time we introduced and applied the high-order 3D Voronoi tessellation method for identification of isolated galaxies, pairs and triplets using the SDSS DR5 spectroscopical survey. We revealed that compact pairs ($R_h < 150$ kpc) and triplets ($R_h < 200$ kpc) are more isolated in average than systems in geometric samples, thus they are characterized by different isolation degree. The wider pair (triplet), the smaller isolation degree is observed. Small values of parameters p_e and t_e are the evidence of loose environment of these systems (they have not a "free space" to be the isolated groups). Thus, we consider wide geometric pairs and triplets as accidental ones in the common field. We compared the luminosities of single galaxies and galaxies in geometric pairs and triplets. It was shown that galaxies in isolated pairs and triplets are two times more luminous than isolated galaxies. On one hand it is the evidence of our geometric method accuracy. On the other hand, we can conclude that in such small groups as pairs and triplets the luminosity-density relation is observed.

We considered dark matter content in these groups. The median values of $M_{\rm vir}/L$ for our samples limited by different criteria are $12\,M_\odot/L_\odot$ for isolated

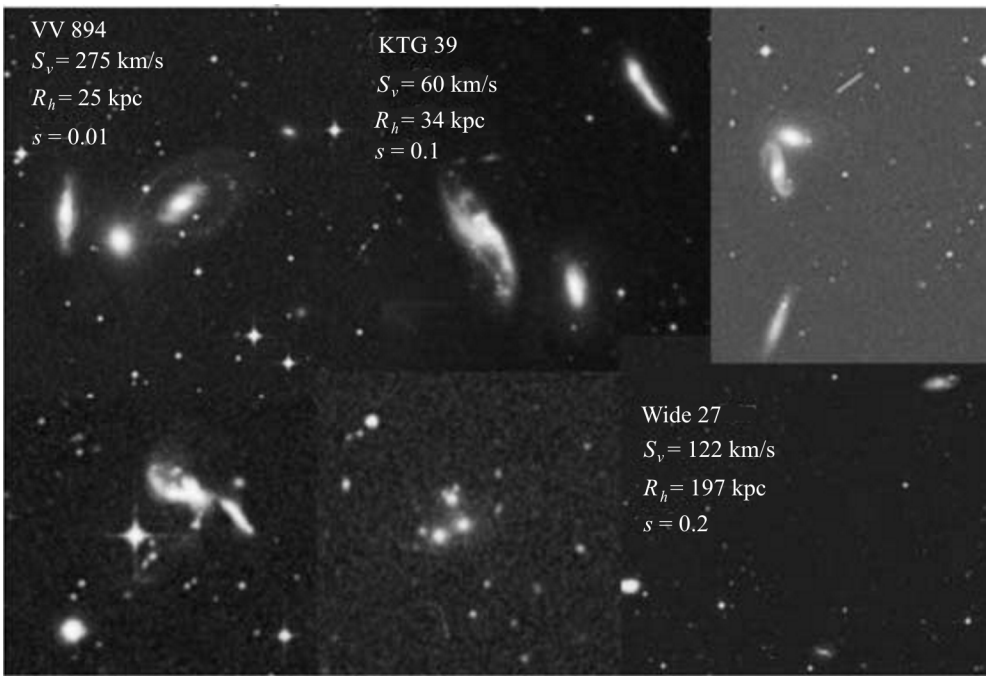

Fig. 4.11. Galaxy triplets from the SDSS spectroscopic survey

pairs, $44\,M_\odot/L_\odot$ for isolated triplets, 7 (8) $M_\odot/L_\odot$ for most compact pairs (triplets) with $R < 50$ (100) kpc. Note, that for most compact (close or interacting) systems is not very large difference in dark matter content for pairs and triplets, but for isolated triplets the $M_{\rm vir}/L$ is larger in three times than for pairs. These results are in agreement with works of other authors. We also found that the pair/triplet is less isolated system (in denser environment), when $M_{\rm vir}/L$ greater. This relation testifies that galaxy systems in denser environment have greater rms velocity (because of $M_{\rm vir} \sim S_v^2$ at fixed distance between galaxies). The $p, t - M_{\rm vir}/L$ dependencies are observed only for compact systems (up to 150—200 kpc for pairs and up to 250—300 kpc for triplets).

We at first obtained the values of "mass-to-luminosity" ratio for sparsely galaxy groups, which were identified by the Voronoi tessellation method in the Local Supercluster and from SDSS spectroscopic survey (Fig. 4.12).

We studied physical properties of very poor groups (3—10 galaxies) with the aim to estimate localization and content of the dark matter. The main samples of these groups were selected from the catalogue of the Local Supercluster by Voronoi tessellation and dynamical methods. We estimated a median value of the mass-to-luminosity ratio for poor LS groups (4—10 members) and find $M_{\rm vir}/L = 34\,M_\odot L_\odot$ and $50\,M_\odot L_\odot$, for the Voronoi tessellation and dynamical methods, respectively. We expect to derive more precise

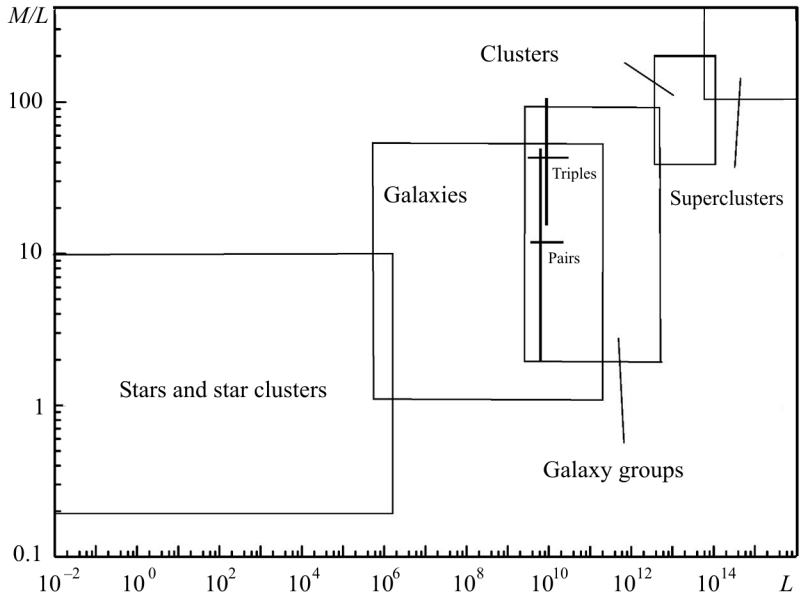

Fig. 4.12. "Mass-to-luminosity ratio" diagram for galaxy systems of different population (star clusters, galaxies, galaxy groups, clusters and superclusters), where our result [60] for sparsely populated galaxy groups is pointed

values of the parameters as the catalogue of LS galaxy groups is refined and improved. We studied the dynamical and colour properties of LS galaxy triplets compared to samples of Northern & Southern triplets and Interacting triplets. Analysis of morphological content and crossing times provides evidence that LS triplets are dynamically younger systems whereas N&S and Interacting triplets are older.

The Dressler effect may be observed even in such poor groups as galaxy triplets. Median values of the mass-to-luminosity ratio for LS triplets, N&S triplets, Interacting triplets are $35\,M_{\odot}/L_{\odot}$, $47\,M_{\odot}/L_{\odot}$, $13\,M_{\odot}/L_{\odot}$, respectively. The derived results led us to conclude about the dark matter distribution that for the dynamically younger sparsely groups (triplets), dark matter is more likely associated with the individual galaxy halos, for the interacting and late sparsely groups the dark matter lies in a common halo of galaxy groups.

Acknowledgements

We acknowledge the usage of the HyperLeda database (http://leda.univ-lyon1.fr) and SIMBAD data systems.

Funding for SDSS-III has been provided by the Alfred P. Sloan Foundation, the Participating Institutions, the National Science Foundation, and the U.S. Department of Energy Office of Science. The SDSS-III web site is

http://www.sdss3.org/. SDSS-III is managed by the Astrophysical Research Consortium for the Participating Institutions of the SDSS-III Collaboration including the University of Arizona, the Brazilian Participation Group, Brookhaven National Laboratory, University of Cambridge, Carnegie Mellon University, University of Florida, the French Participation Group, the German Participation Group, Harvard University, the Instituto de Astrofisica de Canarias, the Michigan State/Notre Dame/JINA Participation Group, Johns Hopkins University, Lawrence Berkeley National Laboratory, Max Planck Institute for Astrophysics, Max Planck Institute for Extraterrestrial Physics, New Mexico State University, New York University, Ohio State University, Pennsylvania State University, University of Portsmouth, Princeton University, the Spanish Participation Group, University of Tokyo, University of Utah, Vanderbilt University, University of Virginia, University of Washington, and Yale University.

Bibliography

1. M.S. Alonso, B. Tissera, G. Coldwell, D. Lambas, Galaxy pairs in the 2dF survey — II. Effects of interactions on star formation in groups and clusters, Mon. Not. R. Astron. Soc. **352**, 1081 (2004).
2. N.A. Bahcall, L.M. Lubin, V. Dorman, Where is the dark matter?, Astrophys. J. **447**, L81—L85 (1995).
3. R. Barrena, M. Ramella, W. Boschin, M. Nonino, A. Biviano, E. Mediavilla, VGCF detection of galaxy systems at intermediate redshifts, Astron. Astrophys. **444**, 685 (2005).
4. E.G. Barton, M.J. Geller, S.J. Kenyon, Tidally Triggered Star Formation in Close Pairs of Galaxies, Astrophys. J. **530**, 660 (2000).
5. E.G. Barton, M.J. Geller, S.J. Kenyon, Tidally Triggered Star Formation in Close Pairs of Galaxies. II. Constraints on Burst Strengths and Ages, Astrophys. J. **582**, 668 (2003).
6. C. Benn J., Wall, Structure on the largest scales: constraints from the isotropy of radio source counts, Mon. Not. R. Astron. Soc. **272**, 678 (1995).
7. M. Blanton, D. Eisenstein, D. Hogg, D. Schlegel, J. Brinkmann, Relationship between Environment and the Broadband Optical Properties of Galaxies in the Sloan Digital Sky Survey, Astrophys. J. **629**, 143 (2005).
8. V. Bernd, The Influence of Environment on Galaxy Evolution. Planets, Stars and Stellar Systems, Vol. 6, by Oswalt, D. Terry; Keel, C. William, Springer, 207 (2013).
9. R.S. Bogart, R.F. Wagoner, Clustering effects among clusters of galaxies and quasi-stellar sources, Astrophys. J. **181**, 609 (1973).
10. V.F. Cardone et al., Secondary infall model and dark matter scaling relations in intermediate-redshift early-type galaxies, Mon. Not. R. Astron. Soc. **416**, 1822 (2011).
11. M. Ceccarelli, C. Valotto, D. Lambas, N. Padilla, R. Giovanelli, M. Haynes, Galaxy Peculiar Velocities and Infall onto Groups, Astrophys. J. **622**, 853 (2005).
12. A.D. Chernin, A.V. Ivanov, A.V. Trofimof, S. Mikkola, Configurations and morphology of triple galaxies: evidence for dark matter?, Astron. Astrophys. **281**, 685 (1994).
13. P. Coles, J. Barrow, Microwave background constraints on the Voronoi model of large-scale structure, Mon. Not. R. Astron. Soc. **244**, 557 (1990).

14. P.H. Coleman, L. Pietronero, The fractal structure of the Universe, Phys. Rep. **213**, 311 (1992).
15. M. Cooper, J. Newman, D. Madgwick, B. Gerke, R. Yan, M. Davis, Measuring Galaxy Environments with Deep Redshift Surveys, Astrophys. J. **634**, 833 (2005).
16. C. Da Rocha, B.L. Ziegler, C. Mendes de Oliveira, Intragroup diffuse light in compact groups of galaxies — II. HCG 15, 35 and 51, Mon. Not. R. Astron. Soc. **388**, 1433 (2008).
17. R. De Propris, Ch. Conselice, J. Liske, S. Driver, D. Patton, A. Graham, P. Allen, The Millennium Galaxy Catalogue: The Connection between Close Pairs and Asymmetry; Implications for the Galaxy Merger Rate, Astrophys. J. **666**, 212 (2007).
18. A. Dressler, Galaxy morphology in rich clusters — Implications for the formation and evolution of galaxies, Astrophys. J. **236**, 351 (1980).
19. H. Ebeling, G. Wiedenmann, Detecting structure in two dimensions combining Voronoi tessellation and percolation, Phys. Rev. **47**, 704 (1993).
20. M. Einasto, J. Einasto, V. Muller, P. Heinamaki, D.L. Tucker, Environmental enhancement of loose groups around rich clusters of galaxies, Astron. Astrophys. **401**, 851 (2003).
21. J. Einasto et al., Structure and formation of Superclusters. XIII. The void probability function, Mon. Not. R. Astron. Soc. **248**, 593 (1990).
22. A. Elyiv, O. Melnyk, I. Vavilova, High-order 3D Voronoi tessellation for identifying Isolated galaxies, Pairs and Triplets, Mon. Not. R. Astron. Soc. **394**, 1409 (2009).
23. E. Escalera, A. Mazure, Wavelet analysis of subclustering: an illustration, Abell 754, Astrophys. J. **388**, 23 (1992).
24. P. Flin, I.B. Vavilova, Structure and properties of A1226, A1228, A1257, Astrophysical Letters and Communications. **36**, 113 (1997).
25. A.M. Garsia, General study of group membership. II. Determination of nearby groups, Astron. Astrophys. Suppl. Ser. **100**, 47 (1993).
26. M.J. Geller, S.J. Kenyon, E.G. Barton, T.H. Jarrett, L.J. Kewley, Infrared Properties of Close Pairs of Galaxies, Astron. J. **132**, 2243 (2006).
27. B.F. Gerke et al., The DEEP2 Galaxy Redshift Survey: First Results on Galaxy Groups, Astrophys. J. **625**, 6 (2005).
28. M. Girardi, P. Manzato, M. Mezzetti, G. Giuricin, F. Limboz, Observational mass-to-light ratio of galaxy systems: from poor groups to rich clusters, Astrophys. J. **569**, 720 (2002).
29. J.A. Gonzales, H. Quevedo, M. Salgado, D. Sudarsky, Measuring the Diffuse Optical Light in Abell 1651, Astron. Astrophys. **362**, 835 (2000).
30. V. Icke, R. van de Weygaert, Fragmenting the universe, Astron. Astrophys. **184**, 16 (1987).
31. V. Icke, R. van de Weygaert, The galaxy distribution as a Voronoi foam, Quart. JRAS **32**, 85 (1991).
32. S. Ikeuchi, E. Turner, Quasi-periodic structures in the large-scale galaxy distribution and three-dimensional Voronoi tessellation, Mon. Not. R. Astron. Soc. **250**, 519 (1991).

33. J. Jackson, A critique of Rees's theory of primordial gravitational radiation, Mon. Not. R. Astron. Soc. **156**, 1 (1972).
34. I. Karachentsev, The virial mass-luminosity ratio and the instability of different galactic systems, Astrofizika. **2**, 81 (1966).
35. I. Karachentsev, Catalogue of isolated pairs of galaxies in the northern hemisphere, Soobshchenia SAO **7**, 1 (1972).
36. I. Karachentsev, Double Galaxies (Nauka, Moscow, 1987), in Russian.
37. I. Karachentsev, V. Karachentseva, V. Lebedev, Galaxy triplets and problem of hidden mass, Izvestiya SAO **27**, 67 (1989).
38. I.D. Karachentsev, Criterion for bound groups of galaxies. Application to the local volume, Astron. Astrophys. Trans. **6**, 1 (1994).
39. I.D. Karachentsev, A.V. Kasparova, Global Properties of Nearby Galaxies in Various Environments, Astronomy Letters **31**, 152 (2005).
40. I. Karachentsev, D. Makarov, Orbital velocity of the Sun and the apex of the Galactic center, Astron. J. **111**, 794 (1996).
41. I.D. Karachentsev, The Local group and other neighboring galaxy groups, Astron. J. **129**, 178 (2005).
42. V.E. Karachentseva, The catalogue of the isolated galaxies, Soobsheniya SAO. **8**, 3 (1973).
43. V.E. Karachentseva, I.D. Karachentsev, A.L. Sherbanobsky, Isolated triplets of galaxies. I. The list. Izvestia SAO. **11**, 3 (1979).
44. V.E. Karachentseva, I.D. Karachentsev, Southern isolated galaxy triplets, Astronomy Reports. **44**, 501 (2000).
45. V.E. Karachentseva, O.V. Melnyk, I.B. Vavilova, D.I. Makarov, Triplets of galaxies in the local supercluster. 2. Virial masses and sum of individual masses, Kinemat. Phys. Celest. Bodies. **21**, 217 (2005).
46. G. Kauffmann, S. White, T. Heckman, B. Menard, J. Brinchmann, S. Charlot, C. Tremonti, J. Brinkmann, The environmental dependence of the relations between stellar mass, structure, star formation and nuclear activity in galaxies, Mon. Not. R. Astron. Soc. **353**, 713 (2004).
47. T. Kiang, Random Fragmentation in Two and Three Dimensions, Zeitschrift fur Astrophysik. **64**, 433 (1966).
48. R. Kim et al., Detecting Clusters of Galaxies in the Sloan Digital Sky Survey. I. Monte Carlo Comparison of Cluster Detection Algorithms, Astron. J. **123**, 20 (2002).
49. D.S. Lambas, P.B. Tissera, M.S.Alonso, G. Coldwell, Galaxy pairs in the 2dF survey — I. Effects of interactions on star formation in the field, Mon. Not. R. Astron. Soc. **346**, 1189 (2003).
50. J. Lewis et al. The 2dF Galaxy Redshift Survey: the environmental dependence of galaxy star formation rates near clusters, Mon. Not. R. Astron. Soc. **334**, 673 (2002).
51. R.C. Lindenbergh, Limits of Voronoi Diagrams, PhD Thesis, preprint (math-ph/0210345) (2002).
52. P. Lopes, R. de Carvalho, R. Gal et al., The Northern Sky Optical Cluster Survey. IV. An Intermediate-Redshift Galaxy Cluster Catalog and the Comparison of Two Detection Algorithms, Astron. J. **128**, 1017 (2004).

53. D.I. Makarov, I.D. Karachentsev, A new catalogue of multiple galaxies in the local supercluster small galaxy groups, ASP Confer. Ser. **209**, 40 (2000).
54. C. Marinoni, M. Davis, J. Newman, A. Coil, Three-dimensional Identification and Reconstruction of Galaxy Systems within Flux-limited Redshift Surveys, Astrophys. J. **580**, 122 (2002).
55. J.A. Materne, The structure of nearby clusters of galaxies. Hierarchical clustering and an application to the Leo region, Astron. Astrophys. **63**, 401 (1978).
56. T. Matsuda, E. Shima, Topology of the supercluster-void structure, Prog. Theo. Phys. **71**, 205 (1984).
57. O.V. Melnyk, Interacting galaxies in sparsely populated groups, Astron. Letters **32**, 302 (2006).
58. O.V. Melnyk, A.A. Elyiv, I.B. Vavilova, The Structure of the Local Supercluster of galaxies detected by three-dimensional Voronoi's tessellation methods, Kinemat. Phys. Celest. Bodies **22**, 283 (2006).
59. O.V. Melnyk, I.B. Vavilova, Triplets of galaxies in the local supercluster. 3. Configuration properties, Kinemat. Phys. Celest. Bodies. **22**, 422 (2006).
60. O. Melnyk, A. Elyiv, I. Vavilova, Mass-to-Luminosity relation for galaxy pairs and triplets in the different environment, Kinemat. Phys. Celest. Bodies. **25**, 64 (2009).
61. O.V. Melnyk, I.B. Vavilova, Dark matter in very poor galaxy groups, Adv. Space Res. **42**, 591 (2008).
62. O. Melnyk, S. Mitronova, V. Karachentseva, Colours of isolated galaxies selected from the Two-Micron All-Sky Survey, Mon. Not. R. Astron. Soc. **438**, 548 (2014).
63. O.V. Melnyk, D.V. Dobrycheva, I.B. Vavilova, Morphology and color indices of galaxies in pairs: Criteria for the classification of galaxies, Astrophysics. **55**, 293 (2012).
64. J. Mulchaey, D. Davis, R. Mushotzky, D. Burstein, An X-Ray Atlas of Groups of Galaxies, Astrophys. J. Suppl. Ser. **145**, 39 (2003).
65. B. Nikolic, H. Cullen, P. Alexander, Star formation in close pairs selected from the Sloan Digital Sky Survey, Mon. Not. R. Astron. Soc. **355**, 874 (2004).
66. E. Panko, P. Flin, A Catalogue of Galaxy Clusters and Groups Based on the Muenster Red Sky Survey, The Journal of Astronomical Data. **12**, 1 (2006).
67. C. Park, R. Gott III, C. Yun-Young, Transformation of Morphology and Luminosity Classes of the SDSS Galaxies, Astrophys. J. **674**, 784 (2008).
68. D.R. Patton, R.G. Carlberg, R.O. Marzke, C.J. Pritchet, L.N. da Costa, P.S. Pellegrini, New Techniques for Relating Dynamically Close Galaxy Pairs to Merger and Accretion Rates: Application to the Second Southern Sky Redshift Survey, Astrophys. J. **536**, 153 (2000).
69. D.R. Patton et al., Dynamically Close Galaxy Pairs and Merger Rate Evolution in the CNOC2 Redshift Survey, Astron. J. **565**, 208 (2002).
70. D.R. Patton, J.K. Grant, L. Simard, A Hubble Space Telescope Snapshot Survey of Dynamically Close Galaxy Pairs in the CNOC2 Redshift Survey, Astron. J., **130**, 2043 (2005).
71. G. Paturel, Study of the large Virgo cluster area from taxonomy, Astron. Astrophys. **71**, 106 (1979).
72. P.J.E. Peebles, E.J. Groth, Statistical analysis of catalog of extragalactic objects. I. Theory, Astrophys. J. **185**, 413 (1973).

73. F. Prada et al., Observing the Dark Matter Density Profile of Isolated Galaxies, Astrophys. J. **598**, 260 (2003).
74. M. Ramella, W. Boschin, D. Fadda, M. Nonino, Finding galaxy clusters using Voronoi tessellations, Astron. Astrophys. **368**, 776 (2001).
75. F. Reda, D. Forbes, A. Beasley, E. O'Sullivan, P. Goudfrooij, The photometric properties of isolated early-type galaxies, Mon. Not. R. Astron. Soc. **354**, 851 (2004).
76. V.C. Rubin, Fluctuations in the space distributions of the galaxies, Proc. NASA **40**, 541 (1954).
77. S.F. Shandarin, Percolation theory and cell structure of the Universe, Pis'ma v Astron. Zh. **9**, 195 (1983) (in Russian).
78. E. Slezak, A. Bijaoui, G. Mars, Identification of structures from galaxy counts: use of wavelet transform, Astron. Astrophys. **227**, 301 (1990).
79. A.S. Szalay, I. Budavari, A. Connolly et al., Spatial clustering of galaxies in large data bases. Technical report MSR-TR-2002-86. Available from: <http://archiv.org/ftp/cs/papers/0208015.pdf> (2002).
80. D.S.L. Soares, The Identification of Physical Close Galaxy Pairs, Astron. J. **134**, 71 (2007).
81. J. Stocke, B. Keeney, A. Lewis, H. Epps, R. Schild, Very Isolated Early-Type Galaxies, Astron. J. **127**, 1336 (2004).
82. M. Subba Rao, A. Szalay, Statistics of pencil beams in Voronoi foams, Astrophys. J. **391**, 483 (1992).
83. M. Subba Rao, A. Szalay, S. Gulkis, P. von Gronefeld, Microwave background fluctuations due to the Sunyaev—Zel'dovich effects in pancakes, Astrophys. J. **420**, 474 (1994).
84. E. Tago, J. Einasto, E. Saar, E. Tempel, M. Einasto, J. Vennik, V. Muller, Groups of galaxies in the SDSS Data Release 5. A group-finder and a catalogue, Astron. Astrophys. **479**, 927 (2008).
85. A.V. Trofimov, A.D. Chernin, Wide triplets of galaxies and the problem of hidden mass, Astron. Zh. **72**, 308 (1995).
86. R.B., Tully Light on Dark Matter, Publ. Astron. Soc. of Australia. **21**, 408 (2004).
87. R.B. Tully, L. Rizzi, A.E. Dolphin et al., Associations of dwarf galaxies, Astron. J. **132**, 729 (2006).
88. R. van de Weygaert, V. Icke, Fragmenting the universe. II — Voronoi vertices as Abell clusters, Astron. Astrophys. **213**, 1 (1989).
89. R. van de Weygaert, Quasi-periodicity in deep redshift surveys, Mon. Not. R. Astron. Soc. **249**, 159 (1991).
90. R. van de Weygaert, Fragmenting the Universe. 3: The constructions and statistics of 3-D Voronoi tessellations, Astron. Astrophys. **283**, 361 (1994).
91. R. van de Weygaert, W. Schaap, The Cosmic Web: Geometric Analysis, astro-ph/0708.1441v1 (2007).
92. I.B. Vavilova, P. Flin, Mapping the Jagiellonian Field of Galaxies, ASP Conference Ser. **125**, 186 (1997).
93. I.B. Vavilova, Large-Scale Structure of the Universe: Observations and Methods, Educational textbook for students. Taras Shevchenko National University of Kyiv (1998) (in Ukrainian).

94. I.B. Vavilova, Karachentseva V.E., Makarov D.I., Melnyk O.V., Triplets of galaxies in the local supercluster. I. Kinematic and virial properties, Kinematika I Fizika Nebesnyh Tel. **21**, 3 (2005).
95. I.B. Vavilova, Cluster and wavelet analysis for detachment of the structures of galaxy clusters: comparison, in: V. Di Gesu et al. (Eds.), Data analysis in Astronomy. World Scientific Publishing (1997), 297.
96. I.B. Vavilova, On the Use of Fractal Concepts in Analysis of Distributions of Galaxies, In: Examining the Big Bang and Diffuse Background Radiations, IAU Symp. Ser. **168**, Eds. M.C. Kafatos and Y. Kondo (1996) 473.
97. I.B. Vavilova, O.V. Melnyk, A.A. Elyiv, Morphological properties of isolated galaxies vs. isolation criteria, Astron. Nachr. **330**, 1004 (2009).
98. S. Verley et al., The AMIGA sample of isolated galaxies. V. Quantification of the isolation, Astron. Astrophys. **472**, 121 (2007).
99. G. Voronoi, Nouvelles applications des parameters continues a la theorie des formes quadratques. Deuxieme Memorie: recherches sur les paralleloedres primitives, Reine Angew. Math. **134**, 198 (1908).
100. B.A. Vorontsov-Velyaminov, R.I. Noskova, V.P. Arkhipova, The catalog of interacting galaxies by Vorontsov-Velyaminov, Astron. Astrophys. Trans. **20**, 717 (2001).
101. S. Weinmann, F. van den Bosch, X. Yang, H. Mo, Properties of galaxy groups in the Sloan Digital Sky Survey — I. The dependence of colour, star formation and morphology on halo mass, Mon. Not. R. Astron. Soc. **366**, 2 (2006).
102. B. Williams, J. Peacock, A. Heavens, Large-scale periodicity — Problems with cellular models, Mon. Not. R. Astron. Soc. **252**, 43 (1991).
103. D.F. Woods, M.J. Geller, E.J. Barton, Tidally Triggered Star Formation in Close Pairs of Galaxies: Major and Minor Interactions, Astron. J. **132**, 197 (2006).
104. S.D.M. White, The hierarchy of correlation function and its relation to other measures of galaxy clustering, Mon. Not. R. Astron. Soc. **186**, 145 (1979).
105. C.K. Xu, Y.C. Sun, X.T. He, The Near-Infrared Luminosity Function of Galaxies in Close Major-Merger Pairs and the Mass Dependence of the Merger Rate, Astrophys. J. **603**, L73 (2004).
106. L. Zaninetti, On the Large-Scale Structure of the Universe as given by the Voronoi Diagrams, Chin. J. Astron. Astrophys. **6**, 387 (2006).
107. L. Zaninetti, New Analytic Results for Poissonian and non-Poissonian Statistics of Cosmic Voids, Rev. Mex. Astron. Astrofis. **48**, 209 (2012), arXive 1209.4759.
108. F. Zwicky, On the clustering of nebulae. I, Astrophys. J. **95**, 555 (1942).

5 CHAPTER

INTERACTION IN THE DARK SECTOR

Yu.L. Bolotin, A.V. Kostenko, O.A. Lemets, D.A. Yerokhin

5.1. Introduction

The discovery of the accelerated expansion of the Universe [43, 47] completely changed our understanding of the composition of the Universe, and led to the replacement of the traditional Big Bang model with the Standard Cosmological Model (SCM). This model turned out to be immensely successful a vast number of observations can be reconciled if we assume that we live in a planar Universe undergoing accelerated expansion [13], for which the current relative densities of dark energy (DE), dark matter (DM), baryonic matter and radiation are, respectively, $\Omega_{\text{de}0} \approx 0.73$, (DM) $\Omega_{dm0} \approx 0.23$, $\Omega_{b0} \approx 0.04$ and $\Omega_{r0} \approx 5 \times 10^{-5}$.

Unlike fundamental theories, physical models only reflect the current state of our understanding of the process or phenomenon that they were created to describe. A model's flexibility plays a big role in its success — a model must be able to modernize and evolve as new information comes in. For this reason, the evolution of any broadly applied model is accompanied by multiple generalizations that aim is to resolve conceptual problems as well to explain the ever-increasing array of observations. In the case of the SCM, one of the more promising way of generalization is the replacement of the cosmological constant with a more complicated, dynamic form of dark energy [3,8,25] as well as the inclusion of interaction between the dark components [4,11,40,60,63].

Typically, DE models are based on scalar fields minimally coupled to gravity, and do not implement the explicit coupling of the field to the background matter. However there is no fundamental reason for this assumption in the

absence of an underlying symmetry which would suppress the coupling. Given that we do not know the true nature of neither DE nor DM, one cannot exclude that there exists a coupling between them. Whereas new forces between DE and normal matter particles are heavily constrained by observations (e.g. in the Solar System and gravitational experiments on Earth), this is not the case for DM particles. In other words, it is possible that the dark components interact with each other, while not being coupled to standard model particles. In the absence of the aforementioned underlying symmetry, the study of the interaction of DE and DM is an important and promising research direction. Moreover, disregarding the potential existence of an interaction between dark components may result in misinterpretations of the observational data. Since the gravitational effects of DE and of DM are opposite (i.e., gravitational repulsion versus gravitational attraction), even a small change of their relative concentrations can have an effect on cosmological dynamics (see, for example, Chapter 1). Models where the DM component of the Universe interacts with the DE field were originally proposed as solutions to the cosmic coincidence problem, since in the attractor regime, both DE and DM scale in the same way. It is remarkable that the scaling solutions in such models can lead to late-time acceleration, while this is not possible in the absence of coupling. It can also produce interesting new features in the large-scale structure. Therefore, the possibility of DE-DM interaction must be looked at with the utmost seriousness.

5.2. Physical mechanism of energy exchange

Models where DM interacts with the DE field can be realized if we only make an obvious assumption: the mass of the cold DM particles is a function of the DE field responsible for the present acceleration of the Universe. Variable-mass particles generally arise in models where the scalar (quintessence) field is coupled to the non-baryonic DM. Such a coupling represents a particularly simple and relatively general form of modified gravity. These particles appear, in fact, in scalar-tensor models and in simple versions of higher-order gravity theories in which the action is a function of the Ricci scalar. In the Lagrangian, these couplings could be of the form $g(\varphi)m_0\bar{\psi}\psi$ or $h\left(\varphi\right)m_0^2\phi^2$ for a fermionic or bosonic DM represented by ψ and ϕ, respectively, where the functions g and h of the quintessence field φ can, in principle, be arbitrary.

The inclusion of interaction leads to the appearance of a source in the right side of the "conservation equation". The quotation marks denote the presence of a flux from one dark component to the other.

Let's now look at the various approaches we can take to introduce interaction in the dark sector. DE represents the simplest explanation of the acceleration of the Universe within the SCM paradigm. DE is generally associated with a cosmological constant, and can be thought of as vacuum energy.

We define [57] a vacuum energy, V, as being the proportionality coefficient between the metric and the energy-momentum tensor

$$T^{\mu}_{\nu} = V g^{\mu}_{\nu}. \tag{5.1}$$

Comparing this with the energy-momentum tensor of a perfect fluid

$$T^{\mu}_{\nu} = (\rho + p)\, u^{\mu} u_{\nu} - p g^{\mu}_{\nu} \tag{5.2}$$

the vacuum energy density and pressure with $\rho = -p = V$. A vacuum energy that is homogeneous throughout spacetime, $\nabla_{\mu} V = 0$, is equivalent to a cosmological constant in Einstein gravity $\Lambda = 8\pi G V$. We will consider the possibility of a time and/or space dependent vacuum energy. From Eq. (5.1) we have

$$\nabla_{\mu} T^{\mu}_{\nu} = F_{\nu}, \quad F_{\mu} \equiv \nabla_{\mu} V. \tag{5.3}$$

We can therefore identify an inhomogeneous vacuum, $\nabla_{\mu} V \neq 0$, with an interacting vacuum, $F_{\mu} \neq 0$. The conservation of the total energy-momentum (including matter fields and vacuum energy)

$$\nabla_{\mu} \left({T_{(\mathrm{de})}}^{\mu}_{\nu} + {T_{(\mathrm{dm})}}^{\mu}_{\nu} \right) = 0 \tag{5.4}$$

implies that the vacuum ${T_{(\mathrm{de})}}^{\mu}_{\nu}$ or DE transfers energy-momentum to or from the matter fields ${T_{(\mathrm{dm})}}^{\mu}_{\nu}$

$$\nabla_{\mu} {T_{(\mathrm{de})}}^{\mu}_{\nu} = -{T_{(\mathrm{dm})}}^{\mu}_{\nu} = F_{\nu}. \tag{5.5}$$

Now we must see what kind of an effect the interaction of the dark components will have on the actual dynamics, i.e. on the Friedmann equations, and obtain the general equations of motion for DE interacting with DM [54]. We assume a Universe formed by only DM and DE. The equations of motion that describe the dynamics of the Universe as a whole are the Einstein field equations

$$R_{\mu\nu} - \frac{1}{2} R g_{\mu\nu} = 8\pi G \left({T_{(\mathrm{de})}}_{\mu\nu} + {T_{(\mathrm{dm})}}_{\mu\nu} \right) \tag{5.6}$$

whereas the conservation equations for each component are

$$\begin{aligned} \nabla^{\nu} {T_{(\mathrm{de})}}_{\mu\nu} &= F_{\mu}, \\ \nabla^{\nu} {T_{(\mathrm{dm})}}_{\mu\nu} &= -F_{\mu}, \end{aligned} \tag{5.7}$$

where the respective energy momentum tensor for the component i ($i = \mathrm{dm}, \mathrm{de}$) is

$$T_{(i)\mu\nu} = (\rho_i + p_i)\, u_{\mu} u_{\nu} - p_i g_{\mu\nu} \tag{5.8}$$

here u_μ is the velocity of the fluid (the same for each one) and ρ_i and p_i are, respectively, the density and pressure of the fluid i measured by an observer with velocity u_μ. F_μ is the 4-vector of interaction between dark components and its form is not known a priori. Equations (5.7) can be projected on the time or on the space direction of the comoving observer. We project these equations onto to the velocity u^μ

$$\begin{aligned} u^\mu \nabla^\nu T_{(\mathrm{dm})\mu\nu} &= -u^\mu F_\mu, \\ u^\mu \nabla^\nu T_{(\mathrm{de})\mu\nu} &= u^\mu F_\mu \end{aligned} \tag{5.9}$$

and in other part orthogonal to the velocity using the projector $h_{\beta\mu} = g_{\beta\mu} - -u_\beta u_\mu$

$$\begin{aligned} h^{\mu\beta} \nabla^\nu T_{(\mathrm{dm})\mu\nu} &= -h^{\mu\beta} F_\mu, \\ h^{\mu\beta} \nabla^\nu \nabla^\nu T_{(\mathrm{de})\mu\nu} &= h^{\mu\beta} F_\mu. \end{aligned} \tag{5.10}$$

Using (5.8) in (5.9) we obtain energy conservation equations for each dark component

$$\begin{aligned} u^\mu \nabla_\mu \rho_{\mathrm{dm}} + (\rho_{\mathrm{dm}} + p_{\mathrm{dm}}) \nabla_\mu u^\mu &= u^\mu F_\mu, \\ u^\mu \nabla_\mu \rho_{\mathrm{de}} + (\rho_{\mathrm{de}} + p_{\mathrm{de}}) \nabla_\mu u^\mu &= -u^\mu F_\mu. \end{aligned} \tag{5.11}$$

On the other hand, substitution (5.8) in (5.11) leads to the Euler equations for every component,

$$\begin{aligned} h^{\mu\beta} \nabla_\mu p_{\mathrm{dm}} + (\rho_{\mathrm{dm}} + p_{\mathrm{dm}}) u^\mu \nabla_\mu u^\beta &= -h^{\mu\beta} F_\mu, \\ h^{\mu\beta} \nabla_\mu p_{\mathrm{de}} + (\rho_{\mathrm{de}} + p_{\mathrm{de}}) u^\mu \nabla_\mu u^\beta &= h^{\mu\beta} F_\mu. \end{aligned} \tag{5.12}$$

These formulas describe the interaction of the dark components. If we want to move further, we need to choose a model (metric), which will be done later.

5.3. Phenomenology of Interacting Models

We have already stated that since there is no fundamental theoretical approach that may specify the functional form of the coupling between DE and DM, presently coupling models are necessarily phenomenological ones. Of course, one can always provide arguments in favour of a certain type of correlation. However, until the creation of a microscopic theory of dark components, the effectiveness of any phenomenological model will be defined only by how well it corresponds to observations.

We assumed that the background metric is described by the flat FLRW metric. In the comoving coordinates we choose $u^\mu = (1, 0, 0, 0)$. With this choice

$$\begin{aligned} \nabla_\mu u^\mu &= 3H, \\ u^\mu \nabla_\mu u^\nu &= 0. \end{aligned} \tag{5.13}$$

Using notation $u^\mu F_\mu = Q(a)$ let's transform the equations (5.11) to the final form

$$\begin{aligned} \dot{\rho}_{\mathrm{dm}} + 3H\rho_{\mathrm{dm}} &= Q, \\ \dot{\rho}_{\mathrm{de}} + 3H(\rho_{\mathrm{de}} + p_{\mathrm{de}}) &= -Q \end{aligned} \tag{5.14}$$

The function $Q(a)$ is known as the interaction function depending on the scale factor. We note that the equations (5.14) are satisfied identically (taking into account the condition $h^{\mu\nu}F_\nu = 0$), and do not produce any new equations.

The sign of Q defines the direction of the flux of energy:

$$Q\begin{cases}>0\\<0\end{cases} \rightarrow \text{energy transfer is } \begin{cases}\text{dark energy} \rightarrow \text{dark matter}\\ \text{dark matter} \rightarrow \text{dark energy}\end{cases}.$$

We will focus our attention on DE in the form of a scalar field φ. In this case

$$w_{\rm de} = w_\varphi = \frac{p_\varphi}{\rho_\varphi} = \frac{\frac{1}{2}\dot\varphi^2 - V(\varphi)}{\frac{1}{2}\dot\varphi^2 + V(\varphi)}. \tag{5.15}$$

The modified (by interaction) Klein—Gordon equation is

$$\ddot\varphi^2 + 3H\dot\varphi + \frac{dV}{d\varphi} = -\frac{Q}{\dot\varphi}. \tag{5.16}$$

It is useful to note that the system (5.12), which describes the interacting dark components, can be transformed into the standard form that corresponds to non-interacting components by re-defining the parameters $w_{\rm de}$ and $w_{\rm dm} = 0$ [12]. If we write the equations (5.14) in the form

$$\dot\rho_i + 3H(1 + w_{{\rm eff},i})\rho_i = 0,\ i = {\rm de}, {\rm dm} \tag{5.17}$$

then

$$w_{\rm eff,dm} = -\frac{Q}{3H\rho_{\rm dm}},\ w_{\rm eff,de} = w_{\rm de} + \frac{Q}{3H\rho_{\rm de}}. \tag{5.18}$$

If we "turn off" the interaction ($Q = 0$), we return to the original equation of state (EOS) parameters: $w_{\rm eff,dm} = w_{\rm dm} = 0$, $w_{\rm eff,de} = w_{\rm de}$.

The system (5.14) has be given an alternative interpretation. It is convenient to introduce the effective pressures $\Pi_{\rm dm}$ and $\Pi_{\rm de}$ [6]

$$Q \equiv -3H\Pi_{\rm dm} = +3H\Pi_{\rm de} \tag{5.19}$$

with the help of which

$$\begin{aligned}\dot\rho_{\rm dm} + 3H(\rho_{\rm dm} + \Pi_{\rm dm}) = 0,\\ \dot\rho_{\rm de} + 3H(\rho_{\rm de} + p_{\rm de} + \Pi_{\rm de}) = 0.\end{aligned} \tag{5.20}$$

In this case the conservation equations formally look as those for two independent fluids. A coupling between them has been mapped onto the relation $\Pi_{\rm dm} = -\Pi_{\rm de}$.

In order to illustrate how interaction between the dark components acts on cosmological dynamics, consider the time evolution of the ratio $r \equiv \rho_{\rm dm}/\rho_{\rm de}$,

$$\dot r = \frac{\rho_{\rm dm}}{\rho_{\rm de}}\left(\frac{\dot\rho_m}{\rho_m} - \frac{\dot\rho_{\rm de}}{\rho_{\rm de}}\right) = 3Hr\left(w_{\rm de} + \frac{1+r}{\rho_{\rm dm}}\frac{Q}{3H}\right). \tag{5.21}$$

Let's analyse the obtained expression [6]. We take $r = r_0 a^{-\xi}$ (r_0 is the energy-density ratio at the present time and ξ is a constant, non-negative parameter). In this case, for the interaction term, we obtain

$$\frac{Q}{3H\rho_{\rm dm}} = -\frac{w_{\rm de} + \frac{\xi}{3}}{1+r}. \tag{5.22}$$

Eq. (5.22) demonstrates that by choosing a suitable interaction between both components, we may produce any desired scaling behavior of the energy densities. The uncoupled case, corresponding to $Q = 0$, is given by $\xi/3 + w_{\rm de} = 0$. The SCM model (the special uncoupled case) corresponds to $w_{\rm de} = -1,\ \xi = 3$. Generally, interacting models are parameterized by deviations from $\xi = -3w_{\rm de}$. Any solution which deviates from $\xi = -3w_{\rm de}$ represents a testable, non-standard cosmological model. For $\xi > 0$, interaction Q (5.22) becomes very small for $a \ll 1$. Consequently, the interaction is not relevant at high redshifts. This guarantees the existence of an early matter-dominated epoch. Note also that energy transfer from DE to DM, i.e. $w_{\rm de} + \frac{\xi}{3} < 0$.

During comparisons of model dynamics with observational results, it is useful to analyse all dynamic variables as functions of redshift, not of time. Let's use the fact that

$$\frac{d}{dt} = \frac{d}{dz}\frac{dz}{da}\frac{da}{dt} = -(1+z)H(z)\frac{d}{dz}$$

and transform the base equations (5.14) to the form

$$\begin{aligned} \frac{d\rho_{\rm dm}}{dz} - \frac{3}{1+z}\rho_{\rm dm} &= -\frac{Q(z)}{(1+z)H(z)}, \\ \frac{d\rho_{\rm de}}{dz} - \frac{3}{1+z}(1+w_{\rm de})\rho_{\rm de} &= \frac{Q(z)}{(1+z)H(z)}. \end{aligned} \tag{5.23}$$

Also, let's introduce [54] the dimensionless interaction function $I_Q(z)$,

$$I_Q(z) \equiv \frac{1}{\rho^0_{\rm crit}(1+z)^3 H(z)} Q\,(z)\,.$$

Moving to relative densities, we finally get

$$\begin{aligned} \frac{d\Omega_{\rm dm}}{dz} - \frac{3}{1+z}\Omega_{\rm dm} &= -(1+z)^2 I_Q(z), \\ \frac{d\Omega_{\rm de}}{dz} - \frac{3}{1+z}(1+w_{\rm de})\Omega_{\rm de} &= (1+z)^2 I_Q(z). \end{aligned} \tag{5.24}$$

The function $I_Q(z)$ is useful during analysis of the observational data [54].

Simple Linear Models. In general, the coupling term Q can take any possible form $Q = Q\left(H, \rho_{\rm dm}, \rho_{\rm de}, t\right)$. However, physically, it makes more sense that the coupling will be time-independent. Among the time-independent options, preference is given to a factorized H dependence $Q = Hq(\rho_{\rm dm}, \rho_{\rm de})$. During this kind of factorization, the effects of the coupling on the dynamics of $\rho_{\rm dm}$ and $\rho_{\rm de}$ become effectively independent from the evolution of the Hubble scale H. The latter is related to the fact that the time derivatives that go into the conservation equation can be transformed in the following way: $d/dt \rightarrow$ $\rightarrow Hd/d\ln a$. It is important to note [64] that the decoupling of the dynamics of the two dark components from H is valid in any theory of gravity, because it is based on the conservation equations. Any coupling of this type can be approximated at late times by a linear expansion

$$q = q_0^* + q_{\rm dm}^* \left(\rho_{\rm dm} - \rho_{\rm dm,0}\right) + q_{\rm de}^* \left(\rho_{\rm de} - \rho_{\rm de,0}\right) \tag{5.25}$$

the constants $q_0^*, q_{\rm dm}^*, q_{\rm de}^*$ can always be redefined in order to give the coupling q the form

$$q = q_0 + q_{\rm dm}\rho_{\rm dm} + q_{\rm de}\rho_{\rm de}. \tag{5.26}$$

Special cases of this general expression:

$$\begin{array}{ll} q \propto \rho_{\rm dm}, & q_0 = q_{\rm de} = 0; \\ q \propto \rho_{\rm de}, & q_0 = q_{\rm dm} = 0; \\ q \propto \rho_{\rm total}, & q_0 = 0,\ q_{\rm dm} = q_{\rm de}. \end{array} \tag{5.27}$$

Let's look at these special cases in greater detail. It can be shown [48], that the introduction of the coupling function δ(a) between DE and DM as

$$\delta(a) = \frac{d\ln m_\psi(a)}{d\ln a} \tag{5.28}$$

(see Section 2) results in the following equation for the evolution of the DM energy density $\rho_{\rm dm}$

$$\dot{\rho}_{\rm dm} + 3H\rho_{\rm dm} - \delta\left(a\right) H\rho_{\rm dm} = 0. \tag{5.29}$$

The time dependence of the DM energy density is easily obtained as the solution of (5.24)

$$\rho_{\rm dm}(a) = \rho_{\rm dm}^{(0)} a^{-3} \exp\left(-\int\limits_a^1 \delta(a')d\ln a'\right). \tag{5.30}$$

This solution shows that the interaction causes $\rho_{\rm dm}$ to deviate from SCM scaling a^{-3}. This is related to the fact that if DE is decaying into DM particles, this component will dilute more slowly as compared with its conserved evolution. Consider the simple example of a constant coupling δ. In this case we obtain

$$\rho_{\rm dm}(a) = \rho_{dm,0} a^{-3+\delta}. \tag{5.31}$$

The deviation from the standard evolution is characterized by a positive interaction constant δ.

Conservation of the total energy density implies that the DE density should obey

$$\dot{\rho}_{\rm de} + 3H\left(\rho_{\rm de} + p_{\rm de}\right) + \delta(a) H \rho_{\rm dm} = 0. \tag{5.32}$$

The solution of this equation for a constant EOS parameter $w_{\rm de}$ and constant coupling δ is

$$\rho_{\rm de}(a) = \rho_{\rm de,0} a^{-3(1+w_{\rm de})} + \frac{\delta \rho_{\rm dm,0}}{\delta + 3w_{\rm de}} \left(a^{-3(1+w_{\rm de})} - a^{-3+\delta}\right). \tag{5.33}$$

The first term is the usual evolution of DE at $\delta = 0$. From this solution, it is easy to see that one must require a positive value of the coupling $\delta > 0$ in order to have a positive value of $\rho_{\rm de}$ for earlier epochs of the Universe. For $w_{\rm de} = -1$, $\delta \neq 0$ this expression reduced to

$$\rho_{\Lambda}(a) = \rho_{\Lambda,0} - \frac{\delta \rho_{\rm dm,0}}{3-\delta} a^{-3+\delta}. \tag{5.34}$$

This expression can be interpreted in terms of a time-dependent cosmological constant $\Lambda(t)$ (see section 5.5.1)

Before going further, let's also write, without any additional comments, the forms of the densities of energy $\rho_{\rm de}(a)$ and $\rho_{\rm dm}(a)$ for the case of $Q = \delta H \rho_{\rm de}$ ($\delta = \text{const}$):

$$\begin{aligned} \rho_{\rm de}(a) &= \rho_{\rm de0} a^{-[3(1+w_{\rm de})+\delta]}, \\ \rho_{\rm dm}(a) &= \frac{-\delta \rho_{\rm de0}}{3w_{\rm de}+\delta} a^{-[3(1+w_{\rm de})+\delta]} + \left(\rho_{\rm dm0} + \frac{\delta \rho_{\rm de0}}{3w_{\rm de}+\delta}\right) a^{-3}. \end{aligned} \tag{5.35}$$

5.3.1. Non-linear interaction in the dark sector

We have already stated multiple times that our current lack of understanding of the structure of the dark components leaves us with only dimensional limitations on the choice of the form of interaction between them. Previously, we analysed linear interactions: the interaction term in the conservation equations of the individual components is proportional either to DM density, to DE density, or to a linear combination of both densities. However, from a physical point of view, an interaction between two components should depend on the product of the abundances of the individual components, as, for instance, in chemical or nuclear reactions. Consequently, a product coupling, i.e., an interaction proportional to the product of DM density and DE density looks more appealing. An analysis of cosmological models with specific non-linear interactions was performed in [7, 30, 38].

Following [6], we investigate, in a flat Universe, the dynamics of a simple two-component model ($\rm de + dm$) with a number of non-linear interactions.

Motivated by the structure

$$\rho_{\rm dm} = \frac{r}{1+r}\rho,\ \rho_{\rm de} = \frac{1}{1+r}\rho,\ r \equiv \frac{\rho_{\rm dm}}{\rho_{\rm de}},\ \rho = \rho_{\rm dm} + \rho_{\rm de}, \tag{5.36}$$

we consider the ansatz concern to effective pressure ($Q = -3H\Pi$)

$$\Pi = -\gamma \rho^m r^n \,(1+r)^s, \tag{5.37}$$

where γ is a positive coupling constant. The powers m, n, s specify the interaction. For fixed values m, n, s the only free parameter is γ. A linear dependence of Π on ρ corresponds to $m = 1$. The effective interaction pressure Π is proportional to powers of products of the densities of the components for the special cases $m = s$. Notice that, according to Friedmann's equations, $\rho \propto H^2$. This implies that the interaction quantity Q is not necessarily linear in the Hubble rate. For $m = s$ the ansatz (5.31) is equivalent to

$$Q = 3\gamma H \rho_{\rm de}^{m-n} \rho_{\rm dm}^n = 3\gamma H \rho_{\rm de}^m r^n. \tag{5.38}$$

The ansatz (5.31) also includes the previously analysed linear cases. The combination $(m, n, s) = (1, 1, -1)$ corresponds to $Q = 3\gamma H \rho_{\rm dm}$, while $(m, n, s) = (1, 0, -1)$ reproduces $Q = 3\gamma H \rho_{\rm de}$. We can therefore state that the ansatz (5.31) contains a large variety of interactions, which have been studied in the literature (see [6]) as special cases.

We consider now three particular combinations of the parameters (m, n, s) which give rise to analytically solvable models with non-linear interaction terms.

Case $\boldsymbol{Q = 3H\gamma \dfrac{\rho_{\rm dm}\rho_{dx}}{\rho}}$**,** $\boldsymbol{(m, n, s) = (1, 1, -2)}$. For such an interaction, the conservation equations for ρ and r are reduced to

$$\begin{aligned} \rho' &= -\left(1 + \frac{w_{\rm de}}{1+r}\right)\rho, \\ r' &= r\,(w_{\rm de} + \gamma), \end{aligned} \tag{5.39}$$

where the prime denotes differentiation with respect to $\ln a$. The solutions of this system are

$$\begin{aligned} r &= r_0 a^{3(w_{\rm de}+\gamma)}, \\ \rho &= \rho_0 a^{-3(1+w_{\rm de})} \left[\frac{1 + r_0 a^{3(w_{\rm de}+\gamma)}}{1+r_0}\right]^{\frac{w_{\rm de}}{w_{\rm de}+\gamma}}, \\ \rho_{\rm dm} &= \rho_{\rm dm0} a^{-3(1-\gamma)} \left[\frac{1 + r_0 a^{3(w_{\rm de}+\gamma)}}{1+r_0}\right]^{-\frac{\gamma}{w_{\rm de}+\gamma}}, \\ \rho_{\rm de} &= \rho_{\rm de0} a^{-3(1+w)} \left[\frac{1 + r_0 a^{3(w_{\rm de}+\gamma)}}{1+r_0}\right]^{-\frac{\gamma}{w_{\rm de}+\gamma}}. \end{aligned} \tag{5.40}$$

An ansatz $r = r_0 a^{-\xi}$ for the energy density ratio corresponds to $\gamma = -(w_{\rm de} + \xi/3)$. For $a \ll 1$ (matter-dominated epoch), we obtain the correct behaviour of the density $\rho \propto a^{-3}$. The SCM model is recovered for $w_{\rm de} = -1$, $\gamma = 0$ ($\xi = 3$).

Case $\boldsymbol{Q = 3H\gamma\dfrac{\rho_{\rm dm}^2}{\rho}}$, $\boldsymbol{(m, n, s) = (1, 2, -2)}$. The analytical solution in this case is

$$\begin{gathered} r = r_0 \frac{w_{\rm de}}{(w_{\rm de} + \gamma r_0)\, a^{-3w_{\rm de}} - \gamma r_0}, \\ \rho = \rho_0 a^{-3\left(1 - \frac{\gamma w_{\rm de}}{w_{\rm de} - \gamma}\right)} \left[\frac{(w_{\rm de} + \gamma r_0)\, a^{-3w_{\rm de}} + r_0\,(w_{\rm de} - \gamma)}{w_{\rm de}(1 + r_0)}\right]. \end{gathered} \tag{5.41}$$

For $a \ll 1$ (the high redshift limit) the ratio r becomes a constant, $r \to |w|/\gamma$. In the opposite limit ($a \gg 1$), $r \propto a^{-3}$, as in the SCM case.

Case $\boldsymbol{Q = 3H\gamma\dfrac{\rho_{\rm de}^2}{\rho}}$, $\boldsymbol{(m, n, s) = (1, 0, -2)}$. For $w_{\rm de} < 0$, i.e. $w_{\rm de} = -|w_{\rm de}|$ the solutions are

$$\begin{gathered} r = \left(r_0 - \frac{\gamma}{|w_{\rm de}|}\right) a^{-3|w_{\rm de}|} + \frac{\gamma}{|w_{\rm de}|}, \\ \rho = \rho_0 a^{-3\left(1 - \frac{w_{\rm de}^2}{|w_{\rm de}| + \gamma}\right)} \left[\frac{|w_{\rm de}| + \gamma + (|w_{\rm de}|\, r_0 - \gamma)\, a^{-3|w_{\rm de}|}}{|w_{\rm de}|\,(1 + r_0)}\right]^{\frac{|w_{\rm de}|}{|w_{\rm de}| + \gamma}}. \end{gathered} \tag{5.42}$$

The ratio r scales as $a^{-3|w_{\rm de}|}$ for $a \ll 1$. For $w_{\rm de} = -1$, this coincides with the scaling of its SCM counterpart. In the opposite limit $a \gg 1$ (far future), the ρ -solution corresponds to matter dominated period, $\rho \propto a^{-3\left(1 - \frac{w_{\rm de}^2}{|w_{\rm de}| + \gamma}\right)}$, which generally does not correspond to a de-Sitter phase.

In conclusion of this section, let's try to solve the opposite problem. Instead of postulating the form of the interaction, let's fixate the ratio

$$r = \frac{\rho_{\rm dm}}{\rho_{\rm de}} = f(a), \tag{5.43}$$

where $f(a)$ is any differentiable function of the scale factor. We then have

$$\begin{gathered} \dot\rho_{\rm dm} = \dot\rho_{\rm de} f + \rho_{\rm de} f'\, \dot a; \\ \dot\rho_{\rm de} = \frac{\dot\rho_{\rm dm}}{f} - \frac{\rho_{\rm dm} f' \dot a}{f^2},\ f' = \frac{df}{da}. \end{gathered} \tag{5.44}$$

From this, we find that

$$Q = \frac{f}{1 + f}\left(\frac{f'}{f} a - 3w_{\rm de}\right) H \rho_{\rm de}. \tag{5.45}$$

To see that the interaction is non-linear in nature, note that $f/(1+f) = \Omega_{\rm dm}$. Therefore,

$$Q = \left(\frac{f'}{f}a - 3w_{\rm de}\right) H\rho_{\rm de}\Omega_{\rm dm}. \tag{5.46}$$

We note that if $f = a^{\xi}$, then

$$Q = (\xi - 3w_{\rm de})\, H\rho_{\rm de}\Omega_{\rm dm}. \tag{5.47}$$

For SCM $\xi = 3$, $w_{\rm de} = -1$ and we return to the obvious result — $Q = 0$.

5.4. Structure of phase space of models with interaction

The evolution of an Universe filled with interacting components can be effectively analysed in terms of dynamical systems theory. Let us consider the following coupled differential equations for two variables

$$\begin{aligned} \dot{x} &= f(x, y, t), \\ \dot{y} &= g(x, y, t). \end{aligned} \tag{5.48}$$

We will be interested in so-called autonomous systems, for which the functions f and g do not contain explicit time-dependent terms. A point (x_c, y_c) is said to be a fixed point or a critical point of the autonomous system if

$$f(x_c, y_c) = g(x_c, y_c) = 0. \tag{5.49}$$

A critical point (x_c, y_c) is called an attractor when it satisfies the condition

$$(x(t), y(t)) \to (x_c, y_c) \ \text{ for } t \to \infty. \tag{5.50}$$

Let's look at the behavior of the dynamical system (5.48) around the critical point. For this purpose, let us consider small perturbations around the critical point

$$x = x_c + \delta x, \ \ y = y_c + \delta y \tag{5.51}$$

Substituting into Eqs. (5.48) leads to the first-order differential equations:

$$\frac{d}{dN}\begin{pmatrix}\delta x \\ \delta y\end{pmatrix} = \hat{M}\begin{pmatrix}\delta x \\ \delta y\end{pmatrix}. \tag{5.52}$$

Taking into account the specifics of the problem that we are solving, we made the change $\dfrac{d}{dt} \to \dfrac{d}{dN}$, where $N = \ln a$. The matrix $\hat{M}$ is given by

$$\hat{M} = \begin{pmatrix} \dfrac{\partial f}{\partial x} & \dfrac{\partial f}{\partial y} \\ \dfrac{\partial g}{\partial x} & \dfrac{\partial g}{\partial y} \end{pmatrix}. \tag{5.53}$$

The general solution for the linear perturbations is

$$\begin{aligned} \delta x &= C_1 e^{\lambda_1 N} + C_2 e^{\lambda_2 N}, \\ \delta y &= C_3 e^{\lambda_1 N} + C_4 e^{\lambda_2 N}. \end{aligned} \tag{5.54}$$

The stability around the fixed points depends on the nature of the eigenvalues.

We will look at the interacting dark components as a dynamical system described by the equations [62]

$$\begin{aligned} \rho'_{\rm de} + 3(1 + w_{\rm de})\rho_{\rm de} &= -Q, \\ \rho'_{\rm dm} + 3(1 + w_{\rm dm})\rho_{\rm dm} &= Q. \end{aligned} \tag{5.55}$$

Here, a prime denotes the derivative with respect to the e-folding time $N = \ln a$. Note that, what although the interaction can significantly change the cosmological evolution, with proper interactions, the system is still an autonomous system. We consider the following specific interaction forms, which were already analysed before:

$$Q_1 = 3\gamma_m \rho_{\rm dm},\ Q_2 = 3\gamma_d \rho_{\rm de},\ Q_3 = 3\gamma_{\rm tot}\rho_{\rm tot}. \tag{5.56}$$

Let's write the effective EOS parameters for both DE and dark matter:

$$Q = Q_1,\ w_{\rm eff,de} = w_{\rm de}\left(\Omega_{\rm de}\right) + \gamma_m \frac{1 - \Omega_{\rm de}}{\Omega_{\rm de}},\ w_{\rm eff,dm} = w_{\rm dm} - \gamma_m, \tag{5.57}$$

$$Q = Q_2,\ w_{\rm eff,de} = w_{\rm de}\left(\Omega_{\rm de}\right) + \gamma_d,\ w_{\rm eff,dm} = w_{\rm dm} - \gamma_d \frac{\Omega_{\rm de}}{1 - \Omega_{\rm de}}, \tag{5.58}$$

$$Q = Q_3,\ w_{\rm eff,de} = w_{\rm de}\left(\Omega_{\rm de}\right) + \gamma_m \frac{1}{\Omega_{\rm de}},\ w_{\rm eff,dm} = w_{\rm dm} - \frac{\gamma_{\rm tot}}{1 - \Omega_{\rm de}}. \tag{5.59}$$

The system (5.55) can be turned into a system of equations for fractional density energies

$$\begin{aligned} \Omega'_{\rm dm} &= 3 f_j \Omega_{\rm dm}\Omega_{\rm de}, \\ \Omega'_{\rm de} &= -3 f_j \Omega_{\rm dm}\Omega_{\rm de}. \end{aligned} \tag{5.60}$$

where $j = 0, 1, 2, 3$. Here $j = 0$ corresponds to the non-interacting case $f_0 = w_{\rm de} - w_{\rm dm}$.

For $j = 1, 2, 3$ (Q_1, Q_2, Q_3):

$$\begin{aligned} f_j &= w_{\rm eff,de\ }{}_j - w_{\rm eff,dm\ }{}_j, \\ f_1 &= f_0 + \frac{\gamma_m}{\Omega_{\rm de}}, \\ f_2 &= f_0 + \frac{\gamma_d}{1 - \Omega_{\rm de}}, \\ f_3 &= f_0 + \frac{\gamma_{\rm tot}}{\Omega_{\rm de}\left(1 - \Omega_{\rm de}\right)}. \end{aligned} \tag{5.61}$$

Let us now obtain the critical points of the autonomous system (5.59) by imposing the conditions $\Omega'_{\rm dm} = \Omega'_{\rm de} = 0$ and $\Omega_{\rm dm} + \Omega_{\rm de} = 1$. Critical points can be broken up into the following categories. The critical point M is the matter dominated phase with $\Omega_{\rm dm} = 1$ and the critical point E is the DE dominated phase with $\Omega_{\rm de} = 1$. If $f_j \propto 1/\Omega_{\rm dm}$ or $f_j \propto 1/\Omega_{\rm de}$ these two fixed points may not exist. Besides the above two fixed points, there are other solutions with $f_j = 0$. Note that an attractor is one of the stable critical points of the autonomous system.

If we analyse the linear perturbations about the critical point $\left(\bar{\Omega}_{\rm de}, \bar{\Omega}_{\rm de}\right)$ of the dynamical system Eqs. (5.60) and linearize them, we get

$$\hat{M} = \begin{pmatrix} 3f\left(\bar{\Omega}_{\rm de}\right)\bar{\Omega}_{\rm de} & 3\left(f\left(\bar{\Omega}_{\rm de}\right)\bar{\Omega}_{\rm dm} + f'\bar{\Omega}_{\rm dm}\bar{\Omega}_{\rm de}\right) \\ -3f\left(\bar{\Omega}_{\rm de}\right)\bar{\Omega}_{\rm de} & -3\left(f\left(\bar{\Omega}_{\rm de}\right)\bar{\Omega}_{\rm dm} + f'\bar{\Omega}_{\rm dm}\bar{\Omega}_{\rm de}\right) \end{pmatrix}. \tag{5.62}$$

Here, $f' \equiv df/d\Omega_{\rm de}$. The two eigenvalues of the matrix $\hat{M}$ that determine the stability of the corresponding critical point are

$$\begin{aligned} \lambda_1 &= 0, \\ \lambda_2 &= 3f\left(2\Omega_{\rm de} - 1\right) - 3f'\Omega_{\rm de}\left(1 - \Omega_{\rm de}\right). \end{aligned} \tag{5.63}$$

When λ_2 is positive, the corresponding critical point is an unstable node. "Unstable" means that the present phase will evolve, eventually, to other phases. When λ_2 is negative, the corresponding critical point is a stable node and the phase will last long.

Let's analyse the structure of phase space with non-linear interactions of the type (5.37). For the system of equations (5.55) the eigenvalues of the matrix $\hat{M}$ are roots of the equation

$$\begin{gathered} \lambda^2 + \left[2 + w_{\rm de} - w_{\rm de}\left(1 + w_{\rm de}\right)\frac{\partial_r \Pi}{\Pi}\right]\lambda + \left(1 + w_{\rm de} + w_{\rm de}\partial_\rho \Pi\right) = 0, \\ \partial_r \Pi \equiv \frac{\partial \Pi}{\partial r},\ \partial_\rho \Pi \equiv \frac{\partial \Pi}{\partial \rho}. \end{gathered} \tag{5.64}$$

The Eq. (5.64) has the solutions

$$\begin{aligned} \lambda_\pm = \frac{1}{2}\Bigg\{\left[w_{\rm de}\left(1 + w_{\rm de}\right)\frac{\partial_r \Pi}{\Pi} - \left(2 + w_{\rm de}\right)\right] \pm \\ \pm\sqrt{\left(2 + w_{\rm de} - w_{\rm de}\left(1 + w_{\rm de}\right)\frac{\partial_r \Pi}{\Pi}\right)^2 - 4\left(1 + w_{\rm de} + w_{\rm de}\partial_\rho \Pi\right)}\Bigg\}, \end{aligned} \tag{5.65}$$

where we have to require $1 + w_{\rm de} + w_{\rm de}\partial_\rho \Pi \neq 0$. In case these solutions are non-degenerate and real, they describe a stable critical point for $\lambda_\pm < 0$, an

unstable critical point for $\lambda_{\pm} > 0$ and a saddle if λ_+ and λ_- have different signs. For complex eigenvalues $\lambda_{\pm} = \alpha \pm i\beta$, it is the sign of α that determines the character of the stationary point. For $\alpha = 0$ the critical point is a center, for $\alpha < 0$ it is a stable focus, and for $\alpha > 0$ it is an unstable focus.

5.5. Examples of realization of interaction in the dark sector

5.5.1. $\Lambda(t)$ the simplest possibility of interaction of the dark components

Possibly the simplest explanation of the observed accelerated expansion of the Universe is DE in the form of a cosmological constant Λ, which modifies the Einstein equations

$$G^{\mu\nu} = 8\pi G T^{\mu\nu} \rightarrow G^{\mu\nu} = 8\pi G T^{\mu\nu} + \Lambda g^{\mu\nu}. \tag{5.66}$$

It is well known that flat models with a very small cosmological term (SCM) are in good agreement with almost all sets of cosmological observations. From the theoretical viewpoint, however, at least two problems arise: the so-called cosmological constant problem and the so-called coincidence problem. Attempts to resolve these problems on a phenomenological level are mainly tied to the introduction of interaction between the dark components. In cosmological models with interaction, Λ is necessarily a time-dependent quantity: the vacuum energy density is a time-dependent quantity because of its coupling with the other matter fields, the characteristics of which depend on time.

Historically, the possibility of a time varying $\Lambda(t)$ was first advanced in the paper by Bronstein [15]. A summary of the evolving ideas and their state at the beginning of the XX century can be seen in the review papers by Peebles and Ratra [42], Lima [36], and J.M. Overduin and F.I. Cooperstock [40]. An overview of the current state of the $\Lambda(t)$ problem can be found in [44].

From Eq. (5.66) the Bianchi identities imply that the coupling between a $\Lambda(t)$ term and DM particles must be of the type

$$u_\mu T^{\mu\nu}_{dm;\nu} = -u_\mu \left(\frac{\Lambda}{8\pi G} g^{\mu\nu}\right)_{;\nu} \tag{5.67}$$

or, equivalently,

$$\dot{\rho}_{\rm dm} + 3H\rho_{\rm dm} = -\dot{\rho}_\Lambda, \tag{5.68}$$

where $\rho_\Lambda = \Lambda/8\pi G$ is the energy density of the cosmological constant. This equation necessarily requires some kind of energy exchange between matter and vacuum energy, e.g. through vacuum decay into matter, or vice versa. It must be emphasized that the equation of state of the vacuum energy density retains its usual form $p_\Lambda(t) = -\rho_\Lambda(t)$, despite the fact that Λ evolves with time.

It should be noted [36] that the equation (5.68) may be rewritten to yield an expression for the rate of entropy production in the $\Lambda(t)$ model as

$$T\frac{dS}{dt} = -\frac{\dot{\Lambda}a^3}{8\pi G}. \tag{5.69}$$

From this equation, it immediately follows that Λ must over the course of time $\dot{\Lambda} < 0$ ($dS/dt > 0$), while the energy is transferred from the decaying vacuum to the material component.

Although we have been using the notation $\Lambda(t)$, the truth is that, in the majority of the papers, it depends only implicitly on the cosmological time through the scale factor $\Lambda = \Lambda(a)$ or the Hubble parameter $\Lambda = \Lambda(H)$, or even a combination of them. Phenomenological models with a variable cosmological constant are listed and reviewed in [40].

All these models have the same general defect: the expression defining $\Lambda(t)$ is obtained either using dimensional arguments or in a completely ad hoc way. The interaction between matter and DE cannot be derived in these models from the principle of least action in a relativistically covariant form. The expression defining $\Lambda(t)$ is obtained either using dimensional arguments or in a completely ad hoc way. Essentially, we have come face to face with the previously described general problem that plagues interaction in the dark sector. In the absence of a microscopic theory of interaction, we are prevented from pointing out the exact mechanisms of energy transfer between the components.

In the field of the Lagrangian description of the dynamic cosmological constant, a certain degree of progress was achieved within the framework of so-called $\Lambda\,(T)$ gravity [45]. In this theory the cosmological constant is a function of the trace of the energy-momentum tensor T. Within the framework of this approximation, the dynamics of the time-dependent cosmological constant can be described directly in terms of interacting components with the densities ρ_Λ and $\rho_{\rm dm}$,

$$\begin{aligned} \dot{\rho}_{\rm dm} + 3H\rho_{\rm dm} &= Q, \\ \dot{\rho}_\Lambda + 3H\left(\rho_\Lambda + p_\Lambda\right) &= -Q, \end{aligned} \tag{5.70}$$

where Q is the rate of the energy transfer from DE to DM,

$$Q = 3H\rho_{\rm dm}\frac{\Lambda' + 2\Lambda''\rho_{\rm dm}}{1 + 3\Lambda' + 2\Lambda''\rho_{\rm dm}}. \tag{5.71}$$

Here $\Lambda' = \dfrac{d\Lambda}{dT}$. We see that in this case, the interaction retains H dependence, but is now a non-linear function of $\rho_{\rm dm}$. We return to a linear dependence when $\dfrac{\Lambda''}{\Lambda'}\rho_{\rm dm} \ll 1$.

5.5.2. Interacting models in $f(R)$ -gravity

One of the possible ways to explain the acceleration of the Universe is to modify Einstein gravity by making the substitution $Rn \to f(R)$. The action in $f(R)$ gravity in the Jordan frame is

$$S = \frac{1}{2\kappa}\int d^4x\sqrt{-g}f(R) + S_m\left(g^{\mu\iota},\psi\right),\ S_m = \int d^4x\sqrt{-g}L_m\left(g^{\mu\iota},\psi\right), \quad (5.72)$$

where R is the Ricci scalar, $\kappa = 8\pi G$, and $L^{(m)}$ is the matter Lagrangian. and ψ represents all matter fields. It is possible to transform the action (5.72) from the original Jordan frame to the Einstein frame by using conformal transformations [31, 46]. In the Einstein frame, the model contains a coupling between the canonical scalar fields (DE) and the non-relativistic matter.

The variation (5.72) with respect to the metric $g_{\mu\nu}$ yields the field equation

$$f'R_{\mu\nu} - \frac{1}{2}fg_{\mu\nu} - \nabla_\mu\nabla_\nu f' + g_{\mu\nu}\Box f'' = kT^{(m)}_{\mu\nu},\ f' \equiv \frac{df}{dR}. \quad (5.73)$$

Here, the matter stress-energy tensor $T^{(m)}_{\mu\nu}$ is

$$T^{(m)}_{\mu\nu} = -\frac{2}{\sqrt{-g}}\frac{\delta\left(\sqrt{-g}L_m\right)}{\delta\left(g^{\mu\nu}\right)} \quad (5.74)$$

$f(R)$ gravity may be written as a scalar-tensor theory, by introducing a Legendre transformation $\{R, f\} \to \{\phi, U\}$ defined as

$$\begin{aligned} \phi &\equiv f'(R), \\ U\left(\phi\right) &\equiv R\left(\phi\right)f' - f\left[R\left(\phi\right)\right]. \end{aligned} \quad (5.75)$$

In this representation the field equations of $f(R)$ gravity can be derived from a Brans—Dicke type action given by

$$S = \frac{1}{2\kappa}\int d^4x\sqrt{-g}\left(\phi R - U(\phi) + L_m\right). \quad (5.76)$$

This is the so-called Jordan frame representation of the action. One can perform a canonical transformation and rewrite the action (5.76) in what is called the Einstein frame. Rescaling the metric as

$$g_{\mu\nu} \to \tilde{g}_{\mu\nu} = f'\,g_{\mu\nu} \quad (5.77)$$

and redefining $\phi \to \tilde{\phi}$ with

$$d\tilde{\phi} = \sqrt{\frac{3}{2k}}\frac{d\phi}{\phi} \quad (5.78)$$

the original theory can be mapped onto the Einstein frame, in which the 'new' scalar field $\tilde{\phi}$ couples minimally to the Ricci curvature and has canonical kinetic energy,

$$S = \int d^4x\sqrt{-g}\left[\frac{\tilde{R}}{2\kappa} - \frac{1}{2}\partial^\mu\tilde{\phi}\,\partial_\mu\tilde{\phi} - V(\tilde{\phi})\right] + S_m\left(e^{-2\beta\tilde{\phi}}\tilde{g}_{\mu\nu}, \psi\right). \tag{5.79}$$

The self-interacting potential $V(\tilde{\phi})$ is given by

$$V(\tilde{\phi}) = \frac{Rf' - f}{2\kappa f'^2}. \tag{5.80}$$

Clearly, a coupling of the scalar field $\tilde{\phi}$ with the matter sector is now induced. The strength of this coupling $\beta = \sqrt{1/6}$ 6 is fixed and is the same for all matter fields.

Taking $\tilde{g}_{\mu\nu}$ and $\tilde{\phi}$ as two independent variables, the variations of the action (5.79) yield the following field equations

$$\tilde{G}_{\mu\nu} = \kappa\left(\tilde{T}^{\tilde{\phi}}_{\mu\nu} + \tilde{T}^m_{\mu\nu}\right), \tag{5.81}$$

$$\Box\tilde{\phi} - \frac{dV(\tilde{\phi})}{d\tilde{\phi}} = -\beta\sqrt{\kappa}\tilde{T}^m, \tag{5.82}$$

where $\tilde{T}^m \equiv \tilde{g}^{\mu\nu}\tilde{T}^m_{\mu\nu}$. The latter equation shows that the evolution of the field ϕ is directly coupled to matter. Radiation, for which $\tilde{T}^m = 0$, is an obvious exception.

For a spatially flat homogeneous isotropic Universe the field equation (5.82) reduces to

$$\ddot{\phi} + 3H\dot{\phi} + \frac{dV}{d\phi} = -\beta\sqrt{\kappa}\rho_m. \tag{5.83}$$

Utilizing the usual definitions of density and pressure of a scalar field, the equation (5.83)can be transformed into

$$\dot{\rho}_\phi + 3H\left(1 + w_\phi\right)\rho_\phi = -Q,\ Q = \beta\sqrt{\kappa}\dot{\phi}\rho_m \tag{5.84}$$

In the final expressions (the formulas (5.84) and (5.86)), we opted not to write the tildes overhead. Let's now move to the Einstein frame for the matter conservation equation, which has the standard form $\dot{\rho}_m + 3H\rho_m = 0$ in the Jordan frame. The transfer is realized by the transforms

$$d\tilde{t} = \sqrt{F}dt,\ \tilde{a} = \sqrt{F}a,\ \tilde{H} = \frac{1}{\tilde{a}}\frac{d\tilde{a}}{d\tilde{t}} = \frac{1}{\sqrt{F}}\left(H + \frac{\dot{F}}{2F}\right),\ F = e^{-2\beta\sqrt{\kappa}\phi}. \tag{5.85}$$

Performing the transforms, we will obtain

$$\dot{\rho}_m + 3H\rho_m = Q. \tag{5.86}$$

The equations (5.84) and (5.86) represent a standard system of interacting components. It is important to note that interaction is "created" by our deviation from general relativity. Interaction vanishes when $\phi = \text{const}$ i.e. when $f(R)$ is linear function of R.

5.6. Interacting DE models in fractal cosmology

The fractal properties of quantum gravity theories in D dimensions have been explored in several contexts. To start off, the renormalizability of perturbative gravity at and near two topological dimensions drew much interest to $D = 2 + \epsilon$ models, with the hope of improving our understanding of the $D = 4$ case better [22, 29, 59].

Assuming that matter is minimally coupled with gravity, the total action is [16]

$$S = S_g + S_{\mathrm{m}}, \tag{5.87}$$

where S_g is

$$S_g = \frac{M_p^2}{2} \int \mathrm{d}\varrho(x)\, \sqrt{-g}\, (R - 2\lambda - \omega \partial_\mu v \partial^\mu v), \tag{5.88}$$

and

$$S_{\mathrm{m}} = \int \mathrm{d}\varrho \sqrt{-g} \mathcal{L}_{\mathrm{m}} \tag{5.89}$$

is the matter action. Here, g is the determinant of the dimensionless metric $g_{\mu\nu}$, $M_p^{-2} = 8\pi G$ is reduced Planck mass, R is the Ricci scalar, λ is the bare cosmological constant, and the term proportional to ω has been added because v, like the other geometric field $g_{\mu\nu}$, is now dynamical. Note that $d\varrho(x)$ is Lebesgue—Stieltjes measure generalizing the D-dimensional measure $\mathrm{d}^D x$. The scaling dimension of ϱ is $[\varrho] = -D\alpha \neq -D$, where $\alpha > 0$ is a positive parameter.

The derivation of the Einstein equations goes almost like it does in scalar-tensor models. Taking the variation of the action (5.87) with respect to the Friedmann—Robertson—Walker (FRW) metric $g_{\mu\nu}$, one can obtain the Friedmann equations in a fractal Universe, as was shown in [17]

$$\left(\frac{D}{2} - 1\right) H^2 + H\frac{\dot{v}}{v} - \frac{1}{2}\frac{\omega}{D-1}\dot{v}^2 = \frac{1}{M_p^2(D-1)}\rho + \frac{\lambda}{D-1} - \frac{k}{a^2}, \tag{5.90}$$

$$\frac{\Box v}{v} - (D-2)\left(H^2 + \dot{H} - H\frac{\dot{v}}{v} + \frac{\omega}{D-1}\dot{v}^2\right) + \frac{2\lambda}{D-1} = \frac{1}{M_p^2(D-1)}\left[(D-3)\rho + (D-1)p\right], \tag{5.91}$$

where $H = \dot{a}/a$ is the Hubble parameter, ρ and p are the total energy density and pressure of the ideal fluid composing the Universe. The parameter k denotes the curvature of the Universe, where $k = -1, 0, +1$ for the close, flat and open Universe, respectively. Clearly, when $v = 1$, Eqs. (5.90) and (5.91) transform to the standard Friedmann equations in Einstein GR.

If $\rho + p \neq 0$, the following (purely gravitational) equation is valid:

$$\dot{H} + (D-1)H^2 + \frac{2k}{a^2} + \frac{\Box v}{v} + H\frac{\dot{v}}{v} + \omega(v\Box v - \dot{v}^2) = 0. \tag{5.92}$$

The continuity equation in fractal cosmology takes the form

$$\dot{\rho} + \left[(D-1)H + \frac{\dot{v}}{v}\right](\rho + p) = 0, \tag{5.93}$$

when $v = 1$ and $D = 4$, we recover the standard Friedmann equations in four dimensions, Eqs. (5.90) and (5.91) (no gravitational constraint):

$$H^2 = \frac{1}{3M_p^2}\rho + \frac{\lambda}{3} - \frac{k}{a^2}, \tag{5.94}$$

$$H^2 + \dot{H} = -\frac{1}{6M_p^2}(3p + \rho) + \frac{\lambda}{3}. \tag{5.95}$$

On the other hand, for the measure weight

$$v = t^{-\beta}, \tag{5.96}$$

where β is given by $\beta \equiv D(1-\alpha)$, the gravitational constraint is switched on. The UV regime, in fact, describes short scales at which inhomogeneities should play some role. If these are small, the modified Friedmann equations define a background for perturbations rather than a self-consistent dynamics.

Recently [32] the holographic, new agegraphic and ghost DE models in the framework of fractal cosmology were investigated. In the next section we consider the universe in which DE interacting with DM.

For four-dimensional space with a FRW-metric in the fractal case, and the natural parameterization of the function as $v = t^{-\beta}$, the equations (5.93) transform to:

$$\dot{\rho}_m + \left(3H - \beta t^{-1}\right)\rho_m = Q, \tag{5.97}$$

$$\dot{\rho}_x + (1+w)\left(3H - \beta t^{-1}\right)\rho_x = -Q, \tag{5.98}$$

where ρ_m and ρ_x are densities of DM and DE respectively, and w is the EOS parameter for DE. It is convenient to use the relative energy densities of DE and DM in accordance with standard definitions:

$$\Omega_m = \frac{\rho_m}{3M_p^2H^2},\ \Omega_x = \frac{\rho_x}{3M_p^2H^2}. \tag{5.99}$$

The above equation can be written in terms of these density parameters as the following:

$$\begin{aligned}\dot{\Omega}_m + \left(3H - \beta t^{-1}\right)\Omega_m + 2\Omega_m\frac{\dot{H}}{H} &= \frac{Q}{3M_p^2H^2},\\ \dot{\Omega}_x + (1+w_x)\left(3H - \beta t^{-1}\right)\Omega_x + 2\Omega_x\frac{\dot{H}}{H} &= -\frac{Q}{3M_p^2H^2},\end{aligned} \tag{5.100}$$

where the dot denotes a derivative with respect to the cosmic time t. The differential equation for the Hubble parameter has the form

$$\dot{H} + H^2 - \frac{\beta H}{2t} + \frac{\beta(\beta+1)}{2t^2} + \frac{\omega\beta^2}{3t^{2(\beta+1)}} = -\frac{1}{2}((1+3w)\Omega_x + \Omega_m)H^2. \tag{5.101}$$

In order to obtain the Friedmann equation in terms of the relative densities, it is necessary to introduce the fictitious density in same way as $\Omega_k = k/(a^2H^2)$. So, we introduce the fractal relative density:

$$\Omega_f = \frac{\omega\dot{v}^2}{6H^2} - \frac{\dot{v}}{Hv}. \tag{5.102}$$

Taking into account the ansatz $v = t^{-\beta}$, we obtain the equation of motion for fractal relative density

$$\Omega_f = \frac{\omega\beta^2}{6H^2t^{2(\beta+1)}} + \frac{\beta}{Ht}. \tag{5.103}$$

Thus, the Friedman equation can be re-written in a very elegant form

$$\sum_{\alpha=k,f,x,m}\Omega_\alpha \equiv 1. \tag{5.104}$$

Note that within the framework of this definition, the values of the relative densities Ω_x or Ω_m can exceed 1.

5.6.1. Linear interaction of DM and DE

Below, we consider the simplest form of interaction — a linear combination of the decompositions densities of DM and DE in a flat Friedmann—Robertson—Walker fractal Universe with:

$$Q \equiv H(\delta\rho_x + \gamma\rho_m). \tag{5.105}$$

In this case, the equations of motion take the form

$$\begin{aligned}\dot{\Omega}_m + \left(3H - \beta t^{-1}\right)\Omega_m + 2\Omega_m\frac{\dot{H}}{H} &= H(\delta\Omega_x + \gamma\Omega_m),\\ \dot{\Omega}_x + (1+w_x)\left(3H - \beta t^{-1}\right)\Omega_x + 2\Omega_x\frac{\dot{H}}{H} &= -H(\delta\Omega_x + \gamma\Omega_m),\\ \dot{\Omega}_f + \left(\frac{\dot{H}}{H} + 2(1+\beta)t^{-1}\right)\Omega_f - \frac{(1+2\beta)\beta}{Ht} &= 0.\end{aligned} \tag{5.106}$$

Since the equations explicitly depend on time, it is not possible to find their analytical solution.

5.6.2. Analyzable case of DM—DE interaction

The analytical solution can be found only in the case when the Hubble parameter is inversely proportional to time, which is typical, for example, at the stage of nonrelativistic matter dominance. Suppose that at this stage the Hubble parameter has the form $H = \sigma t^{-1}$. Then the equations (5.100) take the following form

$$\begin{aligned} \Omega_m' &= \theta\Omega_m + \sigma\delta\Omega_x, \\ \Omega_x' &= -\delta\gamma\Omega_m + \upsilon\Omega_x, \end{aligned} \tag{5.107}$$

where $\theta = 2+\gamma\sigma+\beta-3\sigma,\ \upsilon = 2-(1+w)(3\sigma-\beta)-\delta\sigma$, and the prime denotes a derivative with respect to the logarithm of cosmic time $' \equiv \dfrac{d}{d\ln t}$. Note also that the parameter θ is physically meaningful under condition $\sigma > 0$, because we do not consider the collapsing universe. In this regime of evolution of the Universe the system of equations is autonomous and can be solved exactly. The characteristic equation of the system (5.107) has the form

$$\tau^2 - (\theta+\upsilon)\tau + \delta^2\sigma\gamma + \theta\upsilon = 0, \tag{5.108}$$

its roots are equal to:

$$\tau_\pm = \frac{\theta+\upsilon}{2}\left[1 \pm \sqrt{1 - 4\frac{(\delta^2\sigma\gamma+\theta\upsilon)}{(\theta+\upsilon)^2}}\right]. \tag{5.109}$$

Let us consider possible types of solutions, and indicate the critical points that correspond to them. As one can see, this model contains many parameters, making it cumbersome to analyze. Note that due to this feature, the system describes all possible types of critical points typical of coarse equilibrium states.

Recall that the values of β in the IR and UV regimes are $\beta_{\mathrm{IR}} = 0$ and $\beta_{\mathrm{UV}} = 2$, respectively. The UV regime, in fact, describes short scales at which inhomogeneities should play some role. If these are small, the modified Friedmann equations define a background for perturbations rather than a self-consistent dynamics.

There are six types of critical points:

1. Stable node $\tau_\pm \in \Re,\ \tau_\pm < 0, \tau_+ > \tau_- > 0,\ \theta+\upsilon < 0,\ 4(\delta^2\sigma\gamma+\theta\upsilon) < (\theta+\upsilon)^2,\ \delta^2\sigma\gamma+\theta\upsilon > 0$.

2. Unstable node: $\tau_\pm \in \Re,\ \tau_\pm > 0,\ \tau_+ > \tau_- > 0,\ \theta+\upsilon > 0,\ 4(\delta^2\sigma\gamma+\theta\upsilon) < (\theta+\upsilon)^2,\ \delta^2\sigma\gamma+\theta\upsilon > 0$.

3. Saddle point: $\tau_\pm \in \Re,\ \tau_+\tau_- < 0,\ \delta^2\sigma\gamma+\theta\upsilon < 0$.

4. Stable spiral point: $\tau_\pm \in \mathbb{C}, \tau\pm = \tau_1 \pm i\tau_2,\ \tau_1, \tau_2 \in \Re\ \tau_1, \tau_2 > 0, \theta+\upsilon < 0,\ (\theta+\upsilon)^2 < 4(\delta^2\sigma\gamma+\theta\upsilon)$.

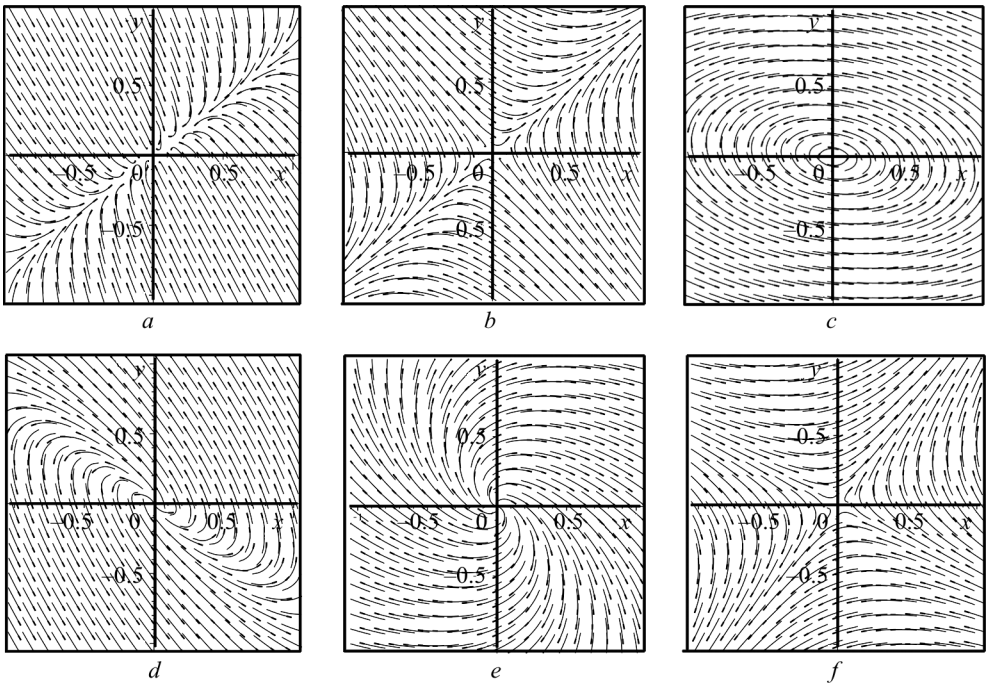

Fig. 5.1. Phase portraits for some types of critical points for $w = -1$: a — stable node, $\gamma = -2$, $\sigma = 3$, $\beta = -1$, $\delta = 3$, b — stable focus, $\gamma = -3$, $\sigma = 1$, $\beta = 2$, $\delta = 3$, c — center, $\gamma = 3$, $\sigma = 3$, $\beta = -1$, $\delta = 1$, d — unstable focus, $\gamma = 3$, $\sigma = 1$, $\beta = 2$, $\delta = 3$, e — unstable node, $\gamma = 3$, $\sigma = -3$, $\beta = 2$, $\delta = 3$, f — saddle, $\gamma = 3$, $\sigma = -3$, $\beta = 1$, $\delta = -2$

5. Unstable spiral point: $\tau_{\pm} \in \mathbb{C}$, $\tau\pm = \tau_1 \pm i\tau_2$, $\tau_1, \tau_2 \in \Re$ $\tau_1, \tau_2 < 0$, $\theta + \upsilon > 0$, $(\theta + \upsilon)^2 < 4(\delta^2\sigma\gamma + \theta\upsilon)$.

6. Elliptic fixed point $\tau_{\pm} \in \Im$, $\tau_{\pm} = \pm i\tau$, $\tau \in \Re$, $\theta = \upsilon$, $\delta^2\sigma\gamma + \theta\upsilon > 0$.

This completes a variety of critical points in the system (5.107). Some types of critical points that are typical for this system are shown in Fig. 5.1.

In most cases, the eigenvalues of the linearized system (5.107) will have eigenvalues with either positive, or negative and/or zero real parts. In these cases it is important to identify which orbits are attracted to the singular point, and which are repelled away as the independent variable (usually t) tends to infinity.

The local dynamics of a singular point may depend on one or more parameters. When small continuous changes in the parameter result in dramatic changes in the dynamics, the singular point is said to undergo a bifurcation. The values of the parameters which result in a bifurcation at the singular point can often be located by examining the linearized system. Singular point bifurcations will only occur if one (or more) of the eigenvalues of the linearized system is a function of the parameter. The bifurcations are located at

the parameter values for which the real part of an eigenvalue is zero. The Fig. 5.1 actually shows such bifurcations. Different types of critical points correspond to different values of parameters and hence different roots (5.109) of the characteristic equation (5.108).

5.7. Interacting holographic DE

The cosmological constant problem consists of the enormous difference (120 orders of magnitude) between the observed DE density in the form of the cosmological constant and its 'expected' value. The expectations are based on quite natural assumptions concerning the cutoff parameter of the integral that represents the density of zero-point vacuum oscillations. The holographic principle allows replacing 'natural assumptions' by more rigorous quantitative estimates.

In any effective quantum field theory defined in a spatial region of a characteristic size L and using an ultraviolet cutoff Λ, the entropy of the system has the form $S \propto \Lambda^3 L^3$. For example, fermions situated at the nodes of a spatial lattice of characteristic size L and period Λ^{-1} are in one of the $2^{(\Lambda L)^3}$ states. Consequently, the entropy of such a system is $S \propto \Lambda^3 L^3$. In accordance with the holographic principle, this quantity should satisfy the inequality [23]

$$L^3\Lambda^3 \leq S_{\rm BH} \equiv \frac{1}{4}\frac{A_{\rm BH}}{l_p^2} = \pi L^2 M_p^2, \tag{5.110}$$

where $S_{\rm BH}$ is the entropy of a black hole and $A_{\rm BH}$ is the surface area of a black hole event horizon, which in the simplest case coincides with the surface of a sphere of the radius L. Relation (5.110) shows that the value of the infrared (IR) cutoff cannot be chosen independently of the value of the ultraviolet (UV) cutoff [23]. In other words, physics at small UV scales depends on the physical parameters at large IR scales. For instance, when inequality (5.110) tends to an exact equality,

$$L \sim \Lambda^{-3} M_p^2. \tag{5.111}$$

Effective field theories with UV cutoff (5.111) necessarily involve numerous states having a gravitational radius exceeding the size of the region within which the theory is defined. In other words, for any cutoff parameter a sufficiently large volume exists in which the entropy in quantum field theory exceeds the Bekenstein limit. To verify this, we note that the effective quantum field theory is usually required to be capable of describing the system at the temperature $T \leq \Lambda$. For $T \gg 1/L$, this system has the thermal energy $M \sim L^3T^4$ and entropy $S \sim L^3T^3$. Condition (5.110) is satisfied for $T \leq \left(M_p^2/L\right)^{1/3}$, which corresponds to the gravitational radius $r_g \sim L(LM_p) \gg L$. To overcome this difficulty, an even stringent limitation is proposed in [23] for the IR cutoff,

$L \sim \Lambda^{-1}$, which excludes all states that are within the limits of their gravitational radii. Taking into account that

$$\rho_{\text{vac}} \approx \frac{\Lambda^4}{16\pi^2},$$

we can rewrite condition (5.110) as

$$L^3\rho_\Lambda \leq LM_p^2 \equiv 2M_{\text{BH}}, \tag{5.112}$$

where M_{BH} is the mass of the black hole of the gravitational radius L. So, by the order of magnitude, the total energy contained in a region of size L does not therefore exceed the mass of the black hole of the same size. The quantity ρ_Λ is conventionally called the holographic DE (HDE).

In the cosmological context we are interested in, if the total energy contained in a region of size L is postulated to not exceed the mass of the black hole of the same size, i.e.,

$$L^3\rho_\Lambda \leq M_{\text{BH}} \sim LM_p^2. \tag{5.113}$$

we reproduce the relation between small and large scales in a natural way. If inequality (5.113) were violated, the Universe would only be composed of black holes. Applying this relation to the Universe as a whole, it is natural to identify the IR scale with the Hubble radius H^{-1}.

$$\rho_\Lambda \sim L^{-2}M_p^2 \sim H^2M_p^2. \tag{5.114}$$

Taking into account that $M_p \simeq 1.2 \times 10^{19}\,\text{GeV}$; $H_0 \simeq 1.6 \times 10^{-42}\,\text{GeV}$. The last quantity is in good agreement with the observed value of DE density $\rho_\Lambda \sim 3 \times 10^{-47}\ \text{GeV}^4$. Therefore, in the framework of holographic dynamics, no problem with the cosmological constant exists.

We represent the holographic DE density as

$$\rho_{_L} = 3c^2M_p^2L^{-2}. \tag{5.115}$$

The coefficient $3c^2$ ($c > 0$) is introduced for convenience, and M_p further stands for reduced Planck mass: $M_p^{-2} = 8\pi G$.

There are many opportunities to choose from the infrared cutoff scale and, therefore, the same number of HDE models. Some of these models are flawed: a problem with the equation of state arises in choosing the Hubble radius as the IR scale: in this case, the HDE does not account for the accelerating expansion of the Universe. The first thing that suggests itself is to replace the Hubble radius by the particle horizon $R_p = a\int_0^t \frac{dt}{a} = a\int_0^a \frac{da}{Ha^2}$. Regretfully, such a replacement does not yield the desired result. For solving this and other problems that arise in the models with HDE, models of interacting HDE was proposed.

The HDE model with interaction between DE and DM was first investigated by B. Wang, Y.G. Gong, and E. Abdalla in [58]. As mentioned above, if dark energy interacts with cold dark matter, the continuity equations for them are

$$\dot{\rho}_{dm} + 3H\rho_{\rm dm} = Q, \tag{5.116}$$

$$\dot{\rho}_L + 3H(\rho_L + p_L) = -Q. \tag{5.117}$$

where Q represent the interaction term.

The interaction between the dark components in the HDE model has been extensively studied in [49]. It was found that the introduction of interaction may not only alleviate the cosmic coincidence problem, but also help to arrive at or cross the phantom divide line.

Next, we consider some models of interacting HDE, the main difference between them consists in the the choice of the infrared cutoff scale. There are various choices for the forms of Q. The most common choice is

$$Q = 3\alpha H\rho,$$

where α is a dimensionless constant, and ρ is taken to be the density of HDE, DM, or the sum of them. In this section, unless otherwise stated, we will consider the case

$$Q = 3\alpha H\rho_L. \tag{5.118}$$

We will obtain some useful expressions, without specifying the type of HDE. For the beginning we can differentiating in time the expression, we obtain a simple relation To start, we differentiate both sides of the expression (5.115) with respect to time in order to find

$$\dot{\rho}_L = -2\rho_L \frac{\dot{L}}{L}, \tag{5.119}$$

substitute this expression in the conservation equations can be obtain the effective equation of state parameter for the interacting HDE:

$$w_L \equiv \frac{p_L}{\rho_L} = \frac{2}{3}\frac{\dot{L}}{LH} - \alpha - 1. \tag{5.120}$$

5.7.1. The HDE with the Hubble radius as an IR Cut-off

Setting $L = H^{-1}$ in the above bound and working with the equality, it becomes

$$\rho_H = 3\,c^2 M_p^2 H^2. \tag{5.121}$$

The effective equation of state parameter takes the form

$$w_H = -\frac{2}{3}\frac{\dot{H}}{H^2} - \alpha - 1, \tag{5.122}$$

It is easily seen that in the case when the interaction between HDE and DM is reduced to the decay of the HDE, interaction parameter $\alpha > 0$, that contributes to the accelerated expansion of the universe. In this case, the Friedmann

equation has the exact solution, so for the Hubble parameter, we obtain

$$H = \frac{2(1-\alpha c^2)}{3-2\alpha c^2}\frac{A}{t}, \tag{5.123}$$

where A is an integration constant, and t is the cosmic time. The time dependence of the scale factor $a(t)$ has the form

$$a(t) = a_0 t^{\frac{2(1-\alpha c^2)}{3-2\alpha c^2}}, \tag{5.124}$$

where a_0 is an integration constant. In conclusion, we find for this model, the deceleration parameter is $q = -1 - \dfrac{\dot{H}}{H^2}$:

$$q(t) = \frac{1}{2(1-2\alpha c^2)}, \tag{5.125}$$

is easily seen that if we assume in equations (5.123)—(5.125) $\alpha = 0$, we obtain expressions for the universe filled by the non-relativistic matter. As seen in this model, the deceleration parameter is constant throughout the evolution of the universe and, therefore, can not explain change of phases slow (matter dominated) expansion to the accelerated (DE dominated) expansion of the universe.

Evidently, a change of ρ_H/ρ_m needs a corresponding change of c^2. Within the framework of this model so far, a dynamical evolution of the energy density ratio is impossible. In the article [41], the authors not only consider $L = H^{-1}$ model, but also studied the case of $c(t)$. In this case, the deceleration parameter is not a constant, which makes it possible (for the appropriate choice depends $c(t)$) to describe transient acceleration (see Section 5.8.3). As a way out it has been suggested again to replace the Hubble scale by the various suitable cosmological scales, like the event horizon.

5.7.2. Interacting HDE with the event horizon as an IR Cutoff

Although the suggesting as the infrared cutoff the scale Hubble radius that is the most simple and theoretically motivated, we have seen above such a choice can not provide the observed Universe even in the presence of interaction between HDE and DM. And furthermore, if the interaction rate is given by $Q = 9c^2\alpha M_p^2 H^3$ ($\alpha > 0$), it happens that the matter density ρ_m becomes negative for $a \ll 1$. This problem does not occur for $\alpha < 0$. Nevertheless, the case $\alpha < 0$ is disfavored by observational constraints.

In this subsection we will consider the cosmological models where the infrared cutoff scale is applied to the cosmological event horizon [33]. In this case,

$$L_f = a(t)\int_t^\infty \frac{1}{a(t')}dt'. \tag{5.126}$$

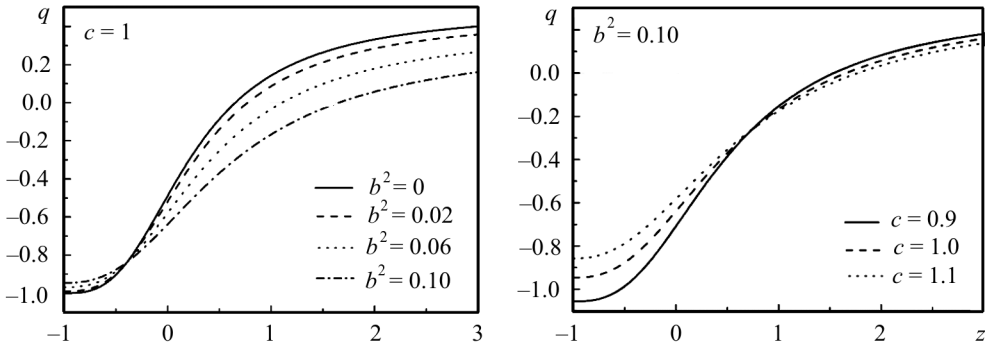

Fig. 5.2. On the left picture display the volution of the deceleration parameter q with a fixed parameter c. In this plot, we take $c = 1$, $\Omega_{f0} = 0.73$, and vary α as 0, 0.02, 0.06, and 0.10, respectively [61]. The right picture represent the evolution of the deceleration parameter q with a fixed coupling α. In this plot, we take $\alpha = 0.10$, $\Omega_{f0} = 0.73$, and vary c as 0.9, 1.0 and 1.1, respectively [61]

This horizon is the boundary of the volume which a stationary observer may ultimately observe. In the presence of big rip at $t = t_s$, ∞ in (5.126) must be replaced with t_s. Using

$$\dot{L}_f = HL_f - 1. \tag{5.127}$$

Substituting (5.126) to (5.120) yields

$$w = -\frac{1}{3} - \frac{2}{3c}\sqrt{\Omega_f} - \alpha. \tag{5.128}$$

Then we can compute the deceleration parameter

$$q = -\frac{\ddot{a}}{aH^2} = \frac{1}{2} + \frac{3}{2}w\Omega_f = \frac{1}{2} - (1 + 3\alpha)\Omega_f - \frac{1}{c}\Omega_f^{3/2}. \tag{5.129}$$

So, that to reveal the effect of interaction to the evolution of the Universe, the cases with dependence of the interaction parameter α for the deceleration parameter q are shown in Fig. 5.2. On the left picture in Fig. 5.2, we fix $c = 1$ and take the coupling constant α as 0, 0.02, 0.06, and 0.10, severally. Furthermore, the cases with a immutable α and various values of c are also interesting. The right picture represent fixing the coupling constant $\alpha = 0.10$, was plotted the evolution diagram of the deceleration parameter q with different values of c (here we take the values of c as 0.9, 1.0, and 1.1, severally). From Fig. 5.2 we find that the Universe passed an early deceleration and a late-time acceleration. Fig. 5.2 displays that, for a constant parameter c, the cosmic acceleration starts earlier for the cases with interaction than the ones without coupling (formerly, it was discussed by Amendola in [2]). Besides, the stronger the coupling both DE and DM is the earlier the acceleration of Universe began. Nevertheless, the cases with smaller coupling will lead to bigger acceleration conclusively in the distant future.

5.7.3. Interacting Holographic Ricci DE

The present subsection concentrates on the holographic Ricci DE (RDE) model. In this model, the IR cutoff length scale L takes the form of the absolute value of Ricci scalar curvature $|\mathcal{R}|^{-1/2}$, indeed in this instance the density of the holographic DE is $\rho_{\mathcal{R}} \propto \mathcal{R}$.

The energy density of DE in the interacting RDE model is defined as [28]

$$\rho_{\mathcal{R}} = 3\alpha M_p^2 \left(\dot{H} + 2H^2 + \frac{k}{a^2}\right), \tag{5.130}$$

where α is a dimensionless parameter. Note that $\rho_{\mathcal{R}}$ is proportional to the Ricci scalar curvature

$$\mathcal{R} = -6 \left(\dot{H} + 2H^2 + \frac{k}{a^2}\right). \tag{5.131}$$

In this subsection, for completeness and following article [55] a relativistic matter will be also considered as one of the components filling the Universe.

The time evolution of the scale factor $a(t)$ is described by the Friedmann equation

$$H^2 = \frac{1}{3M_p^2}(\rho_{\mathcal{R}} + \rho_m + \rho_\gamma + \rho_k), \tag{5.132}$$

where $\rho_{\mathcal{R}}$, ρ_m, ρ_γ and ρ_k represent energy density of DE, matter, radiation, and curvature, respectively. The interaction rate is given by

$$Q = \gamma H \rho_{\mathcal{R}}, \tag{5.133}$$

where γ is a dimensionless parameter. The energy density of radiation is given by $\rho_\gamma = \rho_{\gamma 0} a^{-4}$, where $\rho_{\gamma 0}$ is the present value of radiation density. We adopt a convention that $a(t_0) = 1$ for the present age of the Universe $t_0 \approx 14$ Gyr. According to Eq. (5.14) with Q in Eq. (5.133), the interaction can be relevant if $\gamma\rho_{\mathcal{R}}$ and ρ_m are comparable, whether or not the Universe is in the radiation-dominated epoch.

Combining with Eqs. (5.130) and (5.14), the Friedmann equation (5.132) is written as

$$\frac{\alpha}{2}\frac{d^2H^2}{dx^2} - \left(1 - \frac{7\alpha}{2} - \frac{\alpha\gamma}{2}\right)\frac{dH^2}{dx} - (3 - 6\alpha - 2\alpha\gamma)H^2 - \\ - \frac{\rho_{\gamma 0}}{3M_p^2}e^{-4x} - \{1 - \alpha(1+\gamma)\}ke^{-2x} = 0, \tag{5.134}$$

where $x = \ln a$. The solution to Eq. (5.134) is obtained as

$$\frac{H^2}{H_0^2} = A_+ e^{\sigma_+ x} + A_- e^{\sigma_- x} + A_\gamma e^{-4x} + A_k e^{-2x}, \tag{5.135}$$

where

$$\sigma_{\pm} = \frac{2 - 7\alpha - \alpha\gamma \pm \sqrt{(2-\alpha)^2 - 2\alpha(\alpha+2)\gamma + \alpha^2\gamma^2}}{2\alpha}, \tag{5.136}$$

$\Omega_{\gamma 0} = \rho_{\gamma 0}/\rho_{c0}$, $\Omega_{k0} = -k/H_0^2$ and $\rho_{c0} = 3M_p^2 H_0^2$. Note that $\sigma_{\pm}$ can be imaginary for sufficiently large α and γ. This implies that there is a parameter region where H^2 has oscillatory behavior. However, this region is not phenomenologically viable. The constants $\Omega_{\gamma 0}$ and Ω_{k0} are the present value of Ω_γ and Ω_k, respectively. The constants A_γ, A_k and $A_\pm$ are given by

$$A_\gamma = \Omega_{\gamma 0}, \tag{5.137}$$

$$A_k = \Omega_{k0}, \tag{5.138}$$

$$A_\pm = \pm\frac{\alpha(\sigma_\mp + 3)\Omega_{k0} + 2\Omega_{\Lambda 0} - \alpha(1-\Omega_{\gamma 0})(\sigma_\mp + 4)}{\alpha(\sigma_+ - \sigma_-)}. \tag{5.139}$$

In the non-interaction ($\gamma = 0$), Eq. (5.135) the result reduces to be obtained in [28]. In this case, the constants in Eq. (5.136) are $\sigma_+ = -4 + 2/\alpha$ and $\sigma_- = -3$.

Replacing Eq. (5.135) to Eq. (5.130), the Ricci DE density is given by

$$\rho_{\mathcal{R}} = \rho_{c0} \sum_{i=+,-} \alpha \left(\frac{\sigma_i}{2} + 2\right) A_i e^{\sigma_i x}. \tag{5.140}$$

Moreover, the matter density is

$$\rho_m = \rho_{c0} \sum_{i=+,-} \left\{1 - \alpha \left(\frac{\sigma_i}{2} + 2\right)\right\} A_i e^{\sigma_i x}. \tag{5.141}$$

The equation of state of DE can be found by substituting Eq. (5.140) into the following expression:

$$w_{\mathcal{R}} = -1 - \frac{1}{3}\left(\gamma + \frac{1}{\rho_{\mathcal{R}}}\frac{d\rho_{\mathcal{R}}}{dx}\right). \tag{5.142}$$

In Eqs. (5.140) and (5.141), the term proportional to $e^{\sigma_- x}$ is dominant in the past $a \ll 1$, while the term proportional to $e^{\sigma_+ x}$ is dominant in the future $a \gg 1$. As an illustration, let us consider the case $\alpha = 0.45$ and $\gamma = 0.15$ which corresponds to $\sigma_+ \approx 0.25$ and $\sigma_- \approx -3.0$. In the past $a \ll 1$, the ratio of Eq. (5.141) to Eq. (5.140) is $\rho_m/\rho_{\mathcal{R}} \approx \alpha^{-1}(2 + \sigma_-/2)^{-1} - 1 \approx 3.4$, while $\rho_m/\rho_{\mathcal{R}} \approx \alpha^{-1}(2 + \sigma_+/2)^{-1} - 1 \approx 0.045$ in the future $a \gg 1$.

5.8. Impact of interaction on cosmological dynamics

5.8.1. Transition from decelerated to accelerated expansion through interaction

In SCM, the transition from decelerated to accelerated expansion is related to the increase of the relative density of the cosmological constant. During analysis of interaction in the dark sector, we ask ourselves an obvious question: can we build a viable cosmological model in which this transition is the result of interaction in the dark sector [64, 65]. The question appears to be a valid one, since interaction regulates the relative densities of the accelerating (DE) and decelerating (matter) components.

We assume the dark components interact with each other according to

$$\begin{aligned} \dot{\rho}_{\rm dm} + 3H\rho_{\rm dm} &= \frac{\dot{f}}{f}\rho_{\rm dm}, \\ \dot{\rho}_{\rm de} + 3H\left(1+w\right)\rho_{\rm de} &= -\frac{\dot{f}}{f}\rho_{\rm dm}, \end{aligned} \tag{5.143}$$

where the interaction is described by a time dependent function $f(t)$. Let's write the Friedmann equations in the form

$$\begin{aligned} 3H^2 &= 8\pi G\rho, \\ \frac{\dot{H}}{H^2} &= -\frac{3}{2}\left(1+\frac{p}{\rho}\right), \end{aligned} \tag{5.144}$$

where $\rho = \rho_{\rm dm} + \rho_{\rm de}$, $p = p_{\rm de}$. The matter energy density behaves as

$$\rho_{\rm dm} = \rho_{\rm dm,0}\left(\frac{a_0}{a}\right)^3 \frac{f}{f_0}. \tag{5.145}$$

Because the total energy has to be conserved, the DE density therefore, behaves according to

$$\dot{\rho}_{\rm de} + 3H\left(1+w_{\rm eff}\right)\rho_{\rm de} = 0,\ w_{\rm eff} \equiv w + \frac{\dot{f}}{3Hf}r, \tag{5.146}$$

where $r = \rho_{\rm dm}/\rho_{\rm de}$. In the case of $r = {\rm const}$ we find that

$$w_{\rm eff} = -\frac{\dot{f}}{3Hf},\ w = \left(1+r\right)w_{\rm eff}. \tag{5.147}$$

Under this condition, the total equation of state is

$$\frac{p}{\rho} = \frac{p_{\rm de}}{\rho_{\rm de}+\rho_{\rm dm}} = \frac{w}{1+r} = w_{\rm eff}. \tag{5.148}$$

From the last equation (5.144), the deceleration parameter $q = -1 - \dfrac{\dot{H}}{H^2}$ is

$$q = \frac{1}{2}\left(\frac{3p}{\rho} + 1\right). \tag{5.149}$$

Using (5.147) and (5.148), we obtain

$$q = \frac{1}{2}\left(1 - \frac{\dot{f}}{Hf}\right). \tag{5.150}$$

The sign of q crucially depends on the ratio $\frac{\dot{f}}{Hf}$. For $\frac{\dot{f}}{Hf} < 1$ we have $q > 0$, i.e., decelerated expansion. For $\frac{\dot{f}}{Hf} > 1$ we have $q < 0$ and accelerated expansion. If, in particular, f is such that the ratio $\frac{\dot{f}}{Hf}$ changes from $\frac{\dot{f}}{Hf} < 1$ to $\frac{\dot{f}}{Hf} > 1$, this corresponds to a transition from decelerated to accelerated expansion under the condition of a constant energy density ratio r. Consequently, this transition occurs solely due to interaction.

The analysed case of $r = \text{const}$ seems exotic, and clearly contradicts SCM, where $r \propto a^{-3}$. But, as we saw, it is exactly this dependence that is found in the context of holographic DE models. This relation has the attractive feature that, by identifying the infrared cutoff length with the present Hubble scale, the corresponding ultraviolet cutoff energy density turns out to be of the order of the observed value of the cosmological constant parameter. However, the choice of infrared cutoff length is not consistent with the accelerated expansion of the Universe. As we see, this clear contradiction can become a positive feature [64], if we take into account interaction in the dark sector.

5.8.2. Interacting models as solutions to the cosmic coincidence problem

For constant w_{de}, the energy density of DE scales as $\rho_{\text{de}} \propto$ $\propto a^{-3(1+w_{\text{de}})}$. Observations constrain w_{de} to be very close to -1. Thus, the DE density varies relatively slowly with the scale factor. The matter density, in contrast, scales as $\rho_{\text{dm}} \propto a^{-3}$. This leads to the "well-known coincidence problem": while the matter and DE densities today are nearly within a factor of two of each other, at early times $\rho_{\text{dm}} \gg \rho_{\text{de}}$, and in the far future we expect $\rho_{\text{de}} \gg \rho_{\text{dm}}$. It would appear, then, that we live in a very specific time. Now the question is why is it happening now? Is it a mere coincidence or is there some deep underlying reason behind it? For the sake of viability any cosmological model should give an answer to this question. Models attempting to solve the coincidence problem must take into account interactions between components. Attempts to resolve the coincidence problem as a consequence of interaction between the matter sector and DE have a rich history [19, 21, 26, 37].

Let's analyse the main approaches we can take to resolving the coincidence problem in models with interaction in the dark sector. The key idea is exceedingly simple [21]. A numeric ratio of the "coincidence" is the ratio $r \equiv \rho_{\rm dm}/\rho_{\rm de}$. As we saw in Section 5.3, if we assume that $r \propto a^{-\xi}$, then it can be shown that ξ is related directly to the interaction between the dark components — Q (see Eq. (5.14)). In SCM $\xi = 3$. Therefore, for any value $\xi < 3$ the coincidence problem is less severe than for the SCM model. Let's stop and think about that statement. Using the first Friedmann equation for a spatially flat Universe, and the conservation equation we obtain ($8\pi G = 1$)

$$\dot{r} = 3Hr\left[w_{\rm de} + \frac{Q}{9H^3}\frac{(r+1)^2}{r}\right]. \tag{5.151}$$

For $Q > 0$ (i.e., when energy transfers from DE to DM) the ratio r evolves more slowly than in the SCM model. This certainly alleviates the coincidence problem.

Using

$$\dot{r} = \dot{H}\frac{dr}{dH},\ \dot{H} = -\frac{1}{2}\left(\rho_{\rm dm} + \rho_{\rm de} + p_{\rm de}\right) = -\frac{3}{2}\frac{1 + w_{\rm de} + r}{1 + r}H^2. \tag{5.152}$$

Let's write (5.151) as

$$\frac{dr}{dH} = \frac{I}{H},\ I \equiv -2r\frac{1+r}{1+w_{\rm de}+r}\left[w_{\rm de} + \frac{Q}{9H^3}\frac{(r+1)^2}{r}\right]. \tag{5.153}$$

The Eq. (5.153) can be integrated whenever an expression for the interaction Q in terms of H and r is given. Three following linear models for the coupling were considered

$$Q = 3\alpha H\left(\rho_{\rm dm} + \rho_{\rm de}\right),\ Q = 3\beta H\rho_{\rm dm},\ Q = 3\gamma H\rho_{\rm de},$$

where the phenomenological parameters, α, β, and η are dimensionless, positive constants. Consider as example the first model. This model fits very well data from SN Ia, CMB, and large scale structure formation provided $\alpha < 2.3 \times 10^{-3}$ [39]. The remarkable property of this model is that the ratio r tends to a stationary but unstable value at early times, r_s^+ and to a stationary and stable value, r_s^-, (an attractor) at late times. Consequently, as the Universe expands, $r\,(a)$ smoothly evolves from r_s^+ to the attractor solution r_s^-.

5.8.3. The problem of transient acceleration

Unlike fundamental theories, physical models only reflect the current state of our understanding of a process or phenomenon for the description of which they were developed. The efficiency of a model is to a significant extent determined by its flexibility, i.e., its ability to update when new information appears. Precisely for this reason, the evolution of any broadly applied model is accompanied by numerous generalizations aimed at resolving conceptual problems, as well as a description of the ever increasing number of observations. In the case of the SCM, these generalizations can be divided into two main classes. The first is composed of generalizations that replace the cosmological constant with more complicated dynamic forms of DE, for which the possibility of their interaction with DM must be taken into account. Generalizations pertaining to the second class are of a more radical character. The ultimate goal of these generalizations (explicit or latent) consists in the complete renunciation of dark components by means of modifying Einstein's equations. The generalizations of both the first and second classes can be demonstrated by means of a phenomenon that has been termed "transient acceleration".

Barrow [10] was among the first to indicate that transient acceleration is possible in principle. He showed that within quite sound scenarios that explain the current accelerated expansion of the Universe, the possibility was not excluded of a return to the era of domination of nonrelativistic matter and, consequently, to decelerating expansion. Therefore, the transition to accelerating expansion does not necessarily mean eternal accelerating expansion. Moreover, in Barrow's article, it was shown to be neither the only one possible nor the most probable course of events.

5.8.4. Observational evidence

Based on the independent observational data, including SNe-Ia brilliance curves, signatures of baryon acoustic oscillations (BAO) in the galaxy distribution and fluctuations in the cosmic microwave background (CMB), it was shown in [53] that the acceleration with which the Universe expands has reached its maximum value and is decreasing at present (Fig. 5.3). In terms of the deceleration parameter, this means that this parameter has reached its minimum value and is increasing at present. Hence, the main result of the analysis in Ref. [53] is that the SCM is not the only explanation of the observational data (although it is the simplest), and the accelerated expansion of the Universe in which DE presently dominates is merely a transition phenomenon. We note that it is also shown in Ref. [53] that using the Chevallier—Polarski—Linder (CPL) parametrization,

$$w(z) = w_0 + \frac{w_a\, z}{1+z}, \tag{5.154}$$

for the EOS parameter does not allow us to unambiguously combinine data obtained from observations of close supernova, such as SNe-Ia, and of the CMB anisotropy. A possible resolution of this contradiction is to renounce this parameterization and adopt a different one. In Ref. [53], a parameterization was proposed that is capable of uniting these arrays of data:

$$w(z) = -\frac{1 + \tanh\left[(z - z_t)\Delta\right]}{2}. \tag{5.155}$$

In this approximation, $w = -1$ at the early stages of the evolution of the Universe, and w increases to its maximum value $w \sim 0$, at small z. Figure 5.3 shows the dependence of the deceleration parameter q restored using the parameterization (5.155).

In 2010, in the framework of the Supernova Cosmology Project (SCP), the most recent array of data on bursts of supernova was published [1], which includes 557 events, making it the largest present-day body of data in this field. Moreover, the array of data on supernova with small red shifts ($z < 0.3$) has been significantly enlarged.

At present, there are already several studies [34, 35] in which these observations are analyzed in order to check the hypothesis of transient acceleration. All the authors agree that the final answer can only be given by the repeated, more precise observations. Moreover, it seems that in order to obtain consistent results, the entire technique of data handling has to be corrected. For example, as shown in [34, 35] (Fig. 5.4), there are contradictions between the data obtained from observations of SNe-Ia and BAO at small red shifts and CMB observations at large z. The contradiction consists in the fact that the analysis of two separate series of data yields opposite results. For example, when only the SNe-Ia and BAO data are used, the probability that the acceleration rate of the expansion of the Universe has already reached its maximum $z \sim 0.3$ and is at present starting to decrease turns out to be quite high. However, if these data are supplemented with the CMB observations, the results of the analysis change substantially and no deviations from the SCM model are revealed.

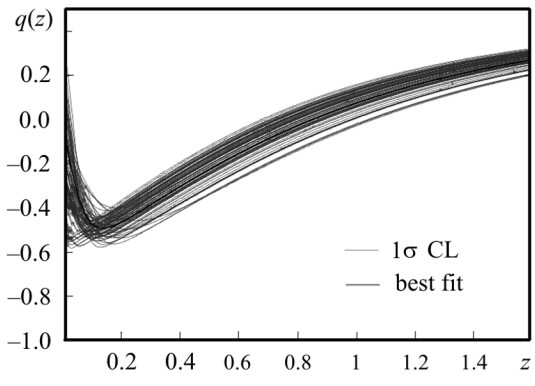

Fig. 5.3. The cosmological deceleration parameter $q(z)$, reconstructed using a combination of SN Ia, BAO and CMB data and the ansatz (5.155). The solid red lines show the best fit reconstructed results, while the dashed green lines show reconstructed results within 1σ CL [53]

Therefore, the restoration of the DE evolutionary dependence

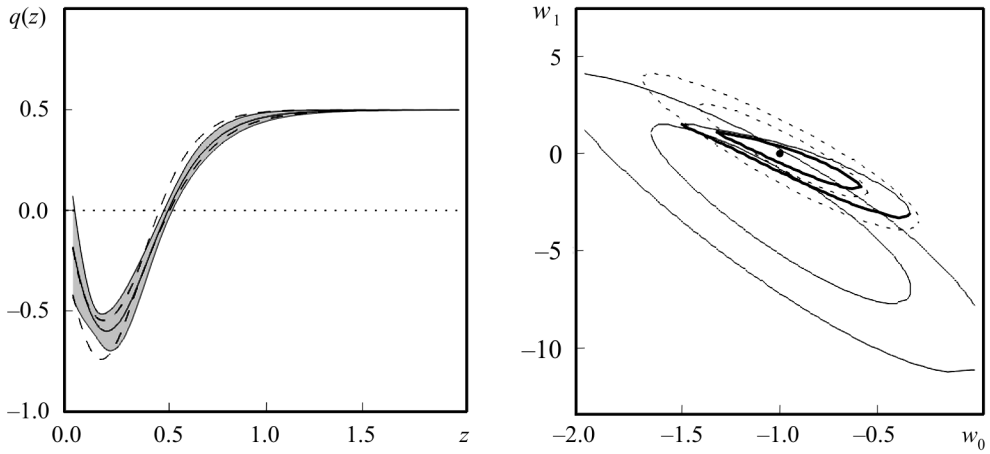

Fig. 5.4. The left panel represent the results reconstructed from Union2 + BAO and show the evolutionary behaviors of $q(z)$ at the 68.3 % confidence level. The gray regions and the regions between two long dashed lines show the results without and with the systematic errors in the SNIa, respectively. The right panel represent the 68.3 % and 95 % confidence level regions for w_0 versus w_1 in the CPL parametrization, $w = w_0 + w_1 z/(1+z)$. In the right panel, the system error in the SNIa is considered. The dashed, solid and thick solid lines represent the results obtained from Union2S, Union2S + BAO and Union2S + BAO + CMB, respectively. The point at $w_0 = -1$, $w_1 = 0$ represents the spatially flat ΛCDM model

and the answer to the question of whether the expansion of our Universe will decelerate or if the accelerating expansion will go on forever (as in the SCM) depends strongly on the data obtained from observations of SNE-Ia, their quality, the technique used in the reconstruction of the cosmological parameters (such as $q(z), w(z)$ and $\Omega_{\rm de}$), and actual parameterization of the DE equation of state. For a detailed answer to this question, we must wait for more precise observational data and find methods of their analysis that are less model-dependent.

Decaying cosmological constant and transient acceleration. As a simple example of transient acceleration, we consider a model with a decaying cosmological constant:

$$\dot{\rho}_m + 3\frac{\dot{a}}{a}\rho_m = -\dot{\rho}_\Lambda, \tag{5.156}$$

where ρ_m and ρ_Λ are the densities of the DM energy and of the cosmological constant Λ. A the early stages of the expansion of the Universe, when ρ_Λ is quite small, such a decay does not influence cosmological evolution in any way. At later stages, as the DE contribution increases, its decay has an ever increasing effect on the standard dependence of the DM energy density $\rho_m \propto a^{-3}$ on the scale factor a. We consider the deviation to be described by a function of the scale factor $\epsilon(a)$

$$\rho_m = \rho_{m,0} a^{-3+\epsilon(a)}, \tag{5.157}$$

where $a_0 = 1$ in the present epoch. Other fields of matter (radiation, baryons) evolve independently and are conserved. Hence, the DE density has the form

$$\rho_\Lambda = \rho_{m0} \int_a^1 \frac{\epsilon(\tilde{a}) + \tilde{a}\epsilon' \ln(\tilde{a})}{\tilde{a}^{4-\epsilon(a)}} d\tilde{a} + \mathrm{X}, \tag{5.158}$$

where the prime denotes the derivative with respect to the scale factor and X is the integration constant. If radiation is neglected, the first Friedmann equation takes the form

$$H = H_0 \left[\Omega_{b,0} a^{-3} + \Omega_{m0}\varphi(a) + \Omega_{\mathrm{X},0}\right]^{1/2}, \tag{5.159}$$

The function $\varphi(a)$ is then written as

$$\varphi(a) = a^{-3+\epsilon(a)} + \int_a^1 \frac{\epsilon(\tilde{a}) + \tilde{a}\epsilon' \ln(\tilde{a})}{\tilde{a}^{4-\epsilon(a)}} d\tilde{a}, \tag{5.160}$$

where $\Omega_{\mathrm{X},0}$, is the relative contribution of the constant X to the common relative density. To proceed, it is necessary to make some assumptions concerning the concrete form of $\epsilon(a)$. Here, we follow the original work [24], and consider the simplest case

$$\epsilon(a) = \epsilon_0 a^\xi \ = \epsilon_0 (1+z)^{-\xi}, \tag{5.161}$$

where ϵ_0 and ξ can take both positive and negative values. It follows from the expression (5.158) that

$$\rho_\Lambda = \rho_{m0}\epsilon_0 \int_a^1 \frac{[1 + \ln(\tilde{a}^\xi)]}{\tilde{a}^{4-\xi-\epsilon_0\tilde{a}^\xi}} d\tilde{a} + \mathrm{X}. \tag{5.162}$$

We note that the case $\epsilon_0 = 0$ corresponds to the SCM, i.e., $\mathrm{X} \equiv \rho_\Lambda$. Using the formulas presented above, it is not difficult to also obtain the dependences for the relative densities $\Omega_b(a)$, $\Omega_m(a)$ and $\Omega_\Lambda(a)$:

$$\Omega_b(a) = \frac{a^{-3}}{\mathrm{A} + a^{-3} + \mathrm{B}^{-1}\varphi(a)}, \tag{5.163a}$$

$$\Omega_m(a) = \frac{a^{-3+\epsilon(a)}}{\mathrm{D} + \mathrm{B}a^{-3} + \varphi(a)}, \tag{5.163b}$$

$$\Omega_\Lambda(a) = \frac{\mathrm{D} + \varphi(a) - a^{-3+\epsilon(a)}}{\mathrm{D} + \mathrm{B}a^{-3} + \varphi(a)}, \tag{5.163c}$$

where $\mathrm{A} = \Omega_{\mathrm{X},0}/\Omega_{b,0}$, $\mathrm{B} = \Omega_{b,0}/\Omega_{m0}$ and $\mathrm{D} = \Omega_{\mathrm{X},0}/\Omega_{m0}$.

Within this simple model, it is practically possible to obtain any dynamics of the Universe with the aid of an appropriate choice of the parameters ϵ_0 and ξ. The case of immediate interest is where $\epsilon_0 > 0$ and ξ takes on large positive

values ($\xi \gtrsim 0.8$). The solid curve in Fig. 5.5 shows the dependence of the deceleration parameter for $\xi = 1.0$ and $\epsilon_0 = 0.1$. We note that at present, for these parameters, when $a \sim 1$, the expansion of the Universe is accelerating, but the dominance of DE is not eternal, unlike in the case of the SCM, and when $a \gg 1$, the Universe will enter a new era of dominance of nonrelativistic matter. Such a form of dynamic behavior is unusual for most models with $\Lambda(t)$ or models with interacting quintessence discussed in the literature, but it is characteristic of the so-called thawing [18] and hybrid [5] potentials that follow from string theory or M-theory.

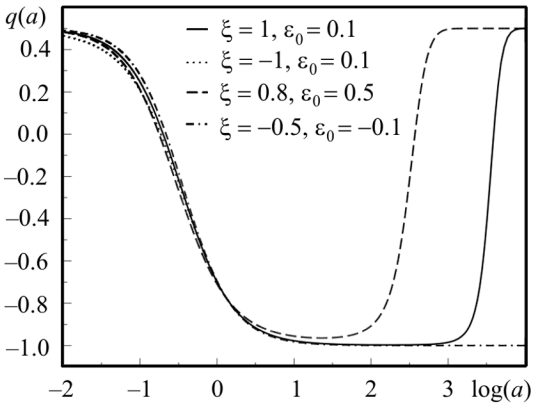

Fig. 5.5. The deceleration parameter as function of $\log(a)$ for some selected values of ϵ_0 and ξ

To better represent the phenomenon of transient acceleration, we find the explicit form of the deceleration parameter $q = -a\ddot{a}/\dot{a}^2$, in this model:

$$q(a) = \frac{3}{2}\frac{\Omega_{b,0}a^{-3} + \Omega_{m0}a^{\epsilon(a)-3}}{\Omega_{b,0}a^{-3} + \Omega_{m0}\varphi(a) + \Omega_{\mathrm{X},0}} - 1, \tag{5.164}$$

The parameter q is represented as a function of $\log(a)$ for different values of ξ and ϵ_0 in Fig. 5.5. We note that in the distant past ($a \ll 1$), the deceleration parameter $q(a) \to 1/2$, which corresponds to a matter-dominated Universe. However, for certain values of parameter ξ, a long (but finite, in contrast to the case of the SCM) era of accelerated expansion sets in. In the distant future ($a \gg 1$), the Universe again returns to decelerated expansion ($q > 0$).

Transient acceleration in an Universe with the interacting components. We consider a spatially flat Universe consisting of three components: DE, DM, and baryons. The first Friedmann equation for such a Universe has the form

$$3M_{\mathrm{Pl}}^2H^2 = \rho_{\mathrm{de}} + \rho_m + \rho_b, \tag{5.165}$$

where, as usual, ρ_{de} is the DE density, ρ_m is the DM energy density, ρ_b is the baryon energy density. The equation of state for DE has the form $p_{\mathrm{de}} = w\rho_{\mathrm{de}}$.

When interaction is present, the conservation equations become

$$\begin{gathered}\dot{\rho}_{\mathrm{de}} + 3H(1+w)\rho_{\mathrm{de}} = -Q;\\ \dot{\rho}_m + 3H\rho_m = Q.\end{gathered} \tag{5.166}$$

The conservation equation for the baryon component is

$$\dot{\rho}_b + 3H\rho_b = 0 \;\Rightarrow\; \rho_b = \rho_{b0}\left(\frac{a_0}{a}\right)^3. \tag{5.167}$$

The total density is $\rho = \rho_m + \rho_b + \rho_{\rm de}$. Without loss of generality, we assume that the energy density ρ_m is expressed as

$$\rho_m = \tilde{\rho}_{m0} \left(\frac{a_0}{a}\right)^3 f(a), \tag{5.168}$$

where $\tilde{\rho}_{m0}$ and a_0 are constants and $f(a)$ is an arbitrary differentiable function of the scale factor. From (5.166) and (5.168), we obtain

$$Q = \rho_m \frac{\dot{f}}{f} = \tilde{\rho}_{m0} \left(\frac{a_0}{a}\right)^3 \dot{f}. \tag{5.169}$$

Let's take

$$f(a) = 1 + g(a). \tag{5.170}$$

In the absence of interaction, $f(a) = 1$; therefore, the function $g(a)$ is responsible for interaction. Then, taking into account that

$$\dot{f} = \dot{g} = \frac{dg}{da}\dot{a}, \tag{5.171}$$

we obtain

$$Q = \tilde{\rho}_{m0} \frac{dg}{da} \dot{a} \left(\frac{a_0}{a}\right)^3. \tag{5.172}$$

This means that

$$\rho_m = \tilde{\rho}_{m0} \left(1 + g\right) \left(\frac{a_0}{a}\right)^3, \tag{5.173}$$

where $\rho_{m0} = \rho_m(a_0)$ if the interaction exists, and $\tilde{\rho}_{m0}$ in the absence of interaction. The two initial values of the DM density are related as

$$\rho_{m0} = \tilde{\rho}_{m0} \left(1 + g_0\right), \tag{5.174}$$

where $g_0 \equiv g(a_0)$. As can be seen from (5.169) when $Q > 0$, DE decays into DM, $\frac{dg}{da} > 0$. When $\frac{dg}{da} < 0$, the decay proceeds in the opposite direction. From (5.166) and (5.172) we obtain

$$\dot{\rho}_{\rm de} + 3H \left(1 + w\right) \rho_{\rm de} = -\tilde{\rho}_{m0} \frac{dg}{da} \dot{a} \left(\frac{a_0}{a}\right)^3. \tag{5.175}$$

When $w = \text{const}$ the solution of (5.175) has the form

$$\begin{aligned} \rho_{\rm de} = \left(\rho_{m0} + \tilde{\rho}_{m0} g_0\right) \left(\frac{a_0}{a}\right)^{3(1+w)} - \tilde{\rho}_{m0} \left(\frac{a_0}{a}\right)^3 g + \\ + 3w \tilde{\rho}_{m0} a_0^3 a^{-3(1+w)} \int\limits_{a_0}^{a} da g a^{3w-1}. \end{aligned} \tag{5.176}$$

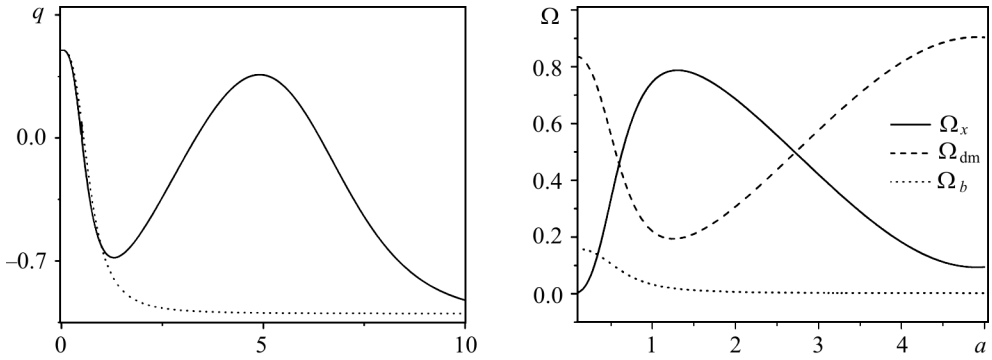

Fig. 5.6. On the left: the dependencies of relative densities on the scale factor for $n = 7$ and $\sigma = 1.5$ (on the left). On the right: the dependencies of deceleration parameter on the scale factor in the model with interacting DE and DM $q(a)$(solid line) with $n = 7$ and $\sigma = 1.5$ in comparison to SCM (dashed line)

We rewrite the second Friedmann equation in terms of $g(a)$

$$\frac{\ddot{a}}{a} = -\frac{1}{6}\left\{\tilde{\rho}_{m0}\left(1+g\right)\left(\frac{a_0}{a}\right)^3 + \rho_{b0}\left(\frac{a_0}{a}\right)^3 + (1+3w)\times\right.$$
$$\times\left[\left(\rho_{m0}+\tilde{\rho}_{m0}g_0\right)\left(\frac{a_0}{a}\right)^{3(1+w)} - \tilde{\rho}_{m0}\left(\frac{a_0}{a}\right)^3 g + \right. \tag{5.177}$$
$$\left.\left. + 3w\tilde{\rho}_{m0}a_0^3 a^{-3(1+w)}\int\limits_{a_0}^{a} daga^{3w-1}\right]\right\}.$$

To solve Eqn. (5.177) it is necessary to define the function $g(a)$. Since the nature of DE and DM is unknown, it is impossible to indicate the form of $g(a)$ based on first principles; therefore, we introduce the interaction in this model in such a way as to make the that the dynamics of the model be consistent with observational data.

Consider the interaction for which the function $g(a)$ is represented as $g\left(a\right) = a^n \exp\left(-a^2/\sigma^2\right)$, where n is a natural number and σ is a positive real number. The existence of transient acceleration implies that the DE density starts to decrease, i.e., its decay occurs, $\dfrac{dg}{da} > 0$. This condition requires that n and σ satisfy the inequality $n\sigma^2 > 2$.

In Fig. 5.6, the dependences of the relative densities on the scale factor are shown for $n = 7$ and $a = \sigma = 1,5$. The model considered permits ensuring transient acceleration for a certain choice of the interaction parameters, but it is indistinguishable from the SCM for large (as well as small) values of the scale factor.

5.9. Constraint on the coupled DE models

5.9.1. Cosmography as a way of testing models with interaction

The method used in this section for testing interaction between dark components is fully based on the cosmological principle and has been termed "cosmography". The cosmological principle allows us to construct the metric of the Universe and take the first steps toward the interpretation of cosmological observations. Like kinematics, that is, the part of mechanics that describes the motion of bodies regardless of the forces causing this motion, cosmography only represents the kinematics of cosmological expansion.

The rate at which the Universe expands is determined by how the Hubble parameter $H(t)$ depends on time. A measure of this dependence is the deceleration parameter $q(t)$. For a more complete description of the kinematics of cosmological expansion, it is useful to consider an extended set of parameters:

$$\begin{aligned} H(t) &= \frac{1}{a}\frac{da}{dt}, \\ q(t) &= -\frac{1}{a}\frac{d^2a}{dt^2}\left(\frac{1}{a}\frac{da}{dt}\right)^{-2}, \\ j(t) &= \frac{1}{a}\frac{d^3a}{dt^3}\left(\frac{1}{a}\frac{da}{dt}\right)^{-3}, \\ s(t) &= \frac{1}{a}\frac{d^4a}{dt^4}\left(\frac{1}{a}\frac{da}{dt}\right)^{-4}, \\ l(t) &= \frac{1}{a}\frac{d^5a}{dt^5}\left(\frac{1}{a}\frac{da}{dt}\right)^{-5}. \end{aligned} \tag{5.178}$$

We will not make any phenomenological assumptions about the dynamics of the dark components. Based solely on kinematics (cosmography), we will show [56], that the observation of distant SNIa offers the possibility of testing the energy transport from the vacuum sector to the nonrelativistic matter sector which includes DM. We show that the measurements of the third order term in the expansion of the luminosity distance relation with respect redshift z (jerk) allows us to detect the energy transport. Higher order terms in the expansions (snap, crackle, etc.) control the velocity, acceleration of energy transport.

We analyse, for simplicity, a two-component fluid with effective pressure and energy

$$p = p_{\rm de},\ \rho = \rho_{\rm de} + \rho_{\rm dm}. \tag{5.179}$$

The conservation condition can be rewritten to the form

$$\frac{1}{a^3}\frac{d}{dt}\left(\rho_{\rm dm}a^3\right) + \frac{1}{a^{3(1+w_{\rm de})}}\frac{d}{dt}\left(\rho_{\rm de}a^{3(1+w_{\rm de})}\right) = 0. \tag{5.180}$$

The first term describes the net rate of absorption of energy per unit time in a unit of comoving volume transfered out of the decaying DE to the nonrelativistic DM. The relation (5.180) can be written as

$$\frac{1}{a^3}\frac{d}{dt}\left(\rho_{\rm dm}a^3\right)=\gamma(t),\ \ \frac{1}{a^{3(1+w_{\rm de})}}\frac{d}{dt}\left(\rho_{\rm de}a^{3(1+w_{\rm de})}\right)=-\gamma(t). \tag{5.181}$$

The function $\gamma(t)$ describes the interaction between the two dark components. Integration of (5.181) gives

$$\begin{gathered}\rho_{\rm dm}a^3=\rho_{\rm dm0}a_0^3+\int\limits_{t_0}^{t}\gamma(t)a^3dt,\\ \rho_{\rm de}a^{3(1+w_{\rm de})}=\rho_{\rm dm0}a_0^{3(1+w_{\rm de})}+\int\limits_{t_0}^{t}\gamma(t)a^{3(1+w_{\rm de})}dt.\end{gathered} \tag{5.182}$$

Using (5.182), we find

$$\begin{gathered}\ddot{a}=\frac{1}{2}\left[-\frac{A(a)}{a^2}-\frac{(1+3w_{\rm de})\,B(a)}{a^{2+3w_{\rm de}}}\right],\\ A(a)\equiv\frac{1}{3}\rho_{\rm dm}a^3,\ \ B(a)\equiv\frac{1}{3}a^{3(1+w_{\rm de})}.\end{gathered} \tag{5.183}$$

Lets's represent (5.183) in the form

$$qH^2=\frac{1}{2}\left[\frac{A(a)}{a^3}+\frac{(1+3w_{\rm de})\,B(a)}{a^{3(1+w_{\rm de})}}\right]. \tag{5.184}$$

To describe higher derivatives of the scale factor we use the cosmographical parameters (5.178) and to describe the interaction we introduce the dimensionless transfer parameter

$$\nu(t)\equiv\frac{\gamma(t)}{3H^3}. \tag{5.185}$$

Deriving by time both sides of (5.183), we obtain the basic relations connecting the jerk ($j(t)$) to the transfer density parameter ($\nu(t)$)

$$\begin{gathered}j-\frac{3}{2}w_{\rm de}\nu=\Omega_{\rm dm}+\frac{1}{2}\,(1+3w_{\rm de})\,(2+3w_{\rm de})\,\Omega_{\rm de},\\ j-\frac{3}{2}w_{\rm de}\nu-1=\frac{9}{2}w_{\rm de}\,(1+w_{\rm de})\,\Omega_{\rm de}-\Omega_c,\ \ \Omega_c\equiv-\frac{k}{a^2H^2}.\end{gathered} \tag{5.186}$$

Since

$$q=\frac{1}{2}\Omega_{\rm dm}+\frac{1+3w_{\rm de}}{2}\Omega_{\rm de} \tag{5.187}$$

for any Ω_c, we obtain

$$j-\frac{3}{2}w_{\rm de}\nu+q=\frac{3}{2}\Omega_{\rm dm}+\frac{1}{2}\,(1+3w_{\rm de})\,(1+w_{\rm de})\,\Omega_{\rm de}. \tag{5.188}$$

In the special case of the flat model ($\Omega_{\rm dm} + \Omega_{\rm de} = 1$) the formula (5.188) reduces to

$$j - \frac{3}{2} w_{\rm de} \nu + q = -\frac{3}{2} \Omega_{\rm dm} \left(4 + 3w_{\rm de}\right) w_{\rm de} + \frac{3}{2} \left(1 + 3w_{\rm de}\right) \left(1 + w_{\rm de}\right). \quad (5.189)$$

Therefore, interaction between nonrelativistic matter and DE is described by the third (and and higher) derivate of the scale factor.

5.9.2. Statefinder diagnostic for interacting models

The lack of a microscopic theory of dark components, as well as our inability to properly interpret the results of observations, has led to the creation of many phenomenological models. To start off, we pick out the models that do not explicitly contradict fundamental theories and observations. This process can be divided into two phases. First, we test how well the model corresponds to certain fundamental physical principles, as well as how well it corresponds to "well studied" areas of parameters. Second, models must be in agreement with the massive amount of data that has been obtained by modern cosmology. Obviously, the second step should come after the first. It must be said, however, that on the fundamental level, most of today's popular models stand their ground, which means that we are forced to test them using observations. Among the most popular testing methods are the so-called Om-diagnostic [51] and the use of a method based on the introduction of so-called statefinder parameters [50].

At the heart of Om-diagnostics is a construct that depends only on the Hubble parameter

$$\mathrm{O}m(x) \equiv \frac{h^2(x) - 1}{x^3 - 1}, \; x = 1 + z, \; h(x) = \frac{H(x)}{H_0}. \quad (5.190)$$

For a planar Universe composed of DE with an EOS parameter $w = \text{const}$ and non-relativistic matter

$$h^2(x) = \Omega_{m0} x^3 + \left(1 - \Omega_{m0}\right) x^\alpha, \; \alpha = 3(1 + w). \quad (5.191)$$

Therefore,

$$\mathrm{O}m(x) = \Omega_{m0} + \left(1 - \Omega_{m0}\right) \frac{x^\alpha - 1}{x^3 - 1}. \quad (5.192)$$

From this relation, it follows that $\mathrm{O}m(x) = \Omega_{m0}$ for when DE is the cosmological constant ($\alpha = 0$), and $\mathrm{O}m(x) > \Omega_{m0}$ for the quintessence case ($\alpha > 0$), $\mathrm{O}m(x) < \Omega_{m0}$ for phantom energy ($\alpha < 0$). Therefore, measurements of $\mathrm{O}m(x)$, which are equivalent to measurements of the Hubble parameter at two different redshifts, provide us with a possible test, and help us to choose an adequate DE model.

As it turns out, Om-diagnostics is proved to be ineffective when analysing models with interaction. The reason is simple. The derivative $\dot{H}$ is related to the deceleration parameter

$$q = -1 - \left(\dot{H}/H\right)^2 = 1/2\,(1 + 3w_{\rm de}\Omega_{\rm de})$$

and does not depend on whether or not both components are interacting. On the other hand,

$$\frac{\ddot{H}}{H^3} = \frac{9}{2}\left(1 + \frac{p_{\rm de}}{\rho}\right) + \frac{9}{2}\left[w_{\rm de}\,(1 + w_{\rm de})\,\frac{\rho_{\rm de}}{\rho} - w_{\rm de}\frac{\Pi}{\rho} - \frac{\dot{w}_{\rm de}}{3H}\frac{\rho_{\rm de}}{\rho}\right]. \qquad (5.193)$$

Unlike with H and $\dot{H}$, the second derivative $\ddot{H}$ does depend on the interaction between the components. Consequently, in order discriminate between models with different interactions or between interacting and non-interacting models, it is desirable to additionally characterize cosmological dynamics by parameters that depend on $\ddot{H}$. This role is filled by the statefinder parameters

$$r \equiv \frac{\dddot{a}}{aH^3},\ \ s \equiv \frac{r - 1}{3(q - 1/2)}. \qquad (5.194)$$

The parameters are dimensionless, and are constructed from the scale factor and its derivatives. The parameter r is the next (after the Hubble parameter and the deceleration parameter) member of the set of kinematic characteristics that describe the Universe's expansion. The parameter s is a combination of q and r, chosen in such a way so as not to depend on the density of dark energy. What are the reasons behind this choice? The characteristics chosen to describe dark energy can be either geometric, if they are derived directly from the space-time metric, or physical, if they depend on the characteristics of the fields that represent dark energy. Physical characteristics are, obviously, model-dependent, while geometric characteristics are more universal. Moreover, the latter are free from the uncertainties that arise during measurements of physical values like density of energy. For this very reason, geometric characteristics are more reliable during analysis of DE models. The values of the geometric parameters with a good degree of precision, are reconstructed from cosmological data. After this, statefinder parameters can be successfully used to identify various DE models.

For a planar Universe filled with a two-component liquid, composed of non-relativistic matter (dark matter + baryons) and dark energy with the relative density $\Omega_{\rm de}$,the statefinder parameters take on the form

$$\begin{aligned} r &= 1 + \frac{9}{2}\Omega_{\rm de}w_{\rm de}(1 + w_{\rm de}) - \frac{3}{2}\Omega_{\rm de}\frac{\dot{w}_{\rm de}}{H}; \\ s &= 1 + w_{\rm de} - \frac{1}{3}\frac{\dot{w}_{\rm de}}{w_{\rm de}H}; \quad w_{\rm de} \equiv \frac{p_{\rm de}}{\rho_{\rm de}}. \end{aligned} \qquad (5.195)$$

Let's write the statefinder parameters $\{r, s\}$ for a) the cosmological constant; b) for time-independent $w_{\rm de}$; c) quintessence

$$\begin{aligned} &a)\,\{r,s\} = \{1,0\};\\ &b)\,\{r,s\} = \left\{1+\frac{9}{2}\Omega de(1+w_{\rm de}), 1+w_{\rm de}\right\};\\ &c)\,\{r,s\} = \left\{1+\frac{12\pi G\dot\varphi^2}{H^2}+\frac{8\pi G\dot V}{H^3}, \frac{2\left(\dot\varphi^2+\frac{2\dot V}{H}\right)}{\dot\varphi^2-2V}\right\}. \end{aligned} \tag{5.196}$$

Much like with $Om(x)$-diagnostics, the statefinder parameters demonstrate the clear difference between the cosmological constant and dynamical forms of DE.

For interacting ($Q = -3\Pi H$) two-component fluids (de, dm) in a flat Universe, the statefinder parameters take the form [66]

$$r = 1+\frac{9}{2}\frac{w_{\rm de}}{1+R}\left[1+w_{\rm de}-\frac{\Pi}{\rho_{\rm de}}-\frac{\dot w_{\rm de}}{3w_{\rm de}H}\right],\ R\equiv\frac{\rho_{\rm dm}}{\rho_{\rm de}}, \tag{5.197}$$

$$s = 1+w-\frac{\Pi}{\rho_{\rm de}}-\frac{\dot w_{\rm de}}{3Hw_{\rm de}}. \tag{5.198}$$

For non-interacting models i.e., for $\Pi = 0$, these parameters reduce to (5.195).

Previously, we saw that the scaling solution of the form $R \propto a^{-\xi}$, where ξ is a constant parameter in the range [0, 3], can be obtained when the DE component decays into the pressureless matter fluid. If $w_{\rm de} = \text{const}$, it can be shown [66] that the interactions which produce the scaling solutions are given by

$$\Pi = \rho_{\rm de}\left(w_{\rm de}+\frac{\xi}{3}\right)\frac{R_0\,(1+z)^\xi}{1+R_0\,(1+z)^\xi}. \tag{5.199}$$

Inserting this into Eqs. (5.197) and (5.198) yields the following expressions for the statefinder parameters

$$r = 1+\frac{9}{2}\frac{w_{\rm de}}{1+R_0\,(1+z)^\xi}\left[1+w_{\rm de}-\left(w_{\rm de}+\frac{\xi}{3}\right)\frac{R_0\,(1+z)^\xi}{1+R_0\,(1+z)^\xi}\right], \tag{5.200}$$

$$s = 1+w_{\rm de}-\left(w_{\rm de}+\frac{\xi}{3}\right)\frac{R_0\,(1+z)^\xi}{1+R_0\,(1+z)^\xi}. \tag{5.201}$$

5.9.3. Observational data

For the observational data, the observational Hubble parameter data $H(z)$ have become an effective probe both in cosmology and astrophysics compared with the SNe Ia data, the CMB data, and the baryonic acoustic oscillation (BAO) data, and it is more rewarding to investigate the observational $H(z)$ data directly. The reason is quite simple, it is obvious that these probes all use the distance scale (e.g., the luminosity distance d_L, the shift parameter R, or the distance parameter A) measurement to determine cosmological parameters, which needs to integrate the Hubble parameter and therefore lose the fine structure and some more important information of $H(z)$. The Hubble parameter depends on the differential age as a function of redshift z in the form

$$H(z) = -\frac{1}{1+z}\frac{dz}{dt}. \tag{5.202}$$

which provides a direct measurement for $H(z)$ through a determination of dz/dt.

In order to obtain constraints on cosmological parameters, we use Pearson's chi-squared test. This test, sometimes called the χ^2 (Chi-square) — test, is most commonly used when testing hypotheses about distribution laws. In many practical problems, the exact dispersion law is unknown, and is therefore a hypothesis that demands statistical verification.

χ^2 for $H(z)$ can be defined as

$$\chi^2_H = \sum_{i=1}^{13} \frac{[H(z_i) - H_{\rm obs}(z_i)]^2}{\sigma^2_{hi}}, \tag{5.203}$$

where σ_{hi} is the 1σ uncertainty in the $H(z)$ data.

As it is known, the baryonic oscillations at recombination are expected to leave baryonic acoustic oscillations (BAO) in the power spectrum of galaxies. The expected BAO scale depends on the scale of the sound horizon at recombination, and on the transverse and radial scales at the mean redshift $z_{\rm BAO} = 0.35$ of galaxies in the survey. Eisenstein in [27] measured the quantity

$$A = \frac{\sqrt{\Omega_m}}{E(z_{\rm BAO})^{1/3}}\left[\frac{1}{z_{\rm BAO}}\int_0^{z_{\rm BAO}} \frac{dz'}{E(z')}\right]^{2/3}, \tag{5.204}$$

The SDSS BAO measurement [27] gives $A_{\rm obs} = 0.469(n_s/0.98) - 0.35 \pm 0.017$ where the scalar spectral index is taken to be $n_s = 0.963$, as measured by WMAP7. In this case, χ^2 can be defined as

$$\chi^2_{\rm BAO} = \frac{(A - A_{\rm obs})^2}{\sigma^2_A}. \tag{5.205}$$

Meanwhile, the locations of the peaks in the CMB temperature power spectrum in l-space depend on the comoving scale of the sound horizon at recombination, and on the angular distance to recombination. This is summarized by the so-called CMB shift parameter R [14] which is related to cosmology by

$$R = \sqrt{\Omega_{m0}} \int_0^{z_{\rm rec}} \frac{dz'}{E(z')}, \tag{5.206}$$

where $z_{\rm rec} \approx 1091.3$ is the redshift of recombination. The 7-year WMAP data gives a shift parameter $R = 1.725 \pm 0.018$. In this case, χ^2 can be defined as

$$\chi^2_{\rm CMB} = \frac{(R - R_{\rm obs})^2}{\sigma_R^2}. \tag{5.207}$$

Notice that both A and R are independent of H_0, thus these quantities can provide robust constraint as complement to $H(z)$ on DE models.

It is commonly believed that SNe Ia all have the same intrinsic luminosity, and thus can be used as "standard candles". Recently, the Supernova Cosmology Project (SCP) collaboration have released their Union2 compilation which consists of 557 SNe Ia. The Union2 compilation is the largest published and spectroscopically confirmed SNe Ia sample to date. Theoretically, the distance modulus can be calculated as

$$\mu = 5 \log \frac{d_L}{\rm Mpc} + 25 = 5 \log_{10} H_0 d_L - \mu_0, \tag{5.208}$$

where $\mu_0 = 5 \log_{10}[H_0/(100\ {\rm km/s/Mpc})] + 42 \cdot 38$, and the luminosity distance d_L can be calculated using $d_L = \frac{(1+z)}{H_0} \int_0^z \frac{dz'}{E(z')}$. Then χ^2 from SNe Ia data is:

$$\chi^2_{\rm SN} = A - \frac{B^2}{C} + \ln\left(\frac{C}{2\pi}\right), \tag{5.209}$$

where $A = \sum_i^{557} (\mu^{\rm data} - \mu^{\rm th})^2/\sigma_i^2$, $B = \sum_i^{557} \mu^{\rm data} - \mu^{\rm th}/\sigma_i^2$, $C = \sum_i^{557} 1/\sigma_i^2$, $\mu^{\rm data}$ is the distance modulus obtained from observations and σ_i is the total uncertainty of SNe Ia data.

5.9.4. Comparison of the cosmological parameters in different models

In this section, we will compare cosmological parameters with various models. Table 5.1 contains the best-fit values of parameters for three different models with interactions in the dark sector. In Fig. 5.7 you can find the probability contours for $w_{\rm de}$ versus δ for different models. The

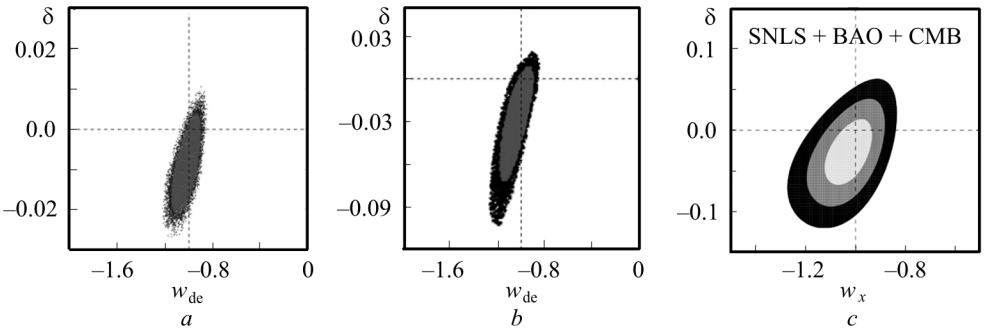

Fig. 5.7. The 68.3 % and 95.4 % confidence level contours for $w_{\rm de}$ versus δ with SNeIa + BAO + CMB in different models. $Q = 3\delta H\rho_m$ (a); $Q = 3\delta H\rho_{\rm de}$ (b); $\rho_m = \rho_{m0}a^{-3+\delta}$ (c); The dashed lines represent $\delta = 0$ and $w_{\rm de} = -1$

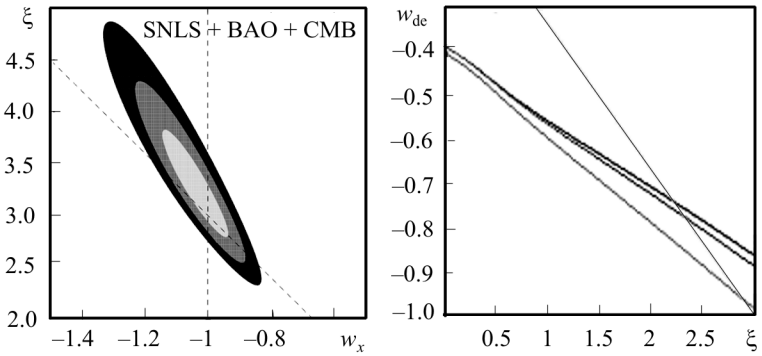

Fig. 5.8. Left: probability contours in the varying coupling models on the $(w_{\rm de}, \xi)$ plane marginalized over $\Omega_{\rm de0}$. The line $\xi = -3w_{\rm de}$ corresponds to the uncoupled models. In this case we have the constraint $2.66 < \xi < 4.05$ (95 % CL). Right: contour Plots of the first three Doppler peaks and the first trough location in the $(\xi, w_{\rm de})$ plane with $\Omega_{m0} = 0.2$ and $h = 0.71$. The upper line corresponds to the non-interacting case $(\xi + 3w_{\rm de} = 0)$

interaction term δ is near zero. Note, however, that even such a small value of interaction can facilitate the solution coincidence problem.

Let us now consider a situation in which the ratio of DE and DM has the following relation:

$$\frac{\rho_{\rm de}}{\rho_m} = \frac{\rho_{\rm de0}}{\rho_{m0}}a^{\xi}, \tag{5.210}$$

where ξ is a constant which quantifies the severity of the coincidence problem. In the absence of the coupling δ with constant $w_{\rm de}$, the energy density of DE scales as $\rho_{\rm de} \propto a^{-3(1+w_X)}$. Here the ratio $\rho_{\rm de}/\rho_m$ is proportional to $a^{-3w_{\rm de}}$, namely, the $\xi = -3w_{\rm de}$ case in Eq. (5.210). Note that the standard SCM model corresponds to $w_{\rm de} = -1$ and $\xi = 3$.

As we see from Fig. 5.8 (left), the ΛCDM model, which corresponds to the point $(w_{\rm de}, \xi) = (-1, 3)$, is within the 1σ contour bound. We remind that the uncoupled models are characterized by the line $\xi = -3w_X$. Thus, provided that

Table 5.1. **The best-fit value of the parameters $\{\Omega_{m0}, w_{\rm de}, \delta\}$ for the $Q = 3\delta H\rho_m$, $Q = 3\delta H\rho_{\rm de}$ and $\rho_m = \rho_{m0}a^{-3+\delta}$ with 1-σ and 2-σ uncertainty for SNe Ia + BAO + CMB data**

Model	$\Omega_{m,0}$	$w_{\rm de}$	δ
$Q = 3\delta H\rho_m$	$0.274^{+0.029}_{-0.029}$	$-1.02^{+0.12}_{-0.13}$	$-0.009^{+0.013}_{-0.012}$
$Q = 3\delta H\rho_{\rm de}$	$0.272^{+0.030}_{-0.030}$	$-1.02^{+0.09}_{-0.09}$	$-0.023^{+0.039}_{-0.040}$
$\rho_m = \rho_{m0}a^{-3+\delta}$	$0.270^{+0.040}_{-0.050}$	$-1.03^{+0.12}_{-0.15}$	$-0.03^{+0.06}_{-0.05}$
ΛCDM	$0.270^{+0.019}_{-0.019}$	$-1.0710^{+0.0775}_{-0.0775}$	0

the points are not on the line $\xi = -3w_{\rm de}$, the coupled models are observationally allowed in the parameter regions $2.66 < \xi < 4.05$ (95 % CL). From Fig. 5.8 (left) it is obvious that the scaling models with $\xi = 0$ are excluded from the data.

In Fig. 5.8 (right) the noninteraction line (solid yellow) stays well beyond the reach of the parameter space allowed by the CMB data. This includes the concordance SCM model as well. Thus, the scaling model is better consistent with the CMB data and it is compatible with a larger parameter space than the noninteracting standard model.

Bibliography

1. R. Amanullah et al., The Hubble Space Telescope Cluster Supernova Survey: The Type Ia Supernova Rate in High-Redshift Galaxy Clusters, arXiv:1010.5786v1. (2010).
2. L. Amendola, Acceleration at $z > 1$?, Mon. Not. Roy. Astron. Soc. **342**, 221 (2003).
3. L. Amendola and S. Tsujikawa, Dark Energy, Theory and Observations (Cambridge University Press, Cambridge, 2010).
4. L. Amendola, Coupled quintessence, Phys. Rev. D. **62**, 043511 (2000).
5. J.S. Alcaniz, R. Silva, F.C. Carvalho, Zong-Hong Zhu, Class. Quantum Grav. **26**, 105023 (2009).
6. F. Arevalo, A. de Ciencias, W. Zimdahl, Cosmological dynamics with nom-linear interactions, arXiv: 1112.5095
7. M. Baldi, Time dependent couplings in the dark sector: from background evolution to nonlinear structure formation, Mon. Not. Roy. Astron. Soc. **411**, 1077 (2011).
8. K. Bamba, S. Capozziello, S. Nojiri and S. Odintsov, Dark energy cosmology: the equivalent description via different theoretical models and cosmography tests, Astrophys. Space Sci. **342**, 155—228 (2012).
9. V. Barger, E. Guarnaccia, and D. Marfatia, Phys. Lett. B **635**, 61 (2006).
10. J. Barrow, R. Bean and J. Magueijo, Can the Universe escape eternal acceleration, Mon. Not. Roy. Astron. Soc. **316**, 41 (2000).
11. A.P. Billyard and A.A. Coley, Interactions in scalar field cosmology, Phys. Rev. D **61**, 083503 (2000).
12. C. Bohmer, G. Caldera-Cabral, R. Lazkoz, and Roy Maartens, Dynamics of dark energy with a coupling to dark matter, Phys. Rev. D **78**, 023505 (2008).
13. Yu.L. Bolotin, D.A. Erokhin, O.A. Lemets, Expanding Universe: slowdown or speedup?, Phys. Usp. **55**, 876—918, (2012).
14. J.R. Bond, G. Efstathiou, and M. Tegmark, Forecasting cosmic parameter errors from microwave background anisotropy experiments, Mon. Not. Roy. Astron. Soc. **291**, L33—L41 (1997).
15. M. Bronstein, On the expanding universe, Physikalische Zeitschrift der Sowjetunion, Bd. **3**, 73—82 (1933).
16. G. Calcagni, Fractal universe and quantum gravity, Phys. Rev. Lett. **104**, 251301 (2010).
17. G. Calcagni, Quantum field theory, gravity and cosmology in a fractal universe, J. High Energy Phys. **03**, 120 (2010).

18. R.R. Caldwell and E.V. Linder, Phys. Rev. Lett. **95**, 141301 (2005).
19. S. del Campo, R. Herrera, D. Pavon, Interacting models may be key to solve the cosmic coincidence problem, J. Cosmol. Astropart. Phys. 0901:020. (2009).
20. T. Chiba, Phys. Rev. D **73**, 063501 (2006).
21. L. Chimento, A. Jakubi, D. Pavon, and W. Zimdahl, Interacting quintessence solution to the coincidence problem, Phys. Rev. D **67**, 083513 (2003).
22. S.M. Christensen and M.J. Duff, Quantum gravity in $2 + \varepsilon$ dimensions, Phys. Lett. B **79**, 213 (1978).
23. A.G. Cohen, D.B. Kaplan, and A.E. Nelson, Effective field theory, black holes, and the cosmological constant, Phys. Rev. Lett. **82**, 4971 (1999).
24. F.E.M. Costa, J.S. Alcaniz, Cosmological consequences of a possible, Phys. Rev. D **81**, 043506 (2010).
25. E.J. Copeland, M. Sami and S. Tsujikawa, Dynamics of dark energy, Int. J. Mod. Phys. D. **15**, 1753 (2006).
26. C. Egan, C. Lineweaver, Dark-Energy Dynamics Required to Solve the Cosmic Coincidence, Phys. Rev. D **78**, 083528 (2008).
27. D.J. Eisenstein et al., Detection of the Baryon Acoustic Peak in the Large-Scale Correlation Function of SDSS Luminous Red Galaxies, Astrophys. J. **633**, 560 (2005).
28. C. Gao, F. Wu, X. Chen, Y. G. Shen, A Holographic Dark Energy Model from Ricci Scalar Curvature, Phys. Rev. D. **79**, 043511 (2009).
29. R. Gastmans, R. Kallosh, and C. Truffin, Quantum gravity near two dimensions, Nucl. Phys. B. **133**, 417 (1978).
30. Jian-Hua He, Bin Wang, and E. Abdalla, Testing the interaction between dark energy and dark matter via latest observations, Phys. Rev. D **83**, 063515 (2011).
31. Jian-Hua He, Bin Wang, Elcio Abdalla, Deep connection between $f(R)$ gravity and the interacting dark sector model, arXiv:1109.1730. (2011).
32. K. Karami et al., Holographic, new agegraphic and ghost dark energy models in fractal cosmology, arXiv:1201.6233. (2012).
33. M. Li, A Model of Holographic Dark Energy, Phys. Lett. B **603**, 1 (2004).
34. Zhengxiang Li, Puxun Wu, and Hongwei Yu, Examining the cosmic acceleration with the latest Union2 supernova data, arXiv:1011.1982v1. (2010).
35. Zhengxiang Li, Puxun Wu and Hongwei Yu, Probing the course of cosmic expansion with a combination of observational data, J. Cosmol. Astropart. Phys. 1011:031, (2010).
36. J.A.S. Lima, Alternative Dark Energy Models: An Overview, Braz. J. Phys. **34**, 194 (2004).
37. S.Z.W. Lip, Interacting Cosmological Fluids and the Coincidence Problem, Phys. Rev. D **83**, 023528 (2011).
38. G. Mangano, G. Miele, and V. Pettorino, Coupled quintessence and the coincidence problem, Mod. Phys. Lett. A **18**, 831 (2003).
39. G. Olivares, F. Atrio-Barandela, and D. Pavon, Dynamics of interacting quintessence models: Observational constraints, Phys. Rev. D **77**, 063513 (2008).
40. J. Overduin, F. Cooperstock, Evolution of the Scale Factor with a Variable Cosmological Term. Phys. Rev. D **58**, 043506 (1998).
41. D. Pavon, W. Zimdahl, Holographic dark energy and cosmic coincidence, Phys. Lett. B **628**, 206-210 (2005).

42. P.J.E. Peebles and B. Ratra, Rev. Mod. Phys. **75**, 559 (2003).
43. S. Perlmutter et al., SUPERNOVA COSMOLOGY PROJECT collaboration, Measurements of Ω and Λ from 42 high-redshift supernovae, Astrophys. J. **517**, 565 (1999).
44. V. Poitras, Constraints on $\Lambda(t)$-cosmology with power law interacting dark sectors, arXiv:1205.6766. (2012).
45. N. Poplawski, A Lagrangian description of interacting dark energy, arXiv: 0608031. (2006).
46. N.J. Poplawski, Interacting dark energy in $f(R)$ gravity, Phys. Rev. D **74**, 084032 (2006).
47. A.G. Riess et al., SUPERNOVA SEARCH TEAM collaboration, Observational evidence from supernovae for an accelerating universe and a cosmological constant, Astron. J. **116**, 1009 (1998).
48. R. Rosenfeld, Reconstruction of interacting dark energy models from parameterizations, Phys. Rev. D **75**, 083509 (2007).
49. H.M. Sadjadi and M. Honardoost, Phys. Lett. B **647**, 231 (2007).
50. V. Sahni, T. Saini, A. Starobinsky, U. Alam, Statefinder — a new geometrical diagnostic of dark energy, JETP Lett. **77**, 201—206 (2003).
51. V. Sahni, A. Shafieloo, A.A. Starobinsky, two new diagnostics of dark energy, Phys. Rev. D **78**, 103502 (2008).
52. R.J. Scherrer, Phys. Rev. D **73**, 043502 (2006).
53. Arman Shafieloo, Varun Sahni, Alexei A. Starobinsky,Is cosmic acceleration slowing down?, Phys. Rev. D. **80**, 101301 (2009).
54. F.C. Solano, U. Nucamendi, Reconstruction of the interaction term between dark matter and dark energy using SNe Ia, BAO, CMB, H(z) and X-ray gas mass fraction, arXiv:1207.0250. (2012).
55. Masashi Suwa, Takeshi Nihei, Observational constraints on the interacting Ricci dark energy model, Phys. Rev. D. **81**, 023519 (2010).
56. M. Szydlowski, Cosmological model with energy transfer, Phys. Lett. B **632**, 1—5 (2006).
57. D. Wands, J. De-Santiago, and Y. Wang, Inhomogeneous and interacting vacuum energy, Class. Quantum Grav. **29**, 145017 (2012).
58. B. Wang, Y.G. Gong, and E. Abdalla, Phys. Lett. B **624**, 141 (2005).
59. S. Weinberg, Ultraviolet divergences in quantum gravity, in General relativity, an Einstein centenary survey, S.W. Hawking and W. Israel (eds.) (Cambridge University Press, Cambridge U.K., 1979).
60. C. Wetterich, The cosmon model for an asymptotically vanishing time-dependent cosmological "constant", Astron. Astrophys. **301**, 321—328 (1995).
61. Jingfei Zhang, Xin Zhang, Hongya Liu, Statefinder diagnosis for the interacting model of holographic dark energy, Phys. Lett. B **659**, 26—33 (2008).
62. Yi Zhang, Hui Li, A New Type of Dark Energy Model, arXiv: 1003.2788. (2010).
63. W. Zimdahl, D. Pavon, and L.P. Chimento Interacting quintessence, Phys. Lett. B **521**, 133 (2001).
64. W. Zimdahl, Dark energy:a unifying view, Int. J. Mod. Phys. D **17**, 651 (2008).
65. W. Zimdahl, Accelerated expansion through interaction, arXiv:0812.2292. (2008).
66. W. Zimdahl, D. Pavon, Statefinder parameters for interacting dark energy, Gen. Rel. Grav. **36**, 1483—1491 (2004).

6 CHAPTER

STERILE NEUTRINO DARK MATTER

A.M. Boyarsky, D.A. Iakubovskyi

6.1. Dark matter problem and particle physics

The nature of dark matter (DM) is among the most intriguing questions of modern physics. There is a body of strong and convincing evidence of its existence. Indeed, numerous independent tracers of gravitational potential (observations of the motion of stars in galaxies and galaxies in clusters; emissions from hot ionized gas in galaxy groups and clusters; 21 cm line in galaxies; both weak and strong gravitational lensing measurements) demonstrate that the dynamics of galaxies and galaxy clusters cannot be explained by the Newtonian potential created by visible matter only. Moreover, cosmological data (analysis of the cosmic microwave background anisotropies and of the statistics of galaxy number counts) shows that the cosmic large scale structure started to develop much before decoupling of photons at recombination of hydrogen in the early Universe and, therefore, much before ordinary matter could start clustering. This body of evidence points at the existence of a new substance, universally distributed in objects of all scales and providing a contribution to the total energy density of the Universe at the level of about 25 %. The relative abundance of baryonic dark matter is strongly constrained by numerous microlensing experiments probing the Massive Compact Halo Objects (see e.g. [7, 74, 99], for an overview see [136] and references therein) and the results of Big Bang Nucleosynthesis [62]. Attempts to explain dark matter by the existence of primordial black holes has not been fully successful (see e.g. [55,56]). No attempts to explain the dark matter phenomenon by the modification of Einsteinian gravity and/or Newtonian laws of dynamics has been successful in explaining the dark matter at the cluster and cosmologi-

cal scales (see the recent discussion in [65,194], see also [17,134] for alternative viewpoints). Therefore, a microscopic origin of dark matter phenomenon (i.e. a new particle or particles) remains the most plausible hypothesis (see e.g. recent review of [22, 23, 69, 179] and refs. therein). Therefore, a microscopic origin of dark matter phenomenon (i.e. a new particle or particles) remains the most plausible hypothesis.

The only electrically neutral and long-lived particle in the Standard Model of particle physics (SM) are neutrinos. As the experiments show that neutrinos have mass, they could play the role of dark matter particles. Neutrinos are involved in weak interactions that keep these particles in the early Universe in thermal equilibrium down to the temperatures of few MeV. At smaller temperatures, the interaction rate of weak reactions drops below the expansion rate of the Universe and neutrinos "freeze out" from the equilibrium. Therefore, a background of relic neutrinos was created just before primordial nucleosynthesis. As interaction strength and, therefore, decoupling temperature and concentration of these particles are known, their present day density is fully defined by the sum of the masses for all neutrino flavors. To constitute the whole DM this mass should be about 11.5 eV (see e.g. [104]). Clearly, this mass is in conflict with the existing experimental bounds: measurements of the electron spectrum of β-decay put the combination of neutrino masses below 2 eV [21] while from the cosmological data one can infer an upper bound of the sum of neutrino masses is $\sum m_i \lesssim 1$ eV [105]. The fact that neutrinos could not constitute 100 % of DM follows also from the study of phase space density of DM-dominated objects that should not exceed the density of degenerate Fermi gas: fermionic particles could play the role of DM in dwarf galaxies only if their mass is above few hundreds of eV (the so-called 'Tremaine—Gunn bound' [181], for review see [45] and references therein) and in galaxies if their mass is above few tens of eV. Moreover, as the mass of neutrinos is much smaller than their decoupling temperature, they decouple relativistic and become non-relativistic only in matter-dominated epoch ("hot dark matter"). For such a dark matter the history of structure formation would be very different and the Universe would look rather differently nowadays [63]. All these strong arguments prove convincingly that *dominant fraction of dark matter* cannot be made of the Standard Model neutrinos and therefore *the Standard Model of elementary particles does not contain a viable DM candidate.* Therefore, the DM particle hypothesis necessarily implies an extension of the SM.

Phenomenologically little is known about the properties of DM particles. The mass of fermionic DM particles is limited from below by the 'Tremaine—Gunn bound' [1]. They are not necessarily stable, but their lifetime (with respect

[1] A much weaker bound, based on the Liouville theorem, can be applied for bosonic DM, see e.g. [118, 119].

to radiative decay) should significantly exceed the age of the Universe (see e.g. [44]); DM particles should have become non-relativistic sufficiently early in the radiation-dominated epoch (although a sub-dominant fraction might have remained relativistic much later).

A lot of attention has been devoted to the class of dark matter candidates called *weakly interacting massive particles* (WIMPs) (see e.g. [23, 72] for review). These hypothetical particles generalize the neutrino DM [102]: they also interact with the SM sector with roughly electroweak strength, however their mass is large enough so that these particles become non-relativistic already at decoupling. In this case the present day density of such particles depends very weakly (logarithmically) on the mass of the particle as long as it is heavy enough. This "universal" density happens to be within the order of magnitude consistent with DM density (the so-called "*WIMP miracle*"). Due to their large mass and interaction strength, the lifetime of these particles would be extremely short and therefore some special symmetry has to be imposed in the model to ensure their stability.

The interest for this class of candidates is due to their potential relation to the electroweak symmetry breaking, which is being tested at the LHC in CERN. In many models trying to make the Standard Model "natural" like, for example, supersymmetric extensions of the Standard Model, there are particles that could play the role of WIMP dark matter candidates. The WIMP searches are important scientific goals of many experiments. Dozens of dedicated laboratory experiments are conducted to detect WIMPs in the Galaxy halo by testing their interaction with nucleons (*direct detection experiments*) (see e.g. [160] and references therein). Searches for the annihilation products of these particles (*indirect detection*) are performed by PAMELA, Fermi and other high-energy cosmic missions (see e.g. reviews [20, 101]). No convincing signals has been observed so far in either "direct" or "indirect" searches.

Additionally, no hints of new physics at electroweak scale had turned up at the LHC or in any other experiments. This makes alternative approaches to the DM problem ever more viable.

6.2. Sterile neutrino dark matter

Another viable generalization of the neutrino DM idea is given by *sterile neutrino dark matter* scenario [3,4,9,64,66,170], see [49,95] for review. Sterile neutrino is a right-chiral counterpart of the left-chiral neutrinos of the SM (called '*active*' neutrinos in this context). Adding these particles to the SM Lagrangian makes neutrinos massive and is therefore their existence provides a simple and natural explanation of the observed neutrino flavor oscillations. These particles are singlet leptons because they carry no charges with respect to the Standard Model gauge groups (hence the name), and therefore

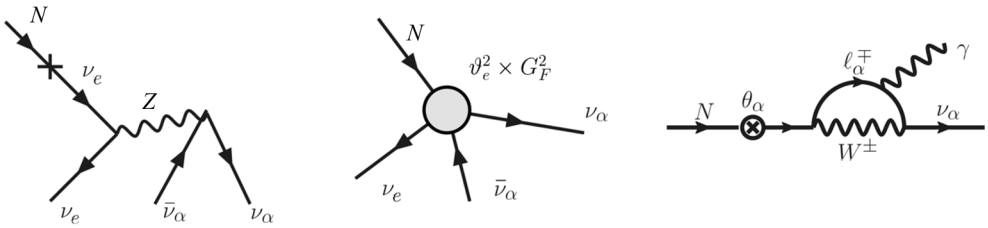

Fig. 6.1. Example of interactions of sterile neutrino. Left: decay of sterile neutrino $N \to$ $\to \nu_e \nu_\alpha \bar{\nu}_\alpha$ through neutral current interactions. A virtual ν_e is created and the quadratic mixing (marked by symbol "$\times$") is proportional to θ^2. Center: at energies $E_N \ll M_Z$, the process in the left panel can be described by the Fermi-like interaction with the "effective" Fermi constant $\theta_e \times G_F$. Right: Two-body radiative decay $N \to \gamma + \nu_\alpha$ of sterile neutrino. The energy of the photon is $E_\gamma = \dfrac{1}{2} M_N$

along with their Yukawa interaction with the active neutrinos (= 'Dirac mass') they can have a Majorana mass term (see e.g. [2] for details). They interact with the matter via creation of virtual active neutrino (quadratic mixing) and in this way they effectively participate in weak reactions (see e.g. Fig. 6.1). At energies much below the masses of the W and Z-bosons, their interaction can be described by the analog of the Fermi theory with the Fermi coupling constant G_F suppressed by the active-sterile neutrino mixing angle θ — the ratio of their Dirac to Majorana masses (Fig. 6.1):

$$\theta_\alpha^2 = \sum_{\text{sterile N}} \left| \frac{m_{\text{Dirac},\,\alpha}}{M_{\text{Majorana}}} \right|^2 \tag{6.1}$$

(this mixing can be different for different flavours α).

It was observed long ago that such particles can be produced in the Early Universe through mixing with active neutrinos [64] and have a correct relic density for any mass [3, 10, 11, 64, 98, 168, 170].

The existence of sterile neutrinos is motivated by the *observational phenomena beyond the Standard Model* (unlike WIMPs that are motivated first of all by the theoretical considerations of stability of the Higgs mass against quantum corrections that could require a fine-tuning of parameters of the model). Namely, sterile neutrinos would provide a simple and natural explanation of the *neutrino flavour oscillations* [129, 135, 151, 196]. However, a *single* sterile neutrino would be unable to explain the two observed mass splittings between Standard Model neutrinos — at least two sterile neutrinos are needed for that. Moreover, should sterile neutrino play the role of DM, its mixing with active neutrinos would be too small to contribute significantly to the flavor oscillations — its life time should be very large and, therefore, interaction strength should be too feeble [9, 40]. Therefore, in order to explain dark matter and

neutrino mass (one for each SM flavor), the minimal model should contain 3 right-handed neutrinos [9]. In such a model, the lowest mass eigen-state of the active neutrinos will be (almost) zero and the sum of neutrino masses $\sum m_\nu \approx \kappa\sqrt{|\Delta m^2_{\rm atm}|}$, where $\kappa = 1$ or 2 for normal (inverted) hierarchy [40]. This is one of the predictions of such a model.

In spite of the fact that dark matter sterile neutrino plays essentially no role in the neutrino oscillations, the fact that three particles are needed to explain *both* dark matter and neutrino oscillations is crucial. As we will see below, primordial properties of sterile neutrino dark matter are determined by two other sterile neutrinos.

If the masses of the two sterile neutrinos, responsible for neutrino oscillations, are below ∼2 GeV (mass of c-quark), such particles can be searched with existing experimental techniques [76, 77]. This is a unique situation when one can directly test the nature of neutrino oscillations in 'intensity frontier' [83] experiments. For masses above 2 GeV the searches become more difficult.

It turns out that in the region of masses between 100 MeV and electroweak scale out-of equilibrium reactions with these two sterile neutrinos are capable of generating the observed matter—antimatter asymmetry of the Universe (baryogenesis) [12]. These observations motivated a lot of recent efforts for developing this model, called the νMSM — *Neutrino Minimal Standard Model* (see [49] for review). Therefore, finding these particles in intensity frontier experiments would provide an unparalleled possibility to test baryogenesis in laboratory. Moreover, if some particles are found in such experiments it will be possible not only to check whether they are responsible for baryogenesis or not, but also unambiguously predict the properties of sterile neutrino DM.

Because its interaction with the Standard Model particles is very feeble, sterile neutrino does not need to be stable. The decay channel for sterile neutrinos of all masses is to 3 (anti)neutrinos (Fig. 6.1, left panel) [2]. However, the most characteristic feature of sterile neutrino DM is its ability to decay to photon and neutrino (with cosmologically long lifetime) [4,66,143], see Fig. 6.1, right panel. The emitted photon is almost mono-energetic (the width of the DM decay line is determined entirely by the motion of DM particles). Although the lifetime of the DM particles turns out to be *much longer than the age of the Universe*, humongous amount of these particles around us implies that the combined emission may be sizable.

If dark matter is made of sterile neutrinos, detecting astrophysical signal from their decay (the "indirect detection") may be the only way to identify this particle experimentally. However, it may be possible to prove the dark matter origin of observed signal unambiguously using its characteristic properties.

[2] For masses above 1 MeV additional decay channels become kinematically possible.

In summary, one sees that three sterile with the masses below electroweak scale form a minimal testable model that provides a unified description of three major *observational* problems "beyond-the-Standard-Model" [9, 12, 49, 54]:

1. neutrino flavour oscillations;
2. the absence of primordial anti-matter in the Universe;
3. existence of dark matter.

6.2.1. Production of sterile neutrinos in the early Universe

The active-sterile neutrino mixing is strongly suppressed at temperatures above a few hundred MeV (see e.g. [142]) and peaks roughly at [64]

$$T_{\rm peak} \sim 130 \left(\frac{M_{N_{\rm DM}}}{1\ {\rm keV}}\right)^{1/3}\ {\rm MeV}. \tag{6.2}$$

Sterile neutrinos DM are never in thermal equilibrium (see e.g. [49]) and their number density is significantly smaller than that of the active neutrinos (that is why they can account for the observed DM abundance without violating 'Tremaine—Gunn bound'). In particular, the shape of the primordial momentum distribution of thus produced sterile neutrinos is roughly proportional to that of the active neutrinos [66]:

$$f_{N_{\rm dm}}(t,p) = \frac{\chi}{e^{p/T_\nu(t)}+1}, \tag{6.3}$$

where the normalization $\chi \sim \theta^2_{\rm dm} \ll 1$ and where $T_\nu(t)$ is the temperature of the active neutrinos [3]. Comparing the production temperatures Eq. (6.2) of DM sterile neutrinos with their masses shows that they are produced relativistically in the radiation-dominated epoch. Indeed, for the primordial DM distribution of the form (6.3) one has $\langle p\rangle \sim T_{\rm peak} \gtrsim M_{N_{\rm dm}}$ for $M_{N_{\rm dm}} \lesssim 40$ GeV. Relativistic particles stream out of the overdense regions and erase primordial density fluctuations at scales below the *free-streaming horizon* (FSH) — particles' horizon when they becomes nonrelativistic (for a detailed discussion of characteristic scales see e.g. [35] and references therein). This effect influences the formation of structures. If DM particles decouple nonrelativistically (*cold* DM models, CDM) the structure formation occurs in a "bottom-up" (or "hierarchical") manner: specifically, smaller scale objects form first and then merge into the larger ones [144]. CDM models fit modern cosmological data well. In the case of particles, produced relativistically and *remaining relativistic* into the matter-dominated epoch (i.e. *hot* DM, HDM), the structure formation goes in a "top-down" fashion [200], where the first structures to collapse have

[3] The true distribution of sterile neutrinos is in fact colder than that shown in Eq. (6.3). Specifically, the maximum of $p^2 f_{N_1}(p)$ occurs at $p/T_\nu \approx 1.5$—1.8 (depending on $M_{N_{\rm dm}}$), as compared with $p \approx 2.2 T_\nu$ for the case shown in Eq. (6.3) [10, 11].

sizes comparable to the Hubble size [27, 29, 68]. The HDM scenarios contradict large-scale structure (LSS) observations [63]. Sterile neutrino DM that is produced relativistic and is then redshifted to nonrelativistic velocities in the radiation-dominated epoch is an intermediate, *warm dark matter* (WDM) candidate [3, 28, 66]. Structure formation in WDM models is similar to that in CDM models at distances above the free streaming scale. Below this scale density fluctuations are suppressed, compared with the CDM case. The free-streaming scale can be estimated as [29]

$$\lambda_{\rm FS}^{co} \sim 1 \text{ Mpc} \left(\frac{\text{keV}}{M_{N_{\rm dm}}}\right) \frac{\langle p_N \rangle}{\langle p_\nu \rangle}. \tag{6.4}$$

where 1 Mpc is the (comoving) horizon at the time when momentum of active neutrinos $\langle p_\nu \rangle \sim 1$ keV. If the spectrum of sterile neutrinos is nonthermal, then the moment of non-relativistic transition and $\lambda_{\rm FS}^{co}$ is shifted by $\langle p_N \rangle / \langle p_\nu \rangle$.

This mechanism specifies a *minimal* amount of sterile neutrinos that will be produced for given M_1 and θ_1. The requirement that 100 % of DM be produced via such mixing places an *upper bound* on the mixing angle θ_1 for a given mass. This conclusion can only be affected by entropy dilution arising from the decay of some heavy particles below the temperatures given in Eq. (6.2) [13, 24].

The production of sterile neutrino DM may substantially change in the presence of lepton asymmetry when the resonant production (RP) of sterile neutrinos [170] occurs, analogous to the Mikheyev—Smirnov—Wolfenstein effect [128, 195]. When the dispersion relations for active and sterile neutrinos cross each other at some momentum p, the effective transfer of an excess of active neutrinos (or antineutrinos) to the population of DM sterile neutrinos occurs. The maximal amount of sterile neutrino DM that can be produced in such a way is determined by the value of lepton asymmetry, $\eta_L \equiv |n_\nu - n_{\bar\nu}|/s$, where s is the entropy of relativistic species in plasma. The present DM abundance $\Omega_{\rm dm} \sim 0.25$ translates into the requirement of $\eta_L \sim 10^{-6}\,(\text{keV}/M_{N_{\rm dm}})$ in order for RP sterile neutrinos to constitute the dominant fraction of DM. One notices that the resonant production occurs only for values of lepton asymmetry, η_L much larger than the measured value of baryon asymmetry of the Universe: $\eta_B \equiv n_B/s \sim 10^{-10}$ [146]. Such a value of η_L does not contradict to any observations though. Indeed, the upper bounds on η_L are based on either primordial nucleosynthesis (BBN) or CMB measurements (as chemical potential of neutrinos would carry extra radiation density) [88, 103]. These bounds read $|\eta_L| \lesssim$ few $\times\, 10^{-3}$ (see e.g. [58, 121, 165]). We see, therefore, that the lepton asymmetry, required for resonant sterile neutrino production is still considerably smaller than the upper limit. Notice, that at epochs prior to BBN even $\eta_L \sim 1$ is possible (if this lepton asymmetry disappears later). Such a scenario is realized e.g. in the *Neutrino Minimal Standard Model*, νMSM (see [49] for review), where the lepton asymmetry keeps being generated below

the sphaleron freeze-out temperature and may reach $\eta_L \sim 10^{-2} \div 10^{-1}$ before it disappears at $T \sim$ few GeV [168].

6.2.2. Structure formation with sterile neutrino dark matter

Non-negligible velocities of 'warm' sterile neutrinos alter the power spectrum of density fluctuations at scales below the free-streaming horizon scale. Additionally, the suppression of the halo mass function below a certain scale [19] and different history of formation of first structures affects the way the first stars were formed and therefore the reionization history of the Universe, abundance of the oldest (*Population III*) stars, etc. [73, 80, 169, 172, 197, 198].

The effects of suppression of the matter power spectrum are probed with the *Lyman-α forest method* [81, 163, 186—188] (see [35] for critical overview of the method and up-to-date bounds). Using neutral hydrogen as a tracer of overall matter overdensity, one can reconstruct the power spectrum of density fluctuations at redshifts $2 < z < 5$ and scales 0.3—5 h/Mpc (in comoving coordinates) by analyzing Lyman-α absorption features in the spectra of distant quasars.

If all DM is made of sterile neutrinos with a simple Fermi-Dirac-like spectrum of primordial velocities (6.3), the matter power spectrum has a sharp (cut-off like) suppression (as compared to ΛCDM) at scales below the free-streaming horizon (6.4) (similar to the case of 'thermal relics' [28]). In this case the *Lyman-α forest data* [35, 81, 163, 187, 188, 191] puts such strong constraints at their free-streaming length, which can be expressed as the *lower bound* on their mass $M_{N_{\rm dm}} \geq 8$ keV (at 3σ CL) [35]. Such WDM models produce essentially no observable changes in the Galactic structures (see [35, 59, 138, 162, 175]) and therefore, from the observational point of view such a sterile neutrino DM (although formally 'warm') would be indistinguishable from pure CDM.

On the other hand, resonantly produced sterile neutrinos have spectra that significantly differ from those in the non-resonant case [98, 170]. The primordial velocity distribution of RP sterile neutrinos contains narrow resonant (*cold*) *plus* a nonresonant (*warm*) components — CWDM model (see [35, 36] for details) [4]. In the CWDM case, however, Lyman-α constraints allow a significant fraction of DM particles to be very warm [35]. This result implies for example, that sterile neutrino with the mass as low as 1—2 keV is consistent with all cosmological data [36].

The first results [107] demonstrate that RP sterile neutrino DM, compatible with the Lyman-α bounds [36], do change the number of substructure of a Galaxy-size halo and their properties. Qualitatively, structures form in

[4] Axino and gravitino models may have similar spectra of primordial velocities, c.f. [84].

these models in a bottom-up fashion (similar to CDM). The way the scales are suppressed in CWDM models is more complicated (and in general less severe for the same masses of WDM particles), as comparable with pure warm DM models. The first results of [107] demonstrate that the resonantly produced sterile neutrino DM models, compatible with the Lyman-α bounds of [36], do change the number of substructure of a Galaxy-size halo and their properties. The discrepancy between the number of observed substructures with small masses and those predicted by ΛCDM models (first pointed out in [89, 137]) can simply mean that these substructures did not confine gas and are therefore completely dark (see e.g. [18, 53, 117, 173]). This is not true for larger objects. In particular, CDM numerical simulations invariably predict several satellites "too big" to be masked by galaxy formation processes, in contradiction with observations [51,89,137,176]. Resonantly produced sterile neutrino DM with its non-trivial velocity dispersion, turns out to be "warm enough" to amend these issues [107] (and "cold enough" to be in agreement with Lyman-α bounds [36]).

Ultimate investigation of the influence of dark matter decays and of modifications in the evolution of large scale structure in the 'sterile neutrino Universe' as compared with the ΛCDM model requires a holistic approach, where all aspects of the systems are examined within the same set-up rather than studying the influence of different features one-by-one. Potentially observable effects of particles' free streaming and decays are expected in terms of

- formation and nature of the first stars [73, 158, 169, 177];
- reionization of the Universe [26, 80, 96, 122, 198];
- the structure of the intergalactic medium as probed by the Lyman-α forest [35, 36, 159, 163, 188—191];
- the structure of dark matter haloes as probed by gravitational lensing [70, 124, 133, 171, 189];
- the structure and concentration of haloes of satellite galaxies [107, 114, 115, 147, 166].

The results of this analysis will be confronted with measured cosmological observables, using various methods: Lyman-α analysis (with BOSS/SDSS-III [161] or X-Shooter/VLT [185]), statistics and structure of DM halos, gravitational lensing, cosmological surveys).

The weak lensing surveys can be used to probe further clustering properties of dark matter particles as sub-galactic scales, as the next generation of these surveys will be able to measure the matter power spectrum at scales down to 1—10 h/Mpc with a few percent accuracy. The next generation of lensing surveys (such as e.g. KiDS [86], LSST [111], WFIRST [78], Euclid [16]) can provide sensitivity, compatible with the existing Lyman-α bounds [124, 171]. As in the case of the Lyman-α forest method the main challenge for the weak lensing is to properly take into account baryonic effects on matter power spectrum. The suppression of power spectrum due to primordial dark matter velocities can

be extremely challenging to disentangle from the modification of the matter power spectrum due to baryonic feedback [61, 164, 190]. Finally, the modified concentration mass relation, predicted in the CWDM models, including those of resonantly produced sterile neutrinos [36, 116] can be probed with the weak lensing surveys (see e.g. [87, 120]) if their sensitivity can be pushed to halo masses below roughly $10^{12}\,M_\odot$.

6.2.3. Sterile neutrinos as decaying dark matter

Although the lifetime of any realistic decaying dark matter should be much longer than the age of the Universe (see e.g. [44]), the huge amount of potentially decaying dark matter particles in a typical halo could produce a sizable decay signal. For example, there are $\sim 10^{75}$ dark matter particles with a $\sim$1 keV mass in the halo of Andromeda galaxy. With the lifetime of the order of the age of the Universe, this would lead to $\sim 10^{57}$ decays per second, releasing $\sim 10^{45}$ erg/s. For comparison, the total X-ray luminosity of the Andromeda galaxy in the 0.1—2.4 keV band is 6 orders of magnitude smaller, $(1.8 \pm 0.3) \times 10^{39}$ erg/s [178], which immediately tells us that the lifetime of such particles should be at least 6 orders of magnitude longer than the age of the Universe.

Sterile neutrino is an example of decaying dark matter candidate. The astrophysical search for decaying DM is very promising. First of all, a positive result would be conclusive, as the DM origin of any candidate signal can be unambiguously checked. Indeed, the decay signal is proportional to the *column density* $S = \int \rho_{\rm dm}(r) dr$ along the line of sight and not to the $\int \rho^2_{\rm dm}(r) dr$ (as it is the case for annihilating DM). As a result, a vast variety of astrophysical objects of different nature would produce a comparable decay signal (c.f. [38, 42, 46]). Therefore

• one has a freedom of choosing the observational targets, avoiding complicated astrophysical backgrounds;

• if e.g. a candidate spectral line is found, its surface brightness profile may be measured (as it does not decay quickly away from the centers of the objects), distinguished from astrophysical emissions (that usually decay in outskirts) and compared among several objects with the same expected signal. This allows to distinguish the decaying DM signal from any possible astrophysical background and therefore makes astrophysical search for the decaying DM another type of direct (rather than indirect) detection experiment.

The case of the astrophysical search for decaying DM has been presented in the recent White Papers [1,32]. This approach has been illustrated on the recent claim of [108] that a spectral feature at $E \sim 2.5$ keV in the *Chandra* observation of Willman 1 can be interpreted a DM decay line. Ref. [47] demonstrated that such an interpretation is ruled out by archival observations of M31 and Fornax/Sculptor dSphs with high significance (see also [109, 130]).

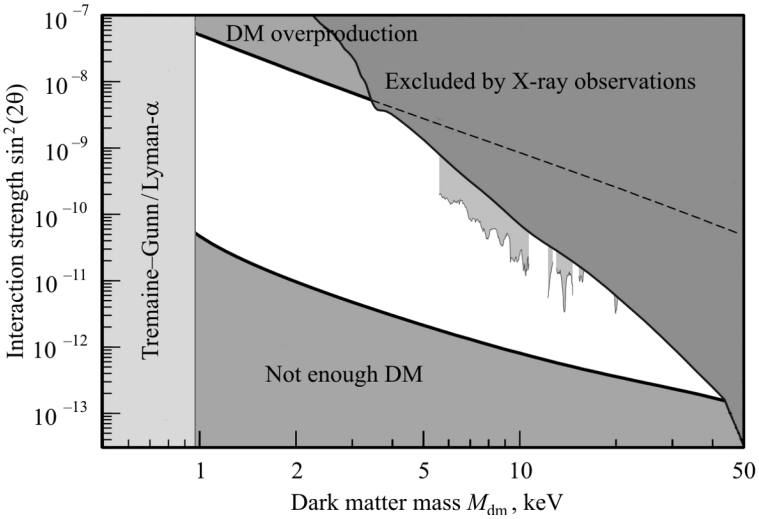

Fig. 6.2. The allowed region of parameters of sterile neutrino dark matter in the νMSM (white unshaded region) confronted with existing and projected experimental bounds. For any combination of mass and mixing angle between two black curves the necessary amount of dark matter can be produced (given the presence of certain amount of lepton asymmetry in the plasma, generated by two other sterile neutrinos). The blue shaded region in the upper right corner is excluded by the non-observation of decaying DM line in X-rays [5,34,37,39,42, 43, 110, 153, 192]. Gray regions between $\sim$5 keV and $\sim$20 keV show *expected sensitivity* from a *combination of a large number of archival observations* (as described in Section 6.5.1). The gaps are due to the presence of strong instrumental lines at certain energies (where the combination method does not provide any improvement over earlier bounds). The lower limit of $\sim$ 5 keV is due to the presence of instrumental lines and absorption edge at energies 1—2.5 keV and emission of the Milky way, dominating at lower energies. In the region below 1 keV sterile neutrino DM is 'too light' and is ruled out based on 'Tremaine—Gunn' like arguments [45] and on the Lyman-α analysis [35, 36]

The 'Tremaine—Gunn bound' restricts the lowest energies in which one can search for the fermionic decaying DM to the *X-ray range*. An extensive search of the DM decay signal in the keV range using archive data was conducted recently, using *XMM-Newton*, *Chandra* and *Suzaku* observations of extragalactic diffuse X-ray background, galaxies and galaxy clusters [5, 6, 34, 37, 39, 41—43, 48, 110, 153, 154, 192]. This search allowed to probe large part of the parameter space of decaying DM (between 0.5 keV and $\sim$14 MeV) and establish a *lower bound* on the lifetime of dark matter decay for both DM $\to \nu + \gamma$ and also DM $\to \gamma + \gamma$ (the latter would be the case e.g. for axion or majoron [100]). The combined restrictions on the lifetime (see [44]) turns out to exceed 10^{26} s, almost independent on the mass.

Let us consider the implications of the negative results of searches for decaying dark matter line in the νMSM, taking it as a minimal (baseline) model. Its parameter space is presented in Fig. 6.2. For any combination of mass and

mixing angle between two black curves the necessary amount of dark matter can be produced (given the presence of certain amount of lepton asymmetry in the plasma). If interaction strength is too high, too much dark matter is produced in contradiction with observations. If the interaction strength is too low — one cannot account for 100 % of dark matter with sterile neutrinos and additional "dark" particles would be needed). The shaded region in the upper right corner is excluded due to non-observation of decaying dark matter line with X-ray observatories [5, 6, 34, 37, 39, 41—43, 48, 110, 153, 154, 192]. Confronting the requirement to produce the correct DM abundance with the X-ray bounds, one is able to deduce the upper limit on the mass of sterile neutrino DM to be about 50 keV [37]. Finally, a lower limit on the mass of DM sterile neutrino $M_N \sim 1$—2 keV comes from the analysis of the Lyman-α forest data [35,36] [5]. As a result, the combination of X-ray bounds and computations of primordial abundance shows that in the νMSM the parameter space of sterile neutrino DM is *bounded on all sides*.

6.3. Decaying dark matter signal from different objects

In this Chapter we analyze dark matter distributions in several hundreds of dark matter-dominated objects in the Local Universe (redshift $z < 0.3$) in order to estimate the dark matter decay map and determine optimal observational targets and detection strategy. We demonstrate that the expected dark matter decay signal (proportional to the "*dark matter column density*") increases slowly with the mass of the object. We determine a relation between the dark matter column density and the mass of the halo and demonstrate that the *scatter of this relation* can be predicted based on the existing numerical simulations of structure formation. Therefore, decaying dark matter would produce a unique all-sky signal, with a known slow-varying angular distribution — a signal that can be easily distinguished from any possible astrophysical background and therefore makes the astrophysical search for decaying dark matter an "almost direct" detection experiment.

6.3.1. Dark matter column density

The flux from the dark matter decay from a given direction (in photons s^{-1} cm^{-2}) is given by

$$F_{\rm dm} = \frac{\Gamma E_\gamma}{m_{\rm dm}} \int\limits_{\text{fov cone}} \frac{\rho_{\rm dm}(\mathbf{r})}{4\pi|\mathbf{D}_L + \mathbf{r}|^2} d\mathbf{r}. \tag{6.5}$$

[5] Notice, that the lower bound on the mass of sterile neutrino DM, produced via non-resonant mixing (having a simple Fermi-Dirac-like spectrum) is at tension with the upper bound on the mass, coming from X-ray observations (see e.g. [34, 35] and refs. therein).

Here $\mathbf{D}_L$ is the *luminosity* distance between an observer and the centre of an observed object, $\rho_{\rm dm}(\mathbf{r})$ is the dark matter density, and the integration is performed over the dark matter distribution inside the (truncated) cone — solid angle, spanned by the field of view (FoV) of the X-ray satellite. In case of distant objects [6], Eq. (6.5) can be simplified:

$$F_{\rm dm} = \frac{M_{\rm dm}^{\rm fov}\Gamma}{4\pi D_L^2}\frac{E_\gamma}{m_{\rm dm}}, \tag{6.6}$$

where $M_{\rm dm}^{\rm fov}$ is the mass of dark matter within a telescope field of view, $m_{\rm dm}$ — mass of the dark matter particle. In the case of small FoV, Eq. (6.6) simplifies to

$$F_{\rm dm} = \frac{\Gamma \mathcal{S}_{\rm dm}\Omega E_\gamma}{4\pi m_s}, \tag{6.7}$$

where

$$\mathcal{S}_{\rm dm} = \int\limits_{\rm l.o.s.} \rho_{\rm dm}(r)dr \tag{6.8}$$

is the *dark matter column density* (the integral goes along the line of sight), $\Omega \ll 1$ — FoV solid angle.

Decay signal of the Milky Way halo. Because we reside in the inner part of Milky Way dark matter halo, it is the only object whose dark matter decay signal would be spread across the whole sky. The dark matter column density for the Milky Way halo is calculated using the expression [43]

$$\mathcal{S}_{\rm dm}^{\rm MW}(\phi) = \int\limits_0^\infty \rho_{\rm dm}\left(\sqrt{r_\odot^2 + z^2 - 2zr_\odot\cos\phi}\right)dz, \tag{6.9}$$

where ϕ is the off-the-Galactic-center region, so that for the direction with galactic coordinates (l, b)

$$\cos\phi = \cos b\cos l. \tag{6.10}$$

and $r_\odot = 8$ kpc is the distance from the Earth to the Sun.

It can be seen (e.g. [37, 42, 43]) that the function $S_{\rm dm}^{\rm MW}$ can change only by a factor of few, when moving from the Galactic center ($\phi = 0°$) to the anti-center ($\phi = 180°$). That is, the Milky Way contribution to the decay is an all-sky signal. This is in stark contrast with the annihilating dark matter, where only few degrees around the Galactic Center represent a "region-of-interest".

Decaying dark matter signal from extragalactic objects. Let us now compare how contributions of other Galactic and extragalactic dark matter dominated objects compares with the column density of the Milky Way.

[6] Namely, if luminosity distance D_L is much greater than the characteristic scale of the dark matter distribution.

To properly compare the dark matter distributions in different objects, fitted by different density profiles, one needs to *average* dark matter column density within a central part of an object:

$$\mathcal{S} = \frac{2}{r_*^2} \int\limits_0^{r_*} r dr \int dz\, \rho_{\rm dm}(\sqrt{r^2+z^2}). \tag{6.11}$$

Integral over z extends to the virial boundary of a dark matter halo (and can be extended all the way to infinity, as the integral converges). The definition (6.11) implies that $\mathcal{S}$ is proportional to the dark matter surface density within r_* ($\mathcal{S} \propto \rho_* r_*$), where ρ_* is the average dark matter central density and r_* is its characteristic scale [7].

It has been argued for some time that ρ_* and r_* *for galaxies* are inversely proportional (for review see e.g. [91], see [67, 75] for recent results). Similar result, *extended to cluster scales*, was originally discussed in [42]. If this were true, the dark matter column density and hence expected signal would be the same for different objects.

To investigate this result and to study the distribution of dark matter column density in the objects in Local Universe, we altogether with coauthors [46] produced a catalog of more than 1000 dark matter density profiles of about 300 unique dark matter-dominated objects of all types, from dwarf spheroidal satellites of the Milky Way to galaxy clusters. It spans more than 8 orders of magnitude in the halo masses and more than four orders of magnitude in r_* (0.2 kpc $\lesssim r_* \lesssim 2.5$ Mpc).

The resulting dependence of dark matter column density on the type and mass of the objects is shown in Fig. 6.3. By studying dark matter distribution in a large dataset of cosmic objects of different scale including dwarf, spiral and elliptical galaxies, galaxy groups and galaxy clusters [46] we found the following relation between the characteristic dark matter column density $\mathcal{S}$ and the halo mass $M_{\rm halo}$ [8]:

$$\lg \mathcal{S} = 0.21 \lg \frac{M_{\rm halo}}{10^{10}\, M_\odot} + 1.79 \tag{6.12}$$

(with $\mathcal{S}$ in $M_\odot {\rm pc}^{-2}$).

The fit to the data without the dwarf spheroidal galaxies (dSphs) has the slope $\approx$0.23, much better quality of fit, and coincides extremely well with the results of N-body simulations [113] for isolated halos (black dashed-dotted line on Fig. 6.3). At masses below $10^{10}\, M_\odot$ no isolated halos were resolved in [113]

[7] For Navarro—Frenk—White (NFW) dark matter profile [139, 140] $\rho_* = \rho_s$ and $r_* = r_s$. For other types of DM distributions, see [46] for relations between (ρ_*, r_*) and their characteristic density and radius.

[8] We use M_{200} as halo mass $M_{\rm halo}$. A proper definition of M_{200} can be found e.g. in [113].

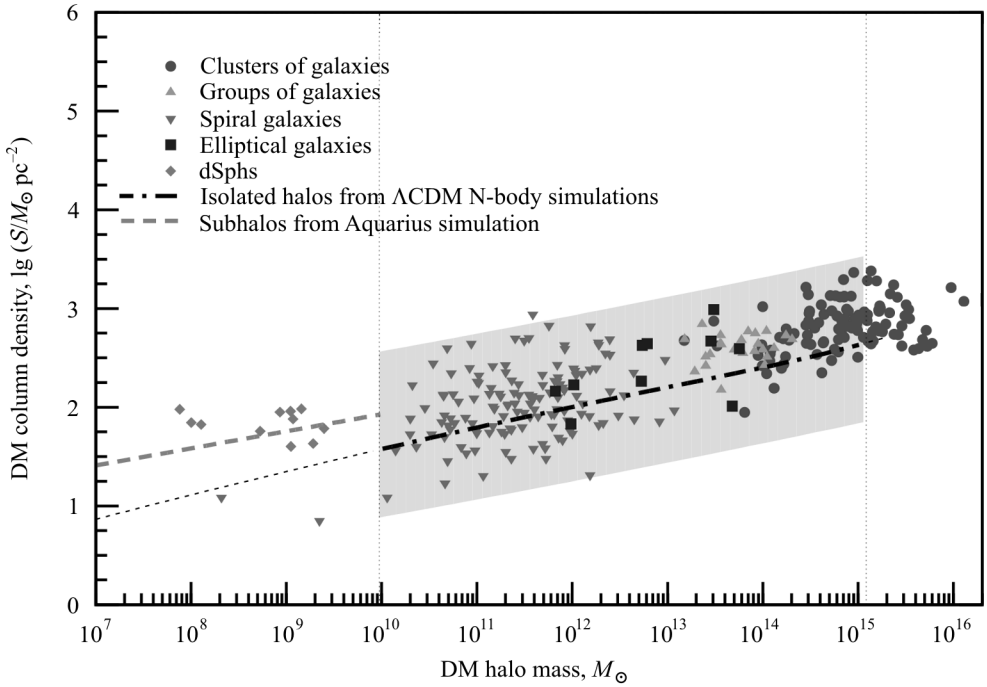

Fig. 6.3. **Column density $\mathcal{S}$ as a function of halo mass $M_{\rm halo}$.** The black dashed-dotted line is the $\mathcal{S} - M_{\rm halo}$ relation obtained from N-body simulations [113], using the WMAP fifth year cosmological parameters [90]. The shaded region shows the 3σ scatter in the simulation data. The vertical lines indicate the mass range probed by simulations. The dotted line is the theoretical prediction from the toy model for isolated halos [52, 113]. The gray dashed line showns the results from the Aquarius simulation for satellite halos [174]

and a simple toy model [52, 113] was used to predict the relation between parameters of NFW profile in a given cosmological scenario. The model (dotted line in the Fig. 6.3) fits well the results for the few spiral galaxies in this range. *Thus the agreement between observations and predictions from ΛCDM extend over more than eight orders of magnitude in mass.*

Comparison of observational data with N-body simulations indicates that, despite the presence of various systematic errors in the data, the dark matter distributions in the observed objects exhibit an universal property — a systematic change of the average column density $\mathcal{S}$ as a function of the object mass ($\mathcal{S} \propto M_{\rm halo}^{0.2}$, relation (6.12)). This is different from the flat $\mathcal{S} = {\rm const}$ dependence, previously suggested [67, 75, 91]. The latter is based, in our view, on a confusion between the properties of isolated and non-isolated halos. Excellent agreement with pure dark matter simulations suggest also that the observed scaling dependence is insensitive to the presence of baryons, details of local environment, formation history.

The relation (6.12) can be used to search for deviations from cold dark matter model (e.g. warm dark matter models [28]) or modifications of gravity at large scales [71]. This motivates the dedicated astronomical observations with all the data processed in a uniform way. Studies of galaxies with the masses below $10^{10}\,M_\odot$ and galaxy clusters would be especially important.

Various scaling relations are known in astrophysics ("fundamental plane relation" for elliptical galaxies [92], "Tully—Fisher relation" for spiral galaxies [183], etc.). The relation (6.12) discussed in this Section differs in one crucial aspect: *it extends uniformly to all classes of objects at which dark matter is observed*. It would be very difficult to explain such a relation within Modified Newtonian dynamics [127] theory considered as an alternative to dark matter. That is why this relation, further confirmed, studied and understood analytically, may serve as one more evidence of the existence of dark matter.

6.4. Existing X-ray bounds on decaying dark matter parameters

Table 6.1 summarizes existing works that put bounds on decaying dark matter from observations of individual objects. In this Table, we do not discuss the claim [149] that the intensity of the Fe XXVI Lyman-γ line at 8.7 keV, observed in [93], cannot be explained by standard ionization and recombination processes, and that the dark matter decay may be a possible explanation of this apparent excess. Spectral resolution of current missions does not allow to reach any conclusion. However, barring an *exact* coincidence between energy of decay photon and Fe XXVI Lyman-γ, this claim may be tested with the new missions, discussed in Section 6.5.2.

6.5. Strategy of further searches for decaying dark matter

The objects with the largest dark matter decay signal turn out to be the nearby galaxy clusters. However, the detection of the dark matter decay line from galaxy clusters in X-rays is complicated by the fact that most of them show strong emission precisely in keV range [9]. Indeed, the virial theorem immediately tells us that the temperature of the intercluster medium is

$$T_{\rm gas} \sim G_N\, m_{\rm p}\, \mathcal{R} \rho_* r_*^2, \tag{6.13}$$

where ρ_*, r_* are characteristic density and size, $\mathcal{R}$ is a typical overdensity in objects of a given type, $m_{\rm p}$ is the proton mass. For galaxy clusters the overdensity $\mathcal{R} \sim 10^3$ and size $r_* \sim 1$ Mpc, the temperature $T_{\rm gas}$ is always in the

[9] When searching for decaying dark matter signatures in other energy ranges, e.g. in the GeV range, galaxy clusters become the best targets, see e.g. [60].

Table 6.1. **Summary of existing X-ray observations of different objects performed by different groups**

Reference	Object	Instrument	Cleaned exp, ks
[39]	Diffuse X-ray background	HEAO-1, XMM-Newton	224, 1450
[41]	Coma & Virgo galaxy clusters	XMM-Newton	20, 40
[42]	Large Magellanic Cloud	XMM-Newton	20
[155]	Milky Way halo	Chandra/ACIS-S3	Not specified
[192] [a]	M31 (central 5′)	XMM-Newton	35
[156]	Abell 520 galaxy cluster	Chandra/ACIS-S3	67
[43]	Milky Way halo, Ursa Minor dSph	XMM-Newton	547, 7
[5]	Milky Way halo	Chandra/ACIS	1500
[48]	Galaxy cluster 1E 0657−56 ("Bullet")	Chandra/ACIS-I	450
[31]	Milky Way halo	X-ray microcalorimeter	0.1
[199] [b]	Milky Way halo	INTEGRAL/SPI	5500
[34]	M31 (central 5—13′)	XMM-Newton/EPIC	130
[37] [b]	Milky Way halo	INTEGRAL/SPI	12200
[110]	Ursa Minor	Suzaku/XIS	70
[157]	Draco dSph	Chandra/ACIS-S	32
[108] [c]	Willman 1	Chandra/ACIS-I	100
[50] [d]	M31, Fornax, Sculptor	XMM-Newton/EPIC, Chandra/ACIS	400, 50, 162
[131] [e]	Willman 1	Chandra/ACIS-I	100
[132]	Segue 1	Swift/XRT	5
[30]	M33	XMM-Newton/EPIC	20—30
[193]	M31 (12—28′ off-center)	Chandra/ACIS-I	53
[109]	Willman 1	XMM-Newton	60
[97]	Ursa Minor, Draco	Suzaku/XIS	200, 200

[a] Mistakes on calculating the bound, see discussion in [34]. [b] INTEGRAL/SPI is sensitive at 20 keV—7 MeV. [c] Claimed presence of 2.5 keV feature. [d] Did not put any bounds, only checked of the origin of 2.5 keV feature. [e] Re-analyzed the same observation of Willman 1, did not find 2.5 keV feature.

keV range, which makes it hard to detect a dark matter decay line against a strong X-ray continuum.

The optimal targets for detection the dark matter line become X-ray faint objects, such as dwarf spheroidal galaxies which do not contain any X-ray gas [42]. However archival observations of dwarf spheroidal galaxies have rather short exposure.

Objects with comparable column density and X-ray quiet (at least in energies above 1—2 keV) are the *nearby spiral galaxies*. Of these objects the Milky Way (including Large Magellanic Cloud (LMC) and Small Magellanic Cloud (SMC) satellites) and Andromeda galaxy had been observed for the longest (combined) time. The strongest bounds on parameters of decaying dark matter particles come from either Milky Way halo [43] or the central part of the Andromeda galaxy [34].

The strongest existing bounds (those of [34, 42, 43]) used the X-ray observations of LMC, Milky Way and Andromeda galaxy whose effective exposure was below 200 ksec (see Table 6.1) [10].

In this situation of the current generation of X-ray telescopes there are two possible ways to further improve the existing bounds and probe the theoretically interesting regions of particle physics models:

• Deep (few mega-seconds) [11] observations of the most X-ray quiet objects. "*Classical*" dwarf spheroidal galaxies (Ursa Minor, Draco, Sculptor, Fornax), where the dark matter content can be determined robustly, are the preferred targets. The problem with this approach is the limited visibility of some of these objects and large investment (about 10 %) of the annual observational time of the satellite (total observational time available each year for XMM-Newton and Chandra satellites is about half of the calendar year, i.e. 14—15 Msec). Allocating time for such an observation in the absence of a candidate line is hardly possible. On the other hand, observations of these objects would provide an important confirmation of the signal, detected with some other means.

• Total exposure of all observations of dark matter-dominated objects with the X-ray satellites is several orders of magnitude longer than any possible single observation. Therefore a possible way to advance with the existing X-ray instruments is *to combine a large number* of X-ray observations of different dark matter-dominated objects. The idea is that the spectral position of the dark matter decay line is the same for all these observations, while the astrophysical backgrounds in the combined spectrum would "average out", producing a smooth continuum against which a small line would become visible. Naively, such a dataset, uniformly processed, should allow to improve the existing bounds by at least an order of magnitude *and* study spatial dependence of each candidate line.

• Finally, drastic improvement in the decaying dark matter search is possible with a *new generation of spectrometers*, having large field of view and energy resolution close to several eV [1, 31, 32, 145]. In Section 6.5.2, we discuss this possibility in more detail.

[10] For Milky Way halo [43], total exposure of the combined blank sky dataset was ∼547 ks, but due to subtraction of instrumental background with ∼145 ks exposure, the errorbars of the subtracted spectrum were mainly defined by the exposure of the background.

[11] Even longer exposure will not improve the situation, as the error bars will begin to be dominated by systematic uncertainties, see the next Section 6.5.1 for detailed discussion.

6.5.1. Advance with existing missions: stacking of observations

Significant improvement of sensitivity for decaying DM line with the current X-ray missions (*XMM-Newton, Chandra, Suzaku*) is quite challenging. Indeed, an improvement by an order of magnitude would require an increase of observational time by *two* orders of magnitude. The best existing constraints in X-rays are based on observations with exposure of several hundreds of ks. Therefore, one would need $\gtrsim$10 Ms of dedicated X-ray observations. Such a huge cleaned exposure is extremely difficult to obtain for a *single* DM-dominated object (for example, the whole year of observational programme of the *XMM-Newton* satellite is only 14.5 Ms).

Using archive of the *XMM-Newton* observations [12] it is possible to collect about 20 Ms of observations of nearby spiral and irregular galaxies [33] (galaxy clusters have much stronger emission in the keV range and their combined analysis would require a completely different strategy). Therefore a possible way to advance with the existing X-ray instruments is to combine a large number of X-ray observations of different DM-dominated objects. The idea is that the spectral position of the DM decay line is the same for all these observations, while the astrophysical backgrounds in the combined spectrum would "average out", producing a smooth continuum against which a small line would become visible. Naively, this should allow to improve the existing bounds by at least an order of magnitude.

However, this turns out to be a highly non-trivial task. Indeed, such a large exposure means that the statistical errors in each energy bin can be as small as 0.1 %. To extract meaningful bounds one would need therefore *comparably small* systematic errors. However, the level of systematics of the *XMM-Newton* is much higher (at the level 5—10 %, see e.g. [79]) due to the instrument's degradation with time and variability of the instrumental (=cosmic-ray induced) background that constitutes a significant part of a signal in each energy bin (and becomes a dominant component above few keV (c.f. [57, 94, 141, 152]). The exposure of 'closed filter' dataset [13] is $\sim$1 Ms. As a result, the usual practice of subtraction of rescaled instrumental background data (see e.g. [57, 94, 148]) would mean at least $\sim$3 times larger errorbars due to the smaller exposure of the instrumental dataset. Moreover, the instrumental component of the *XMM-*

[12] *XMM-Newton* has the largest 'grasp' (=product of the field-of-view and effective area) as compared to *Chandra* and *Suzaku*, which would allow to collect the largest amount of photons from 'diffuse sources', such as the signal from DM decays in the DM halos of the nearby galaxies.

[13] A special dataset (obtained with the filter of the X-ray telescope closed, so that no X-ray photons can reach the detector) created specifically to determine the (time-averaged) shape of the instrumental background and used to remove the most prominent instrumental features from observations of diffuse sources, see e.g. [94, 112].

Newton background is self-similar only on average which would introduce additional errors (at the level of few %, see [43]). Another standard procedure of working with diffuse sources — subtraction of the 'blank sky' data [14] will not be applicable in this case as well. First of all, such a dataset would also contain decaying dark matter line originating from the decays in the Milky Way halo (this fact has been exploited before to put bounds on decaying DM in [5, 43]). Secondly, subtracting the 'blank sky' data would again reduce all the advantages of a large dataset by lowering statistics (as the exposure of the latest blank-sky co-added observations is again of the order of ∼1 Ms).

This means that to *take all the advantages of this long-exposure dataset, one cannot use the standard data-processing methods*. Therefore, an alternative method of data analysis has to be developed, that has the sensitivity towards the searching for narrow lines at the level, dictated by the statistics of the combined dataset. The results will be reported in [33]. The estimated level of sensitivity of this method is shown as the gray line in Fig. 6.2.

6.5.2. X-ray micro-calorimeters

Really significant progress (that allows, for example, to cover the whole region of parameter space in Fig. 6.2) in searching for decaying DM cannot be achieved with the existing instruments by simply increasing the exposure of observations. Indeed, the width of the DM decay line, $\Delta E/E_\gamma$ is determined by the virial velocities of DM particles in halos and ranges from $\mathcal{O}(10^{-4})$ for dwarf spheroidal galaxies to $\mathcal{O}(10^{-3})$ for the Milky Way-size galaxies to 10^{-2} for galaxy clusters. If the spectral resolution is much bigger than the width of the line, one averages the photons from the line with the background photons over a large energy bin. This is the case for all existing X-ray missions, whose detectors are based on CCD technology (c.f. [182]) and where the spectral resolution is at the level $\Delta E/E \gtrsim 10^{-2}$, see Fig. 6.4. Therefore, *an X-ray spectrometer with the energy resolution at least* $\Delta E/E \sim 10^{-3}$ *is crucial for detection of a decaying DM line.*

The technology behind such spectrometers (known as *X-ray micro-calorimeters*, see e.g. [125, 150]) has been actively developed by the high-energy astrophysical community in the last decades. There is a strong interest for building such a spectrometer, and different versions of high resolution X-ray missions had been proposed in response to the ESA and NASA calls (including the ESA's call for Fundamental Physics Roadmap), see e.g. [15, 32, 82, 145, 180]. Astrophysical interest to X-ray spectrometer is motivated by a number of important applications to observational cosmology, providing crucial insight into the nature of dark matter by studying the structure of the "cosmic web".

[14] Combination of many observations of X-ray quiet parts of the sky [57, 152]. Unlike the 'closed filter' dataset collects the physical emission from the Milky Way.

In particular,

• search for missing baryons in the cosmic filaments; through their emission and absorption;

• trace the evolution and physics of clusters out to their formation epoch;

• usage of gamma-ray bursts as backlight to observe the warm-hot intergalactic media in absorption;

• study the evolution of massive star formation using gamma-ray bursts to trace their explosions back to the early epochs of the Universe ($z \sim 6$) (see e.g. [15, 82, 145]).

The first spectrometer based on this technology was flown (albeit unsuccessfully) on *Suzaku* mission [85] and another one is being planned for the Astro-H [14, 180]. However, currently planned and proposed X-ray micro-calorimeter missions (Astro-H [180], Athena [15], ORIGIN [82], etc.) are not optimal for the purpose of decaying dark matter search. These missions are optimized for the astrophysical goals and have limited field-of-view (usually, much below 1 deg^2), good angular resolution and narrow energy range.

On the contrary, the key parameters that determine the sensitivity of the proposed instrument for decaying dark matter search are (see Fig. 6.4):

• a spectral resolution $\Delta E/E \lesssim 10^{-3}$ over the range of energies 0.5—25 keV (this is the minimal energy range, that would allow to probe the parameter space of our baseline model, the νMSM);

• large *'grasp'* $\sim 10^3$—10^4 cm$^2 \cdot$ deg^2. There are essentially two possibilities to achieve such a grasp. One can either launch a non-imaging spectrometer

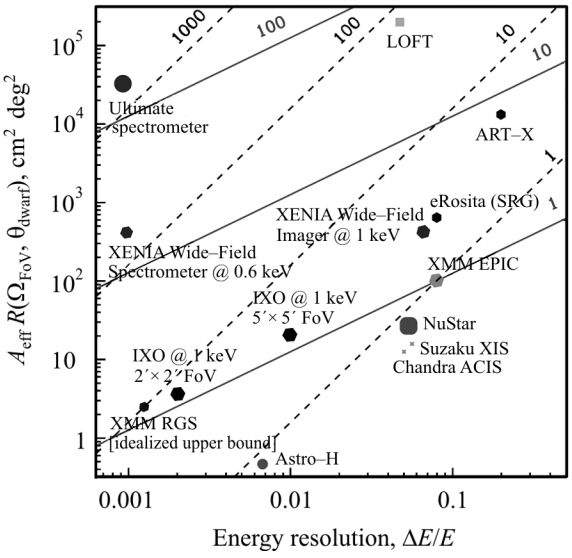

Fig. 6.4. Comparison of sensitivities of existing and proposed/planned X-ray missions for the detection of the DM decay line in a nearby dwarf spheroidal galaxy of the angular size of 1 deg. The sensitivity of XMM-Newton EPIC camera is taken as a reference. Solid lines indicate improvement of the sensitivity by factors of 1, 10 and 100 (the top left is the most sensitive). The dashed lines show the improvement of the sensitivity towards the detection of a strong line (in an effectively background free regime). See also [31, 32]

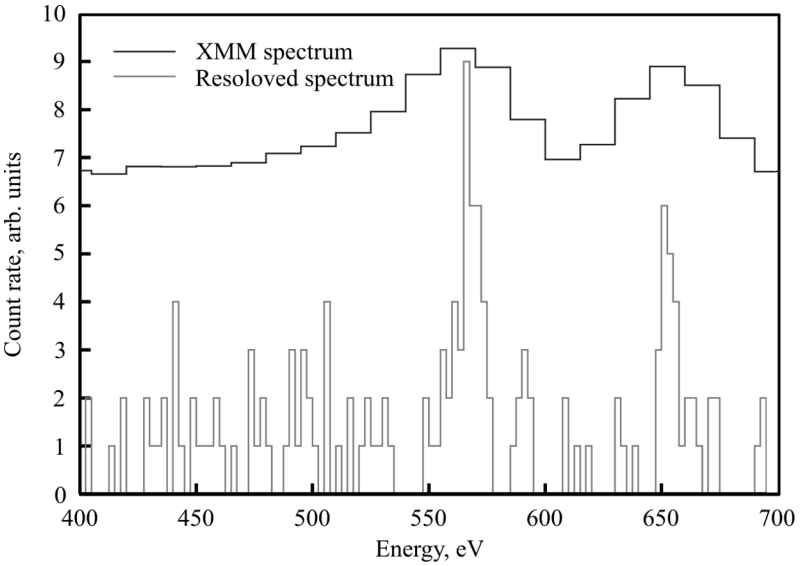

Fig. 6.5. Galactic diffuse background (observed with *XMM-Newton* (red) and the same data, observed with the X-ray spectrometer (XQC project [126])

(with a 'collimator' having a field-of-view as large as $\sim 10^2$ deg^2) [15]; or install mirrors (thus increasing the effective area beyond the geometric size of the detectors, probably to as much as 10^3 cm^2). The latter option allows to have also imaging capabilities, however, it is usually extremely costly to cover the required energy range and to have sufficiently large (at least $1^\circ \times 1^\circ$) field of view.

Fig. 6.4 summarizes the data on sensitivity of existing and proposed missions and demonstrates that none of them would provide a sufficient improvement with respect to the existing constraints (see [31, 32] for discussion).

Currently, there exists a project (the *X-ray quantum calorimeter*, XQC [126]) that can be considered a prototype of the proposed mission. It has the field of view of about 1 sr (3.5×10^3 deg^2), an effective area of ~ 1 cm^2 and the energy resolution of 10 eV over the energy range 0.1—4 keV [126] [16]. This calorimeter has been flown several times on sounding rockets [126]. Although

[15] Making field-of-view significantly larger than about $10^\circ \times 10^\circ$ would of course further increase the sensitivity towards the line detection. However, in this case it would become challenging to identify the nature of the candidate line (if found), as in this case none of the nearby DM dominated objects with large angular size (Andromeda galaxy, Large and Small Magellanic clouds, Virgo cluster) will look like 'hot spots' of DM decays. Moreover, in this case it will not be possible to build a DM surface brightness profile as one varies the directions off the Galactic Center and investigate whether it is consistent with DM distribution in the Milky Way.

[16] A similar calorimeter used in Suzaku was capable of delivering a similar resolution up to the maximal energy range of 12 keV [85].

each flight had been very short (about 100 s), it allowed to demonstrate that the Milky Way emission in the energy range 0.1—1 keV (which looks as a continuum in the spectra obtained with X-ray imaging instruments, see e.g. [57, 123] is actually a "forest" of thin lines (see Fig. 6.5). Because of its superior spectral resolution, decaying DM bounds based on the ∼100 s exposure of the flight of this spectrometer [126] are comparable with 10^4 s of the *XMM-Newton* exposure [31].

To detect a dark matter decay line, that is much weaker than the lines resolved with the XQC spectrometer, a significantly longer exposure (∼1 year) would be required. The requirement to keep the cryostat of such a spectrometer in the stable regime, means that one cannot use the sounding rockets, but rather needs to use a satellite (probably, staying in Low Earth Orbit, unlike *XMM-Newton* or *Chandra*). The project therefore becomes a small-to-medium scale cosmic mission.

6.5.3. Laboratory searches for sterile neutrino DM

Finally, several words should be said about laboratory searches of DM sterile neutrinos. As Fig. 6.2 demonstrates, their mixing angle is always smaller than $\sim 10^{-4}$ (even for the lightest admissible masses of ∼1 keV). This makes their laboratory searches extremely challenging. One possibility would be to measure the event-by-event kinematics of β-decay products [25]. This experiment, however, is plagued by the bremsstrahlung emission of the finite state electrons that changes their energy. Other possibilities of searches for the keV-scale sterile neutrinos are discussed e.g. in [8,106,184]. All these experiments require essentially background-free regime and it is not clear whether any of them can realistically touch cosmologically interesting region of parameters of sterile neutrino.

6.6. Conclusion

After almost 20 years of research the sterile neutrino remains a viable dark matter candidate. Observations of neutrino flavor oscillations further increased the interest to this candidate. Recent discovery of a Higgs like particle with the mass 125—126 GeV and absence of signs of new physics at the LHC or in DM direct detection experiments call for alternative (not related to electroweak symmetry breaking) testable beyond the Standard Model (BSM) models (including dark matter). Attempts to solve all BSM problems with particles with masses below electroweak scale [49, 167] provide an novel approach to the problem of naturalness of the SM.

Dedicated cosmic experiment, an X-ray spectrometer, searching for signatures of decaying dark matter, has a capability to identify the dark matter particle. Combination of this experiment with the searches for neutral leptons

at beam-target experiments gives a unique possibility to resolve experimentally three major BSM problems: the nature of neutrino flavor oscillations; the mechanism of generation of matter-antimatter asymmetry in the Universe; and the existence of dark matter. It could provide not only a possibility to detect new particles, but also do independent cross checks of the mechanisms of DM production and baryogenesis. Even negative results would allow to shed a light on the DM properties and therefore restrict the class of extensions of the SM.

Although the current data, describing formation of structures, is fully consistent with the ΛCDM 'concordance' model, sterile neutrino DM (that can be 'warm', 'cold' or 'mixed' (cold + warm)) is also fully compatible with the observations. Future cosmic surveys will be able to measure the matter power spectrum with the sufficiently high precision to detect the imprints that such DM leaves in the matter power spectrum at sub-Mpc scales.

Bibliography

1. K. Abazajian, Detection of Dark Matter Decay in the X-ray. In astro2010: The Astronomy and Astrophysics Decadal Survey, vol. 2010 of ArXiv Astrophysics e-prints, 1 (2009); 0903.2040.
2. K. Abazajian et al., Light Sterile Neutrinos: A White Paper (2012); 1204.5379.
3. K. Abazajian, G.M. Fuller, and M. Patel, Sterile neutrino hot, warm, and cold dark matter, Phys. Rev. D **64**, 023501 (2001); astro-ph/0101524.
4. K. Abazajian, G.M. Fuller, and W.H. Tucker, Direct detection of warm dark matter in the X-ray, Astrophys. J. **562**, 593—604 (2001); astro-ph/0106002.
5. K. Abazajian and S.M. Koushiappas, Constraints on sterile neutrino dark matter, Phys. Rev. D **74**, 023527 (2006); astro-ph/0605271.
6. K.N. Abazajian, M. Markevitch, S.M. Koushiappas, and R.C. Hickox, Limits on the Radiative Decay of Sterile Neutrino Dark Matter from the Unresolved Cosmic and Soft X-ray Backgrounds, Phys. Rev. D **75**, 063511 (2007); arXiv:astro-ph/0611144.
7. C. Alcock et al., Binary Microlensing Events from the MACHO Project, Astrophys. J. **541**, 270—297 (2000).
8. S. Ando and A. Kusenko, Interactions of keV sterile neutrinos with matter, Phys. Rev. D **81**, 113006 (2010); 1001.5273.
9. T. Asaka, S. Blanchet, and M. Shaposhnikov, The nuMSM, dark matter and neutrino masses, Phys. Lett. B **631**, 151—156 (2005); hep-ph/0503065.
10. T. Asaka,M. Laine, and M. Shaposhnikov, On the hadronic contribution to sterile neutrino production, J. High Energy Phys. **06**, 053 (2006); hep-ph/0605209.
11. T. Asaka, M. Laine, and M. Shaposhnikov, Lightest sterile neutrino abundance within the νMSM, J. High Energy Phys. **01**, 091 (2007); hep-ph/0612182.
12. T. Asaka and M. Shaposhnikov, The νMSM, dark matter and baryon asymmetry of the universe, Phys. Lett. B **620**, 17—26 (2005); arXiv:hep-ph/0505013.
13. T. Asaka, M. Shaposhnikov, and A. Kusenko, Opening a new window for warm dark matter, Phys. Lett. B **638**, 401—406 (2006); hep-ph/0602150.
14. http://astro-h.isas.jaxa.jp/index.html.en.
15. X. Barcons et al., Athena (Advanced Telescope for High ENergy Astrophysics) Assessment Study Report for ESA Cosmic Vision 2015—2025 (2012); 1207.2745.
16. J.P. Beaulieu et al., EUCLID: Dark Universe Probe and Microlensing Planet Hunter. In V. Coudé Du Foresto, D.M. Gelino, and I. Ribas (ed.) Pathways Towards Habitable Planets, vol. 430 of Astronomical Society of the Pacific Conference Series, 266 (2010); 1001.3349.

17. J.D. Bekenstein and R.H. Sanders, TeVeS/MOND is in harmony with gravitational redshifts in galaxy clusters, Mon. Not. R. Astron. Soc. **421**, L59—L61 (2012); 1110.5048.
18. A.J. Benson, C.S. Frenk, C.G. Lacey, C.M. Baugh, and S. Cole, The effects of photoionization on galaxy formation — II. Satellite galaxies in the Local Group, Mon. Not. R. Astron. Soc. **333**, 177—190 (2002); arXiv:astro-ph/0108218.
19. A.J. Benson et al., Dark Matter Halo Merger Histories Beyond Cold Dark Matter: I — Methods and Application to Warm Dark Matter (2012); 1209.3018.
20. L. Bergstrom, Saas-Fee Lecture Notes: Multi-messenger Astronomy and Dark Matter (2012); 1202.1170.
21. J. Beringer et al., Review of Particle Physics, Phys. Rev. D **86**, 010001 (2012).
22. G. Bertone, *Particle Dark Matter: Observations, Models and Searches* (Cambridge University Press, Cambridge, 2010).
23. G. Bertone, D. Hooper, and J. Silk, Particle dark matter: Evidence, candidates and constraints, Phys. Rept. **405**, 279—390 (2005); hep-ph/0404175.
24. F. Bezrukov, H. Hettmansperger, and M. Lindner, keV sterile neutrino Dark Matter in gauge extensions of the Standard Model, Phys. Rev. D **81**, 085032 (2010); 0912.4415.
25. F. Bezrukov and M. Shaposhnikov, Searching for dark matter sterile neutrinos in the laboratory, Phys. Rev. D **75**, 053005 (2007); arXiv:hep-ph/0611352.
26. P.L. Biermann and A. Kusenko, Relic keV sterile neutrinos and reionization, Phys. Rev. Lett. **96**, 091301 (2006); astro-ph/0601004.
27. G.S. Bisnovatyi-Kogan, Cosmology with a nonzero neutrino rest mass, Astronomicheskij Zhurnal **57**, 899—902 (1980).
28. P. Bode, J.P. Ostriker, and N. Turok, Halo formation in warm dark matter models, Astrophys. J. **556**, 93—107 (2001); astro-ph/0010389.
29. J.R. Bond, G. Efstathiou, and J. Silk, Massive neutrinos and the large-scale structure of the universe, Phys. Rev. Lett. **45**, 1980—1984 (1980).
30. E. Borriello, M. Paolillo, G. Miele, G. Longo, and R. Owen, Constraints on sterile neutrino dark matter from XMM–Newton observation of M33, ArXiv e-prints (2011); 1109.5943.
31. A. Boyarsky, J.W. den Herder, A. Neronov, and O.Ruchayskiy, Search for the light dark matter with an x-ray spectrometer, Astropart. Phys. **28**, 303—311 (2007); astro-ph/0612219.
32. A. Boyarsky, J.W. den Herder, O. Ruchayskiy et al., The search for decaying Dark Matter (2009); A white paper submitted in response to the Fundamental Physics Roadmap Advisory Team (FPR-AT) Call for White Papers, 0906.1788.
33. A. Boyarsky, D. Iakubovskyi, and O. Ruchayskiy, Analysis of stacked spectra of nearby galaxies observed with XMM-Newton (2012); to appear.
34. A. Boyarsky, D. Iakubovskyi, O. Ruchayskiy, and V. Savchenko, Constraints on decaying dark matter from XMM-Newton observations of M31, Mon. Not. R. Astron. Soc. **387**, 1361—1373 (2008); arXiv:0709.2301.
35. A. Boyarsky, J. Lesgourgues, O. Ruchayskiy, and M. Viel, Lyman-alpha constraints on warm and on warm-plus-cold dark matter models, J. Cosm. Astropart. Phys. **0905**, 012 (2009); 0812.0010.
36. A. Boyarsky, J. Lesgourgues, O. Ruchayskiy, and M. Viel, Realistic sterile neutrino dark matter with keV mass does not contradict cosmological bounds, Phys. Rev. Lett. **102**, 201304 (2009); 0812.3256.

37. A. Boyarsky, D. Malyshev, A. Neronov, and O. Ruchayskiy, Constraining DM properties with SPI, Mon. Not. R. Astron. Soc. **387**, 1345—1360 (2008); 0710.4922.
38. A. Boyarsky, A. Neronov, O. Ruchayskiy, and I. Tkachev, Universal properties of Dark Matter halos, Phys. Rev. Lett. **104**, 191301 (2010); 0911.3396
39. A. Boyarsky, A. Neronov, O. Ruchayskiy, and M. Shaposhnikov, Constraints on sterile neutrino as a dark matter candidate from the diffuse X-ray background, Mon. Not. R. Astron. Soc. **370**, 213—218 (2006); astro-ph/0512509.
40. A. Boyarsky, A. Neronov, O. Ruchayskiy, and M. Shaposhnikov, The masses of active neutrinos in the νMSM from X-ray astronomy, J. Exp. Theor. Phys. Lett. **83** (4), 133—135 (2006), hep-ph/0601098.
41. A. Boyarsky, A. Neronov, O. Ruchayskiy, and M. Shaposhnikov, Restrictions on parameters of sterile neutrino dark matter from observations of galaxy clusters, Phys. Rev. D **74**, 103506 (2006); astro-ph/0603368.
42. A. Boyarsky, A. Neronov, O. Ruchayskiy, M. Shaposhnikov, and I. Tkachev, Strategy to search for dark matter sterile neutrino, Phys. Rev. Lett. **97**, 261302 (2006); astro-ph/0603660.
43. A. Boyarsky, J. Nevalainen, and O. Ruchayskiy, Constraints on the parameters of radiatively decaying dark matter from the dark matter halo of the milky way and ursa minor, Astron. Astrophys. **471**, 51—57 (2007); astro-ph/0610961.
44. A. Boyarsky and O. Ruchayskiy, Bounds on Light Dark Matter (2008); 0811.2385.
45. A. Boyarsky, O. Ruchayskiy, and D. Iakubovskyi, A lower bound on the mass of Dark Matter particles, J. Cosm. Astropart. Phys. **0903**, 005 (2009); 0808.3902.
46. A. Boyarsky, O. Ruchayskiy, D. Iakubovskyi, A.V. Macciò, and D. Malyshev, New evidence for dark matter (2009); 0911.1774.
47. A. Boyarsky, O. Ruchayskiy, M.G. Walker, S. Riemer-Sørensen, and S.H. Hansen, Searching for Dark Matter in X-Rays: How to Check the Dark Matter origin of a spectral feature, Mon. Not. Roy. Astron. Soc. **407**, 1188—1202 (2010); 1001.0644.
48. A. Boyarsky, O. Ruchayskiy, and M. Markevitch, Constraints on parameters of radiatively decaying dark matter from the galaxy cluster 1e0657 – 56, Astrophys. J. **673**, 752 (2008); astro-ph/0611168.
49. A. Boyarsky, O. Ruchayskiy, and M. Shaposhnikov, The role of sterile neutrinos in cosmology and astrophysics, Ann. Rev. Nucl. Part. Sci. **59**, 191 (2009); 0901.0011.
50. A. Boyarsky et al., Searching for dark matter in X-rays: how to check the dark matter origin of a spectral feature, Mon. Not. R. Astron. Soc. **407**, 1188—1202 (2010); 1001.0644.
51. M. Boylan-Kolchin, J.S. Bullock, and M. Kaplinghat, Too big to fail? The puzzling darkness of massive Milky Way subhalos, Mon. Not. R. Astron. Soc. **415**, L40—L44 (2011); 1103.0007.
52. J.S. Bullock et al., Profiles of dark haloes: evolution, scatter and environment, Mon. Not. R. Astron. Soc. **321**, 559—575 (2001); arXiv:astro-ph/9908159.
53. J.S. Bullock, A.V. Kravtsov, and D.H. Weinberg, Reionization and the Abundance of Galactic Satellites, Astrophys. J. **539**, 517—521 (2000); arXiv:astro-ph/0002214.

54. L. Canetti, M. Drewes, and M. Shaposhnikov, Sterile Neutrinos as the Origin of Dark and Baryonic Matter (2012); 1204.3902.
55. F. Capela, M. Pshirkov, and P. Tinyakov, Constraints on Primordial Black Holes as Dark Matter Candidates from Star Formation, ArXiv e-prints (2012); 1209.6021.
56. B.J. Carr, Primordial Black Holes: Do They Exist and Are They Useful? In *Inflating Horizon of Particle Astrophysics and Cosmology* (Universal Academy Press Inc. and Yamada Science Foundation, 2005); astro-ph/0511743.
57. J.A. Carter and A.M. Read, The XMM-Newton EPIC background and the production of background blank sky event files, Astron. Astrophys. **464**, 1155—1166 (2007); arXiv:astro-ph/0701209.
58. E. Castorina et al., Cosmological lepton asymmetry with a nonzero mixing angle $\theta_1 3$, Phys. Rev. D **86**, 023517 (2012); 1204.2510.
59. P. Colin, O. Valenzuela, and V. Avila-Reese, On the Structure of Dark Matter Halos at the Damping Scale of the Power Spectrum with and without Relict Velocities, Astrophys. J. **673**, 203—214 (2008); 0709.4027.
60. C. Combet et al., Decaying dark matter: a stacking analysis of galaxy clusters to improve on current limits, ArXiv e-prints (2012); 1203.1164.
61. M.P. van Daalen, J. Schaye, C.M. Booth, and C.D. Vecchia, The effects of galaxy formation on the matter power spectrum: A challenge for precision cosmology, Mon. Not. Roy. Astron. Soc. **415**, 3649—3665 (2011); 1104.1174.
62. A. Dar, Baryonic Dark Matter and Big Bang Nucleosynthesis, Astrophys. J. **449**, 550 (1995); arXiv:astro-ph/9504082.
63. M. Davis, G. Efstathiou, C.S. Frenk, and S.D. White, The Evolution of Large Scale Structure in a Universe Dominated by Cold Dark Matter, Astrophys. J. **292**, 371—394 (1985).
64. S. Dodelson and L.M. Widrow, Sterile-neutrinos as dark matter, Phys. Rev. Lett. **72**, 17—20 (1994); hep-ph/9303287.
65. S. Dodelson, The Real Problem with MOND, Int. J. Modern Phys. D **20**, 2749—2753 (2011); 1112.1320.
66. A.D. Dolgov and S.H. Hansen, Massive sterile neutrinos as warm dark matter, Astropart. Phys. **16**, 339—344 (2002); hep-ph/0009083.
67. F. Donato et al., A constant dark matter halo surface density in galaxies, Mon. Not. R. Astron. Soc. **397**, 1169—1176 (2009); 0904.4054.
68. A.G. Doroshkevich, M.I. Khlopov, R.A. Sunyaev, A.S. Szalay, and I.B. Zeldovich, Cosmological impact of the neutrino rest mass, New York Academy Sciences Annals **375**, 32—42 (1981).
69. M. Drees and G. Gerbier, Mini–Review of Dark Matter: 2012, ArXiv e-prints (2012); 1204.2373.
70. R.M. Dunstan, K.N. Abazajian, E. Polisensky, and M. Ricotti, The Halo Model of Large Scale Structure for Warm Dark Matter (2011); 1109.6291.
71. G. Dvali, G. Gabadadze, and M. Porrati, 4D gravity on a brane in 5D Minkowski space, Phys. Lett. B **485**, 208—214 (2000); arXiv:hep-th/0005016.
72. J.L. Feng, Dark matter candidates from particle physics and methods of detection, Ann. Rev. Astron. Astrophys. **48**, 495—545 (2010); 1003.0904.
73. L. Gao and T. Theuns, Lighting the Universe with filaments, Science **317**, 1527 (2007); 0709.2165.

74. E.I. Gates, G. Gyuk, and M.S. Turner, The Local Halo Density, Astrophys. J. Lett. **449**, L123 (1995); astro-ph/9505039.
75. G. Gentile, B. Famaey, H. Zhao, and P. Salucci, Universality of galactic surface densities within one dark halo scale-length, Nature **461**, 627—628 (2009); 0909.5203.
76. D. Gorbunov and M. Shaposhnikov, How to find neutral leptons of the numsm? J. High Energy Phys. **10**, 015 (2007); arXiv:0705.1729 [hep-ph].
77. D. Gorbunov and M. Shaposhnikov, Search for GeV-scale sterile neutrinos responsible for active neutrino masses and baryon asymmetry of the universe, Submitted to European Strategy Preparatory Group.
78. J. Green et al., Wide-Field InfraRed Survey Telescope (WFIRST) Final Report, ArXiv e-prints (2012); 1208.4012.
79. M. Guainazzi et al., Epic status of calibration and data analysis. XMM-Newton calibration technical report, EPIC Concortium (2012), http://xmm2.esac.esa.int/docs/documents/CAL-TN-0018.ps.gz.
80. S.H. Hansen and Z. Haiman, Do we need stars to reionize the universe at high redshifts? Early reionization by decaying heavy sterile neutrinos, Astrophys. J. **600**, 26—31 (2004); astro-ph/0305126.
81. S.H. Hansen, J. Lesgourgues, S. Pastor, and J. Silk, Closing the window on warm dark matter, Mon. Not. R. Astron. Soc. **333**, 544—546 (2002); astro-ph/0106108.
82. J.W. den Herder et al., ORIGIN: Metal creation and evolution from the cosmic dawn (2011); 1104.2048.
83. J. Hewett et al., Fundamental Physics at the Intensity Frontier (2012); 1205.2671.
84. K. Jedamzik, M. Lemoine, and G. Moultaka, Gravitino, axino, Kaluza—Klein graviton warm and mixed dark matter and reionisation, J. Cosm. Astropart. Phys. **0607**, 010 (2006); astro-ph/0508141.
85. R. Kelley et al., The Suzaku high resolution X-ray spectrometer, Publ. Astron. Soc. Jpn. **59**, 77 (2007).
86. Kilo-degree survey (kids). http://www.astro-wise.org/projects/KIDS/.
87. L.J. King and J.M.G. Mead, The mass-concentration relationship of virialized haloes and its impact on cosmological observables, Mon. Not. R. Astron. Soc. **416**, 2539—2549 (2011); 1105.3155.
88. D. Kirilova, On Lepton asymmetry and BBN, Progress in Particle and Nuclear Physics **66**, 260—265 (2011).
89. A. Klypin, A.V. Kravtsov, O. Valenzuela, and F. Prada, Where Are the Missing Galactic Satellites? Astrophys. J. **522**, 82—92 (1999); arXiv:astro-ph/9901240.
90. E. Komatsu et al., Five-Year Wilkinson Microwave Anisotropy Probe Observations: Cosmological Interpretation, Astrophys. J. Suppl. Ser. **180**, 330—376 (2009); 0803.0547.
91. J. Kormendy and K.C. Freeman, Scaling Laws for Dark Matter Halos in Late-Type and Dwarf Spheroidal Galaxies. In S. Ryder, D. Pisano, M. Walker, and K. Freeman (eds.) Dark Matter in Galaxies, vol. 220 of IAU Symposium, 377 (2004); arXiv:astro-ph/0407321.
92. J. Kormendy and S. Djorgovski, Surface photometry and the structure of elliptical galaxies, Ann. Rev. Astron. Astrophys. **27**, 235—277 (1989).

93. K. Koyama et al., Iron and Nickel Line Diagnostics for the Galactic Center Diffuse Emission, Publ. Astron. Soc. Jpn. **59**, 245—255 (2007); arXiv:astro-ph/0609215.
94. K.D. Kuntz and S.L. Snowden, The EPIC-MOS particle-induced background spectra, Astron. Astrophys. **478**, 575—596 (2008).
95. A. Kusenko, Sterile neutrinos: the dark side of the light fermions, Phys. Rept. **481**, 1—28 (2009); 0906.2968.
96. A. Kusenko, Sterile dark matter and reionization (2006); astro-ph/0609375.
97. A. Kusenko, M. Loewenstein, and T.T. Yanagida, Moduli dark matter and the search for its decay line using Suzaku X-ray telescope, ArXiv e-prints (2012); 1209.6403.
98. M. Laine and M. Shaposhnikov, Sterile neutrino dark matter as a consequence of νMSM-induced lepton asymmetry, J. Cosm. Astropart. Phys. **6**, 31 (2008); arXiv:0804.4543.
99. T. Lasserre et al., Not enough stellar mass Machos in the Galactic halo, Astron. Astrophys. **355**, L39—L42 (2000); arXiv:astro-ph/0002253.
100. M. Lattanzi and J.W.F. Valle, Decaying warm dark matter and neutrino masses, Phys. Rev. Lett. **99**, 121301 (2007); 0705.2406.
101. J. Lavalle and P. Salati, Dark Matter Indirect Signatures, Comptes Rendus Physique **13**, 740—782 (2012); 1205.1004.
102. B.W. Lee and S. Weinberg, Cosmological lower bound on heavy-neutrino masses, Phys. Rev. Lett. **39**, 165—168 (1977).
103. J. Lesgourgues and S. Pastor, Cosmological implications of a relic neutrino asymmetry, Phys. Rev. D **60**, 103521 (1999); hep-ph/9904411.
104. J. Lesgourgues and S. Pastor, Massive neutrinos and cosmology, Phys. Rept. **429**, 307—379 (2006); astro-ph/0603494.
105. J. Lesgourgues and S. Pastor, Neutrino mass from Cosmology, Adv. High Energy Phys. **2012**, 608515 (2012); 1212.6154.
106. W. Liao, keV scale ν_R dark matter and its detection in β decay experiment, Phys. Rev. D **82**, 073001 (2010); 1005.3351.
107. M. Lovell et al., The Haloes of Bright Satellite Galaxies in a Warm Dark Matter Universe, Mon. Not. R. Astron. Soc. to appear (2011); 1104.2929.
108. M. Loewenstein and A. Kusenko, Dark Matter Search Using Chandra Observations of Willman 1, and a Spectral Feature Consistent with a Decay Line of a 5 keV Sterile Neutrino, Astrophys. J. **714**, 652—662 (2010); 0912.0552.
109. M. Loewenstein and A. Kusenko, Dark Matter Search Using XMM-Newton Observations of Willman 1, Astrophys. J. **751**, 82 (2012); 1203.5229.
110. M. Loewenstein, A. Kusenko, and P.L. Biermann, New Limits on Sterile Neutrinos from Suzaku Observations of the Ursa Minor Dwarf Spheroidal Galaxy, Astrophys. J. **700**, 426—435 (2009); 0812.2710.
111. LSST Science Collaborations et al. LSST Science Book, Version 2.0, ArXiv e-prints (2009); 0912.0201.
112. D.H. Lumb, R.S. Warwick, M. Page, and A. De Luca, X-ray background measurements with xmm-newton epic, Astron. Astrophys. **389**, 93—105 (2002); astro-ph/0204147.

113. A.V. Macciò, A.A. Dutton, and F.C. van den Bosch, Concentration, spin and shape of dark matter haloes as a function of the cosmological model: WMAP1, WMAP3 and WMAP5 results, Mon. Not. R. Astron. Soc. **391**, 1940—1954 (2008); 0805.1926.
114. A.V. Macciò and F. Fontanot, How cold is dark matter? Constraints from Milky Way satellites, Mon. Not. R. Astron. Soc. **404**, L16—L20 (2010); 0910.2460.
115. A.V. Macciò, S. Paduroiu, D. Anderhalden, A. Schneider, and B. Moore, Cores in warm dark matter haloes: a Catch 22 problem, Mon. Not. R. Astron. Soc. **424**, 1105—1112 (2012); 1202.1282.
116. A.V. Macciò, O. Ruchayskiy, A. Boyarsky, and J.C. Munoz-Cuartas, The inner structure of haloes in Cold + Warm dark matter models, Mon. Not. R. Astron. Soc. (2012); 1202.2858.
117. A.V. Macciò et al., Luminosity function and radial distribution of Milky Way satellites in a ΛCDM Universe, Mon. Not. R. Astron. Soc. **402**, 1995—2008 (2010); 0903.4681.
118. J. Madsen, Phase-space constraints on bosonic and fermionic dark matter, Phys. Rev. Lett. **64**, 2744—2746 (1990).
119. J. Madsen, Generalized Tremaine-Gunn limits for bosons and fermions, Phys. Rev. D **44**, 999—1006 (1991).
120. R. Mandelbaum, U. Seljak, and C.M. Hirata, Halo mass — concentration relation from weak lensing, J. Cosm. Astropart. Phys. **0808**, 006 (2008); 0805.2552.
121. G. Mangano, G. Miele, S. Pastor, O. Pisanti, and S. Sarikas, Constraining the cosmic radiation density due to lepton number with Big Bang Nucleosynthesis, J. Cosm. Astropart. Phys. **1103**, 035 (2011); 1011.0916.
122. M. Mapelli, A. Ferrara, and E. Pierpaoli, Impact of dark matter decays and annihilations on reionization, Mon. Not. Roy. Astron. Soc. **369**, 1719—1724 (2006); astro-ph/0603237.
123. M. Markevitch et al., Chandra Spectra of the Soft X-Ray Diffuse Background, Astrophys. J. **583**, 70—84 (2003); astro-ph/0209441.
124. K. Markovic, S. Bridle, A. Slosar, and J. Weller, Constraining warm dark matter with cosmic shear power spectra, J. Cosm. Astropart. Phys. **1101**, 022 (2011); 1009.0218.
125. D. McCammon, Thermal Equilibrium Calorimeters — An Introduction, 1. Topics in Applied Physics (Springer, 2005); URL http://books.google.ch/books?id=zUxm2EHppcwC.
126. D. McCammon et al., A High Spectral Resolution Observation of the Soft X-Ray Diffuse Background with Thermal Detectors, Astrophys. J. **576**, 188—203 (2002); astro-ph/0205012.
127. M. Milgrom, A modification of the Newtonian dynamics — Implications for galaxies, Astrophys. J. **270**, 371—389 (1983).
128. S.P. Mikheev and A.Y. Smirnov, Resonance enhancement of oscillations in matter and solar neutrino spectroscopy, Sov. J. Nucl. Phys. **42**, 913—917 (1985).
129. P. Minkowski, $\mu \to e\gamma$ at a rate of one out of 1-billion muon decays? Phys. Lett. B **67**, 421 (1977).
130. N. Mirabal and D. Nieto, Willman 1: An X-ray shot in the dark with Chandra (2010); 1003.3745.

131. N. Mirabal and D. Nieto, Willman 1 in X-rays: Can you tell a dwarf galaxy from a globular cluster? ArXiv e-prints (2010); 1003.3745.
132. N. Mirabal, Swift observation of Segue 1: constraints on sterile neutrino parameters in the darkest galaxy, Mon. Not. R. Astron. Soc. **409**, L128—L131 (2010); 1010.4706.
133. M. Miranda and A.V. Macciò, Constraining Warm Dark Matter using QSO gravitational lensing (2007); 0706.0896.
134. J.W. Moffat and V.T. Toth, Comment on "The Real Problem with MOND" by Scott Dodelson, arXiv:1112.1320; ArXiv e-prints (2011); 1112.4386.
135. R.N. Mohapatra and G. Senjanovic, Neutrino mass and spontaneous parity nonconservation, Phys. Rev. Lett. **44**, 912 (1980).
136. M. Moniez, Microlensing as a probe of the Galactic structure: 20 years of microlensing optical depth studies, General Relativity and Gravitation **42**, 2047—2074 (2010); 1001.2707.
137. B. Moore et al., Dark matter substructure within galactic halos, Astrophys. J. **524**, L19—L22 (1999); arXiv:astro-ph/9907411.
138. R.K. de Naray, G.D. Martinez, J.S. Bullock, and M. Kaplinghat, The Case Against Warm or Self-Interacting Dark Matter as Explanations for Cores in Low Surface Brightness Galaxies (2009); 0912.3518.
139. J.F. Navarro, C.S. Frenk, and S.D.M. White, The Structure of Cold Dark Matter Halos, Astrophys. J. **462**, 563—575 (1996); astro-ph/9508025.
140. J.F. Navarro, C.S. Frenk, and S.D.M. White, A universal density profile from hierarchical clustering, Astrophys. J. **490**, 493—508 (1997); astro-ph/9611107.
141. J. Nevalainen, M. Markevitch, and D. Lumb, Xmm-newton epic background modeling for extended sources, Astrophys. J. **629**, 172—191 (2005); astro-ph/0504362.
142. D. Notzold and G. Raffelt, Neutrino Dispersion at Finite Temperature and Density, Nucl. Phys. B **307**, 924 (1988).
143. P.B. Pal and L. Wolfenstein, Radiative decays of massive neutrinos, Phys. Rev. D **25**, 766 (1982).
144. P.J.E. Peebles, *The large-scale structure of the universe* (Princeton University Press, Princeton, N.J., 1980), 435 p.
145. L. Piro, J.W. den Herder, T. Ohashi et al., EDGE: Explorer of diffuse emission and gamma-ray burst explosions, Experimental Astronomy **23**, 67—89 (2009); 0707.4103.
146. Planck Collaboration et al., Planck 2013 results. XVI. Cosmological parameters, ArXiv e-prints (2013); 1303.5076.
147. E. Polisensky and M. Ricotti, Constraints on the Dark Matter Particle Mass from the Number of Milky Way Satellites, Phys. Rev. D **83**, 043506 (2011); 1004.1459.
148. J. Pradas and J. Kerp, XMM-Newton data processing for faint diffuse emission. Proton flares, exposure maps and report on EPIC MOS1 bright CCDs contamination, Astron. Astrophys. **443**, 721—733 (2005); arXiv:astro-ph/0508137.
149. D.A. Prokhorov and J. Silk, Can the Excess in the FeXXVI Ly Gamma Line from the Galactic Center Provide Evidence for 17 keV Sterile Neutrinos? (2010); 1001.0215.

150. F. Porter, Low-temperature detectors in x-ray astronomy. Nuclear Instruments and Methods in Physics Research Section A: Accelerators, Spectrometers, Detectors and Associated Equipment **520**, 354—358 (2004); URL http://www.sciencedirect.com/science/article/pii/S0168900203031681.
151. P. Ramond, The family group in grand unified theories (1979); hep-ph/9809459.
152. A.M. Read and T.J. Ponman, The xmm-newton epic background: Production of background maps and event files, Astron. Astrophys. **409**, 395—410 (2003); astro-ph/0304147.
153. S. Riemer-Sørensen, S.H. Hansen, and K. Pedersen, Sterile Neutrinos in the Milky Way: Observational Constraints, Astrophys. J. Lett. **644**, L33—L36 (2006); astro-ph/0603661.
154. S. Riemer-Sørensen and S.H. Hansen, Decaying dark matter in Draco, Astron. Astrophys. **500**, L37—L40 (2009); 0901.2569.
155. S. Riemer-Sørensen, S.H. Hansen, and K. Pedersen, Sterile Neutrinos in the Milky Way: Observational Constraints, Astrophys. J. Lett. **644**, L33—L36 (2006); arXiv:astro-ph/0603661.
156. S. Riemer-Sørensen, K. Pedersen, S.H. Hansen, and H. Dahle, Probing the nature of dark matter with cosmic x rays: Constraints from "dark blobs" and grating spectra of galaxy clusters, Phys. Rev. D **76**, 043524 (2007); arXiv:astro-ph/0610034.
157. S. Riemer-Sørensen and S.H. Hansen, Decaying dark matter in the Draco dwarf galaxy, Astron. Astrophys. **500**, L37—L40 (2009).
158. E. Ripamonti,M. Mapelli, and A. Ferrara, The impact of dark matter decays and annihilations on the formation of the first structures, Mon. Not. Roy. Astron. Soc. **375**, 1399—1408 (2007); astro-ph/0606483.
159. E. Ripamonti, M. Mapelli, and A. Ferrara, Intergalactic medium heating by dark matter, Mon. Not. Roy. Astron. Soc. **374**, 1067—1077 (2007); astro-ph/0606482.
160. T. Saab, An Introduction to Dark Matter Direct Detection Searches and Techniques (2012); 1203.2566.
161. D.J. Schlegel et al., SDSS-III: The Baryon Oscillation Spectroscopic Survey (BOSS). In American Astronomical Society Meeting Abstracts, vol. 39 of Bulletin of the American Astronomical Society, No. 132.29 (2007).
162. A. Schneider, R.E. Smith, A.V. Maccio, and B. Moore, Nonlinear Evolution of Cosmological Structures in Warm Dark Matter Models (2011); 1112.0330.
163. U. Seljak, A. Makarov, P. McDonald, and H. Trac, Can sterile neutrinos be the dark matter? Phys. Rev. Lett. **97**, 191303 (2006); astro-ph/0602430.
164. E. Semboloni, H. Hoekstra, J. Schaye, M.P. van Daalen, and I.J. McCarthy, Quantifying the effect of baryon physics on weak lensing tomography, Mon. Not. R. Astron. Soc. **417**, 2020—2035 (2011); 1105.1075.
165. P.D. Serpico and G.G. Raffelt, Lepton asymmetry and primordial nucleosynthesis in the era of precision cosmology, Phys. Rev. D **71**, 127301 (2005); astro-ph/0506162.
166. S. Shao, L. Gao, T. Theuns, and C.S. Frenk, The phase space density of fermionic dark matter haloes (2012); 1209.5563.
167. M. Shaposhnikov, Is there a new physics between electroweak and Planck scales? (2007); 0708.3550.

168. M. Shaposhnikov, The νMSM, leptonic asymmetries, and properties of singlet fermions, J. High Energy Phys. **08**, 008 (2008); 0804.4542.
169. B.W. O'Shea and M.L. Norman, Population III star formation in a Lambda WDM universe, Astrophys. J. **648**, 31—46 (2006); astro-ph/0602319.
170. X.-D. Shi and G.M. Fuller, A new dark matter candidate: Non-thermal sterile neutrinos, Phys. Rev. Lett. **82**, 2832—2835 (1999); astro-ph/9810076.
171. R.E. Smith and K. Markovic, Testing the Warm Dark Matter paradigm with large-scale structures, Phys. Rev. D **84**, 063507 (2011); 1103.2134.
172. J. Sommer-Larsen, P. Naselsky, I. Novikov, and M. Gotz, Inhomogenous Primordial Baryon Distributions on Sub-Galactic Scales: High-z Galaxy Formation with WDM, Mon. Not. Roy. Astron. Soc. **352**, 299 (2004); astro-ph/0309329.
173. R.S. Somerville, Can Photoionization Squelching Resolve the Substructure Crisis? Astrophys. J. Lett. **572**, L23—L26 (2002); arXiv:astro-ph/0107507.
174. V. Springel et al., The Aquarius Project: the subhaloes of galactic haloes, Mon. Not. R. Astron. Soc. **391**, 1685—1711 (2008); 0809.0898.
175. L.E. Strigari et al., A large dark matter core in the fornax dwarf spheroidal galaxy? Astrophys. J. **652**, 306—312 (2006); arXiv:astro-ph/0603775.
176. L.E. Strigari, C.S. Frenk, and S.D.M. White, Kinematics of Milky Way satellites in a Lambda cold dark matter universe, Mon. Not. R. Astron. Soc. **408**, 2364—2372 (2010); 1003.4268.
177. J. Stasielak, P.L. Biermann, and A. Kusenko, Thermal evolution of the primordial clouds in warm dark matter models with kev sterile neutrinos, Astrophys. J. **654**, 290—303 (2007); arXiv:astro-ph/0606435.
178. R. Supper et al., ROSAT PSPC survey of M 31, Astron. Astrophys. **317**, 328—349 (1997).
179. M. Taoso, G. Bertone, and A. Masiero, Dark Matter Candidates: A Ten-Point Test, J. Cosm. Astropart. Phys. **0803**, 022 (2008); 0711.4996.
180. T. Takahashi et al., The ASTRO-H Mission. In Society of Photo-Optical Instrumentation Engineers (SPIE) Conference Series, vol. 7732 of Presented at the Society of Photo-Optical Instrumentation Engineers (SPIE) Conference (2010); 1010.4972.
181. S. Tremaine and J.E. Gunn, Dynamical role of light neutral leptons in cosmology, Phys. Rev. Lett. **42**, 407—410 (1979).
182. H. Tsunemi et al., Development of a large format charge-coupled device (CCD) for applications in X-ray astronomy, Nucl. Instr. and Methods in Phys. Research A **579**, 866—870 (2007).
183. R.B. Tully and J.R. Fisher, A new method of determining distances to galaxies, Astron. Astrophys. **54**, 661—673 (1977).
184. H. de Vega, O. Moreno, E.M. de Guerra, M.R. Medrano, and N. Sanchez, Role of sterile neutrino warm dark matter in rhenium and tritium beta decays, Nucl. Phys. B **866**, 177 (2013); 1109.3452.
185. J. Vernet et al., X-shooter, the new wide band intermediate resolution spectrograph at the ESO Very Large Telescope, Astron. Astrophys. **536**, A105 (2011); 1110.1944.
186. M. Viel, G.D. Becker, J.S. Bolton, and M.G. Haehnelt, Warm Dark Matter as a solution to the small scale crisis: new constraints from high redshift Lyman-alpha forest data, ArXiv e-prints (2013); 1306.2314.

187. M. Viel, J. Lesgourgues, M.G. Haehnelt, S. Matarrese, and A. Riotto, Constraining warm dark matter candidates including sterile neutrinos and light gravitinos with wmap and the Lyman-alpha forest, Phys. Rev. D **71**, 063534 (2005); astro-ph/0501562.
188. M. Viel, J. Lesgourgues, M.G. Haehnelt, S. Matarrese, and A. Riotto, Can sterile neutrinos be ruled out as warm dark matter candidates? Phys. Rev. Lett. **97**, 071301 (2006); astro-ph/0605706.
189. M. Viel, K. Markovic, M. Baldi, and J. Weller, The Non-Linear Matter Power Spectrum in Warm Dark Matter Cosmologies, Mon. Not. R. Astron. Soc. (2011); 1107.4094.
190. M. Viel, J. Schaye, and C.M. Booth, The impact of feedback from galaxy formation on the Lyman-alpha transmitted flux (2012); 1207.6567.
191. M. Viel et al., How cold is cold dark matter? Small scales constraints from the flux power spectrum of the high-redshift Lyman-alpha forest, Phys. Rev. Lett. **100**, 041304 (2008); 0709.0131.
192. C.R. Watson, J.F. Beacom, H. Yuksel, and T.P. Walker, Direct x-ray constraints on sterile neutrino warm dark matter, Phys. Rev. D **74**, 033009 (2006); astro-ph/0605424.
193. C.R. Watson, Z. Li, and N.K. Polley, Constraining sterile neutrino warm dark matter with Chandra observations of the Andromeda galaxy, J. Cosm. Astropart. Phys. **3**, 18 (2012); 1111.4217.
194. R. Wojtak, S.H. Hansen, and J. Hjorth, Gravitational redshift of galaxies in clusters as predicted by general relativity, Nature **477**, 567—569 (2011), 1109.6571.
195. L. Wolfenstein, Neutrino oscillations in matter, Phys. Rev. D **17**, 2369—2374 (1978).
196. T. Yanagida, Horizontal gauge symmetry and masses of neutrinos, Prog. Theor. Phys. **64**, 1103 (1980).
197. N. Yoshida, A. Sokasian, L. Hernquist, and V. Springel, Early Structure Formation and Reionization in a Warm Dark Matter Cosmology, Astrophys. J. **591**, L1—L4 (2003); astro-ph/0303622.
198. B. Yue and X. Chen, Reionization in the Warm Dark Matter Model, Astrophys. J. **747**, 127 (2012); 1201.3686.
199. H. Yuksel, J.F. Beacom, and C.R. Watson, Strong Upper Limits on Sterile Neutrino Warm Dark Matter, Phys. Rev. Lett. **101**, 121301 (2008); 0706.4084.
200. Y.B. Zel'dovich, Gravitational instability: An approximate theory for large density perturbations, Astron. Astrophys. **5**, 84—89 (1970).

7 CHAPTER

SEARCH FOR EFFECTS BEYOND THE STANDARD MODEL OF PARTICLES IN LOW COUNTING EXPERIMENTS

F.A. Danevich, V.V. Kobychev, V.I. Tretyak

In fundamental physics,
if something can be tested,
it should be tested.
L.B. Okun [355]

7.1. Introduction

Properties of particles and interactions — and, in particular, properties of neutrino and weak interactions — play a key role not only in particle physics, but also in cosmology and astrophysics. Measurements of neutrino fluxes from the Sun, from cosmic rays in atmosphere, from reactors and accelerators give strong evidence of neutrino oscillations, an effect which cannot be explained in framework of the Standard Model of particles. Search for neutrinoless double beta decay is considered now as an unique tool to study properties of neutrino. Study of this extremely rare nuclear decay with the help of nuclear spectrometry methods, without building of rather expensive accelerators, allows to investigate quite wide range of interesting and important effects beyond the Standard Model: nature of neutrino (is neutrino Dirac or Majorana particle), an absolute scale and the mass scheme of neutrino, to check the lepton number conservation, examine existence of hypothetical Nambu—Goldstone bosons (majorons) and right-handed currents in weak interaction.

Experiments with neutrino detectors, in addition to fundamental investigations of neutrino oscillation parameters, provide important knowledge of electromagnetic properties of neutrino, examine possible existence and mixing with heavy neutrino. Furthermore, the experiments directed to detect solar or/and reactor neutrinos can study

neutrino flux from the Earth providing an unique information on our planet structure.

Development of sensitive experimental technique to search for double beta decay, the rarest process ever observed, allow in parallel to study several hypothetical particles and processes, such as decay of electron or nucleons, violation of the Pauli principle, search for mass of photon, etc. Another direction of astroparticle (underground) physics is search for axions, hypothetical particles predicted to explain the strong CP problem in quantum chromodynamics. Axions are also considered as very promising candidates to explain dark matter in the Universe.

There is an evidence for a large amount of invisible (dark) matter in the Universe, which reveals itself only through gravitational interaction. Weakly interacting massive particles (WIMPs), in particular neutralino predicted by the Minimal Supersymmetric extensions of the Standard Model, are considered as one of the most acceptable components of the dark matter. A few current large scale projects to search for dark matter require development of massive (hundreds and thousands kg) ultra-low background detectors which contain certain elements (or variety of elements), have low energy threshold, are extremely radiopure, and are able to distinguish very weak effect from background.

Scintillation detectors possess range of unique properties for the low counting experiments: low radioactive contamination, presence of different elements, stability over tens of years of operation, reasonable price. Moreover, development, during the last decade, of the technique of low temperature scintillating bolometers give a "second wind" for the scintillation method allowing to reach very high energy resolution and low energy threshold, excellent particle discrimination ability, which are especially important features for the next generation double beta and dark matter experiments.

Double β decay and dark matter experiments demand super-low radioactive background which can be reached only in deep underground laboratories and with detectors constructed with super-pure materials. Development of experimental methods to search for the rare events gives possibility to search for other rare processes in nuclear and particle physics, such as transition of nuclei to super-dense state, nuclear decays with cluster emission, rare β and α decays.

We present here brief reviews of current status and describe several recent results obtained in the field over last few years.

7.2. Double beta decay

7.2.1. Basic theory and experimental status

Double beta (2β) decay of atomic nuclei was considered by Maria Goeppert—Mayer in 1935 as nuclear process changing a nuclear charge by two units [257]. As an example, scheme of decay of ^{116}Cd is shown in Fig. 7.1.

Two neutrino (2ν) double beta decay, a process of transformation of nuclei with simultaneous emission of two electrons (positrons) and two antineutrinos (neutrinos):

$$(A, Z) \to (A, Z + 2) + 2e^- + 2\bar{\nu_e},$$
$$(A, Z) \to (A, Z - 2) + 2e^+ + 2\nu_e$$

is allowed in the Standard Model (SM). In addition to decay with emission of two positrons, capture of electron with positron emission, and double electron capture are possible:

$$e^- + (A, Z) \to (A, Z - 2) + e^+ + 2\nu_e,$$
$$2e^- + (A, Z) \to (A, Z - 2) + 2\nu_e.$$

However, being the second order process in weak interaction, 2β decay is characterized by an extremely low probability: to-date it is the rarest decay observed in direct laboratory experiments. It was detected only for 11 nuclides; corresponding half lives are in the range of 10^{18}—10^{24} yr [410, 411]. The positive experiments where the two neutrino double beta decay was observed, and experiments giving the most stringent limits on two neutrino channel are listed in Table 7.1 (more detailed information, especially on geochemical experiments

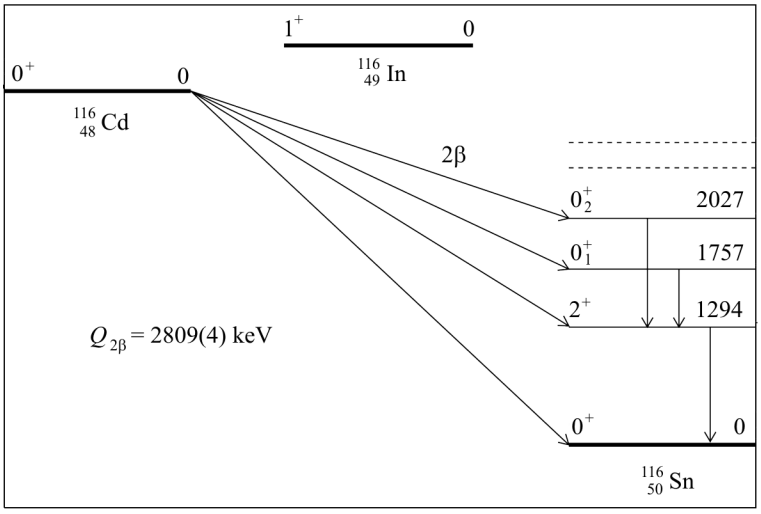

Fig. 7.1. Decay scheme of ^{116}Cd. Energies of excited levels and emitted γ quanta are in keV. $Q_{2\beta}$ is the double beta decay energy [57]

Table 7.1. **Half lives relatively to $2\nu2\beta^-$ decay. The data are presented for transitions to the ground states of the daughter nuclei. Transitions to the first 0_1^+ excited levels of the daughter nuclei ($0^+ \to 0_1^+$) are observed for ^{100}Mo and ^{150}Nd. If two uncertainties are given, the first one is statistical, and the second one is systematic**

Isotope	$T_{1/2}$, years	Experimental method	Ref.
^{48}Ca	$(4.3^{+2.4}_{-1.1} \pm 1.4) \times 10^{19}$	Enriched ^{48}Ca in time-projection chamber	[65]
	$(4.2^{+3.3}_{-1.3}) \times 10^{19}$	Enriched ^{48}Ca between planar Ge detectors	[168]
	$(4.4^{+0.5}_{-0.4} \pm 0.4) \times 10^{19}$	Tracking calorimeter NEMO-3	[413]
^{76}Ge	$(9.0 \pm 1.0) \times 10^{20}$	HPGe detectors with enriched ^{76}Ge	[418]
	$(1.1^{+0.6}_{-0.3}) \times 10^{21}$	Same	[332]
	$(8.4^{+1.0}_{-0.8}) \times 10^{20}$	”	[167]
	$(1.1 \pm 0.2) \times 10^{21}$	”	[4]
	$(1.77 \pm 0.01^{+0.13}_{-0.11}) \times 10^{21}$	”	[261]
	$(1.55 \pm 0.01^{+0.19}_{-0.15}) \times 10^{21}$	”	[291]
	$(1.74 \pm 0.01^{+0.18}_{-0.16}) \times 10^{21}$	”	[215]
^{82}Se	$(1.2 \pm 0.1 \pm 0.4) \times 10^{19}$	Geochemical	[318]
	$(1.08^{+0.26}_{-0.06}) \times 10^{20}$	Enriched ^{82}Se in time-projection chamber	[228]
	$(8.3 \pm 1.0 \pm 0.7) \times 10^{19}$	Tracking calorimeter NEMO-2	[45]
	$(9.6 \pm 0.3 \pm 1.0) \times 10^{19}$	Tracking calorimeter NEMO-3	[46]
^{96}Zr	$(3.9 \pm 0.9) \times 10^{19}$	Geochemical	[280]
	$(2.1^{+0.8}_{-0.4}) \times 10^{19}$	Tracking calorimeter NEMO-2	[44]
	$(9.4 \pm 3.2) \times 10^{18}$	Geochemical	[429]
	$(2.35 \pm 0.14 \pm 0.16) \times 10^{19}$	Tracking calorimeter NEMO-3	[36]
^{100}Mo	$(3.3^{+2.0}_{-1.0}) \times 10^{18}$	Enriched ^{100}Mo between plastic scintillators and proportional chambers	[419]
	$(1.2^{+0.5}_{-0.3}) \times 10^{19}$	Enriched ^{100}Mo between plastic scintillators in a proportional chamber (ELEGANT V)	[221]
	$(9.5 \pm 0.4 \pm 0.9) \times 10^{18}$	Tracking calorimeter NEMO-2	[202]
	$(7.6^{+2.2}_{-1.4}) \times 10^{18}$	^{100}Mo foil between Si(Li) detectors	[22]
	$(6.82^{+0.38}_{-0.53} \pm 0.68) \times 10^{18}$	^{100}Mo foil in time-projection chamber	[387]
	$(7.2 \pm 0.9 \pm 1.8) \times 10^{18}$	^{100}Mo in ionization chamber with liquid argon	[50]
	$(2.1 \pm 0.3) \times 10^{18}$	Geochemical	[265]
	$(7.11 \pm 0.02 \pm 0.54) \times 10^{18}$	Tracking calorimeter NEMO-3	[46]
^{100}Mo	$(6.1^{+1.8}_{-1.1}) \times 10^{20}$	HPGe γ spectrometry of ^{100}Mo sample	[71]
$0^+ \to 0_1^+$	$(9.3^{+2.8}_{-1.7}) \times 10^{20}$	HPGe γ spectrometry of ^{100}Mo samples	[78]
	$(5.9^{+1.7}_{-1.1} \pm 0.6) \times 10^{20}$	HPGe γ spectrometry of ^{100}Mo sample	[166]
	$(5.7^{+1.3}_{-0.9} \pm 0.8) \times 10^{20}$	Tracking calorimeter NEMO-3	[48]
	$(5.5^{+1.2}_{-0.8} \pm 0.3) \times 10^{20}$	HPGe γ spectrometry of ^{100}Mo sample	[281]
	$(6.9^{+1.0}_{-0.8} \pm 0.7) \times 10^{20}$	HPGe γ spectrometry of ^{100}Mo sample	[91]
^{114}Cd	$>1.3 \times 10^{18}$ at 90 % CL	$CdWO_4$ crystal scintillator	[92]
^{116}Cd	$(2.6^{+0.9}_{-0.5}) \times 10^{19}$	^{116}Cd foil between plastic scintillators in a proportional chamber (ELEGANT IV)	[222]
	$(2.9^{+0.4}_{-0.3}) \times 10^{19}$	$^{116}CdWO_4$ crystal scintillators	[200]

End of the tabl. 7.1

Isotope	$T_{1/2}$, years	Experimental method	Ref.
	$(3.75 \pm 0.35 \pm 0.21) \times 10^{19}$	Tracking calorimeter NEMO-2	[47]
	$(2.88 \pm 0.04 \pm 0.16) \times 10^{19}$	Tracking calorimeter NEMO-3	[413]
^{128}Te	$(1.8 \pm 0.7) \times 10^{24}$	Geochemical	[317]
	$(7.7 \pm 0.4) \times 10^{24}$	Geochemical	[150]
	$(2.4 \pm 0.4) \times 10^{24}$	Geochemical	[329]
^{130}Te	$(2.60 \pm 0.28) \times 10^{21}$	Geochemical	[287]
	$(7.5 \pm 0.3 \pm 2.3) \times 10^{20}$	Geochemical	[317]
	$(2.7 \pm 0.1) \times 10^{21}$	Geochemical	[150]
	$(7.9 \pm 1.0) \times 10^{20}$	Geochemical	[404]
	$(6.1 \pm 1.4^{+2.9}_{-3.5}) \times 10^{20}$	Cryogenic bolometer with TeO_2 crystals	[42]
	$(9.0 \pm 1.4) \times 10^{20}$	Geochemical	[329]
	$(7.0 \pm 0.9 \pm 1.1) \times 10^{20}$	Tracking calorimeter NEMO-3	[43]
^{136}Xe	$>1.0 \times 10^{22}$ at 90 % CL	Scintillation detector with liquid xenon enriched in ^{136}Xe	[148]
	$>8.5 \times 10^{21}$ at 90 % CL	High-pressure proportional counter filled by enriched ^{136}Xe	[245]
	$(2.11 \pm 0.04 \pm 0.21) \times 10^{21}$	EXO time projection chamber filled by liquid enriched ^{136}Xe	[8]
	$(2.38 \pm 0.02 \pm 0.11) \times 10^{21}$	KamLAND-Zen liquid scintillator loaded by enriched ^{136}Xe	[243]
^{150}Nd	$(1.88^{+0.66}_{-0.39} \pm 0.19) \times 10^{19}$	^{150}Nd sample in time-projection chamber	[39]
	$(6.75^{+0.37}_{-0.42} \pm 0.68) \times 10^{18}$	^{150}Nd sample in time-projection chamber	[387]
	$(9.11^{+0.25}_{-0.22} \pm 0.63) \times 10^{18}$	Tracking calorimeter NEMO-3	[35]
^{150}Nd $0^+ \to 0^+_1$	$(1.33^{+0.36+0.27}_{-0.23-0.13}) \times 10^{20}$	HPGe γ spectrometry of ^{150}Nd sample	[79]
^{160}Gd	$>1.9 \times 10^{19}$ at 90 % CL	Gd_2SiO_5(Ce) crystal scintillator	[201]
^{186}W	$>2.3 \times 10^{19}$ at 90 % CL	$ZnWO_4$ crystal scintillators	[93]
^{238}U	$(2.0 \pm 0.6) \times 10^{21}$	Radiochemical	[415]

with ^{82}Se, ^{128}Te, ^{130}Te can be found in [410, 411]). Estimation of average half lives of the nuclides is proposed in [70]. It should be stressed, that comparison of the measured half lives of different isotopes relatively to the two neutrino mode allows to tune theoretical calculations for the neutrinoless mode (see below), important to derive values of the effective neutrino mass from experimental data.

In 1937 Ettore Majorana has introduced a true neutral neutrino equivalent to its antiparticle (Majorana neutrino, $\nu \equiv \bar{\nu}$) [323]. In 1939 W.H. Furry [240] considered at the first time possibility of neutrinoless double beta ($0\nu2\beta$) decay, a process of transformation of (A, Z) to $(A, Z \pm 2)$ through exchange of virtual Majorana neutrinos and accompanied by emission of only electrons or

positrons:

$$(A, Z) \rightarrow (A, Z \pm 2) + 2e^{\mp}.$$

Neutrinoless 2β decay of atomic nuclei is forbidden in the SM because this process violates the lepton number by two units [52, 53, 75, 225, 227, 229, 253, 259,347,374,420,421,435]. However, this decay is predicted in many SM extensions which expect in a natural way that the neutrino is a Majorana particle with non-zero mass. While experiments on neutrino oscillations already gave evidence that the neutrino is massive [216,341], these experiments are sensitive only to neutrino mass differences. Double beta decay experiments are considered to-date as the best instrument to determine an absolute scale of neutrino mass, establish the neutrino mass hierarchy, probe the nature of the neutrino (is it a Majorana or a Dirac particle?), test conservation of the lepton number.

The half life of $0\nu2\beta$ decay is inversely proportional to the square of the effective Majorana mass of neutrino $\langle m_\nu \rangle$:

$$(T_{1/2}^{0\nu2\beta})^{-1} = G^{0\nu}(Q_{\beta\beta}, Z) \times |M^{0\nu}|^2 \times \langle m_\nu \rangle^2 \text{ with } \langle m_\nu \rangle = |\Sigma U_{ej}^2 m_{\nu_i}|, \quad (7.1)$$

where $G^{0\nu}(Q_{\beta\beta}, Z)$ is the phase space integral, $M^{0\nu}$ is the nuclear matrix element, m_{ν_i} are the mass eigenstates of neutrino, U_{ej} — matrix elements of mixing between the mass eigenstates and flavor states of neutrino.

Experimental investigations of double β decay are carried out by different approaches: geochemical (measurements of daughter isotopes in old minerals containing element of interest), radiochemical (detection of alpha activity of daughter nuclei in a sample of uranium), direct counting methods by using nuclear detectors. According to Yu.G. Zdesenko [435], the last approach can be divided in two different classes: (a) experiments using a "passive" source placed near detectors; and (b) experiments involving an "active" source, in which a detector contains 2β decay candidate nuclei and thus serves as both source and detector simultaneously.

Developments in the experimental techniques during the last two decades lead to an impressive improvement of sensitivity to the neutrinoless mode of $2\beta^-$ decay up to 10^{23}—10^{25} yr. Readers can find an interesting historical review of double beta decay studies in [76]. History of false discoveries of this rare process is presented in [409]. Results of the most sensitive experiments to search for $0\nu2\beta^-$ decay are given in Table 7.2.

In more general terms the half life relatively to the $0\nu2\beta$ decay should include also admixtures of hypothetical right-handed currents in weak interactions:

$$(T_{1/2}^{0\nu})^{-1} = C_{mm}^{0\nu}(\frac{\langle m_\nu \rangle}{m_e})^2 + C_{m\lambda}^{0\nu}\langle\lambda\rangle\frac{\langle m_\nu \rangle}{m_e} + C_{m\eta}^{0\nu}\langle\eta\rangle\frac{\langle m_\nu \rangle}{m_e} + \\ + C_{\lambda\lambda}^{0\nu}\langle\lambda\rangle^2 + C_{\eta\eta}^{0\nu}\langle\eta\rangle^2 + C_{\lambda\eta}^{0\nu}\langle\lambda\rangle\langle\eta\rangle,$$

Table 7.2. **Results of the most sensitive experiments to search for $0\nu2\beta^-$ decay. If not specified explicitly, the limits are given for the transition to the ground state of the daughter nuclei. The values of the effective Majorana neutrino mass $\langle m_\nu \rangle$ and coupling constants $\langle \lambda \rangle$, $\langle \eta \rangle$ derived from high sensitivity $0\nu2\beta$ decay experiments are also presented. The limits on $\langle m_\nu \rangle$ and $\langle \eta \rangle$ from the observation of 2β decay of ^{128}Te were derived under assumption that the 2β decay of this isotope is due to the neutrinoless decay [150]**

Isotope	$T_{1/2}$, years	CL, %	m_ν, eV	$\eta(10^{-6})$	$\lambda(10^{-8})$	Experimental method	Ref.
^{48}Ca	$>1.4\times10^{22}$ $>5.8\times10^{22}$	90				CaF_2 crystal scintillators	[353] [416]
^{76}Ge	$>7.4\times10^{24}$ $>1.9\times10^{25}$ $>1.57\times10^{25}$ $(2.23^{+0.44}_{-0.31})\times$ $\times10^{25}$	90 90 90 68	 <0.35 <(0.33—1.35) 0.32 ± 0.03	<1.1 $0.692^{+0.058}_{-0.056}$	<0.64 $0.305^{+0.026}_{-0.025}$	HPGe detectors from enriched ^{76}Ge	[261] [291] [5] [290]
^{82}Se	$>2.7\times10^{22}$	68				^{82}Se foil in time-projection chamber	[228]
	$>2.7\times10^{22}$	90	<(1.7—4.9)	<3.8		NEMO-3	[46]
^{96}Zr	$>9.1\times10^{21}$	90				NEMO-3	[36]
^{100}Mo	$>5.5\times10^{22}$ $>4.2\times10^{22}$ $>4.9\times10^{22}$ $>4.6\times10^{23}$ $>8.9\times10^{22}$	90 90 90	<(2.1)—4.8 <(0.7—2.8)	 <(3.2—4.7) <2.5	 <(2.4—2.7) 	^{100}Mo foil between plastic scintillators in proportional chamber (ELEGANT V) NEMO-3 NEMO-3	[220] [46] [48]
^{114}Cd	$>1.1\times10^{21}$	90				$CdWO_4$ crystal scintillator	[92]
^{116}Cd	$>1.7\times10^{23}$ $>1.4\times10^{22}$ $>1.4\times10^{22}$ (0^+_1) $>2.9\times10^{22}$ (2^+_1)	90	<(1.5—1.7)	<2.2	<2.5	$^{116}CdWO_4$ crystal scintillators	[200]
^{128}Te	$>1.1\times10^{23}$ $(7.2\pm0.4)\times$ $\times10^{24}$	90	 <(1.1—1.5)		 <5.3	TeO_2 cryogenic bolometers Geochemical	[42] [150]
^{130}Te	$>2.1\times10^{23}$ $>3.0\times10^{24}$ $>3.1\times10^{22}$ (2^+_1)	90	<(1.6—2.4) <(0.19—0.68)		<(0.9—5.3)	TeO_2 cryogenic bolometers	[42] [41] [42]
^{134}Xe	$>5.8\times10^{22}$	90				Liquid xenon scintillation detector	[148]
^{136}Xe	$>3.4\times10^{23}$ $>2.6\times10^{23}$ $>1.2\times10^{24}$	90	<(1.8)—5.2 <2.9	<4.4	<2.3	Time projection chamber with ^{136}Xe Liquid xenon scintillation detector	[424] [148]
^{150}Nd	$>1.2\times10^{21}$	90				Time projection chamber with ^{150}Nd foil	[387]
	$>1.8\times10^{22}$	90	<(4.0—6.8)			NEMO-3	[35]
^{160}Gd	$>1.3\times10^{21}$	90				Gd_2SiO_5(Ce) crystal scintillator	[201]
^{186}W	$>1.1\times10^{21}$	90				$CdWO_4$ crystal scintillators	[200]

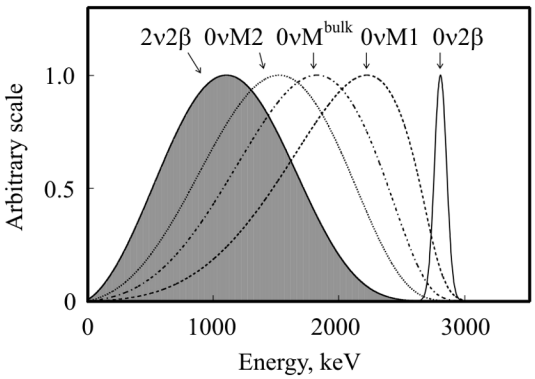

Fig. 7.2. Response functions of a detector with the energy resolution 4 % (full width at the half of peak maximum, FWHM) for the 2ν and 0ν modes of the 2β decay of ^{116}Cd

where $\langle\lambda\rangle$ describes the coupling between the right-handed lepton current and right-handed quark current, and $\langle\eta\rangle$ describes the coupling between the right-handed lepton current and left-handed quark current. The effective Majorana neutrino mass and the right-handed current coupling constants derived from the most sensitive $0\nu2\beta$ decay experiments are presented in Table 7.2.

Neutrinoless 2β decay may also occur due to existence of majorons, hypothetical neutral pseudoscalar zero mass (or very light) Nambu—Goldstone bosons, which couple to Majorana neutrinos and may be emitted in the neutnoless 2β decay [180, 181, 246]. The most sensitive experiments to search for majorons are presented in Table 7.3.

According to the Schechter—Valle theorem [383], observation of neutrinoless double β decay implies the Majorana nature of neutrinos with non-vanishing mass. Generally speaking, the neutrinoless double beta decay can be mediated by different hypothetical processes beyond the SM.

Broad energy spectra of two electrons are expected in case of two neutrino 2β decay and neutrinoless double β decay with emission of one, two and bulk [342] majorons. A sharp peak with the energy equal to $Q_{\beta\beta}$ and the width determined by the energy resolution of a detector is expected in a case of $0\nu2\beta$ decay (see Fig. 7.2).

Table 7.3. **The most sensitive experiments to search for double β decay with majoron emission. All the limits are given at 90 % CL**

Isotope	$T_{1/2}$, years	Experimental method	Ref.
^{76}Ge	$>1.7 \times 10^{22}$	HPGe detectors with enriched ^{76}Ge	[87]
^{82}Se	$>1.5 \times 10^{22}$	NEMO-3	[49]
^{100}Mo	$>2.7 \times 10^{22}$	NEMO-3	[49]
^{116}Cd	$>8.0 \times 10^{21}$	$^{116}CdWO_4$ crystal scintillators	[200]
^{128}Te	$>7.2 \times 10^{24}$	Geochemical	[150]
^{130}Te	$>2.2 \times 10^{21}$	TeO_2 cryogenic bolometers	[42]
^{136}Xe	$>5.0 \times 10^{23}$	Liquid xenon scintillation detector	[148]
^{150}Nd	$>1.5 \times 10^{21}$	NEMO-3	[35]

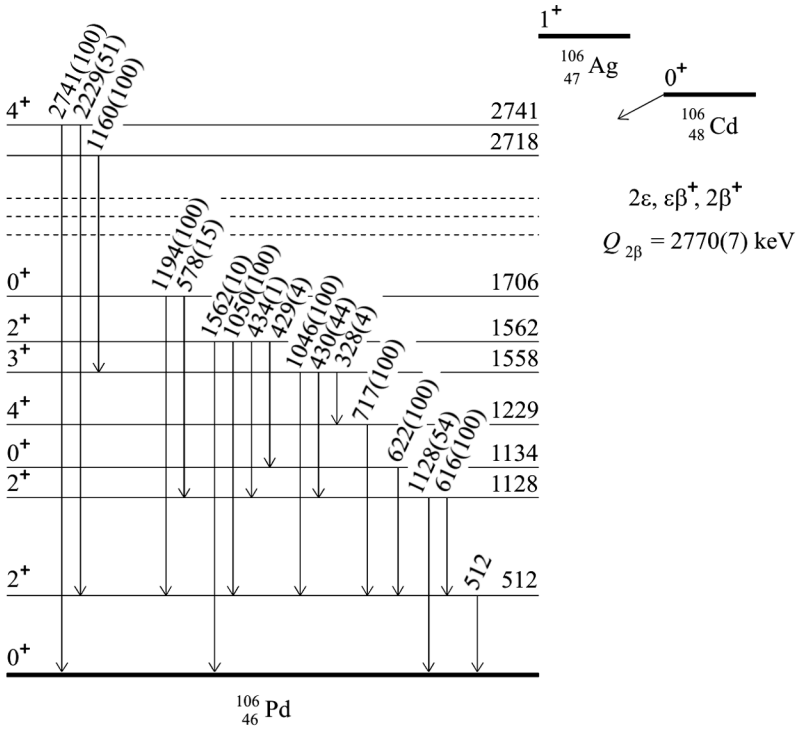

Fig. 7.3. Decay scheme of ^{106}Cd. Energies of excited levels and emitted γ quanta are in keV (relative intensities of γ quanta are given in parentheses). $Q_{2\beta}$ is the double beta decay energy

Several high sensitivity double beta decay projects are in preparation or in R&D stage: CANDLES (search for 2β decay of ^{48}Ca with the help of CaF_2 scintillators [433]), CUORE (^{130}Te, low temperature TeO_2 bolometers [40, 234]), GERDA [385] and MAJORANA [3] (^{76}Ge, semiconductor high-purity germanium detectors), LUICFER (^{82}Se, ZnSe scintillating bolometers operated at 20 mK [254]) and SuperNEMO (track detector based on NEMO-3 technology [72]), AMoRE (^{100}Mo, $CaMoO_4$ crystal scintillators [314]), EXO (^{136}Xe, time-projection chamber filled by liquid xenon with detection of scintillation [23]) and KamLAND-Zen (^{136}Xe dissolved in large volume liquid scintillator [405]), SNO+ (^{150}Nd, neodymuim loaded liquid scintillator [178]). All the experiments (except the CANDLES and CUORE projects in their first stages) intend to use hundred kilograms of enriched isotopes.

Experimental investigations are concentrated mostly on $2\beta^-$ decays, processes with emission of two electrons. Results for double positron decay ($2\beta^+$), electron capture with positron emission ($\varepsilon\beta^+$), and capture of two electrons from atomic shells (2ε) are much more modest (as an example, the decay scheme of ^{106}Cd is presented in Fig. 7.3). The most sensitive experiments give li-

Table 7.4. **Results of the most sensitive experiments to search for double electron capture (2ε), electron capture with emission of positron ($\varepsilon\beta^+$), and double positron emission ($2\beta^+$). In those cases where it is not specified, the limits are given for the transitions to the ground state of the daughter nuclei. Results correspond to 90 % CL, except of [98, 145, 328] which correspond to 68 % CL**

Isotope	Modes and channels of decay	$T_{1/2}$, years	Experimental method	Ref.
^{40}Ca	$2\nu2\varepsilon$	$>5.9 \times 10^{21}$	CaF_2(Eu) crystal scintillators	[94]
^{64}Zn	$2\nu2$K	$>1.1 \times 10^{19}$	$ZnWO_4$ crystal scintillators	[95]
	$0\nu2\varepsilon$	$>3.2 \times 10^{20}$	Same	
	$2\nu\varepsilon\beta^+$	$>1.0 \times 10^{21}$	”	
	$0\nu\varepsilon\beta^+$	$>8.7 \times 10^{20}$	”	
^{74}Se	$0\nu2\varepsilon(2_2^+, 1204.2$ keV)	$>5.5 \times 10^{18}$	HPGe γ spectrometry of enriched ^{74}Se	[73]
^{78}Kr	$2\nu2$K	$>1.5 \times 10^{21}$	Proportional counter with enriched ^{78}Kr	[244]
^{96}Ru	$0\nu2$K	$>1.2 \times 10^{19}$	HPGe γ spectroscopy of Ru sample	[96]
	$2\nu\varepsilon\beta^+$	$>2.5 \times 10^{18}$	Same	
	$2\nu2\beta^+$	$>3.9 \times 10^{18}$	”	
^{106}Cd	$2\nu2\varepsilon$	$>3.6 \times 10^{20}$	^{106}Cd foil between HPGe (TGV)	[378]
	$2\nu\varepsilon\beta^+$	$>4.1 \times 10^{20}$	^{106}Cd sample between NaI(Tl) detectors	[98]
	$0\nu\varepsilon\beta^+$	$>3.7 \times 10^{20}$	Same	
	$(2\nu + 0\nu)\ 2\beta^+$	$>1.6 \times 10^{20}$	”	
	$0\nu2\varepsilon$	$>1.3 \times 10^{21}$	$^{106}CdWO_4$ crystal scintillator	[99]
	$0\nu\varepsilon\beta^+$	$>2.6 \times 10^{21}$	Same	
	$2\nu2\beta^+$	$>6.0 \times 10^{20}$	”	
	$0\nu2\beta^+$	$>1.3 \times 10^{21}$	”	
^{108}Cd	$2\nu2$K	$>1.1 \times 10^{18}$	$CdWO_4$ crystal scintillator	[92]
	$0\nu2\varepsilon$	$>1.0 \times 10^{18}$	Same	
^{120}Te	$2\nu\varepsilon\beta^+$	$>7.6 \times 10^{19}$	TeO_2 cryogenic bolometers	[26]
	$0\nu\varepsilon\beta^+$	$>1.9 \times 10^{21}$	Same	
^{130}Ba	$2\varepsilon + \varepsilon\beta^+ + 2\beta^+$	$(2.2 \pm 0.5) \times 10^{21}$	Geochemical	[328]
^{132}Ba	2ε	$>2.2 \times 10^{21}$	Geochemical	[328]
^{136}Ce	$2\nu2K$	$>3.2 \times 10^{16}$	$CeCl_3$ crystal scintillator	[100]
	$0\nu2K$	$>3.0 \times 10^{16}$	Same	
	$2\nu\varepsilon\beta^+$	$>2.4 \times 10^{16}$	”	
	$0\nu\varepsilon\beta^+$	$>9.0 \times 10^{16}$	”	
	$2\nu2\beta^+$	$>1.8 \times 10^{16}$	Gd_2SO_5(Ce) crystal scintillator	[201]
	$0\nu2\beta^+$	$>6.9 \times 10^{17}$	CeF_3 crystal scintillator	[145]
^{156}Dy	$2\nu2K$	$>6.1 \times 10^{14}$	HPGe γ spectrometry	[101]
	$0\nu2K$	$>1.7 \times 10^{16}$	Same	
	$(2\nu + 0\nu)\ \varepsilon\beta^+$	$>1.9 \times 10^{16}$	”	
^{180}W	$2\nu2$K	$>1.0 \times 10^{18}$	$ZnWO_4$ crystal scintillators	[95]
	$0\nu2\varepsilon$	$>1.3 \times 10^{18}$	Same	
^{190}Pt	$2\nu2K$	$>8.4 \times 10^{14}$	HPGe γ spectrometry	[102]
	$0\nu2K$	$>5.7 \times 10^{15}$	Same	
	$2\nu\varepsilon\beta^+$	$>9.2 \times 10^{15}$	”	

mits on the 2ε, $\varepsilon\beta^+$ and $2\beta^+$ processes on the level of 10^{16}—10^{21} yr (see Table 7.4). Reasons for this situation are: (1) lower energy releases in 2ε, $\varepsilon\beta^+$ and $2\beta^+$ processes in comparison with those in $2\beta^-$ decay, that result in lower probabilities of the processes, as well as making background supp ression difficult; (2) usually lower natural abundances of $2\beta^+$ isotopes (which are typically lower-than 1 % with only few exceptions). Nevertheless, studies of neutrinoless 2ε and $\varepsilon\beta^+$ decays are important to explain the mechanism of neutrinoless $2\beta^-$ decay: is it due to non-zero neutrino mass or to the right-handed admixtures in weak interactions [266]. Another important motivation to search for double electron capture appears from a possibility of a resonant process due to energy degeneracy between initial and final state of mother and daughter nuclei. Such a coincidence could give a resonant enhancement of the neutrinoless double electron capture. The possibility of the resonant neutrinoless double electron capture was discussed time ago in [149,398,422,432], where an enhancement of the rate by some orders of magnitude was predicted. Such a resonant process could occur if the energy of transition ($Q_{\beta\beta}$) minus two binding energies of electrons on atomic shells of daughter nucleus is near to the energy of the ground or an excited level ($E_{\rm exc}$) of a daughter isotope. Fig. 7.4 shows results of calculations [99] for one of the most promising isotopes ^{106}Cd.

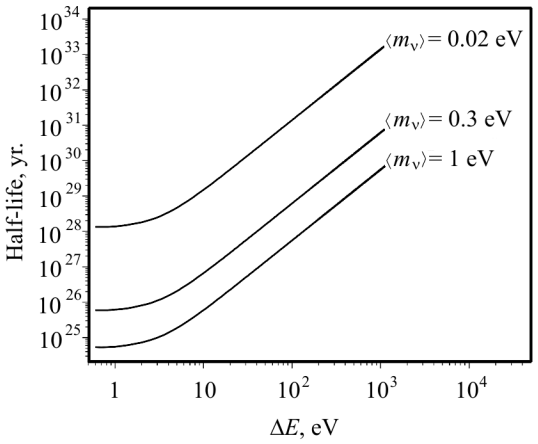

Fig. 7.4. Calculated dependence of the half life of ^{106}Cd relatively to the resonant $0\nu2\varepsilon$ capture to excited levels of ^{106}Pd on parameter ΔE (see text) for different values of the effective neutrino mass [99]

The half life relatively to $0\nu2\varepsilon$ decay is expected to become shorter with decrease of the difference between the initial and the final state of mother anddaughter nuclei:

$$\Delta E = Q_{\beta\beta} - E_{\rm exc} - (E_{b_i} + E_{b_j}),$$

where E_{b_i} and E_{b_j} are the energies of binding electrons on i and j shells of daughter atoms (a combination $i = j$ is also possible). The potentially 2ε active nuclei having excited levels with energies satisfying such a condition are listed in Table 7.5.

It should be stressed that the present accuracy of the data on the energy of 2β decay (which come from the accuracy of atomic mass measurements) in most of the cases is on the level of a few keV. Therefore, precise measurements

Table 7.5. **Double electron capture processes with possibility of resonant enhancement due to energy degeneracy between initial and final state of mother and daughter nuclei**

Transition, isotopic abundance [147], energy of decay (keV) [57]	Energy (E_b) of binding electrons	Double electron capture from level(s)	ΔE, keV	Experimental limits on $T_{1/2}$	Theoretical estimations of $T_{1/2}$
^{74}Se $\to$ ^{74}Ge, 0.89(4) %, 1209.7(0.6)	$E_b(\mathrm{L_1}) = 1.4$	2L$_1$, 2^+, 1204.2	2.7 ± 0.6	$>5.5 \times 10^{18}$ [73]	
^{78}Kr $\to$ ^{78}Se, 0.355(3) %, 2846.4(2.0)	$E_b(\mathrm{L_1}) = 1.7$	2L$_1$, (2^+), 2838.5	4.5 ± 2		
^{96}Ru $\to$ ^{96}Mo, 5.54(14) %, 2718(8)	$E_b(\mathrm{K}) = 20.0$ $E_b(\mathrm{L_1}) = 2.9$	KL$_1$, 2^+, 2700.2 2L$_1$, 2712.7	-5.1 ± 8 -0.5 ± 8	$>2.2 \times 10^{19}$ [96,97] $>5.1 \times 10^{19}$ [96,97]	
^{106}Cd $\to$ ^{106}Pd, 1.25(6) %, 2770(7)	$E_b(\mathrm{K}) = 24.4$	2K, 2717.6	3.6 ± 7	$>1.4 \times 10^{20}$ [99]	
^{112}Sn $\to$ ^{112}Cd , 0.97(1) %, 1919(4)	$E_b(\mathrm{K}) = 26.4$	2K, 0^+, 1871.0	-5.4 ± 4	$>1.4 \times 10^{18}$ [203] $>9.2 \times 10^{19}$ [74]	$\sim 10^{29}$ [149], 1.4×10^{29} [398]
^{124}Xe $\to$ ^{124}Te, 0.0952(3) %, 2864.4(2.2)	$E_b(\mathrm{L_1}) = 4.9$	2L$_1$, 2853.2 2L$_1$, 2,3, 2858.9	1.4 ± 2.2 -4.3 ± 2.2		9×10^{24}—2×10^{33} [307]
^{130}Ba $\to$ ^{130}Xe, 0.106(1) %, 2630.1(2.9)	$E_b(\mathrm{K}) = 34.6$ $E_b(\mathrm{L_1}) = 5.5$	2K, 2544.4 2L$_1$, 2608.4	6.5 ± 2.9 0.7 ± 2.9	$>4.0 \times 10^{21}$ [80] $(2.2 \pm 0.5) \times 10^{21}$ [328] $>4.0 \times 10^{21}$ [80] $(2.2 \pm 0.5) \times 10^{21}$ [328]	
^{136}Ce $\to$ ^{136}Ba, 0.185(2) %, 2419(13)	$E_b(\mathrm{K}) = 37.4$ $E_b(\mathrm{L_1}) = 6.0$	2K, 0^+, 2315.3 2K, 2349.5 2L$_1$, $(1^+, 2^+)$, 2392.1 2L$_1$, $(1^+, 2^+)$, 2399.9	28.8 ± 13 -5.3 ± 13 14.9 ± 13 7.1 ± 13	 $>2.4 \times 10^{15}$ [90] $>4.1 \times 10^{15}$ [90]	5×10^{29} [398], 1×10^{23}—7×10^{29} [307] 1×10^{23}—2×10^{33} [307] 8×10^{22}—3×10^{31} [307] 8×10^{22}—5×10^{31} [307]
^{152}Gd $\to$ ^{152}Sm, 0.20(1) %, 55.70(18)	$E_b(\mathrm{K}) = 46.8$	KL$_1$, g.s. 0^+	1.2 ± 0.2		5×10^{24} [398], 10^{26} [226], 2×10^{23}—2×10^{31} [307]
^{156}Dy $\to$ ^{156}Gd, 0.056(3) %, 2010(6)	$E_b(\mathrm{K}) = 50.2$ $E_b(\mathrm{L_1}) = 8.4$	2K, 2^+, 1914.8 KL$_1$, 1^-, 1946.4 KL$_1$, 0^-, 1952.4 2L$_1$, 0^+, 1988.5 2L$_1$, 2^+, 2003.8	-3 ± 6 7 ± 6 1 ± 6 7 ± 6 -6 ± 6	$>1.1 \times 10^{16}$ [101] $>9.6 \times 10^{15}$ [101] $>2.6 \times 10^{16}$ [101] $>1.9 \times 10^{16}$ [101] $>3.0 \times 10^{14}$ [101]	8×10^{23}—8×10^{30} [307]
^{162}Er $\to$ ^{162}Dy, 0.139(5) %, 1844.2(2.7)	$E_b(\mathrm{K}) = 53.8$ $E_b(\mathrm{L_1}) = 9.0$	KL$_1$, 2^+, 1782.7	-1.3 ± 2.7		

^{164}Er → ^{164}Dy, 1.601(3) %, 23.7(2.1)	E_b(L$_1$) = 9.0	2L$_1$, g.s. 0$^+$	5.7±2.1		4×10^{23}—5×10^{32} [128]
^{168}Yb → ^{168}Er, 0.123(3) %, 1422(4)	E_b(K) = 57.5	KL$_1$, 1$^-$, 1358.9	−4.2±4		4×10^{23}—5×10^{29} [128]
	E_b(N$_1$) = 0.45	2N, 0$^+$, 1422.1	−1.0±4		1×10^{24}—8×10^{32} [128]
^{180}W → ^{180}Hf, 0.12(1) %, 144(4)	E_b(K)= 65.4	2K, g.s. 0$^+$	13.2±4	>1.3×10^{18} [107]	3×10^{27}—5×10^{30} [123],
					3×10^{22}—4×10^{27} [128]
^{184}Os → ^{184}W, 0.02(1) %, 1451.2(1.0)	E_b(K) = 69.5	2K, 0$^+$, 1322.1	−9.9±1		3×10^{22}—2×10^{27} [128]
^{190}Pt → ^{190}Os, 0.014(1),%, 1383(6)	E_b(N$_1$) = 0.65	2N, (0,1, 2)$^+$, 1382.4	−0.7±6	>2.9×10^{16} [119]	3×10^{23}—6×10^{31} [128]

of atomic mass difference for the potentially interesting isotopes and accurate determination of the excited levels characteristics (spin, parity, decay channels) are requested. Meanwhile, development of experimental technique to search for double electron capture in different nuclei is important. The resonant double electron capture experiments can be realized both by the "passive" and "active" source techniques. One should keep in mind that nuclei with high nuclear charge Z are favorable from the point of view of the decay probability.

Recently several experiments were performed to search for resonant double electron capture. Scintillation technique was applied to investigate ^{106}Cd [99] and ^{180}W [95], while ultra-low background HPGe γ spectrometry was used to search for resonant processes in ^{74}Se [73], ^{96}Ru [96,97], ^{156}Dy, ^{158}Dy [101] and ^{190}Pt [102]. According to estimations [226, 389], in case of ^{152}Gd and ^{164}Er the sensitivity can be comparable to the favored $0\nu2\beta^-$ decays of nuclei. However, the energy release in double electron capture of these nuclei is expected to be very low (several keV) which makes certain difficulties to carry out high sensitivity experiments.

7.2.2. Search for 2β processes with the help of low background γ spectrometry

Search for 2β processes in ^{96}Ru, ^{104}Ru, ^{156}Dy, ^{158}Dy, ^{190}Pt and ^{198}Pt. A search for 2β decay of ^{96}Ru and ^{104}Ru was carried out by using a ruthenium sample with mass of 473 g with the HPGe detector GeCris (468 cm^3) over 986 h, and in the GeMulti setup (four HPGe detectors, ≈225 cm^3 volume each one) over 1176 h in the Gran Sasso underground laboratory of INFN (Italy). The measurements allowed to establish limits on 2β processes in ruthenium on the level of $T_{1/2} \sim 10^{18}$—10^{19} yr [96,97]. In 2010 the ruthenium (the total mass of the initial material was increased to ≈900 g) was purified by electron beam melting to remove potassium (the activity of ^{40}K in the ruthenium before the purification was 3.3 ± 0.6 Bq/kg, while

after the purification the activity was reduced by one order of magnitude). Now measurements are in progress in the GeMulti set-up. We estimate a sensitivity of the experiment to search for 2β processes in ^{96}Ru and ^{104}Ru at the level of 10^{20}—10^{21} yr depending on the decay channel.

A search for 2β decay of dysprosium was realized for the first time with the help of an ultra-low background HPGe γ detector of 244 cm^3 volume. After 2512 h of data taking with a 322 g sample of Dy_2O_3 limits on 2β processes in ^{156}Dy and ^{158}Dy have been established at the level of $T_{1/2} \sim 10^{14}$—10^{16} yr [101].

The measurements performed over 1815 h with a 42.5 g sample of platinum with the GeCrys HPGe γ spectrometer were used to set limits on double β processes in ^{190}Pt in the range of $T_{1/2} \sim 10^{14}$—10^{16} yr [102]. The search for the possible resonant $0\nu 2\varepsilon$ capture to the 1382.4 keV level was realized for the first time.

Main results of investigations of possible resonant neutrinoless double electron capture in ^{96}Ru, ^{156}Dy, ^{158}Dy and ^{190}Pt are summarized in Table 7.5.

7.2.3. Two neutrino 2β decay of ^{100}Mo to the first 0^+ excited level of ^{100}Ru

A 1199 g sample of molybdenum oxide with molybdenum enriched in ^{100}Mo to 99.5 % was measured over 18120 h in the GeMulti set-up. Two γ quanta of 540 keV and of 591 keV emitted in the deexcitation process after $2\nu 2\beta$ decay of ^{100}Mo to the 0_1^+ excited level of ^{100}Ru ($E_{\rm exc} = 1131$ keV) were observed both in coincidence and in the sum spectra (the sum spectrum is shown in Fig. 7.5 together with the background data). The measured half life $T_{1/2} = 6.9^{+1.0}_{-0.8}(\text{stat.}) \pm 0.7(\text{syst.}) \times 10^{20}$ yr [91] is in agreement with positive results obtained in previous experiments [48, 71, 281].

7.2.4. Double β experiments with the help of scintillation detectors

Search for 2β processes in ^{64}Zn, ^{70}Zn, ^{180}W and ^{186}W with low background $ZnWO_4$ crystal scintillators. A search for 2β processes in ^{64}Zn, ^{70}Zn, ^{180}W and ^{186}W has been performed in the low background DAMA/R&D set-up at the Gran Sasso underground laboratory by using $ZnWO_4$ crystal scintillators. First results of the experiment were reported in [93, 103]. New improved half life limits on double beta decay of Zn and W isotopes were set on the level of 10^{18}—10^{21} yr by analysis of the total 0.3487 kg × yr exposure [95]. In particular, limits on 2β decay in ^{64}Zn were set as: $T_{1/2}^{2\nu 2K} \geq 1.1 \times 10^{19}$ yr, $T_{1/2}^{0\nu 2\varepsilon} \geq 3.2 \times 10^{20}$ yr, $T_{1/2}^{2\nu\varepsilon\beta^+} \geq 9.4 \times 10^{20}$ yr, and $T_{1/2}^{0\nu\varepsilon\beta^+} \geq 8.5 \times 10^{20}$ yr (all the limits at 90 % confidence level). The energy

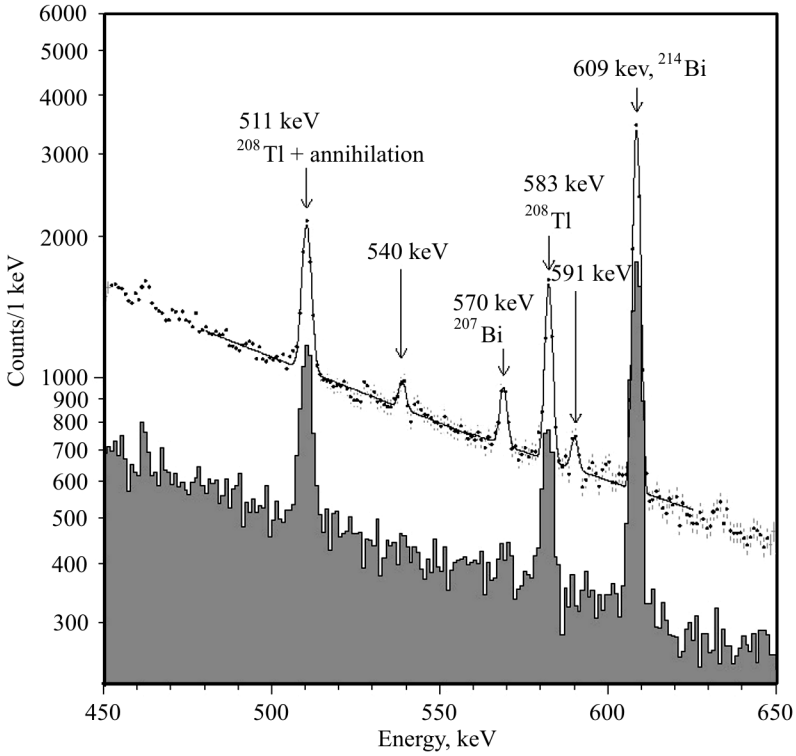

Fig. 7.5. The energy spectrum collected for 18120 h with the 1199 g $^{100}MoO_3$ sample (top) and the background spectrum collected for 7711 h (bottom; normalized to 18120 h)

spectrum of the $ZnWO_4$ crystal scintillator $\oslash 41 \times 27$ mm measured over 2798 h, corrected for the energy dependence of detection efficiency, together with the $2\nu 2K$ peak of ^{64}Zn with $T_{1/2}^{2\nu 2K} = 1.1 \times 10^{19}$ yr excluded at 90 % C.L. is presented in Fig. 7.6. The measured energy spectrum of the $ZnWO_4$ scintillation crystals (the total exposure is 0.349 kg × yr) together with the GEANT4 simulated response functions for $\varepsilon\beta^+$ process in ^{64}Zn excluded at 90 % C.L. is shown in Fig. 7.7 together with the most important components of the background.

The $0\nu 2\varepsilon$ decay in ^{180}W was restricted to the level of $T_{1/2} \geq 1.3 \times 10^{18}$ yr (possibility of this decay can be increased through the resonant enhancement).

Search for 2β decay of cerium with $CeCl_3$ crystal scintillators. A search for 2β processes in ^{136}Ce, ^{138}Ce and ^{142}Ce has been performed over 1638 h by using a 6.9 g $CeCl_3$ crystal scintillator. New improved half life limits have been obtained, in particular for ^{136}Ce: $T_{1/2}^{2\nu 2K} \geq 3.2 \times 10^{16}$ yr, $T_{1/2}^{0\nu 2K} \geq 3.0 \times 10^{16}$ yr, $T_{1/2}^{2\nu\varepsilon\beta^+} \geq 2.4 \times 10^{16}$ yr, $T_{1/2}^{0\nu\varepsilon\beta^+} \geq 0.9 \times 10^{17}$ yr [100].

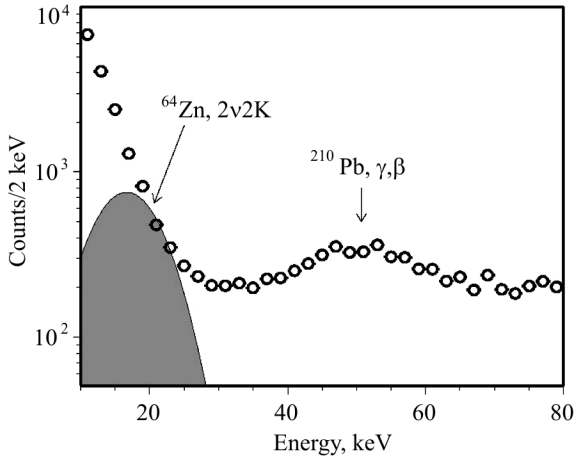

Fig. 7.6. The energy spectrum of the $ZnWO_4$ crystal scintillator $\oslash 41 \times 27$ mm measured over 2798 h, corrected for the energy dependence of detection efficiency, together with the $2\nu 2K$ peak of ^{64}Zn with $T_{1/2}^{2\nu 2K} = 1.1 \times 10^{19}$ yr excluded at 90 % C.L.

The development of radiopure $CeCl_3$ scintillators is of particular interest: a resonant 0ν double electron capture in ^{136}Ce is possible to a few excited levels of ^{136}Ba.

Search for double β processes in ^{106}Cd, ^{108}Cd, ^{114}Cd and ^{116}Cd with the help of cadmium tungstate crystal scintillators. Search for double beta processes in ^{108}Cd and ^{114}Cd was realized by using data of the low background experiment with $CdWO_4$ crystal scintillator at the the Gran Sasso underground laboratory. The $CdWO_4$ detector, experimental set-up, measurements and data analysis are described in detail in [104]. Fits of the measured spectra in different energy regions give the limits on double β processes in ^{108}Cd and ^{114}Cd (at 90 % CL): $T_{1/2}^{2\nu 2K}(^{108}\mathrm{Cd}) \geq 1.1 \times 10^{18}$ yr, $T_{1/2}^{0\nu 2\varepsilon}(^{108}\mathrm{Cd}) \geq 1.0 \times 10^{18}$ yr, $T_{1/2}^{2\nu 2\beta}(^{114}\mathrm{Cd}) \geq 1.3 \times 10^{18}$ yr, $T_{1/2}^{0\nu 2\beta}(^{114}\mathrm{Cd}) \geq$ $\geq 1.1 \times 10^{21}$ yr [92].

Cadmium tungstate crystals enriched in ^{106}Cd (231 g, isotopic abundance of ^{106}Cd 66 %) [105] and in ^{116}Cd (1868 g, 82 %) [77] were developed (see section 7.9.2) to search for 2β decay of ^{106}Cd and ^{116}Cd. The scintillators show excellent optical and scintillation properties thanks to a careful purification of initial materials and to the use of the low-thermal-gradient Czochralski technique to grow the crystals. Limits on different channels of 2β decay of ^{106}Cd: $T_{1/2}^{0\nu 2\varepsilon} \geq 3.6 \times 10^{20}$ yr, $T_{1/2}^{2\nu\varepsilon\beta^+} \geq 7.2 \times 10^{19}$ yr, $T_{1/2}^{0\nu\varepsilon\beta^+} \geq 2.1 \times 10^{20}$ yr, $T_{1/2}^{2\nu 2\beta^+} \geq 2.5 \times 10^{20}$ yr, $T_{1/2}^{0\nu 2\beta^+} \geq 2.1 \times 10^{20}$ yr were derived from the 1320 h experiment [106]. The resonant $0\nu 2\varepsilon$ processes were restricted as $T_{1/2}^{0\nu 2K} \geq$ $\geq 1.4 \times 10^{20}$ yr and $T_{1/2}^{0\nu KL} \geq 3.2 \times 10^{20}$ yr. An analysis of 6591 h data is in progress. A new phase of the experiment with the enriched $^{106}CdWO_4$ crystal in coincidence with the GeMulti set-up is in preparation.

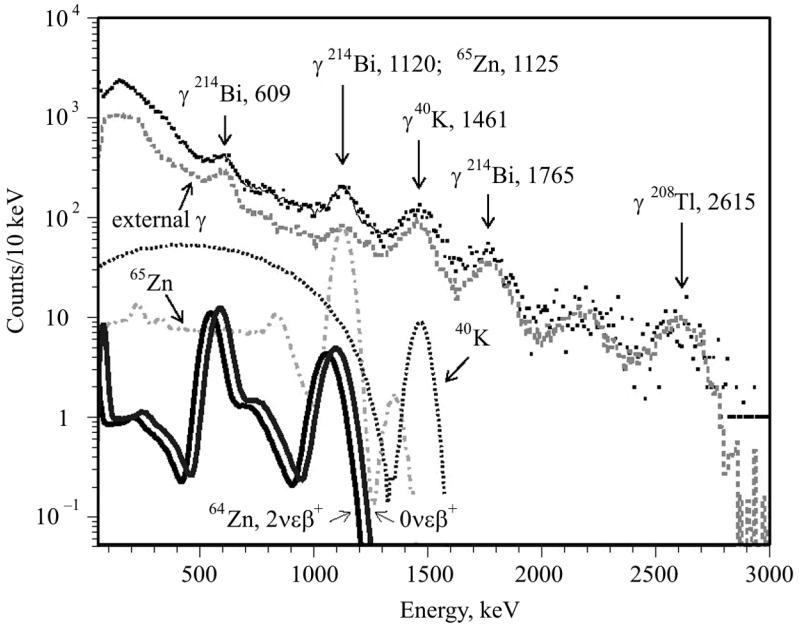

Fig. 7.7. The measured energy spectrum of the $ZnWO_4$ scintillation crystals (the total exposure is 0.349 kg × yr) together with the GEANT4 simulated response functions for $\varepsilon\beta^+$ process in ^{64}Zn excluded at 90 % C.L. The most important components of the background are shown. The energies of γ lines are in keV

A low background experiment to search for double β decay of ^{116}Cd with the help of the enriched $^{116}CdWO_4$ crystal scintillators is in progress. We estimate a sensitivity of a 5 yr experiment (depending on a level of background) as $T_{1/2} \sim (0.5—1.5) \times 10^{24}$ yr. It corresponds, taking into account the recent calculations of matrix elements [270, 298, 388], to the effective neutrino mass $\langle m_\nu \rangle \approx 0.4—1.4$ eV.

Development of crystal scintillators, rather promising technique to search for double beta decay, will be discussed in section 7.9.2.

7.3. Search for solar axions

7.3.1. Introduction of axions

The general form of the Hamiltonian of quantum chromodynamics (QCD) contains a term that violates the CP symmetry in the strong interaction [179, 282]. However, this violation is not observed experimentally. For example, only upper (and very strict) limit is measured for the neutron electric dipole moment, which is related with the CP violating term: $d < 2.9 \times 10^{-26}\ e \times$ cm [347]. This contradiction is known as the strong CP problem of QCD. One of the most simple and elegant solutions of this

contradiction was proposed by Peccei and Quinn in 1977 [359,360] by introducing a new global symmetry. The spontaneous violation of the PQ symmetry at the energy scale f_a totally suppresses the CP violating term in the QCD Hamiltonian. Weinberg [426] and Wilczek [431] have independently shown that this model leads to existence of axion — a new pseudo-scalar neutral particle. The mass of axion is connected with the scale of the PQ symmetry violation: $m_a(\text{eV}) \approx 6 \times 10^6 / f_a(\text{GeV})$.

The interaction of axion with different components of usual matter is described by different effective coupling constants: $g_{a\gamma}$ (interaction with photons), g_{ae} (electrons), g_{aN} (nucleons), which are also inversely proportional to f_a and those values are unknown (additionally, one should note that relations of $g_{a\gamma}$, g_{ae}, g_{aN} with f_a are model dependent).

In the first works, the energy of the PQ symmetry violation was considered to be close to the scale of the electro-weak symmetry violation and, therefore, the axion mass is $\approx$ 100 keV. But this value of the axion mass was soon excluded by experiments with radioactive sources, reactors and accelerators (see reviews [51, 179, 282, 283, 319, 347, 368, 369] and references therein). Then the standard axion (known as PQWW by names of authors) was substituted by other models which allow much bigger values of f_a up to the Planck mass of 10^{19} GeV: the hadronic axion model (KSZV) [284, 384] and the model of the GUT axion (DFSZ) [212,441]. The axion mass and the coupling constants $g_{a\gamma}$, g_{ae}, g_{aN}, which are inversely proportional to f_a, can have very small values (m_a down to 10^{-12} eV) in these models, and these axions are sometimes named as "invisible". It should be noted that, besides the solution of the strong CP problem, axion is one of the best candidates on the role of the dark matter particles [51, 146, 283, 319, 368, 369, 393].

If axions exist, the Sun can be an intensive source of these particles. They can be born: (1) in the interaction of thermal γ quanta with fluctuating electromagnetic fields within the Sun due to the Primakoff effect and (2) in nuclear magnetic transitions in nuclides present in the Sun.

The first effect generates the continuous spectrum of axions with energy up to $\sim$20 keV and the mean value of 4.2 keV [152]. The total thermal axion flux on Earth depends on the coupling constant $g_{a\gamma}$ as $\varphi = (g_{a\gamma} \times 10^{10}\ \text{GeV})^2\ 3.5 \times \times 10^{11}\ \text{cm}^{-2}\ \text{s}^{-1}$. The relation of the axion mass m_a with $g_{a\gamma}$ is model dependent; for example, this flux is equal (in terms of m_a) to $\varphi = (m_a/1\ \text{eV})^2\ 7.4 \times\ 10^{11}\ \text{cm}^{-2}\ \text{s}^{-1}$ in the model with GUT axion, whereas other models can possess a deeply suppressed axion-photon coupling constant [152].

In the second effect, de-excitation of excited nuclear levels in magnetic (M1) transitions can produce quasi-monoenergetic axions instead of gamma quanta, due to axion-nucleon coupling g_{aN}. The total energy of axions is equal to the energy of gamma quanta. These levels can be excited by thermal movement of nuclei (the temperature of the solar core is equal to $\approx$1.3 keV,

and, therefore, only low-lying levels, like 14.4 keV level of ^{57}Fe or 9.4 keV level of ^{83}Kr, are excited effectively). Other possibility of populating the excited levels is the nuclear reactions in the Sun (for example, the 477.6 keV level of ^{7}Li is populated in the main *pp* cycle).

In spite of the theoretical attractivity of axions, any direct experimental evidences of their existence are still absent. Indirect astrophysical and cosmological arguments give advantage to the axion mass in the range 10^{-6}—10^{-2} eV or about 10 eV [51, 284, 319, 347, 368, 369]. The laboratory searches for axion are based on several possible mechanisms of axion interactions with the ordinary matter [51, 283, 319, 368, 369]: (1) the inverse Primakoff effect, i.e. conversion of axion to photon in laboratory magnetic field (an example of such the experiment is CAST [443]) or in a crystal detector (for example, NaI(Tl) [144]); (2) the Compton conversion of axion to photon (analogue of the Compton effect) $a + e \to \gamma + e$ [122]; (3) the decay of axion to two photons $a \to \gamma\gamma$ [122]; (4) the axioelectric effect of interaction with an atom $a + (A, Z) \to e + (A, Z)^+$ (analogue of photoeffect) [122]; (5) the resonant absorption of axions emitted in nuclear M1 transitions in a radioactive source, a nuclear reactor or the Sun by the analogue nuclei in a target (see details below). It should be noted that these mechanisms are based on different kinds of interactions of axion with matter, they are sensitive to different coupling constants ($g_{a\gamma}$, g_{ae}, g_{aN}), and the limits on the values of the constants and on the axion mass are model dependent. Thus, diverse experiments are mutually complementary. While the most of experiments concern the axion-photon coupling constant $g_{a\gamma}$, only the mechanism (5) is related to the axion-nucleon constant g_{aN} both in emission and in absorption of axion. This allows to exclude uncertainty related to the values of $g_{a\gamma}$ and g_{ae}.

Coming to the Earth, such quasi-monoenergetic axions could resonantly excite corresponding levels of the same nuclei (^{7}Li, ^{57}Fe, ^{83}Kr, ...). In the subsequent deexcitation process, γ quanta are emitted; they can be observed with the help of some detectors located near a sample with ^{7}Li, ^{57}Fe, ^{83}Kr, ... nuclei (or incorporating these nuclei). Experiments searching for these γ's have the following advantages: (1) probability of emission of such axions at birth and at capture is related only with coupling constant of axions with nucleons g_{aN}; uncertainties related with $g_{a\gamma}$, g_{ae} dissapear; (2) flux of ^{7}Li axions is directly related with the main *pp* cycle, which determines luminosity of the Sun (in contrast to axions, connected with thermal excitation of ^{57}Fe and ^{83}Kr which have some uncertainties in their solar abundances and distribution of temperature inside the Sun). Summary of all experiments searched for resonant excitation of nuclei by solar axions is given in Table 7.6.

As one can see from Table 7.6, the best limits on axion mass in the resonant excitation experiments were obtained in measurements with ^{57}Fe. However, it should be noted that, because energy of ^{57}Fe excited level is 14.4 keV, axions

with mass greater than 14.4 keV (if they exist) just cannot be emitted instead of γ quanta in ^{57}Fe deexcitation. What is why experiments with ^{7}Li, which has greater excitation energy of 477.6 keV, are also valuable: it is important to set in ^{7}Li measurements m_a limit lower than 14.4 keV widening a window in excluded axion masses to [477.6, 0.145] keV limits. This was done at the first time in [107]; improved results were reached in [108].

7.3.2. Limit on axion mass from measurements with different samples containing lithium

In previous experiments searching for solar ^{7}Li axions, peak at energy of 477.6 keV was not observed, and only limits on the peak amplitude and the corresponding mass of the axions m_a were set: (1) in [305], Li sample with mass of 61 g was measured with HPGe detector 78 cm^3 during 2667 h that gave $m_a < 32$ keV; (2) in [204], LiOH target of 3.9 kg was measured with HPGe 160 cm^3 during 3036 h resulting in $m_a < 16$ keV. Both these experiments were performed at the Earth level.

Recently, the following samples were measured in the Gran Sasso underground laboratory of the INFN (Italy) with low background HPGe detectors to search for solar ^{7}Li axions:

• LiF powder 243 g, HPGe 408 cm^3, 722 h; it was found that the sample is polluted by U/Th at ∼0.5 Bq/kg, see Fig. 7.8;

• LiF powder 47 g (of different producer), HPGe 408 cm^3, 914 h; polluted by U/Th at 0.2 Bq/kg;

• LiF(W) crystal 224 g, HPGe 244 cm^3, 633 h; radiopure, U/Th $<$ $<$ 0.02 Bq/kg, see Fig. 7.9.

Table 7.6. **Summary of searches for quasi-monoenergetic solar axions coupled to nucleons through resonant excitation of nuclei**

Axion source, E_γ (keV)	Short description	$\lim m_a$ (keV)	Year [Ref.]
^{7}Li, $E_\gamma = 477.6$	HP Ge 78 cm^3, Li 61.4 g, 2667 h	32.0^a	2001 [305]
	HP Ge 160 cm^3, LiOH 3.9 kg, 3028 h	16.0^b	2005 [204]
	HP Ge 408 cm^3, LiF powder 243 g, 722 h	13.9^b	2008 [107]
	HP Ge 244 cm^3, LiF crystal 553 g, 4044 h	8.6^b	2012 [108]
^{57}Fe, $E_\gamma = 14.4$	Si(Li), Fe 33 mg (^{57}Fe 95 %), 1472 h	0.745^a	1998 [306]
	Si(Li), Fe 16 mg (^{57}Fe 80 %), 712 h	0.360^b	2007 [207]
	Si PIN, Fe 206 mg (^{57}Fe 96 %), 334 h	0.216^a	2007 [348]
	Si(Li), Fe 290 mg (^{57}Fe 91 %), 2028 h	0.159^a	2009 [205]
	Total Earth heat flux	1.6	2009 [185]
	Si(Li), Fe 1.26 g (^{57}Fe 91 %), 1075 h	0.145^a	2010 [206]
^{83}Kr, $E_\gamma = 9.4$	PC^c 243 cm^3, Kr gas 1.7 g, 564 h	5.5^a	2004 [274]

^{a} At 95 % C.L. ^{b} At 90 % C.L. ^{c} Proportional counter.

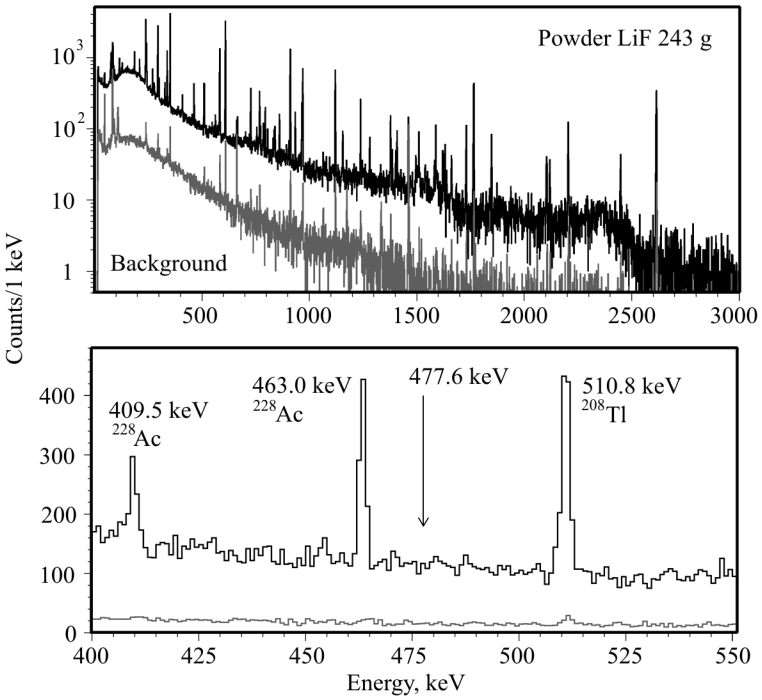

Fig. 7.8. Energy spectrum of LiF powder 243 g measured with HPGe detector 408 cm^3 during 722 h at LNGS in comparison with background

The 477.6 keV peak was not observed in any measurements; only limit on the peak area and corresponding axion mass can be derived as:

$$m_a = 1.55 \times 10^{11} \times (S/\varepsilon N_7 t)^{1/4} \text{ eV},$$

where m_a is in eV, S is the area of the peak, ε is the efficiency of registration of the 477.6 keV γ quanta by the detector, N_7 is the number of ^{7}Li nuclei in the target, t is the time of measurement in seconds. While the LiF powder shown in Fig. 7.8 was polluted, nevertheless it gave slightly better limit on axion mass of $m_a < 13.9$ keV at 90 % C.L. than other two samples, due to better efficiency reached with greater HPGe detector [107].

However, it was clear that in the following measurements a LiF(W) crystal should be used because of its radiopurity. Bigger sample was prepared with mass of 553 g. It was measured in the underground conditions of the Gran Sasso underground laboratory with HPGe detector 244 cm^3 during 4044 h. Only limits on U/Th pollutions were set as < 0.01 Bq/kg, see Fig. 7.10 (left). With the values of: $S < 37$, $\varepsilon = 2.3 \times 10^{-2}$, $N_7 = 1.2 \times 10^{25}$, the following limit was obtained: $m_a < 8.6$ keV at 90 % C.L. This is the best limit for the ^{7}Li axion mass to-date.

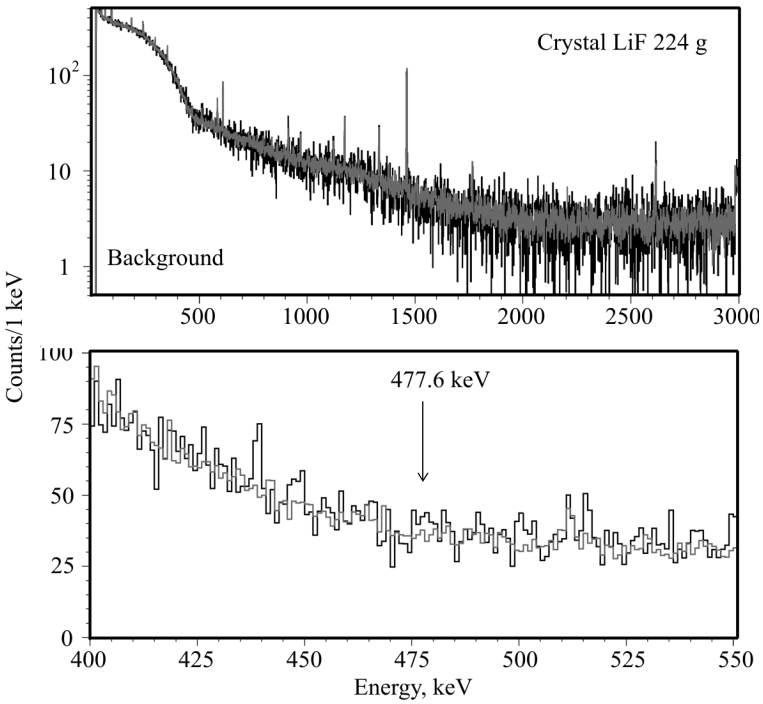

Fig. 7.9. Spectrum measured with LiF(W) crystal 224 g with HPGe 244 cm^3 during 633 h. In lower panel, region around the expected energy of 477.6 keV is shown in more detail

The best limit on axion mass related only with the g_{aN} coupling constant was determined in a similar search with ^{57}Fe nuclei: $m_a < 145$ eV [206]. However, as we already noted, possible masses of axions which could be born in ^{57}Fe deexcitation cannot be greater than 14.4 keV. Thus, a window of 14.4—16.0 keV in axion masses was not closed in previous experiments (14.4 keV — maximum axion mass emitted in ^{57}Fe; 16.0 keV — limit on sensitivity in previous experiments with ^{7}Li). Now this window is closed. Current situation with limits on axion masses from resonant excitation experiments is shown in Fig. 7.10 (right).

7.3.3. Resonance capture of solar ^{57}Fe axions and heat flow of the Earth

It is possible to obtain upper limit on the axion mass if — very conservatively — to suppose that the total heat flow of the Earth is caused exclusively by resonance capture of solar axions inside the Earth [185]. According to the contemporary conceptions [25], the Earth mantle (which gives ∼68 % of the Earth's mass) contains 6.26 % of Fe; core (∼32 % of the Earth's

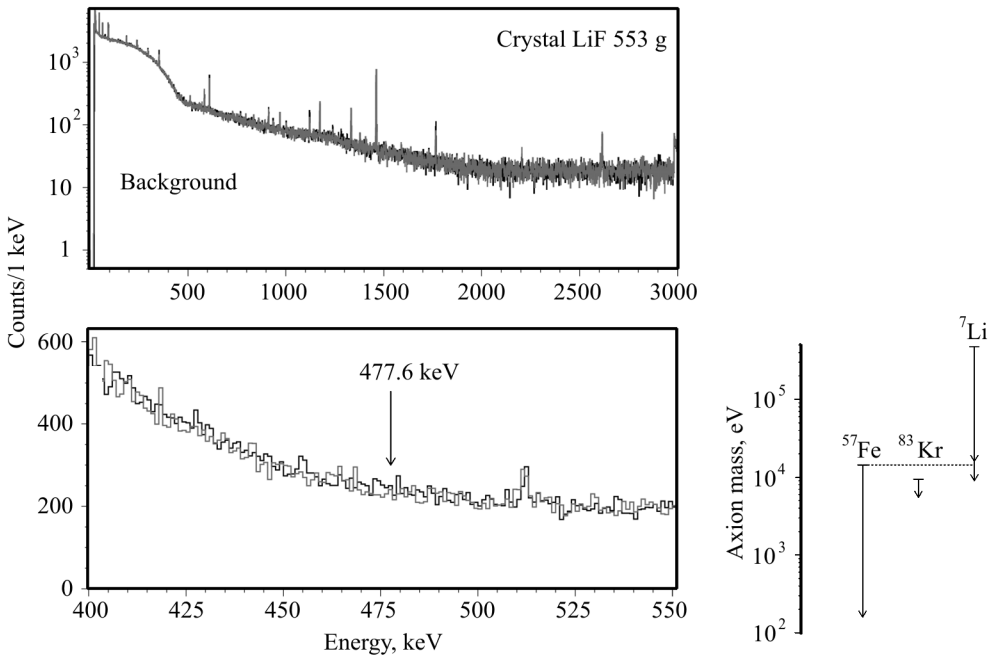

Fig. 7.10. Left: Energy spectrum of LiF(W) crystal measured during 4044 h with HPGe 244 cm^3. Right: Current situation with limits on axion masses from resonant excitation experiments. Empty arrow shows improvement reached in measurements with LiF targets

mass) contains 78.0—87.5 % of Fe. Altogether, the Earth in total consists of 29.6—32.6 % of Fe; isotopic natural abundance of ^{57}Fe is 2.119 %; this gives the number of ^{57}Fe nuclei in the Earth as: $N_{57} = (4.0—4.4) \times 10^{47}$.

Flux of ^{57}Fe axions from the Sun is estimated as the greatest one [263] because of small excitation energy of ^{57}Fe (14.4 keV) and big occurrance of Fe in the Sun. Number of resonance captures per 1 sec in a target at the Earth with N_{57} nuclei of ^{57}Fe is equal [207]:

$$R = 4.5 \times 10^{-33} N_{57} (m_a/1 \text{ eV})^4.$$

In each capture, energy of 14.4 keV is released; it is totally absorbed in the Earth. Equalizing this energy release to the Earth's heat flux (which is equal $(31—46) \times 10^{12}$ W in different estimations, see details in [185]; here we will take maximal value of 46×10^{12} W and minimal value of $N_{57} = 4.0 \times 10^{47}$), one can get:

$$m_a = 1.8 \text{ keV}.$$

The mass of axion m_a cannot be greater than this value. If to subtract energy release from radioactive decays of U/Th chains and ^{40}K in the Earth (conservative estimation is 20×10^{12} W [233]), this limit can be slightly improved:

$$m_a < 1.6 \text{ keV}.$$

Both these values are better than that obtained here earlier for ^{7}Li ($m_a < 8.6$ keV) and for ^{83}Kr ($m_a < 5.5$ keV [274], but worse than limits from specialized experiments with ^{57}Fe (145—745 eV, see Table 7.6). It should be also noted that this estimation has evident drawback: such a limit depends on our knowledge of the Earth structure.

7.3.4. Possible experiment with the TGV detector: sensitivity to the mass of solar ^{57}Fe axions

Limit on the solar ^{57}Fe axion mass could be further improved in measurements with the TGV detector (Telescope Germanium Vertical, created by JINR, Dubna, Russia in collaboration with France, Czech Republic, Slovakia). The TGV set-up [379] consists of 32 HPGe detectors $\varnothing 60 \times 6$ mm with total sensitive volume $\sim$400 cm^3; it is installed in the Modane underground laboratory (France, 4800 m w.e.). Currently it is used for search for 2β decays of ^{106}Cd (with thin $\sim$50 μm ^{106}Cd foils located between HPGe detectors). Energy threshold of the detector allows to detect X-rays/γ quanta with energy more than 5—6 keV.

After finish of the experiment with ^{106}Cd, the TGV set-up could be used for search for the solar ^{57}Fe axions with energy of 14.4 keV. For their effective registration, thin foils, as in case of ^{106}Cd, should be used; and it is important that low enough energy threshold is already achieved with the set-up.

Sensitivity of possible experiment is estimated: it is related with the maximal value of the product εN_{57}. Calculations for Fe foils' thickness from 10 to 100 μm show that after 50—70 μm, value of εN_{57} is increased only slightly due to self-absorption in the sample ($\varepsilon N_{57} \approx 7 \times 10^{20}$ for a foil with 100 % enrichment in ^{57}Fe).

For measurements with ^{57}Fe, $m_a = 2.15 \times 10^8 \times [S/\varepsilon N_{57} t]^{1/4}$ eV. In measurements during $t = 1$ year and 0 events in the peak of 14.4 keV, maximal sensitivity to m_a can be reached with 16 samples of ^{57}Fe of 100 % enrichment and thickness $d = 50$ μm (total mass of ^{57}Fe — 12.8 g): $m_a < 9.2$ eV. More real estimation (8 samples of ^{57}Fe, 80 % enrichment, $d = 70$ μm, total mass of ^{57}Fe — 9.0 g) is the following: $m_a < 33$ eV. It is $\sim$5 times better than the most stringent limit known today ($m_a < 145$ eV [206]).

7.3.5. Search for solar axions emitted in the M1-transition of ^{7}Li* with Borexino CTF

The described above searches for ^{7}Li solar axion ($E =$ = 478 keV) were performed with resonant absorption on ^{7}Li target. Non-resonant interactions of mono-energetic axions have much lower cross-sections, but it can be compensated by using larger targets. Other possible reactions for detections of ^{7}Li solar axions are interactions with electrons by Compton

axion to photon conversion $a + e \rightarrow e + \gamma$ and the axioelectric effect $a + e + Z \rightarrow e + Z$ (cross-sections of these reactions are defined by axion-electron g_{ae} coupling constant), as well as the Primakoff conversion on nuclei $a + Z \rightarrow \gamma + Z$ and the decay of the axion into two γ quanta (amplitudes of these processes depend on axion-photon coupling $g_{a\gamma}$); Z is the charge of the nucleus. All these reactions would lead to appearance of 478 keV peak in the energy spectrum of a calorimeter. In this chapter we describe an experimental search for ^{7}Li solar axions performed with the prototype of the Borexino detector [1], Counting Test Facility (CTF).

CTF is a large liquid scintillation detector constructed in order to test the key concepts of Borexino, namely the possibility to purify a large mass of liquid scintillator down to the level of contamination for U and Th of 10^{-16} g/g. The detector is placed in the Hall C of the Gran Sasso underground laboratory. The active volume of CTF is 4 tons of liquid scintillator contained in a transparent spherical nylon vessel, 2 m diameter and 0.5 mm thick, which is viewed by 100 PMTs with light concentrators mounted on a support structure. The construction is immersed in 1000 m^3 of high purity shielding water, contained in an external cylindrical tank 10 m diameter and 11 m high. The water shielding covers the scintillator against gamma quanta emitted by radioactive contaminants in the PMTs and their support structure and by nuclei capturing neutrons generated within the walls of the experimental hall. On the bottom of the tank, 16 upward-looking PMTs of the muon-veto system are mounted, for detection of the Cherenkov light of muons that cross the water. One can find a detailed description of the CTF in [157].

The extremely low background level and the large mass of the CTF allowed to set limits on many processes including hypothetical particles and interactions. The data taken during 548 days of live-time in the CTF-3 campaign, when the detector was filled by 3.75 t of pseudo-cumene (1,2,4-trimethylbenzene) with PPO (2,5-diphenyloxazole, 1.5 g/L), have been used by the Borexino collaboration to set limits on the properties of axion.

The response functions of the detector for the above listed reactions of axions were obtained by Monte-Carlo simulation. No statistically significant indications on axion interactions were found. Using the experimental data one can set new, model independent, upper limits on constants of interaction of axion with electrons, photons and nucleons: $g_{ae}g_{aN} \leq (1.0\text{—}2.4) \times 10^{-10}$ at $m_a \leq 450$ keV and $g_{a\gamma}g_{aN} \leq 5 \times 10^{-9}$ GeV^{-1} at $m_a \leq 10$ keV. For heavy axions the limits $g_{ae} < (0.7\text{—}2.0) \times 10^{-8}$ and $g_{a\gamma} < 10^{-9}\text{—}10^{-8}$ at 100 keV $< m_a <$ 400 keV are obtained in assumption that g_{aN} depends on m_a as for KSVZ axion model [122]. All the limits were set at 90 % CL.

[1] The detector Borexino is described in the next chapter.

7.4. Study of neutrino properties in underground experiments

7.4.1. The Borexino detector at the Laboratori Nazionali del Gran Sasso

The detector CTF (Counting Test Facility) described in the end of the previous chapter is a prototype of the Borexino, a large liquid scintillation detector, which was designed for real-time detection of low-energy solar neutrinos. The primary aim of Borexino is detection of monoenergetic ^{7}Be neutrino with energy of 862 keV, emitted in solar *pp*-cycle in the electron capture reaction of $^7\mathrm{Be}(e,\nu)^7\mathrm{Li}$. The measurement of this flux provides an information on the mass and mixture matrix of neutrino. Additionally, the unique properties of the detector (large target mass and very high radiopurity) have been used in order to obtain limits on probabilities of many hypothetical processes.

The Borexino detector is placed in the Hall C of the Gran Sasso underground laboratory, on the depth of 3600 m of water equivalent. The active mass of the target scintillator in Borexino is 278 tons of pseudo-cumene (PC, 1,2,4-trimethylbenzene), doped with a fluorescent dye (1.5 g/L of PPO, 2,5-diphenyloxazole). The scintillator is contained in a thin (125 μm) transparent spherical nylon vessel (the volume is 315 m^3) which is enclosed in two concentric buffers (323 and 567 tons of PC with admixture of 5.0 g/L of dimethylphthalate, a component quenching the PC scintillation light). The two PC buffers are separated by a thin transparent nylon film to prevent diffusion of radon towards the scintillator. The scintillator and the buffers are contained in a stainless steel sphere (SSS, $\oslash$13.7 m) which is surrounded by a 18.0 m diameter, 16.9 m high domed water tank (WT), containing 2100 tons of ultrapure water as an additional shield. The scintillation light is detected via 2212 8-inch PMTs uniformly distributed on the inner surface of the SSS and directed to the center of the sphere. Additional 208 8-inch PMTs are placed on the external surface of the SSS to view the water tank, serving as a muon veto; they detect the Cherenkov light radiated by muons in the water shield. The key features of the Borexino detector are described in [158, 159].

The first physical run of the detector started on 16 May, 2007. The main achievement of the Borexino Collaboration was the first real-time direct measurement of the low energy (0.862 MeV) ^{7}Be solar neutrinos which had been performed from an analysis of data obtained during 192 live days in the period from 16 May, 2007 to 12 April, 2008, totaling a 41.3 ton$\times$yr fiducial exposure to solar neutrinos [160].

7.4.2. The first direct real-time measurement of ^{7}Be solar neutrino flux

Before the observations performed by Borexino, the real-time measurements were available only for high-energy solar neutrinos (more than 4.5 MeV) with water Cherenkov detectors SuperKamiokande [181—183] and SNO [390,391]. The flux of lower (sub-MeV) energy solar neutrinos was measured by the chlorine-argon [182] and gallium-germanium [242,256,380] radiochemical detectors which integrate the neutrino flux over periods of ∼1 month and cannot provide spectral information. The preferred explanation of the observed lack of electron neutrinos in the flux was the mechanism of neutrino flavour oscillations. The oscillations were observed also for atmospheric neutrinos [401], for reactor anti-neutrinos [276] and for accelerator neutrinos [278,334].

Solar neutrinos are detected in Borexino through their elastic scattering on electrons in the scintillator. Electron neutrinos interacting through charged and neutral currents have a cross section ∼5 times larger than muon neutrinos and tau neutrinos in the energy range of interest, because ν_μ and ν_τ interact only through neutral currents. The electrons scattered by neutrinos are detected by means of the scintillation light retaining the information on the energy, while information on the direction of the scattered electrons is lost. The basic signature for the monoenergetic 862 keV ^{7}Be neutrinos is the Compton-like edge of the recoil electrons at 665 keV.

The interaction rate of ^{7}Be solar neutrinos in the pseudo-cumene target is expected to be of 0.5 counts/(ton × day), so the requirements to the radioactive contamination of the target are extremely strict. The thick layers of the shield cover the internal part of the detector and screen the target from the external radioactivity. The liquids are purified during the filling of the detector. Position sensitivity of the detector (as obtained from the PMTs timing data via a time-of-flight algorithm) allows to distinguish events in the innermost spherical part of the active target, approximately 1/3 of the scintillator (78.5 tons); the external layer of the target serves as an active shield. Alpha and beta/gamma particles can be distinguished by different scintillation pulse shape for alphas and gammas [163].

In the spectrum in the Fig. 7.11, one can see ^{14}C beta-decays (Q_β = = 156 keV) in the low energy part (<100 photoelectrons, p.e.); the peak around 200 p.e. due to alpha decay of ^{210}Po (5.14 MeV) is moved to the lower energies by alpha-quenching (about 13 times) of pseudo-cumene. The Compton-like edge at 300—350 p.e. is created by solar ^{7}Be neutrinos. The spectral continuum from 400 to 900 p.e. is created by β^+ decay of cosmogenic ^{11}C which is produced by neutron spallation from ^{12}C by muons *in situ*.

The Bi-Po fast chains allow to define the content of U and Th in the scintillator (assuming non-broken equilibrium in the families): $1.6(1) \times 10^{-17}$ g

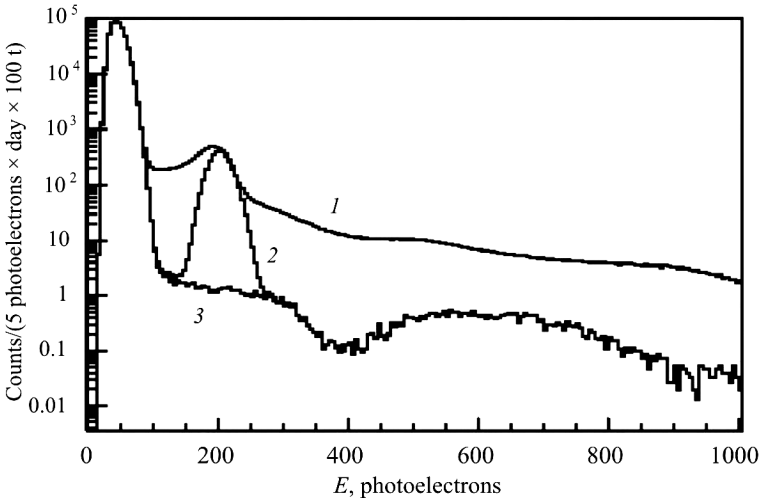

Fig. 7.11. The charge spectra of Borexino measured during 192 live days, all curves scaled to exposure of 100 days × ton: line *1* — after base cuts suppressing time-correlated events related to muons, ^{214}Bi—^{214}Po chains, and pile-ups (removing about 0.7 % of events); line *2* — after fiducial cut removing events in the external part of the target; line *3* — after the statistical subtraction of the alpha-emitting contaminants, mainly ^{210}Po

[^{238}U]/g and $6.8(15) \times 10^{-18}$ g[^{232}Th]/g. The ^{85}Kr content in the scintillator is dangerous because it overlaps with the expected spectrum of ^{7}Be solar neutrinos. The activity of ^{85}Kr in the detector was estimated via the rare decay sequence $^{85}\mathrm{Kr} \to {}^{85m}\mathrm{Rb}$ ($\tau = 1.5\,\mu$s, branching ratio 0.43 %) $\to {}^{85}$Rb that allows to apply the delayed coincidences technique; the activity is 29(14) counts/(day × 100 tons). The light yield is about 500 p.e./MeV, and the energy resolution is $\sim 5\,\% \cdot (E/1\,\mathrm{MeV})^{-1/2}$.

The spectral fit of the spectrum in the 160—2000 keV energy region gives the solar ^{7}Be scattering rate equal to $49 \pm 3(\mathrm{stat.}) \pm 4(\mathrm{syst.})$ counts/(day · 100 t) (see Fig. 7.12). The main background components have amplitudes (in the same units) of $25 \pm 3(\mathrm{stat.}) \pm 2(\mathrm{syst.})$ for ^{85}Kr β^- decay (this is in a good agreement with the independent measurement of ^{85}Kr activity, see above); $25 \pm \pm 1(\mathrm{stat.}) \pm 2(\mathrm{syst.})$ for ^{11}C β^+ decay; and $23 \pm 2(\mathrm{stat.}) \pm 2(\mathrm{syst.})$ for ^{210}Bi β^- decay together with scattering of CNO solar neutrinos which should produce a very similar spectrum.

The expected flux of ^{7}Be neutrinos for the Standard Solar Model with high metallicity [62] is $5.08(25) \times 10^{9}\,\mathrm{cm}^{-2} \cdot \mathrm{s}^{-1}$, which would give 74(4) counts/(day · 100 t) if no oscillations occur. The scenario of MSW-LMA (Large Mixing Angle, Mikheev—Smirnov—Wolfenstein effect of neutrino flavour oscillation in matter) would give the rate of 48 ± 4 counts/(day · 100 t), which is consistent with the measured rate. The MSW-LMA scenario predicts the dominant mode of neutrino oscillations to be the matter oscillations for

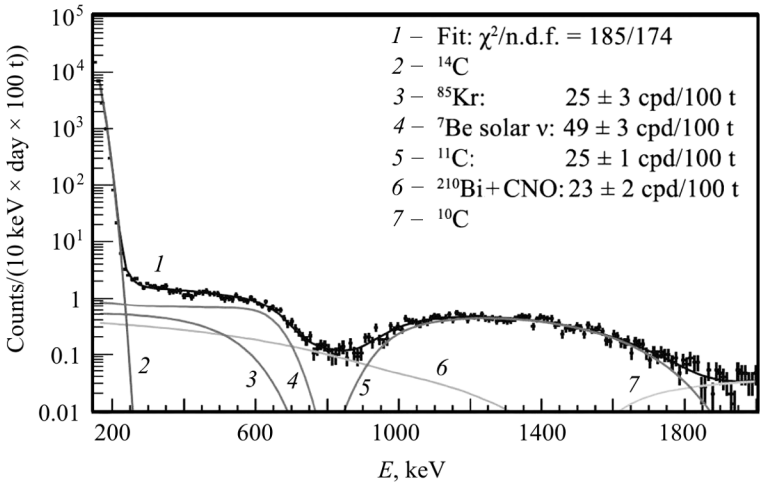

Fig. 7.12. The spectral fit in 160—2000 keV region

$E > 3\,\text{MeV}$ and the vacuum oscillations for $E < 0.5\,\text{MeV}$. Before the Borexino result, the direct measurements of the electron neutrino survival probability P_{ee} were performed only for energies $E > 5\,\text{MeV}$, in the matter-dominant region [390, 391]. The measurement of P_{ee} around the transition region is an important test of the MSW-LMA scenario.

7.4.3. The limit on electromagnetic properties of neutrino from Borexino measurements

A minimal extension of the electroweak standard model with a massive neutrino requires a non zero neutrino magnetic moment proportional to the neutrino mass [239, 315, 324]. The experimental evidence from solar and reactor neutrinos has demonstrated that neutrinos are massive, and should thus possess a non-null magnetic moment. The non-zero values of neutrino mass yields the lower limit for the magnetic moment to be $4 \times 10^{-20}\mu_{\text{B}}$ [64] where $\mu_{\text{B}} = e/2m_e$ is the Bohr magneton. The current experiments are not sensitive enough for such low magnetic moments, but larger values are possible in other extensions of the Standard Model [89, 248].

In case of a non-null neutrino magnetic moment, a new term

$$\left(\frac{d\sigma}{dT}\right)_{\text{EM}} = \mu_\nu^2 \frac{\pi\alpha_{\text{EM}}^2}{m_e^2}\left(\frac{1}{T} - \frac{1}{E_\nu}\right)$$

should be added to the standard electroweak cross section

$$\left(\frac{d\sigma}{dT}\right)_{\text{W}} = \frac{2G_F^2 m_e}{\pi}\left(g_L^2 + g_R^2\left(1 - \frac{T}{E_\nu}\right)^2 - g_L g_R \frac{m_e T}{2E_\nu^2}\right),$$

where E_ν is the neutrino kinetic energy and T is the recoil electron kinetic energy. At the low energy, $\left(\frac{d\sigma}{dT}\right)_{\rm EM} \sim \frac{1}{T}$. The coupling of neutrinos to an electromagnetic field due to a neutrino magnetic moment is expressed by a 3×3 matrix. Dirac neutrinos can have both diagonal and off-diagonal (transition) moments, whereas the Majorana neutrino can have only transitional moments.

The analysis of Borexino data with the same statistics as for the measurements of ^{7}Be solar neutrino allowed to set the upper limit on the neutrino magnetic moment to be $5.4 \times 10^{-11}\mu_{\rm B}$ (90 % CL) which was the best experimental limit on the time of publication (currently, the best limit is set for the electron anti-neutrino in a reactor experiment [249], $3.2 \times 10^{-11}\mu_{\rm B}$). The sensitivity of Borexino to the magnetic moment, due to the larger target, is about 10 times better than it was obtained for similar search performed by the Borexino Collaboration in the CTF detector [164], $5.5 \times 10^{-10}\mu_{\rm B}$.

The searches of different electromagnetic properties of neutrino had been performed [164] with the second phase of the CTF detector (CTF-2), the pilot version of the Borexino detector described above. The liquid scintillator used at this stage was a phenylxylylethane (PXE, $C_{16}H_{18}$) with p-diphenylbenzene (para-terphenyl) as a primary wavelength shifter at a concentration of 2 g/L, along with a secondary wavelength shifter 1,4-bis-(2-methylstyrol)-benzene (bis-MSB) at 20 mg/L. The density of the scintillator is 0.99 kg/L. The total number of target electrons in CTF-2 $N_e = 1.36 \times 10^{30}$, the live time of data taking $t = 32.1$ days.

If neutrinos have mass and the flavour lepton number is not conserved, then the heavier neutrino flavours could decay to lighter ones: $\nu_H \to \nu_L + \gamma$. The above-mentioned minimal extension of the Standard Model (modified by non-zero neutrino mass and non-conservation of the flavour lepton number) predicts the lifetime for neutrino via this channel as high as $\tau/m_\nu \approx 10^{29}$ yr/eV. In the laboratory frame, the spectrum of photons emitted by decaying ultra-relativistic neutrino is described [208] as

$$\frac{dN}{dE_\gamma} = \frac{m_\nu}{\tau}\frac{1-\alpha+2\alpha E_\gamma/E_\nu}{E_\nu^2},$$

where E_γ and E_ν are energies of the gamma quantum and the decaying neutrino, respectively. The parameter α defines the angular distribution of the photon, relative to the spin of the decaying neutrino in the neutrino rest frame:

$$\frac{dN}{d(\cos\vartheta)} = \frac{1+\alpha\cos\vartheta}{2},$$

where ϑ is the angle between photon momentum and the spin of neutrino in the rest frame. This parameter relates to the space-time structure of the decay

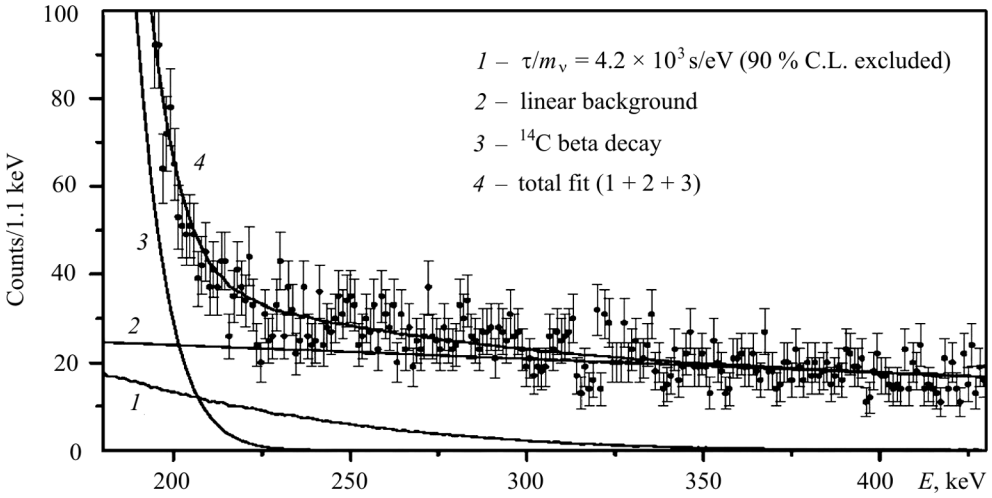

Fig. 7.13. Monte Carlo simulation of the signal in CTF-2 from radiative decay of solar neutrino for $\tau/m_\nu = 4.2 \times 10^3$ s/eV ($\alpha = 0$) and the experimental background data of CTF-2 for 32.1 days of live time

vertex and should be 0 for Majorana neutrino, $-1 \leq \alpha \leq 1$ for Dirac neutrino; for the case of total parity violation, $\alpha = \pm 1$.

The CTF detector is irradiated by the flux of solar neutrinos and can detect the gamma quanta emitted in this neutrino radiative decay. The limits on the ratio of lifetime of neutrino to their mass had been derived from a likelihood function analysis at 90 % CL (Fig. 7.13): $\tau/m_\nu > 4.2 \times 10^3$ s/eV ($\alpha = 0$), $\tau/m_\nu > 9.7 \times 10^3$ s/eV ($\alpha = +1$) and $\tau/m_\nu > 1.5 \times 10^3$ s/eV ($\alpha = -1$).

The sensitivity of the Borexino detector to this process is estimated to be two orders of magnitude better, but the results of searches of the neutrino radiative decay with this detector are still not published. The limit for radiative decay obtained in CTF-2 of Borexino is the best for laboratory searches (in reactors, accelerators, etc.) of this process, but it is much less restrictive than the astrophysical limits from the solar gamma ray flux (7×10^9 s/eV [370]) and from distortion of CMB spectrum (lifetime $< 4 \times 10^{20}$ s for $m_{\min} < < 0.14$ eV [337]).

7.4.4. Limits on the heavy neutrino mixing in solar ^{8}B decay

In the previous chapter, the radiative decay of light massive neutrino $\nu_H \to \nu_L + \gamma$ had been discussed. For heavy neutrino with the mass $\geq 2m_e$, this mode of decay can be accompanied by decay into a light neutrino and electron-positron pair: $\nu_H \to \nu_L + e^+ + e^-$ (see Fig. 7.14).

This heavy neutrino due to its mass can be only a small admixture to the three neutrino flavours of the Standard Model. It cannot be coupled (or this

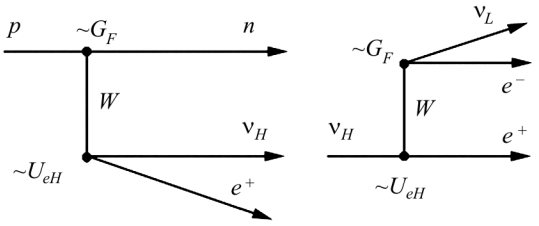

Fig. 7.14. (left) Emission of heavy neutrino in a positronic beta decay (for example, in the decay of $^8\mathrm{B} \to \to {}^8\mathrm{Be} + e^+ + \nu_H$). (right) Decay of the heavy neutrino into a light neutrino and electron-positron pair

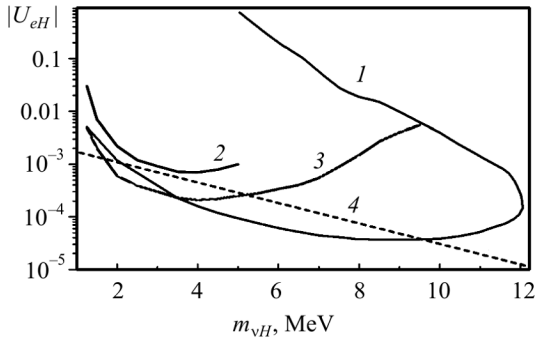

Fig. 7.15. The excluded values (90% CL) in the $m_{\nu_H} - U_{eH}$ parameters space. The experimental limits are obtained: *1* — from CTF-2 data [162]; *2, 3* — from reactor neutrino experiments [209] and [264], respectively; *4* — from search of $\pi \to e\nu$ decay in accelerator experiment [169]. The plot is taken from [162]

coupling is very small) to Z^0 boson because only contribution of three types of neutrino to the decay width of Z^0 is observed. However, the hypothetical heavy sterile neutrino is predicted by many extensions of the Standard Model and proposed as candidate to the dark matter particles [165,214]. Possible indications of sterile neutrino existence have been obtained in accelerator experiments LSND [321] and recently in MiniBooNE [333].

The rest frame width of the decay of heavy neutrino can be described as [386]

$$\Gamma = \frac{G_F^2}{192\pi^3} m_{\nu_H}^2 |U_{eH}|^2 |U_{eL}|^2 h(m_e^2/m_{\nu_H}^2).$$

The U_{eH} (small) and U_{eL} ($\sim$1) are the mixing parameters of heavy and light neutrinos to the electron neutrinos, $h(m_e^2/m_{\nu_H}^2)$ is the phase space factor. The probability of the electron-positron pair decay mode is predicted to be, in general, much higher than that of the radiative decay. The emission of the heavy neutrino with mass <15 MeV is kinematically allowed in the beta decay of ^{8}B; thus, these neutrinos, if exist, can contribute to the solar neutrino flux and their decay to e^+e^- pair can be registered in Earth-based experiments.

The data of CTF-2 experiment described in the previous chapter had been used by the Borexino Collaboration to restrict the mass and U_{eH} parameters of the heavy neutrino [162]. The data were collected during 29.1 days in August—September 2000. The in-flight decay of a solar boron neutrino to e^+e^- pair in the sensitive volume of the detector would result in registration of event with energy equal to the full energy of the neutrino. All the observed events with

energy >4.5 MeV were associated with muons. The partial suppression of non-muonic high-energy events by the muon veto had been taken into account. The non-observation of the sought decays leads to the restrictions on the mass and mixture parameter of the heavy neutrino shown in Fig. 7.15.

7.4.5. Limits on the solar electron antineutrino flux with the Borexino Counting Test Facility

A small antineutrino flux from the Sun is not completely excluded. One of possible production mechanisms is the neutrino-antineutrino conversion due to spin-flavour precession, induced by a neutrino non-diagonal magnetic moment and originally proposed as a possible solution to the observed solar neutrino deficit [383]. This could be a sub-dominant process in addition to the MSW-LMA solution of the solar neutrino problem. A random magnetic field in the convection zone of the Sun can increase the flux of $\tilde{\nu}_e$ through spin/flavour conversion [336]. Such enhancement would improve the detectability of a neutrino magnetic moment down to the level of $10^{-12}\mu_{\mathrm{B}}$.

The electron antineutrinos can be detected in CTF by the inverse beta decay of protons $\tilde{\nu}_e + p \to n + e^+$ with a threshold of 1.806 MeV. The cross section for this process is two orders of magnitude higher than that for $\tilde{\nu}_e$ elastic scattering on electron. In organic scintillators, the inverse beta decay reaction generates a prompt signal from the positron and a delayed one, following the neutron capture on protons $n + p \to d + \gamma + 2.22\,\mathrm{MeV}$. The total energy released by the positron after annihilation is $E = T + 2m_e c^2$, where T is the positron kinetic energy. Neglecting the small neutron recoil, the visible prompt energy is $E_{\tilde{\nu}_e} - 0.78$ MeV. The capture of thermalized neutrons on protons with a mean life-time of ∼200—250 μs provides a delayed tag for this reaction in a LS detector, allowing significant reduction of background. Neutron capture on ^{12}C is also possible but with a much smaller probability.

The data obtained in CTF-3 during 855.6 days of data collection (764.2 days of live time) were processed using the series of cuts for suppressing backgrounds. For example, the event pairs with the distance of >0.7 m between the prompt and delayed events were rejected, as well as the events tagged by the muon veto system.

Taking into account the 62(2) % efficiency of registration after the applied cuts, the estimated background sources for 764.2 days of CTF-3 live time were the following: 0.08 expected events of accidental coincidences; 0.37 events from reactor antineutrinos; 0.8(3) events of scattering of fast neutrons on target protons; 0.07(3) events of scattering of fast neutrons on target ^{12}C with exciting 4.4 MeV level of this nuclei. The cosmogenic activity that can simulate the inverse beta decay (mainly ^{8}He and ^{9}Li nuclei created by muons by spallation

of ^{12}C) was reduced to 10^{-4} simulating events by setting a 2 s veto time window after every muon crossing the set-up. The background from $^{13}C(\alpha, n)^{16}O$ reaction is negligible due to very low content of alpha active nuclides in the CTF scintillator (mainly ^{210}Po with activity of $\sim$20 μBq/t).

Only one candidate event had been observed. Its prompt energy was 4.37 MeV, so one cannot exclude the chance that this event is the de-excitation of the 4.4 MeV level of ^{12}C (excited by a muon-induced fast neutron) with the following thermalization and capture of the neutron. Taking into account the estimated background of 1.3 ± 0.7 events, the upper limit (with 90 % CL) on number of events that should be excluded for given condition is 3.3.

The hypothetical flux of $\tilde{\nu}_e$'s from ^{8}B, assuming no spectral distortion, can be obtained from the following equation:

$$\varphi_{\tilde{\nu}_e} = \frac{N_{\tilde{\nu}_e}}{N_p t \varepsilon \langle\sigma\rangle},$$

where $N_{\tilde{\nu}_e}$ is the number of detected events, $N_p = 2.25 \times 10^{29}$ is the number of target protons, $t = 6.60 \times 10^7$ s is the live time, $\varepsilon = 62\,\%$ is the mean detection efficiency, and $\langle\sigma\rangle = 3.4 \times 10^{-42}$ cm^2 is the mean cross-section over the ^{8}B neutrino spectrum in the energy range of interest. An upper limit for the electron antineutrino flux, assuming no distortion in the ^{8}B spectrum, is derived from the upper limit of 3.3 candidate events. The ^{8}B solar electron antineutrino flux limit (90 % CL) is $<1.1 \times 10^5$ cm^{-2} s^{-1}, or $<1.9\,\%$ of the ^{8}B neutrino flux. This experiment was the first search for solar anti-neutrino flux including the low-energy range of 1.8—4 MeV. The sensitivity of the Borexino detector to the ratio $\frac{\varphi_{\tilde{\nu}_e}}{\varphi_{\nu_e}}$ (^{8}B) is estimated to be three orders of magnitude better, $\sim 10^{-5}$ in all the range $E_\nu > 1.8$ MeV. All current limits are summarized in Table 7.7.

Table 7.7. **Experimental constraints on the flux (in cm$^{-2} \cdot$ s^{-1}) of solar $\tilde{\nu}_e$'s. The measured flux in the table is the limit on the flux within the experimental energy range (in MeV) at 90 % CL. The total flux is the limit scaled to the total energy range. The version BP04 of the Standard Solar Model [63] predicts a $\tilde{\nu}_e$'s flux from ^{8}B equal to $(5.79 \pm 1.33) \times 10^6$ cm$^{-2} \cdot$ s^{-1}**

	LSD	SK	KamLAND	SNO	CTF
Exposure, kt · yr	0.094	92.2	0.28	0.584	0.0078
Energy range of $\tilde{\nu}_e$	7—17	8—20	8.3—14.8	4—14.8	1.8—20
Measured flux of $\tilde{\nu}_e$	$<0.46 \times 10^5$	$<1.32 \times 10^4$	$<3.7 \times 10^2$	$<3.4 \times 10^4$	$< 1.06 \times 10^5$
Total flux of $\tilde{\nu}_e$	$<1 \times 10^5$	$<4 \times 10^4$	$<1.3 \times 10^3$	$<5.2 \times 10^4$	$< 1.08 \times 10^5$
$\frac{\varphi_{\tilde{\nu}_e}}{\varphi_{\nu_e}}$ (^8B)	$\leq 1.7 \times 10^{-2}$	$\leq 0.7 \times 10^{-2}$	$\leq 2.2 \times 10^{-4}$	$\leq 1 \times 10^{-2}$	$\leq 1.9 \times 10^{-2}$
Ref., year	[320], 1996	[402], 2003	[277], 2004	[392], 2004	[161], 2006

7.5. Searches for the electric charge non-conservation

The conservation of the electric charge is one of the fundamental laws of standard quantum electrodynamics based on underlying principle of gauge invariance. In accordance with the Weinberg theorem [427], charge conservation (CC) is also related with masslessness of the photon. Nevertheless, the possibility that the electric charge conservation may be broken in future unified gauge theories and the implications of such a violation have been intensively discussed in literature [340, 355—358, 423]. We would like to note that for fundamental questions any "a priori" argument based on pure esthetic or other principles could give wrong results (as it was demonstrated, for instance, with parity conservation), and on some level we could face unexpected things. In 1992, Lev Okun wrote: "In spite of the fact that at present we have no theoretically self-consistent framework for a description of violation of charge conservation or the exclusion principle, experimentalists should not stop testing these most fundamental concepts of modern physics. In fundamental physics, if something can be tested, it should be tested" [355]. Because of its fundamental status, law of charge conservation should be verified with the best possible to-date accuracy.

Since the electron is the lightest electrically charged particle, its stability implies charge conservation. The electron's life time was estimated using the following indirect considerations:

(a) In [367], balance of electric currents in the Earth atmosphere was examined. If the disbalance current (200 A) is caused by the electron decay, with number of electrons in the Earth of 2×10^{51} one can derive limit on the electron life time $\tau_e > 5 \times 10^{22}$ yr;

(b) In [322], it was noted that expansion of the Universe could be caused by disbalance in the electric charge on the level of 2×10^{-18}; then from time of life of the Universe of 10^{10} yr follows $\tau_e > 10^{28}$ yr;

(c) In [269], a relation between the electron life time τ_e and mass of gamma quantum m_γ was obtained in framework of the SU(5) model as: $\tau_e = 10^{-25}(m_Z/m_\gamma)^2$ yr where $m_Z = 91.2$ GeV is the mass of the Z boson. Limits on the m_γ value were derived from observations of the magnetic field of Jupiter as $m_\gamma < 6 \times 10^{-16}$ eV [211] and from intergalactic magnetic field as $m_\gamma < 2 \times 10^{-27}$ eV [177]. From that follows $\tau_e > 10^{27}$ yr and $\tau_e > 10^{51}$ yr, respectively; however, these limits are model-dependent.

The following schemes were proposed to test the charge conservation in direct laboratory experiments which are continuing since 1959:

(1) to look for decay of electron to gamma quantum and electron neutrino: $e^- \to \gamma + \nu_e$, first discussed in [232] (ν_e is supposed here for conservation of the lepton number);

(2) to search for decay of electron into invisible modes, like $e^- \to \nu_e\bar{\nu}_e\nu_e$ [232] or disappearance;

(3) to search for decay of electron into *invisible* with excitation of neighboring nucleus (first proposed in [267]);

(4) to look for charge non-conserving (CNC) beta decay [232];

(5) to search for CNC decays of other charged particles (protons, or pairs of protons, etc.).

We discuss here processes (1)—(4) while more details on the process (5) will be given in the next section.

(1) Decay of electron to γ quantum and neutrino. Because both emitted particles are (almost) massless, they are kinematically equivalent and each of them has energy equal to half of energy available. In case of a free electron, energy of γ quantum is $E_\gamma = m_e c^2/2 = 255.5$ keV ($m_e c^2$ is the electron mass). If an electron is bound on atomic shell with binding energy E_b, energy of γ quantum will be $E_\gamma = (m_e c^2 - E_b)/2$. Because of non-zero velocity of an atomic shell electron, the Doppler broadening should be taken into account (as it was noted in [124] at the first time). The expected shape is the Gaussian with the width at half maximum FWHM $= 0.104 \times E_\gamma \times \sqrt{E_b}$ (all values — in keV). F.e., for K electrons in Ge detector ($E_b = 11.1$ keV), FWHM is 86.7 keV that is quite big value compared with typical Ge energy resolution of 1—2 keV at energy $\simeq$250 keV. Energy release in a detector is equal $E_d = E_\gamma = (m_e c^2 - E_b)/2$ if an electron decay occurs outside a detector's sensitive volume. However, if decay occurs in a detector itself, a vacation which is created in the atomic shell will be filled in the subsequent deexcitation process with emission of cascade of X rays and Auger electrons with total energy E_b; thus total energy release in the detector is $E_d = E_\gamma + E_b = (m_e c^2 + E_b)/2$. An expected response function of a detector will be the sum of many Gaussians with proper centers and widths which takes into account all atomic shells in atoms or molecules located in a detector itself and in surrounding materials. Further details can be found in [293].

The $e^- \to \gamma + \nu_e$ CNC decay is still not observed, and only limits on the electron life time were established. The first experimental restriction $\tau_e(e^- \to \gamma + \nu_e) > 1.0 \times 10^{18}$ yr was set in 1959 in short (6.5 h) measurements at the Earth level with NaI(Tl) scintillator of 1287 cm^3 [232]. The most restrictive to-date value was obtained with massive (near 4 tons) CTF Borexino detector installed deep underground (3600 m w.e.) in the Gran Sasso underground laboratory as $\tau_e(e^- \to \gamma + \nu_e) > 4.2 \times 10^{26}$ yr [59]. All experimental results are summarized in Table 7.8.

(2) Decay of electron into invisible modes. In result of electron decay into particles which leave detector without interaction (f.e., two neutrinos and one antineutrino [232]) or just electron disappearance (f.e., into extra dimensions [37]), an electron hole will be created in atomic shell. In the subsequent

deexcitation process this hole will be filled by electrons from higher shells, and cascade of X rays and Auger electrons will be emitted; total released energy will be equal to the binding energy E_b of the disappeared electron on the atomic shell. If this decay occurs inside some detector, peak at energy E_b should be observed. For Ge, NaI(Tl) and Xe detectors, which were used in searches for $e^- \to invisible$ up to now, E_b values for K electrons are equal $E_b(\mathrm{Ge}) = 11.1$ keV, $E_b(\mathrm{I}) = 33.2$ keV, $E_b(\mathrm{Xe}) = 34.6$ keV. In all experiments, except of [110], decays of K electrons were searched for. In the DAMA experiment [110] with massive (around 100 kg) NaI(Tl) scintillators, low energy threshold of $\simeq$2 keV was reached, and this allowed to investigate L electrons with $E_b(\mathrm{I})$ $\simeq$5 keV at the first time. There are 8 electrons on L atomic shell compared with 2 electrons on K shell, and factor 4 in the electron number together with big mass of the detector, low background and big time of measurements resulted in the best to-date limit $\tau(e^- \to invisible) > 2.4 \times 10^{24}$ yr at 90 % C.L. Results of all experimental searches for CNC decay $e^- \to invisible$ are summarized in Table 7.8.

(3) Decay $e^- \to$ invisible with excitation of nuclear levels. In 1987 Holjevic et al. [267] proposed additional approach for testing the charge conservation: to search for processes in which electron disappears and the

Table 7.8. **Experimental limits on the electron life time at 68 % (90 %) C.L. for channels: $e^- \to invisible$ and $e^- \to \nu_e\gamma$. Best limits are in bold**

Detector	Volume, cm^3	Time of measurement, h	Limit on $\tau_e(e^- \to invisible)$, yr	Limit on $\tau_e(e^- \to \nu_e\gamma)$, yr	Year [Ref.]
NaI(Tl)	1287	6.5	1.0×10^{18}	1.0×10^{19}	1959 [232]
NaI(Tl)	348	$110^a, 362^b$	2.0×10^{21}	4.0×10^{22}	1965 [339]
Ge(Li)	66	1185	5.3×10^{21} [c]	–	1975 [395]
NaI(Tl)	1539	515	2.0×10^{22}	3.5×10^{23}	1979 [299]
Ge(Li)	130	$3760^a, 3616^b$	2.0×10^{22}	3.0×10^{23}	1983 [124]
HP Ge	135	8850	–	$1.5(1.1) \times 10^{25}$	1986 [54]
HP Ge	3×140	1662	$2.7(1.7) \times 10^{23}$	–	1991 [373]
NaI(Tl)	17×10570	2823	1.2×10^{23}	–	1992 [223]
HP Ge	591	3199	–	$2.4(1.2) \times 10^{25}$	1993 [67]
HP Ge	$48 + 2 \times 209$	$13404^a, 7578^b$	$4.3(2.6) \times 10^{23}$	$3.7(2.1) \times 10^{25}$	1995 [9]
BaF_2	2×103	986	–	3.2×10^{21}	1996 [21]
Xe[d]	2000	$2340^a, 257^b$	1.5×10^{23}	$2.0(1.0) \times 10^{25}$	1996 [109]
HP Ge	132	12600	1.3×10^{24}	–	1998 [295]
NaI(Tl)	9×2643	5354	$\mathbf{4.2(2.4) \times 10^{24}}$	–	1999 [110]
Xe[d]	2000	8336	–	$3.4(2.0) \times 10^{26}$	2000 [111]
$C_{16}H_{18}$[d]	4.2×10^6	770	–	$\mathbf{-(4.6) \times 10^{26}}$	2002 [59]
HP Ge	437	33233	–	$1.9(1.0) \times 10^{26}$ [e]	2007 [293]

[a] For channel $e^- \to invisible$. [b] For channel $e^- \to \nu_e\gamma$. [c] At 84% C.L. [d] Liquid scintillator. [e] This result was critisized in [210] as being overestimated at $\simeq$5 times.

neighboring nucleus is left in an excited state. Such a process is analogous to the usual electron capture but does not change the nucleus' charge: $(A, Z) + e^- \to \to (A, Z)^* + \nu_e$, and sometime it is named the CNC electron capture. It includes both the weak boson and photon mediating processes and gives possibility to investigate both the lepton and quark sectors [224, 267].

Levels with energies up to $m_e c^2 - E_b$ can be excited, but it is supposed that the lowest levels with difference in spin between the ground and excited state $\Delta J = 0, 1$ are fed with higher probability, and that K electrons are mostly involved being the closest to the nucleus. Deexcitation γ quanta can be observed with a proper detector located close to a sample (or containing atoms under investigation). Up to now, only 5 experiments searching for CNC electron capture were performed in which NaI(Tl) and liquid Xe scintillators were used; results are summarized in Table 7.9.

(4) CNC beta decay. CNC β decay, first considered for testing the charge conservation in [232], is a process in which the $(A, Z) \to (A, Z + 1)$ transformation is not accompanied by the emission of an electron. It is supposed that instead of an e^-, a massless particle is emitted (for example, a ν_e, a γ quantum, etc.): $(A, Z) \to (A, Z + 1) + (\nu_e$ or γ, etc.$) + \bar{\nu}_e$. In this case the energy available in the (A, Z) decay is increased of 511 keV, that are normally spent for the electron rest mass. This makes possible some transitions to the ground or excited states of the daughter $(A, Z + 1)$ nucleus which are energetically forbidden for the normal, charge conserving β decay $(A, Z) \to$

Table 7.9. **Experimental life time limits on the electron disappearance with nuclear levels excitation of ^{23}Na, ^{127}I and ^{129}Xe. Best values are in bold**

Nucleus, E_{exc}	Life time limits τ, yr				
	[267] 90 % C.L.	[224] 68 % C.L.	[112] 90 % C.L.	[113] 90 % C.L.	[139] 68 % C.L.
^{23}Na					
440.0 keV			$\mathbf{1.5 \times 10^{23}}$		
^{127}I					
57.6 keV	2.1×10^{21}	5.8×10^{22}	$\mathbf{2.4 \times 10^{23}}$		
202.9 keV	1.9×10^{21}	5.6×10^{22}	$\mathbf{2.0 \times 10^{23}}$		
375.0 keV	2.4×10^{21}		$\mathbf{1.8 \times 10^{23}}$		
418.0 keV	2.4×10^{21}		1.6×10^{23}		$\mathbf{1.2 \times 10^{24}}$
^{129}Xe					
39.6 keV				$\mathbf{1.1 \times 10^{24}}$	
236.1 keV				$\mathbf{3.7 \times 10^{24}}$	
318.2 keV				$\mathbf{2.2 \times 10^{24}}$	
321.7 keV				$\mathbf{2.5 \times 10^{24}}$	
411.5 keV				$\mathbf{2.3 \times 10^{24}}$	

Table 7.10. **Limits on life time established in direct experiments to search for charge non-conserving β decay. Best limit is in bold**

CNC β decay	Target, weight	Technique, detector	τ_{CNC}, yr (C.L.)	Year [Ref.]
$^{87}Rb \to {}^{87m}Sr$	RbF, 30 g	CS [a], NaI(Tl)	1.8×10^{16}	1960 [399]
$^{87}Rb \to {}^{87m}Sr$	Rb_2CO_3, 400 g	CS, Ge(Li)	1.9×10^{18} (90 %)	1979 [352]
$^{71}Ga \to {}^{71}Ge$	Ga, 300 kg	CS, prop. counter	2.3×10^{23} (90 %)	1980 [69]
$^{87}Rb \to {}^{87m}Sr$	Rb_2CO_3, 800 g	CS, Si(Li)	7.5×10^{19} (90 %)	1983 [417]
$^{113}Cd \to {}^{113m}In$	$CdCl_2$, 1.5 kg	CS, Si(Li), NaI(Tl)	1.4×10^{18} (90 %)	1983 [376]
$^{71}Ga \to {}^{71}Ge$	$GaCl_3$—HCl, 101 t + Ga, 57 t	CS, prop. counter	$\mathbf{3.5 \times 10^{26}}$ (68 %)	1996 [351] [b]
$^{73}Ge \to {}^{73}As$	Ge, 952 g	RT [c], HP Ge	2.6×10^{23} (90 %)	2002 [296]
$^{136}Xe \to {}^{136}Cs$	Xe, 6.5 kg [d]	RT, LXe	1.3×10^{23} (90 %)	2004 [140]
$^{115}In \to {}^{115m}Sn$	In, 928 g	RT, HP Ge	4.1×10^{20} (90 %)	2005 [174]
$^{139}La \to {}^{139}Ce$	$LaCl_3$, 50 g	RT, $LaCl_3$(Ce)	1.0×10^{18} (90 %)	2006 [141]
$^{100}Mo \to {}^{100}Tc$	$^{100}MoO_3$, 1199 g	RT, 4 HP Ge	4.5×10^{19} (90 %)	2010 [91]

[a] CS means chemical separation of the daughter product. [b] Accounting for contribution from the solar neutrinos, the limit for ^{71}Ga was improved to $\tau_{CNC} > 1.4 \times 10^{27}$ yr in [406]. [c] RT means real-time experiment. [d] 68.8 % ^{136}Xe.

$\to (A, Z+1)+e^- + \bar{\nu}_e$. The CNC β decay was searched for in several experiments since 1960. Only lower limits on the corresponding life times were established in the range of 10^{16}—10^{26} yr (see Table 7.10). We note here that capture of solar neutrinos $(A, Z) + \nu_e \to (A, Z+1) + e^-$ results in the same daughter nucleus $(A, Z+1)$ as in the CNC β decay, and these processes cannot be distinguished if daughter nuclei are extracted by chemical separation which was traditional techniques for experiments investigating solar neutrinos. The same techniques was used in searches for CNC β decay up to 2002 when the real-time approach was proposed and applied at the first time [296]. The best to-date limit was derived from the data of the SAGE and GALLEX solar neutrino experiments which used near 100 t of Ga [351].

7.6. Searches for invisible decays of nucleons and disappearance of matter

The baryon (B) and lepton (L) numbers are considered in the Standard Model (SM) as conserved values [2]. However, any underlying symmetry principle behind this fact is unknown, unlike f.e. the gauge invariance in electrodynamics which guarantees the masslessness of the photon and absolute conservation of the electric charge. Many extensions of the SM, in particular, grand unified theories consider conservation of B and L charges as approximate

[2] At non-perturbative level, B and L are not conserved even in the SM; however these effects are important at high energies ($\simeq$100 GeV) in the early Universe but are non-observable at current low temperatures [268].

law; they incorporate B and L violating interactions and predict decays of protons and neutrons bounded in nuclei. The processes with $\Delta B = 1$, $\Delta B = 2$, $\Delta(B - L) = 0$, $\Delta(B - L) = 2$ have been discussed in literature [309, 349].

Stimulated by theoretical predictions, nucleon instability has been searched for in many underground experiments with the help of massive detectors such as IMB, Fréjus, Kamiokande, SuperKamiokande and others (for experimental activity see [83, 292, 361] and references therein). About 90 decay modes have been investigated; however, no evidence for the nucleons (N) decay has been found. A complete summary of the experimental results is given in the Review of Particle Physics [347]. For the modes in which the nucleon decays to particles strongly or electromagnetically interacting in the detector's sensitive volume, the obtained life time limits are in the range of 10^{30}—10^{34} yr, while for decays to only weakly interacting products (neutrinos) the bounds were up to 10 orders of magnitude lower and only during the last decade they were significantly improved.

Interest to invisible decays of nucleons (and/or di- and tri-nucleons) and their disappearance is related with recently developed theories in which our world is described as a brane inside higher-dimensional space [37, 217, 218]. Particles, initially confined to the brane, may escape to extra dimensions (ED), thus disappearing for a normal observer. While energy, momentum, electric charge, etc. are conserved in full space, their balance could be broken in our 3-dimensional world. Tunneling of particles to EDs is predicted to be a generic property of massive matter [377]. Arkani-Hamed, Dimopoulos, and Dvali wrote in [38]: "The presence and properties of the extra dimensions will be investigated by looking for any loss of energy from our 3-brane into the bulk".

Theoretical estimations of the corresponding life times are quite uncertain because even the number of extra dimensions is unknown. Dubovsky [219] gives τ values for electron as $\tau(e \to \mathit{nothing}) = 9.0 \times 10^{25}$ yr in case of three EDs, and for proton $\tau(p \to \mathit{nothing}) = 9.2 \times 10^{34}$ yr for four EDs [3]. Recently a novel baryon number violating process, in which two neutrons in a nucleus disappear, emitting a bulk majoron $nn \to \chi$, was discussed by Mohapatra et al. [342]; the expected life time was estimated as $\sim 10^{32-39}$ yr. Also mechanisms for the tri-nucleon decay have been discussed; in recent theory by Babu et al. [58] processes with $\Delta B = 1, \Delta B = 2$ are forbidden but tri-nucleon decays with $\Delta B = 3$ are allowed.

Up to now we do not know which mode of nucleon decay is realized in the nature; different theories give different values for the nucleon's life time and

[3] We are using the following classification of decay channels: decay to *nothing* means disappearance (tunneling to EDs); decay to *invisible* means disappearance or decay to weakly interacting particles (one or few neutrinos of any flavors, majorons, etc.). Channel to *anything* means any possible mode of decay.

disagree which mode of decay is the most probable. In this relation experimental limits on the nucleons life time independent on the decay mode are also interesting and important. We will concentrate below on experiments where τ limits for nucleons (also di- and tri-nucleons) independent on mode or on their decays into *invisible* were established. The following approaches were used to set the τ limits:

(1) Spontaneous fission of ^{232}Th. In 1958, Flerov et al. derived limit on nucleon life time from an experiment searching for the spontaneous fission of ^{232}Th [237]. It was assumed (following idea [372]) that decay or disappearance of p or n in ^{232}Th will blow up the nucleus: it can be destroyed in the initial N decay or in the subsequent deexcitation of the nucleus. From the limit on ^{232}Th spontaneous fission [237] $T_{1/2} > 1.0 \times 10^{21}$ yr and taking into account that ^{232}Th contains 90 protons and 142 neutrons, the following limits were derived (see Table 7.11 for summary): $\tau(p \to anything) > 1.2 \times 10^{23}$ yr, $\tau(n \to anything) > 1.8 \times 10^{23}$ yr. These limits are considered as independent on mode [347] but, in fact, the τ values depend (inside a factor of few) on type of decay, see f.e. [272] [4].

(2) Geochemical search. In [231] the bounds on N decay to *invisible* were determined on the basis of mass-spectrometric measurements with Te ore samples (2.5×10^9 yr old) by looking for the possible daughter nuclide ^{129}Xe ($^{130}\text{Te} \to ... \to {}^{129}\text{Xe}$).

(3) Radiochemical method. In the experiment [235] the target of 1710 kg of potassium acetate $KC_2H_3O_2$, which contained 9.7×10^{27} atoms of ^{39}K, was exposed deep underground (4400 m w.e.) for about one year. Then, the candidate daughter ^{37}Ar, which could be created in result of nucleon disappearance in ^{39}K and subsequent evaporation of additional nucleon ($^{39}\text{K} \to ... \to {}^{37}\text{Ar}$), was extracted and its activity was measured as 0.3 ± 0.6 decays per day, which leads to the nucleon's life time limit $\tau(N \to invisible) > 1.1 \times 10^{26}$ yr. Reanalysis of these data in [407] allowed to set limits also for the nn and pn invisible decays.

(4) Study of the neutron production rate in deuterium. The decay or disappearance of proton bounded in deuterium nucleus, which consists only of proton and neutron, will result in the appearance of free neutron: $d \to n + ?$. Appearance of free neutrons was investigated in a shielded liquid scintillator enriched in deuterium [213], as well as in D_2O target with mass of 267 kg, installed at Reactor 5 of the Centrale Nucleaire de Bugey (France) and well shielded against cosmic rays and natural radioactivity; this allowed to set the best current limit for the p decay to *anything* as $\tau > 4.0 \times 10^{23}$ yr [408]. Analysis of the data collected with massive (1000 t) D_2O detector in the Sudbury Neutrino

[4] Spontaneous fission of ^{232}Th was observed in 1995; measured half life is $T_{1/2} = (1.2 \pm \pm 0.4) \times 10^{21}$ yr [155].

Table 7.11. **Lower limits on the life time for N, NN and NNN decays into invisible channels established in various approaches. The best limits for specific channels are in bold**

Nucleon(s) decay	τ limit, yr and C.L.	Year [Ref.]	Short explanation
$p \to anything$	1.2×10^{23}	1958 [237]	Limit on ^{232}Th spontaneous fission
	3.0×10^{23}	1970 [213]	Search for free n in liquid scintillator enriched in deuterium ($d \to n+?$)
	$\mathbf{4.0 \times 10^{23}}$ 95 %	2001 [408]	Free n in reactor experiment with D_2O
$\to invisible$	7.4×10^{24}	1977 [231]	Geochemical search for $^{130}\mathrm{Te} \to ... \to {}^{129}\mathrm{Xe}$
	1.1×10^{26}	1978 [235]	Radiochemical search for $^{39}\mathrm{K} \to ... \to {}^{37}\mathrm{Ar}$
	1.9×10^{24} 90 %	2000 [142]	Search for ^{128}I decay in ^{129}Xe detector
	$\simeq 10^{28}$	2002 [10]	Free n in the SNO D_2O volume
	1.1×10^{26} 90 %	2003 [60]	Search for ^{12}B decay in CTF detector
	3.5×10^{28} 90 %	2003 [434]	Free n in the SNO D_2O volume
	$\mathbf{2.1 \times 10^{29}}$ 90 %	2004 [11]	Search for γ with $E_\gamma = 6$—7 MeV emitted in ^{15}N deexcitation in SNO detector
$n \to anything$	$\mathbf{1.8 \times 10^{23}}$	1958 [237]	Limit on ^{232}Th spontaneous fission
$\to \nu_\mu \overline{\nu}_\mu \nu_\mu$	5.0×10^{26} 90 %	1979 [310]	Massive liquid scint. detector fired by ν_μ in result of n decays in the whole Earth [a,b]
	1.2×10^{26} 90 %	1991 [127]	Fréjus iron detector fired by ν_μ [b]
$\to \nu_e \overline{\nu}_e \nu_e$	3.0×10^{25} 90 %	1991 [127]	Fréjus iron detector fired by ν_e [c]
$\to \nu_i \overline{\nu}_i \nu_i$	2.3×10^{27} 90 %	1997 [255]	Search for bremsstrahlung γ with $E_\gamma > 100$ MeV emitted due to sudden disappearance of n magnetic moment (from Kamiokande data) [d]
$\to \nu_i \overline{\nu}_i \nu_i \overline{\nu}_i \nu_i$	1.7×10^{27} 90 %	1997 [255]	The same approach [d]
$\to invisible$	8.6×10^{24}	1977 [231]	Geochemical search for $^{130}\mathrm{Te} \to ... \to {}^{129}\mathrm{Xe}$
	1.1×10^{26}	1978 [235]	Radiochemical search for $^{39}\mathrm{K} \to ... \to {}^{37}\mathrm{Ar}$
	4.9×10^{26} 90 %	1993 [403]	Search for γ with $E_\gamma = 19$—50 MeV emitted in ^{15}O deexcitation in Kamiokande detector
	1.8×10^{25} 90 %	2003 [60]	Search for ^{11}C decay in CTF detector
	1.9×10^{29} 90 %	2004 [11]	Search for γ with $E_\gamma = 6$—7 MeV emitted in ^{15}O deexcitation in SNO detector
	$\mathbf{5.8 \times 10^{29}}$ 90 %	2006 [33]	Search for correlated decays in KamLAND detector
$nn \to \nu_\mu \overline{\nu}_\mu$	6.0×10^{24} 90 %	1991 [127]	Fréjus iron detector fired by ν_μ [e]
$\to \nu_e \overline{\nu}_e$	1.2×10^{25} 90 %	1991 [127]	Fréjus iron detector fired by ν_e [f]
$\to invisible$	1.2×10^{25} 90 %	2000 [142]	Search for ^{127}Xe decay in ^{129}Xe detector
	4.9×10^{25} 90 %	2003 [60]	Search for ^{10}C and ^{14}O decay in CTF
	4.2×10^{25} 90 %	2004 [407]	Radiochemical search for $^{39}\mathrm{K} \to ... \to {}^{37}\mathrm{Ar}$ [g]
	$\mathbf{1.4 \times 10^{30}}$ 90 %	2006 [33]	Search for correlated decays in KamLAND detector
$pp \to invisible$	5.5×10^{23} 90 %	2000 [142]	Search for ^{127}Te decay in ^{129}Xe detector
	$\mathbf{5.0 \times 10^{25}}$ 90 %	2003 [60]	Search for ^{11}Be decay in CTF detector
	1.9×10^{24} 90 %	2006 [143]	Search for decays $^{134}\mathrm{Te} \to ... \to {}^{134}\mathrm{Xe}$ in ^{136}Xe detector

End of the tabl. 7.11

Nucleon(s) decay	τ limit, yr and C.L.	Year [Ref.]	Short explanation
$pn \to invisible$	$\mathbf{2.1 \times 10^{25}}$ 90 %	2004 [407]	Radiochemical search for $^{39}\mathrm{K} \to ... \to {}^{37}\mathrm{Ar}$ [g]
	3.2×10^{23} 90 %	2006 [143]	Search for decays $^{134}\mathrm{I} \to {}^{134}\mathrm{Xe}$ in $^{136}\mathrm{Xe}$ detector
$ppp \to invisible$	$\mathbf{3.6 \times 10^{22}}$ 90 %	2006 [143]	Search for decays $^{133}\mathrm{Sb} \to ... \to {}^{133}\mathrm{Cs}$ in $^{136}\mathrm{Xe}$ detector
$ppn \to invisible$	$\mathbf{2.7 \times 10^{22}}$ 90 %	2006 [143]	Search for decays $^{133}\mathrm{Te} \to ... \to {}^{133}\mathrm{Cs}$ in $^{136}\mathrm{Xe}$ detector
$pnn \to invisible$	$\mathbf{1.4 \times 10^{22}}$ 90 %	2006 [143]	Search for decays $^{133}\mathrm{I} \to ... \to {}^{133}\mathrm{Cs}$ in $^{136}\mathrm{Xe}$ detector

[a] The result of [310] was reestimated in [127] to be more than one order of magnitude lower. [b] The limit is also valid for $p \to \nu_\mu \overline{\nu}_\mu \nu_\mu$ decay. [c] The limit is also valid for $p \to \nu_e \overline{\nu}_e \nu_e$ decay. [d] $i = e, \mu, \tau$. [e] The limit is also valid for pn and pp decays into $\nu_\mu \overline{\nu}_\mu$. [f] The limit is also valid for pn and pp decays into $\nu_e \overline{\nu}_e$. [g] On the basis of the data of [235].

Observatory (SNO) located on the depth of 6000 m w.e. (Canada) lead to limit $\tau(p \to invisible)$ around 10^{28} yr [10, 434].

(5) Search for prompt γ quanta emitted by a nucleus in a de-excitation process after N decays within the inner nuclear shell (valid for invisible channels). Energies of the emitted γ quanta in the range of 19—50 MeV were investigated with the Kamiokande detector [403]. In search for the 6—7 MeV γ quanta with the SNO detector [11], the best limit for the p decay to *invisible* was set as $\tau(p \to invisible) > 2.1 \times 10^{29}$ yr.

(6) Search for bremsstrahlung γ quanta emitted because of a sudden disappearance of the neutron magnetic moment (limits depend on the number of emitted neutrinos) [255].

(7) Considering the Earth as a target with nucleons which decay by emitting electron or muon neutrinos; these neutrinos can be detected by a large underground detector [127, 310] (valid for decay into neutrinos with specific flavors).

(8) Very often daughter nuclei created after N disappearance in mothers are unstable. Search for their radioactive decay (time-resolved from prompt products) can be performed with a proper low background detector (especially effective if mother nuclei are incorporated in a detector itself). Such investigations were done with liquid Xe scintillators (enriched by ^{129}Xe [142] or ^{136}Xe [143]) and with the BOREXINO Counting Test Facility (CTF), a 4 t liquid scintillation detector [60].

(9) Search for radioactive decay of daughter nuclei (with character half lives in the range of seconds or minutes) can be combined with registration of prompt energy release after N decay or disappearance. Such a combined approach was

used with the massive (currently the world's largest low background liquid scintillator, 1000 t) KamLAND detector [33] that allowed to establish the best τ limits (near 10^{30} yr) for n and nn decays to *invisible*.

All experimental results on searches for invisible decays of nucleons are summarized in Table 7.11.

Concluding this section, we would like to note that decays to *invisible* or disappearance were searched for not only for nucleons but also for other constituents of matter. Experiments on disappearance of electrons were described in the previous section; best limits on life time τ are on the level of $\simeq 10^{24}$ yr [110, 113]. Upper limits on the branching ratio λ for decay of positronium into *invisible* were obtained in [61]; in particular, for the direct annihilation $e^+e^- \to$ *invisible* $\lambda < 2.1 \times 10^{-8}$. Decay of unstable particles into *invisible* was looked for with the BABAR detector that gives $\lambda < 2.2 \times 10^{-4}$ for B^0 mesons [55] and $\lambda < 3.0 \times 10^{-4}$ for $Y(1S)$ [56], and with the BES detector λ limits are $\simeq 10^{-2}$ for η, η' [6] and J/ψ [7]. Astrophysical bounds for tunneling of γ quanta into EDs — that leads to additional cooling of stars — were discussed in [238].

7.7. Search for spontaneous emission of heavy clusters

The spontaneous emission of nuclear fragments heavier than α particles and lighter than the most probable fission fragments, named cluster decay, was theoretically predicted in 1980 [381] and experimentally observed at the first time in 1984 [14, 241, 375]. Up to date, spontaneous emission of clusters ranging from ^{14}C to ^{34}Si from near twenty trans-lead nuclei (from ^{221}Fr to ^{242}Cm) have been observed with branching ratios relative to α decay from 10^{-9} down to 10^{-16} and partial half lives from 3.2×10^3 yr up to 1.2×10^{20} yr [156, 414]. In all these decays double magic nucleus ^{208}Pb, or nuclei close to ^{208}Pb, are produced that even allows to consider this domain of cluster decays as "lead radioactivity" [414], analogously to "α radioactivity". For about ten cases, only the half life limits are known with the highest value of $T_{1/2} > 5.0 \times$ $\times 10^{21}$ yr for decay $^{232}\mathrm{Th} \to {}^{24-26}\mathrm{Ne} + {}^{208-206}\mathrm{Hg}$ [155, 156].

A new region of parent nuclei, for which cluster radioactivity can be observed experimentally, was predicted recently [366]: these are the nuclei with $Z = 56$—64 and $N = 58$—72; daughter nuclei are close to double magic $^{100}_{50}$Sn. First searches in this domain were performed resulting only in limit $T_{1/2} > 3.5$ h for $^{114}\mathrm{Ba} \to {}^{12}\mathrm{C} + {}^{102}\mathrm{Sn}$ [262].

The most widely used technique in experiments on cluster radioactivity is based on solid state nuclear track detectors which are able to register track of heavy cluster emitted from thin sample while rejecting much more numerous low energy α particles with great efficiency [156]. In few first measurements also Si detector telescopes were applied [375]. Ge detectors were used in two

experiments looking for γ rays from created in cluster decay nuclear residuals: ^{24}Na in decay of ^{233}U (where the limit $T_{1/2} > 1.7\times10^{17}$ yr was established) [66], and various clusters in decays of Hg isotopes (with $T_{1/2}$ limits up to few by 10^{21} yr) [170].

Very interesting approach — search for the initial energy release and subsequent decay (or chains of decays) of created clusters (which usually are radioactive) — was used in experiment [138] to look for possible cluster decays of ^{127}I. In this research mother ^{127}I nuclei were incorporated in the NaI(Tl) detector (natural abundance of ^{127}I is 100 % [147]) that ensured high efficiency of detection of the decays. The data used were collected deep underground (about 3600 m w.e.) at the Gran Sasso underground laboratory by using the highly radiopure $\simeq$100 kg NaI(Tl) set-up of the DAMA experiment (DAMA/NaI) devoted mainly for investigation of Dark Matter particles [146]. The set-up consisted of 9 NaI(Tl) scintillators with mass of $\simeq$9.7 kg each; the analyzed statistics was 33834 kg $\cdot$ days.

Using table of atomic masses [57], one can find that 215 different decay modes are possible for ^{127}I nucleus with positive energy release Q. However, the most interesting are those with emission of double magic nucleus $^{48}_{20}$Ca and its neighbor $^{49}_{21}$Sc: they have the highest Q values of 28.9 and 29.4 MeV, respectively [57]. Nucleus ^{48}Ca created in decay $^{127}_{53}\mathrm{I} \rightarrow {}^{48}_{20}\mathrm{Ca} + {}^{79}_{33}\mathrm{As}$ is practically stable, $T_{1/2}(2\beta) \simeq 4\times10^{19}$ yr, but supplementary nucleus ^{79}As has quite short half life of 9.01 m, and in its decay emits γ quanta with energy of 0.432 MeV (probability 1.49 %) and 0.365 MeV (1.86 %) [236]. The sequence of events searched for was the following: (1) first event with energy >5 MeV (from initial cluster decay with $Q = 28.9$ MeV; here the NaI(Tl) quenching factor for ions with high stopping power was taken into account); (2) $\Delta t < 270$ s between the first and the second events; (3) energy release in one of NaI(Tl) between 1.00 and 1.85 MeV (from electron emitted in β decay); (4) coincident energy release in other NaI(Tl) between 0.365 and 0.432 MeV ($\pm2\sigma$ energy resolution) from emitted γ quanta. Efficiency to detect such a sequence of events was calculated with Monte Carlo program as 3.6×10^{-4} [138]. Number of registered events in the experimental data, which satisfy the selection criteria, was found as 348, in full agreement with the expected number of random coincidences (361 ± 5). This gives the following limit for the life time:

$$\tau({}^{127}_{53}\mathrm{I} \rightarrow {}^{48}_{20}\mathrm{Ca} + {}^{79}_{33}\mathrm{As}) > 6.8\times10^{21} \text{ yr at } 90\,\% \text{ C.L.}$$

For other possible modes of ^{127}I cluster decay, investigated in this work (^{24}Ne + ^{103}Tc, ^{28}Mg + ^{99}Nb, ^{30}Mg + ^{97}Nb, ^{32}Si + ^{95}Y, ^{34}Si + ^{93}Y, ^{49}Sc + + ^{78}Ge) also only τ limits were found; they were in the range of 2.8×10^{21} yr to 2.1×10^{24} yr, up to 3 orders of magnitude higher than the best τ limits established for other perspective nuclides in other works.

7.8. Rare α and β decays

While α decay is well known nuclear phenomenon with more than 100 years history, interest to its investigation even increased during last years. At present days researches are concentrated mainly on studies of short-living exotic isotopes close to the proton drip line, decays of superheavy elements, and on search for α activity of naturally occurring isotopes. Despite alpha decay is energetically allowed for several primordial natural elements from cerium to uranium, during the 20th century α activity was observed (apart from uranium and thorium families) only for neodymium, samarium, gadolinium, hafnium, osmium and platinum. Recently two extremely rare α decays were discovered. Alpha activity of bismuth, being considered the heaviest stable element, was observed with the half life $T_{1/2} = 1.9 \times 10^{19}$ yr (the longest measured $T_{1/2}$ for α decays) by using a BGO crystal (bismuth germanate, $Bi_4Ge_3O_{12}$) as a low-temperature scintillating bolometer [325]. Alpha decay of tungsten (isotope ^{180}W) with $T_{1/2} = 1.1 \times 10^{18}$ yr was detected [186] with the help of cadmium tungstate crystal scintillators.

Isotopes ^{50}V, ^{115}In and ^{113}Cd are only three nuclei which enable study of four-fold forbidden β decays in a practical way, when rare β decay is not masked by much more rapid β decays. The high order of forbiddeness leads to high half lives, in the range of 10^{14}—10^{17} yr. It should be noted an interesting possibility of an independent estimation of neutrino mass in case of a very low energy of β decay of ^{115}In to the first excited level of daughter nucleus.

Usually investigations of rare α and β decays are by-products of experiments aimed to search for double beta decay and dark matter, measure neutrino fluxes, screening of materials for development of ultra-low background nuclear spectrometry.

7.8.1. Beta decay of ^{113}Cd

Isotope ^{113}Cd is present in the natural composition of cadmium with abundance of 12.22 %, however, it is β unstable with $Q_\beta = 320(3)$ keV [57]. Radioactivity of ^{113}Cd was observed for the first time only in 1970 [260], after a number of unsuccessful attempts since 1940 (see references in [260]). Then this decay was investigated in works [15, 199, 258, 338].

The most precise study of β decay of ^{113}Cd (measurement of $T_{1/2}$ and spectrum shape) was realized in [104] by using a low background $CdWO_4$ crystal scintillator to investigate the β decay of ^{113}Cd with precision better than those of the previous studies. The $CdWO_4$ crystal with mass of 434 g, used in the experiment [199] and then stored during last 10 years in the Solotvina Underground Laboratory on a depth of 1000 m w.e., was transported in a lead container by surface and immediately placed underground in the Gran Sasso underground laboratory to avoid its cosmogenic activation. It was installed in a

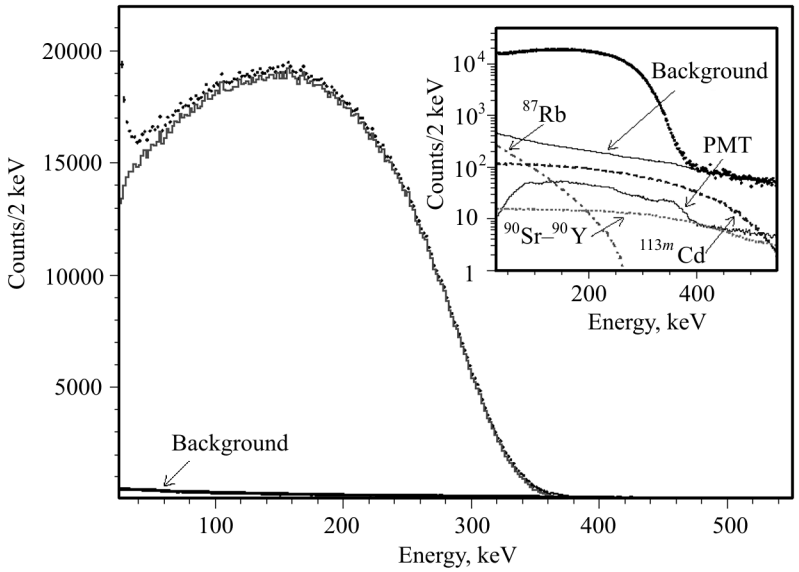

Fig. 7.16. The raw energy spectrum of the $CdWO_4$ scintillator measured over 2758 h in the low background set-up is shown by dots. The energy spectrum, obtained after the PMT noise rejection and the correction for related efficiency and the subtraction of the background, is shown by histogram. (Inset) The raw spectrum is shown together with the model of the background and its main components: β spectra of ^{87}Rb, ^{113m}Cd and ^{90}Sr—^{90}Y, and the contribution from the external γ quanta from PMTs in these experimental conditions

low background DAMA/R&D set-up (see e.g. [136]) surrounded by low radioactive shield of high purity Cu, Pb, Cd and polyethylene/paraffin to reduce the external background. The whole shield has been closed inside a Plexiglas box, continuously flushed by high purity N_2 gas. An event-by-event data acquisition system records amplitude, arrival time of event, and shape of scintillation signal with a 20 MS/s transient digitizer. Data were accumulated during 2758 h. The abundance of ^{113}Cd in the $CdWO_4$ crystal was determined with precise mass spectrometric measurements. Contribution of radioactive contamination in the crystal in the region of the ^{113}Cd β spectrum was estimated by the time-amplitude and pulse-shape analyzes of the collected data, and with the help of GEANT4 software package [13]. Mass spectrometry was also used to check presence of radioactive elements. Pulse-shape analysis allowed to reject α events and PMT noise, and to reach quite low energy threshold of 28 keV.

The signal to background ratio was equal 56/1, which is the best value among all to-date experiments. More than 2.4×10^6 events were collected, and half life of ^{113}Cd was determined as:

$$T_{1/2} = (8.04 \pm 0.05) \times 10^{15} \text{ yr}.$$

Accumulated during 2758 h spectrum with its fit by a model function and components of background are shown in Fig. 7.16.

7.8.2. First observation of β decay of ^{115}In to the first excited level of ^{115}Sn

In accordance with the last tables of atomic masses [57], mass difference between ^{115}In and ^{115}Sn is equal to 499 ± 4 keV. It is enough to populate in β decay of ^{115}In not only the ground state but also the first excited level of ^{115}Sn with $E_{\text{exc}} = 497.4$ keV. However, because of extremely low energy release of 1.6 ± 4 keV and related with this low probability, decay to ^{115}Sn* was observed only very recently [173].

In the experiment carried out in the underground conditions of the Gran Sasso underground laboratory, a high purity indium metal sample with natural composition (95.71 % of ^{115}In) and mass of 928 g was measured during 2762 h in the ultra-low background set-up with four HPGe γ detectors of 225 cm^3

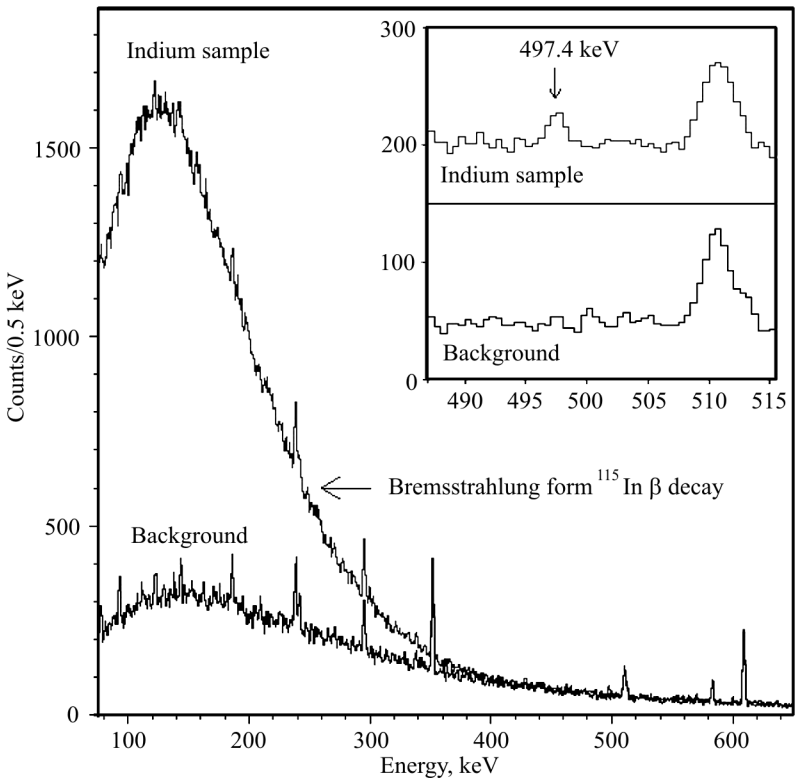

Fig. 7.17. Experimental spectrum of the In sample (accumulated for 2762 h) and background spectrum (1601 h) measured with four HPGe detectors in the energy interval 70—600 keV. The region of 600—2800 keV, where the spectra are practically indistinguishable, is not shown. Background is normalized to the same counting time. In the inset, the region of the 497.4 keV peak is shown in more detail; here, the In spectrum is shifted upward by 150 counts

volume each. A γ spectrum of the In sample in comparison with background is shown in Fig. 7.17. All lines (except of line at 497.4 keV) were related with natural, cosmogenic or man-made nuclides; their rates in background and the In sample were equal inside the statistical uncertainties. The line at 497.48 ± 0.21 keV was present only in the In spectrum, with area of 90 ± 22 counts. The energy of the peak is in agreement with the expected energy of γ quantum (497.358 ± 0.024 keV) emitted in deexcitation of the first excited level of ^{115}Sn. Counting rate in the peak corresponds to probability of 1.2×10^{-6} (relatively to decay to the ground state), and to half life of 3.7×10^{20} yr (see Fig. 7.18).

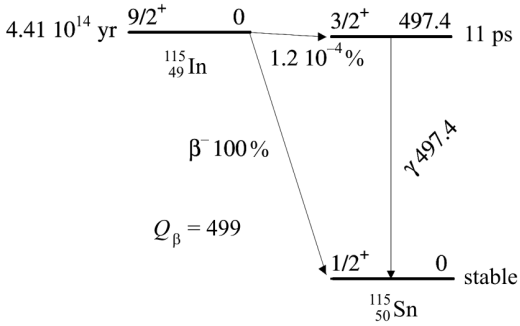

Fig. 7.18. New scheme of ^{115}In→^{115}Sn decay

The observation of ^{115}In →^{115}Sn* decay was recently confirmed also in measurements [27,430]. In accordance with the atomic mass tables [57], the value of $Q_\beta = 1.6 \pm 4.0$ keV was considered as possibly the lowest energy release in β decays (to be compared with 2.555 keV for ^{163}Ho, and 2.469 keV for ^{187}Re). To resolve this puzzling situation, the masses of ^{115}In and ^{115}Sn atoms were measured with unprecedent accuracy of ≃10 eV in [345]. This gives for decay to the ground ^{115}Sn state Q_β value of 497.489 ± 0.010 keV. Taking into account energy of the first ^{115}Sn excited level $E_{\rm exc} = 497.334 \pm 0.022$ keV, the Q_β value for decay to this level is 155 ± 24 eV, i.e. this decay really has the lowest known value of Q_β.

We have here a paradoxical situation: we know masses of ^{115}In and ^{115}Sn (near 115 GeV each) with accuracy of 10 eV, while the energy of the first ^{115}Sn excited level (which has energy 497 keV, i.e. 5 orders of magnitude lower) is known with worse accuracy of 22 eV giving the biggest contribution to the overall error bar of 24 eV. Measurements of $E_{\rm exc}$ with much better accuracy of ≃5 eV is currently realized at the INR, Kyiv.

7.8.3. Alpha decay of natural europium

Two naturally occurring europium isotopes (^{151}Eu and ^{153}Eu) are potentially α active. A CaF_2(Eu) crystal scintillator with mass of 370 g was used to search for α decay of ^{151}Eu ($Q_\alpha = 1.964$ MeV). While Eu is present in the crystal as a dopant with mass fraction of only ∼0.4 %, theoretical estimations (on the basis of work [365]) of the expected half life gave the value of $T_{1/2} \approx 4 \times 10^{18}$ yr, which is reachable with current experimental techniques.

Measurements were performed over 7426 h by using the DAMA/R&D set-up at the Gran Sasso underground laboratory. An event-by-event data acquisi-

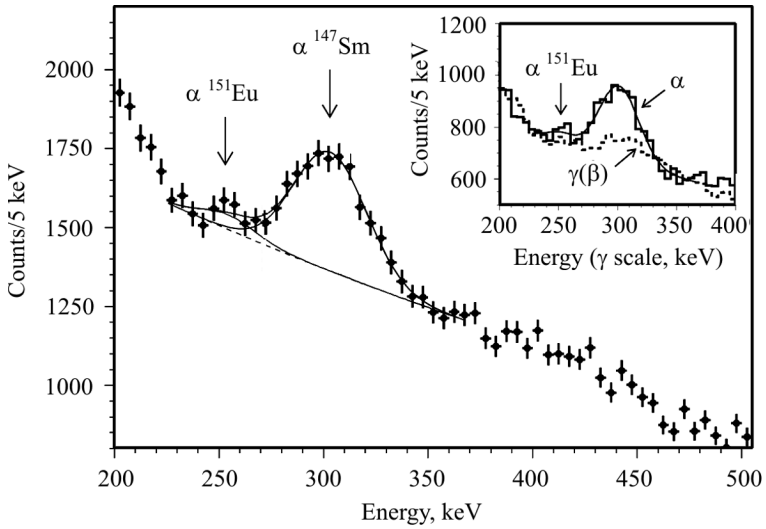

Fig. 7.19. Low energy part of the spectrum measured during 7426 h in the low background set-up with the $CaF_2(Eu)$ scintillator. The peculiarity on the left of the ^{147}Sm peak can be attributed to the decay of ^{151}Eu with $T_{1/2} = 5 \times 10^{18}$ yr. (Inset) Spectra obtained by applying the pulse-shape discrimination technique shown by dashed ($\gamma(\beta)$ component) and solid (α component) lines

tion system has been recording amplitude, arrival time of event, and shape of scintillation signal with a 160 MS/s transient digitizer over a window of 3125 ns. Response of the detector to γ quanta and α particles was measured with a set of external radioactive sources and by using the trace internal pollution of the crystal by α decaying nuclides. In accordance with measured α/β ratio [5], the expected energy of ^{151}Eu peak in γ scale of the $CaF_2(Eu)$ scintillator is 245(36) keV. The concentration of Eu in the crystal was checked with the help of the Inductively Coupled Plasma Mass Spectrometry analysis as 0.4 %, which is in agreement with the data provided by producer of the scintillator.

Internal radioactive contamination of the crystal by ^{40}K, U/Th chains and other nuclides was determined — on the level of mBq/kg — by the time-amplitude analysis and simulation of radioactive decays with the GEANT4 package. Peaks of alpha particles were identified in the data as being caused by α particles despite rather modest pulse shape discrimination between $\gamma(\beta)$ and α events in the $CaF_2(Eu)$ scintillator.

Measured spectrum of the $CaF_2(Eu)$ scintillator is shown in Fig 7.19. Peculiarity on the left of the ^{147}Sm peak has energy of 255(7) keV, in agreement with the expected energy of ^{151}Eu α decay. Pulse shapes of events in this peculi-

[5] The detector energy scale is measured with γ sources, thus the notation "α/γ ratio" could be more adequate. However, because γ rays interact with matter by means of the energy transfer to electrons, we are using the traditional notation "α/β ratio".

arity correspond to shapes caused by α particles. Determined experimentally half life $T_{1/2} = (5^{+11}_{-3}) \times 10^{18}$ yr [116] is in accordance with theoretical predictions.

This first indication should be confirmed in other experiments. One of the possibilities could be the use of $Li_6Eu(BO_3)_3$ crystals as a cryogenic bolometer with energy resolution for alpha particles at the level of several keV [117, 326].

7.8.4. α activity of natural tungsten

A first indication of the alpha decay of ^{180}W (the expected energy of alpha particles is 2460(5) keV [57], isotopic abundance of ^{180}W is $\delta = 0.12(1)\,\%$ [147]), with a half life $T_{1/2} \sim 10^{18}$ yr was obtained in the measurements with low background $CdWO_4$ crystal scintillators [186], and then was confirmed with $CaWO_4$ crystals as scintillators [436] and scintillating bolometers [184]. Recently the observation was also confirmed in measurements with low background $ZnWO_4$ crystals scintillators in the DAMA/R&D at the Gran Sasso underground laboratory [118]. There is a peculiarity in the α spectrum of a few $ZnWO_4$ detectors accumulated over 3197 kg · h of exposure at the energy of 325(11) keV. This energy in the γ scale corresponds to the α particle energy of 2358(80) keV. These alpha events can be ascribed to the α decay of ^{180}W with the half life $T_{1/2} = (1.3^{+0.6}_{-0.5}) \times 10^{18}$ yr. This result is in agreement with the data published earlier. It should be stressed that the isotope ^{180}W has the lowest ever measured specific α activity ($\simeq$2 decays per year per gram of the natural tungsten to be compared with the value of $\simeq$100 for natural bismuth).

7.8.5. First detection of α decay of ^{190}Pt to excited level of ^{186}Os

All six naturally occurring isotopes of platinum are potentially α unstable. However, only for one of them, ^{190}Pt (with the biggest energy release of $Q_\alpha = 3251(6)$ keV), α decay to the ground state of ^{186}Os was experimentally observed. The currently recommended half life value is $T_{1/2} = (6.5 \pm 0.3) \times 10^{11}$ yr. However, the first excited level of ^{186}Os ($J^\pi = 2^+$) has quite low energy: $E_{\rm exc} = 137.2$ keV, and energy available to α particle in decay to this level, $Q^*_\alpha = 3114(6)$ keV, is high enough to make the decay to be observed (theoretical estimations are in the range of $T_{1/2} = 10^{13}$—10^{14} yr). This allowed to detect the $^{190}\mathrm{Pt} \to {}^{186}\mathrm{Os}(2^+_1)$ decay through detection of the 137.2 keV γ quantum with the help of an ultra-low background HPGe detector even using a platinum sample with natural isotopic composition with very low percentage of ^{190}Pt (0.012(2) % [147]).

The measurements were performed deep underground in the Gran Sasso underground laboratory. Two platinum crucibles with the total mass of 42.6 g

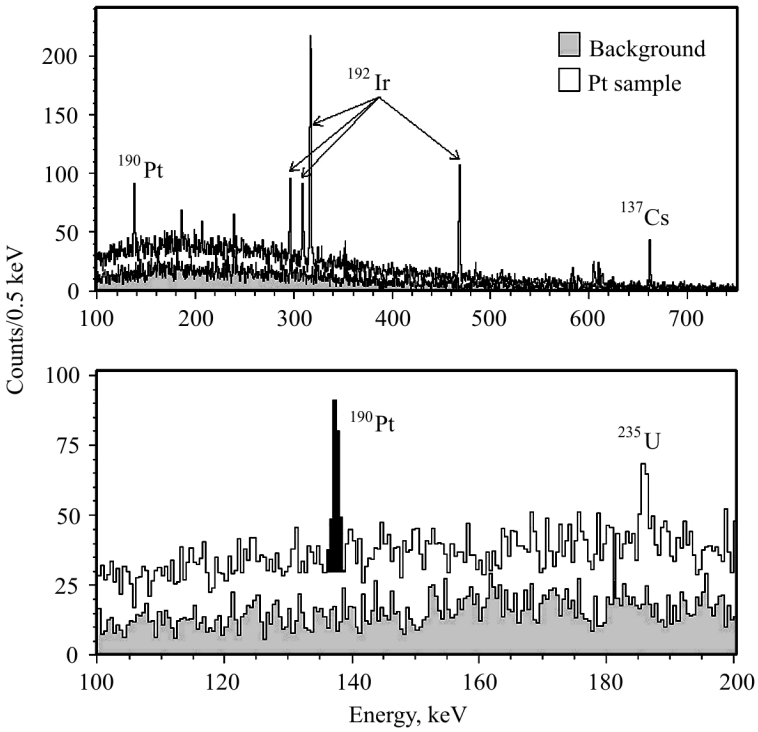

Fig. 7.20. Energy spectrum of the Pt sample with mass of 42.6 g measured over 1815 h (upper part), and in more detail around the 137 keV region (lower part). The background spectrum (measured without the Pt sample during 1046 h but normalized here to 1815 h) is also shown (filled histogram)

were used as a Pt sample. Data with the Pt were collected with HPGe detector of 468 cm^3 volume during 1815.4 h, while background spectrum of the detector was measured over 1045.6 h. The energy resolution of the detector is FWHM = = 2.0 keV for the 1332 keV γ line of ^{60}Co. To reduce external background, the detector was shielded by layers of low-radioactive copper (∼10 cm) and lead (∼20 cm); the set-up has been continuously flushed by high purity nitrogen (stored deep underground for a long time) to avoid presence of residual environmental radon. Part of the spectrum accumulated with the Pt sample in comparison with the background in the energy range of 100—700 keV is shown in Fig. 7.20.

The peak at energy of 137.1 ± 0.1 keV after α decay of ^{190}Pt to the 2_1^+ excited level of ^{186}Os is clearly visible in the Pt spectrum being absent in the background. Its area of 132 ± 17 counts corresponds to $T_{1/2} = 2.6^{+0.4}_{-0.3}(\text{stat.}) \pm$ $\pm\, 0.6(\text{syst.}) \times 10^{14}$ yr. An updated scheme of the ^{190}Pt decay is shown in Fig. 7.21. Half life limits for α decays of other platinum isotopes with emission of γ quanta were also obtained for the first time on the level of 10^{16}—10^{18} yr [119].

7.9. Development of experimental technique to search for rare nuclear and sub-nuclear processes

Searches for double beta decay, dark matter, hypothetical decays and processes, investigations of rare α and β decay require development of particle detectors with very low radioactive contamination, high energy resolution, very low energy threshold (especially important to search for the two neutrino electron capture and direct interaction of dark matter particles), containing certain elements (to study α, β and 2β decays) or variety of elements (for dark matter detectors). Most of scintillation materials possess unique properties required for high-sensitivity rare decay experiments: presence of certain elements, low level of intrinsic radioactivity, reasonable spectrometric characteristics, pulse-shape discrimination ability. Most of the crystal scintillators can be applied as cryogenic scintillating bolometers, which are extremely promising detectors thanks to high energy resolution and excellent particle discrimination. Here we briefly discuss development of low background scintillation detectors for low counting experiments.

7.9.1. Radioactive contamination of scintillators

Double beta decay and dark matter projects require low as much as possible — in ideal case zero — background of a detector in a region of interest. Radioactive contamination of scintillation material is the major cause of background as far as appropriate shielding against external irradiation is provided. A summary of radioactive contamination of scintillators is given in Table 7.12 [191]. The most dangerous radionuclides for 2β experiments are ^{226}Ra and ^{228}Th with daughters (^{214}Bi and ^{208}Tl) with energies of β decay of 3270 keV and 4999 keV, respectively.

Naturally occurring ^{40}K usually provides rather high counting rate up to 1461 keV. Anthropogenic ^{90}Sr is also troublesome radionuclide because it is in

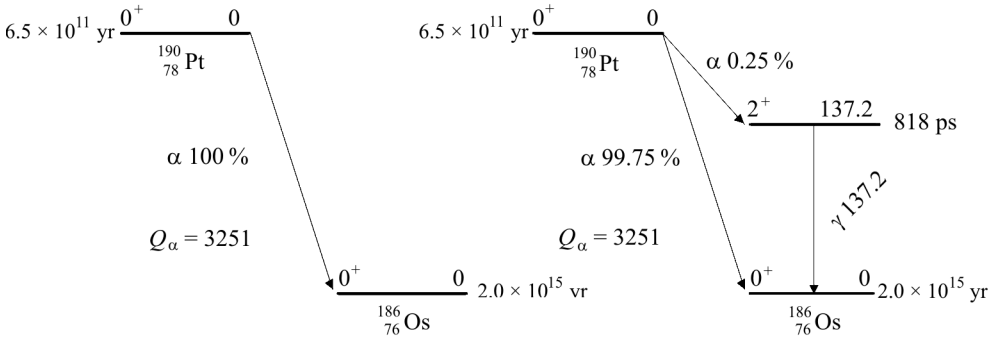

Fig. 7.21. Old (left) and new (right) schemes of α decay of ^{190}Pt

Table 7.12. **Radioactive contamination of scintillators (mBq/kg). Data for germanium crystals of HPGe detectors are given for comparison**

Scintillator	Total α activity (U + Th)	^{228}Th	^{226}Ra	^{40}K	Particular radioactivity	References
$MgWO_4$	5700 ± 400	<50	<50	<1600		[196]
$CaWO_4$	400—1400	<0.2—0.6	5.6—7	<12		[175, 193, 271, 436]
$ZnWO_4$	0.2	0.002	0.002	<0.4	0.5 (^{65}Zn)	[118]
$CdWO_4$	0.3—2	<0.003—0.039	<0.004	0.3—3.6	558 (^{113}Cd)	[104, 189, 200, 247]
					<3—30 (^{113m}Cd)	
$PbWO_4$	$(53—79) \times 10^3$	<13	<10		$(53—79) \times 10^3$	[190]
$PbWO_4$ (from ancient lead)					<4 (^{210}Pb)	[18]
$PbMoO_4$					$(67—192) \times 10^3$	[437]
$CaMoO_4$	<10	0.04	0.13	<3		[31]
Li_2MoO_4	<300	<12	<21	170		[81, 82]
$ZnMoO_4$	73 ± 2	<(0.3—1.1)	<1.1—8.1			[88, 251]
YAG		70	170	3300		[271]
YAG:Nd	<20					[188]
$Li_6Eu(BO_3)_3$		<130	<70	<1500	949 (^{152}Eu)	[117]
					212 (^{154}Eu)	
BGO		<0.4—6	<1.2	<7	$7—3 \times 10^3$ (^{207}Bi)	[68, 183]
GSO(Ce)	40—217	2.3—100	0.3	<14	1200 (^{152}Gd)	[201, 425]
Lu_2SiO_5(Ce)					3.9×10^7 (^{176}Lu) [a]	
NaI(Tl)	0.08—2.4	0.009—0.02	0.012—0.2	0.6		[24, 84, 134]
CsI(Tl)		0.0015—0.009	0.009—0.010		6 (^{134}Cs)	[313, 442]
					14—61 (^{137}Cs)	
$LaCl_3$(Ce)		<0.4	<34		4.1×10^5 (^{138}La)	[135]
$LaBr_3$					3.2×10^5 [b]	
LuI_3					1.6×10^7 (^{176}Lu) [a]	
LiF(W)		<20	<20	<66		[107]
CaF_2(Eu)	8	0.1—0.13	1.1—1.3	<7	10 (^{152}Eu)	[116, 354]
CeF_3	3400	1100	<60	<330		[114]
BaF_2		400	1400			[176]
Plastic scintillator		<0.00013				[34]
Liquid scintillator	$\approx 10^{-6}$	$(0.21—1.2) \times 10^{-6}$ (^{232}Th)	$(0.043—6.3) \times 10^{-6}$ (^{238}U)	$<7 \times 10^{-5}$	0.3 (^{14}C)	[19, 126, 397]
HPGe		$<2 \times 10^{-5}$	$<2 \times 10^{-5}$			[215, 294]

[a] Calculated value based on ^{176}Lu half life, isotopic composition and chemical formulae of LuI_3 and Lu_2SiO_5 compounds. [b] Calculated value based on ^{138}La half life, isotopic composition and chemical formula of $LaBr_3$ compound.

equilibrium with ^{90}Y with high energy of decay $Q_\beta = 2280$ keV (in addition, both ^{90}Sr and ^{90}Y are nuclides rather hard to measure due to absence of γ rays detectable by HPGe γ spectrometers). Presence of cosmogenic radioactivity should be also controlled and decreased as much as possible. A reachable (and *measurable* with present instrumentation) level of tens μBq/kg is discussed now (see, e.g. [31, 34, 120, 190, 433, 439]. However, further progress in the searching for 2β decay and dark matter will be possible only using crystal scintillators with higher radiopurity.

7.9.2. Development of crystal scintillators for double β decay experiments

High sensitivity experiments to search for double β processes in different nuclei are strongly required both for theoretical and experimental reasons. Scintillation detectors are rather promising technique from this point of view. Indeed, there are several scintillation materials containing elements with potentially 2β active isotopes. It is worth to mention a pioneer work of der Mateosian and Goldhaber to search for neutrinoless double β decay of ^{48}Ca by using enriched in ^{48}Ca and ^{40}Ca CaF_2(Eu) crystal scintillators [327]. Several high sensitivity studies of the double β decay processes were performed using crystal scintillators, which contain candidate nuclei: ^{40}Ca [137], ^{48}Ca [353,416], ^{70}Zn and ^{64}Zn [93,95,103,192], ^{106}Cd [105,189,200], ^{108}Cd and ^{114}Cd [92,200], ^{116}Cd [200], ^{130}Ba [176], ^{136}Ce and ^{138}Ce [100,114], ^{160}Gd [171,201,297], ^{180}W and ^{186}W [93, 194, 200]. For instance in the Solotvina experiment [200] with the cadmium tungstate scintillators enriched in ^{116}Cd one of the lowest in the 2β experiments counting rate of 0.04 counts/(year keV kg) was reached in the energy window 2.5—3.2 MeV where a peak from $0\nu2\beta$ decay of ^{116}Cd is expected.

The half life limit on neutrinoless double β decay of ^{116}Cd was set as $T_{1/2} \geq 1.7 \times 10^{23}$ years at 90 % C.L., which leads to one of the strongest restriction on the effective Majorana neutrino mass $\langle m_\nu \rangle \leq$ (1.5—1.7) eV. A number of large-scale scintillator-based projects to search for neutrinoless double β decay with sensitivity on the level of the inverted hierarchy of neutrino mass have been proposed [88, 120, 121, 172, 433, 439, 444]. The projects intend to use 10^2—10^3 kg of double β active isotopes. It should be also mentioned SuperNEMO double β decay project [279,362] aiming to utilize a large amount of plastic or liquid scintillators.

It should be stressed, that the energy resolution in a high sensitivity neutrinoless double β decay experiment aiming to explore inverted hierarchy of the neutrino mass (such an experiment should have a sensitivity to the effective neutrino mass on the level of 0.02—0.05 eV, which corresponds to half lives $T_{1/2} \sim 10^{26-28}$ yr) plays a crucial role due to irremovable background

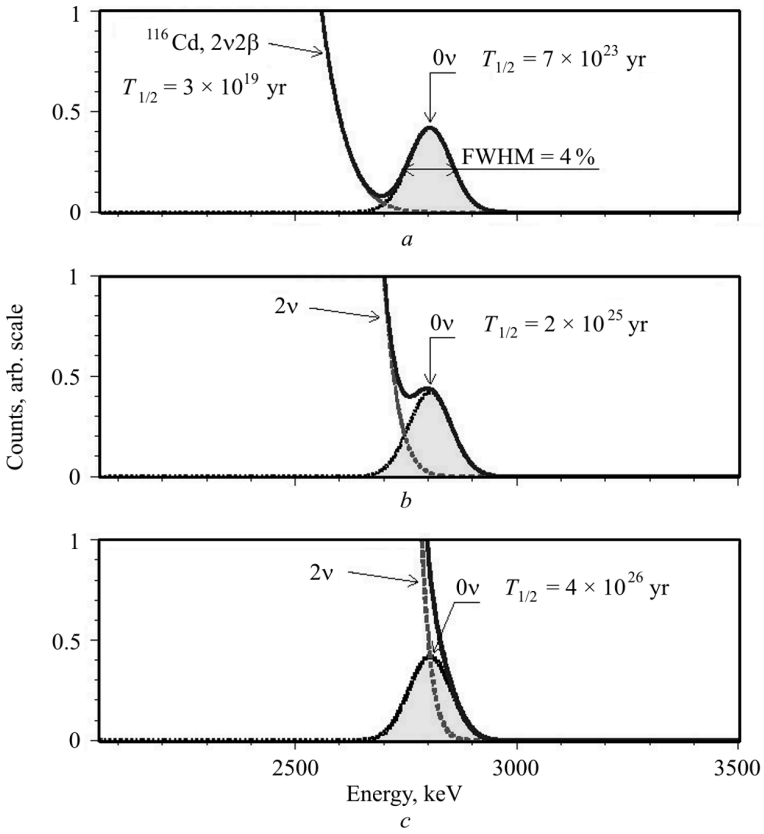

Fig. 7.22. Spectra of 0ν and $2\nu2\beta$ decays for different half life of ^{116}Cd relatively to $0\nu2\beta$ decay. Due to not perfect energy resolution, the $2\nu2\beta$ decay provides irremovable background in the region of the $0\nu2\beta$ peak

coming from two neutrino decay [438]. Importance of energy resolution for high sensitivity $0\nu2\beta$ decay experiments is demonstrated in Fig. 7.22, where the energy resolution FWHM = 4 %, a typical for scintillation experiment, is taken to show the problem of background coming from two neutrino mode. At the same time, rather modest energy resolution of scintillation detectors (typically a full width at the half of maximum is 100—150 keV for 1—3 MeV γ quanta) limits their application in high sensitivity experiments. Cryogenic scintillation bolometers (see e.g. [88, 251, 252, 363, 364]) with a typical energy resolution of a few keV looks extremely perspective technique for future neutrinoless double β decay experiments able to explore even the normal hierarchy of the neutrino mass (half life sensitivity on the level of 10^{28}—10^{30} years) [438]. At present $CdWO_4$ [252], ZnSe [187], $CaMoO_4$ [314] and recently developed $ZnMoO_4$ [88, 251, 273, 346] are considered as the most promising materials for high sensitivity cryogenic double β decay experiments.

Development of molybdates to search for neutrinoless double β decay of ^{100}Mo. ^{100}Mo is one of the most promising candidates for 2β experiments because of its high transition energy ($Q_{2\beta} = 3034.40 \pm 0.17$ keV [371]) and comparatively high isotopic abundance $\delta = 9.82 \pm 0.31\,\%$ [147]. There exist several crystal scintillators containing molybdenum: molybdate of calcium ($CaMoO_4$) [31, 123, 285], cadmium ($CdMoO_4$) [330, 364], lead ($PbMoO_4$) [197, 335, 363, 437], lithium-zinc ($Li_2Zn_2(MoO_4)_3$) [85], lithium (Li_2MoO_4) [81, 82], zinc ($ZnMoO_4$) [251, 273, 346] (the main properties of the molybdates are presented in Table 7.13). However, $CdMoO_4$ contains β active ^{113}Cd ($T_{1/2} = 8.04 \times 10^{15}$ yr [104], $\delta = 12.22\,\%$ [147]). In addition ^{113}Cd has very high cross section for capture of thermal neutrons 20600(4000) barn [236], which leads to γ background from neutron-gamma capture up to the energy of several MeV. Disadvantage of $PbMoO_4$ (even supposing that crystals would be produced from low-radioactive ancient lead [16,17,198]) is high effective Z value which causes stronger interactions with background γ quanta, and comparatively low concentration of molybdenum. $Li_2Zn_2(MoO_4)_3$ has low light yield. Besides the material is hard to grow. Here we describe recent performance of the most promising crystal scintillators containing molybdenum for cryogenic 2β experiments: $CaMoO_4$, Li_2MoO_4 and $ZnMoO_4$.

The only known molybdate crystal scintillator with reasonable light output at room temperature is calcium molybdate ($CaMoO_4$) proposed in [285] to search for the 0ν double beta decay of ^{100}Mo. The scintillation properties and the radioactive contamination of $CaMoO_4$ crystals produced by two companies in Ukraine and Russia have been studied. The best energy resolutions 10.3 % and 4.7 % for the 662 and 2615 keV γ lines were obtained with the $CaMoO_4$ sample of $\oslash 38 \times 20$ mm produced in Ukraine. Three components of the scintillation decay ($\approx$0.7 μs, 4 μs and 17 μs) and their intensities for α particles and γ quanta were observed, that allows to discriminate α particles and γ quanta. The temperature dependences of the light output and pulse shape were tested in the temperature range from -175 to $+40$ °C. The radiopurity

Table 7.13. **Main characteristics of molybdates promising for experiments to search for $0\nu2\beta$ decay of ^{100}Mo**

Crystal	Density, g/cm^3	Melting point, °C	Index of refraction	Wavelength of emission max, nm	Concentration of Mo, %
Li_2MoO_4	3.0—3.1	701		580	55.2
$Li_2Zn_2(MoO_4)_3$	4.38	890	2.0	550—610	46.1
$CaMoO_4$	4.2—4.3	1445—1480	1.98	520	48.0
$ZnMoO_4$	4.3	1003	1.9	585—625	42.6
$CdMoO_4$	4.35	1175	2.2	550	35.2
$PbMoO_4$	6.95	1060	2.4	540	26.1

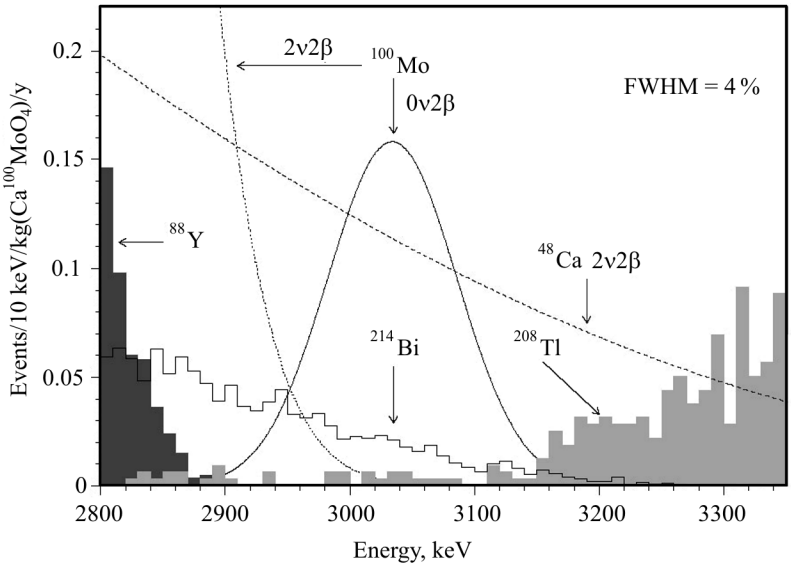

Fig. 7.23. Calculated backgrounds from the $2\nu2\beta$ decay of ^{48}Ca ($T^{2\nu}_{1/2} = 4\times10^{19}$ yr), internal pollutions by ^{208}Tl and ^{214}Bi (both with 0.1 mBq/kg), and ^{88}Y isotope from cosmogenic activity. The amplitude of the ^{88}Y distribution corresponds to 1000 decays in $CaMoO_4$, while the expected ^{88}Y cosmogenic activity is 4 events/kg/year during 5 years. Distributions for ^{100}Mo are shown for $T^{2\nu}_{1/2} = 7 \times 10^{18}$ yr and $T^{0\nu}_{1/2} = 10^{24}$ yr

of $CaMoO_4$ crystals was estimated in the low background measurements in the Solotvina underground laboratory. $CaMoO_4$ scintillators produced in Ukraine show contamination by uranium and thorium (particularly by ^{210}Po) at the level of 0.4—0.5 Bq/kg. The contamination of the $CaMoO_4$ crystal produced in Russia is one–two orders of magnitude higher.

Perspectives for high sensitivity experiments to search for the $0\nu2\beta$ decay of ^{100}Mo are discussed in [31]. The energy resolution of 4—5 % (looks realistic for ordinary scintillation detector) is enough to reach a sensitivity at the level of 10^{25} yr. The contamination of crystals by ^{226}Ra and ^{232}Th should not exceed the level of 0.1 mBq/kg. Disadvantage of $CaMoO_4$ is presence of $2\nu2\beta$ active isotope ^{48}Ca with abundance in natural calcium on the level of $\delta = 0.187\,\%$ [147], which creates background at $Q_{2\beta}$ energy of ^{100}Mo [31]. Therefore the $2\nu2\beta$ decay of ^{48}Ca restricts the sensitivity of an experiment to search for the $0\nu2\beta$ decay of ^{100}Mo by using $CaMoO_4$ crystal scintillators. Calculated background components ($2\nu2\beta$ decay of ^{48}Ca, internal pollutions by ^{208}Tl, ^{214}Bi and ^{88}Y isotopes are presented at Fig. 7.23 together with a peak of $0\nu2\beta$ decay of ^{100}Mo corresponding to the half life $T^{0\nu}_{1/2} = 10^{24}$ yr. To avoid the effect of ^{48}Ca, calcium molybdate crystals from enriched isotope ^{100}Mo and from calcium depleted in ^{48}Ca were developed [286]. A final goal

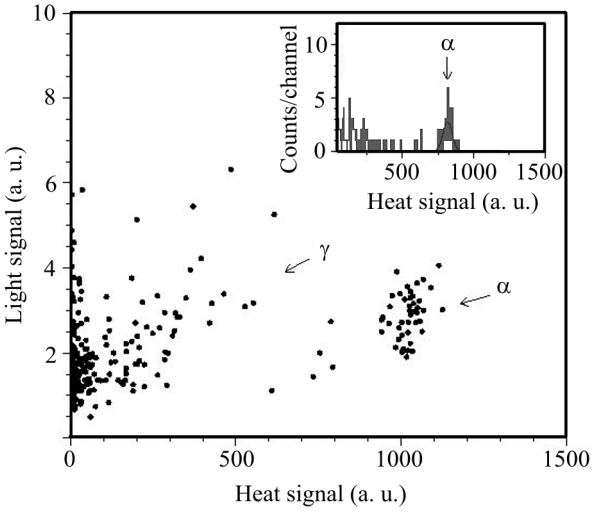

Fig. 7.24. Scatter plot of the light signal versus heat signal for 37 h background exposition with Li_2MoO_4 crystal $\oslash 25 \times \times 0.9$ mm. (Inset) Distribution of heat signals. Fit of α peak by Gaussian function with the energy resolution FWHM = 9 % is shown by solid line [81]

of the AMoRE collaboration (Korea, Russia, Ukraine, China) is a large scale high sensitivity experiment to search for $0\nu2\beta$ decay of ^{100}Mo by using enriched in ^{100}Mo and depleted in ^{48}Ca calcium molybdate crystals as cryogenic scintillating bolometers [314].

A sample of Li_2MoO_4 crystal ($\oslash 25 \times 0.9$ mm) was measured over 37 h as bolometer at ≈10 mK in the CUORE R&D set-up [363] in the Gran Sasso underground laboratory. In addition to the heat signal, the scintillation light was read by an additional Ge bolometer. Light output of the sample was estimated as 7 % relatively to $CdMoO_4$ crystal $10 \times 10 \times 2$ mm. Taking into account relative light outputs of $CdMoO_4$ and $CaMoO_4$ at 9 K [330], this corresponds to ≈20 % of $CaMoO_4$. Light output for α particles is ≈30 % relatively to γ quanta, which allows to discriminate α and $\gamma(\beta)$ events (see Fig. 7.24).

The peak observed in the heat signal spectrum is probably due to contamination of the crystal by ^{210}Pb (or ^{210}Po if the equilibrium is broken). However, it could be due to contamination of the set-up. Therefore one can give only limit on activity of ^{210}Po in the sample as ≤0.3 Bq/kg. Radiopurity of a Li_2MoO_4 crystal with mass of 34 g was also measured at the Gran Sasso underground laboratory with an ultra-low background HPGe γ spectrometer [82]. Li_2MoO_4 had shown good perspectives as a possible detector to search for double beta decay of molybdenum, and resonant capture of hypothetical solar axions on ^{7}Li [81]. However, taking into account rather low purity grade of the raw materials used to produce the tested Li_2MoO_4 sample (the crystal was obtained by a solid state synthesis technique from MoO_3 and Li_2CO_3 powders both of 99.5 % purity), further R&D to improve the material would be useful.

Recently developed $ZnMoO_4$ [273,346] is surely one of the most promising molybdates. For the first time comparatively large $ZnMoO_4$ single crystals

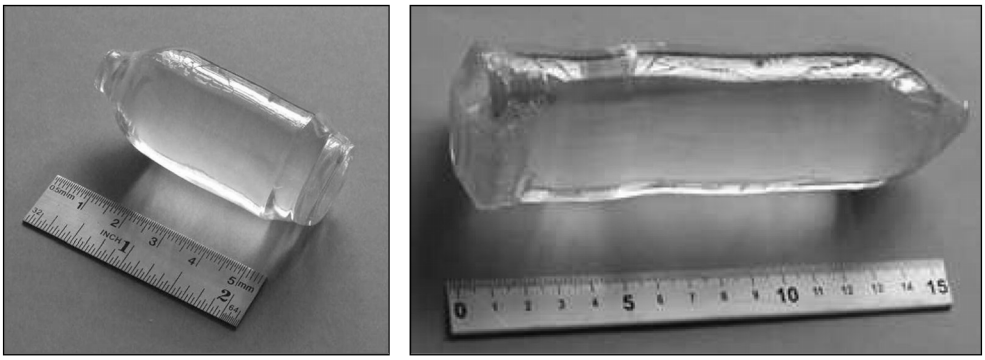

Fig. 7.25. Boules of $^{106}CdWO_4$ (left) and $^{116}CdWO_4$ (right) single crystals grown by the low-thermal-gradient Czochralski process

were grown by the Czochralski and Kyropoulos methods from a melt [273]. Luminescence of the compound was measured under X ray excitation in the temperature range 85—400 K and properties of $ZnMoO_4$ crystal as cryogenic low temperature scintillator were checked for the first time [251]. Radioactive contamination of the $ZnMoO_4$ crystal was estimated as $\leq$0.3 mBq/kg (^{228}Th) and 8 mBq/kg (^{226}Ra). Thanks to the simultaneous measurement of the scintillation light and the phonon signal, the α particles can be discriminated from the γ/β interactions. The detector also shows a clear ability to discriminate the α induced background without the light measurement, thanks to a different shape of the thermal signal that characterizes γ/β and α particle interactions.

An important advantage of $ZnMoO_4$ in comparison to $CaMoO_4$ is lower melting temperature which allows to apply the so called low-thermal-gradient Czochralski technique to produce crystals from enriched ^{100}Mo. Obvious advantages of the low-thermal-gradient method in comparison to the conventional Czochralski technology are higher quality of crystals, high utilization factor of the initial charge (up to 90 %), closed platinum crucible providing a shield against evaporation from ceramic details, potentially the most radioactively contaminated part of a growing set-up. Thanks to good particle discrimination ability and high scintillation properties at low temperatures, $ZnMoO_4$ compound is extremely promising for the search of neutrinoless 2β decay of ^{100}Mo [251]. Further development of this material is in progress [88].

Development of $CdWO_4$ crystal scintillators from enriched isotopes ^{106}Cd and ^{116}Cd. The Solotvina experiment [200] has demonstrated important properties of $CdWO_4$ crystals required for a high sensitivity ^{116}Cd 2β decay experiments. Another application of $CdWO_4$ scintillating crystals is search for double β processes in ^{106}Cd. One of the highest for $2\beta^+$ nuclides value of $Q_{2\beta} = 2770$ keV allows three modes of decay: decay with emission of two positrons ($2\beta^+$), electron capture with emission of positron ($\varepsilon\beta^+$) and

double electron capture (2ε, see the decay scheme of ^{106}Cd in Fig. 7.3). ^{106}Cd looks as one of the most promising nuclei to study the $2\beta^+$ processes.

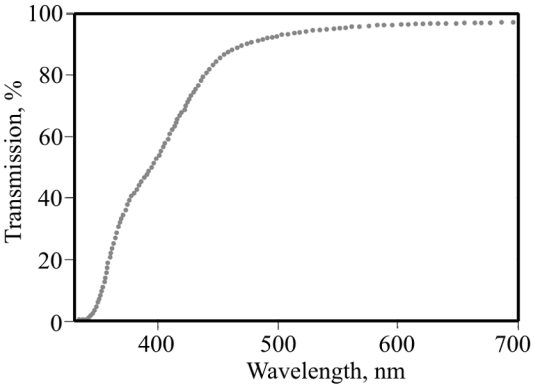

Fig. 7.26. The optical transmission curve of $^{106}CdWO_4$ crystal 50 mm long measured with a thin sample of the crystal in reference beam

A cadmium tungstate crystal scintillator enriched in ^{106}Cd to 66 % (natural abundance is 1.25 %) was developed [105] with the aim to realize an experiment to search for double beta processes in ^{106}Cd. Sample of cadmium enriched in ^{106}Cd was purified by vacuum distillation. Cadmium tungstate compound for crystal growth was synthesized from solutions. Contamination of the enriched cadmium and synthesized compounds were controlled by mass-spectrometry and atomic absorption spectroscopy. The absolute isotopic composition of the enriched cadmium was accurately determined by thermal ionisation mass-spectrometry. In particular, the concentration of ^{106}Cd is 66 %, while abundance of β active isotope ^{113}Cd is 3.9 %. A $^{106}CdWO_4$ crystal boule, with mass of 231 g (87 % of initial mass of powder), was grown by the low-thermal-gradient Czochralski technique (see Fig. 7.25, left). The total irrecoverable loss of enriched cadmium, on the stages of purification, raw material production, crystal growth, and scintillation element production, does not exceed 2.3 %.

A $^{106}CdWO_4$ crystal scintillator with mass of 216 g exhibits excellent optical and scintillation properties. In particular, the energy resolution FWHM = 10 % was measured with 662 keV γ quanta of ^{137}Cs source. From the data of transmittance measurements (see Fig. 7.26) an attenuation length of the material 60 ± 7 cm at the wavelength of the emission maximum (490 nm) was derived. Such a high transmittance was newer reported for cadmium tungstate crystals. One could naturally explain this improvement by the deep purification at the stage of the enriched cadmium distillation and of the $^{106}CdWO_4$ compound synthesis, and also by the advantages of the low-thermal-gradient Czochralski technique. An experiment to search for double β processes in ^{106}Cd was performed in the Gran Sasso underground laboratory [99, 106, 115].

Cadmium tungstate crystal scintillator was also developed from cadmium enriched in ^{116}Cd. The enriched cadmium was purified by chemical methods, the most polluted part was additionally purified by vacuum distillation [300]. Cadmium tungstate compounds were synthesized from solutions. A $^{116}CdWO_4$ crystal boule with mass of 1868 g (which is 87 % of the initial charge) was grown by the low-thermal-gradient Czochralski technique (see Fig. 7.25). The abso-

lute isotopic composition of ^{116}Cd in the crystal was determined as 83 % by mass-spectrometry. Crystal scintillators produced from the boule were subjected to characterization that included measurements of transmittance and energy resolution. Low background detector with the enriched $^{116}CdWO_4$ crystal scintillators was installed in the Gran Sasso underground laboratory. Monte Carlo simulation of double β processes in ^{116}Cd was performed to estimate sensitivity of an experiment to search for double β decay of ^{116}Cd [77]. An experiment to search for double beta decay of ^{116}Cd by using the developed crystal scintillators is in progress in the Gran Sasso underground laboratory.

7.9.3. Crystal scintillators for cryogenic experiments to search for dark matter

There is an evidence for a large amount of invisible (dark) matter in the Universe, which reveals itself only through gravitational interaction. Weakly interacting massive particles (WIMPs), in particular neutralino, predicted by the Minimal Supersymmetric extensions of the Standard Model, are considered as one of the most acceptable components of the dark matter [128, 129, 151, 394]. WIMPs can be detected due to their scattering on nuclei producing low energy nuclear recoils. Extremely low counting rate and small energy of recoil nuclei are expected in experiments to search for the WIMPs. Another experimental difficulty is absence of a clear signature of the effect. In fact, near to exponential distributions of the recoils are expected, while background of a nuclear detector has also typically a behavior near to exponential. There are three signatures of the dark matter interaction with matter: dependence of the effect on nuclei (mass and spin), annual and diurnal modulations of counting rate of the recoil events. Direct methods of WIMPs detection are based on registration of ionization or/and excitation of recoil nucleus in the material of the detector itself. At present, the most sensitive direct experiments apply different detectors for WIMPs search: Ge semiconductor detectors [1, 2, 86, 316, 344], cryogenic bolometers [12, 29, 382], noble gases [28, 32, 125, 311] and scintillation detectors: NaI(Tl) [20, 130—132] CsI(Tl) [312, 313].

An interesting possibility to reject background caused by electrons and gamma quanta provides cryogenic technique, which uses simultaneous registration of heat and light signals from crystal scintillators applied already by the CRESST collaboration [29]. These detectors combine excellent energy resolution and low threshold with the ability to discriminate between different types of interactions (electron, alpha or neutron interactions).

A multi target detector with semiconductor and scintillation bolometers is under development by the EURECA collaboration (European Underground

Rare Event Calorimeter Array). It should be stressed, the EURECA project requires a variety of scintillation targets to verify the nature of a detected signal. The most promising scintillators with high light output for cryogenic dark matter search are $ZnWO_4$, $CaWO_4$, and $CaMoO_4$ [304]. Collaboration carries out development of novel materials ($MgWO_4$ [196], $ZnMoO_4$ [346]) as well as further optimization and improvement of $ZnWO_4$, $CaWO_4$, $CaMoO_4$, CaF_2, BGO, Al_2O_3, LiF, ZnSe, $PbWO_4$, $PbMoO_4$.

Relative pulse amplitude of some crystal scintillators (which can be used as an estimation of relative light output) at helium temperature under α particles irradiation measured with bialkali photomultiplier is presented in Table 7.14.

Radioactive contamination of target scintillation crystals will play a key role to decrease background of a detector. Counting rate of a few counts per kg per day in the energy interval 2—20 keV is typical in the present scintillator-based dark matter experiments [20,132,312,428]. However, to elaborate region of WIMP-nucleon scattering cross sections predicted by the different models, background of a detector should be further decreased by a few orders of magnitude. For instance, the EURECA dark matter project calls for background counting rate lower than a few events per keV per 100 kg per year at energies of a few keV [301,302]. The project makes strict enough demands to scintillators: they should not contain paramagnetic elements, possess high light output (more than 1.5×10^4 photons/MeV), a very low level of radioactive impurity. Fig. 7.27 shows simulated by GEANT4 energy spectra of a scintillation detector contaminated by ^{40}K, ^{60}Co, ^{87}Rb, ^{90}Sr—^{90}Y, ^{137}Cs, ^{232}Th, ^{238}U on the level of 0.1 mBq/kg by each radionuclide [195]. Equilibrium of ^{232}Th and ^{238}U chains assumed to be broken: contributions of ^{234}Th + ^{234m}Pa, ^{210}Pb + ^{210}Bi from the ^{238}U family, and ^{228}Ra + ^{228}Ac, ^{212}Pb + ^{208}Th (^{232}Th) are considered separately. The energy resolution dependence on energy is assumed to be described by square root function with FWHM = 10 % for 662 keV γ line of ^{137}Cs. Supposing a suppression factor 10^2—10^3, which can be reached thanks to the active background rejection using a combination of phonon and scintillation signals, radioactive contamination of crystal scintillators should not exceed a level of ∼0.01 mBq/kg for total activity. As one can see in Table 7.12, there is no crystal scintillator satisfying such a strong demand. Therefore, an

Table 7.14. **Relative light output (relative pulse amplitude) *LY* of crystal scintillators at liquid helium temperature under α particles irradiation measured with bialkali photomultiplier [154]**

Sample	*LY*, %	Sample	*LY*, %	Sample	*LY*, %
$CaWO_4$	100	$CaMoO_4$	46	$MgWO_4$	15
$ZnWO_4$	77	$PbWO_4$	24	LiF(W)	<5
ZnSe	61	$PbMoO_4$	21	$ZnMoO_4$	<5

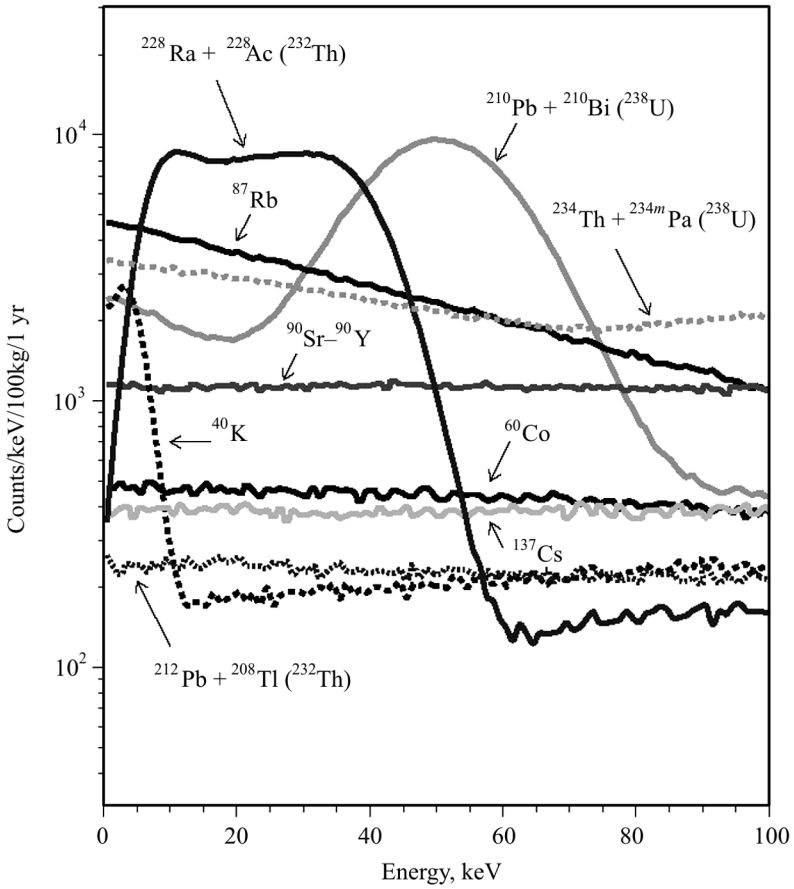

Fig. 7.27. Simulated energy spectra of a scintillation detector contaminated by ^{40}K, ^{60}Co, ^{87}Rb, ^{90}Sr—^{90}Y, ^{137}Cs, ^{232}Th, ^{238}U on the level of 0.1 mBq/kg by each radionuclide

extended R&D are necessary to reach the level of radiopurity requested by the next generation dark matter experiments.

Such an R&D should include the following principal steps [193, 195]:

1. Deep purification of raw materials is supposed to be the most important issue. Metal purification by vacuum distillation, zone melting, and filtering are very promising approaches [133], while further study is necessary for the purification of Ca and Li in order to achieve the required low levels of radioactive contamination.

2. Two to four step re-crystallization, involving screening and assessment of the produced scintillators after each step.

3. Testing at all stages through ultra-low background γ, α, β spectrometry compounds for crystal growing (choice of raw materials, quality control of purified elements and compounds).

4. All work should be done using highly pure reagents, lab-ware and water. All chemistry should be done in a clean room, and, as far as possible, in nitrogen atmosphere. Careful protection from radon should be foreseen.

The low-background scintillation measurements are currently the most appropriate methods of examining the performance of scintillators. R&D of ultra-low-radioactive instrumentation with the sensitivity at the level of 0.01 mBq/kg (able to operate at low, at least liquid nitrogen, temperatures) are necessary. In itself the problem of measurements of crystal scintillators' radiopurity on the level of 0.01 mBq/kg is rather complicated task. Detection of low energy β emitters (e.g., ^{87}Rb, ^{115}In, ^{138}La, ^{176}Lu, ^{187}Re, ^{210}Pb) is particularly difficult. Presence of these radionuclides on the levels dangerous for dark matter experiments can be detected only in produced crystal scintillators under very low background conditions. It should be stressed that measurements of low energy β active radionuclides in crystal scintillators were never realized at such a level of sensitivity.

In addition one should keep in mind also cosmogenic radionuclides. For instance, accumulation of radioactive ^{14}C ($Q_\beta = 156.475$ keV, $T_{1/2} = 5730$ yr), highly undesirable for dark matter experiments, was considered in [440]. The radioactive ^{14}C can be produced by hadronic component of cosmic rays in any materials composed of elements heavier than carbon. Another cosmogenic radionuclide, ^{65}Zn, was observed in comparatively radiopure $ZnWO_4$ scintillators [93,118]. An indication of cosmogenic ^{110m}Ag contamination in $^{116}CdWO_4$ crystal scintillators was reported in [77]. Underground production of detectors, in particular of crystal scintillators, can be requested by the next generation of low background experiments.

Zinc tungstate is a good example of radiopure scintillator (∼0.2—1 mBq/kg level of radioactive contamination) [93, 192, 303]. Nevertheless, at least a ∼20-fold improvement of $ZnWO_4$ radiopurity is still needed for the EURECA experiment, and this represents a significant challenge. Besides, optimization of light collection from crystal scintillators is highly desirable for cryogenic dark matter experiments. The scintillation properties of a zinc tungstate crystal, shaped as a hexagonal prism (height 40 mm, diagonal 40 mm) were determined. An energy resolution of 10.7 % for the 662 keV γ line of ^{137}Cs was measured with the scintillator placed in a light collection set-up similar to that used by the CRESST dark matter search. The light output and decay kinetics of $ZnWO_4$ were examined over the temperature range 7—300 K (see Fig. 7.28 where the temperature dependence is presented) and confirmed to be competitive with those of $CaWO_4$. The radioactive contaminations of the $ZnWO_4$ scintillator measured in the Solotvina underground laboratory do not exceed 0.1—10 mBq/kg (depending on radionuclide). Both scintillation measurements and Monte Carlo simulations show that a hexagonal shape of the scintillation detector provi-

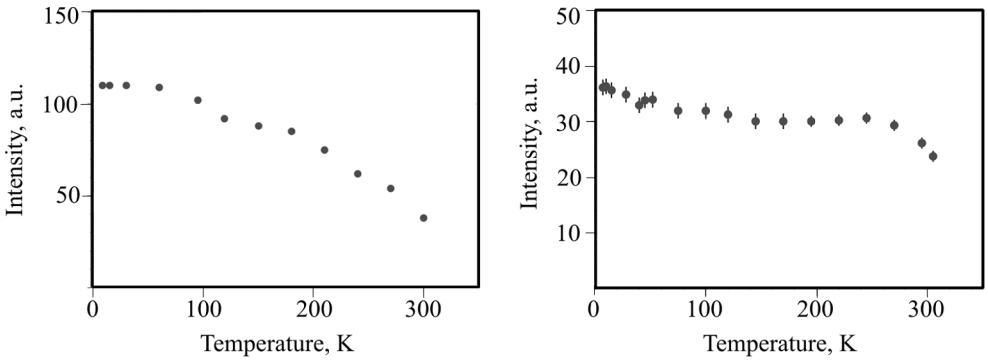

Fig. 7.28. Temperature dependence of the light output of $ZnWO_4$ crystal scintillator for excitation with ^{241}Am particles

Fig. 7.29. Temperature dependence of the light output of the $MgWO_4$ crystal scintillator for excitation with ^{241}Am α particles

des ∼20 % better light output than a cylinder. This study demonstrates the excellent feasibility of $ZnWO_4$ scintillator for cryogenic dark matter experiments.

Calcium tungstate ($CaWO_4$) discovered as scintillator sixty years ago [250, 343] is an appropriate material for cryogenic scintillating bolometers currently used by the CRESST experiment to search for dark matter particles [29, 30, 308, 331, 428]. There is a noticeable variation of radioactive contamination of different $CaWO_4$ samples [175, 436]. The equilibrium of U radioactive chain is typically broken in calcium tungstate crystals, the activity of ^{210}Pb and its daughters dominates in radioactive contamination of $CaWO_4$. Development of radiopure $CaWO_4$ crystal scintillators would be a benefit both for the CRESST and EURECA dark matter experiments.

Recrystallization is expected to be an efficient way to decrease radioactive contamination of crystal scintillators. Effect of recrystallization on radioactive contamination was studied for $CaWO_4$ crystals. Seven samples of $CaWO_4$ crystals were fabricated from three ingots that have been grown using the recrystallization procedure [193]. The radioactive contamination of the crystals was investigated and it was found that ^{210}Po and ^{238}U are the main contributors to the intrinsic α background, the equilibrium of the ^{238}U chain in the crystals is broken. It was demonstrated that the recrystallization process causes significant changes of the radioactive contamination of $CaWO_4$ crystals. It leads to variation in the activity of ^{210}Po (in the range 0.03—1.32 Bq/kg), and ^{238}U (0.04—0.33 Bq/kg) in the crystals. Activity of uranium is decreased thanks to recrystallization. The increase of ^{210}Po activity with time evidenced that ^{210}Po is mainly produced due to ^{210}Pb decay. Therefore radioactive ^{210}Pb should be carefully screened and reduced in raw materials for crystal production. In addition, one needs to study effects of crystal production technology

(crystal growth, annealing, cutting, surface treatment) on their radioactive contamination.

The feasibility of lead molybdate ($PbMoO_4$) and lead tungstate ($PbWO_4$) as detectors for rare event searches has been envisaged in [335] and [234], respectively. The prospects of radiopure $PbWO_4$ and $PbMoO_4$ crystal scintillators as target materials in cryogenic dark matter experiments have been discussed recently [346]. Scintillation properties of $PbWO_4$ and $PbMoO_4$ crystals, as potential cryogenic scintillators for rare event searches, have been studied. The light output and decay kinetics of $PbWO_4$ and $PbMoO_4$ crystals for excitation with ^{241}Am α particles were examined over the temperature range 7—300 K. The α/β ratio was measured with a $PbMoO_4$ crystal scintillator for 5.3 MeV α particles, and the ability to distinguish between signals induced by α particles and γ quanta by pulse shape discrimination was assessed for the $PbMoO_4$ crystal scintillator at 77 K. The energy dependence of the quenching factor for oxygen, molybdenum, tungsten and lead ions at low energy was calculated using a semi-empirical approach [412] with data from the α particle measurements. Both $PbWO_4$ and $PbMoO_4$ crystals are of particular interest for cryogenic experiments to search for dark matter due to the combination of heavy (W, Pb), middle (Mo) and light (O) elements. Nonetheless, the high intrinsic radioactivity due to ^{210}Pb is the main obstacle, limiting the usefullness of these materials for low-background experiments. However, the use of ancient lead for crystal growth should permit to produce lead tungstate and lead molybdate with substantially reduced intrinsic radioactivity to the level of a few mBq/kg [16, 17, 198].

Magnesium tungstate ($MgWO_4$) crystals of $\sim$1 cm^3 volume were obtained for the first time using a flux growth technique. The crystal was subjected to comprehensive characterization that included room temperature measurements of the transmittance, X ray luminescence spectra, afterglow under X ray excitation, relative photoelectron output, energy resolution, non-proportionality of scintillation response to γ quanta, response to α particles, and pulse-shape for γ quanta and α particles. The light output and decay kinetics of $MgWO_4$ were studied over the temperature range 7—305 K. The variation with temperature of the $MgWO_4$ light output in the interval 7—305 K is shown in Fig. 7.29. Under X ray excitation the crystal exhibits an intense luminescence band peaking at a wavelength of 470 nm; the intensity of afterglow after 20 ms is 0.035 %. An energy resolution of 9.1 % for 662 keV γ quanta of ^{137}Cs was measured with a small ($\approx$0.9 g) sample of the $MgWO_4$ crystal (see Fig. 7.30). The photoelectron output of the $MgWO_4$ crystal scintillator is 35 % of that for $CdWO_4$ and 27 % of that for NaI(Tl). The detector showed pulse-shape discrimination ability in measurements with α particles and γ quanta; and that enabled to assess the radioactive contamination of the scintillator. The results of these studies demonstrate the prospect of this material for a variety of scintillation applicati-

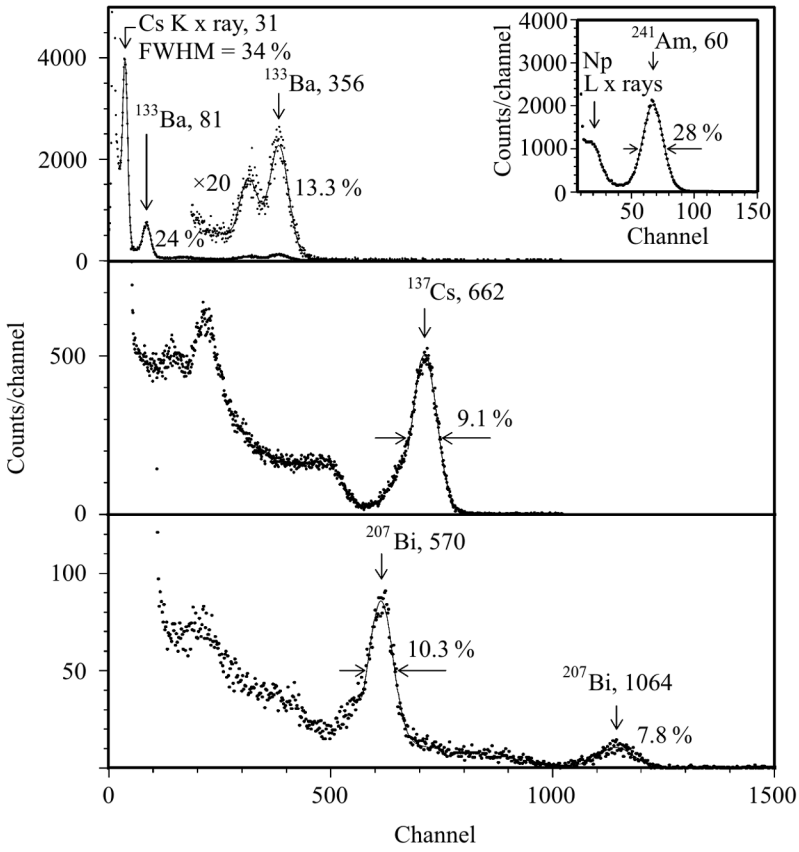

Fig. 7.30. Energy spectra of ^{133}Ba, ^{241}Am (inset), ^{137}Cs, and ^{207}Bi γ rays measured for the $MgWO_4$ scintillation crystal. Fits of the γ peaks are shown as solid lines. Energies of the γ and X ray lines are in keV

ons, including rare event searches [196]. The material can be used for instance in the EURECA project, which require a variety of scintillation targets to verify the nature of a detected signal.

7.9.4. Semi-empirical calculation of quenching factors for ions in scintillators

For a long time it is known that amount of light produced in scintillating material by highly ionizing particles (protons, α particles, heavy ions) is lower than that produced by electrons of the same energy [153]. Thus, in a scintillator calibrated with electron and/or γ sources (which is an usual practice), signals from ions will be seen at lower energies (sometimes up to 40 times) than their real values. Knowledge of these transformation coefficients —

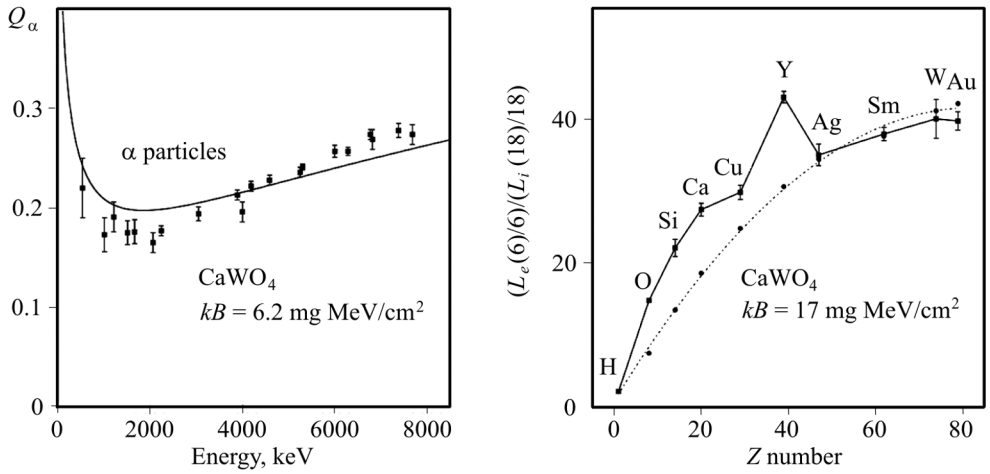

Fig. 7.31. Quenching factors for α particles in $CaWO_4$ and their fit with $kB = 6.2$ mg MeV$^{-1}\cdot$ cm^{-2}

Fig. 7.32. Dependence of inverse of the relative light output at $E_i = 18$ keV, normalized to that for electrons at $E_e = 6$ keV on ion's Z number: squares are experimental points from [350], and circles are calculated values with $kB = 17$ mg MeV$^{-1}\cdot$cm^{-2} found by equating experimental and theoretical values only at one point measured with protons in $CaWO_4$

quenching factors — is extremely important in prediction where the signal should be expected in searches for dark matter particles or in studies of rare α decays.

Semi-empirical method of calculation of quenching factors for scintillators is developed recently [412]. It is based on classical Birks formula [153] with using of the total stopping powers for electrons $(dE/dr)_e$ and ions $(dE/dr)_i$ calculated with the ESTAR [230] and SRIM [396] codes, respectively. The ion quenching factor Q_i at energy E is defined as the ratio of light yield of the ion to that of an electron of the same energy: $Q_i = L_i/L_e$, where

$$L_i = \int_0^E \frac{dE}{1 + kB(\frac{dE}{dr})_i}, \; L_e = \int_0^E \frac{dE}{1 + kB(\frac{dE}{dr})_e}.$$

The method has only one fitting parameter (the Birks factor kB) which can have different values for the same material in different conditions of measurements and data treatment. A hypothesis is used that, once the kB value is obtained by fitting data for particles of one kind and in some energy region (e.g. for a few MeV α particles from internal contamination of a detector), it can be applied to calculate quenching factors for particles of other kind and for other energies (e.g. for low energy nuclear recoils) if all data are

measured in the same experimental conditions and are treated in the same way. Applicability of the method was demonstrated on many examples including materials with different mechanisms of scintillation: organic scintillators (solid C_8H_8, and liquid $C_{16}H_{18}$, C_9H_{12}); crystal scintillators (pure $CdWO_4$, $PbWO_4$, $ZnWO_4$, $CaWO_4$, CeF_3, and doped CaF_2(Eu), CsI(Tl), CsI(Na), NaI(Tl)); liquid noble gases (LXe). Estimations of quenching factors for nuclear recoils are also given for some scintillators where experimental data are absent ($CdWO_4$, $PbWO_4$, CeF_3, $Bi_4Ge_3O_{12}$, LiF, ZnSe). Examples of calculations are given in Fig. 7.31 and 7.32.

Bibliography

1. C.E. Aalseth et al., Experimental constraints on a dark matter origin for the DAMA annual modulation effect, Phys. Rev. Lett. **101**, 251301 (2008).
2. C.E. Aalseth et al., Results from a search for light-mass dark matter with a p-type point contact germanium detector, Phys. Rev. Lett. **106**, 131301 (2011).
3. C.E. Aalseth et al., The proposed Majorana ^{76}Ge double-beta decay experiment, Nucl. Phys. B (Proc. Suppl.) **138**, 217—220 (2005).
4. C.E. Aalseth, F.T. Avignone III, R.L. Brodzinski, J.I. Collar et al., Recent results from the IGEX double-beta decay experiment, Nucl. Phys. B. (Proc. Suppl.) **48**, 223—225 (1996).
5. C.E. Aalseth, F.T. Avignone III, R.L. Brodzinski et al. The IGEX ^{76}Ge neutrinoless double-beta decay experiment: prospect for next generation experiments, Phys. Rev. D **65**, 092007 (2002).
6. M. Ablikim et al., Search for invisible decays of η and η' in $J/\psi \to \phi\eta$ and $\phi\eta'$, Phys. Rev. Lett. **97**, 202002 (2006).
7. M. Ablikim et al., Search for the invisible decay of J/ψ in $\psi(2S) \to \pi^+\pi^- J/\psi$, Phys. Rev. Lett. **100**, 192001 (2008).
8. N. Ackerman et al., Observation of two-neutrino double-beta decay in ^{136}Xe with EXO-200 detector, Phys. Rev. Lett. **107**, 212501 (2011).
9. Y. Aharonov et al., New experimental limits for the electron stability, Phys. Lett. B **353**, 168—172 (1995).
10. Q.R. Ahmad et al., Direct evidence for neutrino flavor transformation from neutral-current interactions in the Sudbury Neutrino Observatory, Phys. Rev. Lett. **89**, 011301 (2002).
11. S.N. Ahmed et al., Constraints on nucleon decay via invisible modes from the Sudbury Neutrino Observatory, Phys. Rev. Lett. **92**, 102004 (2004).
12. Z. Ahmed et al., Search for weakly interacting massive particles with the first five-tower data from the cryogenic dark matter search at the Soudan Underground Laboratory, Phys. Rev. Lett. **102**, 011301 (2009).
13. S. Agostinelli et al., GEANT4 — a simulation toolkit, Nucl. Instrum. Meth. A **506**, 250—303 (2003).
14. D.V. Aleksandrov et al., Observation of the spontaneous emission of ^{14}C nuclei from ^{223}Ra, JETP Lett. **40**, 909—912 (1984).
15. A. Alessandrello et al., Bolometric measurements of the beta spectrum of ^{113}Cd, Nucl. Phys. B (Proc. Suppl.) **35**, 394—396 (1994).

16. A. Alessandrello et al., Measurements on radioactivity of ancient roman lead to be used as shield in searches for rare events, Nucl. Instr. Meth. B **61**, 106—117 (1991).
17. A. Alessandrello et al., The bolometers as nuclear recoil detectors, Nucl. Instr. Meth. A **409**, 451—453 (1998).
18. A. Alessandrello et al., Measurements of internal radioactive contamination in samples of Roman lead to be used in experiments on rare events, Nucl. Instr. Meth. B **142**, 163—172 (1998).
19. G. Alimonti et al., Measurement of the ^{14}C abundance in a low background liquid scintillator, Phys. Lett. B **422**, 349—358 (1998).
20. G.J. Alner et al., Limits on WIMP cross-sections from the NAIAD experiment at the Boulby Underground Laboratory, Phys. Lett. B **616**, 17—24 (2005).
21. R. Alonso, A. Lopez-Garcia, H. Vucetich, On the electron stability measured by the coincidence spectroscopy, Nucl. Instrum. Meth. A **383**, 451—453 (1996).
22. M. Alston-Garnjost, B.L. Dougherty, R.W. Kenney, R.D. Tripp et al., Experimental search for double-β decay of ^{100}Mo, Phys. Rev. C **55**, 474—493 (1997).
23. D. Akimov et al., EXO: an advanced Enriched Xenon double-beta decay Observatory, Nucl. Phys. B (Proc. Suppl.) **138**, 224—226 (2005).
24. J. Amare et al., Background understanding and improvement in NaI scintillators, J. Phys.: Conf. Series **39**, 201—201 (2006).
25. D.L. Anderson, *New Theory of the Earth* (Cambridge, 2007), 405 p.
26. E. Andreotti, C. Arnaboldi, F.T. Avignone III, M. Balata, I. Bandac et al., Search for β^+/EC double beta decay of ^{120}Te, Astropart. Phys. **34**, 643—648 (2011).
27. E. Andreotti et al., Half-life of the β decay $^{115}\mathrm{In}(9/2+) \to {}^{115}\mathrm{Sn}(3/2+)$, Phys. Rev. C **84**, 044605 (2011).
28. J. Angle et al. (XENON Collaboration), First results from the XENON10 dark matter experiment at the Gran Sasso National Laboratory, Phys. Rev. Lett. **100**, 021303 (2008).
29. G. Angloher et al., Commissioning run of the CRESST-II dark matter search, Astropart. Phys. **31**, 270—276 (2009).
30. G. Angloher et al., Limits on WIMP dark matter using scintillating $CaWO_4$ cryogenic detectors with active background suppression, Astropart. Phys. **23**, 325—339 (2005).
31. A.N. Annenkov et al., Development of $CaMoO_4$ crystal scintillators for a double beta decay experiment with ^{100}Mo, Nucl. Instr. Meth. A **584**, 334—345 (2008).
32. E. Aprile et al. (XENON100 Collaboration), First dark matter results from the XENON100 experiment, Phys. Rev. Lett. **105**, 131302 (2010).
33. T. Araki et al., Search for the invisible decay of neutrons with KamLAND, Phys. Rev. Lett. **96**, 101802 (2006).
34. J. Argyriades et al., Results of the BiPo-1 prototype for radiopurity measurements for the SuperNEMO double beta decay source foils, Nucl. Instr. Meth A **622**, 120—128 (2010).
35. J. Argyriades et al., Measurement of the double-β decay half-life of ^{150}Nd and search for neutrinoless decay modes with the NEMO-3 detector, Phys. Rev. C **80**, 032501 (2009).

36. J. Argyriades et al., Measurement of the two neutrino double beta decay half-life of Zr-96 with the NEMO-3 detector, Nucl. Phys. A **847**, 168—179 (2010).
37. N. Arkani-Hamed, S. Dimopoulos, G. Dvali, The hierarchy problem and new dimensions at a millimeter, Phys. Lett. B **429**, 263—272 (1998).
38. N. Arkani-Hamed, S. Dimopoulos, G. Dvali, Large extra dimensions: A new arena for particle physics, Phys. Today, February 2002, p. 35—40.
39. V. Artemiev et al., Half-life measurement of ^{150}Nd 2β decay in the time projection chamber experiment, Phys. Lett. B **345**, 564—568 (1995).
40. C. Arnaboldi et al., Physics potential and prospects for the CUORICINO and CUORE experiments, Astropart. Phys. **20**, 91—110 (2003).
41. C. Arnaboldi et al., Results from the CUORICINO $0\nu\beta\beta$-decay experiment, Phys. Rev. C **78**, 035502 (2008).
42. C. Arnaboldi et al., A calorimetric search on double beta decay of ^{130}Te, Phys. Lett. B **557**, 167—175 (2003).
43. R. Arnold et al., Measurement of the $\beta\beta$ decay half-life of ^{130}Te with the NEMO-3 detector, Phys. Rev. Lett. **107**, 062504 (2011).
44. R. Arnold et al., Double beta decay of ^{96}Zr, Nucl. Phys. A **658**, 299—312 (1999).
45. R. Arnold et al., Double-β decay of ^{82}Se, Nucl. Phys. A **636**, 209—223 (1998).
46. R. Arnold et al., First results of the search for neutrinoless double-beta decay with the NEMO 3 detector, Phys. Rev. Lett. **95**, 182302 (2005).
47. R. Arnold et al., Double-β decay of ^{116}Cd, Z. Phys. C **72**, 239—247 (1996).
48. R. Arnold et al., Measurement of double beta decay of ^{100}Mo to excited states in the NEMO 3 experiment, Nucl. Phys. A **781**, 209—226 (2007).
49. R. Arnold et al., Limits on different majoron decay modes of ^{100}Mo and ^{82}Se for neutrinoless double beta decays in the NEMO-3 experiment, Nucl. Phys. A **765**, 483—494 (2006).
50. V.D. Ashitkov, A.S. Barabash, S.G. Belogurov, G. Carugno et al., Double Beta Decay of ^{100}Mo, JETP Lett. **74**, 529—531 (2001).
51. S.J. Asztalos, L.J. Rosenberg, K. van Bibber et al., Searches for astrophysical and cosmological axions, Annu. Rev. Nucl. Part. Sci. **56**, 293—326 (2006).
52. F.T. Avignone III, G.S. King, Yu.G. Zdesenko, Next generation double-beta decay experiments: metrics for their evaluation, New J. Phys. **7**, 6—46 (2005).
53. F.T. Avignone III, S.R. Elliott, J. Engel, Double beta decay, Majorana neutrinos, and neutrino mass, Rev. Mod. Phys. **80**, 481—516 (2008).
54. F.T. Avignone III et al., New experimental limit on the stability of the electron, Phys. Rev. D **34**, 97—100 (1986).
55. B. Aubert et al., Search for B^0 decays to invisible final states and to $\nu\bar{\nu}\gamma$, Phys. Rev. Lett. **93**, 091802 (2004).
56. B. Aubert et al., Search for invisible decays of the $Y(1S)$, Phys. Rev. Lett. **103**, 251801 (2009).
57. G. Audi, A.H. Wapstra, C. Thibault, The AME2003 atomic mass evaluation (II). Tables, graphs and references, Nucl. Phys. A **729**, 337—676 (2003).
58. K.S. Babu, I. Gogoladze, K. Wang, Gauged baryon parity and nucleon stability, Phys. Lett. B **570**, 32—38 (2003).
59. H.O. Back et al., Search for electron decay mode $e \to \gamma + \nu$ with prototype of Borexino detector, Phys. Lett. B **525**, 29—40 (2002).

60. H.O. Back et al., New limits on nucleon decays into invisible channels with the BOREXINO counting test facility, Phys. Lett. B **563**, 23—34 (2003).
61. A. Badertscher et al., Improved limit on invisible decays of positronium, Phys. Rev. D **75**, 032004 (2007).
62. J.N. Bahcall, A.M. Serenelli, S. Basu, 10,000 standard solar models: a Monte Carlo simulation, Astrophys. J. Suppl. Ser. **165**, 400—431 (2006).
63. J.N. Bahcall, M.H. Pinsonneault, What do we (not) know theoretically about solar neutrino fluxes? Phys. Rev. Lett. **92**, 121301 (2004).
64. A.B. Balantekin, Neutrino magnetic moment, AIP Conf. Proc. **847**, 128—133 (2006).
65. A. Balysh, A. De Silva, V.I. Lebedev, K. Lou et al., Double beta decay of ^{48}Ca, Phys. Rev. Lett. **77**, 5186—5189 (1996).
66. A.Ya. Balysh et al., Radiochemical search for the decay of uranium-233 with the emission of neon-24 using a low-background semiconductor gamma-ray spectrometer, Sov. Phys. JETP **64**, 21—24 (1986).
67. A. Balysh et al., New experimental limits for electron decay and charge conservation, Phys. Lett. B **298**, 278—282 (1993).
68. A. Balysh et al., Radioactive impurities in crystals of bismuth germanate, Pribory i Tekhnika Eksperimenta **1**, 118—122 (1993) (in Russian).
69. I.R. Barabanov et al., Verification of the law of conservation of electric charge, JETP Lett. **32**, 359—361 (1980).
70. A.S. Barabash, Precise half-life values for two-neutrino double-β decay, Phys. Rev. C **81**, 035501 (2010).
71. A.S. Barabash et al., Two neutrino double-beta decay of ^{100}Mo to the first excited 0^+ state in ^{100}Ru, Phys. Lett. B **345**, 408—413 (1995).
72. A.S. Barabash et al., The extrapolation of NEMO techniques to future generation 2β-decay experiments, Phys. At. Nucl. **67**, 1984—1988 (2004).
73. A.S. Barabash, Ph. Hubert, A. Nachab, V. Umatov, Search for β^+EC and ECEC processes in ^{74}Se, Nucl. Phys. A **785**, 371—380 (2007).
74. A.S. Barabash et al., Search for β^+EC and ECEC processes in ^{112}Sn and $\beta^-\beta^-$ decay of ^{124}Sn to the excited states of ^{124}Te, Nucl. Phys. A **807**, 269—281 (2008).
75. A.S. Barabash, Double beta decay experiments, Phys. Part. Nucl. **42**, 613—627 (2011).
76. A.S. Barabash, Double beta decay: Historical review of 75 years of research, Phys. At. Nucl. **74**, 603—613 (2011).
77. A.S. Barabash et al., Low background detector with enriched $^{116}CdWO_4$ crystal scintillators to search for double β decay of ^{116}Cd, J. Instrumentation **06**, P08011 (2011).
78. A.S. Barabash et al., $2\nu\beta\beta$ decay of ^{100}Mo to the first 0^+ excited state in ^{100}Ru, Phys. At. Nucl. 62, 2039—2044 (1999).
79. A.S. Barabash, Ph. Hubert. A. Nachab, V.I. Umatov, Investigation of $\beta\beta$ decay in ^{150}Nd and ^{148}Nd to the excited states of daughter nuclei, Phys. Rev. C **79**, 045501 (2009).
80. A.S. Barabash, R.R. Saakyan, Experimental Limits on $2\beta^+$, Kβ^+, and 2K Processes for ^{130}Ba and on 2K Capture for ^{132}Ba, Phys. At. Nucl. **59**, 179—184 (1996).

81. O.P. Barinova et al, First test of Li_2MoO_4 crystal as a cryogenic scintillating bolometer, Nucl. Instrum. Meth. A **613**, 54—57 (2010).
82. O.P. Barinova et al., Intrinsic radiopurity of a Li_2MoO_4 crystal, Nucl. Instr. Meth. A **607**, 573—575 (2009).
83. R. Barloutaud, Status of the search for matter stability, Nucl. Phys. B (Proc. Suppl.) A **28**, 437—446 (1992).
84. J.C. Barton, J.A. Edgington, Analysis of alpha-emitting isotopes in an inorganic scintillator, Nucl. Instr. Meth. A **443**, 277—286 (2000).
85. N.V. Bashmakova et al., $Li_2Zn_2(MoO_4)_3$ crystal as a potential detector for ^{100}Mo 2β-decay search, Functional Materials **16**, 266—274 (2009).
86. L. Baudis et al., First results from the Heidelberg dark matter search experiment, Phys. Rev. D **63**, 022001 (2001).
87. M. Beck et al., Investigation of the Majoron-accompanied double-beta decay mode of ^{76}Ge, Phys. Rev. Lett. **70**, 2853—2855 (1993).
88. J.W. Beeman et al., A next-generation neutrinoless double beta decay experiment based on $ZnMoO_4$ scintillating bolometers, Phys. Lett. B **710**, 318—323 (2012).
89. N.F. Bell, V. Cirigliano, M.J. Ramsey-Musolf, P. Vogel, M.B. Wise, How magnetic is the Dirac neutrino? Phys. Rev. Lett. **95**, 151802 (2005).
90. P. Belli et al., First limits on neutrinoless resonant 2β captures in ^{136}Ce and new limits for other 2β processes in ^{136}Ce and ^{138}Ce isotopes, Nucl. Phys. A **824**, 101—114 (2009).
91. P. Belli et al., New observation of $2\beta 2\nu$ decay of ^{100}Mo to the 0_1^+ level of ^{100}Ru in the ARMONIA experiment, Nucl. Phys. A **846**, 143—156 (2010).
92. P. Belli et al., Search for double-β decay processes in ^{108}Cd and ^{114}Cd with the help of the low-background $CdWO_4$ crystal scintillator, Eur. Phys. J. A **36**, 167—170 (2008).
93. P. Belli et al., Search for double beta decay of zinc and tungsten with low background $ZnWO_4$ crystal scintillators, Nucl. Phys. A **826**, 256—273 (2009).
94. P. Belli et al., New limits on spin-dependent coupled WIMPs and on 2β processes in ^{40}Ca and ^{46}Ca by using low radioactive CaF_2(Eu) crystal scintillators. Nucl. Phys. B **563**, 97—106 (1999).
95. P. Belli et al., Final result of experiment to search for 2β processes in zinc and tungsten with the help of radiopure $ZnWO_4$ crystal scintillators, J. Phys. G **38**, 115107 (2011).
96. P. Belli et al., Search for double-β decays of ^{96}Ru and ^{104}Ru by ultra-low background HPGe γ spectrometry, Eur. Phys. J. A **42**, 171—177 (2009).
97. P. Belli et al., Search for double β decays of ^{96}Ru and ^{104}Ru with high purity Ge γ spectrometry, Nucl. Phys. At. Energy **11**, 362—366 (2010).
98. P. Belli et al., New limits on $2\beta^+$ decay processes in ^{106}Cd, Astropart. Phys. **10**, 115—120 (1999).
99. P. Belli et al., First results of the experiment to search for 2β decay of ^{106}Cd with the help of $^{106}CdWO_4$ crystal scintillators, Proc. Int. Conf. NPAE-Kyiv2010, 7—12.06.2010, Kyiv, Ukraine — Kyiv, 2011, p. 428—431.
100. P. Belli et al., Search for 2β decay of cerium isotopes with $CeCl_3$ scintillator, J. Phys. G **38**, 015103 (2011).

101. P. Belli et al., First search for double β decay of dysprosium, Nucl. Phys. A **859**, 126—139 (2011).
102. P. Belli et al., First search for double β decay of platinum by ultra-low background HP Ge γ spectrometry, Eur. Phys. J. A **47**, 91 (2011).
103. P. Belli et al., Search for 2β processes in ^{64}Zn with the help of $ZnWO_4$ crystal scintillator, Phys. Lett. B **658**, 193—197 (2008).
104. P. Belli et al., Investigation of β decay of ^{113}Cd, Phys. Rev. C **76**, 064603 (2007).
105. P. Belli et al., Development of enriched $^{106}CdWO_4$ crystal scintillators to search for double β decay processes in ^{106}Cd, Nucl. Instr. Meth. A **615**, 301—306 (2010).
106. P. Belli et al., First results of the experiment to search for 2β decay of ^{106}Cd with the help of $^{106}CdWO_4$ crystal scintillators, AIP Conf. Proc. **1304**, 354—358 (2010).
107. P. Belli et al., ^{7}Li solar axions: Preliminary results and feasibility studies, Nucl. Phys. A **806**, 388—397 (2008).
108. P. Belli et al., Search for ^{7}Li solar axions using resonant absorption in LiF crystal: Final results, Phys. Lett. B **711**, 41—45 (2012).
109. P. Belli et al., Charge conservation and electron lifetime: Limits from a liquid xenon scintillator, Astropart. Phys. **5**, 217—219 (1996).
110. P. Belli et al., New experimental limit on the electron stability and non-paulian transitions in Iodine atoms, Phys. Lett. B **460**, 236—241 (1999).
111. P. Belli et al., Quest for electron decay $e^- \to \nu_e\gamma$ with a liquid xenon scintillator, Phys. Rev. D **61**, 117301 (2000).
112. P. Belli et al., New limits on the nuclear levels excitation of ^{127}I and ^{23}Na during charge nonconservation, Phys. Rev. C **60**, 065501 (1999).
113. P. Belli et al., Charge non-conservation restrictions from the nuclear levels excitation of ^{129}Xe induced by the electron's decay on the atomic shell, Phys. Lett. B **465**, 315—322 (1999).
114. P. Belli et al., Performances of a CeF_3 crystal scintillator and its application to the search for rare processes, Nucl. Instr. Meth. A **498**, 352—361 (2003).
115. P. Belli et al., Search for double-β decay processes in ^{106}Cd with the help of a $^{106}CdWO_4$ crystal scintillator, Phys. Rev. C **85**, 044610 (2012).
116. P. Belli et al., Search for α decay of natural europium, Nucl. Phys. A **789**, 15—29 (2007).
117. P. Belli et al., Intrinsic radioactivity of a $Li_6Eu(BO_3)_3$ crystal and α decays of Eu, Nucl. Instr. Meth. A **572**, 734—738 (2007).
118. P. Belli et al., Radioactive contamination of $ZnWO_4$ crystal scintillators, Nucl. Instr. Meth. A **626—627**, 31—38 (2011).
119. P. Belli et al., First observation of α decay of ^{190}Pt to the first excited level ($E_{\rm exc} = 137.2$ keV) of ^{186}Os, Phys. Rev. C **83**, 034603 (2011).
120. G. Bellini al., High sensitivity 2β decay study of ^{116}Cd and ^{100}Mo with the BOREXINO counting test facility (CAMEO project), Eur. Phys. J. C **19**, 43—55 (2001).
121. G. Bellini et al., High sensitivity quest for Majorana neutrino mass with the BOREXINO counting test facility, Phys. Lett. B **493**, 216—228 (2000).
122. G. Bellini et al., Search for solar axions emitted in the M1-transition of ^{7}Li* with Borexino CTF, Eur. Phys. J. C **54**, 61—72 (2008).

123. S. Belogurov et al., $CaMoO_4$ Scintillation Crystal for the Search of ^{100}Mo Double Beta Decay, IEEE Nucl. Sci. **52**, 1131—1135 (2005).
124. E. Bellotti et al., A new experimental limit on electron stability, Phys. Lett. B **124**, 435—438 (1983).
125. P. Benetti et al., First results from a dark matter search with liquid argon at 87 K in the Gran Sasso underground laboratory, Astropart. Phys. **28**, 495—507 (2008).
126. J. Benziger et al., A scintillator purification system for the Borexino solar neutrino detector, Nucl. Instr. Meth. A **587**, 277—291 (2008).
127. C. Berger et al., Lifetime limits on $(B - L)$-violating nucleon decay and di-nucleon decay modes from the Frejus experiment, Phys. Lett. B **269**, 227—233 (1991).
128. L. Bergstrom, Non-baryonic dark matter: Observational evidence and detection methods, Rep. Prog. Phys. **63**, 793—842 (2000).
129. G. Bertone, D. Hooper, J. Silk, Particle dark matter: Evidence, candidates and constraints, Phys. Rept. **405**, 279—390 (2005).
130. R. Bernabei et al., On the investigation of possible systematics in WIMP annual modulation search, Eur. Phys. J. C **18**, 283 (2000).
131. R. Bernabei et al., The DAMA/LIBRA apparatus, Nucl. Instr. Meth. A **592**, 297—315 (2008).
132. R. Bernabei et al., First results from DAMA/LIBRA and the combined results with DAMA/NaI, Eur. Phys. J. C **56**, 333—355 (2008).
133. R. Bernabey et al., Production of high-pure Cd and ^{106}Cd for $CdWO_4$ and $^{106}CdWO_4$ scintillators, Metallofizika i Noveishije Tekhnologii **30**, 477—486 (2008) (in Russian).
134. R. Bernabei et al., The DAMA/LIBRA apparatus, Nucl. Instr. Meth. A **592**, 297—315 (2008).
135. R. Bernabei et al., Performances and potentialities of a $LaCl_3$:Ce scintillator, Nucl. Instr. Meth. A **555**, 270—281 (2005).
136. R. Bernabei et al., Performances of the ≈100 kg NaI(Tl) set-up of the DAMA experiment at Gran Sasso, Nuovo Cim. A **112**, 545—575 (1999).
137. R. Bernabei et al., Improved limits on WIMP — ^{19}F elastic scattering and first limit on the 2EC2ν ^{40}Ca decay by using a low radioactive CaF_2(Eu) scintillator, Astropart. Phys. **7**, 73—76 (1997).
138. R. Bernabei et al., A search for spontaneous emission of heavy clusters in the ^{127}I nuclide, Eur. Phys. J. A **24**, 51—56 (2005).
139. R. Bernabei et al., Search for charge non-conserving processes in ^{127}I by coincidence technique. Eur. Phys. J. C **72**, 1920 (2012).
140. R. Bernabei et al., The search for rare processes with DAMA/LXe, Proc. Int. Conf. "Beyond 2003", Tegernsee, Germany, 9—14 June 2003, Springer, 2004, p. 365—374.
141. R. Bernabei et al., Search for possible charge non-conserving decay of ^{139}La into ^{139}Ce with $LaCl_3$(Ce) scintillator, Ukr. J. Phys. **51**, 1037—1043 (2006).
142. R. Bernabei et al., Search for the nucleon and di-nucleon decay into invisible channels, Phys. Lett. B **493**, 12—18 (2000).
143. R. Bernabei et al., Search for rare processes with DAMA/LXe experiment at Gran Sasso, Eur. Phys. J. A **27**, s01, 35—41 (2006).

144. R. Bernabei et al., Search for axions by Primakoff effect in NaI crystals, Phys. Lett. B **515**, 6—12 (2001).
145. R. Bernabei et. al., Feasibility of $\beta\beta$ decay searches with Ce isotopes using CeF_3 scintillators, Nuovo Cim. A **110**, 189—195 (1997).
146. R. Bernabei, P. Belli, F. Cappella et al., Dark matter search, Riv. Nuovo Cim. **26**, No. 1, 1—73 (2003).
147. M. Berglund and M.E. Wieser, Isotopic compositions of the elements 2009 (IUPAC Technical Report), Pure Appl. Chem. **83**, 397—410 (2011).
148. R. Bernabei et al., Investigation of $\beta\beta$ decay modes in ^{134}Xe and ^{136}Xe, Phys. Lett. B **546**, 23—28 (2002).
149. J. Bernabeu, A. De Rujula, C. Jarlskog, Neutrinoless double electron capture as a tool to measure the electron neutrino mass, Nucl. Phys. B **223**, 15—28 (1983).
150. T. Bernatowicz, J. Brannon, R. Brazzle, R. Cowsik, C. Hohenberg, and F. Podosek, Neutrino mass limits from a precise determination of 2β-decay rates of ^{128}Te and ^{130}Te, Phys. Rev. Lett. **69**, 2341—2344 (1992).
151. *Particle dark matter. Observations, Models and Searches*, edited by G. Bertone (Cambridge University Press, 2010), 762 p.
152. K. van Bibber, Design for a practical laboratory detector for solar axions, Phys. Rev. D **39**, 2089—20993 (1989).
153. J.B. Birks, *Theory and Practice of Scintillation Counting* (Pergamon, London, 1964).
154. R.S. Boiko et al., Characterisation of scintillation crystals for cryogenic experimental search for rare events, Annual Rep. INR NASU 2008 — Kyiv, 2009, p. 79.
155. R. Bonetti et al., First observation of spontaneous fission and search for cluster decay of ^{232}Th, Phys. Rev. C **51**, 2530—2533 (1995).
156. R. Bonetti, A. Guglielmetti, Measurements on cluster radioactivity — present experimental status, in *Heavy Elements and Related New Phenomena*, ed. by W. Greiner, R.K. Gupta (World Sci., Singapore, 1999), Vol. 2, p. 643—672.
157. Borexino Collaboration, G. Alimonti et al., Light propagation in a large volume liquid scintillator, Nucl. Instrum. Meth. A **440**, 360—371 (2000).
158. Borexino Collaboration, G. Alimonti et al., Science and technology of Borexino: A real time detector for low energy solar neutrinos, Astropart. Phys. **16**, 205—234 (2002).
159. Borexino Collaboration, G. Alimonti et al., The Borexino detector at the Laboratori Nazionali del Gran Sasso, Nucl. Instrum. Meth. A **600**, 568—593 (2009).
160. Borexino Collaboration, C. Arpesella et al., Direct measurement of the ^{7}Be solar neutrino flux with 192 days of Borexino data, Phys. Rev. Lett. **101**, 091302 (2008).
161. Borexino Collaboration, M. Balata et al., Search for electron antineutrino interactions with the Borexino Counting Test Facility at Gran Sasso, Eur. Phys. J. C **47**, 21—30 (2006).
162. Borexino Collaboration, H.O. Back et al., New experimental limits on heavy neutrino mixing in ^{8}B decay obtained with the Borexino Counting Test Facility, JETP Lett. **78**, 261—266 (2003).
163. Borexino Collaboration, H.O. Back et al., Pulse-shape discrimination with the Counting Test Facility, Nucl. Instr. Meth. A **584**, 98—113 (2008).

164. Borexino Collaboration, H.O. Back et al., Study of the neutrino electromagnetic properties with the prototype of the Borexino detector, Phys. Lett. B **563**, 35—47 (2003).
165. A. Boyarsky, A. Neronov, O. Ruchayskiy, M. Shaposhnikov, I. Tkachev, Strategy for searching for a dark matter sterile neutrino, Phys. Rev. Lett. **97**, 261302 (2006).
166. L. De Braeckeleer et al., Measurement of the $\beta\beta$-Decay Rate of ^{100}Mo to the First Excited 0^+ State of ^{100}Ru, Phys. Rev. Lett. **86**, 3510—3513 (2001).
167. R.L. Brodzinski, F.T. Avignone III, J.I. Collar, H. Courant et al., Status report on the International Germanium Experiment, Nucl. Phys. B. (Proc. Suppl.) **31**, 76—81 (1993).
168. V.B. Brudanin, N.I. Rukhadze, Ch. Briancon, V.G. Egorov et al., Search for double beta decay of ^{48}Ca in the TGV experiment, Phys. Lett. B **495**, 63—68 (2000).
169. D.A. Bryman et al., Search for massive neutrinos in the decay $\pi \to e\nu$, Phys. Rev. Lett. **50**, 1546—1549 (1983).
170. E. Bukhner et al., Rare decays of mercury nuclei, Sov. J. Nucl. Phys. **52**, 193—197 (1990).
171. S.F. Burachas et al., A search for ^{160}Gd double beta decay using GSO scintillators, Phys. At. Nucl. **58**, 153—157 (1995).
172. B. Caccianiga, M.G. Giammarchi, Neutrinoless double beta decay with Xe-136 in BOREXINO and the BOREXINO Counting Test Facility, Astropart. Phys. **14**, 15—31 (2000).
173. C.M. Cattadori et al., Observation of β decay of ^{115}In to the first excited level of ^{115}Sn, Nucl. Phys. A **748**, 333—347 (2005).
174. C.M. Cattadori et al., Observation of β decay of ^{115}In to the first excited level of ^{115}Sn, Nucl. Phys. A **748**, 333—347 (2005).
175. S. Cebrian et al., Bolometric WIMP search at Canfranc with different absorbers, Astropart. Phys. **21**, 23—34 (2004).
176. R. Cerulli et al., Performances of a BaF_2 detector and its application to the search for $\beta\,\beta$ decay modes in ^{130}Ba, Nucl. Instr. Meth. A **525**, 535—543 (2004).
177. G.V. Chibisov, Astrophysical upper limits on the photon rest mass, Sov. Phys. Usp. **19**, 624—626 (1976).
178. M. Chen, The SNO liquid scintillator project, Nucl. Phys. B (Proc. Suppl.) **145**, 65—68 (2005).
179. H.-Y. Cheng, The strong CP problem revisited, Phys. Rep. **158**, 1—89 (1988).
180. Y. Chikashige, R.N. Mohapatra, and R.D. Peccei, Are there real goldstone bosons associated with broken lepton number? Phys. Lett. B **98**, 265—268 (1981).
181. Y. Chikashige, R.N. Mohapatra, and R.D. Peccei, Spontaneously broken lepton number and cosmological constraints on the neutrino mass spectrum, Phys. Rev. Lett. **45**, 1926—1929 (1980).
182. B.T. Cleveland et al., Measurement of the solar electron neutrino flux with the Homestake chlorine detector, Astrophys. J. **496**, 505—526 (1998).
183. N. Coron et al., Our -short- experience at IAS and within ROSEBUD with radioactive contaminations in scintillating bolometers: uses & needs, presented at the Workshop on Radiopure scintillators for EURECA (RPSCINT 2008), 9—10 September 2008, Kyiv, Ukraine, p. 12, arXiv:0903.1539 [nucl-ex].

184. C. Cozzini et al., Detection of the natural α decay of tungsten, Phys. Rev. C **70**, 064606 (2004).
185. F.A. Danevich, O.V. Ivanov, V.V. Kobychev, V.I. Tretyak, Heat flow of the Earth and resonant capture of solar ^{57}Fe axions, Kinemat. Phys. Cell. Bodies **25**, 102—106 (2009).
186. F.A. Danevich et al., α activity of natural tungsten isotopes, Phys. Rev. C **67**, 014310 (2003).
187. F.A. Danevich et al., $CdWO_4$, ZnSe and $ZnWO_4$ scintillators in studies of 2β-processes, Instr. Exp. R. **32**, 1059—1064 (1989).
188. F.A. Danevich, V.V. Kobychev, S.S. Nagorny, V.I. Tretyak, YAG:Nd crystals as possible detector to search for 2β and α decay of neodymium, Nucl. Instr. Meth. A **541**, 583—589 (2005).
189. F.A. Danevich et al., Investigation of β^+ β^+ and β^+/EC decay of ^{106}Cd, Z. Physik A **355**, 433—437 (1996).
190. F.A. Danevich et al., Application of $PbWO_4$ crystal scintillators in experiment to search for 2β decay of ^{116}Cd, Nucl. Instr. Meth. A **556**, 259—265 (2006).
191. F.A. Danevich, V.I. Tretyak, Radioactive contamination of scintillators, submitted to Astropart. Phys.
192. F.A. Danevich et al., $ZnWO_4$ crystals as detectors for 2β decay and dark matter experiments, Nucl. Instr. Meth. A **544**, 553—564 (2005).
193. F.A. Danevich et al., Effect of recrystallisation on the radioactive contamination of $CaWO_4$ crystal scintillators, Nucl. Instr. Meth. A **631**, 44—53 (2011).
194. F.A. Danevich et al., Two-neutrino 2β decay of ^{116}Cd and new half-life limits on 2β decay of ^{180}W and ^{186}W, Nucl. Phys. A **717**, 129—145 (2003).
195. F.A. Danevich, On R&D of radiopure crystal scintillators for low counting experiments, Proc. 1st Int. Workshop, Radiopure Scintillators for EURECA, RPScint'2008, 9—10 Sept. 2008, Institute for Nuclear Research, Kyiv, Ukraine, arXiv:0903.1539 [nucl-ex].
196. F.A. Danevich et al., $MgWO_4$ — A new crystal scintillator, Nucl. Instr. Meth. A **608**, 107—115 (2009).
197. F.A. Danevich et al., Feasibility study of $PbWO_4$ and $PbMoO_4$ crystal scintillators for cryogenic rare events experiments, Nucl. Instr. Meth. A **622**, 608—613 (2010).
198. F.A. Danevich et al., Ancient Greek lead findings in Ukraine, Nucl. Instr. Meth. A **603**, 328—332 (2009).
199. F.A. Danevich et al., Beta decay of ^{113}Cd, Phys. Atom. Nucl. 59 (1996) 1—5.
200. F.A. Danevich et al., Search for 2β decay of cadmium and tungsten isotopes: Final results of the Solotvina experiment, Phys. Rev. C **68**, 035501 (2003).
201. F.A. Danevich et al., Quest for double beta decay of ^{160}Gd and Ce isotopes, Nucl. Phys. A **694**, 375—391 (2001).
202. D. Dassie, R. Eschbach, F. Hubert, Ph. Hubert, Two-neutrino double-β decay measurement of ^{100}Mo, Phys. Rev. D **51**, 2090—2100 (1995).
203. J. Dawson et al., A search for various double beta decay modes of tin isotopes, Nucl. Phys. A **799**, 167—180 (2008).
204. A.V. Derbin et al., Search for solar axions emitted in an M1 transition in ^{7}Li* nuclei, JETP Lett. **81**, 365—370 (2005).

205. A.V. Derbin et al., Search for resonant absorption of solar axions emitted in M1 transition in ^{57}Fe nuclei, Eur. Phys. J. C **62**, 755—760 (2009).
206. A.V. Derbin et al., New limit on the mass of 14.4-keV solar axions emitted in an M1 transition in ^{57}Fe nuclei, Phys. At. Nucl. **74**, 596—602 (2010).
207. A.V. Derbin et al., Search for resonant absorption of solar axions emitted in an M1 transition in ^{57}Fe nuclei, JETP Lett. **85**, 12—16 (2007).
208. A.V. Derbin, O.Ju. Smirnov, Search for the neutrino radiative decay with the prototype of the Borexino detector, JETP Lett. **76**, 483—487 (2002).
209. A.V. Derbin et al., Experiment on antineutrino scattering by electrons at a reactor of the Rovno nuclear power plant, JETP Lett. **57**, 768—772 (1993).
210. A. Derbin, A. Ianni, O. Smirnov, Comment on the statistical analysis in "A new experimental limit for the stability of the electron" by H.V. Klapdor-Kleingrothaus, I.V. Krivosheina and I.V. Titkova, arXiv:0704.2047v1 [hep-ex].
211. L. Devis jr., A.S. Goldhaber, M.M. Nieto, Limit on the photon mass deduced from Pioneer-10 observation of Jupiter's magnetic field, Phys. Rev. Lett. **35**, 1402—1405 (1975).
212. M. Dine, W. Fischler, M. Srednicki, A simple solution to the strong CP problem with a harmless axion, Phys. Lett. B **104**, 199—202 (1981).
213. F.E. Dix, Ph. D. Thesis (Case Western Reserve University, 1970).
214. S. Dodelson, L. Widrow, Sterile neutrinos as dark matter, Phys. Rev. Lett. **72**, 17—20 (1994).
215. C. Dörr, H.V. Klapdor-Kleingrothaus, New Monte-Carlo simulation of the Heidelberg—Moscow double beta decay experiment, Nucl. Instr. Meth. A **513**, 596—621 (2003).
216. U. Dore, D. Orestano, Experimental results on neutrino oscillations, Rep. Prog. Phys. **71**, 106201 (2008).
217. S.L. Dubovsky, V.A. Rubakov, P.G. Tinyakov, Brane world: Disappearing massive matter, Phys. Rev. D **62**, 105011 (2000).
218. S.L. Dubovsky, V.A. Rubakov, P.G. Tinyakov, Is the electric charge conserved in brane world? JHEP **08**, 041 (2000).
219. S.L. Dubovsky, Tunneling into extra dimension and high-energy violation of Lorentz invariance, JHEP **01**, 012 (2002).
220. H. Ejiri et al., Limit on the Majorana neutrino mass and right-handed weak current by neutrinoless double β-decay of ^{100}Mo, Phys. Rev. C **63**, 065501 (2001).
221. H. Ejiri, K. Fushimi, T. Kamada, H. Kinoshita et al., Double beta decay of ^{100}Mo, Phys. Lett. B **258**, 17—23 (1991).
222. H. Ejiri, K. Fushimi, R. Hazama, M. Kawasaki, Double beta decays of ^{116}Cd, J. Phys. Soc. Jpn. **64**, 339—343 (1995).
223. H. Ejiri et al., Search for exotic K X-rays from neutral iodine atoms and limits on charge non-conservation, Phys. Lett. B **282**, 281—287 (1992).
224. H. Ejiri et al., Limits on charge nonconservation studied by nuclear excitation of ^{127}I, Phys. Rev. C **44**, 502—505 (1991).
225. H. Ejiri, Double beta decays and neutrino masses, J. Phys. Soc. Japan **74**, 2101—2127 (2005).
226. S. Eliseev et al., Resonant enhancement of neutrinoless double-electron capture in ^{152}Gd, Phys. Rev. Lett. **106**, 052504 (2011).
227. S.R. Elliot, J. Engel, Double-beta decay, J. Phys. G **30**, R183—R215 (2004).

228. S.R. Elliot, A.A. Hahn, M.K. Moe, M.A. Nelson, M.A. Vient, Double beta decay of ^{82}Se, Phys. Rev. C **46**, 1535—1537 (1992).
229. S.R. Elliot, P. Vogel, Double beta decay, Ann. Rev. Nucl. Part. Sci. **52**, 115—151 (2002).
230. http://physics.nist.gov/PhysRefData/Star/Text/contents.html.
231. J.C. Evans Jr., R.I. Steinberg, Nucleon stability: A geochemical test independent of decay mode, Science **197**, 989—991 (1977).
232. G. Feinberg, M. Goldhaber, Microscopic tests of symmetry principles, Proc. Nat. Acad. Sci. U.S. **45**, 1301—1312 (1959).
233. G. Fiorentini, M. Lissia, F. Mantovani, Geo-neutrinos and Earth's interior, Phys. Rep. **453**, 117—172 (2007).
234. E. Fiorini, CUORE: a cryogenic underground observatory for rare events, Phys. Rep. **307**, 309—317 (1998).
235. E.L. Fireman, The depth dependence of ^{37}Ar from ^{39}K and the backgound in solar neutrino studies, Proc. Int. Conf. "Neutrino'77", Baksan Valley, USSR, 18—24 June 1977, Moscow, Nauka, 1978, v. 1, p. 53—59; R.I. Steinberg, J.C. Evans Jr., Decay-mode-independent tests of nucleon stability, Proc. Int. Conf. "Neutrino'77", Baksan Valley, USSR, 18—24 June 1977, Moscow, Nauka, 1978, v. 2, p. 321—326.
236. R.B. Firestone et al., *Table of isotopes* (John Wiley, New York, 1996).
237. G.N. Flerov et al., Spontaneous fission of Th^{232} and stability of nucleons, Sov. Phys. Dokl. **3**, 79—81 (1958).
238. A. Friedland, M. Giannotti, Astrophysical bounds on photons escaping into extra dimensions, Phys. Rev. Lett. **100**, 031602 (2008).
239. K. Fujikawa, R.E. Shrock, Magnetic moment of a massive neutrino and neutrino-spin rotation, Phys. Rev. Lett. **45**, 963—966 (1980).
240. W.H. Furry, On transition probabilities in double beta-disintegration, Phys. Rev. **56**, 1184—1193 (1939).
241. S. Gales et al., Exotic nuclear decay of ^{223}Ra by emission of ^{14}C nuclei, Phys. Rev. Lett. **53**, 759—762 (1984).
242. GALLEX Collaboration, W. Hampel et al., GALLEX solar neutrino observations: Results for GALLEX IV, Phys. Lett. B **447**, 127—133 (1999).
243. A. Gando et al., Measurement of the double-β decay half-life of ^{136}Xe with the KamLAND-Zen experiment, Phys. Rev. C **85**, 045504 (2012).
244. Yu.M. Gavriljuk et al., New stage of search for 2K(2ν) capture of ^{78}Kr, Phys. Atom. Nucl. **69**, 2124—2128 (2006).
245. Yu.M. Gavriljuk, A.M. Gangapshev, V.V. Kuzminov, S.I. Panasenko and S.S. Ratkevich, Results of a search for 2β decay of ^{136}Xe with high-pressure copper proportional counters in Baksan Neutrino Observatory, Phys. Atom. Nucl. **69**, 2129—2133 (2006).
246. G.B. Gelmini, M. Roncadelli, Left-handed neutrino mass scale and spontaneously broken lepton number, Phys. Lett. B **99**, 411—415 (1981).
247. A.Sh. Georgadze et al., Evaluation of activities of impurity radionuclides in cadmium tungstate crystals, Instr. Exp. Technique **39**, 191—198 (1996).
248. H. Georgi, L. Randall, Charge conjugation and neutrino magnetic moments, Phys. Lett. B **244**, 196—202 (1990).

249. Gemma Collaboration, A.G. Beda et al., GEMMA experiment: Three years of the search for the neutrino magnetic moment, Phys. Part. Nucl. Lett. **7**, 406—409 (2010).
250. R.H. Gillette, Calcium and cadmium tungstate as scintillation counter crystals for gamma-ray detection, Rev. Sci. Instr. **21**, 294—301 (1950).
251. L. Gironi, et al., Performance of $ZnMoO_4$ crystal as cryogenic scintillating bolometer to search for double beta decay of molybdenum, JINST **5**, P11007 (2010).
252. L. Gironi et al., $CdWO_4$ bolometers for double beta decay search, Opt. Mat. **31**, 1388—1392 (2008).
253. A. Giuliani, Searches for neutrinoless double beta decay, Acta Phys. Pol. B **41**, 1447—1468 (2010).
254. A. Giuliani, Searches for neutrinoless double beta decay, Acta Phys. Pol. B **41**, 1447—1468 (2010).
255. J.-F. Glicenstein, New limits on nucleon decay modes to neutrinos, Phys. Lett. B **411**, 326—329 (1997).
256. GNO Collaboration, M. Altmann et al., Complete results for five years of GNO solar neutrino observations, Phys. Lett. B **616**, 174—190 (2005).
257. M. Goeppert-Mayer, Double Beta-Disintegration, Phys. Rev. **48**, 512—516 (1935).
258. G. Goessling et al., Experimental study of ^{113}Cd β decay using CdZnTe detectors, Phys. Rev. C **72**, 064328 (2005).
259. J.J. Gomez-Cadenas, J. Martin-Albo, M. Mezzetto, F. Monrabal, M. Sorel, The search for neutrinoless double beta decay, Riv. Nuovo Cim. **35**, 29—98 (2012).
260. W.E. Greth et al., Beta instability in ^{113}Cd, J. Inorg. Nucl. Chem. **32**, 2113—2117 (1970).
261. M. Gunther et al., Heidelberg—Moscow $\beta\beta$ experiment with ^{76}Ge: Full setup with five detectors, Phys. Rev. D **55**, 54—67 (1997).
262. A. Guglielmetti et al., Nonobservation of ^{12}C cluster decay of ^{114}Ba, Phys. Rev. C **56**, 2912—2916 (1997).
263. W.C. Haxton, K.Y. Lee, Red-giant evolution, metallicity, and new bounds on hadronic axions, Phys. Rev. Lett. **66**, 2557—2560 (1991).
264. C. Hagner et al., Experimental search for the neutrino decay $\nu_3 \to \nu_j + e^+ + e^-$ and limits on neutrino mixing, Phys. Rev. D **52**, 1343—1352 (1995).
265. H. Hidaka, C.V. Ly, K. Suzuki, Geochemical evidence of the double β decay of ^{100}Mo, Phys. Rev. C **70**, 025501 (2004).
266. M. Hirsch et al., Nuclear structure calculation of $\beta^+\beta^+$, β^+/EC and EC/EC decay matrix elements, Z. Phys. A **347**, 151—161 (1994).
267. S. Holjevic, B.A. Logan, A. Ljubicic, Nuclear level excitation during charge nonconservation, Phys. Rev. C **35**, 341—343 (1987).
268. G. 't Hooft, Symmetry breaking through Bell-Jackiw anomalies, Phys. Rev. Lett. **37**, 8—11 (1976).
269. J.C. Huang, Stability of the electron in the SU(5) and GWS models, J. Phys. G **13**, 273—284 (1987).
270. F. Iachello, J. Barea, Proc. XIV Int. Workshop on "Neutrino Telescopes", Venice, Italy, March 2011, in press.
271. The ILIAS database on radiopurity of materials, http://radiopurity.in2p3.fr/.

272. A.S. Iljinov, M.V. Mebel, S.E. Chigrinov, Properties of nuclear radioactivity induced by nucleon instability, Sov. J. Nucl. Phys. **37**, 18—26 (1983).
273. L.I. Ivleva et al., Growth and properties of $ZnMoO_4$ single crystals, Crystallography Reports **53**, 1087—1090 (2008).
274. K. Jakovcic et al., A search for solar hadronic axions using ^{83}Kr, Rad. Phys. Chem. **71**, 793—794 (2004).
275. Kamiokande Collaboration, K. S. Hirata et al., Observation of ^{8}B solar neutrinos in the Kamiokande-II detector, Phys. Rev. Lett. **63**, 16—19 (1989).
276. KamLAND Collaboration, S. Abe et al., Precision measurement of neutrino oscillation parameters with KamLAND, Phys. Rev. Lett. **100**, 221803 (2008).
277. KamLAND Collaboration, K. Eguchi et al., High sensitivity search for $\tilde{\nu}_e$'s from the Sun and other sources at KamLAND, Phys. Rev. Lett. **92**, 071301 (2004).
278. K2K Collaboration, M.H. Ahn et al., Measurement of neutrino oscillation by the K2K experiment, Phys. Rev. D **74**, 072003 (2006).
279. M. Kauer (on behalf of the SuperNEMO Collaboration), Calorimeter R&D for the SuperNEMO double beta decay experiment, J. Phys.: Conf. Ser. **160**, 012031 (2009).
280. A. Kawashima, K. Takahashi, A. Masuda, Geochemical estimation of the half-life for the double beta decay of ^{96}Zr, Phys. Rev. C **47**, R2452 (1993).
281. M.F. Kidd, J.H. Esterline, W. Tornow, A.S. Barabash, V.I. Umatov, New results for double-beta decay of ^{100}Mo to excited final states of ^{100}Ru using the TUNL-ITEP apparatus, Nucl. Phys. A **821**, 251—261 (2009).
282. J.E. Kim, G. Carosi, Axions and the strong CP problem, Rev. Mod. Phys. **82**, 557—601 (2010).
283. J.E. Kim, Light pseudoscalars, particle physics and cosmology, Phys. Rep. **150**, 1—177 (1987).
284. J.E. Kim, Weak-interaction singlet and strong CP invariance, Phys. Rev. Lett. **43**, 103—107 (1979).
285. H.J. Kim, et al., Proc. of New View in Particle Physics (VIETNAM'2004), August 5—11, 2004, p. 449.
286. H.J. Kim et al., Neutrino-less double beta decay experiment using $Ca^{100}MoO_4$ scintillation crystals, IEEE Trans. Nucl. Sci. **57**, 1475—1480 (2010).
287. T. Kirsten, H. Richter, E. Jessberger, Rejection of evidence for nonzero neutrino rest mass from double beta decay, Phys. Rev. Lett. **50**, 474—477 (1983).
288. H.V. Klapdor-Kleingrothaus, A. Dietz, H.L. Harney, I.V. Krivosheina, Evidence for neutrinoless double beta decay, Mod. Phys. Lett. A **16**, 2409—2420 (2001).
289. H.V. Klapdor-Kleingrothaus, I.V. Krivosheina, A. Dietz, O. Chkvorets, Search of neutrinoless double beta decay ^{76}Ge in Gran Sasso 1990—2003, Phys. Lett. B **586**, 198—212 (2004).
290. H.V. Klapdor-Kleingrothaus, I.V Krivosheina, The evidence for the observation of $0\nu\beta\beta$ decay: the identification of $0\nu\beta\beta$ events from the full spectra, Mod. Phys. Lett. A **21**, 1547—1556 (2006).
291. H.V. Klapdor-Kleingrothaus et al., Latest results from the Heidelberg—Moscow double beta decay experiment, Eur. Phys. J. A **12**, 147—154 (2001).
292. H.V. Klapdor-Kleingrothaus, A. Staudt, *Non-accelerator Particle Physics* (IoP, Philadelphia, 1995), 531 p.

293. H.V. Klapdor-Kleingrothaus, I.V. Krivosheina, I.V. Titkova, A new experimental limit for the stability of the electron, Phys. Lett. B **644**, 109—118 (2007).
294. H.V. Klapdor-Kleingrothaus et al., GENIUS-TF: A test facility for the GENIUS project, Nucl. Instr. Meth. A **481**, 149—159 (2002).
295. A.A. Klimenko et al., Search for annual and daily dark matter modulations with Ge detectors at Baksan, Phys. At. Nucl. **61**, 1129—1136 (1998).
296. A.A. Klimenko et al., Experimental limit on the charge non-conserving β decay of ^{73}Ge, Phys. Lett. B **535**, 77—84 (2002).
297. M. Kobayashi, S. Kobayashi, Neutrinoless double-beta decay of ^{160}Gd, Nucl. Phys. A **586**, 457—465 (1995).
298. M. Kortelainen, J. Suhonen, Nuclear matrix elements of $0\nu2\beta$ decay with improved short-range correlations, Phys. Rev. C **76**, 024315 (2007).
299. E.L. Koval'chuk, A.A. Pomanskii, A.A. Smol'nikov, A new experimental limit of the $e^- \to \nu_e + \gamma$ decay, JETP Lett. **29**, 145—148 (1979).
300. G.P. Kovtun, A.P. Shcherban', D.A. Solopikhin, V.D. Virich, Z.I. Zelenskaja et al., Production of radiopure natural and isotopically enriched cadmium and zinc for low background scintillators, Functional Materials **18**, 121—127 (2011).
301. H. Kraus et al., EURECA — The European future of cryogenic dark matter searches, J. Phys.: Conf. Series **39**, 139—141 (2006).
302. H. Kraus et al., EURECA — the European future of dark matter searches with cryogenic detectors, Nucl. Phys. B (Proc. Suppl.) **173**, 168—171 (2007).
303. H. Kraus et al., $ZnWO_4$ scintillators for cryogenic dark matter experiments, Nucl. Instr. Meth. A **600**, 594—598 (2009).
304. H. Kraus et al., EURECA — setting the scene for scintillators, Proc. 1st Int. Workshop, Radiopure Scintillators for EURECA, RPScint'2008, 9—10 Sept. 2008, Institute for Nuclear Research, Kyiv, Ukraine, arXiv:0903.1539 [nucl-ex].
305. M. Krcmar et al., Search for solar axions using ^{7}Li, Phys. Rev. D **64**, 115016 (2001).
306. M. Krcmar et al., Search for solar axions using ^{57}Fe, Phys. Lett. B **442**, 38—42 (1998).
307. M.I. Krivoruchenko, F. Simkovic, D. Frekers, A. Faessler, Resonance enhancement of neutrinoless double electron capture, Nucl. Phys. A **859**, 140—171 (2011).
308. R.F. Lang, W. Seidel, Search for dark matter with CRESST, New J. Phys. **11**, 105017 (2009).
309. P. Langacker, Grand unified theories and proton decay, Phys. Rep. **72**, 185—385 (1981).
310. J. Learned, F. Reines, A. Soni, Limits on nonconservation of Baryon Number, Phys. Rev. Lett. **43**, 907—910 (1979).
311. V.N. Lebedenko et al., Result from the First Science Run of the ZEPLIN-III Dark Matter Search Experiment, Phys. Rev. D **80**, 052010 (2009).
312. H.S. Lee et al., Limits on interactions between weakly interacting massive particles and nucleons obtained with CsI(Tl) crystal detectors, Phys. Rev. Lett. **99**, 091301 (2007).
313. H.S. Lee et al., Development of low background CsI(Tl) crystals for WIMP search, Nucl. Instr. Meth. A **571**, 644—650 (2007).

314. S.J. Lee et al., The Development of a Cryogenic Detector with $CaMoO_4$ Crystals for Neutrinoless Double Beta Decay Search, Astropart. Phys. **34**, 732—737 (2011).
315. B.W. Lee, R.E. Shrock, Natural suppression of symmetry violation in gauge theories: Muon- and electron-lepton-number nonconservation, Phys. Rev. D **16**, 1444—1473 (1977).
316. S.T. Lin et al., New limits on spin-independent and spin-dependent couplings of low-mass WIMP dark matter with a germanium detector at a threshold of 220 eV, Phys. Rev. D **79**, 061101 (2009).
317. W.J. Lin et al., Double beta-decay of tellurium-128 and tellurium-130, Nucl. Phys. A **481**, 484—493 (1988).
318. W.J. Lin et al., Geochemically measured half-lives of ^{82}Se and ^{130}Te, Nucl. Phys. A **481**, 477—483 (1988).
319. A. Ljubicic, In search for axions, Rad. Phys. Chem. **74**, 443—453 (2005).
320. LSD Collaboration, M. Aglietta et al., Upper limit on the solar anti-neutrino flux according to LSD data, JETP Lett. **63**, 791—795 (1996).
321. LSND Collaboration, A. Aguilar et al., Evidence for neutrino oscillations from the observation of $\tilde{\nu}_e$ appearance in a $\tilde{\nu}_\mu$ beam, Phys. Rev. D **64**, 112007 (2001).
322. R.A. Lyttleton, H. Bondi, On the physical consequences of a general excess of charge, Proc. Roy. Soc. London A **252**, 313—333 (1959).
323. E. Majorana, Teoria simmetrica dell'elettrone e del positrone, Nuovo Cimento **14**, 171—184 (1937).
324. W.J. Marciano, A.I. Sanda, Exotic decays of the muon and heavy leptons in gauge theories, Phys. Lett. B **67**, 303—305 (1977).
325. P. de Marcillac, N. Coron, G. Dambier, J. Leblanc, J.P. Moalic, Experimental detection of α-particles from the radioactive decay of natural bismuth, Nature **422**, 876—878 (2003).
326. P.D. Marcillac, private communication (2008).
327. E. der Mateosian and M. Goldhaber, Limits for lepton-nonconserving double beta decay of Ca 48, Phys. Rev. **146**, 810—815 (1966).
328. A.P. Meshik et al., Weak decay of ^{130}Ba and ^{132}Ba: Geochemical measurements, Phys. Rev. C **64**, 035205 (2001).
329. A.P. Meshik et al., ^{130}Te and ^{128}Te double beta decay half-lives, Nucl. Phys. A **809**, 275—289 (2008).
330. V.B. Mikhailik et al., Cryogenic scintillators in searches for extremely rare events, J. Phys. D **39**, 1181—1191 (2006).
331. V.B. Mikhailik, H. Kraus, Performance of scintillation materials at cryogenic temperatures, Phys. Stat. Sol. B **247**, 1583—1599 (2010).
332. H.S. Miley, F.T. Avignone III, R.L. Brodzinski, J.I. Collar et al., Suggestive evidence for the two-neutrino double-β decay of ^{76}Ge, Phys. Rev. Lett. **65**, 3092—3095 (1990).
333. MiniBooNE Collaboration, A.A. Aguilar-Arevalo et al., Event excess in the MiniBooNE search for $\tilde{\nu}_\mu \to \tilde{\nu}_e$ oscillations, Phys. Rev. Lett. **105**, 181801 (2010).
334. MINOS Collaboration, P. Adamson et al., Measurement of neutrino oscillations with the MINOS detectors in the NuMI beam, Phys. Rev. Lett. **101**, 131802 (2008).

335. M. Minowa, K. Itakura, S. Moriyama, W. Ootani, Measurement of the property of cooled lead molybdate as a scintillator, Nucl. Instr. Meth. A **320**, 500—503 (1992).
336. O.G. Miranda, T.I. Rashba, A.I. Rez, J.F.W. Valle, Constraining the neutrino magnetic moment with anti-neutrinos from the sun, Phys. Rev. Lett. **93**, 051304 (2004).
337. A. Mirizzi, D. Montanino, P.D. Serpico, Revisiting cosmological bounds on radiative neutrino lifetime, Phys. Rev. D **76**, 053007 (2007).
338. L.W. Mitchel et al., Rare decays of cadmium and tellurium, Phys. Rev. C **38**, 895—899 (1988).
339. M.K. Moe, F. Reines, Charge conservation and the lifetime of the electron, Phys. Rev. B **140**, 992—998 (1965).
340. R.N. Mohapatra, Possible nonconservation of electric charge, Phys. Rev. Lett. **59**, 1510—1512 (1987).
341. R.N. Mohapatra et al., Theory of neutrinos: a white paper, Rep. Prog. Phys. **70**, 1757—1867 (2007).
342. R.N. Mohapatra et al., Neutrino mass, bulk majoron and neutrinoless double beta decay, Phys. Lett. B **491**, 143—147 (2000).
343. R.J. Moon, Inorganic crystals for the detection of high energy particles and quanta, Phys. Rev. **73**, 1210—1210 (1948).
344. A. Morales et al., Improved constraints on WIMPs from the international germanium experiment IGEX, Phys. Lett. B **532**, 8—14 (2002).
345. B.J. Mount et al., Q value of $^{115}\mathrm{In} \to {}^{115}\mathrm{Sn}(3/2+)$: The lowest known energy β decay, Phys. Rev. Lett. **103**, 122502 (2009).
346. L.L. Nagornaya et al., Tungstate and molybdate scintillators to search for dark matter and double beta decay, IEEE Trans. Nucl. Sci. **56**, 2513—2518 (2009).
347. K. Nakamura et al. (Particle Data Group), The Review of Particle Physics, J. Phys. G **37**, 075021 (2010).
348. T. Namba, Results of a search for monochromatic solar axions using ^{57}Fe, Phys. Lett. B **645**, 398—401 (2007).
349. P. Nath, P.F. Perez, Proton stability in grand unified theories, in strings and in branes, Phys. Rep. **441**, 191—317 (2007).
350. J. Ninkovic et al., New technique for the measurement of the scintillation efficiency of nuclear recoils, Nucl. Instrum. Meth. A **564**, 567—578 (2006).
351. E.B. Norman, J.N. Bahcall, M. Goldhaber, Improved limit on charge conservation derived from ^{71}Ga solar neutrino experiments, Phys. Rev. D **53**, 4086—4088 (1996).
352. E.B. Norman, A.G. Seamster, Improved test of nucleon charge conservation, Phys. Rev. Lett. **43**, 1226—1229 (1979).
353. I. Ogawa, R. Hazama, H. Miyawaki et al., Search for neutrino-less double beta decay of ^{48}Ca by CaF_2 scintillator, Nucl. Phys. A **730**, 215—223 (2004).
354. I. Ogawa et al., Double beta decay study of ^{48}Ca by CaF_2 scintillator, Nucl. Phys. A **721**, C525—C528 (2003).
355. L.B. Okun, Note on testing charge conservation and the Pauli exclusion principle, Phys. Rev. D **45**, VI.10—VI.14 (1992).
356. L.B. Okun, *Lepton and Quarks* (North-Holland, Amsterdam, 1982), p. 181—183.

357. L.B. Okun, Tests of electric charge conservation and the Pauli principle, Sov. Phys. Usp. **32**, 543—547 (1989).
358. L.B. Okun, Ya.B. Zeldovich, Paradoxes of unstable electron, Phys. Lett. B **78**, 597—600 (1978).
359. R.D. Peccei, H.R. Quinn, Constraints imposed by CP conservation in the presence of pseudoparticles, Phys. Rev. D **16**, 1791—1797 (1977).
360. R.D. Peccei, H.R. Quinn, CP conservation in the presence of pseudoparticles, Phys. Rev. Lett. **38**, 1440—1443 (1977).
361. D.H. Perkins, Proton decay experiments, Ann. Rev. Nucl. Part. Sci. **34**, 1—52 (1984).
362. F. Piquemal, The SuperNEMO project, Phys. Atom. Nucl. **69**, 2096—2100 (2006).
363. S. Pirro et al., Development of bolometric light detectors for double beta decay searches, Nucl. Instr. Meth. A **559**, 361—363 (2006).
364. S. Pirro et al., Scintillating double-beta-decay bolometers, Phys. Atom. Nucl. **69**, 2109—2116 (2006).
365. D.N. Poenaru, M. Ivascu, Estimation of the alpha decay half-lives, Journal de Physique, **44**, 791—796 (1983).
366. D.N. Poenaru, W. Greiner, New island of cluster emitters, Phys. Rev. C **47**, 2030—2037 (1993).
367. A.A. Pomansky, Proc. Int. Neutrino Conf., Aachen, Germany, 1976, Braunschweig, Vieweg, 1977, p. 671.
368. G.G. Raffelt, Axions — motivation, limits and searches, J. Phys. A **40**, 6607—6620 (2007).
369. G.G. Raffelt, *Stars as Laboratories for Fundamental Physics* (University Chicago Press, Chicago, 1997), 664 p.
370. G.G. Raffelt, Neutrino radiative-lifetime limits from the absence of solar γ rays, Phys. Rev. D **31**, 3002—3004 (1985).
371. S. Rahaman et al., Q values of the ^{76}Ge and ^{100}Mo double-beta decays, Phys. Lett. B **662**, 111—116 (2008).
372. F. Reines, C.L. Cowan, Conservation of the number of nucleons, Phys. Rev. **96**, 1157—1158 (1954).
373. D. Reusser et al., Limits on cold dark matter from the Gotthard Ge experiment, Phys. Lett. B **255**, 143—145 (1991).
374. W. Rodejohann, Neutrino-less double beta decay and particle physics, Int. J. Mod. Phys. E **29**, 1833—1930 (2011).
375. H.J. Rose, G.A. Jones, A new kind of natural radioactivity, Nature **307**, 245—247 (1984).
376. A. Roy et al., Further experimental test of nucleon charge conservation through the reaction ^{113}Cd $\rightarrow$ ^{113m}In + neutrals, Phys. Rev. D **28**, 1770—1772 (1983).
377. V.A. Rubakov, Large and infinite extra dimensions, Phys. Usp. **44**, 871—893 (2001).
378. N.I. Rukhadze et al., New limits on double beta decay of ^{106}Cd, Nucl. Phys. A **852**, 197—206 (2011).
379. N.I. Rukhadze et al., Search for double beta decay of ^{106}Cd in TGV-2 experiment, J. Phys.: Conf. Ser. **203**, 012072 (2010).

380. SAGE Collaboration, J.N. Abdurashitov et al., Measurement of the solar neutrino capture rate by SAGE and implications for neutrino oscillations in vacuum, Phys. Rev. Lett. **83**, 4686—4689 (1999).
381. A. Sandulescu, D.N. Poenaru, F. Greiner, A new decaying mode of heavy nuclei intermediate between nuclear fission and α decay, Sov. J. Part. Nucl. **11**, 528—541 (1980).
382. V. Sanglard et al. (EDELWEISS Collaboration), Final results of the EDELWEISS-I dark matter search with cryogenic heat-and-ionization Ge detectors, Phys. Rev. D **71**, 122002 (2005).
383. J. Schechter, J.W.F. Valle, Neutrino masses in SU(2)×U(1) theories, Phys. Rev. D **22**, 2227—2235 (1980).
384. M.A. Shifman, A.I. Vainstein, V.I. Zakharov, Can confinement ensure natural CP invariance of strong interaction? Nucl. Phys. B **166**, 493—506 (1980).
385. S. Schönert et al., The GERmanium Detector Array (Gerda) for the search of neutrinoless $\beta\beta$ decays of ^{76}Ge at LNGS, Nucl. Phys. B (Proc. Suppl.) **145**, 242—245 (2005).
386. R.E. Shrock, General theory of weak processes involving neutrinos. II. Pure leptonic decays, Phys. Rev. D **24**, 1275—1309 (1981).
387. A. De Silva, M.K. Moe, M.A. Nelson, M.A. Vient et al., Double β decays of ^{100}Mo and ^{150}Nd, Phys. Rev. C **56**, 2451—2467 (1997).
388. F. Simkovic, A. Faessler, V. Rodin, P. Vogel, J. Engel, Anatomy of the $0\nu2\beta$ nuclear matrix elements, Phys. Rev. C **77**, 045503 (2008).
389. F. Simkovic, M.I. Krivoruchenko and A. Faessler, Neutrinoless double-beta decay and double-electron capture, Prog. Part. Nucl. Phys. **66**, 446—451 (2011).
390. SNO Collaboration, B. Aharmim et al., Determination of the ν_e and total ^{8}B solar neutrino fluxes using the Sudbury Neutrino Observatory phase I data set, Phys. Rev. C **75**, 045502 (2007).
391. SNO Collaboration, Q.R. Ahmad et al., Measurement of the rate of $\nu_e + d \rightarrow$ $\rightarrow p+p+e^-$ interactions produced by ^{8}B solar neutrinos at the Sudbury Neutrino Observatory, Phys. Rev. Lett. **87**, 071301 (2001).
392. SNO Collaboration, B. Aharmim et al., Electron antineutrino search at the Sudbury Neutrino Observatory, Phys. Rev. D **70**, 093014 (2004).
393. N.J.C. Spooner, Direct dark matter searches, J. Phys. Soc. Japan **76**, 111016 (2007).
394. S.D. Steffen, Dark-matter candidates. Axions, neutralinos, gravitinos, and axinos, Eur. Phys. J. C **59**, 557—588 (2009).
395. R.I. Steinberg et al., Experimental test of charge conservation and the stability of the electron, Phys. Rev. D **12**, 2582—2586 (1975).
396. http://www.srim.org.
397. F. Suekane, T. Iwamoto, H. Ogawa, O. Tajima and H. Watanabe (for the KamLAND RCNS Group), An overview of the KamLAND 1-kiloton liquid scintillator, arXiv:physics/0404071.
398. Z. Sujkowski, S. Wycech, Neutrinoless double electron capture: A tool to search for Majorana neutrinos, Phys. Rev. C **70**, 052501 (2004).
399. A.W. Sunyar, M. Goldhaber, K-electron capture branch of Sr^{87m}, Phys. Rev. **120**, 871—873 (1960).

400. SuperKamiokande Collaboration, J.P. Cravens et al., Solar neutrino measurements in Super-Kamiokande-II, Phys. Rev. D **78**, 032002 (2008).
401. Super-Kamiokande Collaboration, Y. Fukuda et al., Evidence for oscillation of atmospheric neutrinos, Phys. Rev. Lett. **81**, 1562—1567 (1998).
402. SuperKamiokande Collaboration, Y. Gando et al., Search for $\bar{\nu}_e$ from the Sun at Super-Kamiokande-I, Phys. Rev. Lett. **90**, 171302 (2003).
403. Y. Suzuki et al., Study of invisible nucleon decay, $n \to \nu\nu\bar{\nu}$, and a forbidden nuclear transition in the Kamiokande detector, Phys. Lett. B **311**, 357—361 (1993).
404. N. Takaoka, Y. Motomura, K. Nagao, Half-life of ^{130}Te double-β decay measured with geologically qualified samples, Phys. Rev. C **53**, 1557—1561 (1996).
405. A. Terashima et al., R&D for possible future improvements of KamLAND, J. Phys. Conf. Ser. **120**, 052029 (2008).
406. M. Torres, H. Vucetich, Limits on charge non-conservation from possible seasonal variations of the solar neutrino experiments, Mod. Phys. Lett. A **19**, 639—644 (2004).
407. V.I. Tretyak, V.Yu. Denisov, Yu.G. Zdesenko, New limits on dinucleon decay into invisible channels, JETP Lett. **79**, 106—108 (2004).
408. V.I. Tretyak, Yu.G. Zdesenko, Experimental limits on the proton life-time from the neutrino experiments with heavy water, Phys. Lett. B **505**, 59—63 (2001).
409. V.I. Tretyak, False starts in history of searches for 2β decay, or Discoverless double beta decay, AIP Conf. Proc. **1417**, 129—133 (2011).
410. V.I. Tretyak, Yu.G. Zdesenko, Tables of double beta decay data, At. Data Nucl. Data Tables **6**, 43—90 (1995).
411. V.I. Tretyak, Yu.G. Zdesenko, Tables of double beta decay data — an update, At. Data Nucl. Data Tables **80**, 83—116 (2002).
412. V.I. Tretyak, Semi-empirical calculation of quenching factors for ions in scintillators, Astropart. Phys. **33**, 40—53 (2010).
413. V.I. Tretyak et al., The NEMO-3 results after completion of data taking, AIP Conf. Proc. **1471**, 125—128 (2011).
414. S.P. Tretyakova, G.A. Pik-Pichak, A.A. Ogloblin, The present state and prospects of cluster radioactivity research, Prog. Theor. Phys. Suppl. **146**, 530—535 (2002).
415. A.L. Turkevich, T.E. Economou, G.A. Cowan, Double beta decay of ^{238}U, Phys. Rev. Lett. **67**, 3211—3214 (1991).
416. S. Umehara, T. Kishimoto, I. Ogawa et al., Neutrino-less double-β decay of ^{48}Ca studied by CaF_2(Eu) scintillators, Phys. Rev. C **78**, 058501 (2008).
417. S.C. Vaidya et al., Experimental limit for nucleon stability against charge-nonconserving decay, Phys. Rev. D **27**, 486—492 (1983).
418. A.A. Vasenko, I.V. Kirpichnikov, V.A. Kuznetsov, A.S. Starostin et al., New results in the ITEP/YePI double beta-decay experiment with enriched germanium detectors, Mod. Phys. Lett. A **5**, 1299—1306 (1990).
419. S.I. Vasil'ev, A.A. Klimenko, S.B. Osetrov, A.A. Pomanskii, A.A. Smol'nikov, Observation of the excess of events in the experiment on the search for a two-neutrino double beta decay of ^{100}Mo, JETP Lett. **51**, 622—626 (1990).
420. J.D. Vergados, H. Ejiri, F. Simkovic, Theory of neutrinoless double beta decay, Rep. Prog. Phys. **75**, 106301 (2012).
421. J.D. Vergados, The neutrinoless double beta decay from a modern perspective, Phys. Rept. **361**, 1—56 (2002).

422. M.B. Voloshin, G.V. Mitselmakher, R.A. Eramzhyan, Conversion of an atomic electron into a positron and double $\beta+$ decay, JETP Lett. **35**, 656—659 (1982).
423. M.B. Voloshin, L.B. Okun, Conservation of electric charge, JETP Lett. **28**, 145—149 (1978).
424. J.-C. Vuilleumier, J. Busto, J. Farine, V. Jurgens et al., Search for neutrinoless double-β decay in ^{136}Xe with a time projection chamber, Phys. Rev. D **48**, 1009—1020 (1993).
425. S.C. Wang, H.T. Wong, M. Fujiwara, Measurement of intrinsic radioactivity in a GSO crystal, Nucl. Instr. Meth. A **479**, 498—510 (2002).
426. S. Weinberg, A new light boson? Phys. Rev. Lett. **40**, 223—226 (1978).
427. S. Weinberg, Photons and gravitons in S-matrix theory: Derivation of charge conservation and equality of gravitational and inertial mass, Phys. Rev. B **135**, 1049—1056 (1964).
428. W. Westphal et al., Dark-matter search with CRESST, Czech. J. Phys. **56**, 535—542 (2006).
429. M.E. Wieser, J.R. De Laeter, Evidence of the double β decay of zirconium-96 measured in 1.8×10^9 year-old zircons, Phys. Rev. C **64**, 024308 (2001).
430. J.S.E. Wieslander et al., Smallest known Q value of any nuclear decay: The rare β^- decay of ^{115}In$(9/2+) \to {}^{115}$Sn$(3/2+)$, Phys. Rev. Lett. **103**, 122501 (2009).
431. F. Wilczek, Problem of strong P and T invariance in the presence of instantons, Phys. Rev. Lett. **40**, 279—282 (1978).
432. R.G. Winter, Double K capture and single K capture with positron emission, Phys. Rev. **100**, 142—144 (1955).
433. S. Yoshida et al., CANDLES project for double beta decay of ^{48}Ca, Nucl. Phys. B (Proc. Suppl.) **138**, 214—216 (2005).
434. Yu.G. Zdesenko, V.I. Tretyak, To what extent does the latest SNO result guarantee the proton stability? Phys. Lett. B **553**, 135—140 (2003).
435. Yu.G. Zdesenko, The future of double β decay research, Rev. Mod. Phys. **74**, 663—684 (2002).
436. Yu.G. Zdesenko et al., Scintillation properties and radioactive contamination of $CaWO_4$ crystal scintillators, Nucl. Instr. Meth. A **538**, 657—667 (2005).
437. Yu.G. Zdesenko et al., Lead molybdate as a low-temperature scintillator in the experimental search for the neutrinoless double beta-decay of ^{100}Mo, Instr. Exp. Technique **39**, 364—368 (1996).
438. Yu.G. Zdesenko, F.A. Danevich, V.I. Tretyak, Sensitivity and discovery potential of the future 2β decay experiments, J. Phys. G **30**, 971—981 (2004).
439. Yu.G. Zdesenko et al., CARVEL experiment with $^{48}CaWO_4$ crystal scintillators for the double β decay study of ^{48}Ca, Astropart. Phys. **23**, 249—263 (2005).
440. Yu.G. Zdesenko, O.A. Ponkratenko, V.I. Tretyak, High sensitivity GEM experiment on 2β decay of ^{76}Ge, J. Phys. G **27**, 2129—2146 (2001).
441. A.R. Zhitnitskii, On possible suppression of the axion-hadron interactions, Sov. J. Nucl. Phys. **31**, 260—267 (1980).
442. Y.F. Zhu et al., Measurement of the intrinsic radiopurity of ^{137}Cs/^{235}U/^{238}U/^{232}Th in CsI(Tl) crystal scintillators, Nucl. Instr. Meth. A **557**, 490—500 (2006).
443. K. Zioutas, S. Andriamonje, V. Arsov et al., First results from the CERN axion solar telescope, Phys. Rev. Lett. **94**, 121301 (2005).
444. K. Zuber, Nd double beta decay search with SNO+, AIP Conf. Proc. **942**, 101—104 (2007).

8 CHAPTER

INDIRECT SEARCH FOR DARK MATTER IN THE COSMIC RAY WINDOW

B.I. Hnatyk

8.1. Introduction

More than 80 years ago the seminal work by F. Zwicky [85] introduced a new constituent part of the Universe — unvisible non-luminous gravitationally manifested non-baryonic dark matter (DM). Now the existence of DM is well established by the DM explanation of numerous astronomical observations, including rotational curves of galaxies [71, 72], hot X-ray emitting plasma in clusters of galaxies [32, 57], gravitational lensing effects [69, 81], Big Bang nucleosynthesis yield [63], cosmic microwave background [54], large scale structure of the Universe [47,67,75] and its accelerated expansion [64, 70].

These cosmological DM investigations are complemented by a set of experiments for indirect detection of possible secondary particles from the DM decay or annihilation in the electromagnetic (mainly in X-ray and gamma-ray) or cosmic ray (CR) windows [27] and by a set of running and planned underground laboratory experiments for direct detection of interaction of the DM particles with the matter of detectors [35].

Despite the long history of DM investigation and considerable efforts in direct and indirect detection experiments, till now the unique robust experimental signature of DM is its gravitational interaction. Owing to the fact that DM particles cannot be explained within the Standard Model (SM) frame, the most promising DM investigation is related with high energy collider experiments. Recently the Large Hadron Collider (LHC) team announced the long awaited discovery of the last missing particle of SM — Higgs like

particle with a mass of $m_{\mathrm{H}} \approx 125$ GeV — just in Run 1. Besides the DM problem, there are a lot of arguments for existing of a new physics beyond the SM, e.g. the instability of electroweak vacuum with the threat of quantum tunneling into anti-de-Sitter "Big Crunch" etc. [40]. But, meantime, Run 1 of LHC did not find any signatures of the best-motivated extension of the SM — supersymmetry (SUSY).

There is a hope that the planned Run 2 and Run 3 with higher fluxes and cms protons' energy 14 TeV will be more promising in SUSY search, but simultaneously we expect for looking into physics beyond SM with help of messengers from considerably more powerful cosmic accelerators, namely, using cosmic ray physics.

Cosmic rays were discovered by V. Hess on 7 August 1912 during the balloon flight as an ionizing agent, entering the Earth atmosphere from above. Following investigations have shown that the flux of CRs consists of high energy

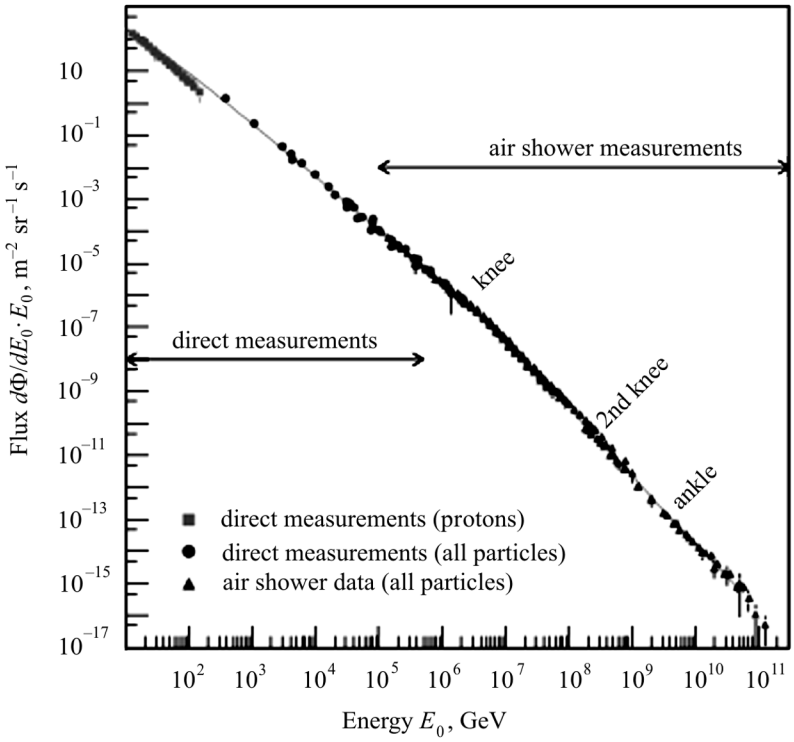

Fig. 8.1. Energy spectrum of cosmic rays. The direct space-based measurements of all-particle spectrum and spectra of different nuclei are possible up to $\sim 10^{14}$ eV. At higher energies the energy spectrum is recovered from air shower measurements. The four main features of spectrum (deviation from a power-law form), namely, softening at $\sim 2.5 \times 10^{15}$ eV (first "knee") and at $\sim 8 \times 10^{17}$ eV ("second knee"), as well as hardening ("ankle") at $\sim 4 \times 10^{18}$ eV and sharp cut-off at $\sim 6 \times 10^{19}$ eV, are presented. Figure is taken from [25]

relativistic particles of different species and covers a wide energy range — from GeV's to hundreds of EeV's. (Fig. 8.1). Atoms and molecules of atmosphere play the role of target particles for accelerated highly relativistic particles in distant cosmic accelerators, therefore secondary particles of the CR-atom collisions reach the surface of Earth. A lot of elementary particles of SM, beginning from positron (discovered by C. Anderson, who shared with V. Hess the Nobel Prize in 1936), were discovered due to the CRs [45].

It is believed that CRs with energies $E \leq 10^{17}$—10^{18} eV are accelerated in Galactic sources, whereas CRs with energies $E > 10^{18}$ eV (ultra-high energy cosmic rays (UHECRs)) are accelerated in the extragalactic sources. Maximum energy of UHECRs ever recorded is 300 EeV, to be compared with a maximum energy of proton in beam $E_p = 7$ TeV in the LHC (the equivalent fixed-target energy of proton-proton collision $\sim 10^{17}$ eV). Such energetic messengers from cosmic ZeVatrons should carry information about physics beyond SM, particularly, about the properties of DM, especially if DM contributes to the CR flux via decay or annihilation processes. Therefore, search for DM physics in the CR window opens an unique possibility to solve the DM enigma.

Decaying or annihilating DM in space produces fluxes of secondary products potentially detectable at the Earth — SM particles, both electrically neutral (photons, neutrinos, neutrons) and charged (electrons, positrons, protons, antiprotons). While the minimum energy of detected extra solar cosmic rays (including nonthermal photons) is of order of $E_{\min} \sim 0.1$ GeV, we expect to check the presence of signatures of decay or annihilation of DM particles with masses $m_\chi \geq E_{\min} \sim 0.1$ GeV in the CR window (in natural units $\hbar = c = k_B = 1$ mass, energy and temperature are expressed in units of energy (erg, eV, etc., typically in GeV), distance and time are expressed in units of inverse energy, the Planck mass is $M_{\rm Pl} = \sqrt{\hbar c/G_N} \approx 1.2 \times 10^{19}$ GeV, where $G_N \approx 6.9 \times \times 10^{-39}$ GeV^{-2} is the Newtonian gravitational constant, and the Fermi coupling constant is $G_F/(\hbar c)^3 \approx 1.2 \times 10^{-5}$ GeV^{-2}).

In Fig. 8.2 the landscape of DM physics is presented, while the main candidates for DM particles with corresponding energy scale and cross-sections for Xenon detector are presented in Fig. 8.3.

Indicated above energy limit of detected CRs allows to expect the registration of decay/annhilation products in the CR window from the heavy enough DM particles, i.e., from thermal relics — weakly interacting massive particles (WIMPs) with 0.1 GeV $\leq m_\chi \leq$ 0.1 PeV [41] and from nonthermally produced massive and supermassive weakly interacting particles (superheavy DM (SHDM) or WIMPZILLAS) [29, 65]. In this review we analyze the results of search for WIMP and SHDM decay/annihilation products in the CR window. To this end we consider the possible manifestations of Galactic WIMPs in multiGeV electron and positron fluxes (sect. 1.2) and SHDM particles in UHECR (multiEeV) fluxes (sect. 1.3).

8.2. Search for WIMP signatures in the Galactic cosmic ray flux

8.2.1. WIMPs as dark matter candidate

Among the zoo of DM candidates in Fig. 8.2 and Fig. 8.3 the most popular ones are WIMPs due to the "WIMP miracle": thermally produced in hot ($T > m_{\rm WIMP}$) early Universe particles with a weak-scale mass ($m_{\rm WIMP} \sim 10$ GeV—1 TeV) and a weak interaction velocity averaged cross-section $\langle \sigma v \rangle = 3 \times 10^{-26}$ cm^3/s give automatically one close to the observable DM abundance $\Omega_{\rm DM} h^2 = 0.120 \pm 0.003$ [41]. Big Bang nucleosynthesis constraint [63] on the baryonic component of the Universe and cold DM (CDM)-philic large scale structure [47,75] rejects any viable SM candidate and demands to look for DM particle(s) Beyond Standard Model (BSM) with SUSY as the most promising theory for extention of SM and with the lightest neutralino (which is its own antiparticle) as a leading WIMP candidate [68].

8.2.2. Antimatter particles in GeV-TeV cosmic ray flux

In the Gev-TeV range a number of running experiments are suitable for detection of charged matter-antimatter particles: PAMELA satellite (e^+, e^-, p, $\bar{p}$), experiment AMS at the International Space Station (ISS) (e^+e^- and anti-nuclei detection), the balloon-borne instrument Advanced

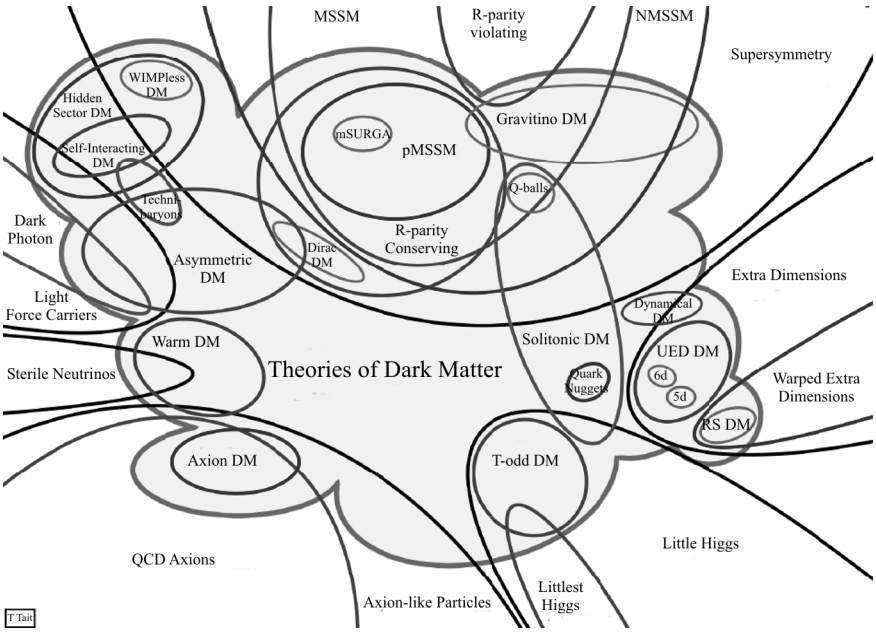

Fig. 8.2. Plethora of dark matter candidates due to T. Tait. Figure is taken from [56]

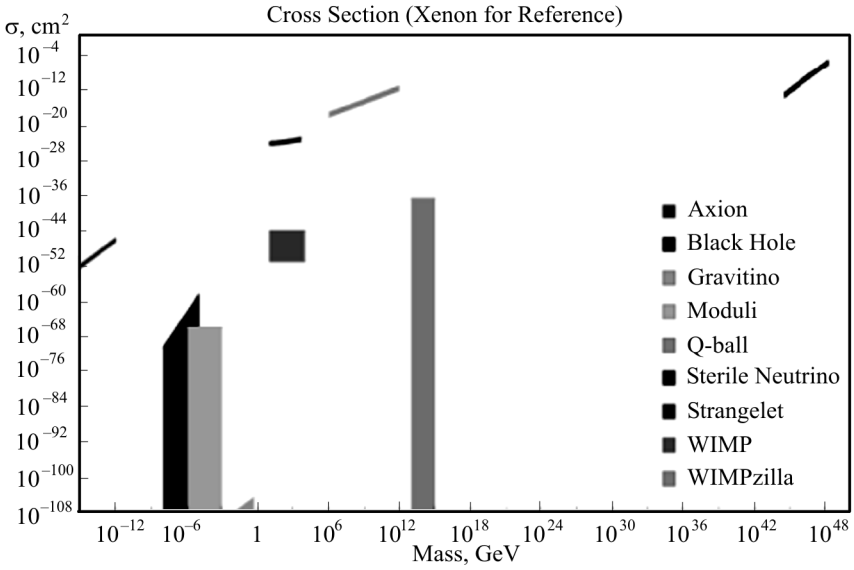

Fig. 8.3. Main dark matter candidates of different masses and their nucleon (Xenon) cross-section compiled by L. Pearce. Figure is taken from [56]

Thin Ionization Calorimeter (ATIC) [62], determination of fluxes of charged leptonic e^+e^- components in the space-born (FERMI-LAT) and ground based (HESS) gamma-telescopes, IceCube neutrino telescope in the Antarctica ice [27]. Recent results of measurements of electron e^-, positron e^+, and total $e^- + e^+$ energy spectra, as well as energy dependence of positron fraction $e^+/(e^+ + e^-)$ in the GeV — hundreds of GeV energy range in PAMELA [1,2,61], FERMI-LAT [3, 4] and AMS [7, 20, 77] experiments, show the unexpected increase in conventional model of CR propagation [60] both of total $e^- + e^+$ flux and positron fraction (from 0.05 at 10 GeV to 0.15 in 200—350 GeV bin, Fig. 8.4). According to the data of ATIC, FERMI-LAT, and HESS the total $e^- + e^+$ flux enhancement continues up to TeV region (Fig. 8.5).

8.2.3. Dark matter explanation of electron-positron anomalies

Two observed electron-positron anomalies (electron-positron enhancement and rising positron fraction) can be naturally explained in the annihilating DM models. DM particle can annihilate into SM particles (protons-antiprotons, electrons-positrons, deuterons-antideuterons, neutrinos and photons) with energies of order of DM masses, i.e., into cosmic ray particles and photons in subGeV-TeV range [39, 73]:

$$\chi + \chi \to q\bar{q},\ W^+W^-,\ \mu^+\mu^-,\ \tau^+\tau^- ... \to e^+e^-,\ p\bar{p},\ D\bar{D},\ \gamma,\ \nu\bar{\nu}.$$

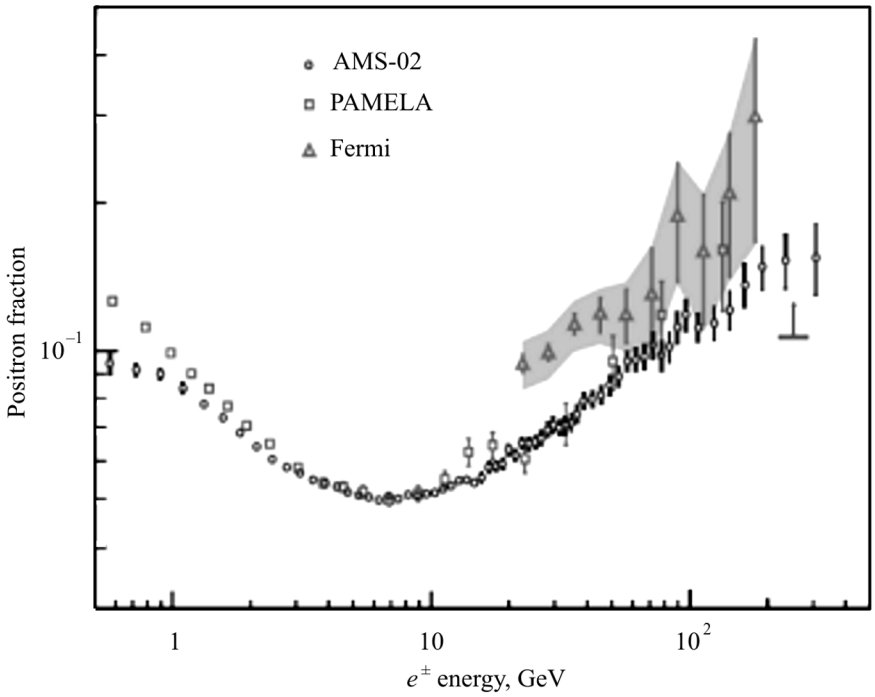

Fig. 8.4. The positron fraction anomaly: increasing of positron fraction in leptonic cosmic ray flux at energy $E \geq 10$ GeV. Observational data of AMS-2 [7], PAMELA [2] and FERMI-LAT [4] are presented. Figure is taken from [7]

Similar CR particles are expected from the metastable decaying DM. Therefore, astrophysical objects with considerable concentration of DM particles (for example, Galactic halo) should contribute to the observed fluxes of GeV-TeV cosmic rays, opening the CR window for indirect detection of DM.

The main contribution to the observed CR electron flux is provided by the Galactic cosmic ray accelerators, mainly, Supernova remnants (SNRs) with their powerful shock waves, where the charged particles of interstellar medium (ISM) (electrons, protons and nuclei of atomic number A and charge Z) are accelerated via diffusive shock acceleration (DSA) up to the maximum energy of order $E_{\max,Z} \sim 10^{15} Z$ eV for nuclei and to somewhat lower energy $E_{\max,e} \sim$ $\sim 10^{13}$ eV for suffering energy losses electrons. Inelastic proton-proton collisions of accelerated relativistic protons with target protons of ISM plasma result in production of secondary leptons

$$pp \to pn\pi^+ \to ppe^+e^-\nu_e\bar{\nu}_e\nu_\mu\bar{\nu}_\mu.$$

Observed positron excess cannot be explained by such a conventional model, within which a secondary positron fraction decreases with energy [59, 60]. Qualitatively it corresponds to the predictions of expected fluxes of animatter from annihilating dark matter in the Galactic halo.

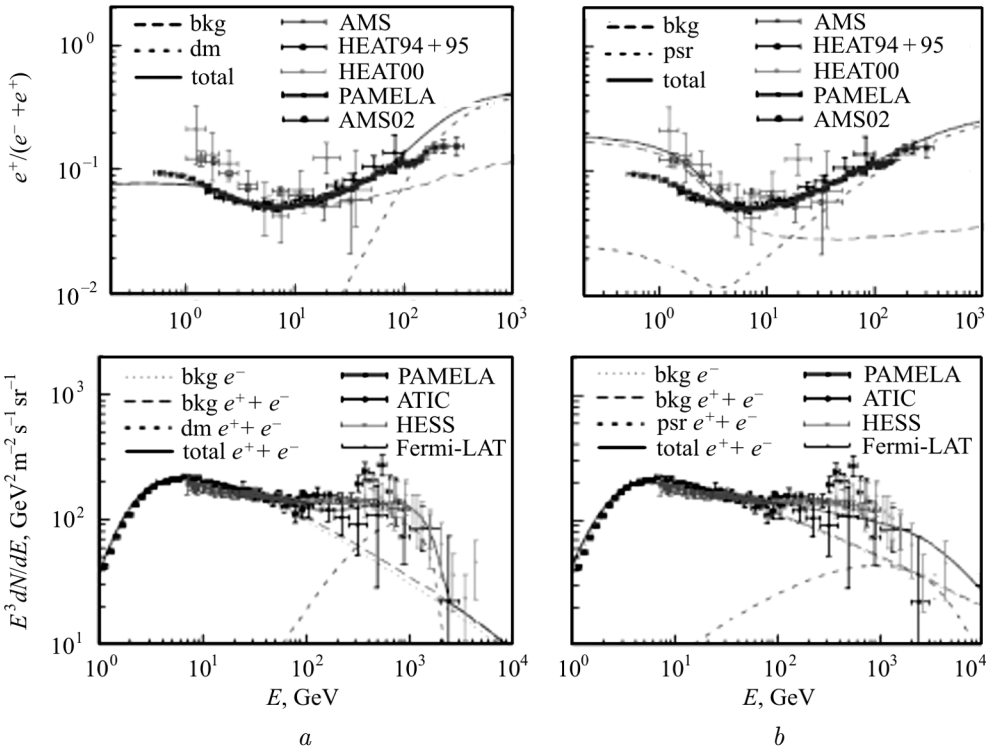

Fig. 8.5. Observational data and theoretical models for the positron fraction (upper row) and electron and positron energy spectrum (lower). Astrophysical background (long dashed lines) and additional contribution from the dark matter annihilation ($\mu^+\mu^-$ channel) (a) or the Galactic pulsar population (b) (short dashed lines) are presented. See text for details. Figure is taken from [83]

In the case of WIMP DM with annihilation rate $\langle\sigma v\rangle = 3 \times 10^{-26}$ cm^3/s and average dark matter density $\sim$0.4 GeV/cm^3 in the Solar neighborhood the required TeV scale masses of DM $M_{\rm DM} \leq 1$ TeV result in considerably low values of the number density and, correspondingly, of the annihilation rate. The expected electron + positron spectral intensity $\Phi(E)$ in $E^3\Phi(E)$ presentation is [19]

$$E^3\Phi(E) = 6 \times 10^{-4} \left(\frac{E}{1\,\text{GeV}}\right) \left(\frac{M_{\rm DM}}{1\,\text{TeV}}\right)^{-2} \theta(M_{\rm DM} - E) B_{\rm tot}\ \text{m}^{-2}\,\text{s}^{-1}\,\text{sr}^{-1}\ \text{GeV}^2, \tag{8.1}$$

where additional "bust factor" $B_{\rm tot} \sim 200$ as a signature of Sommerfeld enhancement effect [19] should be introduced in order to match the observational intensities $E^3\Phi(E)_{\rm obs} \sim 10^2\,\text{m}^{-2}\,\text{s}^{-1}\,\text{sr}^{-1}\,\text{GeV}^2$ in sub-TeV range (Fig. 8.5, 8.6).

There are a lot of works with the DM explanation of electron-positron anomalies [9, 19, 28, 31, 83]. Electron-positron flux from the DM annihilation overlaps the electron and positron CR flux (background flux) from astrophysi-

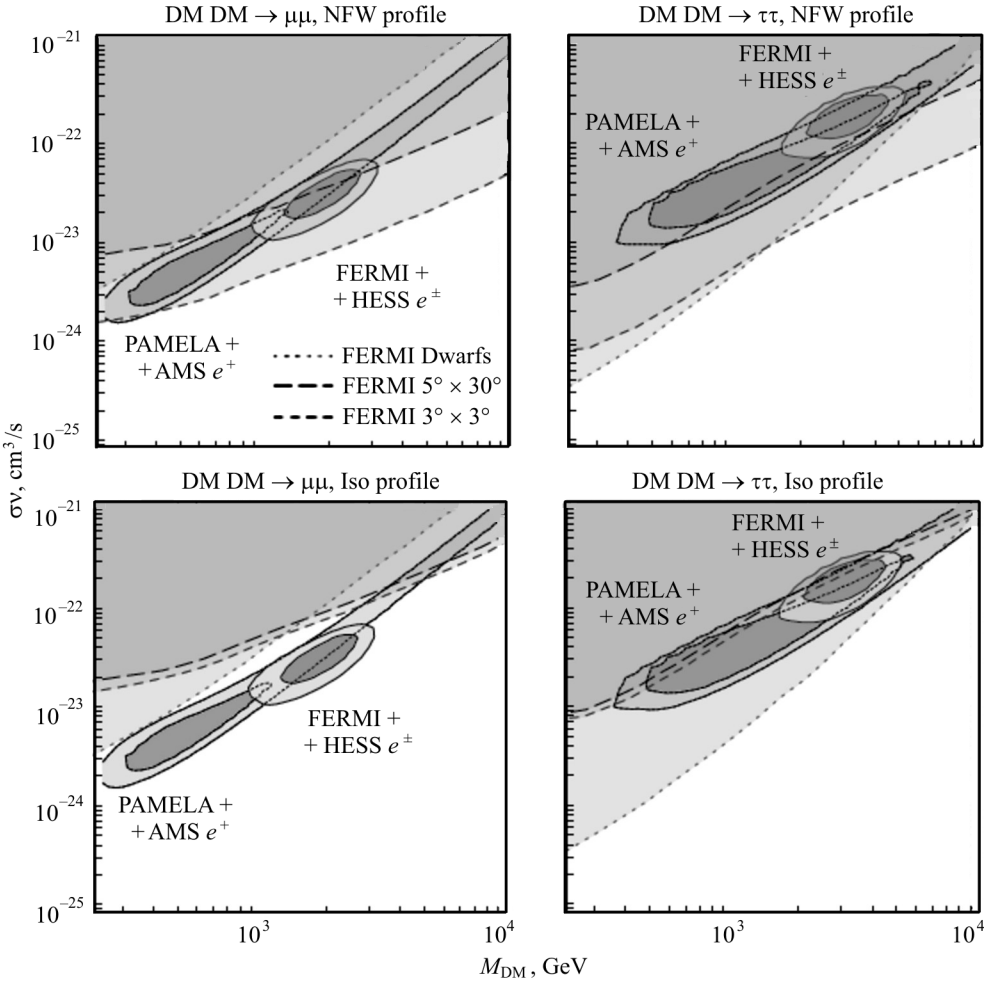

Fig. 8.6. Best fit DM parameters M_{DM} and σv for explanation of the observational positron fraction (AMS-2 and PAMELA data) and total e^+e^- flux (FERMI-LAT and HESS data) (3σ and 5σ contours). Left (right) column corresponds to $\mu^+\mu^-$ ($\tau^+\tau^-$) annihilation channel. Shaded regions show constraints from FERMI-LAT γ-observations of dwarf galaxies and our Galaxy with NFW (upper line) and isothermal (lower line) DM density profiles. Figure is taken from [31]

cal sources in our Galaxy. Background flux includes both primary electrons, accelerated together with nuclei at Supernova remnant shocks, and secondary electrons and positrons, produced in inelastic proton-proton collisions of CR protons with particles of interstellar medium. After escaping the acceleration places, the background particles propagate diffusively into the Galaxy. Primary electrons and positrons from DM annihilation are produced in the whole volume of the Galaxy with the rate, proportional to square of the DM density,

and also propagate diffusively into the Galaxy. Observational flux is the sum of astrophysical background and DM signal, therefore DM interpretation of observations depends strongly on the accuracy of model-dependent calculations of astrophysical (the main free parameters are characteristics of background proton and electron spectra) and DM (the main free parameters are mass $M_{\rm DM}$, cross-section $\langle\sigma v\rangle$, a channel of annihilation, the density profile of the Milky Way DM halo) contributions. Fig. 8.5 from [83] shows the example of such recovering of DM parameters using the data of recent observations. Navarro—Frenk—White distribution of DM with mass of $M_{\rm DM} = 2.3$ TeV and cross-section $\sigma v = 5.0 \times 10^{-23}$ cm^3 s^{-1} gives a reasonable agreement with the observations. But, meantime, a required mass and cross-section are higher than expected.

The situation becomes even worse when observational constraints from FERMI-LAT γ- observations of dwarf galaxies and Galaxy are taken into account. In [31] it is shown that there are some tensions between sub-TeV DM masses, predicted by PAMELA and AMS measurements of the positron fraction, and a few TeV DM masses, predicted by FERMI-LAT and HESS measurements of the total electron-positron flux (Fig. 8.6).

Nevertheless, despite the mentioned problems, the room for DM interpretation of recent observational data concerning the unusual enhancement of electron-positron flux and positron fraction is large enough and new observations are very desirable for estimation or further constraining of the DM parameters.

8.2.4. Astrophysical solutions to electron-positron anomalies

The problem of electron-positron anomalies can have an astrophysical solution. Within more elaborated models of CR generation and propagation an additional flux of electrons and positrons may arise due to the reacceleration of secondary electrons and positrons at Supernova remnant shocks, where the main part of primary nuclei and electrons is accelerated [23, 24, 33, 34, 38, 53, 58, 78]. But there are serious problems in quantitative explanation of observations in the reacceleration approach [28, 59].

Another astrophysical solution: electron and positron acceleration in pulsar wind nebulae (PWNe) [28, 38, 49, 76] looks more promising.

Newly born and fast rotating pulsars are sources of ultrarelativistic pulsar winds, composed of the electron-positron plasma. Strong termination ultrarelativistic shock in free wind, arising from the wind-interstellar medium interaction, accelerates effectively electrons and positrons in equal numbers via DSA, which, in turn, escape PWNe and diffusively propagate into the Galaxy, similarly to the primary CRs from Supernova remnants. An example of explanation of observable data by PWNe model is presented in Fig. 8.5.

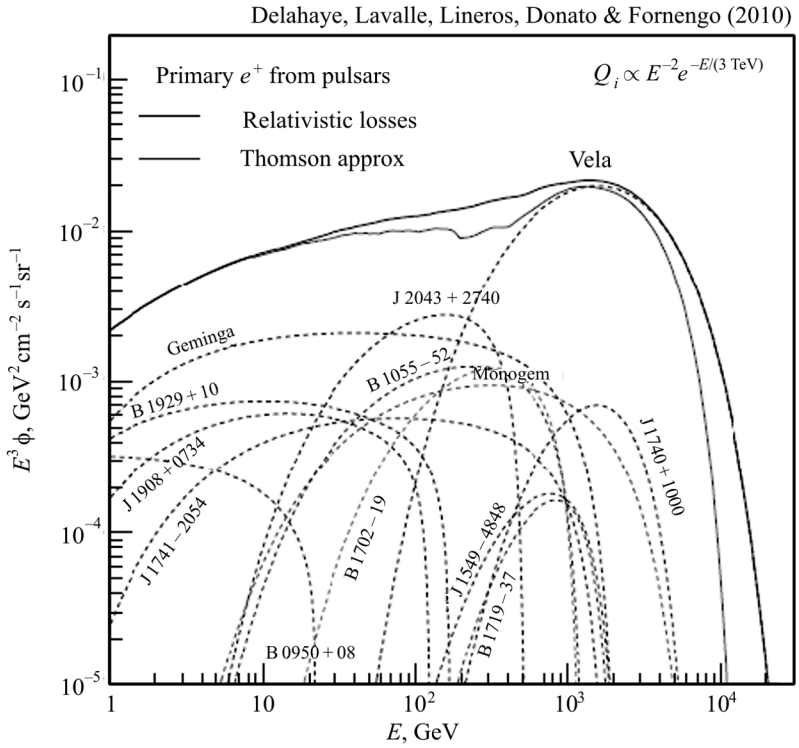

Fig. 8.7. Primary positron energy spectra from nearby pulsars, produced power-law spectra with spectral index $\gamma = 2$ and maximum energy $E_c = 3$ TeV. The cases of nonrelativistic and full relativistic treatment of the energy losses are considered. Figure is taken from [37]

Results of successful modeling of recent AMS-2 data by the sum of contributions of SNRs and PWNe are presented in [38]. Here it is also shown that a few pulsars, which are closer to Earth, may contribute considerably to the electron-positron flux as a result of diffusive propagation of accelerated e^+e^- particles. The most significant contribution is expected from close ($\leq$200—300 pc) and old enough ($\sim 10^5$ yrs) pulsars, especially from the well known close pulsars J 0633 + 1746 (Geminga), B 0656 + 14 (Monogem), B 0833 − 45 (Vela) etc. [37]. In Fig. 8.7 the primary positron energy spectra from nearby pulsars, produced power-law spectra with spectral index $\gamma = 2$ and maximum energy $E_c = 3$ TeV, are presented. The cases of nonrelativistic and full relativistic treatment of the energy losses are shown too.

8.2.5. Electron-positron anomalies and the Vela pulsar wind nebula

Younger ($\leq 10^4$ yrs) pulsars together with their PWNe are still surrounded by SNR shells and accelerated e^+e^- particles are trapped by the magnetic fields of PWNe and SNR shell. And only after fragmentation and decay of SNR shell at the late radiation stage of evolution, the accelerated particles can escape the pulsar region and diffusively propagate into the Galaxy [22]. But the med-age Vela pulsar PSR B 0833 – 45 (characteristic age $t_{\rm Vela} = 11400$ yr) with its PWNe is located in the non-typical Vela SNR without the well developed shell, and the problem of early escaping of accelerated e^+e^- pairs is considerably relaxed.

Vela SNR with Vela pulsar inside belongs to the the Vela complex, which includes the Vela supernova remnant, the binary system γ^2 Velorum with prominent stellar wind bubble IRAS Vela Shell (IVS), and the Gum nebula [80].

In [80] it is shown that the Vela SNR belongs to a subclass of non-Sedov adiabatic remnants in the cloudy interstellar medium (ISM), the dynamics of which is determined by the heating and evaporation of ISM clouds. Observable characteristics of the Vela SNR can be explained as the SN explosion with energy 1.4×10^{50} ergs near the step-like boundary of the ISM with low inter-cloud densities (10^{-3} cm^{-3}) and with the volume-averaged density of clouds evaporated by shock in the north-east (NE) part about four times higher than the one in the south-west (SW) part. The observed asymmetry between the NE and SW parts of the Vela SNR could be explained by the presence of a stellar wind bubble (SWB) blown by the nearest-to-the Earth Wolf—Rayet (WR) star in the γ^2 Velorum system.

In Fig. 8.8 the X-ray map of the Vela SNR from ROSAT All-Sky Survey image (0.1—2.4 keV) [10] and the boundaries of the Vela SNR and stellar wind bubble around the γ^2 Velorum are presented. The extended features outside the boundary of the remnant ("bullets") represent the high velocity fragments of rejected Supernova envelope, which protruded a rarefied SNR shell region. The absence of clear signatures of strong main shock at the edge of SNR, volume-filled X-ray radiation, long-lived bullets as a signature of rarefied circumstellar medium, as well as another arguments, presented in [79, 80], confirm the model of Vela SNR as an untypical one, without regular shell-like structure with a massive swept up magnetised shell of matter of ISM.

Analysis of radio-maps of Vela SNR also confirms peculiarity of the radio-emitting electrons: they are nearly uniformly distributed inside the remnant and do not show the expected shell-like structure [79].

All these arguments support the model of early Vela PWN evolution inside the expanding fragmented Supernova envelope, which decelerates mainly due to the interaction with interstellar cloudlets without forming the regular

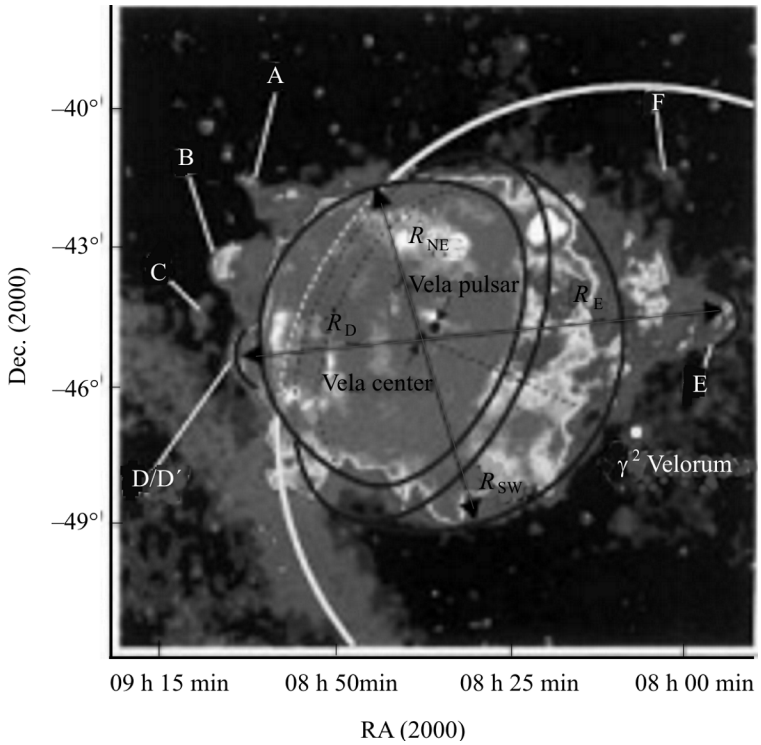

Fig. 8.8. ROSAT All-Sky Survey image (0.1—2.4 keV) of the Vela SNR [10]. A-F are extended features outside the boundary of the remnant ("bullets"). Light grey to white contrast represents the contrast in surface brightness of the factor of 500. Black curves show the NE and SW hemispheres of the Vela SNR. White curve shows the contour of the SWB of γ^2 Velorum. Figure is taken from [80]

shell. Termination shock in pulsar wind will accelerate e^+e^- particles, but downstream region of PWNe will not be inclosed in regular SNR shell and newly accelerated particles can escape from the acceleration region even at very early stages of PWNe formation. Therefore, contrary to the case of typical SNRs, when accelerated particles can escape only from med-age SNRs, we do not expect such a delay in Vela PWN case.

Besides the escaping problem, a contribution of Vela PWN to the observed electron-positron flux is limited by the PWN age. For typical values of diffusion the coefficient Vela PWN can contribute only to the $E \geq 100$ GeV flux (Fig. 8.7). But the analysis of ISM structure around the Vela complex gives evidences for a very rarefied interstellar plasma in this region. In [79, 80] it is shown that the estimate based on the dynamics of expansion of Vela SNR suggests a low value for the ISM density $n_{\rm ISM} \leq 0.01$ cm^{-3}.

Moreover, both the Vela SNR and the γ^2 Velorum SWB could be interacting with the still larger scale SNR, known as the Gum nebula. This nebula is

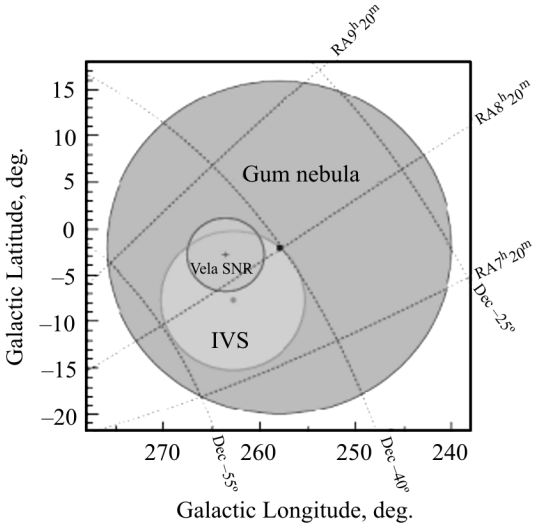

Fig. 8.9. Locations of the Vela SNR (Vela pulsar is shown as a cross), γ^2 Velorum (shown as a circle), IRAS Vela Shell (IVS) bubble and the Gum nebula (center is shown as a square) in Galactic coordinate system. Figure is taken from [80]

a very large region of the ionized gas about 36° in diameter, centered approximately at $(l, b) = (258°, -2°)$ [46], is shown in Fig. 8.9.

Assuming a distance of 400 pc [26] the radius of Gum nebula is about $R_{\rm Gum} \simeq 124(D_{\rm Gum}/400\ {\rm pc})$ pc. This means that both the Vela SNR and γ^2 Velorum with IVS are situated inside the cavity formed by the expansion of SNR associated with the Gum nebula.

The Gum nebula as a very old (0.5—2.0 Myr) SNR should be at the late radiative stage of evolution, which can be modeled with the solution [30] for the shock dynamics. Assuming the current radius 124 pc, the distance to nebula $D_{\rm Gum} = 400 \pm 60$ pc, age ∼1.5 Myr and the explosion energy of $10^{51}E_{51}$ erg, we can find the density of the ISM in which the Gum nebula is expanding:

$$n_{\rm ISM} = 0.07 \left[\frac{t}{1.5\ {\rm Myr}}\right]^{-\frac{7}{6}} \left[\frac{D_{\rm Gum}}{400\ {\rm pc}}\right]^{-\frac{35}{9}} E_{51}^{\frac{17}{72}}\ {\rm cm}^{-3}, \qquad (8.2)$$

The estimate of average density of ISM around the Gum nebula shows that actually the nebula expands into the medium with a much lower density than the typical one in Galactic disk. The low density may suggest the low value of local magnetic field, especially its random component, that determines the value of diffusion coefficient [37]. Moreover, the direction to the Vela complex nearly coincides with the direction of the local spiral arm and the regular component of magnetic field. Corresponding increase of diffusion coefficient results in faster diffusion of electron and positron in 10 GeV—100 GeV range and in increasing of Vela PWN contribution to observed electron-positron enhancement. Future experimental data, especially on the value and direction of anisotropy of electron-positron flux, will be very important in estimating the real contribution of single pulsars, including the Vela one, into antimatter production.

8.3. Search for superheavy dark matter in the ultra high energy cosmic ray flux

8.3.1. Production of superheavy dark matter in the early Universe

Among the viable DM candidates in Fig. 8.3 there are super heavy dark matter (SHDM) particles with masses much larger then unitarity constraint (a few hundred TeV) for the WIMPs, which were in the equilibrium with the thermal plasma in the early Universe. SHDM particles include Q-balls with masses of order 10^9 GeV and WIMPZILLAs with masses of order of GUT scale $\sim 10^{25}$ eV. Such massive particles (often called X-particles) cannot be in thermal equilibrium in the early Universe without overproduction of DM, but there are a number of mechanisms which could produce X-particles as a nonequilibrium component in the early Universe with necessary density at present. Viable mechanisms include gravitational interactions at the end of inflation, thermal production at reheating etc. (see [11, 21, 42, 43] for details).

Due to a very low number density they can have quite strong interaction, but indirect search for such massive particles is possible only (if they are unstable) via the detection of standard model particles from the decay channel. Ultra high energy cosmic ray window $E \geq 10^{18}$ eV is suitable for this search. Traditional mechanisms of cosmic ray production are grounded on an electromagnetic acceleration of some part of the background charged particles up to ultra high energies (so called bottom-up scenario). Decay of massive X-particles also produces the ultra high energy particles with maximum energy of order of $M_X/2$ and with similar to observable spectrum (so called top-down scenario). It is worth to note that the aim of the first proposal of SHDM particles [13] was to explain an unusual energy spectrum of UHECRs, detected in AGASA experiment.

8.3.2. Superheavy dark matter from topological defects

There is an alternative scenario for SHDM production: escaping of short-lived particles from cosmic topological defects (TDs), especially from cosmic strings [82].

Cosmic strings are linear defects that could be formed at a symmetry breaking phase transition in the early Universe [21, 42, 43, 48, 50, 82].

Strings are characterized by the energy scale of symmetry breaking η, which is given by the vacuum expectation value of the corresponding Higgs field, $\langle\phi\rangle = \eta$. The mass per unit length of a string is determined by the energy scale η as $\mu \sim \eta^2$. The gravitational interaction of strings is characterized by dimensionless parameter $G\mu \sim (\eta/m_P)^2$ where G is Newton's constant and $m_P \sim 10^{28}$ eV is the Planck mass.

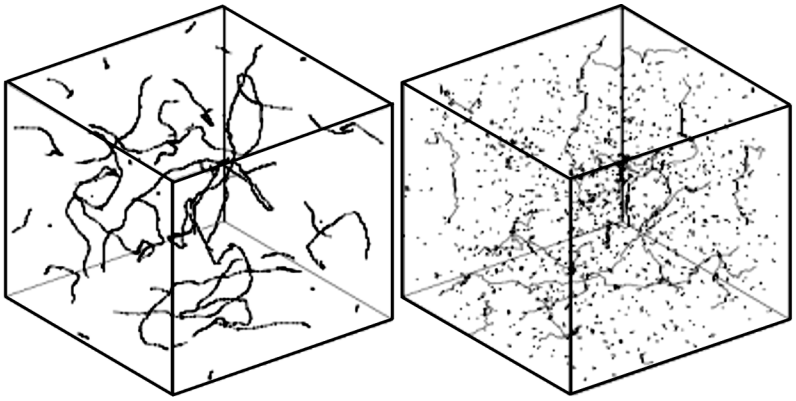

Fig. 8.10. Numerical simulations of the cosmic string network of infinite strings and loops in classical field theory (left) and in the Nambu—Goto approximation (right). Box sizes are of order of the horizon size. Due to the scaling properties the evolving string network structure remains self-similar. Figures are taken from [48]

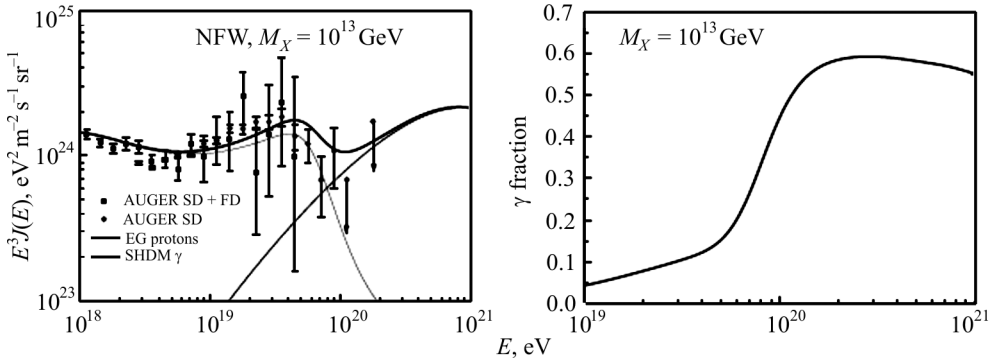

Fig. 8.11. Contribution to the observable spectrum of UHECRs (AUGER data) from ultra high energy photons, produced by the decaying SHDM (left). Fraction of ultra high energy photons in the total flux for the decaying Galactic SHDM with NFW density profile (right). Figures are taken from [6]

Network of strings evolves in a self-similar manner: a horizon-size volume at any time t contains a few long strings stretching across the volume and a large number of small closed loops. The typical distance between long strings and their characteristic curvature radius are both $\sim t$. The typical length of loops being chopped off the long strings is comparable to the scale of the smallest wiggles $l \sim \alpha t$, where α is determined by the gravitational backreaction $\alpha \sim$ $\sim k_g G\mu$, where $k_g \sim 50$. In this case the loops decay within about one Hubble time of their formation. Then, most of the loops at time t have a length $l \sim \alpha t$, and their number density is given by $n_l(t) \sim \alpha^{-1} t^{-3}$.

Strings predicted in some grand unified models respond to external electromagnetic fields as thin superconducting wires. As they move through cosmic magnetic fields, such strings develop electric currents.

Oscillating loops tend to form cusps, where for a brief period of time the string reaches the speed very close to the speed of light. Near a cusp, the string gets contracted by a large factor, its rest energy being turned into kinetic energy. For a string segment of invariant length $\delta l \ll l$, the maximum contraction factor is $\sim l/\delta l$, resulting in a Lorentz factor $\gamma \sim l/\delta l$. Another peculiar feature that one can expect to find on string loops is a kink. It is characterized by a sharp bent, where the string direction changes discontinuously.

It is expected that cosmic strings could be responsible for such astrophysical events as gravitational lensing [74], gravitation wave bursts [36], some examples of gamma-ray bursts [12, 14]. But the most promising signature of the cosmic strings is related to their ability to emit massive X-particles [15, 21, 42, 43]. Besides the ordinary and superconducting (including vortons) cosmic strings, X-particles can be produced by other TDs, such as network of monopoles connected by strings, necklaces and monopoloniums [16].

8.3.3. Superheavy dark matter decay and ultra high energy cosmic ray particles

If SHDM particles are unstable (metastable), they can produce standard model particles via decay. If SHDM particles are stable due to the existence of a some discrete gauge symmetry, and this symmetry is weakly broken, a lifetime of X-particles can be larger than the age of Universe It is believed that the main decay channel is into quarks and leptons. Following hadronization of quarks results in hadron jets with dominance of pions and minor part of nucleons. By-tern, pions decay into leptons (electrons/positrons, neutrinos) and photons. While the hadronization process is described in the QCD frame, the spectra of produced species are also determined mainly by QCD and should be similar to the collider result for $e + e \to \bar{q}q \to$ nucleons + pions [21]. Calculation of the particle energy spectra at the M_X energy scale suggests the flat power-law energy spectrum $N(E) = KE^{-\gamma}$ with $\gamma = 1.9$ with photon dominated flux as a robust signature of decaying origin. The photon/nucleon fraction in the calculated spectra is in the range $N_\gamma(E)/N_n(E) \approx (2\text{—}3)$ [6] (Fig. 8.11). Therefore the X-particles with masses $M_X \geq 10^{21}$ eV and the life time of order of the age of the Universe could contribute to the observable flux of the ultra high energy cosmic rays.

8.3.4. Constrains on superheavy dark matter from recent ultra high energy cosmic ray observations

Secondary relativistic particles produced by the decay of X-particles should contribute to the observable flux of cosmic rays in the energy range $E \leq M_X/2$, i.e., for $M_X \geq 10^{20}$ eV in the ultra high energy cosmic rays range. Very low flux of the ultra high energy cosmic ray demands very large effective areas of detectors (about 3 000 km^2 in the case of Auger surface detectors). Fig. 8.12 shows the dynamics of exposure increasing of running and future cosmic ray detectors.

It is believed that the dominant part of UHECRs is accelerated in astrophysical sources which satisfy the energy requirements, namely, a demand of particle confinement in acceleration region limits the maximum energy of accelerated particle of electric charge Z to the value $E_{\max}(\text{eV}) = 300\, Z\, B(\text{G})\, R(\text{cm})$. Fig. 8.13 shows that a few sources can accelerate UHECRs up to the maximum detected energy 3×10^{20} eV. Among them there are active galactic nuclei (AGN), gamma-ray bursts (GRB), hot spots (the regions of termination shocks) in radiogalaxy lobes, accretion shocks in the intergalactic medium (IGM) around the large scale structure elements (clusters of galaxies, filaments).

Despite the detailed investigations of the UHECR spectrum and presented above list of viable sources, we still have not identified any specific source of

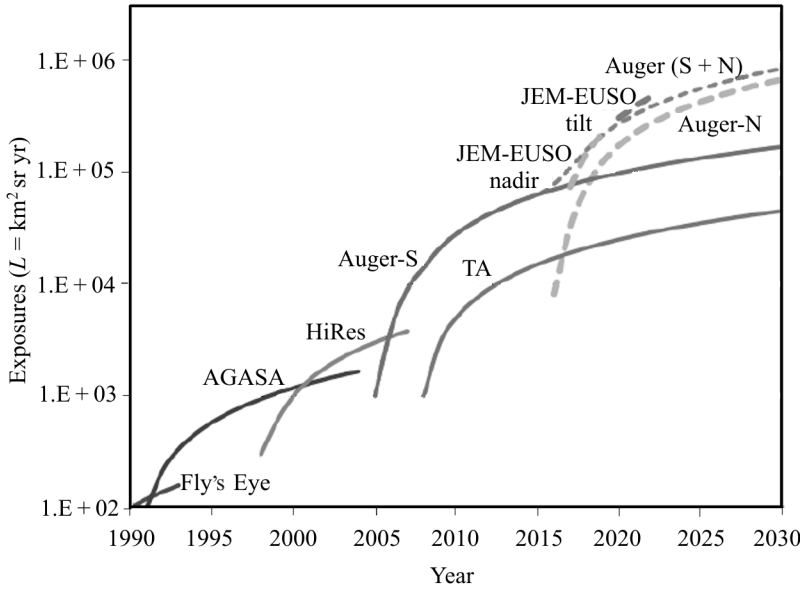

Fig. 8.12. Past (Fly's Eye, AGASA, HiRes (High Resolution Fly's Eye)), present (Auger-South, Telescope Array (TA)) and future (Auger-North, JEM-EUSO (nadir and tilt modes)) experiments for detection of ultra high energy cosmic rays with energy $\geq 10^{18}$ eV. Figure is taken from [8]

UHECRs due to deflections of UHECR trajectories in the intergalactic and Galactic magnetic fields. We do not have robust data on abundances (chemical composition) of UHECRs as well. As result we cannot separate a possible contribution of UHECRs from SHDM decay in total observable flux. But it is promising to search for some distinctive features of SHDM decay. For example, the flux of UHE protons from cosmological sources should be characterized by a sharp steepening at energy 6×10^{19} eV (the well known Greisen—Zatsepin—Kuzmin (GZK) cut-off), i.e., at the threshold energy of the photopion interaction of relativistic protons with the CMB radiation field [44, 84]. Therefore, only sources inside a characteristic radius (aka GZK-radius) of order of $R_{\rm GZK} \leq 50$ Mpc contribute effectively to the UHECR flux in $\sim 10^{20}$ eV range. Meantime, the energy spectrum of UHECRs produced via X-particle decay in the halo of our Galaxy does not suffer from GZK-effect and should extend up to $\sim M_X/2$ region. About ten years ago the AGASA experiment announced the detection of 11 events with energy $E > 10^{20}$ eV without any signatures of the GZK effect, but more recent detectors HiRes, Auger, and Telescope Array have found the robust feature of GZK cut-off in UHECR spectrum, considerably decreasing the possible contribution of DM decaying particles in total flux and shifting DM search window to the highest energies $\geq 10^{20}$ eV. Besides the new detectors with improved statistics, the search for DM features requires the clarification of the nature of detected UHECR particles — their chemical composition, acceleration energy, and energy losses during the propagation etc.

Observable spectrum of UHECRs is a result of joint action of different processes, including acceleration in sources with formation of "generation spectrum", modification of spectrum during the propagation in intergalactic and Galactic magnetic and radiation background fields, generation of air shower in atmosphere. The solution of an inverse problem of recovering the nature of UHECR is a complicated task, to this end it is useful to start with the investigation of proton fraction in the total flux of UHECRs, since hydrogen atoms are the most abundant in the Universe and relativistic protons dominate in the Galactic CR flux.

The propagation of protons in the intergalactic medium induces two distinct features in their spectrum observed at the Earth: mentioned above GZK feature and dip, generated due to pair production process $p + \gamma_{\rm CMB} \rightarrow \rightarrow p + e^+ + e^-$, where the target is provided by the CMB photons. The detection of these features would be a definitive test of the extragalactic origin of UHECRs and of the fact that they are mainly protons [5]. The proton contribution can be estimated using the formalism of the modification factor, first introduced in [17] and defined as the ratio of the spectrum $J_p(E)$ with all energy losses taken into account and the unmodified spectrum $J_p^{\rm un}(E)$, where only adiabatic energy losses (red shift) are included: $\eta(E) = J_p(E)/J_p^{\rm un}$. The spectrum $J_p(E)$ calculated for a power-law generation spectrum $Q_{\rm gen}(E) =$

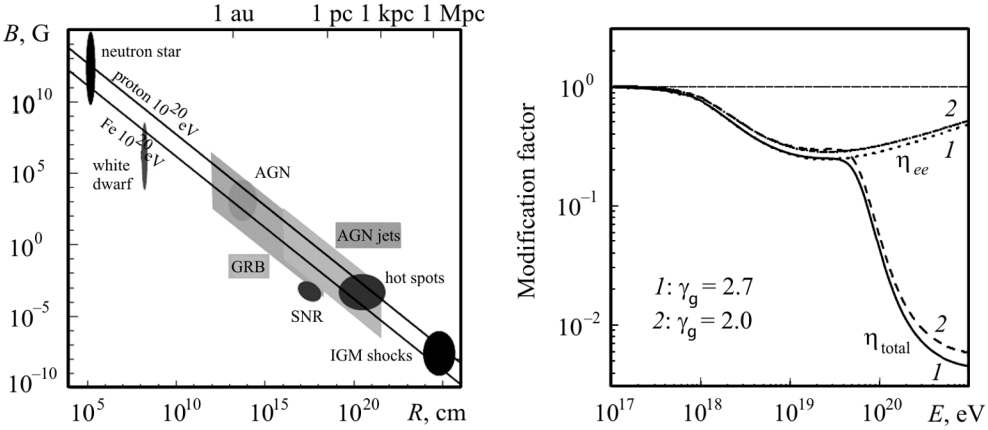

Fig. 8.13. Hillas diagram shows the necessary combination of sizes and magnetic fields of astrophysical objects-candidates for ultra high energy cosmic ray accelerators. Figure is taken from [55]

Fig. 8.14. Modification factor for a power-law generation spectrum with slope $\gamma = 2.0$ (line *2*) and $\gamma = 2.7$ (line *1*). The horizontal line $\eta = 1$ corresponds to adiabatic energy losses only. The curves η_{ee} and $\eta_{\rm tot}$ correspond respectively to the modification factor for adiabatic and pair production energy losses and to the modification factor where all losses are taken into account. Figure is taken from [5]

$= KE^{-\gamma}$ and for a homogeneous distribution of sources, is called "universal spectrum". The important feature of the universal spectrum is its independence of the mode of propagation: it is the same for rectilinear propagation and propagation in arbitrary magnetic fields. In Fig. 8.14 the modification factor as a function of energy for two slopes of the injection spectrum, $\gamma = 2.0$ and $\gamma = 2.7$, is presented.

In Fig. 8.15 the comparison of the modification factor calculated for $\gamma = 2.7$ with the observational data of AGASA, HiRes, Yakutsk and Auger is shown [5]. The dip is well visible in the data at energy below $\sim 4 \times 10^{19}$ eV, above which the photopion production dominates.

Observable spectra show different amplitudes at the same energy, mainly due to systematic errors. In the frame of proton-dominated model the shape of the dip can be used for energy calibration of the detectors. Shifting the energies by a factor λ for each detector in the energy range of the dip one can determine the value of λ that fits the data in the best way for each experiment. This procedure leads to $\lambda = 0.9, 1.2, 0.75$ for AGASA, HiRes and Yakutsk detector, respectively. Agreement of shifted spectra (Fig. 8.16) confirms the proton-dominated composition (more recent data prefer the HiRes spectrum as reference spectrum with the same conclusion about proton spectrum).

From Fig. 8.15 it follows also that the flux of extragalactic protons dominates in the total flux at energy $E > E_{\rm cr} \sim 1 \times 10^{18}$ eV, i.e., the transition

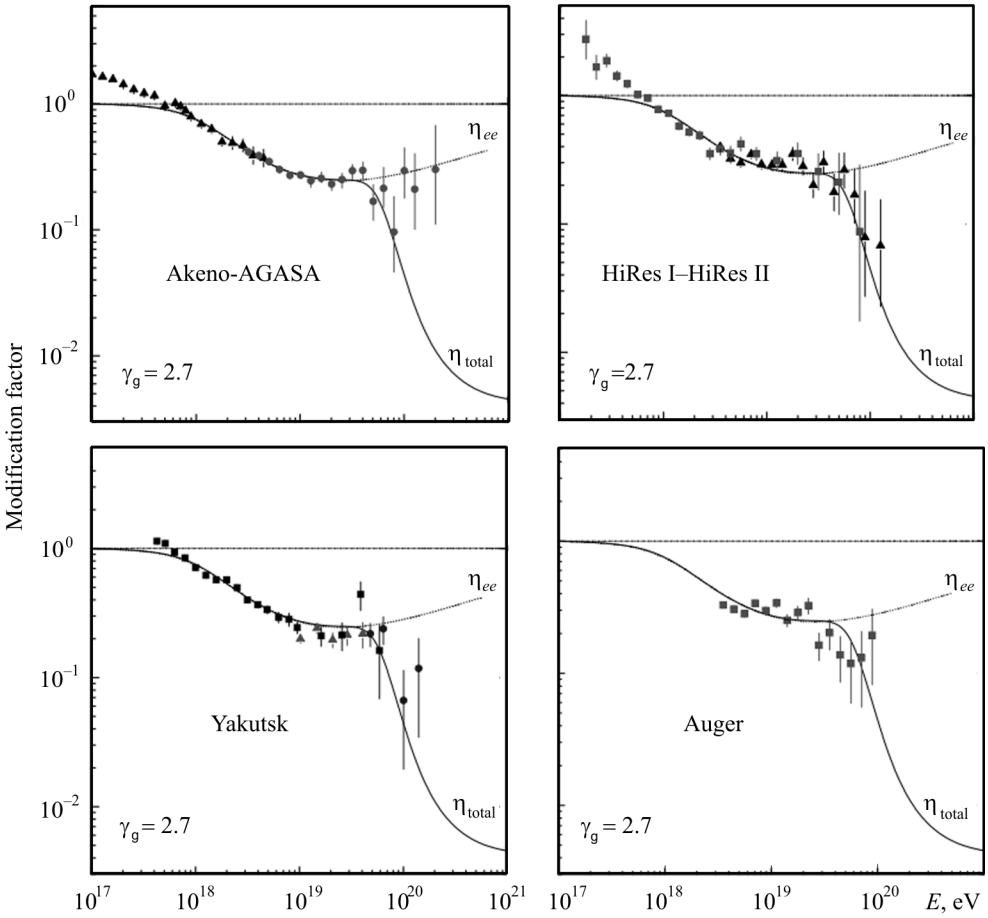

Fig. 8.15. Predicted proton-dominated energy spectrum with dip in comparison with AGASA, HiRes, Yakutsk and Auger data. Figure is taken from [5]

from Galactic to extragalactic cosmic rays takes place at energy $E_{\rm cr}$ [18]. This prediction of proton model is confirmed by the results of KASCADE experiment [51] on the dominance of heavy nuclei (up to iron nuclei) in the Galactic cosmic ray flux in the transition region. The structure of transition region in proton-dominated model is presented in Fig. 8.17. The extragalactic proton spectrum is shown for $Q_{\rm gen} = KE^{-2.7}$ generation spectrum and for propagation in magnetic field $B = 1$ nG with scale $l = 1$ Mpc. The distance between sources is $d = 50$ Mpc. $E_b = E_{\rm cr} = 1 \times 10^{18}$ eV is the beginning of the transition, $E_{\rm Fe}$ is the position of the iron knee and $E_{\rm tr}$ is the energy where the galactic and extragalactic fluxes are equal.

The presented here dip-transition model agrees well with the rigidity model for the origin of the first knee. In this model, the position of the first (proton) knee (Fig. 8.1, $E_p = 2.5 \times 10^{15}$ eV) is determined by the magnetic confinement

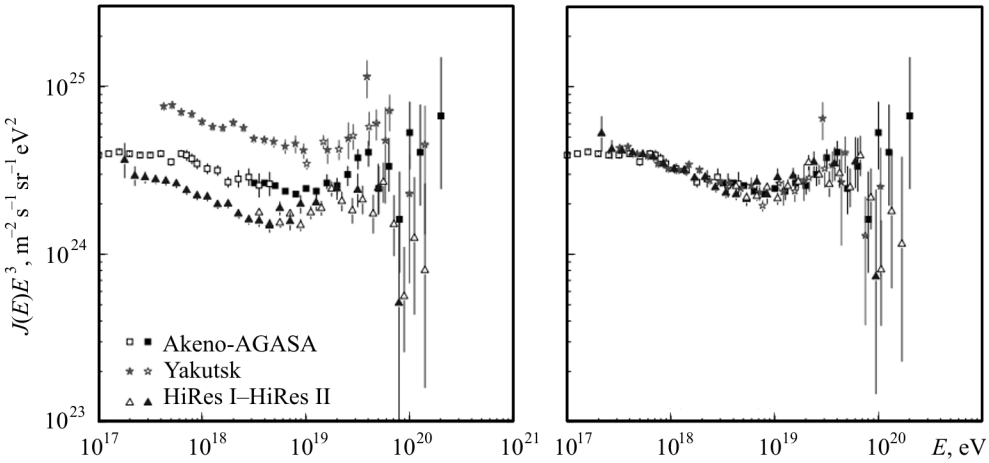

Fig. 8.16. The spectra as measured by Akeno-AGASA, HiRes and Yakutsk arrays (left panel) and after energy calibration by the dip (right panel). Figure is taken from [5]

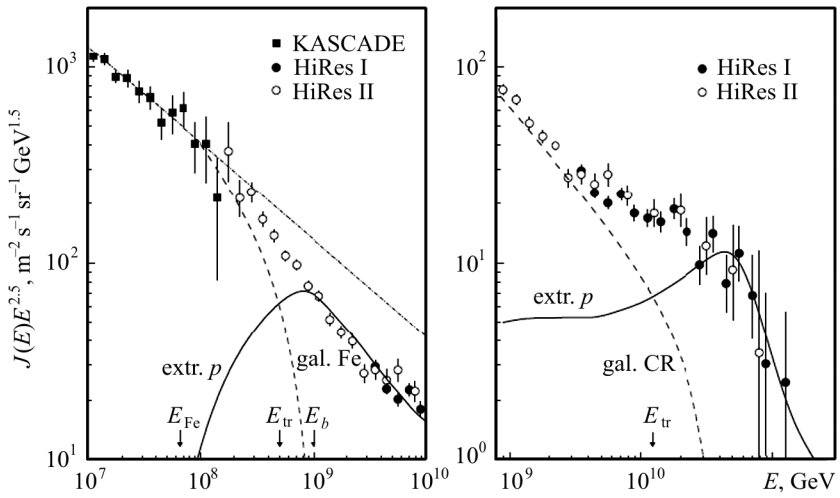

Fig. 8.17. Left panel: transition from Galactic to extragalactic cosmic rays in proton- dominated model (region of the second knee). Right panel: transition in the ankle model for the injection spectrum of extragalactic protons E^{-2}. In both cases the dashed line is obtained as a result of subtracting the extragalactic spectrum from the observed all-particle spectrum. See text for details. Figure is taken from [5]

of protons in the Galactic halo. In this case the knee in the spectrum of nuclei with charge Z is located at $E_Z = ZE_p$. The highest energy knee, due to iron, must be located at $E_{\rm Fe} = 6.5 \times 10^{16}$ eV. At energy $E > E_{\rm Fe}$ the total galactic flux consists mostly of iron.

Proposed for the first time about ten years ago, proton (aka dip) model naturally explains the main properties of extragalactic cosmic ray flux. Very recent data of Auger and Telescope Array are presented in Fig. 8.18.

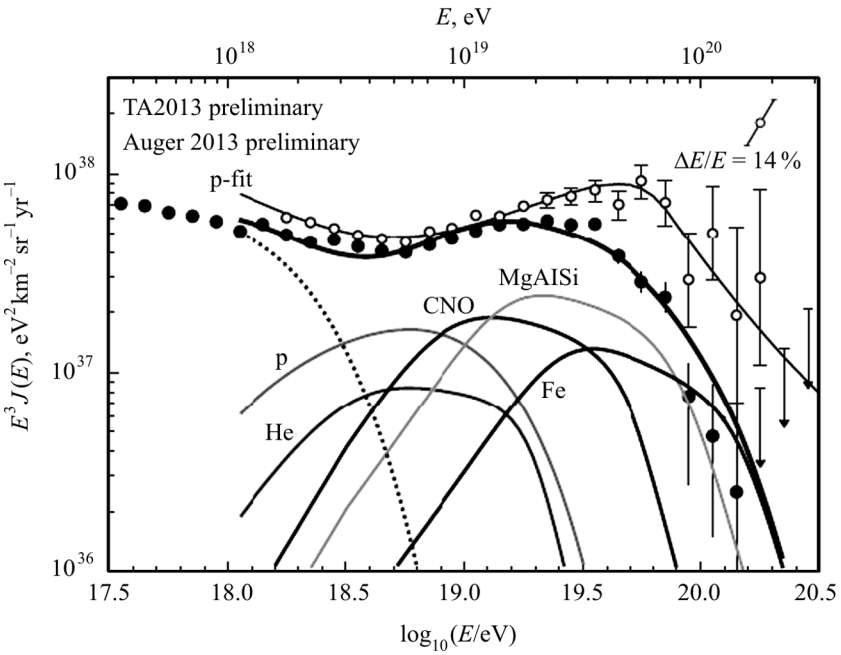

Fig. 8.18. Ultra high energy part of cosmic ray spectrum. Recent results of TA (upper line p-fit) and Auger (black points) collaborations are presented. TA data are fitted according to the proton-dominated dip model, Auger data — according to the ankle model with additional galactic component (dotted line). See text for details. Figure is taken from [52]

The TA-data are very well fitted by the proton model with $E^{-2.39}$ generation spectrum (p-fit line). The Auger data are fitted by the mixed composition model with the maximum acceleration energy of nuclei of charge Z $E_{\max} = 5\times10^{18}Z$ eV and $E^{-2.0}$ generation spectrum. Auger data may be agreed with a proton model as well taking into account the systematic errors $\Delta E/E \sim 14\,\%$. Meantime, the chemical composition is an unresolved problem: TA data agree with a pure proton flux, while Auger data suggest the increasing of fraction of heavy nuclei at the highest energy. The latter case can be explained in mixed composition model, where the extragalactic flux dominates only after the ankle (ankle model) and has a mixed composition of nuclei from protons to irons. The weakness of the ankle model is the need to introduce a new Galactic component at energy up to $\sim 3 \times 10^{18}$ eV.

Both proton and ankle (with mixed composition) models explain UHECR spectrum without the involvement of decaying component produced by SHDM. Additional constraints follow from the recently determined upper limits on ultra high energy photon flux from Auger Surface Detector (SD) and Hybrid (SD and fluorescence telescope) data [66] (Fig. 8.19).

As it was mentioned above, the distinctive feature of SHDM decay is the photon (and neutrino) dominated flux. Of course, this limits disfavor, but do

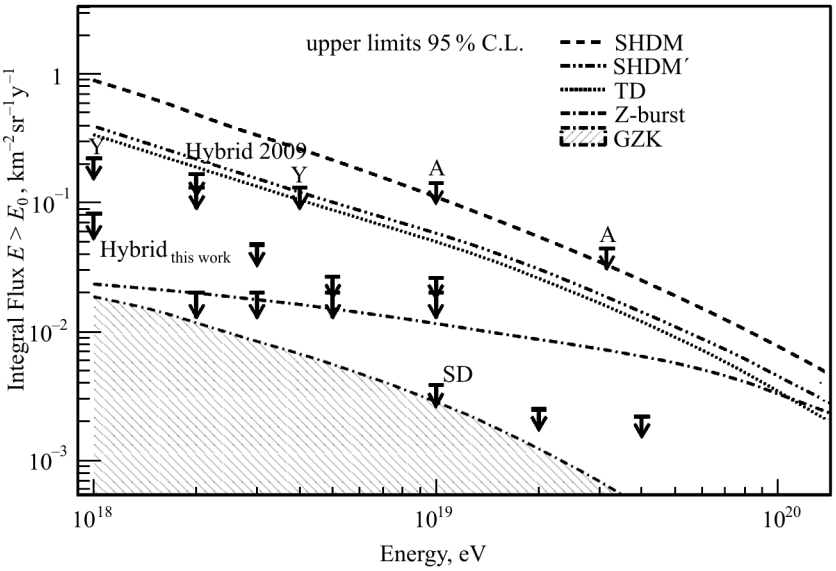

Fig. 8.19. Upper limits on ultra high energy photon flux from Auger Surface Detector (SD) and Hybrid (SD and fluorescence telescope) data [66]. Theoretical predictions from models of super-heavy dark matter (SHDM), topological defects (TD), Z-bursts, and the expected flux due to the Greisen—Zatsepin—Kuzmin (GZK) effect are also presented. Figure is taken from [66]

not exclude the SHDM contribution to the observed UHECR spectrum. New observations with higher statistics in post-GZK range ($E \geq 10^{20}$ eV) are still very promising for indirect detection of SHDM.

8.4. Conclusion

Despite considerable efforts, the indirect search for astrophysical signatures of dark matter has not yet come to fruition. Nevertheless, in quite a number of experiments we expect to find manifestations of dark matter. In addition to the considered above cosmic ray window, a recent indirect dark matter experiments include a search for annihilating or decaying products of dark matter in X-ray, γ-ray and neutrino windows [27]. Improvement of statistics (XMM-NEWTON, FERMI-LAT, AMS etc.) and upgrading (Auger, Telescope Array, IceCube, HESS etc.) of running experiments together with the realization of new experiments (JEM-EUSO, GAMMA-400 etc.) in the near future offer a great promise in the indirect dark matter detection.

Bibliography

1. O. Adriani, G.C. Barbarino, G.A. Bazilevskaya et al., An anomalous positron abundance in cosmic rays with energies 1.5—100 GeV, Nature **458**, 607 (2009).
2. O. Adriani, G.C. Barbarino, G.A. Bazilevskaya et al., Cosmic-Ray Electron Flux Measured by the PAMELA Experiment between 1 and 625 GeV, Phys. Rev. Lett. **106**, 201101 (2011).
3. M. Ackermann, M. Ajello, W.B. Atwood, L. Baldini et al., Fermi LAT observations of cosmic-ray electrons from 7 GeV to 1 TeV, Phys. Rev. D **82**, 092004 (2010).
4. M. Ackermann, M. Ajello, A. Allafort et al., Measurement of Separate Cosmic-Ray Electron and Positron Spectra with the Fermi Large Area Telescope, Phys. Rev. Lett. **108**, 011103 (2012).
5. R. Aloisio, V. Berezinsky, P. Blasi, A. Gazizov et al, A dip in the UHECR spectrum and the transition from galactic to extragalactic cosmic rays, Astropart. Phys. **27**, 76 (2007).
6. R. Aloisio, F. Tortorici, Super Heavy Dark Matter and UHECR Anisotropy at Low Energy, Astropart. Phys. **29**, 307 (2008).
7. AMS Collaboration: M. Aguilar et al., First Result from the Alpha Magnetic Spectrometer on the International Space Station: Precision Measurement of the Positron Fraction in Primary Cosmic Rays of 0.5—350 GeV, Phys. Rev. Lett. **110**, 141102 (2013).
8. L.A. Anchordoqui, G.R. Farrar, J.F. Krizmanic, J. Matthews et al., Roadmap for Ultra-High Energy Cosmic Ray Physics and Astronomy (whitepaper for Snowmass 2013), ArXiv e-prints 1307.5312v2 (2013).
9. N. Arkani-Hamed, D.P. Finkbeiner, T.R. Slatyer, N. Weiner, A theory of dark matter, Phys. Rev. D **79**, 015014 (2009).
10. B. Aschenbach, R. Egger, J. Trümper, Discovery of explosion fragments outside the Vela supernova remnant shock-wave boundary, Nature **373**, 587 (1995).
11. V. Berezinsky, M. Kachelrieß, M.A. Solberg, Supersymmetric superheavy dark matter, Phys. Rev. D **78**, 123535 (2008).
12. V. Berezinsky, B. Hnatyk, A. Vilenkin, Gamma ray bursts from superconducting cosmic strings, Phys. Rev. D **64**, 043004 (2001).
13. V. Berezinsky, M. Kachelrieß, A. Vilenkin, Ultra-high energy cosmic rays without GZK cutoff, Phys. Rev. Lett. **79**, 4302 (1997).
14. V. Berezinsky, B. Hnatyk, A. Vilenkin, Superconducting Cosmic Strings as Gamma-Ray Burst Engines, Baltic Astronomy **13**, 289 (2004).

15. V. Berezinsky, E. Sabancilar, A. Vilenkin, Extremely High Energy Neutrinos from Cosmic Strings, Phys. Rev. D **84**, 085006 (2011).
16. V. Berezinsky, P. Blasi, A. Vilenkin, Signatures of topological defects, Phys. Rev. D **58**, 103515 (1998).
17. V.S. Berezinsky, S.I. Grigorieva, A bump in the ultra-high energy cosmic ray spectrum, Astron. Astrophys. **199**, 1 (1988).
18. V.S. Berezinsky, S.I. Grigorieva, B.I. Hnatyk, Extragalactic UHE proton spectrum and prediction of flux of iron-nuclei at 10^8—10^9 GeV, Nucl. Phys. B Proc. Suppl. **151**, 497 (2006).
19. L. Bergström, Saas-Fee Lecture Notes: Multi-messenger Astronomy and Dark Matter, ArXiv e-prints 1202.1170 (2012).
20. B. Bertucci and the AMS-02 Collaboration, Precision measurement of the electron plus positron spectrum with AMS, Talk at the 33rd ICRC Conference (2013).
21. P. Bhattacharjee, G. Sigl, Origin and Propagation of Extremely High Energy Cosmic Rays, Phys. Rept. **327**, 109 (2000).
22. P. Blasi, E. Amato, Positrons from pulsar winds, High-Energy Emission from Pulsars and their Systems: Proceedings of the First Session of the Sant Cugat Forum on Astrophysics, Astrophys. Space Sci. Proceedings, 624 (2011).
23. K. Blum, Cosmic ray propagation time scales: lessons from radioactive nuclei and positron data, J. Cosmol. Part. Phys. **11**, 37 (2011).
24. K. Blum, B. Katz, E. Waxman, AMS-02 Results Support the Secondary Origin of Cosmic Ray Positrons, Phys. Rev. Let. **111**, 211101 (2013).
25. J. Blumer, R. Engel, J.R. Horandel, Cosmic Rays from the Knee to the Highest Energies, Prog. Part. Nucl. Phys. **63**, 29 (2009).
26. J.C. Brandt, T.P. Stecher, D.L. Crawford, S.P. Maran, The GUM Nebula: Fossil STRÖMGREN Sphere of the VELA X Supernova, Astrophys. J. **163**, L99 (1971)
27. J. Buckley, D.F. Cowen, S. Profumo, A. Archer et al., Cosmic Frontier Indirect Dark Matter Detection Working Group Summary, ArXiv e-prints 1310.7040 (2013).
28. I.Cholis, D. Hooper, Constraining the origin of the rising cosmic ray positron fraction with the boron-to-carbon ratio, Phys. Rev. D **89**, 043013 (2014).
29. D.J.H. Chung, E.W. Kolb, A. Riotto, Superheavy dark matter, Phys. Rev. D **59**, 023501 (1999).
30. D.F. Cioffi, C.F. McKee, E. Bertschinger, Dynamics of radiative supernova remnants Astrophys. J., **334**, 252 (1988).
31. M. Cirelli, M. Kadastik, M. Raidal, A. Strumia, Model-independent implications of the e+, e-, anti-proton cosmic ray spectra on properties of Dark Matter, Nucl. Phys. B **813**, 1 (2009).
32. D. Clowe et al., A direct empirical proof of the existence of dark matter, Astrophys. J. **648**, 109 (2006).
33. R. Cowsik, B. Burch, T. Madziwa-Nussinov, The origin of the spectral intensities of cosmic-ray positrons, Astrophys. J. **786**, 124 (2014).
34. R. Cowsik, B. Burch, Positron fraction in cosmic rays and models of cosmic-ray propagation, Phys. Rev. D **82**, 023009 (2010).
35. P.Cushman, C. Galbiati, D.N. McKinsey, H. Robertson et al., Snowmass CF1 Summary: WIMP Dark Matter Direct Detection, ArXiv e-prints 1310.8327 (2013).

36. T. Damour, A. Vilenkin, Gravitational radiation from cosmic (super)strings: Bursts, stochastic background, and observational windows, Phys. Rev. D **71**, 063510 (2005).
37. T. Delahaye, J. Lavalle, R. Lineros, F. Donato, Galactic electrons and positrons at the Earth: new estimate of the primary and secondary fluxes, Astron. Astrophys. **524**, 51 (2010).
38. M. Di Mauro, F. Donato, N. Fornengo, R. Lineros et al. Interpretation of AMS-02 electrons and positrons data, J. Cosmol. Astropart. Phys. **04**, 006 (2014).
39. F. Donato, Indirect searches for dark matter, Physics of the Dark Universe **4**, 41 (2014).
40. J. Ellis, Theory Summary and Prospects, ArXiv e-prints 1408.5866 (2014).
41. J.L. Feng, Dark Matter Candidates from Particle Physics and Methods of Detection, Ann. Rev. Astron. Astrophys. **48**, 495 (2010).
42. D.S. Gorbunov, V.A. Rubakov, Introduction to the Theory of the Early Universe: Hot Big Bang Theory (World Scientific Pub. Co., Singapore, 2011).
43. D.S. Gorbunov, V.A. Rubakov, Introduction to the Theory of the Early Universe: Cosmological Perturbations and Inflationary Theory (World Scientific Pub. Co., Singapore, 2011).
44. K. Greisen, End to the cosmic ray spectrum?, Phys. Rev. Lett. **16**, 748 (1966).
45. C. Grupen, Early developments: Particle physics aspects of cosmic rays, Astropart. Phys. **53**, 86 (2014).
46. C.S. Gum, A large H II region at galactic longitude 226 deg, Observatory **72**, 151 (1952).
47. E. Hawkins, S. Maddox, S. Cole, D. Madgwick, P. Norberg et al., The 2dF Galaxy Redshift Survey: Correlation functions, peculiar velocities and the matter density of the universe, Mon. Not. Roy. Astron. Soc. **346**, 78 (2003).
48. M. Hindmarsh, Signals of Inflationary Models with Cosmic Strings, Progr. Theor. Phys. Suppl. **190**, 197 (2011).
49. D. Hooper, P. Blasi, P.D. Serpico, Pulsars as the Sources of High Energy Cosmic Ray Positrons, J. Cosmol. Astropart. Phys. **01**, 025 (2009).
50. R. Jeannerot, J. Rocher, M. Sakellariadou, How generic is cosmic string formation in SUSY GUTs, Phys. Rev. D **68**, 103514 (2003).
51. K.-H. Kampert et al., (KASCADE-Collaboration), Proceedings of 27th ICRC, volume "Invited, Rapporteur, and Highlight papers of ICRC 240 (2001).
52. K.-H. Kampert, P. Tinyakov, Cosmic Rays from the Ankle to the Cut-Off, Comptes rendus, Physique **15**, 318 (2014).
53. B. Katz, K. Blum, J. Morag, E. Waxman, What can we really learn from positron flux 'anomalies'?, Mon. Not. Roy. Astron. Soc. **405**, 1458 (2010).
54. E. Komatsu et al., Seven-Year Wilkinson Microwave Anisotropy Probe (WMAP) Observations: Cosmological Interpretation, Astrophys. J. Suppl. **192**, 47 (2011).
55. K. Kotera, A.V. Olinto, The Astrophysics of Ultrahigh-Energy Cosmic Rays, Ann. Rev. Astron. Astrophys. **49**, 119 (2011).
56. A. Kusenko, L.J. Rosenberg, Snowmass-2013 Cosmic Frontier 3 (CF3) Working Group Summary: Non-WIMP dark matter, ArXiv e-prints 1310.8642 (2013).
57. A.D. Lewis, D.A. Buote, J.T. Stocke, Chandra Observations of Abell 2029: The Dark Matter Profile at $<0.01 R_{\rm vir}$ in an Unusually Relaxed Cluster, Astrophys. J. **586**, 135 (2003).

58. Ph. Mertsch, S. Sarkar, AMS-02 data confronts acceleration of cosmic ray secondaries in nearby sources, ArXiv e-prints 1402.0855v2 (2014).
59. I.V. Moskalenko, Cosmic Rays in the Milky Way and Beyond, Nucl. Phys. B Proc. Suppl. **243**, 85 (2013).
60. I.V. Moskalenko, A.W. Strong, Production and Propagation of Cosmic-Ray Positrons and Electrons, Astrophys. J. **493**, 694 (1998).
61. PAMELA Collaboration: O. Adriani et al., The cosmic-ray positron energy spectrum measured by PAMELA, Phys. Rev. Lett. **111**, 081102 (2013).
62. A.D. Panov et al., Possible structure in the cosmic ray electron spectrum measured by the ATIC-2 and ATIC-4 experiments, Astrophys. Space Sci. Trans. **7**, 119 (2011).
63. Particle Data Group Collaboration: B.D. Fields, S. Sarkar, Big Bang nucleosynthesis, Phys. Lett. **667**, 228 (2008).
64. S. Perlmutter, G. Aldering, G. Goldhaber et al., Measurements of Omega and Lambda from 42 high redshift supernovae, Astrophys. J. **517**, 565 (1999).
65. T. Pierog, LHC results and High Energy Cosmic Ray Interaction Models, J. Phys. Conf. Ser. **409**, 012008 (2013).
66. The Pierre Auger Collaboration: P. Abreu, M. Aglietta, E.J. Ahn, I.F.M. Albuquerque et al., The Pierre Auger Observatory III: Other Astrophysical Observations, ArXiv e-prints 1107.4805 (2011).
67. Planck Collaboration: P.A.R. Ade, N. Aghanim, C. Armitage-Caplanet, M. Arnaud et al., Planck 2013 results. XVI. Cosmological parameters, ArXiv e-prints 1303.5076 (2013).
68. P. Pralavorio, Particle Physics and Cosmology, ArXiv e-prints 1311.1769v1 (2013).
69. A. Refregier, Weak Gravitational Lensing by Large-Scale Structure, Ann. Rev. Astron. Astrophys. **41**, 645 (2003).
70. A.G. Riess, A.V. Filippenko, P. Challis et al., Observational evidence from supernovae for an accelerating universe and a cosmological constant, Astron. J. **116**, 1009 (1998).
71. V.C. Rubin, W.K. Ford, Jr., Rotation of the Andromeda Nebula from a Spectroscopic Survey of Emission Regions, Astrophys. J. **159**, 379 (1970).
72. V.C. Rubin, N. Thonnard, W.K. Ford, Jr., Rotational properties of 21 SC galaxies with a large range of luminosities and radii, from NGC 4605 ($R = 4$ kpc) to UGC 2885 ($R = 122$ kpc), Astrophys. J. **238**, 471 (1980).
73. P. Salati, F. Donato, N. Fornengo, Indirect Dark Matter Detection with Cosmic Antimatter, Cambridge University Press 521 (2010).
74. R. Schild, I.S. Masnyak, B.I. Hnatyk, V.I. Zhdanov, Anomalous fluctuations in observations of Q 0957 + 561 A, B: Smoking gun of a cosmic string?, Astron. Astrophys. **422**, 477 (2004).
75. SDSS Collaboration: M. Tegmark et al., Cosmological parameters from SDSS and WMAP, Phys. Rev. D **69**, 103501 (2004).
76. P.D. Serpico, Astrophysical models for the origin of the positron "excess", Astropart. Phys. **39**, 2 (2012).
77. S. Shael and the AMS-02 Collaboration, Precision measurements of the electron spectrum and the positron spectrum with AMS, Talk at the 33rd ICRC Conference (2013).

78. N.J. Shaviv, E. Nakar, T. Piran, Inhomogeneity in Cosmic Ray Sources as the Origin of the Electron Spectrum and the PAMELA Anomaly, Phys. Rev. Lett. **103**, 111302 (2009).
79. I. Sushch, B. Hnatyk, Modelling of the radio emission from the Vela supernova remnant, Astron. Astrophys. **561**, 139 (2014).
80. I. Sushch, B. Hnatyk, A. Neronov, Modeling of the Vela complex including the Vela supernova remnant, the binary system γ^2 Velorum, and the Gum nebula, Astron. Astrophys. **525**, 154 (2011).
81. J.A. Tyson, G.P. Kochanski, I.P. Dell'Antonio, Detailed Mass Map of CL 0024 + 1654 from Strong Lensing, Astrophys. J. **498**, 107 (1998).
82. A. Vilenkin, E. Shellard, Cosmic strings and other topological defects (Cambridge University Press, Cambridge, 1994).
83. Q. Yuan, X.-J. Bi, G.-M. Chen et al., Implications of the AMS-02 positron fraction in cosmic rays, Astropart. Phys. **60**, 1 (2015).
84. G. Zatsepin, V. Kuzmin, Upper limit of the spectrum of cosmic rays, J. Exp. Theor. Phys. Lett. **4**, 78 (1966).
85. F. Zwicky, Spectral displacement of extra galactic nebulae, Helv. Phys. Acta **6**, 110 (1933).

INDEX

ABOUT THE AUTHORS

Petro FOMIN (1930–2011) was the leading Ukrainian scientist in the field of the quantum field theory and cosmology; the founder and head of the Ukrainian Society for Gravity and Relativity Theory. After graduating from the Kharkiv State University in 1953, he entered the postgraduate courses at the same university under the supervision of Prof. A.I. Akhiezer. Since 1957, he worked at the Kharkiv Institute of Physics and Technology, where he defended PhD and DrSci theses. Since 1972 till the end of his life, he worked as the head of Department of Astrophysics and Elementary Particles at the Bogolyubov Institute for Theoretical Physics of the NAS of Ukraine (Kyiv) and, since 1994, also as the head of Department at the Institute of Applied Physics of the NAS of Ukraine (Sumy city). In 1990, P.I. Fomin was elected the Corresponding member of the NAS of Ukraine. P.I. Fomin is the author of well-known fundamental papers in quantum field theory, astrophysics, and theoretical cosmology (more than 170 papers in leading physical journals). Among his most famous results are description of higher-order radiation effects in scattering processes, solutions of superconducting type for fermionic spectrum in quantum electrodynamics, and the pioneer idea of quantum creation of a baby universe from the vacuum as a result of gravitational instability. Laureate of the Barabashov Prize of the National Academy of Sciences of Ukraine (1986) and of the State Prize of Ukraine (2006) for his outstanding achievements in the theoretical physics.

Alina FOMINA, research scientist of the Bogolyubov Institute for Theoretical Physics of the National Academy of Sciences of Ukraine (BITP NASU). She was graduated from the Taras Shevchenko National University of Kyiv (KNU) in 1998 and obtained PhD degree in Theoretical Physics in 2004. Her research interests include cosmology and high-energy astrophysics. Author and co-author of about 20 papers in leading international and Ukrainian physical journals.

Iurii BABYK, junior scientific researcher of the Astro-Informatics Laboratory of the Astro-Space Information-Computing Centre of the Main Astronomical Observatory of the NAS of Ukraine (MAO NASU). Graduated from the Taras Shevchenko National University of Kyiv in 2009 and post-graduated in 2012. Since 2011 he works at the MAO NASU. PhD in Astrophysics and Radio astronomy (2014). Scientific interests: high energy astrophysics, cosmology, galaxy clusters, and dark matter. Visiting scientist at the Dublin Institute for Advanced Studies and at the Dublin City University (2012—2014). Author and coauthor of more than 20 papers and one textbook for students. His scientific activity was awarded by the Grant of the President of Ukraine for young scientists (2014). Additional activity: LOC member of the Annual Young Scientists' Conferences on Astronomy and Space Physics (Kyiv, Ukraine).

Irina VAVILOVA, head of the AstroInformatics Laboratory of the Astro-Space Information-Computing Centre of the Main Astronomical Observatory of the NAS of Ukraine (MAO NASU, Kyiv). Graduated from the Taras Shevchenko National University of Kyiv (KNU) in 1984. She started scientific research in astrophysics at the KNU, where she worked till 2004; in 2004—2007 — at the Dobrov Centre for Research of Scientific Potential and History of Science of the NAS of Ukraine; since 2008 — at the MAO NASU. PhD in Astrophysics and Radio astronomy (1995). Research Fellow at the Maryland University (Maryland, USA), visiting scientist at the Kielce Pedagogical University (Kielce, Poland), Institute for Nuclear Research (Cracow, Poland), University La Sapienza (Rome, Italy), Oxford University (Oxford, UK), and the National Astronomical Research Institute of Thailand (Chang Mai, Thailand). The interests are in extragalaxy astronomy, observational cosmology, mathematical methods in astrophysics, and history of astronomy. Author and coauthor of 7 monographs and textbooks for students, and more than 60 papers in leading astronomical journals. She is awarded the State Order of Princess Olga of 3rd grade (2002), the Honor Diploma of the Presidium of the NAS of Ukraine (2010), and the Fedorov Prize of the NAS of Ukraine (2014) for her scientific research activity.

Olga MELNYK, research scientist of the Astronomical Observatory of the Taras Schevchenko National University of Kyiv (KNU). Graduated from the National Technical University "Kyiv Polytechnical Institute" in 2003. Postgraduate student in 2003—2006 (KNU). PhD degree in Astrophysics and Radioastronomy was obtained in 2007. After that she started working as an junior research scientist at the KNU. In 2009—2013 she has worked at the Department of Astrophysics and Geophysics of the Liege University, Belgium, as a postdoctoral researcher. Since 2014 she is a visitor researcher at the Department of Physics and Astrophysics of the University of Bologna. Her scientific interests are the evolution of galaxies and active galactic nuclei, large scale structure of the Universe. Laureate of the Award of the President of Ukraine for her scientific activity (2014). Author and coauthor of more than 30 papers in leading astronomical journals.

Andrii ELYIV, Senior Research Scientist of the Astro-Informatics Laboratory of the Astro-Space Information-Computing Centre of the Main Astronomical Observatory of the NAS of Ukraine (MAO NASU). He was graduated from the Ivan Franko National University of Lviv in 2003 (BSs) and the Taras Shevchenko National University of Kyiv (MSc) in 2004. PhD degree in Astrophysics and Radioastronomy was obtained in 2007. Scientific interests: High Energy Astrophysics and Optical Astronomy, Large Scale Structure of the Universe. Visiting scientist at the University of Liege, Belgium (2009—2013) and the University of Bologna, Italy (2013—2015). Author and coauthor of more than 30 papers in leading astronomical journals. His scientific activity was awarded by the Grant of the President of Ukraine for young scientists (2011—2012).

Nadiia PULATOVA, junior research scientist of the SRI "Crimean Astrophysical Observatory" of the Taras Shevchenko National University of Kyiv (CrAO, Nauchnyj, Crimea, Ukraine). Graduated from the National Technical University "Kyiv Polytechnical Institute" in 2005 (BSc degree) and the Taras Shevchenko National University of Kyiv (KNU) in 2006 (MSc degree). Postgraduate student in 2006—2009 (KNU). She worked at the Main Astronomical Observatory of the NAS of Ukraine in 2009—2011, since 2011 — at the CrAO. PhD in Astrophysics and Radio astronomy (2011). Postdoctoral Fellow (2013—2014) at the National Astronomical Research Institute of Thailand (Chang Mai, Thailand). The interests are in extragalaxy astronomy. Author and coauthor of more than 20 papers in leading astronomical journals. Her scientific activity was awarded by the Award of the President of Ukraine for young scientists (2013).

Sergey SERGEEV, head of the laboratory of the extragalactic research and gamma-ray astronomy of the SRI "Crimean Astrophysical Observatory" of the Taras Shevchenko National University of Kyiv (CrAO, Nauchny, Crimea, Ukraine). Graduated from the Kazan State University in 1986. Engineer of the Mordovia State University in 1986—1987. Postgraduate student in 1987—1990 (CrAO). Since 1990 he works at the CrAO. PhD and DrSc in Astrophysics and Radio astronomy in 1999 and 2012, respectively. The main scientific interests are the active galactic nuclei, supermassive black holes, observational methods, data analysis, and software development. Author and coauthor of more than 80 papers in the leading astronomical journals (most of them in the international ones). He is honored worker of science and technology of the Autonomous Republic of Crimea of Ukraine as well as the referee of the Astrophysical Journal and Monthly Notices of the Royal Astronomical Society.

Alexey BOYARSKY, assistant professor at the Leiden University (The Netherlands). Graduated from the Moscow Institute for Physics and Technology in 1995. He obtained PhD degree at the Institute for Nuclear Research of the Russian Academy of Sciences in 1999. Postdoctoral fellow in Spinoza Institute (The Netherlands, 1999—2001), Niels Bohr Institute (Denmark, 2001—2003), EPFL (Switzerland, 2003—2005), CERN (2005—2012), ETH Zurich (2007—2011). Research scientist of the Bogolyubov Institute for Theoretical Physics of National Academy of Sciences of Ukraine (BITP NASU, 2008—2012, on leave). His research interests include dark matter phenomenology (structure formation, signature in X- and gamma-rays, sterile neutrinos), particle theory (axions, extra dimensions, quantum anomalies), quantum cosmology (quantum black hole models), quantum Hall effect and integrable systems. Author and co-author of about 60 papers in leading international physical journals.

Dmytro IAKUBOVSKYI, research scientist of the Bogolyubov Institute for Theoretical Physics of National Academy of Sciences of Ukraine ((BITP NASU). Graduated from the Taras Shevchenko National University of Kyiv (KNU) in 2004. He started research activity at the BITP NASU in 2002, where he obtained PhD degree in Theoretical Physics in 2010. His research interests include the dark matter phenomenology, cosmology, and high-energy astrophysics. Author and co-author of about 20 papers in leading international and Ukrainian physical journals. Laureate of the Award of the President of Ukraine for young scientists (2013).

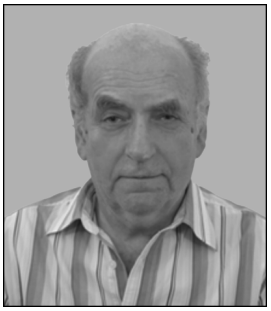

Yuri BOLOTIN is the head of Department of Nuclear Theory and Nonlinear Dynamics, Institute of Theoretical Physics, National Science Center "Kharkiv Institute of Physics and Technology" of the NAS of Ukraine (Kharkiv). After graduating from the Kharkiv State University in 1963 he started research activity at the Kharkiv Institute of Physics and Technology, where he obtained his PhD degree in 1968 (supervisor I.A. Akhiezer) and his Habilitation Doctoral degree in 1988. He is the author of several monographs: Hartee—Fock Method in Nuclear Theory (Naukova Dumka, Kyiv, 1982), Constructive Chaos (Kharkiv, 2005), Regular and chaotic classical and quantum dynamics in multi-well potentials (Cambridge Scientific Publisher, 2011), Chaos: concepts, control and constructive (Springer, 2009), Modern cosmology: Dynamics Universe in problems (Naukova Dumka, Kyiv, 2009). His research interests include nuclear theory, nonlinear dynamics, and cosmology.

Alexander KOSTENKO is a graduate student at the Department of Astronomy and Astrophysics at the University of Toronto (Canada). He started doing research in a wide variety of astrophysical fields while still a student of the V.N. Karazin Kharkiv National University. He obtained his BSc in 2013, being only 18 at the time. His research interests include dark sector cosmology and inflation.

Oleg LEMETS, junior research scientist of the Department of Nuclear Theory and Nonlinear Dynamics at the Institute of Theoretical Physics, National Science Center "Kharkiv Institute of Physics and Technology" of the NAS of Ukraine (Kharkiv). Graduated from the V.N. Karazin Kharkiv National University in 2010. His research interests include the dark matter phenomenology, theoretical cosmology, and interacting dark energy models.

Danylo YEROKHIN is a junior research scientist of the Department of Nuclear Theory and Nonlinear Dynamics at the Institute of Theoretical Physics, National Science Center "Kharkiv Institute of Physics and Technology" of the NAS of Ukraine (Kharkiv). After graduating from the V.N Karazin Kharkiv National University in 2010 he started research activity at the Kharkiv Institute of Physics and Technology. His research interests include the dark energy phenomenology, cosmic inflation, cosmological perturbation theory, and the cosmological model with non-monotonic dependence of the deceleration parameter.

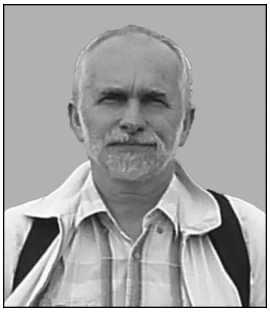

Fedor DANEVICH, head of the Lepton Physics Department of the Institute for Nuclear Research of the National Academy of Sciences of Ukraine (INR NASU, Kyiv). Graduated from the Taras Shevchenko National University of Kyiv in 1980. He started research activities in INR NASU in 1978, where he obtained PhD degree in 1995, and DrSc degree in 2006. He was a visiting scientist at the Max-Planck Institut für Kernphysik (Heidelberg, Germany), Universitá di Firenze and INFN (Florence, Italy), Department of Physics and Mathematics of the University of Insubria (Como, Italy, supported by a fellowship of the Cariplo Foundation), Joint Research Centre of the European Commission (Geel, Belgium), Laboratori Nazionali del Gran Sasso (Assergi, Italy), Istituto Nazionali di Fisica Nucleare (Rome 1 and 2, Italy), Seoul National University (Korea), Centre National de la Recherche Scientifique and the Institut National de Physique Nucléaire et de Physique des Particules (Orsay, France), and other institutions. Research interests include search for double beta decay, dark matter, axions, investigations of rare alpha and beta decays, development of low radioactive technique, R&D of scintillators for astroparticle physics, cryogenic scintillators. Author or co-author of more than 100 articles in leading international physics journals. Laureate of the Sinelnikov Prize of the National Academy of Sciences of Ukraine for outstanding results in physics.

Vladislav KOBYCHEV, senior scientific researcher of the Lepton Physics Department of the Institute for Nuclear Research of the NAS of Ukraine (INR NASU, Kyiv). Graduated from the Taras Shevchenko National University of Kyiv in 1989 (astrophysics). PhD in nuclear and particle physics (INR NASU, 1999). Postdoctoral fellow in National Laboratories of Gran Sasso (Italy, 2001—2003), visiting scientist at the Seoul National University (Korea, 2010—2011), visiting professor at the Daegu National University (Korea, 2012—2013). Research interests include searches for rare and forbidden nuclear processes (double beta decay etc.), axions and dark matter, neutrino physics, exotic properties of particles, Monte Carlo simulation of nuclear detectors. Author and co-author of more than 100 articles in leading international physics journals. Laureate of the Sinelnikov prize of the National Academy of Sciences of Ukraine for outstanding results in physics.

Vladimir TRETYAK is a leading scientific researcher of the Lepton Physics Department of the Institute for Nuclear Research of the National Academy of Sciences of Ukraine (INR NASU, Kyiv). He graduated from the Taras Shevchenko National University of Kyiv in 1980. In 1982, he started research activities in INR NASU, where he obtained PhD degree in 1991. He was a visiting scientist at the Laboratoire de l'Accélérateur Linéaire (Orsay, France), Centre de Recherches Nucleaires (Strasbourg, France), University College London (UK), Laboratori Nazionali del Gran Sasso (Assergi, Italy), Istituto Nazionali di Fisica Nucleare (Rome, Italy), Seoul National University (Korea), Tata Institute of Fundamental Research (Mumbai, India) and other institutions. His research interests include investigations of rare decays in nuclear and particle physics (double beta decay, rare single beta and alpha decays) and searches for exotic processes with violation of electric charge and baryon and lepton numbers (decay of electron, disappearance of nucleons, violation of the Pauli principle). Author or co-author of more than 100 articles in leading international physics journals. Laureate of the Sinelnikov Prize of the National Academy of Sciences of Ukraine for outstanding results in physics.

Bohdan HNATYK is a leading scientific researcher of the Astronomical Observatory of the Taras Shevchenko National University of Kyiv. After graduating from the Lviv State University in 1974 he started research activities at the Institute for Applied Problems of Mechanics and Mathematics and worked on his PhD thesis under the supervision of I.A. Klymyshyn. He obtained his both PhD degree (1983) and Habilitation Doctoral degree (1997) from the Main Astronomical Observatory of the National Academy of Sciences of Ukraine. He is the Laureate of the Barabashov prize of the National Academy of Sciences of Ukraine in field of astronomy (1999). He was a visiting scientist at the Laboratori Nazionali del Gran Sasso of the Istituto Nazionale di Fisica Nucleare (Assergi, Italy), Astronomical Observatory of the Jagiellonian University (Cracow, Poland). He has published more than 70 papers in leading astronomical and physical journals. His research interests include high energy astrophysics, relativistic astrophysics, astrophysics of cosmic rays, cosmology, indirect detection of dark matter.

Монографія є третім томом видання "Темна енергія і темна матерія у Всесвіті". Автори обговорюють астрофізичні прямі й непрямі прояви та властивості темної матерії в галактиках, скупченнях і групах галактик; різноманітні механізми обміну енергією між темною енергією і темною матерією, які розширюють можливості Стандартної космологічної моделі; експериментальні пошуки кандидатів у частинки темної матерії (зокрема стерильні нейтрино, сонячні аксіони, слабко взаємодіючі масивні частинки і надважкі частинки темної матерії) за допомогою космічних і наземних обсерваторій. Монографія призначена для науковців, аспірантів і студентів, які спеціалізуються в позагалактичній астрономії, космології, теоретичній фізиці, ядерній фізиці та астрофізиці високих енергій.

Наукове видання

НАЦІОНАЛЬНА АКАДЕМІЯ НАУК УКРАЇНИ
ІНСТИТУТ ТЕОРЕТИЧНОЇ ФІЗИКИ ім. М.М. БОГОЛЮБОВА
ІНСТИТУТ ЯДЕРНИХ ДОСЛІДЖЕНЬ
ГОЛОВНА АСТРОНОМІЧНА ОБСЕРВАТОРІЯ
НАЦІОНАЛЬНИЙ НАУКОВИЙ ЦЕНТР
"ХАРКІВСЬКИЙ ФІЗИКО-ТЕХНІЧНИЙ ІНСТИТУТ"

МІНІСТЕРСТВО ОСВІТИ І НАУКИ УКРАЇНИ
КИЇВСЬКИЙ НАЦІОНАЛЬНИЙ УНІВЕРСИТЕТ імені ТАРАСА ШЕВЧЕНКА

ТЕМНА ЕНЕРГІЯ І ТЕМНА МАТЕРІЯ У ВСЕСВІТІ

За редакцією академіка НАН України В. ШУЛЬГИ

У ТРЬОХ ТОМАХ

ВАВИЛОВА Ірина, БОЛОТІН Юрій, БОЯРСЬКИЙ Олексій,
ДАНЕВИЧ Федор, КОБИЧЕВ Владислав, ТРЕТЯК Володимир,
БАБИК Юрій, ЯКУБОВСЬКИЙ Дмитро, ГНАТИК Богдан,
СЕРГЕЄВ Сергій

ТЕМНА МАТЕРІЯ: СПОСТЕРЕЖУВАНІ ПРОЯВИ ТА ЕКСПЕРИМЕНТАЛЬНІ ДОСЛІДЖЕННЯ

ТОМ 3

Англійською мовою

Художнє оформлення *Є. Ільницького*
Технічний редактор *О. Бурдік*
Комп'ютерна верстка *Л. Шмагайло*

Підп. до друку 24.03.2015. Формат 70×100/16. Папір офс.
Гарн. Computer Modern. Друк офс. Ум. друк. арк. 30,55. Обл.-вид. арк. 31,44.
Тираж 300 прим. Зам. 4173.

Видавець і виготовлювач Видавничий дім "Академперіодика" НАН України
01004, Київ-4, вул. Терещенківська, 4

Свідоцтво суб'єкта видавничої справи ДК № 544 від 27.07.2001 р.